Experimental Fluid Mechanics

Christophe Bailly
Geneviève Comte-Bellot

Turbulence

Springer

Experimental Fluid Mechanics

More information about this series at http://www.springer.com/series/3837

Christophe Bailly · Geneviève Comte-Bellot

Turbulence

Springer

Christophe Bailly
Laboratoire de Mécanique des Fluides et d'Acoustique
Ecole Centrale de Lyon
Ecully
France

Geneviève Comte-Bellot
Laboratoire de Mécanique des Fluides et d'Acoustique
Ecole Centrale de Lyon
Ecully
France

ISSN 1613-222X ISSN 2197-9510 (electronic)
Experimental Fluid Mechanics
ISBN 978-3-319-16159-4 ISBN 978-3-319-16160-0 (eBook)
DOI 10.1007/978-3-319-16160-0

Library of Congress Control Number: 2015932977

Springer Cham Heidelberg New York Dordrecht London

Printed on acid-free paper

Springer International Publishing AG Switzerland is part of Springer Science+Business Media (www.springer.com)

Foreword

The study of turbulent flows continues to represent a core requirement for many disciplines in the natural sciences and engineering. The lack of a first principle approach to "upscale" turbulence is well known. That is to say, we do not know how to bridge between first principles Navier–Stokes equations-based descriptions of viscous flows and prediction of statistical and structural properties of turbulence. And yet, since turbulence is crucial to many important natural phenomena and engineering processes, the challenges continue to spur research efforts along various directions. And, turbulence must be taught to graduate students, while research scientists and engineers require appropriate introductory texts on the subject.

Since the field is not the result of a cleanly put together set of notions and axioms, the turbulence literature consists of a plethora of concepts, terms, and approaches. This state of the art presents a particularly difficult challenge for students who are at the beginning of their studies in turbulence. They need a textbook that focuses on the fundamentals, on what is established and agreed-upon by the community, without diminishing the wonder about things still unknown. Students require the relevant subjects to be covered with a judicious mix of rigor, physical intuition, and description of empirical facts. Moreover, the topic must be presented in an accessible format that does not diminish the complexities involved.

This second edition of "Turbulence," by Christophe Bailly and Geneviève Comte-Bellot, successfully addresses the desired qualities listed above and thus provides the community with a valuable new textbook. The first edition was published in French in 2003. This edition, now translated into English, expands on the original text. First, updates covering areas of computer simulations and experimental techniques have been made. And, much of the material has been streamlined allowing the text to flow naturally from one subject to another.

The book starts with two introductory chapters overviewing the most important and familiar turbulence phenomena and providing a basic introduction to statistical descriptions of turbulence based on averaging. Then the coverage pivots to wall-bounded turbulent flows, a most important topic. Students are likely to remember elements of this subject from an undergraduate fluid dynamics course, *e.g.,* they may recall using the Moody diagram. This chapter thus provides a natural,

conceptual gateway to the layered intricacies of wall turbulence and to the properties of free shear flows covered in the next chapter. At this point, the coverage moves to more fundamental turbulence physics, with sections on vortex dynamics and homogeneous isotropic turbulence. On the latter topic, the presentation is done both in spectral and physical space. Importantly, it provides sufficient depth to enable students to learn how to perform actual calculations. These sections covering classical topics are then followed by presentations of more recent material, on direct and large eddy simulations, common closures used in the context of Reynolds averaged formulations of turbulence, and the most important experimental techniques. These last three topics can be covered in any desired order.

Many of the chapters contain their own appendices, *i.e.,* materials that may be omitted but may be of interest to more specialized readers. Placing these materials close to the main chapters to which they are most naturally related is quite helpful. Instead of relegating these items to the very end of a book where they could be easily overlooked, the placement in each chapter gently challenges the reader to also examine these more advanced topics.

As notation throughout the book, judiciously the authors use the most commonly used symbols, such as capital letters and over-bars for averaged quantities, "U" for velocity, and so on. They alternate between Gibbs (bold-face vectors and tensors), index or individual component notations, depending on the context as most appropriate. The choice to favor global, mainstream notation greatly facilitates reading the book and should also help with access to the wider research literature.

As a team, Professors Geneviève Comte-Bellot and Christophe Bailly bring to bear the insights from their very distinguished research careers and sustained teaching excellence in the field of turbulence. These qualities come across clearly in this book. The textbook "Turbulence" thus provides a valuable and solid foundation for graduate students and beginning researchers in this important and active field of science and engineering.

December 2014

Charles Meneveau
L.M. Sardella Professor of Mechanical Engineering
Johns Hopkins University

Preface

The motivation for the second edition stemmed in large part from the rapid pace of change in the fields of numerical simulation and experimental techniques. Despite the changes, our goal remains the same: to provide a reference textbook for graduate students, engineers, and research scientists. English is chosen to permit easy communication between workers in the field.

The contents of the present text book is based on the graduate level course taught at Ecole Centrale de Lyon. Over the years, the high standard students who attended the course largely contributed to improve its content and presentation. For students, it contains the essential results as well as details and demonstrations whose oral transmission is often tedious. At a more advanced level, the text provides numerous references which allow the reader to focus on his specific topics of interest. Some sections and appendices, containing developments on more specific subjects, may be skipped during a first reading, but might appear useful at a second one! We have endeavored to provide a wide array of illustrations throughout the book.

The general structure of the book is as follows. After an introduction in Chap. 1 illustrating the interest of turbulent flows, averaged equations and kinetic energy budgets are provided in Chap. 2. The concept of turbulent viscosity as a closure of the Reynolds stress is also introduced. Wall-bounded flows are presented in Chap. 3, and features specific to boundary layers and channel or pipe flows are pointed out. Free shear flows, namely free jets and wakes, are considered in Chap. 4. Chapter 5 deals with vortex dynamics, vorticity being a key element in turbulent flows. Homogeneous turbulence, isotropy, and dynamics of isotropic turbulence are presented in Chaps. 6 and 7. Turbulence is described both in the physical space and in the wavenumber space. Time-dependent numerical simulations are presented in Chap. 8, where an introduction to large eddy simulation is offered. Statistical models of turbulence are examined in Chap. 9. Major experimental techniques, including hot wire anemometry, laser Doppler anemometry, and particle image velocimetry, are finally introduced in Chap. 10. Numerous additional topics are developed in additional sections marked by a star, such as linear stability, the formulation of different models for compressible flow or the refinement of Kolmogorov theory, to name a few, and references are sorted by topics at the end of the book.

We are indebted to many colleagues in the Laboratoire de Mécanique des Fluides et d'Acoustique (LMFA), who helped us by providing materials and by spending time discussing technical points. We would like to warmly acknowledge Christophe Bogey, Thomas Castelain, Philippe Eyraud, Nathalie Grosjean, Faouzi Laadhari, and Julien Weiss. We also would like to express our sincere gratitude to Olivier Marsden, assistant professor at Ecole Centrale de Lyon, and to Antony Coleman, senior researcher (CNRS) at University of Lyon 1, who accepted to read the almost final version of the text, and helped us to provide a polished English manuscript. The remaining errors are, of course, our own.

Ecole Centrale de Lyon, December 2014

Christophe Bailly
Geneviève Comte-Bellot

Contents

Summary of Main Notations

The same notation is sometimes used with different meanings, but it makes sense within the context. For example, the notation f is used for frequency as well as for the coefficient of the longitudinal velocity correlation $f(r)$.

a	Thermal diffusivity $a = \lambda/(\rho c_p)$
a_t	Turbulent thermal diffusivity
c_∞	Speed of sound
C_f	Skin–friction coefficient, see Eq. (1.9)
C_K	Kolmogorov constant $C_K \simeq 1.5$
C_s	Constant of the Smagorinsky model
C_d	Constant of the dynamic Smagorinsky model
C_D	Drag coefficient
C_μ	Constant of the $k_t - \epsilon$ model
d	Dilatation $d = \nabla \cdot \boldsymbol{u}$
$D_v(k)$	Dissipation spectrum, $D_v(k) = 2\nu k^2 E(k)$
e	Specific energy $de = c_v dT$
e_t	Total specific energy $e_t = e + u_i u_i/2$
f	Coefficient of longitudinal velocity correlation $\mathcal{R}_{11}(r, 0, 0)$
g	Coefficient of transverse velocity correlation $\mathcal{R}_{11}(0, r, 0)$
h	Specific enthalpy $dh = c_p dT$
$\boldsymbol{k}$	Wavenumber vector
k_η	Kolmogorov wavenumber $k_\eta = \nu^{-3/4}\epsilon^{1/4}$
k_t	Turbulent kinetic energy, $k_t = \overline{u_i' u_i'}/2$ (incompressible flow)
k_{sgs}	Subgrid-scale energy
L_1, L_f	Longitudinal integral length scale $L_1 = L_f$ for isotropic turbulence
L_2, L_g	Transverse integral length scale $L_2 = L_g$ for isotropic turbulence
l_η	Kolmogorov length scale $l_\eta = \nu^{3/4}\epsilon^{-1/4}$
l_v	Viscous length scale $l_v = \nu/u_\tau$
p	Pressure
$\mathcal{P}$	Mean rate of turbulent kinetic energy production $\mathcal{P} = -\rho\overline{u_i' u_j'}\,\partial\overline{U}_i/\partial x_j$

Pr	Prandtl number $\mathrm{Pr} = \mu c_p/\lambda$
Pr_t	Turbulent Prandtl number $\mathrm{Pr}_t = \nu_t/a_t$
P_w	Wall pressure
r	Specific gas constant
$\mathrm{Re_D}$	Reynolds number $\mathrm{Re}_D = \rho U_d D/\mu = U_d D/\nu$
R_{ij}	Space second-order velocity correlation $R_{ij}(x,r,t) = \overline{u_i'(x,t)u_j'(x+r,t)}$
$\mathcal{R}_{ij}$	Second-order velocity correlation coefficient
$\bar{S}$	Mean shear magnitude $\bar{S} = (2\bar{S}_{ij}\bar{S}_{ij})^{1/2}$
S_ξ	Skewness factor of signal ξ, $S_\xi = \overline{\xi^3}/(\overline{\xi^2})^{3/2}$
$\bar{s}$	Shear magnitude of the filtered velocity field $\bar{s} = \sqrt{2\bar{s}_{ij}\bar{s}_{ij}}$
e_{ij}	Rate-of-strain tensor $e_{ij} = (\partial u_i/\partial x_j + \partial u_j/\partial x_i)/2$, see Eq. (2.10)
s_{ij}	Deviatoric (trace free) part of e_{ij}, see Eq. (2.11)
T	Temperature
T_ξ	Flatness coefficient of signal ξ, $T_\xi = \overline{\xi^4}/(\overline{\xi^2})^2$
t_{ij}	Subgrid-scale stress tensor, $t_{ij} = \rho\bar{u}_i\bar{u}_j - \rho\overline{u_i u_j}$ (incompressible flow)
U_d	Bulk velocity
U_e	Mean free stream velocity of boundary layer
$\boldsymbol{u}$	Velocity vector
u_τ	Wall friction velocity $u_\tau = \sqrt{\tau_w/\rho}$
u_η	Kolmogorov velocity scale $u_\eta = \nu^{1/4}\epsilon^{1/4}$
u'	Root-mean-square velocity fluctuation in isotropic turbulence $u' = \sqrt{2k_t/3}$
u^+	Velocity normalized by the friction velocity $u^+ = u/u_\tau$
x_i	Unit vector in the direction i, $x_2 = (0,1,0)$ in Cartesian coordinates

Greek letters

γ	Ratio of specific heats at constant pressure and volume $\gamma = c_p/c_v$
δ	Boundary layer thickness
δ_1	Displacement thickness of boundary layer
δ_θ	Momentum thickness of boundary layer
δ_{ij}	Kronecker delta $\delta_{ij} = 1$ if $i = j$ and $\delta_{ij} = 0$ if $i \neq j$
ϵ	Dissipation rate of turbulent kinetic energy k_t, see expression (2.22)
ϵ^h	Dissipation rate for a homogeneous flow, see Sect. 6.5
ϵ_{ijk}	Alternating tensor $\epsilon_{ijk} = (i-j)(j-k)(k-i)/2$
ϕ_{ij}	Velocity spectrum tensor
κ	von Kármán constant
λ	Thermal conductivity
λ_1, λ_f	Longitudinal Taylor length scale, $\lambda_1 = \lambda_f$ for isotropic turbulence
λ_2, λ_g	Transverse Taylor length scale, $\lambda_2 = \lambda_g$ for isotropic turbulence
μ	Molecular dynamic viscosity $\mu = \rho\nu$

μ_t	Subgrid-scale or turbulent dynamic viscosity (see Chap. 8)
ν	Molecular kinematic viscosity
ν_t	Subgrid-scale or turbulent kinetic viscosity (see Chap. 8)
$\hat{\nu}_t$	Spectral subgrid-scale or turbulent viscosity
$\bar{\Omega}$	Mean vorticity magnitude $\bar{\Omega} = (2\bar{\Omega}_{ij}\bar{\Omega}_{ij})^{1/2}$
$\boldsymbol{\omega}$	Vorticity vector $\boldsymbol{\omega} = \nabla \times \boldsymbol{u}$
ω_{ij}	Rate of rotation tensor $\omega_{ij} = (\partial u_i/\partial x_j - \partial u_j/\partial x_i)/2$
Θ	Life time of turbulence
ρ	Density
τ_w	Wall shear stress
τ_{ij}	Viscous stress tensor $\tau_{ij} = 2\mu s_{ij}$, see Eqs. (2.6) & (2.12)

Operators and usual decompositions

$\bar{d}/\bar{d}t$	Material derivative along the mean flow, $\bar{d}\bar{F}/\bar{d}t = \partial\bar{F}/\partial t + \partial(\bar{F}\overline{U}_j)/\partial x_j$, see Eq. (2.17)
$\bar{U}_i$	Reynolds average of u_i, $u_i = \bar{U}_i + u_i'$
$\tilde{U}_i$	Favre average of u_i, $\tilde{U}_i = \overline{\rho u_i}/\bar{\rho}$ and $u_i = \tilde{U}_i + u_i''$
$\bar{u}_i$	Space filtering of u_i in large eddy simulation, $\bar{u}_i = G * u_i$ and $u_i = \bar{u}_i + u_i'$
$\tilde{u}_i$	Favre space filtering in large eddy simulation $\bar{\rho}\tilde{u}_i = G * (\rho u_i)$ and $u_i = \tilde{u}_i + u_i''$
$\hat{u}_i$	Fourier transform of the velocity component u_i, see Exp. (6.8)

About the Authors

Christophe Bailly is a Professor of Fluid Dynamics and Acoustics at the Ecole Centrale de Lyon (ECL) in France. He graduated from ECL (1990), received his Ph.D. in Aeroacoustics from the Ecole Centrale Paris in 1994. After one year spent at the Centre National des Etudes Spatiales (CNES), he joined the Laboratoire de Mécanique des Fluides et d'Acoustique (Centre National de la Recherche Scientifique, UMR 5509) at ECL in 1995. As lecturer, he has served in Turbulence at the Ecole Centrale Paris from 1995 to 2006, and serves in aeroacoustics at the Ecole Nationale Supérieure des Techniques Avancées (ENSTA) since 2001. He is also with the Institut Universitaire de France (junior member 2007). His research activities lie in the area of turbulence and aeroacoustics. His is co-author, with Geneviève Comte-Bellot, of one textbook in turbulence, has authored or co-authored more than 90 papers in refereed journals and co-supervised over 24 Ph.D. He is also the recipient of the Yves Rocard Prize from the French Acoustical Society (1996) and of the Alexandre Joannidès Prize from the French Academy of Sciences (Paris, 2001). He is currently an Associate Editor of the American Institute of Aeronautics and Astronautics Journal and an Advisory-Editor for Flow, Turbulence and Combustion.

Geneviève Comte-Bellot obtained her under-graduate diploma in 1953 at the University of Grenoble and her Master degree in Paris in 1954, at the Ecole Normale Supérieure. She chose to obtain the Agrégation which opens the road towards teaching physics and chemistry in high schools. She obtained her Ph Degree in 1963 at the University of Grenoble in the Department of fluid dynamics. Her dissertation was entitled *Turbulent Flow between two parallel walls*. The wind tunnel she specially built permitted to obtain very high Reynolds numbers, an exceptional feature which was never reproduced. Just after having completed her Ph.D., Geneviève Comte-Bellot obtained a post-doc position at the Johns Hopkins University in the team of Professor Stanley Corrsin in Fluid Mechanics. For two years she was in charge of the large *Velvet Windtunnel*, still in operation, where turbulence very close to isotropy could be realized. She studied the decay laws and the Eulerian space-time correlation. Two papers were written and they are today still used as reference. Coming back to France, Geneviève Comte-Bellot, became a

professor at the Ecole Centrale de Lyon, which is connected to the University of Lyon. There, she launched research into aeroacoustics. Many papers were accepted by specialized journals or presented at international meetings. During the same time, Geneviève Comte-Bellot improved and used the constant voltage anemometer. Geneviève Comte-Bellot is corresponding member of the Académie des sciences in Paris, member of the French Académie des technologies and associate member of the American National Academy of Engineering. She is the recipient of the 2014 Fluid Dynamics Prize of the APS (American Physical Society).

Chapter 1
Introduction to Turbulence

1.1 Turbulent Flows

Turbulent flows are characterized by irregular patterns, unpredictable behaviour and the existence of numerous space and time scales. They appear when the source of kinetic energy which drives the fluid in motion is intense and able to overcome the viscosity effects that slow down the fluid. When viscosity predominates, the flow is said to be laminar, and hence regular and predictable. The pioneering work of Boussinesq [592] and Reynolds [663] have defined the first concepts in the study of the turbulent regime. The energy source in a flow can be of various natures: pressure gradients in a pipe flow, initial impulsion for jets, or temperature differences in heated flows where buoyancy takes place.

At the scale of the Earth, solar radiation as well as long range attractive gravitational forces are involved. Oceanic currents such as the Gulfstream in the Atlantic Ocean or the Humboldt stream in the Pacific Ocean have a mean regular motion. Intensity and position fluctuations are, however, observed. The same is true for atmospheric winds. Figure 1.1 displays a map of the winds over the Atlantic Ocean. These maps are used to improve our understanding of weather abnormalities. At high altitudes, the jet streams, with speeds up to 100 km/h, are exploited by plane pilots to optimize their itinerary. Images taken by satellites for weather forecasting are another good daily illustration of the existing irregularities in geophysical flows. Turbulence is therefore encountered everywhere in our terrestrial environment. In astrophysics, the ionized gaseous atmospheres of stars and nebulas are also turbulent, induced by powerful nuclear reactions occurring in their core and leading to an electromagnetic forcing of the flow. Solar winds and Jupiter's red spot are other fascinating examples.

In most industrial applications, substantial energy input or loss often occurs as well. In aeronautics, the high speed and high temperature jet of engines or the relatively low speed wakes generated by the compressor and turbine blades are turbulent. In chemical engineering, turbulence appears in complex confined geometries, especially in the combustion chambers of cars, planes and space launchers. Turbulence, indeed, plays an efficient role in mixing reactants. We use turbulent mixing daily

C. Bailly and G. Comte-Bellot, *Turbulence*, Experimental Fluid Mechanics,
DOI 10.1007/978-3-319-16160-0_1

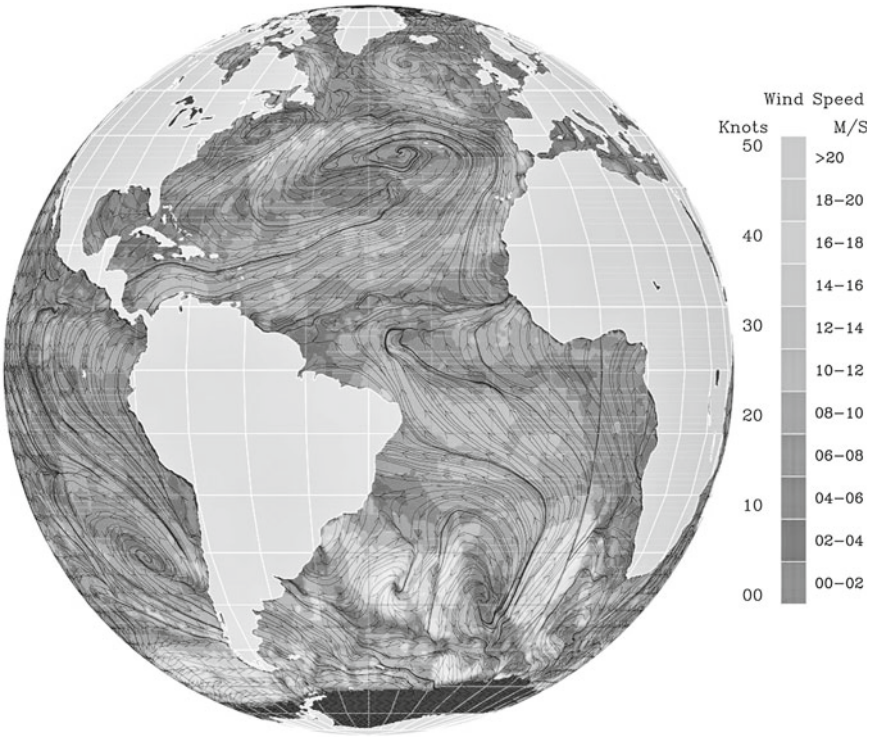

Fig. 1.1 Near-surface wind speeds 10 m above the Atlantic Ocean on August 1, 1999. Data collected by the *SeaWinds* scatterometer onboard NASA's *QuikSCAT* satellite. Courtesy of NASA's Jet Propulsion Laboratory

when adding cream to our coffee or tea. A key contribution is played by the spoon that is turned to achieve a homogeneous beverage. In nuclear engineering, turbulence increases thermal exchange in cooling systems. In acoustics, turbulence disturbs the propagation of sound waves in the atmosphere or in the ocean. Turbulence itself is also an important noise source, the so-called mixing noise in aeroacoustics. It may also induce vibration of structures and fatigue. Noise induced by wall pressure fluctuations is regularly encountered in mechanical engineering including sonar domes in underwater applications, aircraft and car cabin noise, or the protection of payloads during space launcher lift-off, among many other examples.

Turbulent flows can be directly observed, sometimes in a quite spectacular way, as during a volcanic eruption for instance. Intermittent bursts deforming the free plume boundaries are shown in Fig. 1.2. In laboratories, various flow visualization techniques have been developed. For example, emission lines captured in a subsonic round jet are shown in Fig. 1.3. An electrically heated thin wire is placed near the nozzle and oil droplets along the wire produce lines of oil vapor which allow flow visualization for a sufficiently small jet velocity. The picture is taken when the first

Fig. 1.2 Eruption of the subglacial Grimsvötn volcano, Iceland, on May 21, 2011. An initial large plume of smoke and ash rose up to about 17 km height. Until May 25 the eruption scale was larger than that of the 2010 eruption of the Eyjafjallajökull volcano, but did not lead to the air travel chaos caused in April 2010. Courtesy of Thördïs Högnadóttir, Institute of Earth Sciences, University of Iceland

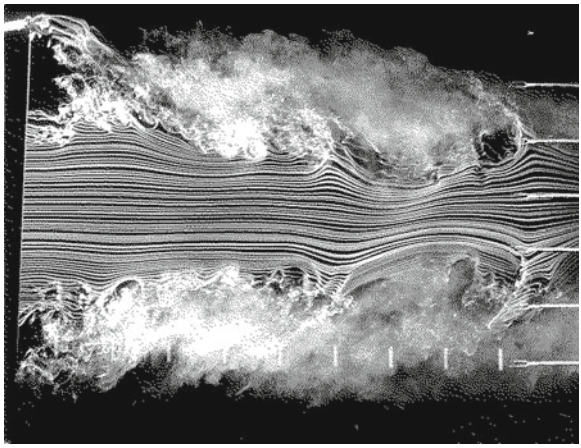

Fig. 1.3 Visualization of emission lines in a round air jet. The nozzle diameter is $D = 15$ cm, the jet velocity is $u_j \simeq 5\ \mathrm{m} \cdot \mathrm{s}^{-1}$ and the Reynolds number is $\mathrm{Re}_D = u_j D/\nu \simeq 5.4 \times 10^4$. The hot wire heating the oil droplets is placed $0.5D$ downstream of the nozzle. In addition, 6 hot-wire probes are located downstream at $4D$. Courtesy of Henry Fiedler

particles reach the downstream side, while others are still on the wire. Large fluctuations are visible near the free edges of the flow, and the vanishing of emission lines downstream corresponds to tridimensional motions out of the visualization plane. Figure 4.2 in Chap. 4 also displays a direct view of a free subsonic jet through a laser sheet. Irregularities on the boundaries of the jet can be described by invoking fractal properties, but the first step is to characterize and analyse the mean flow field.

Turbulent flows are not only characterized by random fluctuations, but also by the presence of coherent structures. This coexistence has been noted in the literature since the 1950s, but it has been dramatically highlighted by the experiments of Crow and Champagne [522] and Laufer [545] in jets, and those of Brown and Roshko

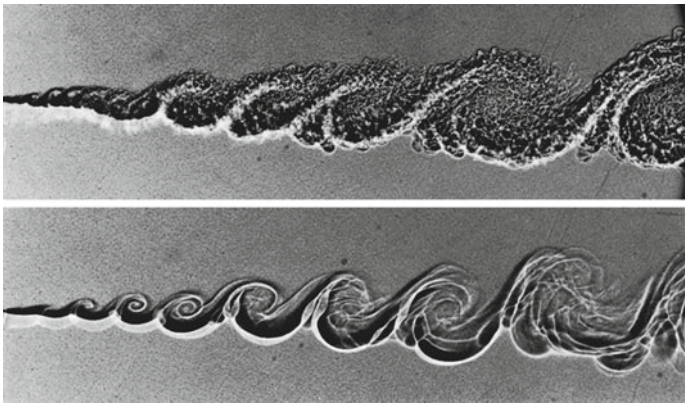

Fig. 1.4 Ombroscopy of a mixing layer between an helium flow at $10\,\mathrm{m}\cdot\mathrm{s}^{-1}$ (*above*) and a nitrogen flow at $3.8\,\mathrm{m}\cdot\mathrm{s}^{-1}$ (*below*). The Reynolds number of the upper flow is ten times higher than that of the lower flow. This variation is obtained by increasing the pressure, and consequently the density of the fluid. An increase in the Reynolds number produces more small structures within the large scales arising from Kelvin-Helmholtz instability waves during the initial laminar mixing at the trailing edge. From Brown and Roshko [474]

[473, 474, 491] and Winant and Browand [497] in mixing layers. The appearance of coherent structures in the first diameters of a jet , as shown in Fig. 4.2 in Chap. 4, is linked to the laminar transition occurring at the nozzle exit. They are also present in mixing layers as illustrated in Fig. 1.4. These large vortical structures are fairly well described by the inviscid stability theory and by the so-called Kelvin-Helmholtz waves, at least during their linear growth. A brief introduction to stability theory is provided in Sect. 1.5. The fully developed turbulent flow appears further downstream, once these coherent structures have vanished. The statistical description then becomes totally relevant and it is possible to determine a mean solution of the flow based on a hypothesis of self-similarity, as presented in Chap. 4. For completeness, coherent structures are also found in wakes generated behind obstacles [28], as well as in wall-bounded turbulent flows. This topic is discussed in Chap. 3, see also Fig. 1.5.

Experimental findings may also be supplemented by numerical simulation of turbulent flows, especially for quantities which are difficult or impossible to directly measure. These numerical experiments are however limited to moderate Reynolds numbers. Nevertheless, they can assess hypotheses used in models, provide a whole picture of turbulent flow in space and in time and guide us to improve experimental set-up where appropriate, and *vice-versa*. Figure 1.5 is another recent example of a simulation of a detached boundary layer in the presence of an adverse pressure gradient. Numerical predictions are continuously improved, and this topic is discussed in Chap. 8.

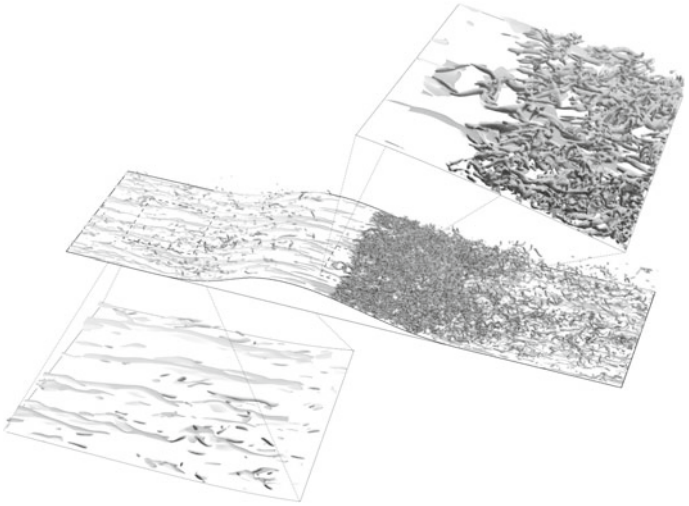

Fig. 1.5 Direct numerical simulation ($2304 \times 385 \times 576$ grid points) of a channel flow with one curved surface inducing an adverse pressure gradient after the bump. The Reynolds number is $\mathrm{Re}^{+} = hu_\tau/\nu = 617$ where h is the half-height of the channel, u_τ the friction velocity and ν the kinematic molecular viscosity. Vortical structures of the separating boundary layer induced by the adverse pressure gradient are represented in *dark grey* while low speed streaks are represented in *light grey*, see Chap. 3. Courtesy of Mathieu Marquillie and Jean-Philippe Laval, refer to Marquillie et al. [643]

1.2 Control Parameters

Turbulence appears when inertial forces prevail over viscosity forces in a flow, which implies that the Reynolds number measuring the relative strength of these two forces must exceed a certain threshold. Determining this value is in general not an easy task, as turbulence takes some time to appear and needs some space to develop. Furthermore, there is no universal transition scenario, even for a given class of flows. The sketch in Fig. 1.6 sums up a classical view of what happens during the transition of a boundary layer developing on a flat plate and without pressure gradient, from a regular flow in the laminar regime to a fully random flow in the turbulent regime. A picture of a turbulent burst taken in a boundary layer of water flow [595] and corresponding to step (e) in Fig. 1.6 is also shown in Fig. 1.7. Transition experimentally starts when the Reynolds number based on the external speed U_{e1} and on the distance x_1 from the leading edge, is of the order of $\mathrm{Re}^{c}_{x_1} \simeq U_{e1}x_1/\nu \simeq 3.2 \times 10^5$, where ν is the kinematic molecular viscosity. This threshold corresponds to the appearance of Tollmien-Schlichting waves associated with the Blasius velocity profile, this topic is briefly described in Sect. 1.6. The Reynolds number still increases with the distance x_1, and a fully turbulent flow is then reached with a thicker boundary layer, as sketched in Fig. 1.13.

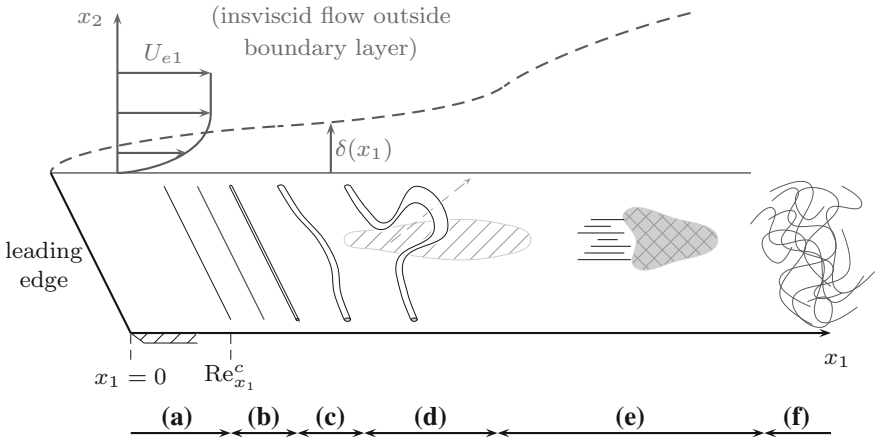

Fig. 1.6 Sketch of the transition of a laminar boundary layer developing over a flat plate with zero pressure gradient. (*a*) Stable laminar flow, (*b*) appearance of Tollmien-Schlichting instability waves, (*c*) nonlinear effects and tridimensional evolution, (*d*) large scale structures such as hairpin vortices, (*e*) growth of bursts and (*f*) fully turbulent boundary layer for $\mathrm{Re}_{x_1} \geq 3 \times 10^6$

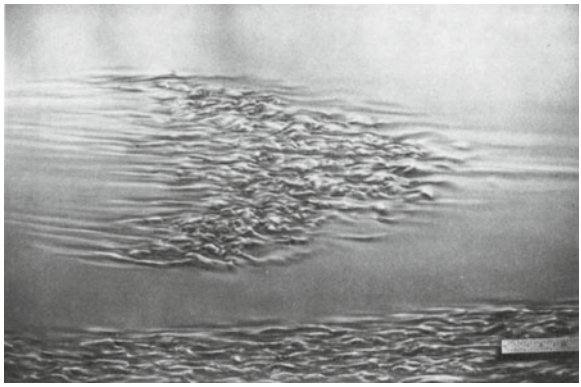

Fig. 1.7 Image of a turbulent burst in a boundary layer of a water flow. The Reynolds number at the center of the burst based on the distance to the leading edge of the flat plane is $\mathrm{Re}_{x_1} = 2 \times 10^5$. See Cantwell et al. [595]

In the seminal experiment of Reynolds [662] regarding the onset of turbulence in a circular pipe flow, the control parameter is again the Reynolds number based on the diameter D and the bulk velocity U_d,

$$\mathrm{Re}_D = \frac{\rho U_d D}{\mu} = \frac{U_d D}{\nu}$$

where ρ is the density, μ the molecular dynamic viscosity and $\nu = \mu/\rho$. The bulk velocity is the average velocity over a cross section of the pipe. In practice, turbulence occurs for a value of the Reynolds number above around $\mathrm{Re}_D \geq 3000$, but this threshold depends on the quality of the facility. Indeed, the laminar pipe flow, also known as the Hagen-Poiseuille flow, is found to be stable for all Reynolds numbers

according to the classical linear stability theory. A laminar circular pipe flow has thus been observed up to a Reynolds number of 10^5 by controlling background noise in order to obtain infinitesimal perturbations [620]. The scenario of the transition to turbulence for one of the most famous flows in fluid dynamics remains only partially understood [647].

The Reynolds number is not the only control parameter encountered to characterize the transition to turbulence. In Rayleigh-Bénard experiment for instance, instabilities appear in a fluid confined between two plates that are maintained at two different temperatures $T_0 + \Delta T$ and T_0, as shown in Fig. 1.8. The control parameter is then the Rayleigh number, defined as

$$\mathrm{Ra} = \frac{g\beta\Delta T h^3}{\nu a}$$

where g is the gravitational acceleration, β the thermal expansion coefficient of the fluid, ΔT the temperature difference between the two plates, h the height between the two plates and a the thermal diffusivity, based on the specific heat at constant pressure c_p and on the thermal conductivity λ in Fourier's law $a = \lambda/(\rho c_p)$. In this experiment, a fluid particle is heated by the lower plate and rises due to the buoyancy or Archimede force while the viscous drag force and heat loss by conduction are opposed to this motion. Similarly, the cooler denser fluid near the upper plate tends to go down. A chaotic fluid motion is therefore expected if the temperature difference ΔT is high enough.

The Rayleigh number represents the relative strength of these forces, and regular convection cells are observed for a Rayleigh number around of 1700 [67]. By increasing the Rayleigh number, or equivalently the temperature difference ΔT, the rotation direction and the size of the cells randomly change. In order to model the experimental chaotic behaviour of this flow, Lorenz [75] developed the following dynamic system,

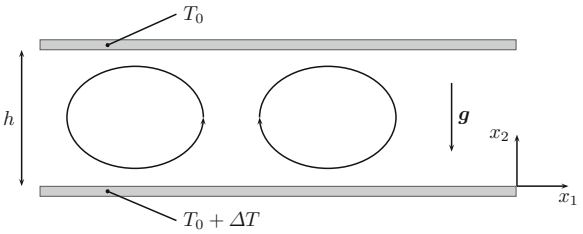

Fig. 1.8 Rayleigh-Bénard cells in a fluid confined between two flat plates at different temperatures. The convective cells are not circular, as there is a $\sqrt{2}$ factor between the vertical wavenumber k_2 and the horizontal wavenumber k_1 [67]

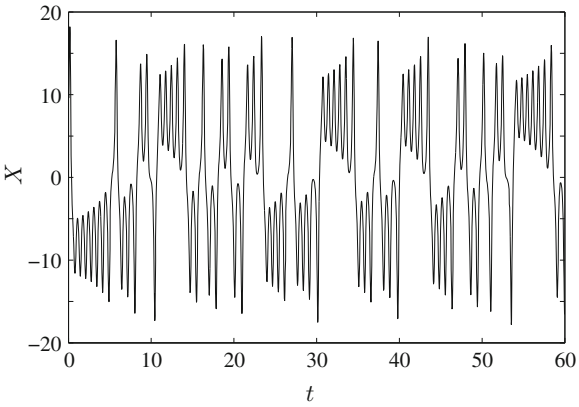

Fig. 1.9 Time history of the X variable in the Lorenz strange attractor [75] for the following values of the parameters $\mathrm{Pr} = 10$, $b = 8/3$ and $r = 28$

$$\begin{cases} \dfrac{dX}{dt} = \mathrm{Pr}(Y - X) \\ \dfrac{dY}{dt} = -XZ + rX - Y \\ \dfrac{dZ}{dt} = XY - bZ \end{cases} \tag{1.1}$$

where $\mathrm{Pr} = \mu c_p/\lambda$ is the Prandtl number, also defined as the ratio ν/a where ν is the kinematic viscosity and a the thermal diffusivity. The control parameter r of the system is proportional to the Rayleigh number, and b represents a shape factor associated with the cell sizes. The X component is roughly proportional to the magnitude $\psi_1(t)$ involved in the stream function $\psi(x_1, x_2, t) = \psi_1(t)\cos(k_2 x_2)\sin(k_1 x_1)$. The time history of $X(t)$ is shown in Fig. 1.9 for illustration. It may be observed that there are fluctuations in the rotation amplitude and direction of the fluid since $\omega_z = -\nabla^2\psi$. This chaotic behaviour, which requires at least three degrees of freedom and a nonlinear autonomous system, is extremely sensitive to initial conditions. Lorenz's work is famous for offering the first strange attractor in the literature. At a high Rayleigh number, the solution becomes completely chaotic and the flow reaches a fully turbulent state.

1.3 Nonlinearity of the Navier-Stokes Equations

The unpredictable feature of turbulence and the existence of a large range of scales interacting with themselves have their origin in the nonlinear behaviour of the Navier-Stokes equations. For an incompressible flow, the Navier-Stokes equations can be written as

$$\rho\left(\frac{\partial \boldsymbol{u}}{\partial t} + \boldsymbol{u}\cdot\nabla\boldsymbol{u}\right) = -\nabla p + \mu\nabla^2\boldsymbol{u} \tag{1.2}$$

where $\boldsymbol{u}$ is the velocity vector, ρ the density, p the pressure and μ the dynamic molecular viscosity of the fluid. These equations display two nonlinear terms, the convective acceleration term $\boldsymbol{u} \cdot \nabla \boldsymbol{u}$ and the pressure term. We will first show how the convection term $\boldsymbol{u} \cdot \nabla \boldsymbol{u}$ causes the numerous scales observed in any turbulent flow.

1.3.1 Generation of Harmonics

Consider the one-dimensional convection problem to simplify algebra,

$$\frac{\partial u}{\partial t} + u \frac{\partial u}{\partial x} = 0$$

with the initial condition $u\,(x, t_0) = A \cos(k_x x)$ à $t = t_0$. A Taylor expansion yields the flow velocity at time $t = t_0 + \Delta t$,

$$\begin{aligned} u\,(x,t) &= u\,(x,t_0) + (t - t_0)\,\frac{\partial u}{\partial t}\,(x,t_0) + \mathcal{O}(\Delta t^2) \\ &= A\cos\,(k_x x) - (t - t_0)\,u\,\frac{\partial u}{\partial x}\,(x,t_0) + \cdots \\ &= A\cos\,(k_x x) + (t - t_0)\,A^2 k_x \cos\,(k_x x)\sin\,(k_x x) + \cdots \\ &= A\cos\,(k_x x) + \underbrace{(t - t_0)\,\frac{A^2 k_x}{2}\sin\,(2k_x x)}_{\text{higher harmonic}} + \cdots \end{aligned}$$

Note the appearance of a higher harmonic, which is directly linked to the nonlinear convective term $\boldsymbol{u} \cdot \nabla \boldsymbol{u}$. The two-dimensional problem is even more complex. We have

$$\begin{cases} \dfrac{\partial u}{\partial t} + u\dfrac{\partial u}{\partial x} + v\dfrac{\partial u}{\partial y} = 0 \\ \dfrac{\partial v}{\partial t} + u\dfrac{\partial v}{\partial x} + v\dfrac{\partial v}{\partial y} = 0 \end{cases} \quad \text{with} \quad \begin{cases} u\,(x,\,y,\,t_0) = A\cos(k_x x)\cos(k_y y) \\ v\,(x,\,y,\,t_0) = A'\cos(k'_x x)\cos(k'_y y) \end{cases}$$

as initial conditions. By introducing a Taylor expansion similar to the one-dimensional problem, the solution for $u(x, y, t)$ becomes

$$\begin{aligned} u\,(x,\,y,\,t) &= u\,(x,\,y,\,t_0) + (t - t_0)\frac{\partial u}{\partial t}\,(x,\,y,\,t_0) + \mathcal{O}(\Delta t^2) \\ &= A\cos\,(k_x x)\cos\left(k_y y\right) + (t - t_0) \times \left\{k_x A^2 \cos(k_x x)\sin(k_x x)\cos^2(k_y y)\right\} \\ &+ \left\{k_y A A' \cos(k_x x)\cos(k'_x x)\sin(k_y y)\cos(k'_y y)\right\} + \cdots \\ &= A\cos(k_x x)\cos(k_y y) + (t - t_0)\,k_x A^2/4\,\sin(2k_x x)\left[\cos(2k_y y) + 1\right] \end{aligned}$$

$$+ (t - t_0)\, k_y A A'/4 \left\{\cos\left[(k_x - k'_x)x\right] + \cos\left[(k_x + k'_x)x\right]\right\}$$
$$\times \left\{\sin\left[(k_y - k'_y)y\right] + \sin\left[(k_y + k'_y)y\right]\right\} + \cdots$$

There is thus generation at the same time of both higher harmonics, that is higher wavenumbers or smaller structures, with the terms $\cos[(k_x + k'_x)x]$ and $\sin[(k_y + k'_y)y]$, and lower harmonics, or larger structures, with the terms $\cos[(k_x - k'_x)x]$ and $\sin[(k_y - k'_y)y]$. In other words, energy transfers occur between large and small structures. Given the recurrence of this phenomenon, a rather broadband spectrum is expected for velocity fluctuations. As may be seen, energy transfer is limited for large structures by geometrical constraints. What about small structures or high wavenumbers?

For small structures, energy transfer is stopped by the molecular viscosity. Indeed, velocity difference between two neighboring fluid particles is reduced by viscous diffusion, in the same way their temperature would coincide due to conduction in a thermal problem. In order to estimate the dissipation scale l_η associated with the viscous molecular dissipation, the time variation of the velocity must balance the viscous term in the Navier-Stokes Equation (1.2). The former term gives,

$$\frac{\partial u}{\partial t} \sim \frac{u_\eta^2}{l_\eta}$$

by taking for the time scale $t \sim l_\eta/u_\eta$, and the latter gives

$$\nu \frac{\partial^2 u}{\partial x^2} \sim \nu \frac{u_\eta}{l_\eta^2}$$

where u_η is the velocity scale associated with l_η. We thus obtain for the corresponding Reynolds number,

$$\mathrm{Re}_\eta = \frac{l_\eta u_\eta}{\nu} \sim 1 \tag{1.3}$$

The l_η scale plays a fundamental role in experiments as well as in numerical simulations, and is known as the Kolmogorov length scale. We will learn to estimate its value later, but its existence should be noted now.

The broadband nature of turbulence spectra can be directly observed in experimental signals. The time history of the longitudinal fluctuating velocity u'_1 measured in a round subsonic jet by hot-wire anemometry is shown in Fig. 1.10a, and displays a rich spectral content. The Kolmogorov scale is about $l_\eta \simeq 0.2$ mm, compared to the jet diameter $D = 8$ cm for a jet Reynolds number $\mathrm{Re}_D \simeq 1.06 \times 10^5$. The turbulence intensity can be characterized by the ratio $\sigma_{u_1} = u'_{1\mathrm{rms}}/\bar{U}_1$ between the root mean square (rms) value of u'_1 and the local mean velocity $\bar{U}_1 \simeq 11.7\ \mathrm{m \cdot s^{-1}}$. In the present case, we have $\sigma_{u_1} \simeq 21.2\,\%$. The probability density function (pdf) is another insightful way of looking into a turbulent signal. For a Gaussian signal, the pdf is given by

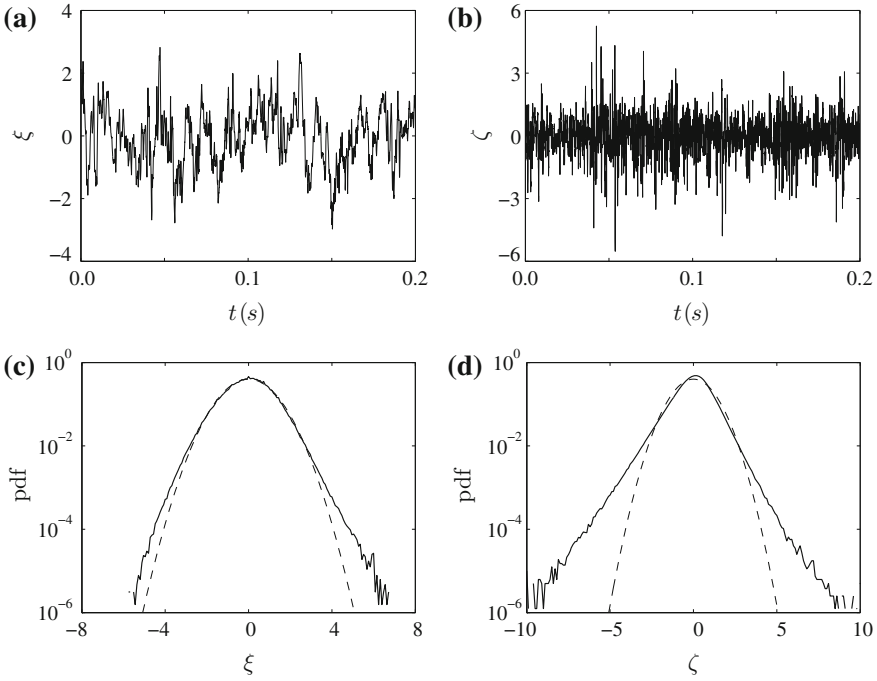

Fig. 1.10 An example of velocity signal measured by hot-wire anemometer in a subsonic round jet at a Reynolds number $\mathrm{Re}_D \simeq 1.06 \times 10^5$, with $D = 8$ cm and $U_j = 19.8\ \mathrm{m \cdot s^{-1}}$. The probe is located at $x_1/D \simeq 11.9$ on the jet centerline. **a** Time history of the fluctuating axial velocity normalized by its rms value, $\xi = u_1'(t)/u_{1\mathrm{rms}}'$. **b** Same representation for the time derivative, $\zeta = \partial_t u_1'(t)/(\partial_t u_1')_{\mathrm{rms}}$. Probability density functions (pdf) of ξ and ζ are shown in (**c**) and (**d**) in *solid lines*, and are compared to a Gaussian distribution in *dashed line*. The skewness and flatness factors are respectively $S_\xi \simeq -0.06$ and $T_\xi \simeq 3.40$ for u_1', and $S_\zeta \simeq -0.38$ and $T_\zeta \simeq 5.15$ for $\partial_t u_1'$. Data provided courtesy of Olivier Marsden (LMFA)

$$p(\xi) = \frac{1}{\sigma\sqrt{2\pi}}\, e^{-\frac{\xi^2}{2\sigma^2}}$$

where σ is the standard deviation. This function is compared to that found for $u_1'(t)$ in Fig. 1.10c, and clearly the velocity signal does not follow a normal distribution. This is a general result for turbulent signals [172] The skewness and flatness factors are respectively $S_\xi \simeq -0.06$ and $T_\xi \simeq 3.40$, to compare to the values $S_\xi = 0$ and $T_\xi = 3$ obtained for a Gaussian signal. The definition of these two coefficients is given below for a centered variable ξ,

$$S_\xi = \frac{\overline{\xi^3}}{(\overline{\xi^2})^{3/2}} \qquad \text{and} \qquad T_\xi = \frac{\overline{\xi^4}}{(\overline{\xi^2})^2} \tag{1.4}$$

The discrepancy with regard to a Gaussian distribution increases for the time derivative, as displayed in Figs. 1.10c, d. This can be explained by the internal intermittency, which is still the subject of numerous studies, as discussed by Sreenivasan and Antonia [195].

1.3.2 Turbulence and Continuum Mechanics

The dissipation length scale l_η is small, but in general remains larger than the mean free path λ_m of fluid molecules. The continuum model can therefore be applied. The ratio between the free mean path and the length of interest, in the present case the Kolmogorov scale, is known as the Knudsen number, $\mathrm{Kn} = \lambda_m / l_\eta$, and the medium is considered to be continuous when $\mathrm{Kn} \leq 0.01$. For an ideal gas, it is useful to note that the kinematic viscosity is well estimated by $\nu \sim c_\infty \times \lambda_m$, where c_∞ is the speed of sound [76]. The exact expression for the free mean path is

$$\lambda_m = \frac{\nu}{c_\infty} \sqrt{\frac{\gamma \pi}{2}}$$

where $\gamma = c_p / c_v$ is the ratio of specific heat, $\gamma = 1.4$ for a diatomic gas. As a result, the Knudsen number can be estimated as follows by using Eq. (1.3),

$$\mathrm{Kn} = \frac{\lambda_m}{l_\eta} \sim \frac{\nu}{c_\infty} \frac{u_\eta}{\nu} \sim \frac{u_\eta}{c_\infty} \ll 1$$

As an illustration, for the turbulent signal examined in Fig. 1.10, the dissipation velocity scale is $u_\eta \simeq 7.3 \times 10^{-2}\ \mathrm{m \cdot s^{-1}}$, which must be compared to the speed of sound $c_\infty = \sqrt{\gamma r T_\infty} \simeq 343.2\ \mathrm{m \cdot s^{-1}}$.

1.3.3 Sensitivity to Initial Conditions

The nonlinearity of the Navier-Stokes equations does not allow the time evolution of turbulent fields to be predicted over a long period. The reason for this is that a small difference in the initial conditions introduces significant differences as time goes by. This sensitivity to initial conditions has been studied for chaotic systems and implies a positive value for the largest Lyapunov exponent. An example in meteorology is that weather forecasts over a period of more than a few days are often risky. Indeed, an initial separation of 1 cm between two fluid particles in the atmosphere results in a 10 km separation within just a day.

The blinking vortices of Aref [64] is a good example to illustrate the unpredictable behaviour of chaotic systems and also to show the benefit in stirring fluids. In this experiment, the plane incompressible and inviscid flow is created by two

point vortices of the same strength and located at $(-a, 0)$ and at $(a, 0)$ respectively. In practice, this can be realized by two rods or agitators animated by motors. During the time interval $2nT \leq t < (2n+1)T$, the first vortex is on while the second is off, and during the interval $(2n+1)T \leq t < 2(n+1)T$, the first vortex is off while the second is on. The two vortices thus blink on and off with a period T. The time dependence imposed on the vortices is essential for adding a dimension to the two-dimensional flow because chaotic behaviour is observed with at least three dimensional systems, either all three spatial as in the Lorenz attractor (1.1) or two spatial with one in time as in the present case. One point of interest here is the position of particles that are originally located in a single spot, in grey in Fig. 1.11, and then advected by the flow. Aref has shown that the control parameter is $\beta = \Gamma T/(2\pi a^2)$, and we recall that the velocity field around a vortex of strength Γ is $u_r = 0$ and $u_\theta = \Gamma/(2\pi r)$ in polar coordinates (r, θ). Each particle thus follows a circular rotation $\Delta\theta = \beta a^2/r^2$ during time T. For a small β, all particles circle more or less round the first vortex. For a given configuration, a very small value of β corresponds to a small switching time T for the blinking vortices, and the integration of particle motion can be interpreted as a simple numerical algorithm corresponding to vortices which act simultaneously. For this steady flow, pathlines and streamlines coincide and no chaotic advection is observed. For a large β, particles can be carried along by the velocity field of the second vortex at its current location when it starts to be active. Particles that are initially concentrated in the single spot, are thereby advected almost everywhere. This chaotic stirring is an efficient way to produce homogeneous solutions in industrial applications [80].

1.3.4 A Remark About Pressure

The second nonlinear term in the Navier-Stokes equation is the pressure term. It may be explicitly written by taking the divergence of Eq. (1.2). For an incompressible flow, this leads to a Poisson equation,

$$\nabla^2 p = -\rho \frac{\partial}{\partial x_i}\left(u_j \frac{\partial u_i}{\partial x_j}\right) = -\rho \frac{\partial u_i}{\partial x_j}\frac{\partial u_j}{\partial x_i} \tag{1.5}$$

whose Green's function is known for an infinite medium,

$$p(\boldsymbol{x}) - p_\infty = \frac{\rho}{4\pi}\int_V \left(\frac{\partial u_i}{\partial y_j}\frac{\partial u_j}{\partial y_i}\right)(\boldsymbol{y})\,\frac{d\boldsymbol{y}}{|\boldsymbol{x}-\boldsymbol{y}|} \tag{1.6}$$

assuming that $p \to p_\infty$ as $\boldsymbol{x} \to \infty$. Every region of the volume V occupied by the fluid thus contributes to the estimation of the pressure field at point $\boldsymbol{x}$. The fact that this contribution is instantaneous comes from the hypothesis of incompressibility, with perturbations traveling at infinite speed, as expected for an elliptic equation. Of course for a compressible medium, there is a time delay to transfer information

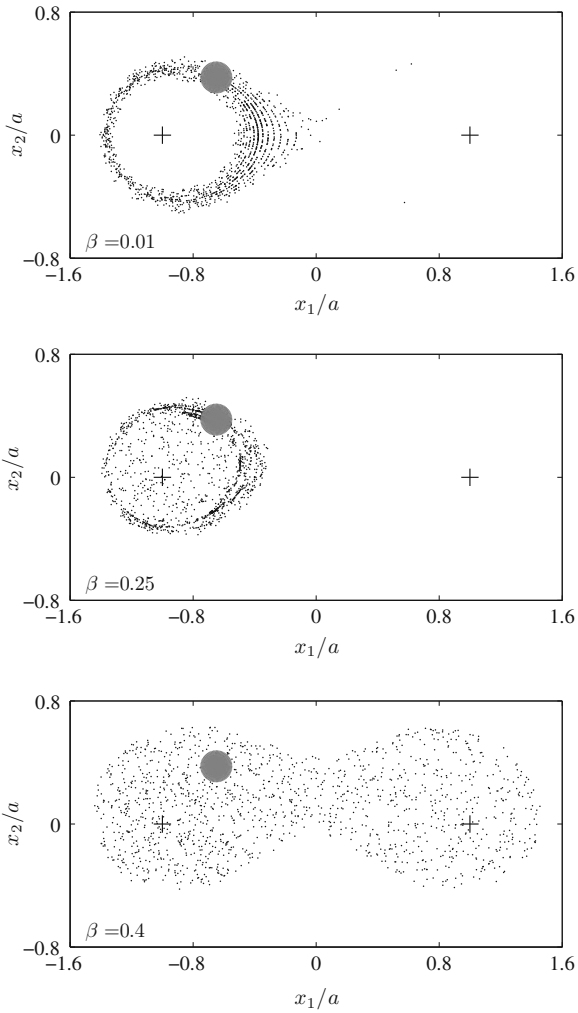

Fig. 1.11 Aref's blinking vortex system [64] for three values of the control parameter $\beta = 0.01, 0.25, 0.40$. The vortex positions are indicated by crosses. The particles are initially concentrated within the *grey* spot. For all plots, the time of stirring is $t = 4000\,T$

from a fluid particle located at $\boldsymbol{y}$ to the observer located at $\boldsymbol{x}$, as briefly presented in Sect. 1.4.2. Substituting the expression of p in the Navier-Stokes Equation (1.2) yields an equation that only depends on the velocity $\boldsymbol{u}$. Nevertheless, this obviously does not make the equation easier to solve. A similar equation links the vorticity field to the velocity field, it is discussed in Chap. 5.

1.4 Some Practical Consequences of Turbulence

On the whole, transport is very efficient in a turbulent flow, be it for momentum, mass or heat. Nonetheless, with this efficiency comes an increase in wall friction which is rarely sought. In what follows, a few examples of the advantages and drawbacks of the turbulent regime are given.

1.4.1 Transport Efficiency

Increase of Diffusion in a Given Geometry
Let us consider the example of the momentum transport over a given distance L, and compare the time of molecular diffusion to the time offered by turbulent diffusion. If only viscous diffusion imposes the motion of the fluid molecules, the time length T_v is determined from the balance between the time derivative of the velocity and the viscosity forces in the Navier-Stoke equation,

$$\frac{\partial \boldsymbol{u}}{\partial t} \sim \nu \nabla^2 \boldsymbol{u} \qquad \text{and hence,} \qquad T_v \sim \frac{L^2}{\nu}$$

For $L = 5$ m, with $\nu = 1.5 \times 10^{-5}$ m^2.s^{-1} in air, this leads to $T_v \simeq 500$ h. If turbulence is present, there is a balance between the time derivative of the velocity and inertial forces,

$$\frac{\partial \boldsymbol{u}}{\partial t} \sim \boldsymbol{u} \cdot \nabla \boldsymbol{u} \qquad \text{hence,} \qquad T_t \sim \frac{L}{u'}$$

Turbulent diffusion therefore results from velocity fluctuations. By choosing $u' \simeq 5$ cm $\cdot$ s^{-1} as an example, one obtains $T_t \simeq 2$ m, demonstrating the efficiency of turbulent transport. Note that the Reynolds number based on the travel distance L actually compares the two characteristic times,

$$\frac{T_v}{T_t} \sim \frac{u' L}{\nu} \sim \mathrm{Re}_L$$

A similar result can be easily derived for heat transport which is governed in an incompressible flow by

$$\frac{\partial \theta}{\partial t} + \boldsymbol{u} \cdot \nabla \theta = a \nabla^2 \theta$$

where a is the thermal diffusion coefficient. Now, with $T_v \sim L^2/a$ and $T_t \sim L/u'$, we have for the ratio of the two time scales

$$\frac{T_v}{T_t} \sim \frac{u' L}{a} \sim \frac{u' L}{\nu} \frac{\nu}{a} = \mathrm{Pr} \times \mathrm{Re}_L$$

where the Prandtl number appears. In air, at atmospheric pressure and at $T = 273\,\mathrm{K}$, $\mathrm{Pr} \simeq 0.73$. In practice, ascending velocities resulting from the work of the buoyancy force near a radiator are sufficient to create such fluctuations in velocity within a room and to ensure a homogeneous temperature.

The efficiency of mixing by turbulent transport is important for the dilution of pollutant waste discharged in rivers, oceans or in the atmosphere. Nonetheless, specific meteorological conditions can hamper rapid dispersion. Figure 1.12 shows a smoke plume released from a chimney in an atmosphere where the mean temperature increases with height above the ground, a situation called *temperature inversion* in meteorology. The plume no longer benefits from buoyancy to rise and only moves away due to the wind.

Expansion of the Free Boundaries of a Flow

A sketch representing the growth of a boundary layer on a flat plate is displayed in Fig. 1.13. This flow has already been introduced in connection with Fig. 1.6. The boundary layer thickens downstream, first slowly because of viscous diffusion in the laminar zone and then quickly due to transverse velocity fluctuations in the turbulent zone. More precisely, the boundary layer thickness δ grows as $\delta^2 \sim \nu t$ in the laminar zone, and as $\delta \sim u_2' t$ in the turbulent zone. The time t offered to either process is imposed by the external velocity $t \sim x_1/U_{e1}$. Assuming that the turbulent boundary layer also starts at the leading edge of the plate, by a tripping device for example, and that the velocity fluctuation normal to the wall is proportional to the free speed U_{e1}, then in the turbulent part, $\delta \sim (u_2'/U_{e1})x_1$. More specifically, the following relations can be respectively derived, based on the self-similar solution of Blasius in

Fig. 1.12 Smoke plume in the presence of a near surface temperature inversion, which hinders vertical turbulent motion and drives the plume horizontally. *The Quays Shopping Centre*, near to An Tiur and Cloghoge, Ireland. Courtesy of Eric Jones

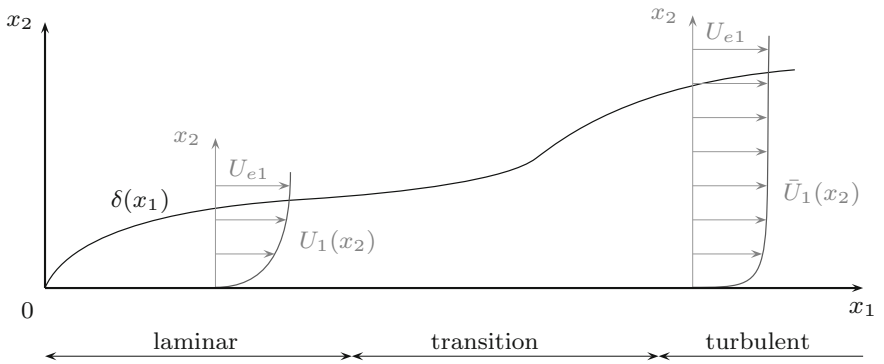

Fig. 1.13 Growth of a boundary layer on a flat plane without external pressure gradient. Transition appears for $\mathrm{Re}_{x_1} = x_1 U_{e1}/\nu \simeq 3.2 \times 10^5$, or equivalently for $\mathrm{Re}_\delta = \delta U_{e1}/\nu \simeq 2800$

the laminar regime [22],

$$\delta \simeq 4.92 \frac{x_1}{\mathrm{Re}_{x_1}^{1/2}} \tag{1.7}$$

and based on a 1/7th power law velocity profile [22] in the turbulent regime,

$$\delta \simeq 0.37 \frac{x_1}{\mathrm{Re}_{x_1}^{1/5}} \tag{1.8}$$

Reduction of Flow Separation Regions

Turbulence is able to bring a high velocity fluid to regions where the fluid motion would naturally be slowed down. This is the case of the aft part of a cylinder where expanding cross-section of the flow requires a deceleration of the fluid and a corresponding increase in pressure, i.e. dp/dx_1 is positive. In practice, it is said that the boundary layer meets an adverse pressure gradient. Naturally the boundary layer will separate from the cylinder, but turbulence can shift the separation point downstream. The location of the separation point S is shown in Fig. 1.14 as a function of the Reynolds number $\mathrm{Re}_D = U_\infty D/\nu$ based on the incoming velocity upstream U_∞ and the diameter D of the cylinder. At least three regimes can be identified: the subcritical one corresponding to a laminar boundary layer separation, the critical regime for $3 \times 10^5 \leq \mathrm{Re}_D \leq 1.5 \times 10^6$ for which a separation bubble followed by a turbulent reattachment occurs, and the super-critical one for which the attached boundary layer is turbulent.

In diffusers, important separation also occurs when the divergence angle becomes too wide, see for instance picture 175 in Van Dyke [28], and hence inhibits the normal functioning of energy recovery. Current studies in active flow control aim to master separation, small pulsed jets are used in experiments on aircraft flaps [579] for instance. An example of control allowing flow reattachment downstream

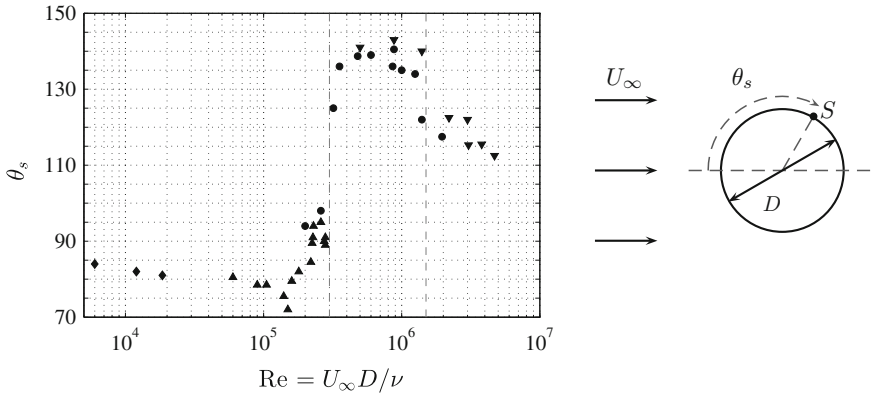

Fig. 1.14 Separation of a boundary layer on a cylinder. The separation point S is located around $\phi_s \simeq 90^o$ for a laminar boundary layer, and around $\phi_s \simeq 135^o$ for a turbulent boundary layer. The origin of angles is taken at the stagnation point. Experimental data (▲ ▼ ♦ ●) from different sources [567, 581]

of the circular cylinder using a pulsed jet [569] is shown in Chap. 10. The velocity field in Fig. 10.24 measured by particle image velocimetry, clearly demonstrates the influence of this pulsed jet.

Decrease of Form or Pressure Drag

Since turbulence transports high velocity fluid into the slow wake of a body, the wake width becomes narrow and the pressure distribution is modified over the surface of the body, thus decreasing its form drag coefficient C_D. In the critical regime, C_D can decrease down to 0.60 whereas it remains at 1.20 in the subcritical or laminar regime. Golf balls make a clever use of this phenomenon. Dimples promote transition of the boundary layer from the laminar to the turbulent regime. In the case of a sphere, drag crisis appears for $\mathrm{Re}_D \simeq 3 \times 10^5$ with a drop in the drag coefficient, from 0.5 to 0.2. The experiments mentioned in the previous paragraph are also used to deflect flows and modify drag and lift of airfoils.

Increase in Thermal Exchanges

Turbulence can bring cold fluid towards a heated wall or conversely hot fluid towards a cold wall, hence increasing heat transfer substantially. Thermal exchangers based on tube bundles, plates or fins use this property. For a flat plate maintained at a constant temperature within a flow parallel to it, the local Nusselt number comparing the convective heat flux at the wall to a pure conductive transfer is given by the two following semi-empirical expressions,

$$\begin{cases} \mathrm{Nu}_{x_1} \simeq 0.324\, \mathrm{Re}_{x_1}^{1/2}\, \mathrm{Pr}^{1/3} & \text{in the laminar regime,} \\ \mathrm{Nu}_{x_1} \simeq 0.0292\, \mathrm{Re}_{x_1}^{4/5}\, \mathrm{Pr}^{1/3} & \text{in the turbulent regime,} \end{cases}$$

where we recall that $\mathrm{Re}_{x_1} = U_{e1}x_1/\nu$ is based on the distance from the leading edge and $\mathrm{Pr} = \mu c_p/\lambda$ the Prandtl number of the fluid. The Nusselt number rapidly varies with the Reynolds number for a turbulent flow, hence indicating an increase in thermal exchanges.

1.4.2 A Few Undesirable Effects

Increase in Wall Friction

Wall friction is greatly increased by turbulence. Indeed transverse velocity fluctuations can bring a high velocity fluid close to the wall resulting in a stiffer mean velocity profile and a higher wall shear-stress $\bar{\tau}_w$. For a pipe flow the skin-friction coefficient C_f is defined by

$$C_f = \frac{\bar{\tau}_w}{\frac{1}{2}\rho U_d^2} \qquad \text{with} \qquad \bar{\tau}_w = \mu \left.\frac{\partial \bar{U}_z}{\partial r}\right|_{\text{wall}} \tag{1.9}$$

where $\bar{U}_z(r)$ is the mean longitudinal velocity. Figure 1.15 illustrates the correlation between the friction coefficient C_f and the Reynolds number $\mathrm{Re}_D = U_d D/\nu$, where D is the pipe diameter and U_d the bulk velocity. In the laminar regime, one has $C_f = 16/\mathrm{Re}_D$ which directly issues from the well-known parabolic velocity profile of the Hagen-Poiseuille flow. In the turbulent regime, numerous laws have been suggested over the years, such as the explicit relation $C_f \simeq 0.0791\,\mathrm{Re}_D^{-1/4}$ by Blasius and valid for $4000 \leq \mathrm{Re}_D \leq 10^5$, and the implicit relationship [22, 30]

$$\frac{1}{C_f^{1/2}} \simeq 4\log_{10}(\mathrm{Re}_D\, C_f^{1/2}) - 0.40 \tag{1.10}$$

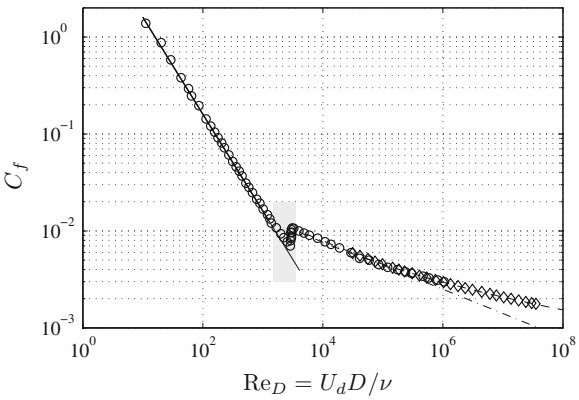

Fig. 1.15 Skin-friction coefficient C_f for a *circular pipe* as a function of the Reynolds number Re_D. Laminar regime: —— $C_f = 16/\mathrm{Re}_D$. Turbulent regime: –·–·– Blasius' relationship $C_f \simeq 0.0791\,\mathrm{Re}_D^{-1/4}$, – – – Eq. (1.11). Data from McKeon et al. [645] ○ Oregon facility and ◇ Princeton superpipe

Recent experimental data have been obtained in Princeton's superpipe [689] at high Reynolds numbers, by increasing the pressure of the air flow up to about 200 bars, and thus by increasing the Reynolds number $\mathrm{Re}_D = \rho U_d D/\mu$ up to 3.5×10^7 due to an increase in the fluid density ρ at a constant temperature, noting that $\mu = \mu(T)$. The following expression of C_f is proposed by McKeon et al. [645]

$$\frac{1}{C_f^{1/2}} \simeq 3.860 \log_{10}(\mathrm{Re}_D\, C_f^{1/2}) - 0.088 \tag{1.11}$$

In Chap. 3, it will be seen that relation 1.11 provides accurate results for the friction velocity $u_\tau = \sqrt{\bar{\tau}_w/\rho}$.

Turbulence and Acoustics

Turbulence generates broadband acoustic radiation, especially the so-called mixing noise for subsonic flows [511], and its intensity increases with the velocity to the power eight, which is certainly the most famous result derived from the aerodynamic noise theory of Lighthill [546]. Lighthill's wave equation can be seen as the generalisation of the Poisson Equation (1.6) for a compressible medium,

$$\frac{\partial^2 \rho'}{\partial t^2} - c_\infty^2 \nabla^2 \rho' = \frac{\partial^2 T_{ij}}{\partial x_i \partial x_j} \quad \text{with} \quad T_{ij} = \rho u_i u_j + (p' - c_\infty^2 \rho')\delta_{ij} - \tau_{ij}$$

where ρ' and p' are respectively the fluctuations in density and in pressure, c_∞ being a speed of sound and τ_{ij} the viscous stress tensor. The solution in free space can be written as,

$$\rho'(\boldsymbol{x}, t) = \frac{1}{4\pi c_\infty^2} \int_V \frac{\partial^2 T_{ij}}{\partial y_i \partial y_j} \left(\boldsymbol{y}, t - \frac{r}{c_\infty} \right) \frac{d\boldsymbol{y}}{r}$$

and the time delay $\tau = r/c_\infty$ related to the propagation of acoustic waves from a fluid particle located at $\boldsymbol{y}$ to the observer located at $\boldsymbol{x}$ is now present.

Broadband shock-associated noise and Mach waves are also present in supersonic jets, and the sound pressure levels of the radiated sound field outside of the jet flow are high enough to be directly visualized, as shown in Fig. 1.16. Acoustic propagation is also affected, the sound field is refracted and scattered by turbulent flows through velocity and temperature fluctuations. Source localizations by antenna or sonars for offshore exploration must taken into account the presence of a non homogeneous flow field. This phenomenon also exists in optics, where telescopes have to handle perturbations caused by the fluctuations of the refractive index of air.

1.5 Introduction to the Inviscid Linear Stability*

We consider the linear growth of small perturbations around a base flow, which should be in principle the laminar solution, and we want to know under what conditions the disturbance will be able to grow. Such analysis enables a better understanding of the

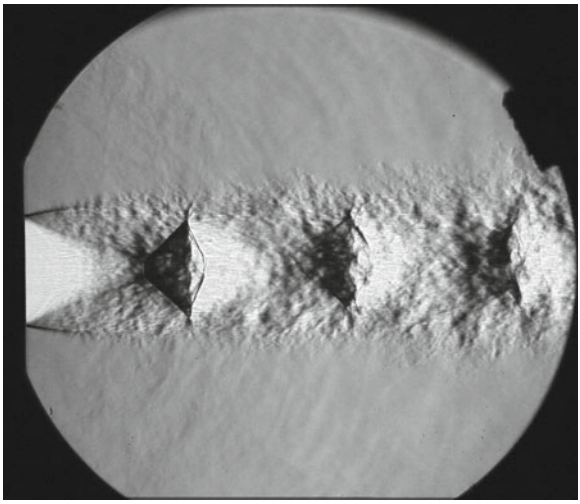

Fig. 1.16 Underexpanded supersonic round jet at Mach number 1.53 and Reynolds number $\mathrm{Re}_D = 1.1 \times 10^6$. The nozzle pressure ratio is NPR $\simeq 3.83$, the velocity is $u_j = 443\ \mathrm{m \cdot s^{-1}}$, the total temperature is $T_t = 32.2\ ^{\mathrm{o}}\mathrm{C}$ and the diameter $D = 38$ mm. For a convergent nozzle, shock-cells are generated to adapt the exit pressure p_e of the jet to the ambient pressure p_∞. Small-scale turbulence inside the jet is also visible. The intense radiated acoustic field can additionally be observed outside of the flow. Courtesy of Benoît André and Thomas Castelain (LMFA)

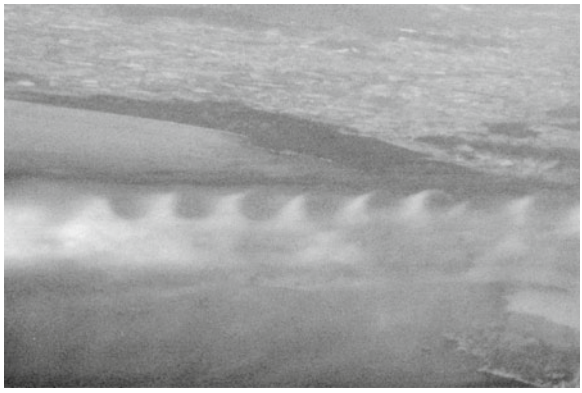

Fig. 1.17 Kelvin-Helmholtz instability occurring in the formation of clouds. Courtesy of Thomas Castelain, during a flight between Catania and Milan (LMFA)

first phase of the boundary layer transition from the laminar to the turbulent regime [54, 55]. These results are also used in numerical simulations of turbulent flows, where specific frequencies are used in order to seed turbulence development [541] at the inflow of the computational domain for instance. Kelvin-Helmholtz waves are certainly the most famous instability waves observed in free shear flows, and it is possible to see them in everyday life with some luck, see Fig. 1.17. These waves can also generate noise in supersonic jets for instance, as shown in Fig. 1.16.

1.5.1 Rayleigh Equation*

The considered base flow is a parallel two-dimensional flow with $U_1 = U_1(x_2)$, $U_2 = U_3 = 0$, whereas the pressure p_∞ and the density ρ_∞ are supposed to be constant. The time-dependent solution for the perturbed field is sought in the form of normal modes

$$\rho' = \hat{\rho}(x_2)e^{i(kx_1-\omega t)} \qquad u_i' = \hat{u}_i(x_2)e^{i(kx_1-\omega t)} \qquad p' = \hat{p}(x_2)e^{i(kx_1-\omega t)}$$

The physical quantities are obtained by taking the real part of the previous expressions. The decomposition $\rho = \rho_\infty + \rho'$, $\boldsymbol{u} = \boldsymbol{U} + \boldsymbol{u}'$ and $p = p_\infty + p'$ is then introduced into Euler's equations,

$$\rho\left(\frac{\partial \boldsymbol{u}}{\partial t} + \boldsymbol{u}\cdot\nabla\boldsymbol{u}\right) = -\nabla p$$

and only linear terms are retained by assuming that the perturbations ρ', $\boldsymbol{u}'$ and p' are small compared to the base flow variables. For the present two-dimensional case, it may be more convenient to express the velocity perturbation using the stream function ψ,

$$\psi = \phi(x_2)\, e^{i(kx_1-\omega t)} \quad \text{with} \quad \begin{cases} u_1' = \dfrac{\partial \psi}{\partial x_2} = \phi'(x_2)\, e^{i(kx_1-\omega t)} \\ u_2' = -\dfrac{\partial \psi}{\partial x_1} = -ik\phi(x_2)\, e^{i(kx_1-\omega t)} \end{cases}$$

and the perturbation of vorticity is then given by,

$$\omega' = \frac{\partial u_2'}{\partial x_1} - \frac{\partial u_1'}{\partial x_2} = -\nabla^2\psi$$

Only two-dimensional perturbations are considered here, as they are known to be the most unstable for the given base flow. Indeed, Squires [37] showed that any inviscid three-dimensional unstable perturbation corresponds to a more two-dimensional unstable one. The perturbation field satisfies the linearized Euler's equations,

$$\begin{cases} \nabla\cdot\boldsymbol{u}' = 0 \\ \rho_\infty\left(\dfrac{\partial u_1'}{\partial t} + U_1\dfrac{\partial u_1'}{\partial x_1} + u_2'\dfrac{dU_1}{dx_2}\right) + \dfrac{\partial p'}{\partial x_1} = 0 \\ \rho_\infty\left(\dfrac{\partial u_2'}{\partial t} + U_1\dfrac{\partial u_2'}{\partial x_1}\right) + \dfrac{\partial p'}{\partial x_2} = 0 \end{cases}$$

and the Fourier transform with respect to x_1 and t gives,

$$\begin{cases} ik\hat{u}_1 + \dfrac{d\hat{u}_2}{dx_2} = 0 \\ -ikc\hat{u}_1 + ikU_1\hat{u}_1 + \hat{u}_2\dfrac{dU_1}{dx_2} + \dfrac{1}{\rho_\infty}ik\hat{p} = 0 \\ -ikc\hat{u}_2 + ikU_1\hat{u}_2 + \dfrac{1}{\rho_\infty}\dfrac{d\hat{p}}{dx_2} = 0 \end{cases}$$

where the complex c is defined so that $\omega = kc$. It is possible to write an equation on the transverse velocity $\hat{u}_2$ for instance, by differentiating the second equation with respect to x_2 and by substituting the remaining unknowns using the two other equations. This yields,

$$(U_1 - c)\left(\frac{d^2\hat{u}_2}{dx_2^2} - k^2\hat{u}_2\right) - \frac{d^2U_1}{dx_2^2}\hat{u}_2 = 0 \tag{1.12}$$

which is Rayleigh's equation (1880). This equation is the starting point for the inviscid stability study of free shear flows. In the spatial theory, which is often the most relevant using a local approach by comparison with experiments, the complex wavenumber $k = k_r + ik_i$ is sought for a given real angular frequency ω in order to obtain non trivial solutions of (1.12) satisfying the boundary conditions $\hat{u}_2(x_2) \to 0$ as $x_2 \to \pm\infty$. The sign of the imaginary part k_i of the wavenumber thus determines the flow stability,

$$u_2' = \hat{u}_2\,(x_2)\, e^{-k_i x_1}\, e^{i(k_r x_1 - \omega t)}$$

Perturbation is spatially amplified if $k_i < 0$, damped if $k_i > 0$, and the marginal or neutral stability is obtained for $k_i = 0$. Hence k_i represents the spatial amplification or growth rate, and the phase velocity of the perturbation is given by $c_r = \omega/k_r$.

A similar discussion arises in the temporal approach. The angular frequency $\omega = \omega_r + i\omega_i$ is then sought as a complex value for a given real wavenumber k. One of the most famous result of the inviscid stability theory was pioneered by Rayleigh. A necessary condition for observing instability waves is that the velocity profile U_1 of the base flow has at least one inflection point. To demonstrate this result, the Rayleigh Equation (1.12) is multiplied by $\hat{u}_2^\star$, the conjugate of $\hat{u}_2$, and similarly, the conjugate of the Rayleigh equation is multiplied by $\hat{u}_2$. This yields,

$$\begin{cases} \hat{u}_2^\star\,\hat{u}_2'' - k^2\left|\hat{u}_2\right|^2 - \dfrac{1}{U_1 - c}\dfrac{d^2U_1}{dx_2^2}\left|\hat{u}_2\right|^2 = 0 \\ \hat{u}_2\,\hat{u}_2''^\star - k^2\left|\hat{u}_2\right|^2 - \dfrac{1}{U_1 - c^\star}\dfrac{d^2U_1}{dx_2^2}\left|\hat{u}_2\right|^2 = 0 \end{cases}$$

where $\hat{u}_2'' = d^2\hat{u}_2/dx_2^2$, and by subtraction,

$$\underbrace{\hat{u}_2^\star\,\hat{u}_2'' - \hat{u}_2\,\hat{u}_2''^\star}_{(\hat{u}_2'\,\hat{u}_2^\star)' - (\hat{u}_2\,\hat{u}_2'^\star)'} - \frac{2ic_i}{|U_1 - c|^2}\frac{d^2U_1}{dx_2^2}\left|\hat{u}_2\right|^2 = 0$$

Hence, by integrating along the transverse direction x_2 and taking into account the boundary conditions for $\hat{u}_2$, the equation becomes

$$c_i \int_{-\infty}^{+\infty} \frac{\left|\hat{u}_2\right|^2}{|U_1 - c|^2}\frac{d^2U_1}{dx_2^2}dx_2 = 0$$

A necessary condition for the growth of instability waves is the vanishing of the integral, thus requiring that U_1 has at least one inflection point, but nothing ensures that $c_i > 0$. A stronger necessary condition was later obtained by Fjørtoft (1950). The following criterion

$$\frac{d^2U_1}{dx_2^2}(U_1 - U_s) < 0$$

must be satisfied somewhere on the velocity profile, where U_s is the velocity at the inflection point. For a monotonic velocity profile, it also means that the spanwise vorticity $\Omega_s = dU_s/dx_2$ at the inflection point has to be a maximum rather than a minimum [37, 55]. These two criteria given by Rayleigh and Fjørtoft are often sufficient in practice for free shear flows, such as mixing layers and jets, and can be extended for compressible flows, see Sect. 1.5.4. A last useful result to mention is Howard's semi-circle theorem (1961), which states that c must lie in the semi-circle,

$$\left[c_r - \frac{1}{2}(U_{1\min} + U_{1\max})\right]^2 + c_i^2 \leq \left[\frac{1}{2}(U_{1\max} - U_{1\min})\right]^2$$

Some stability results dealing with classical base profiles are discussed hereafter.

1.5.2 Plane Mixing Layer⋆

Two-dimensional mixing layer is usually well described analytically by a hyperbolic tangent profile, see Fig. 1.18, which can be written in the following general form,

$$U_1(x_2) = \frac{\mathcal{U}_1 + \mathcal{U}_2}{2} + \frac{\mathcal{U}_1 - \mathcal{U}_2}{2}\tanh\left(\frac{x_2}{2\delta_\theta}\right) = u_m\left[1 + R_u\tanh\left(\frac{x_2}{2\delta_\theta}\right)\right] \tag{1.13}$$

where u_m is the mean velocity in the mixing layer, R_u a parameter associated with the velocity difference $\Delta U = \mathcal{U}_1 - \mathcal{U}_2$ in the shear zone, and δ_θ is the momentum thickness of the shear layer,

$$u_m = \frac{\mathcal{U}_1 + \mathcal{U}_2}{2} \qquad R_u = \frac{\Delta U}{2u_m}$$

$$\delta_\theta = \frac{1}{\Delta U^2} \int_{-\infty}^{+\infty} [U_1(x_2) - \mathcal{U}_2]\,[\mathcal{U}_1 - U_1(x_2)]\,dx_2$$

The length scale δ_θ can also be expressed in terms of the vorticity thickness δ_ω defined as,

$$\delta_\omega = \frac{1}{\Omega_{max}} \int_{-\infty}^{+\infty} \Omega\, dx_2$$

and for the hyperbolic tangent profile (1.13), $\delta_\omega = 4\delta_\theta$. This profile has an inflection point at $x_2 = 0$, which also corresponds to a maximum of the spanwise vorticity, two necessary conditions for the development of Kelvin-Helmholtz instability waves.

The evolution of the spatial wavenumber and of the amplification rate as a function of frequency are shown in Fig. 1.19 for several values of the parameter R_u. For the value $R_u = 1$, that is $\mathcal{U}_2 = 0$, the most amplified mode is obtained for $\omega\delta_\theta/u_m \simeq 0.2067$, corresponding to the frequency,

$$f_0 \simeq 0.033 \frac{u_m}{\delta_\theta} \simeq 0.132 \frac{u_m}{\delta_\omega}$$

and the perturbation amplification over one wavelength $\lambda = 2\pi/k_r$ is

$$\exp\left(-k_i \frac{2\pi}{k_r}\right) \simeq \exp\left(2\pi \times 0.1142/0.2016\right) \simeq 35$$

In other words, the amplitude of the wave is multiplied by 35 each time it travels a distance of one wavelength. The most amplified mode f_0 is usually known as the fundamental mode of the mixing layer. The phase velocity $c_r = \omega/k_r$ and the group velocity v_g,

$$v_g = \frac{dk_r/d\omega}{(dk_r/d\omega)^2 + (dk_i/d\omega)^2}$$

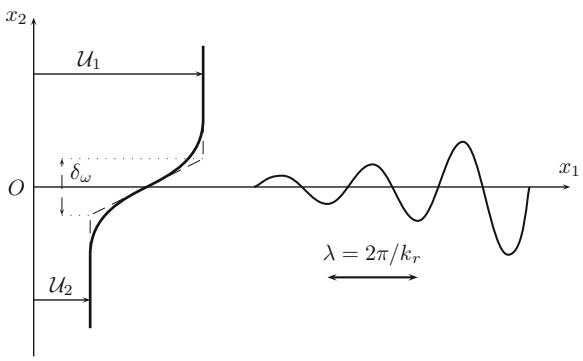

Fig. 1.18 Spatial growth of instability waves in a plane mixing layer. For a hyperbolic tangent profile, the vorticity thickness is $\delta_\omega = 4\delta_\theta$

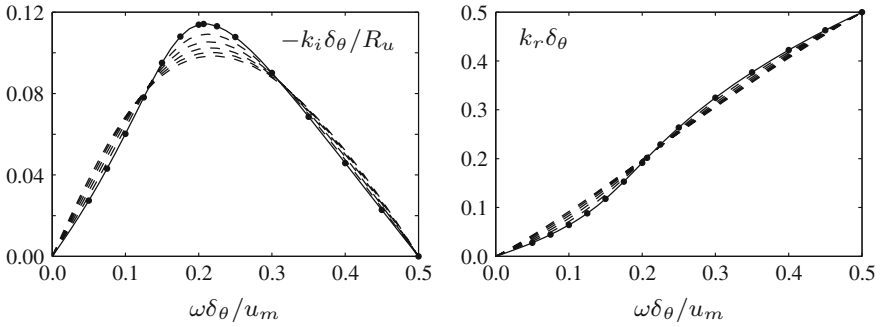

Fig. 1.19 Spatial amplification for the hyperbolic tangent velocity profile (1.13). On the *left* side, the amplification rate normalized by the parameter R_u, $-k_i\delta_\theta/R_u$ and on the *right*, the real part of the wavenumber $k_r\delta_\theta$ in terms of the adimensional frequency $\omega\delta_\theta/u_m$. Computations for $R_u = 0.5$ to $R_u = 1$ with a step of 0.1; the values calculated by Michalke [48] for $R_u = 1$ corresponds to • symbols

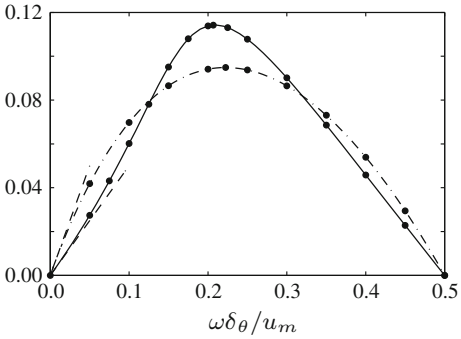

Fig. 1.20 Stability of the hyperbolic tangent velocity profile (1.13) for $R_u = 1$. Amplification $-k_i\delta_\theta$ of the spatial growing mode in solid line, and of the temporal growing mode $\omega_i\delta_\theta/v_g$ in *dashdot line*, as a function of the adimensional frequency $\omega\delta_\theta/u_m$. Points calculated by Michalke [47, 48] are in • symbols, the vortex sheet solution valid as $\omega \to 0$, is plotted in *dashed lines*

that is the velocity at the point corresponding to the maximum amplitude of a wave packet, are functions of the frequency, thus highlighting the dispersive nature of these waves. For the most amplified frequency f_0, $c_r \simeq u_m$ and $v_g = (dk_r/d\omega)^{-1} \simeq 0.66u_m$. The value of the phase velocity can be estimated by measuring the displacement of local maxima of vortices at frequency f_0. The value predicted by the linear stability theory is in good agreement with numerical simulations [470]. An illustration is given later in Sect. 5.4.

Finally, stability analysis based on spatial and temporal growing modes is displayed in Fig. 1.20 by using Gaster's transformation [38], which only holds true for small amplification rates, that is in the neighbourhood of neutral points.

1.5.3 Plane Jet⋆

The initial development of a plane jet can also be described by a hyperbolic tangent velocity profile,

$$\frac{U_1}{U_j} = \frac{1}{2}\left\{1 + \tanh\left[\frac{h_0}{2\delta_\theta}\left(1 - \frac{|x_2|}{h_0}\right)\right]\right\} \tag{1.14}$$

where U_j is the jet exit velocity, h_0 the jet half-width and δ_θ the momentum thickness of the shear layer. This symmetrical velocity profile has two inflection points, and thus two oscillation modes; namely a symmetrical or varicose mode, and an antisymmetrical or sinuous mode. The symmetrical mode is obtained by imposing $u_2' = 0$ on the axis of symmetry, or equivalently $\hat{u}_2 = 0$ at $x_2 = 0$. The antisymmetrical mode is obtained by imposing $u_1' = 0$ on the axis of symmetry, or equivalently $d\hat{u}_2/dx_2 = 0$ at $x_2 = 0$ according to the continuity equation.

An important parameter in the present case is the ratio h_0/δ_θ between the jet half-width and the characteristic length scale of the shear layer. For large values of h_0/δ_θ, the two mixing layers are generally considered as quasi-independent, and behave as in the basic hyperbolic tangent shear profile (1.13) with $U_j = 2u_m$ and $R_u = 1$.

1.5.4 Generalisation of the Rayleigh Equation⋆

In this last paragraph, the generalisation of the Rayleigh equation to compressible perturbations is briefly introduced for a axisymmetrical base flow, $U_r = U_\theta = 0$ and $U_z = U(r)$ in cylindrical coordinates. Mean pressure p_∞ is supposed to be constant in the flow but a mean density profile $\varrho(r)$ is now considered in the decomposition of the density, $\rho = \varrho(r) + \rho'$. A solution for compressible perturbations $(\rho', u_r', u_\theta', u_z', p')$ is still sought as normal modes, e.g. one has for the pressure,

$$p' = \hat{p}\,(r)\, e^{i(kz + n\theta - \omega t)} \quad \text{with} \quad n \in \mathbf{N}$$

In a similar manner to what was undertaken in Sect. 1.5.2, the variable decomposition is introduced in Euler's equation and the energy conservation equation, and only linear terms are retained. Hence,

$$\begin{cases} \dfrac{\partial \rho'}{\partial t} + U\dfrac{\partial \rho'}{\partial z} + u'_r\dfrac{d\varrho}{dr} + \varrho\nabla\cdot\boldsymbol{u}' = 0 \\ \varrho\dfrac{\partial u'_r}{\partial t} + \varrho U\dfrac{\partial u'_r}{\partial z} + \dfrac{\partial p'}{\partial r} = 0 \\ \varrho\dfrac{\partial u'_\theta}{\partial t} + \varrho U\dfrac{\partial u'_\theta}{\partial z} + \dfrac{1}{r}\dfrac{\partial p'}{\partial \theta} = 0 \\ \varrho\dfrac{\partial u'_z}{\partial t} + \varrho u'_r\dfrac{dU}{dr} + \varrho U\dfrac{\partial u'_z}{\partial z} + \dfrac{\partial p'}{\partial z} = 0 \\ \dfrac{\partial p'}{\partial t} + U\dfrac{\partial p'}{\partial z} + \gamma p_\infty\nabla\cdot\boldsymbol{u}' = 0 \end{cases}$$

By taking their Fourier transform with respect to z, θ and t, these equations become,

$$\begin{cases} -i\omega\hat{\rho} + ikU\hat{\rho} + \hat{u}_r\dfrac{d\varrho}{dr} + \varrho\nabla_\perp\cdot\hat{\boldsymbol{u}} = 0 \\ -i\omega\hat{u}_r + ikU\hat{u}_r + \dfrac{1}{\varrho}\dfrac{d\hat{p}}{dr} = 0 \\ -i\omega\hat{u}_\theta + ikU\hat{u}_\theta + i\dfrac{1}{\varrho}\dfrac{n}{r}\hat{p} = 0 \\ -i\omega\hat{u}_z + \hat{u}_r\dfrac{dU}{dr} + ikU\hat{u}_z + \dfrac{1}{\varrho}ik\hat{p} = 0 \\ -i\omega\hat{p} + ikU\hat{p} + \gamma p_\infty\hat{\nabla}\cdot\hat{\boldsymbol{u}} = 0 \end{cases}$$

From this system, the density $\hat{\rho}$ and the three velocity components $\hat{u}_r$, $\hat{u}_\theta$ and $\hat{u}_z$ can be expressed in terms of the pressure perturbation $\hat{p}$,

$$\hat{\rho} = -\frac{1}{\varrho}\frac{d\varrho}{dr}\frac{1}{(kU-\omega)^2}\frac{d\hat{p}}{dr} + \frac{\hat{p}}{c^2} \tag{1.15}$$

$$\varrho\hat{u}_r = i\frac{1}{kU-\omega}\frac{d\hat{p}}{dr} \tag{1.16}$$

$$\varrho\hat{u}_\theta = -\frac{n}{r}\frac{\hat{p}}{kU-\omega} \tag{1.17}$$

$$\varrho\hat{u}_z = -\frac{1}{(kU-\omega)^2}\frac{dU}{dr}\frac{d\hat{p}}{dr} - \frac{k\hat{p}}{kU-\omega} \tag{1.18}$$

where $c = c(r)$ is the mean speed of sound defined by $c^2 = \gamma p_\infty/\varrho$. The equation governing the pressure $\hat{p}$ may then be obtained through the energy conservation equation,

$$i\,(kU-\omega)\,\hat{p} + \gamma p_\infty\nabla_\perp\cdot\hat{\boldsymbol{u}} = 0$$

that is, by replacing the term $\nabla_\perp\cdot\hat{\boldsymbol{u}}$ by its definition,

$$i\,(kU-\omega)\,\hat{p}+\gamma p_\infty\left[\frac{1}{r}\frac{d}{dr}\left(r\hat{u}_r\right)+i\frac{n}{r}\hat{u}_\theta+ik\hat{u}_z\right]=0$$

The velocity components can then be eliminated according to the previous expressions (1.16)–(1.18), which yields

$$\frac{d^2\hat{p}}{dr^2}+\left[\frac{1}{r}-\frac{1}{\varrho}\frac{d\varrho}{dr}-\frac{2k}{kU-\omega}\frac{dU}{dr}\right]\frac{d\hat{p}}{dr}-\left[k^2+\frac{n^2}{r^2}-\frac{(kU-\omega)^2}{c^2}\right]\hat{p}=0 \quad (1.19)$$

This equation is a generalisation of Rayleigh's Equation (1.12) to include compressibility effects for free shear flows [36, 50]. Equation (1.19) describes not only spatial growing instability waves within the flow, but also propagation of acoustic perturbations through the base flow. Without going into details here, Equation (1.15) is reduced to $\hat{\rho}=\hat{p}/c^2$ by neglecting the mean density gradient term, a relation which governs acoustic fluctuations. A generalized inflection point theorem based on this equation can also be stated as follows [34],

$$\frac{d}{dr}\left(\frac{\rho}{n^2+k^2\rho^2}\frac{dU}{dr}\right)=0$$

in the framework of temporal stability.

Evolution of the wavenumber as function of the frequency for the two first modes $n=0$ and $n=1$, is shown in Fig. 1.21. The base profile of the axisymmetric jet is taken as follows,

$$\frac{U}{U_j}=\frac{1}{2}\left\{1+\tanh\left[\frac{r_0}{2\delta_\theta}\left(1-\frac{r}{r_0}\right)\right]\right\}$$

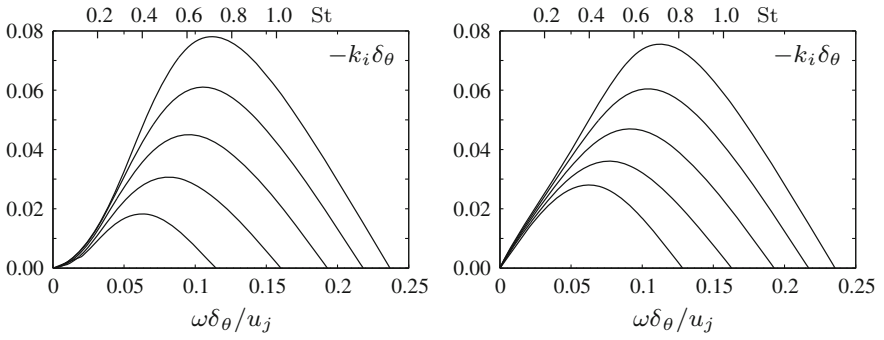

Fig. 1.21 Axisymmetric compressible jet with $r_0/\delta_\theta=20$ and $T_t=T_\infty$, where T_t is the jet stagnation or total temperature and T_∞ the temperature of the ambient medium at rest. Evolution of the amplification rate $-k_i\delta_\theta$ for the plane mode $n=0$ (*left*) and the first azimuthal mode $n=1$ (*right*). The Mach number of the jet varies from $M_j=0.9$ up to $M_j=2.1$ with a step of 0.3; The frequency is also given in terms of Strouhal number $\mathrm{St}=2r_0f/u_j$

where U_j is the jet exit velocity and r_0 the radius of the jet. The density profile is provided by the Crocco-Busemann relation. Stability theory predicts the domination of the first azimuthal mode $n = 1$ as the Mach number M_j increases for cold jets.

The reader may continue on this topic by reading Huerre et al.[41–43] for the distinction between convective and absolute instabilities, and the work of Tam et al. [57, 59, 60] for compressibility effects in jets and mixing layers.

1.6 Orr-Sommerfeld Equation*

The stability study of wall flows, but also that of wakes or jets at low Reynolds number, requires the inclusion of viscous effects. Under the same hypothesis of linearization as in Sect. 1.5, the incompressible perturbations are now governed by the Orr (1907) and Sommerfeld (1908) equation,

$$\left(U_1^\star - c^\star\right)\left(\frac{d^2u_2^\star}{dx_2^{\star 2}} - k^{\star 2}u_2^\star\right) - \frac{d^2U_1^\star}{dx_2^{\star 2}}\,\hat{u}_2^\star = \frac{1}{ik^\star\,\mathrm{Re}_{\delta_1}}\left(\frac{d^2u_2^\star}{dx_2^{\star 2}} - k^{\star 2}u_2^\star\right)^2 \tag{1.20}$$

written using dimensionless variables, denoted by a superscript $\star$. The displacement thickness δ_1 of the boundary layer is the reference length scale, and the free stream velocity of the base flow U_{e1} is the reference velocity scale, and $\mathrm{Re}_{\delta_1} = U_{e1}\delta_1/\nu$. Stability analysis is often more tricky than for inviscid flows and is beyond the scope of the present course [37, 39, 55].

As an illustration, we consider the temporal stability analysis of a laminar boundary layer growing on a flat plate without pressure gradient, the corresponding base flow is thus the Blasius velocity profile. The Orr-Sommerfeld Equation (1.20) can be recast in the following form,

$$\frac{-1}{ik^\star\,\mathrm{Re}_{\delta_1}}\left(\mathcal{L}_2^\star\hat{u}_2^\star\right)^2 + \bar{U}_1^\star\,\mathcal{L}_2^\star\hat{u}_2^\star - \frac{d^2\bar{U}_1^\star}{dx_2^{\star 2}}\hat{u}_2^\star = c^\star\,\mathcal{L}_2^\star\hat{u}_2^\star \tag{1.21}$$

where $\mathcal{L}_2^\star = d^2/dx_2^{\star 2} - k^{\star 2}$. The numerical approach consists in solving an eigenvalue problem, where $c^\star = c_r^\star + ic_i^\star$ is the desired eigenvalue. Therefore, for each value of the Reynolds number Re_{δ_1} and of the axial wavenumber $k^\star = k\delta_1$, the stability is determined by the sign of $c_i^\star = \mathrm{Im}(c^\star)$. Iso-contours of the amplification or growth rate $c_i^\star = c_i/U_{e1}$ are represented as functions of the pair $(\mathrm{Re}_{\delta_1}, k\delta_1)$ in Fig. 1.22. The critical Reynolds number $\mathrm{Re}_{\delta_1}^c \simeq 519.4$ is obtained for $k^c\delta_1 \simeq 0.303$, which yields a wavelength of $\lambda \simeq 7.3\delta$ at the start of transition for the Tollmien-Schlichting instability waves, by using (1.7) to compute the boundary layer thickness δ. The critical phase velocity is $c_r^\star/U_{e1} \simeq 0.3965$ and the critical angular frequency is $\omega^\star\delta_1/U_{e1} \simeq 0.12$. This frequency is also often expressed as $F = \omega/Re_{\delta_1} = \omega\nu/U_{e1}^2$. The largest possible wavenumber is $k_r\delta_1 \simeq 0.36$,

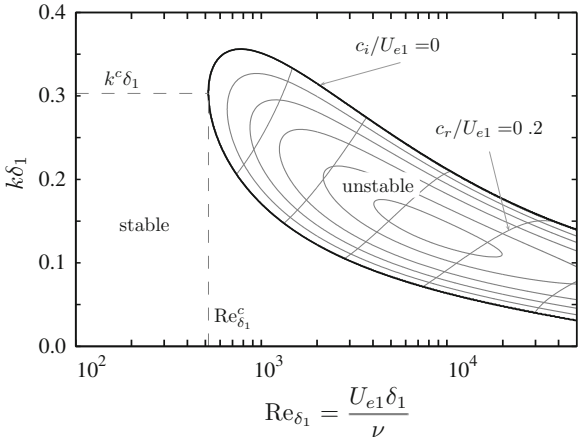

Fig. 1.22 Temporal stability of a laminar boundary layer growing on a flat plate without pressure gradient. The Orr-Sommerfeld Equation (1.21) is solved by a Chebyshev matrix collocation method. The closed curves represent contours of constant growth rate at $c_i/U_{e1} = [0.005, 0.01, 0.015, 0.020, 0.023]$, as a function of the Reynolds number $\mathrm{Re}_{\delta_1} = U_{e1}\delta_1/\nu$ and of the dimensionless wavenumber $k\delta_1$. The neutral curve is in *black*, and the critical value of the Reynolds number is $\mathrm{Re}^c_{\delta_1} \simeq 519.4$, associated with a critical value of the wavenumber $k^c\delta_1$. Isocontours of the phase velocity in the x direction are also plotted for $c_r/U_{e1} = [0.15, 0.20, 0.25, 0.30, 0.35]$

which corresponds to the smallest wavelength $\lambda \simeq 6.2\delta$ for instabilities. Tollmien-Schlichting waves have thus a rather large wavelength compared to δ.

A good agreement is obtained if the wavenumber k of the perturbation is well controlled in experiments, and if nonparallel effects are included in the theory [37], yielding a lower value of the critical Reynolds number $\mathrm{Re}_{\delta_1} \simeq 400$. In practice, the transition from the laminar regime to the turbulent regime is found near $\mathrm{Re}_{x_1} \simeq 3 - 5 \times 10^5$ or equivalently near $\mathrm{Re}_{\delta_1} \simeq 1000$, and the transition is completed for $\mathrm{Re}_{x_1} \simeq 3 \times 10^6$. The reader may refer to the comprehensive reviews by Wazzan [62], Arnal [31] and Reed et al. [54] to continue with this topic.

Chapter 2
Statistical Description of Turbulent Flows

This chapter focuses on the statistical approach to turbulence. On the one hand, it seeks to describe the evolution of mean and turbulent fields, and on the other, to highlight the transfer terms between these two fields. This splitting, introduced in 1883 by Reynolds, is not unique, nor the most satisfactory. Other flow decompositions are given in Chaps. 8 and 9. Nevertheless, the Reynolds approach is still to this date the only one allowing simple statistical assessments of fluid dynamic equations.

2.1 Method of Taking Averages

Any variable occurring in a turbulent field, such as velocity, pressure or temperature, is a random function of position $\boldsymbol{x}$ and time t. The first method to define an average is thus based on a probabilist approach. This means that the same experiment is repeated a larger number of times providing independent realizations of the field. The statistical mean $\bar{F}(\boldsymbol{x}, t)$ of a variable $f(\boldsymbol{x}, t)$ is then defined as

$$\bar{F}(\boldsymbol{x}, t) = \lim_{N \to \infty} \frac{1}{N} \sum_{i=1}^{N} f^{(i)}(\boldsymbol{x}, t)$$

where $f^{(i)}$ is the ith realization. This average will be the one employed throughout this chapter because of convenience when manipulating equations. It is however difficult to be implemented in concrete experiments. Two other methods are therefore involved in special cases. When the turbulent field is stationary, i.e. when time t does not enter into $\bar{F}$, a temporal average is possible, leading to

$$\bar{F}_T(\boldsymbol{x}) = \lim_{T \to \infty} \frac{1}{T} \int_{t_0}^{t_0+T} f\left(\boldsymbol{x}, t'\right) dt'$$

C. Bailly and G. Comte-Bellot, *Turbulence*, Experimental Fluid Mechanics,
DOI 10.1007/978-3-319-16160-0_2

where T is the observation time over only one realization. As an example, a sensor is placed at location $\boldsymbol{x}$ in a jet operated by a constant power supply. The duration T has to be large to permit $\bar{F}_T$ to approach $\bar{F}$. The exact demonstration relies on the hypothesis of ergodicity, which is developed at large by Lumley in his book on stochastic tools in turbulence [77]. Practically, a tangible requirement is that points at sufficiently large separation be uncorrelated. As a result, time T has to be much greater than the largest turbulent time scale encountered in the turbulent field. Moreover this time T depends on the nature of the considered variable f. Even simply for velocity, T differs for measurements dealing with $u(\boldsymbol{x}, t)$ and measurements involving $u'^2(\boldsymbol{x}, t)$ or $u'^4(\boldsymbol{x}, t)$.

When the turbulent field is homogeneous, i.e. when position $\boldsymbol{x}$ does not enter into $\bar{F}$, a spatial average is possible leading to

$$\bar{F}_V(t) = \lim_{V\to\infty} \frac{1}{V} \int_V f\left(\boldsymbol{x}', t\right) d\boldsymbol{x}'$$

As above, the volume V has to be large relative to the turbulent spatial scales involved in the variable f which is considered. The spatial average is generally employed when running computations which generally provide a knowledge of the turbulent field f at all points $\boldsymbol{x}$, and moreover at all times t in the volume V. An example is the turbulence decay in a large box after the initial excitation is turned off.

In the Reynolds decomposition, any physical variable f can be split into its mean part $\bar{F}$ and its fluctuation part f', i.e. $f = \bar{F} + f'$ with $\overline{f'} = 0$. As a convention for what follows, capital letters are employed as often as possible when designating mean physical quantities, in addition to the bar related to the mean operator. It is important to note that in this context, the mean part represents what is reasonably calculable, or at least the deterministic part, as opposed to the random or incoherent fluctuations which will be either modelled or measured.

Some important properties of the averaging operator are now listed. For two random variables $f = f(\boldsymbol{x}, t)$ and $g = g(\boldsymbol{x}, t)$ and a constant α, one easily establishes,

(i) $\overline{f+g} = \overline{F} + \overline{G}$

(ii) $\overline{\alpha f} = \alpha \overline{F}$

(iii) $\overline{\overline{F} g} = \overline{F}\,\overline{G}$

(iv) $\overline{\dfrac{\partial f}{\partial t}} = \dfrac{\partial \overline{F}}{\partial t} \qquad \overline{\dfrac{\partial f}{\partial x_i}} = \dfrac{\partial \overline{F}}{\partial x_i}$

(v) $\overline{\displaystyle\int f dt} = \displaystyle\int \overline{F} dt \qquad \overline{\displaystyle\int f dx_i} = \displaystyle\int \overline{F} dx_i$

Moreover, an important practical rule which will often be employed later on, concerns the product of two variables f and g,

$$\overline{fg} = \bar{F}\,\bar{G} + \overline{f'g'} \tag{2.1}$$

The alert reader may have noticed that the presence of a nonlinear term in the equations does not allow expression of the product as a function of $\bar{F}$ and $\bar{G}$ only, but introduces a new second-moment term $\overline{f'g'}$.

2.2 Reynolds Averaged Navier-Stokes Equations

Prior to considering the implications for turbulence of the Reynolds decomposition in a mean part and a fluctuating part, the fluid dynamics equations must be clearly stated. The reader can refer to classical textbooks in order to review the different local forms of these equations.

2.2.1 The Fluid Dynamics Equations

The fluid dynamics equations take the following forms whether they concern mass, momentum or energy conservation [5],

$$\frac{\partial \rho}{\partial t} + \nabla \cdot (\rho \boldsymbol{u}) = 0 \tag{2.2}$$

$$\frac{\partial (\rho \boldsymbol{u})}{\partial t} + \nabla \cdot (\rho \boldsymbol{u} \otimes \boldsymbol{u}) = -\nabla p + \nabla \cdot \boldsymbol{\tau} \tag{2.3}$$

$$\frac{\partial (\rho h)}{\partial t} + \nabla \cdot (\rho h \boldsymbol{u}) = -\nabla \cdot \boldsymbol{q} + \frac{\partial p}{\partial t} + \boldsymbol{u} \cdot \nabla p + \nabla \boldsymbol{u} : \boldsymbol{\tau} \tag{2.4}$$

where ρ, $\boldsymbol{u}$, p and h designate density, velocity, pressure and enthalpy, respectively. No volume force such as gravity is considered here. The viscous stress tensor $\boldsymbol{\tau}$ is expressed for a Newtonian fluid as,

$$\begin{aligned} \boldsymbol{\tau} &= \mu \left[\nabla \boldsymbol{u} + (\nabla \boldsymbol{u})^t \right] + \lambda_2 \nabla \cdot \boldsymbol{u} \\ &= \mu \left[\nabla \boldsymbol{u} + (\nabla \boldsymbol{u})^t - \frac{2}{3} (\nabla \cdot \boldsymbol{u}) \, \boldsymbol{I} \right] + \mu_b (\nabla \cdot \boldsymbol{u}) \, \boldsymbol{I} \end{aligned} \tag{2.5}$$

where μ, λ_2 and $\mu_b = \lambda_2 + 2\mu/3$ designate the dynamic viscosity, the second viscosity and the bulk viscosity, respectively. To make clear the compact tensorial notations, let us explicit the convective term in (2.3) and the dissipation term in (2.4),

$$[\nabla \cdot (\rho \boldsymbol{u} \otimes \boldsymbol{u})]_i = \frac{\partial}{\partial x_j} (\rho u_i u_j) \qquad \nabla \boldsymbol{u} : \boldsymbol{\tau} = \frac{\partial u_i}{\partial x_j} \tau_{ij}$$

By substituting expression (2.5) into the Navier-Stokes equation (2.3), the thermodynamic pressure is now distinct from the effective or mechanical pressure given by $p - \mu_b \nabla \cdot \boldsymbol{u}$. The classical approach consists in taking $\mu_b = 0$, according to the Stokes hypothesis, and the viscous stress tensor is then simply expressed as,

$$\boldsymbol{\tau} = \mu \left[\nabla \boldsymbol{u} + (\nabla \boldsymbol{u})^t\right] - \frac{2}{3}\mu \left(\nabla \cdot \boldsymbol{u}\right) \boldsymbol{I} \tag{2.6}$$

However, except for a monoatomic gas [71], this assumption is experimentally not satisfied [72, 74] when the determination of μ_b is carried out by measuring sound absorption. It should be noted that this discussion only occurs for compressible flows. Expression (2.5) directly provides the expression of $\boldsymbol{\tau}$ for an incompressible flow, thus satisfying $\nabla \cdot \boldsymbol{u} = 0$. In addition, if the fluid is not Newtonian, in such case as water flows containing polymers or bubbles for drag reduction, other constitutive equations have to be used.

The fluid is presumed to act as an ideal gas, i.e. $p = \rho r T$, and the conductive heat flux is supposedly described by the Fourier law $\boldsymbol{q} = -\lambda \nabla T$. In these relations, r is the ideal gas constant of the studied fluid and λ its thermal conductivity. The use of the enthalpy variable h to write the conservation of energy enables to obtain the temperature T directly by using the relation $dh = c_p dT$, where c_p is the specific heat for a constant pressure. The energy conservation equation can be written in many other forms such as [5],

$$\frac{\partial(\rho e)}{\partial t} + \nabla \cdot (\rho e \boldsymbol{u}) = -\nabla \cdot \boldsymbol{q} - p \nabla \cdot \boldsymbol{u} + \nabla \boldsymbol{u} : \boldsymbol{\tau} \tag{2.7}$$

$$\frac{\partial(\rho e_t)}{\partial t} + \nabla \cdot (\rho e_t \boldsymbol{u}) = \nabla \cdot \left[-\boldsymbol{q} - p\, \boldsymbol{u} + \boldsymbol{\tau} \cdot \boldsymbol{u}\right] \tag{2.8}$$

where $e = c_v T$ and $e_t = e + \boldsymbol{u}^2/2$ are the internal energy and the total energy respectively, with $\rho e_t = p/(\gamma - 1) + \rho \boldsymbol{u}^2/2$ for an ideal gas.

In addition, the following rule obtained by using Eq. (2.2) for any variable f, will also be frequently employed,

$$\frac{\partial(\rho f)}{\partial t} + \nabla \cdot (\rho f \boldsymbol{u}) = \rho \left(\frac{\partial f}{\partial t} + \boldsymbol{u} \cdot \nabla f\right) \tag{2.9}$$

In order to simplify algebra in this statistical study, the flow is assumed incompressible, i.e. $\nabla \cdot \boldsymbol{u} = 0$. Compressible flows, which are more complex, will be briefly described in Chap. 9 as applied to statistical modelling, see Sect. 9.3.1. Therefore, the following will now focus essentially on the Navier-Stokes equation. The case of a dilatable fluid including buoyancy effects, that is to say for which $\rho = \rho(T)$, can be treated as an exercise in order to practice the course.

Some results of continuum mechanics concerning the viscous stress tensor are briefly recalled as to conclude this section. The velocity gradient tensor can be decomposed in the sum of a symmetrical part, the deformation or rate-of-strain tensor e_{ij}, and an anti-symmetrical part, the vorticity tensor ω_{ij},

$$\frac{\partial u_i}{\partial x_j} = \underbrace{\frac{1}{2}\left(\frac{\partial u_i}{\partial x_j} + \frac{\partial u_j}{\partial x_i}\right)}_{e_{ij}} + \underbrace{\frac{1}{2}\left(\frac{\partial u_i}{\partial x_j} - \frac{\partial u_j}{\partial x_i}\right)}_{\omega_{ij}}$$

A physical interpretation of the velocity gradient tensor is given in Sect. 5.3. The vorticity tensor is linked to the vorticity vector $\boldsymbol{\omega} = \nabla \times \boldsymbol{u}$ through the two relations below,

$$\omega_{ij} = \frac{1}{2}\epsilon_{ijk}\omega_k \qquad \omega_k = \frac{1}{2}\epsilon_{ijk}\omega_{ij}$$

Moreover, it is convenient to split the deformation tensor e_{ij} into its isotropic and deviatoric parts by writing,

$$e_{ij} = e_{ij}^{\mathcal{I}} + e_{ij}^{\mathcal{D}} = \frac{1}{3}e_{kk}\delta_{ij} + \left(e_{ij} - \frac{1}{3}e_{kk}\delta_{ij}\right) \tag{2.10}$$

The isotropic or spherical part $e_{ij}^{\mathcal{I}}$ expresses the volume change since

$$\mathrm{tr}(\boldsymbol{e}^{\mathcal{I}}) = e_{ij}^{\mathcal{I}}\delta_{ij} = \frac{1}{3}e_{kk}\,(1+1+1) = \frac{\partial u_k}{\partial x_k} = \nabla \cdot \boldsymbol{u}$$

whereas the deviatoric part $e_{ij}^{\mathcal{D}}$ is such as $\mathrm{tr}(\boldsymbol{e}^{\mathcal{D}}) = 0$, and is also symmetric. From now on, the deviatoric part of the velocity gradient tensor will be denoted s_{ij},

$$s_{ij} \equiv e_{ij}^{\mathcal{D}} \equiv \frac{1}{2}\left(\frac{\partial u_i}{\partial x_j} + \frac{\partial u_j}{\partial x_i}\right) - \frac{1}{3}(\nabla \cdot \boldsymbol{u})\delta_{ij} \tag{2.11}$$

As is clear from the constitutive relation (2.6), the viscous stress tensor is linearly linked to this tensor s_{ij} by,

$$\tau_{ij} = 2\mu s_{ij} \tag{2.12}$$

for a Newtonian fluid satisfying Stokes's hypothesis. At last, the dissipation term $\nabla\boldsymbol{u} : \boldsymbol{\tau}$ appearing in the energy conservation equation (2.4) is always positive, and this result is straightforward by noting that the viscous tensor is symmetric

$$\nabla\boldsymbol{u} : \boldsymbol{\tau} = \frac{\partial u_i}{\partial x_j}\tau_{ij} = \frac{\partial u_j}{\partial x_i}\tau_{ji} = e_{ij}\tau_{ij} = s_{ij}\tau_{ij}$$

and thus $\nabla\boldsymbol{u} : \boldsymbol{\tau} = 2\mu s_{ij}^2 \geq 0$. This dissipation term represents the quantity of mechanical energy transformed into thermal energy by viscous effects, and it is necessarily positive because of the second thermodynamic principle. By developing this expression, is obtained

$$\nabla\boldsymbol{u} : \boldsymbol{\tau} = 2\mu\left(e_{ij}^2 - \frac{1}{3}e_{kk}^2\right) = 2\mu\left[e_{ij}^2 - \frac{1}{3}(\nabla \cdot \boldsymbol{u})^2\right]$$

A final remark is to observe that there is no distinction between e_{ij} and $e_{ij}^{\mathcal{D}} \equiv s_{ij}$ for an incompressible flow of a Newtonian fluid.

2.2.2 Averaged Equations

To derive averaged equations, the Reynolds decomposition is applied to velocity $u_i = \bar{U}_i + u'_i$ and pressure $p = \bar{P} + p'$, as well as to the viscous tensor $\tau_{ij} = \bar{\tau}_{ij} + \tau'_{ij}$. The flow is considered incompressible and density is supposed to be constant. However, we will try to keep general expressions as far as possible in the development. Firstly, from the incompressibility condition,

$$\frac{\partial}{\partial x_i}\left(\bar{U}_i + u'_i\right) = 0$$

one obtains by averaging the equation,

$$\frac{\partial \bar{U}_i}{\partial x_i} = 0 \quad \text{and then,} \quad \frac{\partial u'_i}{\partial x_i} = 0$$

by substraction of the two first equations. Therefore, the instantaneous fluctuating velocity field is incompressible. This property will be employed very often later on. In the same way, from the mass conservation equation (2.2)

$$\frac{\partial}{\partial x_j}\left[\rho\left(\bar{U}_j + u'_j\right)\right] = 0$$

and from the momentum conservation equation (2.3)

$$\frac{\partial}{\partial t}\left[\rho\left(\bar{U}_i + u'_i\right)\right] + \frac{\partial}{\partial x_j}\left[\rho\left(\bar{U}_i + u'_i\right)\left(\bar{U}_j + u'_j\right)\right] = -\frac{\partial\left(\bar{P} + p'\right)}{\partial x_i} + \frac{\partial\left(\bar{\tau}_{ij} + \tau'_{ij}\right)}{\partial x_j} \tag{2.13}$$

the averaging operation leads to the Reynolds averaged equations,

$$\frac{\partial}{\partial x_j}\left(\rho \bar{U}_j\right) = 0 \tag{2.14}$$

$$\frac{\partial\left(\rho \bar{U}_i\right)}{\partial t} + \frac{\partial\left(\rho \bar{U}_i\, \bar{U}_j\right)}{\partial x_j} = -\frac{\partial \bar{P}}{\partial x_i} + \frac{\partial}{\partial x_j}\left[\bar{\tau}_{ij} - \rho\overline{u'_i u'_j}\right] \tag{2.15}$$

The new unknown $-\rho\overline{u'_i u'_j}$ issued from the convective nonlinear term in (2.3), is called the Reynolds stress tensor. Generally this term is larger than the mean viscous stress tensor except for wall-bounded flows, where viscosity effects become preponderant close to the wall. The no-slip boundary condition indeed requires that $\overline{u'_i u'_j} \to 0$ at the wall.

Due to the appearance of the new unknown $-\rho\overline{u'_i u'_j}$, the set of equations giving the mean velocity field $\bar{U}_i$ cannot be solved, and there are more unknowns than

equations. In short, this is called a *closure problem*. Two strategies can then be pursued to surmount the difficulty. The first comes from Boussinesq, and consists of modelling the Reynolds tensor $-\rho\overline{u_i' u_j'}$. Details are given in Sect. 2.5. The second one consists in writing an equation for this unknown tensor, i.e. a transport equation for the Reynolds stress tensor $-\rho\overline{u_i' u_j'}$. However, as one can guess, this new equation will introduce third-moment terms in velocity fluctuations, as shown later with the triple correlation term in Eq. (2.19) for instance, which still requires a closure.

The mean kinetic energy of the fluctuating field k_t, also called the turbulent kinetic energy,

$$k_t \equiv \frac{\overline{u_i' u_i'}}{2} = \frac{\overline{u_1'^2} + \overline{u_2'^2} + \overline{u_3'^2}}{2} \tag{2.16}$$

can be introduced through the contraction of the Reynolds stress tensor

$$-\rho\overline{u_i' u_j'}\,\delta_{ij} = -2\rho k_t$$

It therefore appears instructive to continue the presentation by considering the kinetic energy budget of the mean flow as well as the kinetic energy budget of the fluctuating field.

2.3 Kinetic Energy Budget of the Mean Flow

The equation which describes the kinetic energy $\rho\bar{U}_i^2/2$ of the mean flow can be obtained by multiplying the averaged Navier-Stokes equation (2.15) in the ith direction by the mean velocity $\bar{U}_i$ component,

$$\bar{U}_i \times \left\{ \frac{\partial\left(\rho\bar{U}_i\right)}{\partial t} + \frac{\partial\left(\rho\bar{U}_i\bar{U}_j\right)}{\partial x_j} = -\frac{\partial\bar{P}}{\partial x_i} + \frac{\partial}{\partial x_j}\left[\bar{\tau}_{ij} - \rho\overline{u_i' u_j'}\right] \right\}$$

From the mass conservation equation (2.14), a rule similar to relation (2.9) can easily be derived for an arbitrarily mean flow quantity $\bar{F}$,

$$\frac{\partial\left(\rho\bar{F}\right)}{\partial t} + \frac{\partial}{\partial x_i}\left(\rho\bar{U}_i\bar{F}\right) = \rho\frac{\partial\bar{F}}{\partial t} + \rho\bar{U}_i\frac{\partial\bar{F}}{\partial x_i} \equiv \frac{\bar{d}}{\bar{d}t}(\rho\bar{F}) \tag{2.17}$$

and is here used to rearrange the left-hand side of the previous equation in a conservative form,

$$\bar{U}_i \times \left\{ \frac{\partial(\rho \bar{U}_i)}{\partial t} + \frac{\partial(\rho \bar{U}_i \bar{U}_j)}{\partial x_j} \right\} = \rho \bar{U}_i \frac{\partial \bar{U}_i}{\partial t} + \rho \bar{U}_i \bar{U}_j \frac{\partial \bar{U}_i}{\partial x_j}$$
$$= \rho \frac{\partial}{\partial t}\left(\frac{\bar{U}_i^2}{2}\right) + \rho \bar{U}_j \frac{\partial}{\partial x_j}\left(\frac{\bar{U}_i^2}{2}\right)$$
$$= \frac{\partial}{\partial t}\left(\frac{\rho \bar{U}_i^2}{2}\right) + \frac{\partial}{\partial x_j}\left(\bar{U}_j \frac{\rho \bar{U}_i^2}{2}\right)$$

The other terms can be rewritten thanks to the incompressibility condition for the mean flow, and as a result, the kinetic energy budget can be recast in the following form,

$$\frac{\partial}{\partial t}\left(\frac{\rho \bar{U}_i^2}{2}\right) + \frac{\partial}{\partial x_j}\left(\bar{U}_j \frac{\rho \bar{U}_i^2}{2}\right) = \underbrace{\rho \overline{u_i' u_j'} \frac{\partial \bar{U}_i}{\partial x_j}}_{(a)} - \underbrace{\bar{\tau}_{ij} \frac{\partial \bar{U}_i}{\partial x_j}}_{(b)} \tag{2.18}$$
$$- \underbrace{\frac{\partial\left(\bar{U}_i \bar{P}\right)}{\partial x_i}}_{(c)} + \underbrace{\frac{\partial}{\partial x_j}\left(\bar{U}_i \bar{\tau}_{ij}\right)}_{(d)} - \underbrace{\frac{\partial}{\partial x_j}\left(\bar{U}_i \rho \overline{u_i' u_j'}\right)}_{(e)}$$

Intentionally, let us first consider the last three terms (c), (d) and (e). They respectively represent the power of pressure forces, viscous forces and Reynolds stress forces. It is important to observe that these terms are zero for a homogeneous mean flow. Indeed, they represent pure diffusion transfers and are actually written as a flux divergence form. As a result, the most important terms are term (a) which represent a transfer between the mean flow and the fluctuating flow, and the term (b) which represents the viscous dissipation of the mean flow.

In order to correctly understand the transfer term between the mean field and the turbulent field, it is useful to write down the equation governing the turbulent kinetic energy of the fluctuating field.

2.4 Kinetic Energy Budget of the Fluctuating Field

The turbulent kinetic energy k_t is defined by relation (2.16) and its governing equation can be obtained by writing the general equation for the Reynolds stress tensor, and then contracting indices, the minus sign of $-\rho \overline{u_i' u_j'}$ being left off.

2.4.1 Transport Equation of Reynolds Stresses

The Navier-Stokes equation governing the component u_i' is obtained by subtracting to the initial equation (2.13) its averaged equation (2.15), which leads to,

$$\frac{\partial\left(\rho u_i'\right)}{\partial t}+\frac{\partial}{\partial x_k}\left[\rho\left(u_i'\bar{U}_k+\bar{U}_i u_k'+u_i'u_k'\right)\right]=-\frac{\partial p'}{\partial x_i}+\frac{\partial}{\partial x_k}\left(\rho\overline{u_i'u_k'}+\tau_{ik}'\right)$$

and this equation is denoted as (Σ_i). The dummy summation index is now denoted as k to avoid any confusion with the index j considered in the Reynolds stress component $-\rho\overline{u_i'u_j'}$. Similarly, we can obtain the equation governing the component u_j', denoted as (Σ_j). The transport equation is then obtained by forming $u_j'\Sigma_i+u_i'\Sigma_j$ and by applying the average operator. More specifically, the three following groups are first rearranged,

$$\begin{cases}u_j'\dfrac{\partial}{\partial x_k}\left(\rho u_i'\bar{U}_k\right)+u_i'\dfrac{\partial}{\partial x_k}\left(\rho u_j'\bar{U}_k\right)=\dfrac{\partial}{\partial x_k}\left(\rho u_i'u_j'\bar{U}_k\right)\\ u_j'\dfrac{\partial}{\partial x_k}\left(\rho\bar{U}_i u_k'\right)+u_i'\dfrac{\partial}{\partial x_k}\left(\rho\bar{U}_j u_k'\right)=\rho u_j'u_k'\dfrac{\partial\bar{U}_i}{\partial x_k}+\rho u_i'u_k'\dfrac{\partial\bar{U}_j}{\partial x_k}\\ u_j'\dfrac{\partial}{\partial x_k}\left(\rho u_i'u_k'\right)+u_i'\dfrac{\partial}{\partial x_k}\left(\rho u_j'u_k'\right)=\dfrac{\partial}{\partial x_k}\left(\rho u_i'u_j'u_k'\right)\end{cases}$$

then applying the averaging operator and using the incompressibility condition, one gets

$$\frac{\partial\left(\rho\overline{u_i'u_j'}\right)}{\partial t}+\frac{\partial}{\partial x_k}\left(\rho\overline{u_i'u_j'}\,\bar{U}_k\right)=\mathcal{P}_{ij}+T_{ij}+\Pi_{ij}+D_{ij}-\rho\epsilon_{ij}\tag{2.19}$$

where the different terms in the right-hand side are defined as,

$$\begin{aligned}\mathcal{P}_{ij}&=-\left(\rho\overline{u_j'u_k'}\frac{\partial\bar{U}_i}{\partial x_k}+\rho\overline{u_i'u_k'}\frac{\partial\bar{U}_j}{\partial x_k}\right)\\ \mathcal{T}_{ij}&=-\frac{\partial}{\partial x_k}\left(\rho\overline{u_i'u_j'u_k'}\right)\\ \Pi_{ij}&=-\left(\overline{u_j'\frac{\partial p'}{\partial x_i}}+\overline{u_i'\frac{\partial p'}{\partial x_j}}\right)\\ \mathcal{D}_{ij}&=\frac{\partial}{\partial x_k}\left(\overline{u_j'\tau_{ik}'}+\overline{u_i'\tau_{jk}'}\right)\\ \rho\epsilon_{ij}&=\overline{\tau_{ik}'\frac{\partial u_j'}{\partial x_k}}+\overline{\tau_{jk}'\frac{\partial u_i'}{\partial x_k}}\end{aligned}$$

An interpretation of this budget is presented in Sect. 2.6 for the plane channel flow. This equation can be numerically solved, as an alternative to the modelling of Reynolds stress tensor $-\rho\overline{u_i' u_j'}$. However, and as already mentioned in Sect. 2.2.2, this equation contains a triple correlation term $\mathcal{T}_{ij}$, which requires a closure.

2.4.2 Budget of the Turbulent Kinetic Energy

The transport equation for k_t is directly deduced from (2.19) by contracting the indices and keeping the half-sum, namely $\bar{d}(\rho k_t)/\bar{d}t = (\mathcal{P}_{ii}+\mathcal{T}_{ii}+\Pi_{ii}+\mathcal{D}_{ii}-\rho\epsilon_{ii})/2$. It yields,

$$\frac{\bar{d}(\rho k_t)}{\bar{d}t} = \underbrace{-\rho\overline{u_i' u_k'}\,\frac{\partial \bar{U}_i}{\partial x_k}}_{(a)} \underbrace{-\overline{\tau_{ik}'\frac{\partial u_i'}{\partial x_k}}}_{(b)} \underbrace{-\frac{1}{2}\frac{\partial}{\partial x_k}\rho\overline{u_i' u_i' u_k'}}_{(c)} \underbrace{-\overline{u_i'\frac{\partial p'}{\partial x_i}}}_{(d)} + \underbrace{\frac{\partial}{\partial x_k}\overline{u_i'\tau_{ik}'}}_{(e)} \tag{2.20}$$

Moreover, the pressure term (d) can be rearranged as follows,

$$\Pi = \overline{u_i'\frac{\partial p'}{\partial x_i}} = \frac{\partial}{\partial x_i}\overline{u_i' p'} - \overline{p'\frac{\partial u_i'}{\partial x_i}} = \frac{\partial}{\partial x_i}\overline{u_i' p'} \tag{2.21}$$

and the three terms (c), (d) and (e) can then be rewritten as the divergence of a flux vector $\nabla\cdot\bar{\boldsymbol{J}} = \mathcal{T}+\Pi+\mathcal{D}$ to show that they are transport terms. The triple velocity correlation $\mathcal{T}$ represents the diffusion of the turbulent kinetic energy by the fluctuating velocity, and the terms Π and $\mathcal{D}$ can be associated with diffusion effects through the pressure and the viscous stresses. For homogeneous turbulence, $\nabla\cdot\bar{\boldsymbol{J}} \equiv 0$, the convection of the turbulent kinetic energy is then only balanced by,

$$\frac{\bar{d}(\rho k_t)}{\bar{d}t} = -\rho\overline{u_i' u_j'}\,\frac{\partial \bar{U}_i}{\partial x_j} - \overline{\tau_{ij}'\frac{\partial u_i'}{\partial x_j}} \tag{2.22}$$

namely the transfer term $\mathcal{P}$ between the mean field and the turbulent field on the one hand, see comments of Eq. (2.18), and the viscous dissipation per unit of mass of the turbulent kinetic energy on the other hand, denoted $\rho\epsilon$. This quantity is always positive,

$$\rho\epsilon = \overline{\tau_{ij}'\frac{\partial u_i'}{\partial x_j}} = 2\mu\overline{s_{ij}'^2} \geq 0 \tag{2.23}$$

A simplified expression of the dissipation ϵ, which is often used in practice, is briefly introduced in Eq. (2.26), and discussed later in Sect. 6.5.

By comparing Eqs. (2.18) and (2.20), the energy exchanged between the mean field and the turbulent field can only be carried on through the term $\mathcal{P}$. This term is generally positive, corresponding to an energy supply from the mean field to the

turbulent one, and is called, by abuse of language, the production term. A simple heuristic argument shows that this is true for a sheared flow. Let us take, for example, the case of a boundary layer where $d\bar{U}_1/dx_2 > 0$, and imagine that a fluid particle gets through the grey line from bottom to top, as shown in Fig. 2.1. Thus $u_2' > 0$, and this particle finds itself in the midst of a material animated by a greater mean velocity, thus having a deficit in longitudinal velocity, leading to $u_1' < 0$ and $\overline{u_1' u_2'} < 0$. The same reasoning can be applied to a fluid particle going through to the grey line from top to bottom, or to other flows with a negative mean velocity gradient such as jets. Finally, the $\mathcal{P}$ production term appears to be rather positive.

The principal terms that have been highlighted in the analysis of the kinetic energy budgets for the mean and the turbulent fields are resumed in Fig. 2.2. The rule (2.1) is again illustrated here with the dissipation induced by viscous effects,

$$\overline{\tau_{ij}\frac{\partial u_i}{\partial x_j}} = \bar{\tau}_{ij}\frac{\partial \bar{U}_i}{\partial x_j} + \overline{\tau'_{ij}\frac{\partial u'_i}{\partial x_j}} = \bar{\tau}_{ij}\frac{\partial \bar{U}_i}{\partial x_j} + \rho\epsilon$$

which is split into two contributions in the budget of the kinetic energy of the mean flow (2.18) and of the turbulent flow (2.20). These two terms are production terms in the transport equation for the mean temperature, as shown later in Sect. 9.2.3.

2.5 Turbulent Viscosity: The Boussinesq Model

The most famous and widely used closure for the Reynolds stress tensor is based on the concept of a turbulent viscosity, introduced by Boussinesq. This hypothesis involves expressing the Reynolds stress tensor by analogy with the viscous stress $\boldsymbol{\tau}$.

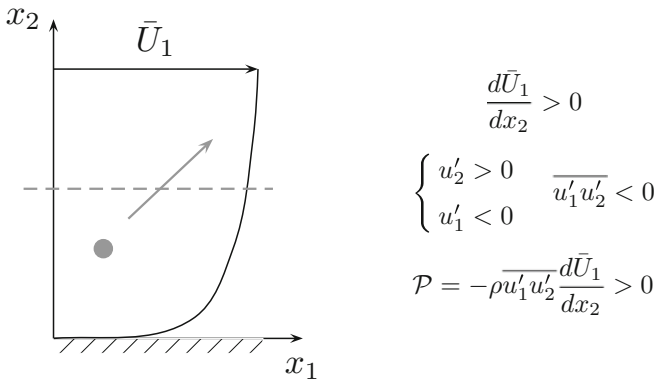

Fig. 2.1 Sketch of a fluid particle moving inside a boundary layer, and heuristic argument to estimate the sign of the production term $\mathcal{P}$

It is therefore assumed that

$$-\rho\overline{u_i'u_j'} = 2\mu_t\bar{S}_{ij} \underbrace{-\frac{2}{3}\rho k_t\delta_{ij}}_{(a)} \tag{2.24}$$

where μ_t is called the dynamic turbulent viscosity or the eddy viscosity. The isotropic term (a) is necessary to satisfy the condition $-\rho\overline{u_i'u_i'} = -2\rho k_t$ by contraction of the indices, that is for $i = j$ and taking the summation over i.

The turbulent viscosity seems on first approach to be a function of the flow $\mu_t = \mu_t(\boldsymbol{x}, t)$, as opposed to the molecular viscosity which is an intrinsic physical property of the fluid. A great challenge in turbulence is to derive a comprehensive formulation for μ_t, and examples will be given in the next chapters. Closure based on a turbulent viscosity model is presented here because it is the basis of most turbulent models used in numerical simulations of the Reynolds averaged Navier-Stokes equations. Chapter 9 treats in detail this issue, but it seems important to already note some consequences of such modelling for the Reynolds stress tensor since the reference to a turbulent viscosity is made throughout the textbook. Note also that approaches following in large eddy simulation are definitively different, and will be discussed in Chap. 8.

Replacing the six unknowns of the Reynolds stress tensor, three normal stresses $-\rho\overline{u_i'^2}$ and three shear stresses $-\rho\overline{u_i'u_j'}$ for $i \neq j$, by a unique unknown function μ_t induces a one-way energy transfer from the mean flow field towards the fluctuating field. Indeed, the term $\mathcal{P}$ takes the form

$$\mathcal{P} = -\rho\overline{u_i'u_j'}\frac{\partial\bar{U}_i}{\partial x_j} = \left(2\mu_t\bar{S}_{ij} - \frac{2}{3}\rho k_t\delta_{ij}\right)\frac{\partial\bar{U}_i}{\partial x_j} = 2\mu_t\bar{S}_{ij}^2 \geq 0$$

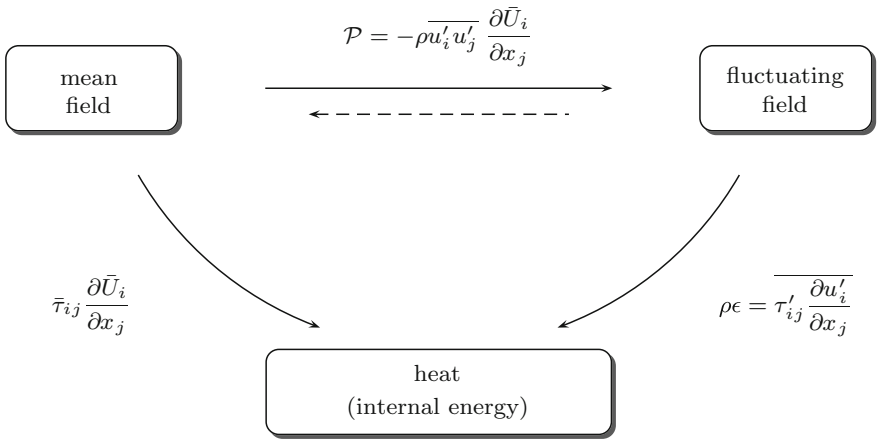

Fig. 2.2 Simplified diagram of energy transfers between the mean and turbulent fields, when neglecting all diffusion terms. The term $\mathcal{P}$ is generally a production term for the fluctuating field

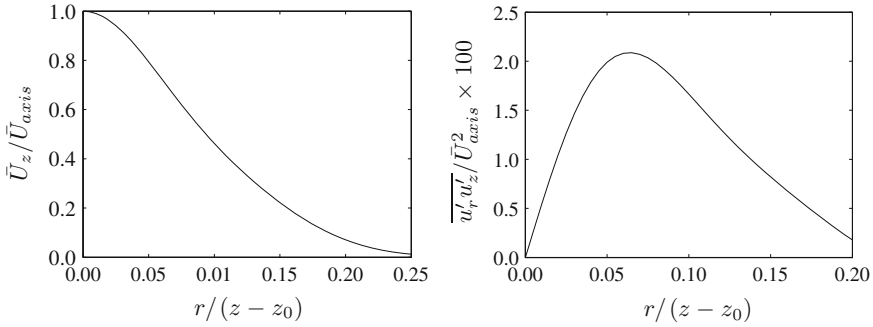

Fig. 2.3 Subsonic round jet at Mach M $= 0.16$ and Reynolds number $\mathrm{Re}_D = 9.5 \times 10^4$. Radial profiles of the mean velocity $\bar{U}_z/\bar{U}_{axis}$ and of the $\overline{u'_r u'_z}/\bar{U}^2_{axis}$ term against the radial distance $r/(z - z_0)$ in the fully developed region of the jet, at a distance larger than $25D$ from the nozzle exit. Data from Hussein et al. [539], see also Chap. 4

as $\mu_t > 0$, which is generally assumed in turbulent models. Moreover, in the case of a mean shear flow, with $\bar{U}_1 = \bar{U}_1(x_2)$ and $\bar{U}_2 = \bar{U}_3 = 0$, the model imposes the Reynolds stress to be zero for an extremum of the mean velocity, as the total strain τ_t seen by the fluid is given by

$$\tau_t = \bar{\tau}_{12} - \rho\overline{u'_1 u'_2} = \mu\frac{d\bar{U}_1}{dx_2} + \mu_t\frac{d\bar{U}_1}{dx_2} = (\mu + \mu_t)\frac{d\bar{U}_1}{dx_2} \tag{2.25}$$

There is no difficulty for symmetrical mean flow fields in 2-D and for axisymmetrical mean fields in 3-D. Figure 2.3 reproduces for example the $\bar{U}_z$ et $\overline{u'_r u'_z}$ profiles measured in a round jet by Hussein et al. [539]. Notice that $\overline{u'_r u'_z}$ is zero on the axis and that the production term $\mathcal{P}$ is positive.

However, at least two famous counterexamples exist regarding asymmetrical mean flows. The first is the wall jet, the experimental profiles of which appear in Fig. 2.4. Clearly $-\rho\overline{u'_1 u'_2}$ and $d\bar{U}_1/dx_2$ are zero for different x_2 positions. The second example concerns a channel flow with a smooth wall on one side and a rough wall on the other, studied by Hanjalić and Launder [618]. In both these cases, the location of the point where $-\rho\overline{u'_1 u'_2} = 0$ is displaced further than the point where $d\bar{U}_1/dx_2 = 0$ by the turbulent region which possesses the most intense velocity fluctuations, that is the jet compared to the wall in the first example, and the rough side compared to the smooth one in the second example.

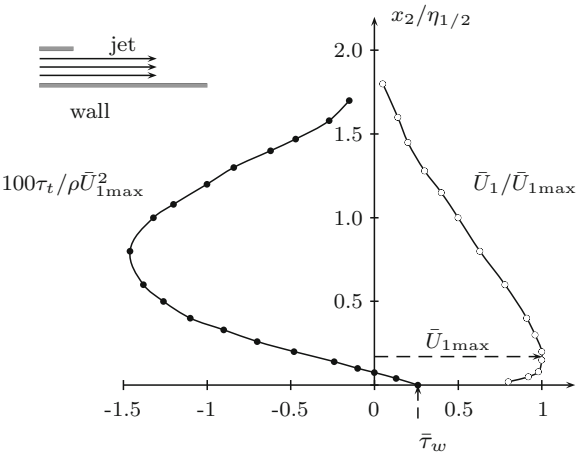

Fig. 2.4 Wall jet, Reynolds number at the nozzle exit Re $\simeq 1.8 \times 10^4$. Mean velocity $\bar{U}_1$ and total shear stress $\tau_t = \mu d\bar{U}_1/dx_2 - \rho\overline{u_1' u_2'}$ profiles as a function of the distance to the wall, $x_2/\eta_{1/2}$, where $\eta_{1/2}$ is the distance for which $\bar{U}_1 = 0.5 \times \bar{U}_{1max}$, and τ_w is the wall shear stress. By moving away from the wall, one first finds the point where $\tau_t = 0$, then the one where $d\bar{U}_1/dx_2 = 0$. Data from Tailland and Mathieu [557].

2.6 An Example: The Turbulent Channel Flow

In order to conclude this chapter and illustrate the turbulent kinetic energy assessment that has been established in a general case, the following section will focus on a fully developed stationary turbulent flow between two flat parallel walls, see Fig. 2.5. This turbulent channel flow is often used as a reference for direct numerical simulation, such for example the calculations of Kim et al. [629], Mansour et al. [640], Moser et al. [642] or Hoyas and Jiménez [621], because it is experimentally well documented, see Laufer [636], Comte-Bellot [604] or Johansson and Alfredsson [625].

A channel flow is found fully developed in experiments when the considered section is far enough from the entrance, $x_1 \geq 120h$, where h is the half-width of the channel. All mean quantities are then stationary and do not depend on x_1 except for the mean pressure. The mean velocity has the form $\bar{U}_1(x_2)$ and $\bar{U}_2 = \bar{U}_3 \equiv 0$. Moreover, the flow is statistically independent from x_3, meaning that x_3 is an homogeneous

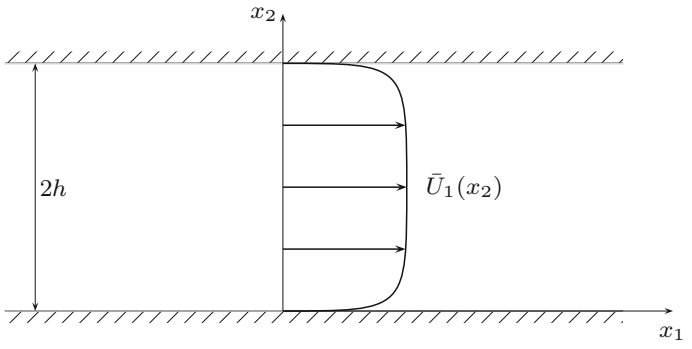

Fig. 2.5 Sketch of the geometry of a turbulent channel flow

direction for the turbulent field. The orientation of the x_3 axis has no influence, which leads to $\overline{u_1'u_3'} = \overline{u_2'u_3'} = 0$ and $\overline{p'u_3'} = 0$. Therefore, x_3 is a principal direction for the tensors, and the Reynolds tensor simplifies as,

$$-\rho\overline{u_i'u_j'} = -\rho \begin{pmatrix} \overline{u_1'^2} & \overline{u_1'u_2'} & 0 \\ \overline{u_1'u_2'} & \overline{u_2'^2} & 0 \\ 0 & 0 & \overline{u_3'^2} \end{pmatrix}$$

Equation (2.19) which governs the velocity correlations $\overline{u_i'u_j'}$, is written for the $i = j$ case, where the i indice is here replaced by the greek letter α so as to indicate that two repeated indices are not summed,

$$\frac{\bar{d}}{\bar{d}t}\left(\rho\overline{u_\alpha'^2}\right) = \mathcal{P}_{\alpha\alpha} + T_{\alpha\alpha} + \Pi_{\alpha\alpha} + \mathcal{D}_{\alpha\alpha} - \rho\epsilon_{\alpha\alpha}$$

The last two terms are often rearranged for incompressible flows. By noting that,

$$\mathcal{D}_{\alpha\alpha} = \mu\frac{\partial^2\overline{u_\alpha'^2}}{\partial x_k\partial x_k} + 2\mu\frac{\partial^2\overline{u_k'u_\alpha'}}{\partial x_k\partial x_\alpha}$$
$$\rho\epsilon_{\alpha\alpha} = 2\mu\overline{\frac{\partial u_\alpha'}{\partial x_k}\frac{\partial u_\alpha'}{\partial x_k}} + 2\mu\frac{\partial^2\overline{u_k'u_\alpha'}}{\partial x_k\partial x_\alpha}$$

the viscous diffusion and dissipation terms are thus combined as follows,

$$\mathcal{D}_{\alpha\alpha} - \rho\epsilon_{\alpha\alpha} = \mu\frac{\partial^2\overline{u_\alpha'^2}}{\partial x_k\partial x_k} - 2\mu\overline{\frac{\partial u_\alpha'}{\partial x_k}\frac{\partial u_\alpha'}{\partial x_k}} \equiv \mathcal{D}^h_{\alpha\alpha} - \rho\epsilon^h_{\alpha\alpha} \tag{2.26}$$

The new dissipation term $\epsilon^h_{\alpha\alpha}$ is not the correct thermodynamic expression of the dissipation, as formulated by Corrsin [68]. This term is sometimes called the isotropic dissipation, even though only homogeneity is required to have the equality between $\epsilon_{\alpha\alpha}$ and $\epsilon^h_{\alpha\alpha}$. This approximation of the exact dissipation is classically used in turbulence models since the transport equation of $\epsilon^h_{\alpha\alpha}$ is much simpler, see Sect. 6.5. At least for the case of the channel flow, the difference between the two expressions remains reasonably small [593].

The transport equation for the $\overline{u_\alpha'^2}$ component can then be recast as,

$$\begin{aligned}\frac{\bar{d}}{\bar{d}t}(\rho\overline{u_\alpha'^2}) = &-2\rho\overline{u_\alpha'u_k'}\frac{\partial\bar{U}_\alpha}{\partial x_k} - \frac{\partial}{\partial x_k}\rho\overline{u_\alpha'u_\alpha'u_k'} \\ &- 2\overline{u_\alpha'\frac{\partial p'}{\partial x_\alpha}} + \mu\frac{\partial^2\overline{u_\alpha'^2}}{\partial x_k\partial x_k} - 2\mu\overline{\frac{\partial u_\alpha'}{\partial x_k}\frac{\partial u_\alpha'}{\partial x_k}} \\ = &\ \mathcal{P}_{\alpha\alpha} + \mathcal{T}_{\alpha\alpha} + \Pi_{\alpha\alpha} + \mathcal{D}^h_{\alpha\alpha} - \rho\epsilon^h_{\alpha\alpha}\end{aligned} \tag{2.27}$$

In this equation, $\mathcal{P}_{\alpha\alpha}$ is the production, $\mathcal{T}_{\alpha\alpha}$ is the turbulent diffusion, $\Pi_{\alpha\alpha}$ is the velocity pressure-gradient correlation, $\mathcal{D}^h_{\alpha\alpha}$ is the viscous diffusion and $\epsilon^h_{\alpha\alpha}$ is the dissipation. The term $\Pi_{\alpha\alpha}$ can also be decomposed as the sum of a pressure diffusion term and a pressure velocity-gradient correlation term, in a similar way as in expression (2.21),

$$\Pi_{\alpha\alpha} = 2\left(-\frac{\partial}{\partial x_\alpha}\overline{u'_\alpha p'} + \overline{p'\frac{\partial u'_\alpha}{\partial x_\alpha}}\right) = \Pi^d_{\alpha\alpha} + \Pi^s_{\alpha\alpha} \tag{2.28}$$

to highlight the specific role of the fluctuating pressure.

Equation (2.27) is now particularized for the case of a fully developed turbulent channel flow. For each normal stress component $\overline{u'^2_\alpha}$, it thus yields

$$\begin{aligned}
0 &= -2\overline{u'_1u'_2}\frac{d\bar{U}_1}{dx_2} + \frac{d}{dx_2}\left(-\overline{u'^2_1u'_2} + \nu\frac{d\overline{u'^2_1}}{dx_2}\right) + \frac{2}{\rho}\overline{p'\frac{\partial u'_1}{\partial x_1}} - 2\nu\overline{\frac{\partial u'_1}{\partial x_k}\frac{\partial u'_1}{\partial x_k}} \\
0 &= 0 + \frac{d}{dx_2}\left(-\overline{u'^2_2u'_2} + \nu\frac{d\overline{u'^2_2}}{dx_2} - \frac{2}{\rho}\overline{u'_2p'}\right) + \frac{2}{\rho}\overline{p'\frac{\partial u'_2}{\partial x_2}} - 2\nu\overline{\frac{\partial u'_2}{\partial x_k}\frac{\partial u'_2}{\partial x_k}} \\
0 &= 0 + \frac{d}{dx_2}\left(-\overline{u'^2_3u'_2} + \nu\frac{d\overline{u'^2_3}}{dx_2}\right) + \frac{2}{\rho}\overline{p'\frac{\partial u'_3}{\partial x_3}} - 2\nu\overline{\frac{\partial u'_3}{\partial x_k}\frac{\partial u'_3}{\partial x_k}}
\end{aligned} \tag{2.29}$$

In these equations, the terms are organized in order to have successively the production term, the diffusion and pressure–velocity correlation terms, the pressure–velocity gradient term and finally the viscous dissipation term. It is essential to note that only the longitudinal component u'_1 receives energy from the mean flow through the production term $\mathcal{P}_{11}$. The transverse velocity components u'_2 and u'_3 can therefore only receive energy from u'_1 through pressure fluctuations. The latter being scalar, there is no privileged direction, which explains why both u'_2 and u'_3 can receive energy. Pressure therefore has a redistribution role relative to the turbulent kinetic energy between the three components of velocity.

Finally, the half-sum of all three equations (2.29) provides the turbulent kinetic energy budget for the channel flow,

$$\begin{aligned}
0 &= -\rho\overline{u'_1u'_2}\frac{d\bar{U}_1}{dx_2} - \frac{1}{2}\frac{d}{dx_2}\rho\overline{u'_iu'_iu'_2} + \mu\frac{d^2k_t}{dx_2^2} - \frac{d}{dx_2}\overline{u'_2p'} - \mu\overline{\frac{\partial u'_i}{\partial x_k}\frac{\partial u'_i}{\partial x_k}} \\
0 &= \mathcal{P} + \mathcal{T} + \mathcal{D}_h + \Pi^d - \rho\epsilon^h
\end{aligned} \tag{2.30}$$

Notice that pressure has an influence only through the transport term

$$\Pi^d \equiv \Pi^d_{ii}/2 = \Pi^d_{22}/2$$

in (2.30). Indeed, one has $\Pi = \Pi^d + \Pi^s$ with $\Pi^s = \Pi^s_{ii}/2 = 0$, and so it is expected that $\Pi^s_{11} = \overline{p'\partial u'_1/\partial x_1}$ is negative whereas Π^s_{22} and Π^s_{33} are expected to be rather positive terms.

These conjectures are confirmed by experiment, and results will be presented in detail in Chap. 3. It is however interesting to notice here that $\overline{u_1'^2}$ is greater than $\overline{u_2'^2}$ and $\overline{u_3'^2}$ in rms since $u_1' \simeq 2.5u_\tau$, $u_2' \simeq u_\tau$ and $u_3' \simeq 1.3u_\tau$, where u_τ is the friction velocity defined by $u_\tau = (\bar{\tau}_w/\rho)^{1/2}$ and $\bar{\tau}_w$ is the shear stress at the wall, namely $\bar{\tau}_w = \bar{\tau}_{12}(x_2 = 0)$.

Direct numerical simulations also complete these analyses, specifically for correlation terms involving pressure, which in general cannot be measured. The budgets of $\overline{u_1'^2}$, $\overline{u_2'^2}$, $\overline{u_3'^2}$ and $\overline{u_1'u_2'}$ computed by Hoyas and Jiménez [621, 622] are shown in Fig. 2.6. For $\overline{u_1'^2}$, the production term is found positive $\mathcal{P}_{11} > 0$. At the wall, the dissipation term is counterbalanced by the viscous diffusion. Moreover, the pressure–velocity correlation gradient term is negative as expected, $\Pi_{11}^s < 0$. The orders of magnitude of the terms involved in the budget of $\overline{u_2'^2}$, $\overline{u_3'^2}$ and $\overline{u_1'u_2'}$ are smaller. Concerning the analysis of the role of pressure, Π_{22}^s is found positive as soon as $x_2^+ > 10$, $\Pi_{33}^s > 0$ and $\Pi_{22}^d + \Pi_{22}^s > 0$. One also knows that $\Pi_{11}^d = \Pi_{33}^d = 0$. The production

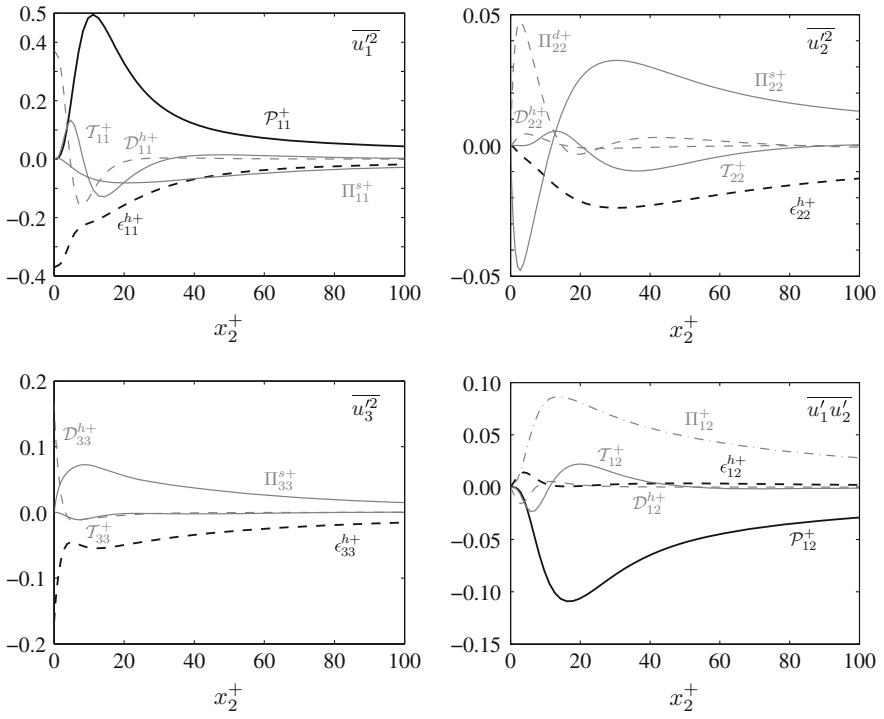

Fig. 2.6 Budgets of $\overline{u_1'^2}, \overline{u_2'^2}, \overline{u_3'^2}$ and $\overline{u_1'u_2'}$ for the channel flow at Reynolds number $\mathrm{Re}^+ = hu_\tau/\nu = 2003$, computed by Hoyas and Jiménez [621, 622]. See Eqs. (2.27) and (2.29) for the notations. Profiles are plotted as a function of the wall variable $x_2^+ = x_2u_\tau/\nu$, where u_τ is the friction velocity, and all terms are made dimensionless with u_τ, ν and ρ

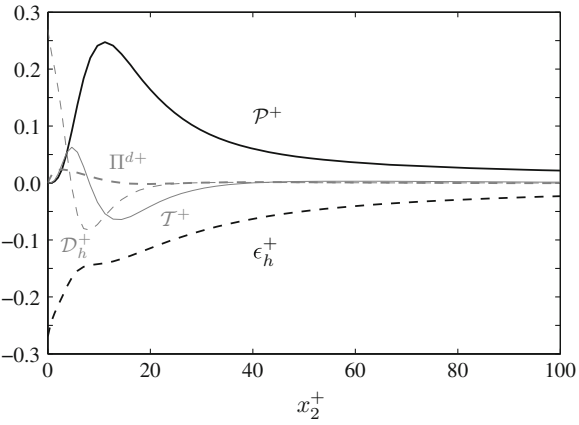

Fig. 2.7 Turbulent kinetic energy budget (2.30) for a channel flow at Reynolds number $\mathrm{Re}^+ = hu_\tau/\nu = 2003$, computed by Hoyas and Jiménez [621, 622]. Profiles are plotted as a function of the wall variable $x_2^+ = x_2 u_\tau/\nu$, and all terms are made dimensionless using u_τ, ν and ρ

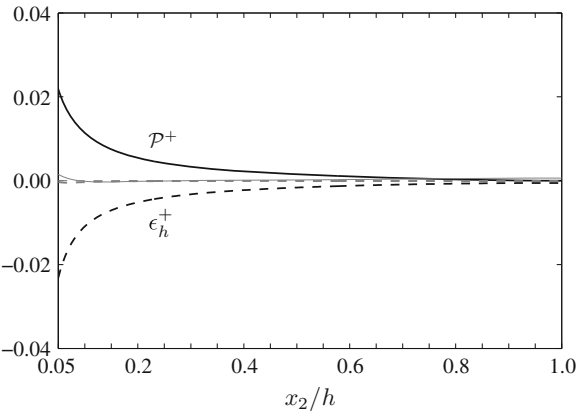

Fig. 2.8 Turbulent kinetic energy budget (2.30) for a channel flow at Reynolds number $\mathrm{Re}^+ = 2003$, computed by Hoyas and Jiménez [621, 622]. Profiles are plotted as a function of x_2/h, and all terms are made dimensionless using u_τ, ν and ρ

term $\mathcal{P}_{12}$ in the budget of $\overline{u_1' u_2'}$ is found negative, and according to (2.19), it can be written as,

$$\mathcal{P}_{12} = -\overline{u_2'^2}\frac{d\bar{U}_1}{dx_2} < 0$$

but this matches a positive production on the Reynolds stress $-\overline{u_1' u_2'}$.

Finally, the turbulent kinetic energy budget is represented in Fig. 2.7, according to Hoyas and Jiménez calculations [621, 622]. The role of pressure through the diffusion term is found to be very weak, even if pressure fluctuations are at the origin of the velocity components u_2' and u_3'. It can be also observed that for $x_2^+ \geq 30$, there is a quasi-equilibrium between dissipation and production. However this balance cannot extend to the center of the channel, where clearly the dissipation still exists, whereas the turbulent kinetic energy production tends to zero. In the budget of k_t shown in Fig. 2.8 as function of the distance x_2/h to the wall, the equilibrium subsists up to $x_2/h \simeq 0.5$. This interval over which production and dissipation are balanced, is characteristic of a wall flow, and this important result is developed in Chap. 3.

Chapter 3
Wall-Bounded Turbulent Flows

Wall turbulent flows are constrained by the presence of at least one rigid wall, which imposes a no-slip boundary condition at its surface. Boundary layers are constrained on one side only and a free edge subsists on the external side. A typical mean velocity profile is sketched in Fig. 3.1a for a cross section far enough from the leading edge as explained in Chap. 1, see Fig. 1.13. The complex indentation of the free edge can however be observed on the instantaneous side view displayed in Fig. 3.14. Channel or pipe flows are completely confined by surrounding walls and there is no place for free edges. A mean velocity profile is shown in Fig. 3.1b for a cross section far enough from the duct entrance. The channel case was examined in Sect. 2.6 when studying the turbulent kinetic energy budget of the flow. In this fully developed regime, the flow velocity characteristics become independent of the longitudinal coordinate x_1. The mean pressure which has to drive the flow, still depends on this longitudinal coordinate. To complete this general view, mean velocity profiles measured in a pipe flow are displayed in Fig. 3.2. The stiffness of these profiles near the wall can be clearly observed as the Reynolds number increases. Obviously different properties are expected to emerge between the external zone of a boundary layer and the central zone of a channel or a pipe. On the contrary, some similar properties may be present in both flows near the walls.

Turbulent boundary layers are present in our environment, e.g. in the atmosphere encompassing the Earth, and are encountered in many engineering applications such as flows over car bodies, over wings and fuselage of planes, around the blades of fans and turbines. Turbulent flows always prevail in ducts supplying water, petroleum or natural gases.

3.1 Friction Velocity

The no-slip boundary condition at $x_2 = 0$ induces a frictional shear at the wall. Its mean value, noted $\bar{\tau}_w$, is along the main flow direction x_1, refer to Fig. 3.1a, and its dimension is the product of density by a square velocity. A friction velocity, noted

C. Bailly and G. Comte-Bellot, *Turbulence*, Experimental Fluid Mechanics,
DOI 10.1007/978-3-319-16160-0_3

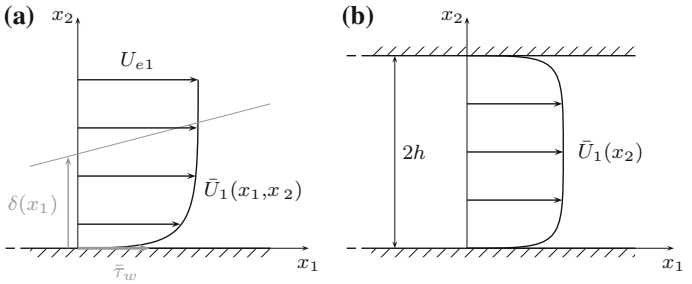

Fig. 3.1 Sketch of two wall-bounded turbulent flows. **a** Mean flow of a boundary layer on a flat plate without mean pressure gradient, with a Reynolds number defined as $\mathrm{Re}_\delta = U_{e1}\delta/\nu$. **b** Mean flow between two parallel plane walls (channel flow) with a Reynolds number defined as $\mathrm{Re}_h = U_d h/\nu$ where U_d is the bulk velocity

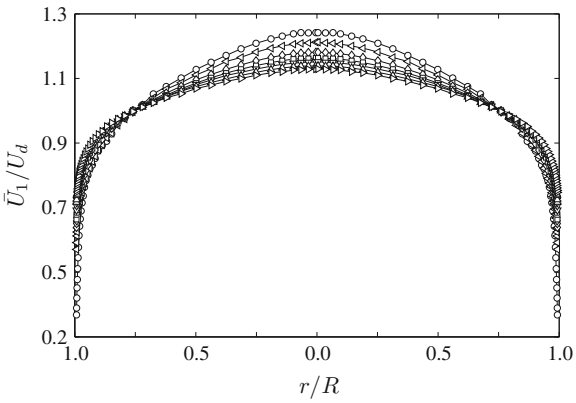

Fig. 3.2 Mean radial velocity profiles in a turbulent pipe flow of diameter $D = 2R$ as a function of the Reynolds number, $\mathrm{Re}_D = U_d D/\nu = 3.2 \times 10^4$ ∘, 9.9×10^4 ◁, 3.1×10^5 ◇, 1.0×10^6 □, 3.1×10^6 ▽, 1.0×10^7 △, 3.5×10^7 ▷, data taken from Zagarola and Smits [689] (Princeton superpipe)

u_τ, can therefore be defined by

$$u_\tau = \sqrt{\bar{\tau}_w/\rho} \tag{3.1}$$

and is often preferred to $\bar{\tau}_w$. The velocity u_τ plays a key role throughout the entire flow, whether concerning the mean field or the most essential characteristics of turbulence. Hence, $\bar{U}_1/u_\tau$ will be considered rather than $\bar{U}_1$ for the mean velocity, and $\overline{u'_\alpha u'_\alpha}/u_\tau^2$ with $\alpha = 1, 2$ or 3, rather than just $\overline{u'_\alpha u'_\alpha}$ for the mean square values of the velocity fluctuations.

For boundary layers, because of their downstream evolution, $\bar{\tau}_w$ as well as u_τ depend on x_1. A significant property of u_τ is that Definition (3.1) even holds for compressible boundary layers, where $\rho = \rho_w$ is the fluid density at the wall which often differs from that in the free stream [608].

For the established flow in circular pipes, the friction velocity u_τ has a typical order of magnitude of 4 % of the bulk velocity U_d, calculated as

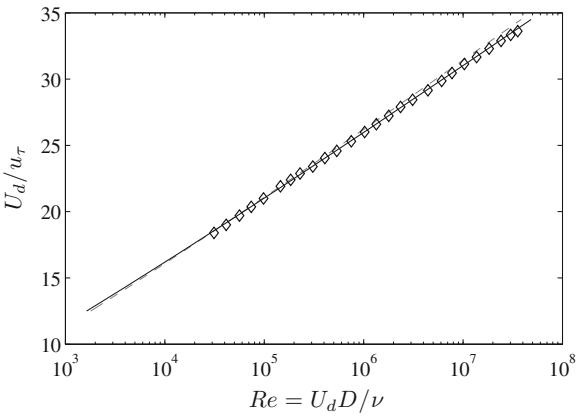

Fig. 3.3 Bulk velocity U_d normalized to the friction velocity u_τ plotted against the Reynolds number $\mathrm{Re}_D = U_d D/\nu$ for a *circular pipe* flow. Computed —— from expression (1.11) and - - - from expression (1.10), ◇ data from McKeon et al. [645] (Princeton group, superpipe)

$$U_d = \frac{1}{\pi R^2}\int_0^R \bar{U}_z(r) 2\pi r dr$$

where $D = 2R$ and $\bar{\boldsymbol{U}} = (\bar{U}_z, 0, 0)$ in cylindrical coordinates. A more precise value is given in Fig. 3.3 by plotting the evolution of U_d/u_τ against the Reynolds number Re_D. The curve is obtained by noting that $U_d/u_\tau = (2/C_f)^{1/2}$ from (1.9), and by substituting the expression of C_f with Eq. (1.11). The skin-friction coefficient C_f, also known as the Fanning friction factor [30], must not be mistaken with the Darcy friction factor f. Indeed, f is linked to the mean pressure drop by,

$$f = -\frac{d\bar{P}}{dx_1}\frac{D}{\rho U_d^2/2}$$

and C_f is connected to the wall shear by

$$C_f = \frac{\bar{\tau}_w}{\rho U_d^2/2}$$

The relation between C_f and f is obtained by writing the equilibrium between the action of pressure and the friction force for a dx_1 cross section of the pipe,

$$\frac{\pi D^2}{4}\left(-\frac{d\bar{P}}{dx_1}\right) dx_1 = \pi D \bar{\tau}_w \, dx_1$$

which leads to

$$\bar{\tau}_w = -\frac{D}{4}\frac{d\bar{P}}{dx_1} \quad \text{and hence,} \quad f = 4C_f$$

3.2 Equation for the Mean Velocity Profile

The case of channels long enough for the flow to become fully developed is first considered. Under these conditions, all longitudinal gradients of mean velocities and of turbulent statistics are zero. In other words, there is no more longitudinal evolution of the mean flow and the flow is perfectly homogeneous in the longitudinal direction. This is a useful reference configuration, already introduced in Sect. 2.6, for the understanding of induced mechanisms at the wall. The case of boundary layer flow is then considered. This type of flow inevitably possesses a longitudinal evolution, but this evolution is slow according to the boundary layer hypothesis, as elaborated by Prandtl [6, 22]. All longitudinal gradients are assumed to be one order of magnitude smaller than the gradients perpendicular to the wall, leading to a quasi-homogeneity in the streamwise direction.

3.2.1 The Plane Channel Flow

The following equations describe the mean velocity field in a plane channel,

$$\begin{cases} 0 = -\dfrac{1}{\rho}\dfrac{\partial \bar{P}}{\partial x_1} - \dfrac{d}{dx_2}\overline{u_1' u_2'} + \nu \dfrac{d^2 \bar{U}_1}{dx_2^2} \\ 0 = -\dfrac{1}{\rho}\dfrac{\partial \bar{P}}{\partial x_2} - \dfrac{d}{dx_2}\overline{u_2' u_2'} \end{cases} \tag{3.2}$$

They are obtained from the general equations derived in Sect. 2.2.2, by considering a stationary mean flow parallel to x_1, i.e. $\bar{U}_1 = \bar{U}_1(x_2)$ and $\bar{U}_2 = \bar{U}_3 = 0$. Integration of the second equation from the wall at $x_2 = 0$, and up to a current point x_2 yields,

$$\bar{P}\,(x_1, x_2) = \bar{P}_w - \rho \overline{u_2' u_2'} \qquad \text{where} \qquad \bar{P}_w \equiv \bar{P}\,(x_1, x_2 = 0)$$

is the mean wall pressure. The substitution of this result in the first equation leads to,

$$0 = -\frac{1}{\rho}\frac{d\bar{P}_w}{dx_1} + \frac{d}{dx_2}\underbrace{\left(-\overline{u_1' u_2'} + \nu \frac{d\bar{U}_1}{dx_2}\right)}_{= \tau_t(x_2)/\rho}$$

and by integration between $x_2 = 0$ and a current point x_2 of the transverse section, one has

$$\frac{d\bar{P}_w}{dx_1} x_2 = -\rho \overline{u_1' u_2'} + \mu \frac{d\bar{U}_1}{dx_2} - \bar{\tau}_w$$

In order to link $\bar{\tau}_w$ to the longitudinal mean pressure gradient, this equation is then particularized by taking $x_2 = h$, corresponding to the median plane of the channel,

where the total stress $\tau_t(x_2) = -\rho\overline{u_1' u_2'} + \mu d\bar{U}_1/dx_2$ is zero. Hence,

$$\frac{d\bar{P}_w}{dx_1} h = -\bar{\tau}_w \tag{3.3}$$

By combining these two last equations and by introducing the friction velocity u_τ defined by (3.1), the equation governing the total mean shear stress is,

$$\tau_t(x_2) = -\rho\overline{u_1' u_2'} + \mu\frac{d\bar{U}_1}{dx_2} = \rho u_\tau^2\left(1 - \frac{x_2}{h}\right) \tag{3.4}$$

A linear dependence is thus found between $\tau_t(x_2)$ and the distance to the wall x_2. The maximum of $\bar{\tau}_w$ occurs at the wall for $x_2 = 0$, and the minimum at the median plane $x_2 = h$ with $\tau_t = 0$. This relation reflects the global influence and meaning of the friction velocity u_τ throughout the entire flow. Note that u_τ can directly be expressed as a function of the longitudinal pressure gradient $d\bar{P}_w/dx_1$, corresponding to the pressure drop in the channel. Similarly for a circular pipe flow, one has $\tau_t(r) = \rho u_\tau^2(1 - r/R)$ with $(R/2)d\bar{P}_w/dx_1 = -\bar{\tau}_w$, where r is the radial distance from the axis and R the pipe radius.

The shear Reynolds stress $-\overline{u_1' u_2'}/u_\tau^2$ is plotted in Fig. 3.4 for a channel flow, to underline the importance taken by this term in the total shear stress $\tau_t(x_2)$ as the Reynolds number increases, by noting that τ_t follows the linear law (3.4). The Reynolds shear stress becomes preponderant for $\mathrm{Re}_h \geq 10^4$, except in the viscous sublayer close to the wall. For smaller Reynolds numbers, $-\overline{u_1' u_2'}/u_\tau^2$ is much smaller

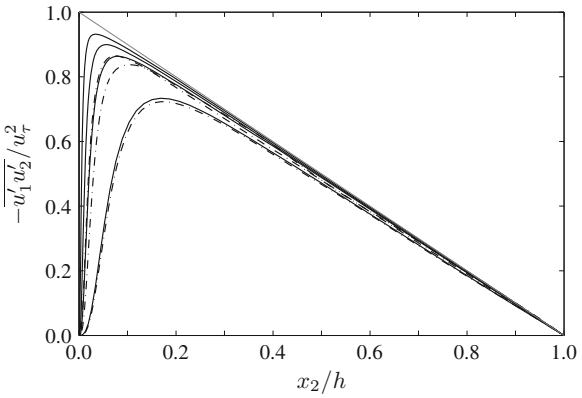

Fig. 3.4 Reynolds shear stress $-\overline{u_1' u_2'}/u_\tau^2$ in a plane channel flow. – – – from Moser et al. [642] at $\mathrm{Re}^+ = u_\tau\delta/\nu \simeq 180, 395, 590$ and —— from Hoyas and Jiménez [642] at $\mathrm{Re}^+ = 180, 550, 950, 2000$. The Reynolds number based on the bulk velocity lies in the interval $2800 \leq \mathrm{Re}_h \leq 43{,}600$. The *curves* approach the total linear shear stress $\tau_t/(\rho u_\tau^2)$ given by (3.4), when the Reynolds number increases.

than the straight line given by (3.4), and the viscous term $(\nu/u_\tau^2)d\bar{U}_1/dx_2$ is responsible for this difference.

3.2.2 The Boundary Layer

The governing equations for boundary layer approximation are reminded in Sect. 3.9. The two-dimensional averaged Navier-Stokes equations can be rearranged as follows [22, 30],

$$\begin{cases} \bar{U}_1 \dfrac{\partial \bar{U}_1}{\partial x_1} + \bar{U}_2 \dfrac{\partial \bar{U}_1}{\partial x_2} = -\dfrac{1}{\rho}\dfrac{dP_e}{dx_1} - \dfrac{\partial \overline{u_1' u_2'}}{\partial x_2} + \nu \dfrac{\partial^2 \bar{U}_1}{\partial x_2^2} \\ \bar{P}(x_1, x_2) = P_e - \rho \overline{u_2' u_2'} \end{cases} \tag{3.5}$$

Moreover $P_e = \bar{P}_w$, where P_e designates the pressure outside the boundary layer and $\bar{P}_w$ is the mean wall pressure. Compared to the channel flow, several differences appear. First of all, notice the presence of a longitudinal pressure gradient which depends on the chosen external flow. For a uniform free stream flow U_{e1} above a flat plate, $dP_e/dx_1 = 0$, and this case is now considered in what follows. The presence of a mean pressure gradient is discussed in the last section of this chapter. Secondly, notice the presence of the wall-normal velocity component $\bar{U}_2$ which allows the boundary layer to grow with x_1.

An integral relation can classically be derived from (3.5), in following von Kármán. As $U_{e1} = \text{cst}$, the mass conservation equation can be written as

$$\frac{\partial}{\partial x_1}(\bar{U}_1 U_{e1}) + \frac{\partial}{\partial x_2}(\bar{U}_2 U_{e1}) = 0$$

The Navier-Stokes equation (3.5) is also recast in order to introduce the velocity difference $\bar{U}_1 - U_{e1}$, and is integrated in the transverse direction from the wall to infinity. This yields,

$$\int_0^\infty \frac{\partial}{\partial x_1}\bar{U}_1\left(\bar{U}_1 - U_{e1}\right) dx_2 + \left[\bar{U}_2\left(\bar{U}_1 - U_{e1}\right)\right]_0^\infty = \left[-\overline{u_1' u_2'} + \nu \frac{\partial \bar{U}_1}{\partial x_2}\right]_0^\infty$$

and thus,

$$U_{e1}^2 \frac{\partial}{\partial x_1}\int_0^\infty \frac{\bar{U}_1}{U_{e1}}\left(\frac{\bar{U}_1}{U_{e1}} - 1\right) dx_2 + 0 = 0 - u_\tau^2$$

Finally, the friction velocity u_τ is governed by

$$u_\tau^2 = U_{e1}^2 \frac{d\delta_\theta}{dx_1} \quad \text{with} \quad \delta_\theta = \int_0^\infty \frac{\bar{U}_1}{U_{e1}}\left(1 - \frac{\bar{U}_1}{U_{e1}}\right) dx_2 \tag{3.6}$$

where δ_θ is the momentum thickness of the boundary layer. This relation is the momentum-integral equation of von Kármán [22] written here for a zero-pressure-gradient boundary layer. The friction velocity therefore appears to be in this case an increasing function of the downstream position x_1 as $d\delta_\theta/dx_1$ is positive. The same property applies to the local skin-friction coefficient defined by,

$$C_f \equiv \frac{\rho u_\tau^2}{\frac{1}{2}\rho U_{e1}^2} = 2\,\frac{d\delta_\theta}{dx_1} \tag{3.7}$$

As early as 1930, the dependence of u_τ or C_f with the local Reynolds number $\mathrm{Re}_{x_1} = U_{e1}x_1/\nu$ has been looked for. Schlichting [22] among others had to make two assumptions. First, C_f in a boundary layer where $U_{e1} = \mathrm{cst}$ is similar to C_f in a channel or pipe flow, i.e.

$$\frac{\bar{\tau}_w}{\rho U_{e1}^2} \simeq 0.0225 \left(\frac{U_{e1}\delta}{\nu}\right)^{-1/4}$$

Secondly, the mean velocity profile is described by a power law $\bar{U}_1/U_{e1} = (x_2/\delta)^{1/n}$, with $n \simeq 7$ for $\mathrm{Re}_\delta = U_{e1}\delta/\nu \simeq 10^5$ for instance. Thus, $\delta_\theta(x_1) = (7/72)\delta(x_1)$ and resolving the differential equation (3.7)

$$\frac{7}{72}\frac{d\delta}{dx_1} \simeq 0.0225 \left(\frac{U_{e1}\delta}{\nu}\right)^{-1/4}$$

Schlichting obtained $\delta(x_1) \simeq 0.37 x_1 \mathrm{Re}_{x_1}^{-1/5}$ and $\delta_\theta(x_1) \simeq 0.036 x_1 \mathrm{Re}_{x_1}^{-1/5}$. Consequently, $C_f(x_1) \simeq 0.0576\,\mathrm{Re}_{x_1}^{-1/5}$ and finally, $u_\tau(x_1)/U_{e1} \simeq 0.17\,\mathrm{Re}_{x_1}^{-1/10}$. For example, by taking $\mathrm{Re}_{x_1} \simeq 10^7$, one gets $u_\tau \simeq 0.034\,U_{e1}$.

Let us now establish an equation similar to (3.4) for the mean shear stress distribution across the boundary layer. Integration of Eq. (3.5) in the transverse direction from the wall to a current point x_2 leads to,

$$\int_0^{x_2} \left(\bar{U}_1\frac{\partial \bar{U}_1}{\partial x_1} + \bar{U}_2\frac{\partial \bar{U}_1}{\partial x_2}\right) dx_2 = -\overline{u_1' u_2'} + \nu\frac{\partial \bar{U}_1}{\partial x_2} - u_\tau^2 \tag{3.8}$$

However, the left-hand side can not be analytically evaluated in the general case, but we know its value for $x_2 = 0$, which is zero, and more interestingly its value for $x_2 = \delta$, which is $-u_\tau^2$. In a first approximation, this term may be assumed to vary linearly with x_2 and be thus written as $-u_\tau^2 x_2/\delta$. This leads to,

$$-\overline{u_1' u_2'} + \nu\frac{\partial \bar{U}_1}{\partial x_2} \simeq u_\tau^2\left(1 - \frac{x_2}{\delta}\right) \quad \text{for} \quad 0 \le x_2 \le \delta \tag{3.9}$$

A justification of this approximation can also be established [22] for a mean velocity profile of the form $\bar{U}_1/U_{e1} = (x_2/\delta)^{1/n}$. The integration of the left-hand side of (3.8) gives $-u_\tau^2(x_2/\delta)^{(n+2)/n} \simeq -u_\tau^2 x_2/\delta$ for classic values of n between 7 and 9.

As a concluding remark, the total mean shear stress is governed by Eq. (3.4) for the channel flow and by Eq. (3.9) for the boundary layer, by noting that $\delta = \delta(x_1)$ and $u_\tau = u_\tau(x_1)$ in the latter case. To simplify notations, only the boundary layer case is considered in what follows, but results for the channel flow are treated in the same manner, in replacing δ by h.

3.3 Viscous Sublayer

Very close to the wall, momentum transfers due to turbulence are nearly zero, due to blocking of normal velocity fluctuations u_2' by the wall, so that $-\rho\overline{u_1'u_2'} \simeq 0$. The viscous stress $\mu d\bar{U}_1/dx_2$ thus dominates the total shear stress $\tau_t(x_2)$. This region is called the viscous sublayer of wall-bounded flows. Of course at the wall, viscosity ensures the no-slip boundary condition and $u_1' = u_2' = 0$. In the same way, the matching of temperature between a heated flow and a wall is ultimately imposed by thermal conduction, and not by turbulent convection and mixing. In this viscous sublayer, Eq. (3.4) or (3.9) reduce to

$$\tau_t(x_2) = \mu\frac{d\bar{U}_1}{dx_2} = \bar{\tau}_w = \rho u_\tau^2$$

indicating that the evolution of the mean velocity with the wall distance is linear as in a Couette flow between two parallel walls, one of which is moving relative to the other. After normalization by the friction velocity u_τ, this linear profile takes the canonical form,

$$\frac{\bar{U}_1}{u_\tau} = \frac{x_2 u_\tau}{\nu} \quad \text{or} \quad \bar{U}_1^+ = x_2^+ \tag{3.10}$$

where following dimensionless wall variables are introduced,

$$\bar{U}_1^+ = \frac{\bar{U}_1}{u_\tau} \quad \text{and} \quad x_2^+ = \frac{x_2}{l_\nu} = \frac{x_2 u_\tau}{\nu} \tag{3.11}$$

The viscous length scale $l_\nu = \nu/u_\tau$ constructed on viscosity and friction velocity, characterizes the influence of the viscous effects induced by the wall. The overall parameters such as δ for the boundary layer or h for the channel are indeed not sufficient to describe the flow. Near the walls, lengths are preferably measured in viscous lengths and velocities in friction velocity. All variables rendered dimensionless by these wall units, l_ν or u_τ, are denoted with a superscript $+$, and there are usually called inner variables. Note that for the viscous length scale, $l_\nu^+ = 1$.

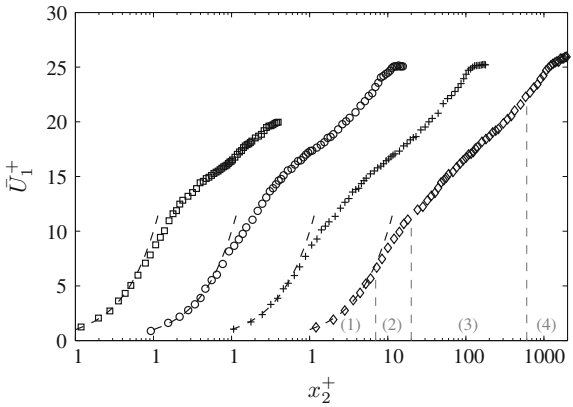

Fig. 3.5 Mean velocity profiles in inner scales, measured in a channel flow at $\mathrm{Re}^+ = u_\tau h/\nu = 390$ □, and in boundary layers at $\mathrm{Re}^+ = u_\tau \delta/\nu = 2900$ ∘, 3400+ and 4100 ◇. The viscous sublayer law (3.10) is plotted in *dashed line*. Data from Khoo et al. [627]

Figure 3.5 illustrates the experimental velocity profiles obtained by Khoo et al. [627] in several boundary layers and in a channel. The predicted law (3.10) for the viscous sublayer is clearly observed up to surely $x_2^+ \simeq 5$. More details about the experimental technique will be given in Chap. 10 because a special calibration rig is required for the sensor, in that case a hot-wire, in order to take into account only the heat taken away by the flow regardless the heat lost to the wall. Figure 3.5 has also the advantage of revealing the four main regions into which a wall-bounded flow can be divided: (1) the viscous sublayer we have just considered, (2) a region beyond the viscous sublayer and called the buffer layer, (3) a region where a logarithmic law appears and (4) a region of adjustment with the outer flow. In what follow, we shall examine these regions, firstly, the logarithmic one.

3.4 The Logarithmic Region

3.4.1 Dimensional Analysis

A dimensional analysis often provides a quick description of a physical law. Here we consider the mean velocity profile $\bar{U}_1$ (m · s^{-1}), which is expected to be a function of the following variables, x_2 (m), u_τ (m · s^{-1}), ν (m^2 · s^{-1}) and δ (m). Only two physical dimensions are involved and the Vaschy-Buckingham Π theorem leads to a relation involving 3 dimensionless parameters,

$$\frac{\bar{U}_1}{u_\tau} = f\left(\frac{x_2 u_\tau}{\nu}, \frac{x_2}{\delta}\right)$$

Two asymptotic forms of this relation can be derived, according to the distance to the wall. Near the wall, that is for $x_2/\delta < 1$ with $x_2^+ \gg 1$, the mean velocity is

depicted with respect to the wall velocity, which is zero there. In contrast near the edge of the boundary layer, for $x_2/\delta \to 1$, the mean velocity is rather compared with the free stream velocity U_{e1} and thus takes the form of a velocity defect law, also called a wake law, so that

$$\begin{cases} \dfrac{\bar{U}_1}{u_\tau} = f_1\left(\dfrac{u_\tau x_2}{\nu}\right) & \text{in the inner layer,} \\ \dfrac{U_{e1} - \bar{U}_1}{u_\tau} = f_2\left(\dfrac{x_2}{\delta}\right) & \text{in the outer layer.} \end{cases}$$

The two variables $u_\tau x_2/\nu = x_2^+$ and x_2/δ are independent, even though x_2 appears in each. For example, the value of $x_2 u_\tau/\nu$ can clearly be modified without affecting x_2/δ. Moreover, the link between the two length scales can be made through the dimensionless number Re^+ based on the friction velocity and the boundary layer thickness,

$$\frac{u_\tau x_2}{\nu} = \frac{u_\tau \delta}{\nu} \times \frac{x_2}{\delta} = \mathrm{Re}^+ \times \frac{x_2}{\delta} \tag{3.12}$$

The parameter $\mathrm{Re}^+ = u_\tau \delta/\nu = \delta^+$ represents the thickness of the boundary layer normalized by the viscous length l_ν. It is known as the Kármán number or the friction Reynolds number, even if it does not display a ratio between inertial and viscous forces here, but rather is an indicator of the disparity between inner and outer scales [614] since $\mathrm{Re}^+ = \delta/l_\nu$. If this Reynolds number is increased, the separation between the inner and the outer scales is increased accordingly. In other words, the same x_2 can insure $x_2/\delta \ll 1$ and belongs to the outer region, and $x_2 u_\tau/\nu \gg 1$, and belongs to the inner region.

At a sufficiently high Reynolds number, both laws can be simultaneously verified in the same region, called an overlap region, as shown in Fig. 3.6. By imposing the continuity of the velocity $\bar{U}_1$ and of its derivative $d\bar{U}_1/dx_2$, the two following relations must be satisfied,

$$\frac{U_{e1}}{u_\tau} - f_1\left(\frac{u_\tau x_2}{\nu}\right) = f_2\left(\frac{x_2}{\delta}\right) \quad \text{and} \quad -\frac{u_\tau}{\nu}\frac{df_1}{d\,(u_\tau x_2/\nu)} = \frac{1}{\delta}\frac{df_2}{d\,(x_2/\delta)}$$

In order to make explicit the two independent variables $u_\tau x_2/\nu$ and x_2/δ, the last relation is multiplied by x_2, which yields

$$\frac{u_\tau x_2}{\nu}\frac{df_1}{d\,(u_\tau x_2/\nu)} = -\frac{x_2}{\delta}\frac{df_2}{d\,(x_2/\delta)} = \mathrm{cst} = \frac{1}{\kappa}$$

where κ is the von Kármán constant. This leads by integration to

$$\frac{\bar{U}_1}{u_\tau} = \frac{1}{\kappa}\ln\left(\frac{u_\tau x_2}{\nu}\right) + B \tag{3.13}$$

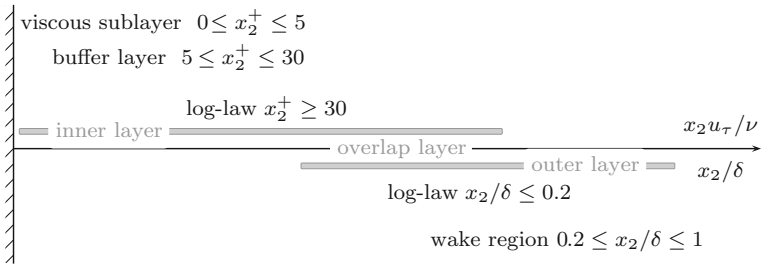

Fig. 3.6 The mean flow regions in a boundary layer

Table 3.1 Values of the constants of the log-law (3.13), see also relation (3.15) for the constant A

Wall-bounded flow	κ	B
Zero-pressure-gradient turbulent boundary layer	0.384	4.17
Turbulent pipe flow	0.41	5.0

in the inner layer, where the additive constant B is the velocity at $x_2^+ = 1$, and

$$\frac{U_{e1} - \bar{U}_1}{u_\tau} = -\frac{1}{\kappa} \ln\left(\frac{x_2}{\delta}\right) + A \tag{3.14}$$

in the outer layer. Values of the constants κ, B and A are experimentally evaluated from canonical flows, see Table 3.1 and examples provided in the next paragraph.

Lastly, two additional remarks can be made. The first one is that the compatibility relation induced by the continuity of the two velocity profiles in the overlap region,

$$\frac{U_{e1}}{u_\tau} = \frac{1}{\kappa} \ln(\mathrm{Re}^+) + A + B \tag{3.15}$$

and the second one is to note that the mean velocity gradient in this log-law is given by

$$\frac{d\bar{U}_1}{dx_2} = \frac{u_\tau}{\kappa x_2} \tag{3.16}$$

without the contribution of ν nor δ.

The log-law of the wall is a remarkable simple form for the mean velocity profile, and has been used successfully in engineering. This presentation has however been simplified in order to only highlight key features. Some other effects of the Reynolds number in a fully developed wall flow [614] or alternative dimensional laws [591, 594, 615, 656] are among topics currently discussed in the literature, but out of the scope of this textbook. In addition, experimental uncertainties and restricted Reynolds number range of most experiments and numerical simulations are entering into the discussion. To continue on this topic, the reader may refer to the reviews

by Gad-el-Hak and Bandyopadhyay [614], Marusic et al. [644] or Smits et al. [675] among others.

3.4.2 Some Examples

The mean velocity profiles measured by Osterlünd [654, 655] in a zero-pressure-gradient boundary layer on a flat plate are shown in Fig. 3.7. The log-law (3.13) approximately starts at $x_2^+ \simeq 30$ in the inner layer, this value being rather independent of the flow Reynolds number. More interestingly and as expected, the x_2 range covered by the log-law extends when the Reynolds number increases. The semi-empirical limit usually adopted is $x_2/\delta \leq 0.2$. This means that the Reynolds number must be high enough to distinguish a log-law, at least $\mathrm{Re}^+ \sim 10^3$, and typically $\mathrm{Re}^+ \sim 10^4$ to see a logarithmic velocity profile over one decade [387, 644].

The log-law can be used to determine u_τ from the mean velocity profile. By plotting $x_2 \partial \bar{U}_1/\partial x_2$ as a function of the distance from the wall x_2, the local minimum is indeed u_τ/κ. Also remember that u_τ is connected to the skin-friction coefficient C_f by $u_\tau = U_{e1}(C_f/2)^{1/2}$. As an illustration, values of C_f obtained by different authors are shown in Fig. 3.8 as a function of the Reynolds number $\mathrm{Re}_{\delta_\theta}$. For example, with $\mathrm{Re}_{\delta_\theta} = 10^3$, one obtains $u_\tau/U_{e1} \simeq 0.04$. At this point, and for an engineering purpose, it is interesting to connect $\mathrm{Re}_{\delta_\theta}$ to Re_{x_1}, which was previously undertaken in Sect. 3.2.2. Assuming that $\delta_\theta \simeq 0.036 x_1 \mathrm{Re}_{x_1}^{-1/5}$ for most boundary layer flows, one gets $\mathrm{Re}_{x_1} \simeq 64\,\mathrm{Re}_{\delta_\theta}^{5/4}$, and therefore $\mathrm{Re}_{x_1} = 3.6 \times 10^5$ for $\mathrm{Re}_{\delta_\theta} = 10^3$.

Experiments by Zagarola and Smits [689], in a pipe with compressed air, already introduced in Sect. 1.4.2, cover a remarkable range of Reynolds numbers with three orders of magnitude $3.2 \times 10^4 \leq \mathrm{Re}_D \leq 3.5 \times 10^7$. Mean velocity profiles are represented in inner variables in Fig. 3.9. The extension of the log-law towards the pipe axis when the Reynolds number increases is again well illustrated. Note that the drop in the central region of the pipe is associated with the crossing of the pipe axis by the probes.

The determination of all the constants in the log-law requires a measurement of the friction velocity independently of the velocity profile. For boundary layers, the friction velocity is usually estimated from the measurement of the friction coefficient C_f by using a hot film measuring device, a Preston tube or miniature weight-measuring wall devices. For confined flows, this can be carried out more accurately through the pressure drop, see for instance expression (3.3) established for the channel flow. By compiling many recent experiments at high Reynolds number [651], it appears that the von Kármán constant κ does not seem to be a universal constant, even for canonical flows. For a zero-pressure-gradient boundary layer, the two coefficients of the log-law (3.13) are taken to be $\kappa \simeq 0.384$ and $B \simeq 4.17$, as shown in Fig. 3.7. The classical value recommended in many textbooks for the von Kármán constant, $\kappa \simeq 0.41$, is a value found for pipe flows, as illustrated in Fig. 3.9.

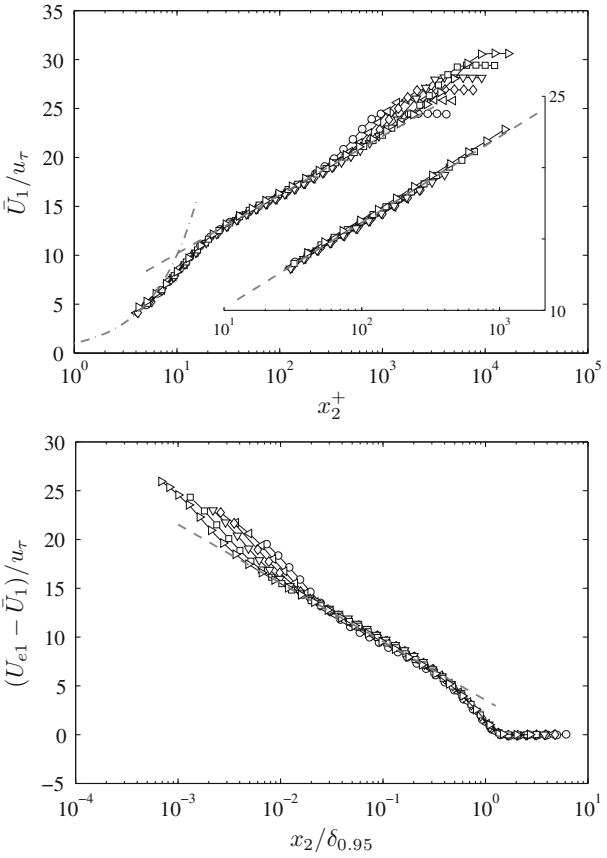

$\mathrm{Re}_{\delta_{0.95}}$	1.7×10^4	2.8×10^4	4.3×10^4	6.9×10^4	1.1×10^5	1.9×10^5
$\mathrm{Re}_{\delta_\theta}$	2.5×10^3	4.3×10^3	6.5×10^3	1.0×10^4	1.7×10^4	2.7×10^4
$\mathrm{Re}^+_{\delta_{0.95}}$	684	1092	1594	2462	3944	6147
	○	◁	◇	▽	□	▷

Fig. 3.7 Mean velocities profiles in a zero-pressure-gradient boundary layer on a flat plate. *Top*, velocity profile in inner scales, -·-·- viscous sublayer law (3.10), – – – log-law (3.13) with $\kappa \simeq 0.384$ and $B \simeq 4.17$, and insert for the range $x_2^+ \geq 30$ and $x_2/\delta \leq 0.2$. *Bottom*, velocity profile in outer scales, – – – wake law (3.14) with $\kappa \simeq 0.384$ and $A \simeq 3.54$. Reynolds numbers are defined by $\mathrm{Re}_{\delta_{0.95}} = U_{e1}\delta_{0.95}/\nu$, $\mathrm{Re}_{\delta_\theta} = U_{e1}\delta_\theta/\nu$ and $\mathrm{Re}^+_{\delta_{0.95}} = u_\tau\,\delta_{0.95}/\nu$, $\delta_{0.95}$ is the wall distance where the velocity is 95 % of the free-stream velocity U_{e1}. Data from Osterlünd [654, 655]

3.4.3 The Balance Between Production and Dissipation

In Chap. 2, the approximate local balance between production and dissipation has already been mentioned regarding the turbulent kinetic energy budget computed

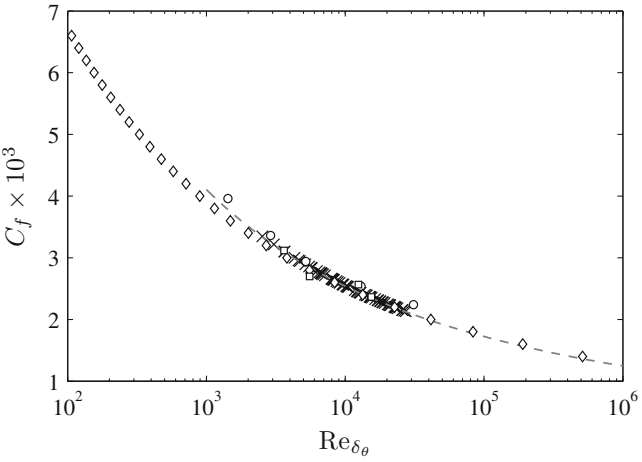

Fig. 3.8 Local skin-friction coefficient C_f as a function of the Reynolds number $\mathrm{Re}_{\delta_\theta}$ for a zero-pressure-gradient boundary layer over a flate plate. Experimental data, $\times$ Osterlünd [654], $\circ$ De Graaff and Eaton [605], $\square$ Andreopoulos et al. [587], $\diamond$ Coles [601] and **- - -** C_f fitted Coles-Fernholtz relation [650, 654] $C_f = 2\left[(1/\kappa)\ln(\mathrm{Re}_{\delta_\theta}) + C\right]^{-2}$ with $\kappa = 0.384$ and $C \simeq 4.08$

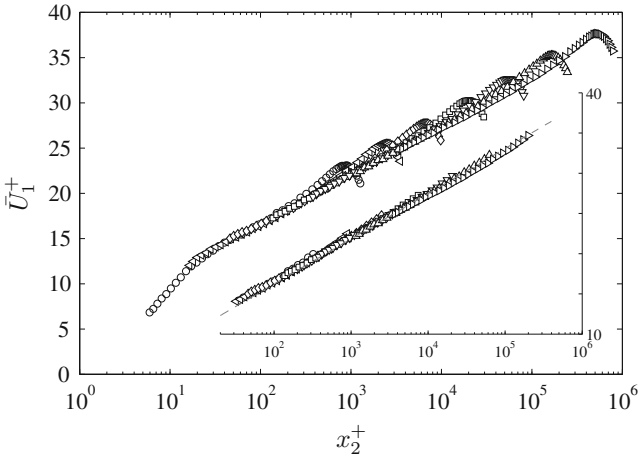

Fig. 3.9 Mean radial velocity profiles in a turbulent pipe flow of diameter $D = 2R$ using inner scaling variables, as a function of the Reynolds number $\mathrm{Re}_D = U_d D/\nu = 3.2 \times 10^4 \circ$; $9.9 \times 10^4 \triangleleft$; $3.1 \times 10^5 \diamond$; 1.0×10^6 $\square$; 3.1×10^6 $\triangledown$; $1.0 \times 10^7 \triangle$; $3.5 \times 10^7 \triangleright$. Insert for the range $x_2^+ \geq 30$ and $x_2/\delta \leq 0.2$ is also shown, and the log-law (3.13) is plotted in *dashed line*, with $\kappa = 0.41$ and $B = 5.0$. Data from Zagarola and Smits [689] (Princeton *superpipe*)

for a channel flow, and reported in Figs. 2.7 and 2.8. This balance is observed for $x_2^+ \geq 30$ and $x_2/h \leq 0.2$, that is in the log-law region of the mean velocity profile. In Fig. 3.10, the ratio of production to homogeneous dissipation obtained for several Reynolds numbers, is plotted as a function of the distance to the wall in inner scale

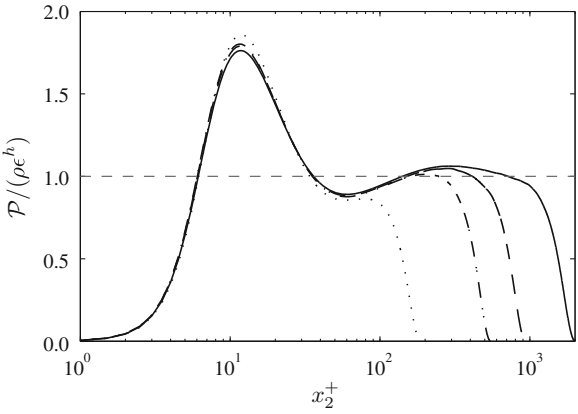

Fig. 3.10 Ratio of production to homogeneous dissipation as a function of the distance to the wall in inner scale, for different Reynolds number in a plane channel flow. ····· $\mathrm{Re}^+ = 180$, –·–·– $\mathrm{Re}^+ = 550$, – – – $\mathrm{Re}^+ = 950$, —— $\mathrm{Re}^+ = 2003$. Numerical data from Hoyas and Jiménez [621, 622]

using the database of Hoyas and Jiménez [621, 622]. On can easily observe that the interval over which production balances dissipation, i.e. $\mathcal{P}/(\rho\epsilon^h) \simeq 1$, increases with the Reynolds number, corresponding to the extension of the log-law region. This balance between production and dissipation holds also for pipe flows, as shown numerically by Eggels et al. [609], for instance, with a systematic comparison of their simulations with those of a plane channel flow at $\mathrm{Re}^+ = 180$. No major difference was observed.

This result is also confirmed by experiments, even though they are difficult to realize. Historically, the turbulent kinetic energy budget in a pipe turbulent flow established by Laufer [637] is one of the first insightful experimental studies, and is redrawn in Fig. 3.11, where the notations of Sect. 2.4.2 have been used. The production term $\mathcal{P}$ and the dissipation term ϵ^h are obtained with a relatively good accuracy. Near the pipe axis, one can clearly observe that the turbulent activity is reduced, but the dissipation subsists, $\epsilon^h \neq 0$, even if $\mathcal{P} = 0$. The transfer term T is difficult to measure and has usually an important error bar. Finally, the pressure

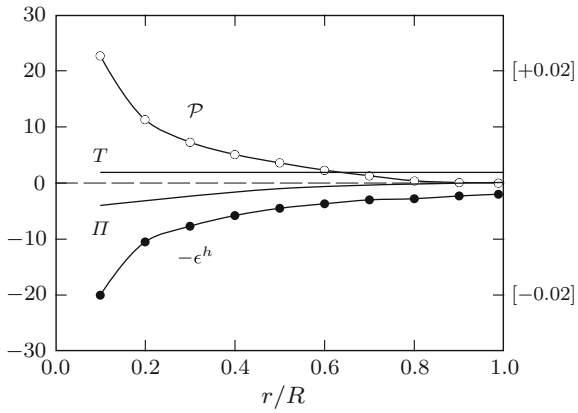

Fig. 3.11 Turbulent kinetic energy budget in the central region of a pipe flow at Reynolds number $\mathrm{Re}_D = 5 \times 10^4$ or $\mathrm{Re}^+ = 1050$, r is the distance to the wall. *Symbols* are measurements by Laufer [637]. All terms are made dimensionless using the radius R and u_τ, and the corresponding values in wall units are indicated in *brackets at right*.

term, $\Pi^d = \partial_{x_i}\overline{u_i' p'}$ in Eq. (2.20) can not directly be measured and is estimated by imposing the budget closure.

The simplification of the turbulent kinetic energy to the balance between production and dissipation implies the existence of a local equilibrium in space. The log-law region appears therefore somewhat isolated from the influence of the wall as well as of the central zone for a channel or pipe flow, or of the edge of a boundary layer, since all the transfer terms are negligible.

Finally, when wall function methods are used to solve averaged Navier-Stokes equations in engineering problems, see Chap. 9, the first mesh point normal to the wall is chosen inside the log-law region. The value of the mean velocity which must be imposed at this point as a boundary condition is then determined using the expression of the log-law combined with the balance between production and dissipation. By this way, grid points are saved since the viscous sublayer is not meshed. An example is provided in Chap. 9 for the k_t–ϵ turbulence model.

3.4.4 Kolmogorov Length Scale

Variation of the Kolmogorov length scale l_η defined as the smallest possible scale related to nonlinear effects, see Sect. 1.3.1, can be estimated in the log-law region. The estimation of l_η is obtained by writing that the order of magnitude of the dissipation is

$$\epsilon = \frac{1}{\rho}\overline{\tau_{ij}'\frac{\partial u_i'}{\partial x_j}} \sim \nu\left(\frac{u_\eta}{l_\eta}\right)^2$$

and by noting that the Reynolds number associated with Kolmogorov's scales is of order unity, that is $l_\eta u_\eta/\nu \sim 1$. The combination of these two relations leads to $l_\eta = (\nu^3/\epsilon)^{1/4}$. Moreover, an expression of ϵ can be derived by writing the balance between production and dissipation in the log-law. Approximating $-\overline{u_1' u_2'}$ by u_τ^2 and $d\bar{U}_1/dx_2$ by $u_\tau/\kappa x_2$ in the production term yields to

$$\rho\epsilon \simeq \mathcal{P} \simeq -\rho\overline{u_1' u_2'}\,\frac{\partial \bar{U}_1}{\partial x_2} \simeq \rho u_\tau^2 \times \frac{u_\tau}{\kappa x_2}$$

from which it follows that $\epsilon \simeq u_\tau^3/\kappa x_2$. The evolution of the Kolmogorov length scale l_η^+ is thus given by,

$$l_\eta^+ = (\kappa x_2^+)^{1/4} \tag{3.17}$$

3.5 The Buffer Layer

One can clearly see in Fig. 3.10 that $\mathcal{P} \gg \epsilon^h$ over the range $6 \leq x_2^+ \leq 20$. This region is located between the viscous sublayer $x_2^+ \leq 5$, and the log-law region $x_2^+ \geq 30$, and is termed the buffer layer. The same observation can be made in Fig. 2.7 which deals with the turbulent kinetic energy budget computed for a channel flow. This result can be easily interpreted if one remembers that the production term is $-\rho\overline{u_1' u_2'}\partial\bar{U}_1/\partial x_2$. Indeed some distance from the wall must be introduced so that the Reynolds stress $-\rho\overline{u_1' u_2'}$ can be generated—it is zero at the wall—but not too much so that the mean velocity gradient $\partial\bar{U}_1/\partial x_2$ can stay high—it is the highest at the wall.

Note that the intersection point between the viscous sublayer and the log-law region must satisfy,

$$x_2^+ = \frac{1}{\kappa}\ln x_2^+ + B$$

which leads to $x_2^+ \simeq 10.2$ with the values of κ and B associated with a zero-pressure-gradient boundary layer, see Table 3.1. This value corresponds to the production peak observed in Fig. 3.10. Moreover, roughly half of the turbulence production occurs between the wall and the beginning of the log-law region. This can be verified by integrating the cumulative production term $\mathcal{P}$ from the wall using numerical data available for the channel flow, refer to Fig. 3.10 for instance. As already mentioned, this region represents a very small part of the boundary layer at high Reynolds numbers. Since a large part of the turbulence production takes place very close to the wall, it is interesting to investigate this region in more detail.

It is now well established both experimentally and numerically that the viscous sublayer is dominated by quasi-streamwise vortices, associated with alternating low and high speed streaks. Streaks are sinuous and narrow regions elongated in the streamwise direction, in which the longitudinal velocity is lower or higher than the local mean velocity $\bar{U}_1(x_2)$. They have been experimentally identified by Kline et al. [633] and Kim et al. [630] among others [664]. The typical length of streaks is $\lambda_1 \simeq 15\delta - 20\delta$, and the mean spacing between low speed streaks is about $\lambda_3^+ \simeq 100$ at $x_2^+ \simeq 10$, with a lognormal distribution and is found independent of the Reynolds number [664, 674]. A general view obtained by numerical simulation is shown in Fig. 1.5. Low speed streaks slightly lift away from the wall in the buffer region and finally break up in a so-called bursting process. Bursts consist of violent intermittent events such as ejections and sweeps, corresponding respectively to outflow of low-speed fluid from the wall and inflow of high-speed fluid toward the wall. A typical joint probability density function $P_{u_1' u_2'}$ of the shear Reynolds stress

$$-\overline{u_1' u_2'} = -\iint u_1' u_2' P_{u_1' u_2'} du_1' du_2'$$

is drawn in Fig. 3.12b. Ejection events of low-speed fluid correspond to the Q_2 quadrant, for which $u_1' < 0$ and $u_2' > 0$, and similarly sweep events of high-speed

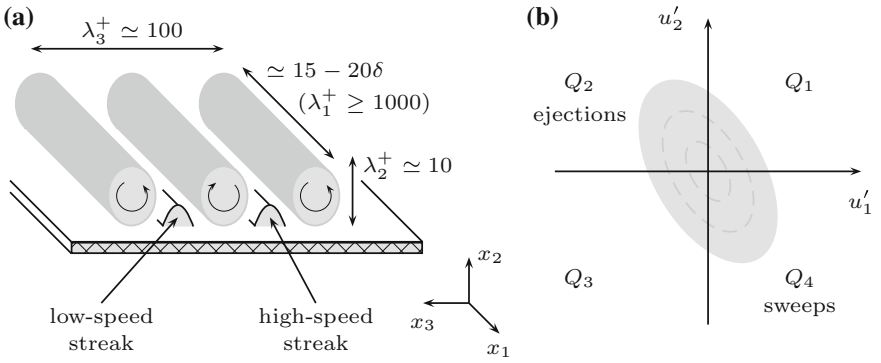

Fig. 3.12 **a** Sketch of low and high speed streaks (not to scale) generated by counter-rotating flows, the streamwise vorticity in gray is associated with successive hairpin vortices attached to the wall. **b** Joint probability density function $P_{u_1'u_2'}$ of the Reynolds stress $-\overline{u_1'u_2'}$ illustrating privileged events in the second and fourth quadrants of the $u_1' - u_2'$ plane [585]

fluid are associated with the Q_4 quadrant [686]. In these two quadrants Q_2 and Q_4, the production term $\mathcal{P}$ is positive, but ejection events dominate in the region $x_2^+ \geq 12$ and are mainly responsible of the turbulent kinetic energy production.

Generation of streaks by two consecutive counter-rotating vortices can be reasonably explained by the advection of fluid from a sheared mean flow, as illustrated in Fig. 3.12a. Formation of streamwise vortices, which have a longitudinal spacing of order $l_1^+ \simeq 400$, by streaks is currently much less well understood. Self-sustaining mechanisms of wall turbulence have nevertheless been proposed as a possible scenario [624, 658], and would provide new concepts of flow control to achieve drag reduction.

The presence of hairpin-shaped or horseshoe vortices is also another characteristic of wall-bounded flows [586, 619]. A general conceptual view has been offered by Adrian [585], and is reproduced in Fig. 3.13, the reader should refer to Robinson [664] for a review on conceptual models. Birth of these structures is found in the buffer region, and they are observed in the logarithmic region with an inclination angle of about 45° to the wall, corresponding to the principal direction of stretching in a shear flow. These structures are strongly elongated at high Reynolds number since the size of the vortex core scales with the viscous length l_ν while its length scales with δ. The whole evolution of such a structure requires a longitudinal distance of approximately 4δ. A new vortex however appears before and a direct instantaneous view therefore reveals more than one structure. Their spacing is about $\Delta x_1^+ \simeq 200$ near the wall and $\Delta x_1^+ \simeq 140$ in the logarithmic region, in agreement with the local convection velocity and leading to hairpin vortex packets [585, 599] and an inclination angle θ. Hairpin vortices are called coherent structures because they possess a sufficiently long life time to define an organised motion [585]. An important topic is the identification of such structures through the localization of vortices, see Sect. 5.9, or by using a proper orthogonal decomposition, see Sect. 6.7.

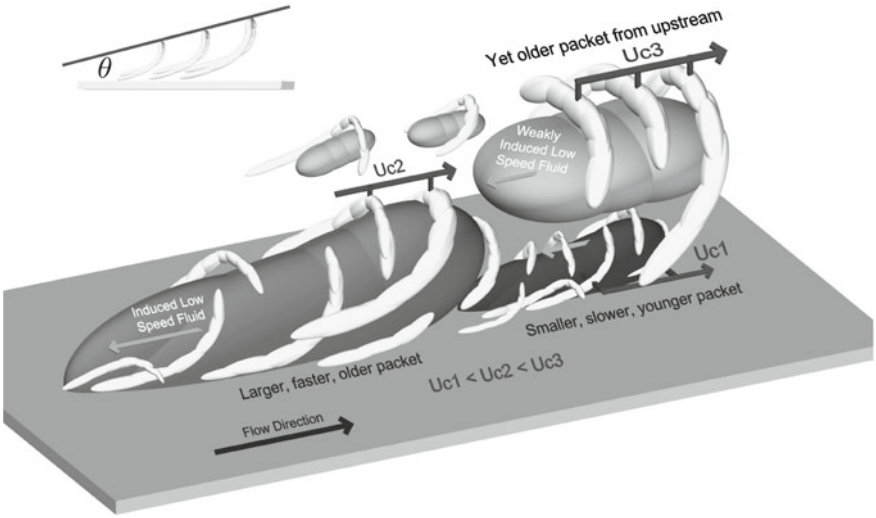

Fig. 3.13 Schematic view of hairpin vortices attached to the wall and growing up, from Adrian et al. [586]. See also Fig. 3.14 for angle $\theta \simeq 18°$

3.6 Free Edges

Far from the walls, the main difference between boundary layers and core regions of pipes or channels comes from the edges exhibited by the first ones. Figure 3.14 illustrates the main feature of a turbulent boundary layer with bulges connected to the hairpins issued from the main energetic part of the boundary layer, namely the buffer layer. Bandyopadhyay [590] has developed a simple model to explain the value of the inclination angle $\theta \simeq 18°$ of the interface slope displayed in Figs. 3.13 and 3.14.

An instantaneous view of the vorticity field through isosurfaces of Q-criterion colored by the wall distance is shown in Fig. 3.15. The turbulent field has been obtained by a compressible direct numerical simulation, and gives an opportunity to mention the importance of numerical simulations in the investigation of near wall turbulence. In this figure, streamwise vortices associated with streaks are visible very close to the wall (dark gray) and the head of some hairpin vortices (light gray) can also be distinguished.

3.6.1 Turbulence Near the Free Edge of Boundary Layers

The outer region of a boundary layer approximately spreads from $x_2/\delta = 0.5$ to $x_2/\delta = 1.2$. It matches the deep notches of the boundary layer edge, as observed in Fig. 3.14. The signal recorded by a sensor is then alternatively turbulent and non

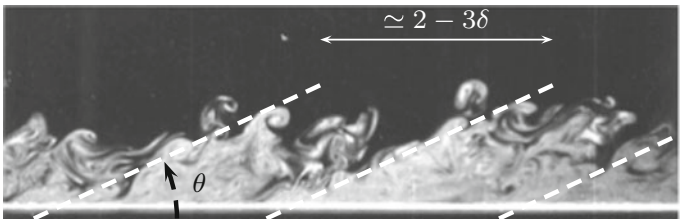

Fig. 3.14 Instantaneous side view of a boundary layer on a flat plate, the external velocity is $U_{e1} = 2.1\,\mathrm{m}\cdot\mathrm{s}^{-1}$, the thickness is $\delta = 7$ cm, the resulting Reynolds number is $\mathrm{Re}_\delta = U_{e1}\delta/\nu \simeq 10^4$, and the friction velocity is $u_\tau = 0.1\,\mathrm{m}\cdot\mathrm{s}^{-1}$ The visualization is obtained by seeding the air flow with incense particles and by illuminating the flow with a laser sheet. The free boundary is marked by large indentations. Note that three-dimensional structures can be folded and cut by the laser sheet. In this experiment, the transition to turbulence is triggered by a thin wire located upstream. Courtesy of Faouzi Laadhari (LMFA)

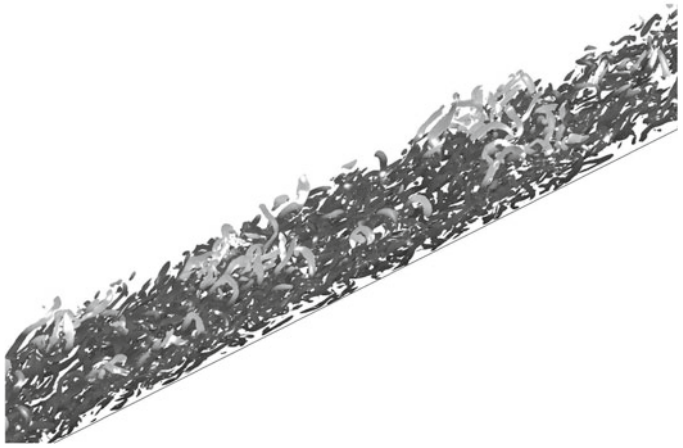

Fig. 3.15 Direct numerical simulation of a boundary layer over a flate plate. The Reynolds number is $\mathrm{Re}_{\delta_\theta} \simeq 1200$ and the Mach number is $M = 0.9$. The size of the displayed domain is $67\delta_\theta$ in the streamwise direction and $10\delta_\theta$ in the spanwise direction. Instantaneous iso-surfaces of Q-criterion field (see Sect. 5.9) colored by wall distance. Courtesy of Olivier Marsden (LMFA)

turbulent, due to passage of notches and bulges over the probe. Figure 3.16 offers an example of such a signal provided by a hot wire anemometer.

The main characteristic to be introduced is the intermittency factor, usually denoted γ. It is defined as the averaged fraction of time during which the sensor receives a turbulent signal, and therefore $0 \leq \gamma \leq 1$. The lower value $\gamma = 0$ matches a non turbulent signal, while $\gamma = 1$ matches a fully turbulent one. As an illustration, the intermittency factor corresponding to the signal plotted in Fig. 3.16 is $\gamma \simeq 0.06$ for a sensor located at $x_2/\delta = 0.9$.

Precise measurement of γ requires a spy sensor fit for turbulence detection. Kovasznay et al. [634] used two parallel and close hot wires in order to obtain

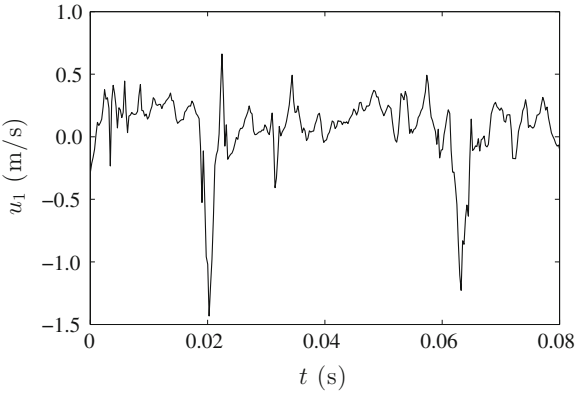

Fig. 3.16 Time signal recorded by a hot wire anemometer located at $x_2/\delta = 0.9$ of a boundary layer in air. The thickness is $\delta = 2.07 \times 10^{-2}$ m and the free stream velocity is $U_{e1} = 8\,\mathrm{m} \cdot \mathrm{s}^{-1}$, which results in a Reynolds number $\mathrm{Re}_\delta = 1.1 \times 10^4$. Two strong bursts coming from inside the boundary layer are visible, with $u_1' < 0$. The skewness factor is therefore negative $S_{u_1'} \simeq -1.6$ and the flattening factor is quite high $T_{u_1'} \simeq 6.3$. More regular fluctuations induced by the free boundary are also visible. The intermittency factor is $\gamma \simeq 0.06$. Data provided courtesy of Faouzi Laadhari (LMFA)

an estimate of $\partial u_1'/\partial x_2$, a part of the fluctuation component of the velocity rotational ω_3' along x_3. Other authors employed a slight thermal marking of the fluid particle belonging to the boundary layer by heating the underlaying wall [545, 589], a technique already developed by Sunyach [495], for the free boundary of a jet. This technique is particularly useful if the boundary layer develops itself in an outer flow which is already turbulent. In any case, a threshold criteria must be set after having examined signal levels to calculate the intermittency factor.

The spy sensor provides a temporal signal $I(t)$ which changes its value from 0 to 1 when a turbulent burst begins to pass, and from 1 to 0 when the end of the burst is achieved. The average of the intermittency function $I(t)$, of course, is γ. A trigger window can be generated by the signal $I(t)$ in order to separate turbulent and non turbulent contributions, and therefore to perform conditional averaging. Various examples can be found in Kovasznay et al. [634] for $\bar{U}_1$, $\bar{U}_2$, $\overline{u_1'^2}$, $\overline{u_1' u_2'}$, as well as the velocity of the free edge of the boundary layer, estimated around $0.97 U_{e1}$, and the privileged locations for entrainment from the free stream, localised in between bursts.

As an illustration, the transverse component of the mean velocity $\bar{U}_2$ is here considered, as shown in Fig. 3.17. Inside turbulent bursts, the transverse velocity $\bar{U}_2^{\mathrm{int}}$ is positive, which corresponds to strong fluid ejections coming from the wall region. The transverse velocity $\bar{U}_2^{\mathrm{ext}}$ is however negative in the potential flow outside of the boundary layer edge, which corresponds to entrainment of external fluid. As a conclusion, let us remember that $\bar{U}_2$ is always slightly positive, even far from the edge of a boundary layer. By once again assuming that the free stream velocity U_{e1} is constant, the integration of the continuity equation leads to

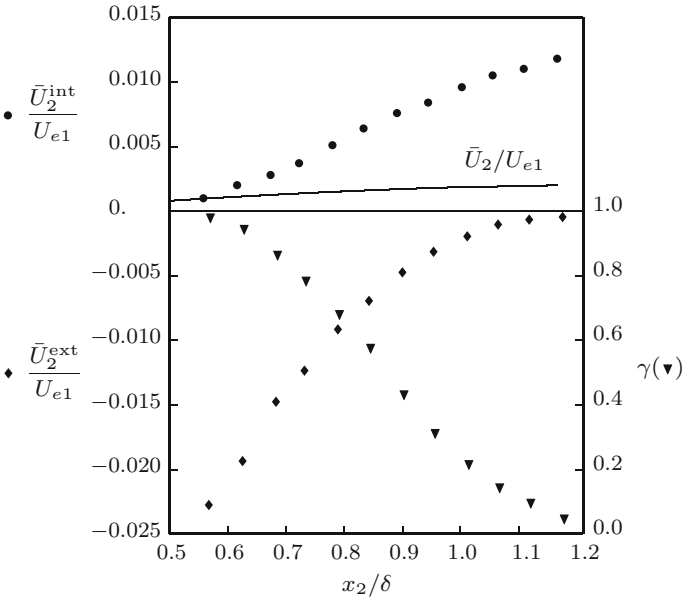

Fig. 3.17 Conditional averaging in the external zone of a boundary layer at $\mathrm{Re}_\delta \simeq 2.9 \times 10^4$. By denoting $\bar{U}_2^{\rm int}$ (•) and $\bar{U}_2^{\rm ext}$ (♦) the fluid velocity in the internal and external edge of a boundary layer, one has $(\bar{U}_2^{\rm int} - \bar{U}_2)/U_{e1} > 0$ inside bursts, and $(\bar{U}_2^{\rm ext} - \bar{U}_2)/U_{e1} < 0$ in the potential outside flow. The intermittent factor γ (▼) is about unity inside the turbulent boundary layer and decreases near its edge. Data from Kovasznay et al. [634]

$$U_{e2} \equiv \bar{U}_2(x_2 \to \infty) = -\int_0^\infty \frac{\partial \bar{U}_1}{\partial x_1} dx_2 = -\int_0^\infty \frac{\partial \left(\bar{U}_1 - U_{e1}\right)}{\partial x_1} dx_2$$

and finally

$$U_{e2} = U_{e1} \frac{d\delta_1}{dx_1} \quad \text{with} \quad \delta_1 = \int_0^\infty \left(1 - \frac{\bar{U}_1}{U_{e1}}\right) dx_2$$

where δ_1 is the boundary layer displacement thickness, which increases with x_1.

Finally, viscosity is expected to be negligible in the outer layer, and the log-law velocity profile is then rather expressed as a defect or wake law (3.14) in the overlap region, as also shown in Fig. 3.7. From various experimental data, Clauser [600] and Coles [602] have proposed to describe the end of the wake law as,

$$\frac{\bar{U}_1}{u_\tau} = \frac{1}{\kappa} \ln\left(\frac{u_\tau x_2}{\nu}\right) + B + \frac{2\Pi}{\kappa} w\left(\frac{x_2}{\delta}\right)$$

where w is a universal function associated with normalization conditions, and Π a parameter. This discussion has been recently revisited and extended by Chauhan et al. [596] who provide a full composite profile fitted to recent experimental data.

3.6.2 Turbulence in the Core Region of Channels or Pipes

An important issue regarding long pipe or channel flows is to define the fully developed turbulent state. One of the best indicator to identify this state is the skewness coefficient $S_{u_1'}$ of the longitudinal fluctuating velocity,

$$S_{u_1'} = \overline{u_1'^3}/\left(\overline{u_1'^2}\right)^{3/2}$$

already introduced in Chap. 1, see expression 1.4. This physical quantity seems complex but has the advantage of varying with x_1, much more rapidly than other classical quantities such as mean velocities or turbulence intensities. This results of the alternation between turbulent bursts bringing high contributions $u_1' < 0$ and laminar and more rapid fluid bringing small contributions $u_1' > 0$, just before the junction of the boundary layers associated with each wall of a plane channel, or with the peripheral walls of a circular duct. An odd order momentum of the probability distribution of the u_1' velocity fluctuation such as $S_{u_1'}$, equal to zero for a Gaussian process, will thus take a negative value of about $S_{u_1'} \simeq -1.8$. After the junction, the flow reorganizes and the existence of initial boundary layers is lost by the turbulent flow. During this process, the absolute value of $S_{u_1'}$ appreciably decreases but the value along the axis remains negative with $S_{u_1'} \simeq -0.40$. More data on this topic can be found in Comte-Bellot [603]. In addition, the skewness coefficient $S_{u_2'}$ of the transverse velocity fluctuations u_2' remains positive, revealing the diffusion of the kinetic energy term $\overline{u_2'^2}$ by u_2' fluctuations, from the wall towards the central zone. The maximum $S_{u_2'} = +0.40$ is reached for $x_2/h \simeq 0.70$, illustrating once more how turbulence has non Gaussian statistics. Of course, $S_{u_2'} = 0$ on the channel or duct axis by symmetry.

Even for a fully turbulent flow, there are two production zones of turbulent kinetic energy, near each wall for a plane channel or all around the circumferential wall for a pipe. As a result, an alternating of structures appears in the central zone. Some experiments offer the possibility to label the origin of structures, for example by locating events $u_2' > 0$ and $u_1' < 0$ associated with each wall. It can then be inferred that structures coming from a given wall go beyond the symmetry plane, or the axis for a pipe, see Sabot and Comte-Bellot [667] and Antonia et al. [589].

3.6.3 Other Results

Many turbulence statistics have been studied in the wall region in order to determine the velocity fluctuation intensity, the spectral distribution of the kinetic energy or the spatio-temporal coherence of the turbulent field for example. For vibroacoustical problems, pressure fluctuations at the wall are also of interest. In what follows, some physical quantities are considered with the velocity fluctuation intensity $\overline{u_\alpha' u_\alpha'}/u_\tau^2$ and the integral length scales.

Figure 3.18 provides for usual practical Reynolds numbers, that is $\mathrm{Re}_h \geq 10^5$, the velocity fluctuation intensities denoted $u^+_{\alpha\mathrm{rms}}$ for $\alpha = 1, 2, 3$ and defined as the square root of $\overline{u'_\alpha u'_\alpha}/u_\tau^2$. Note firstly that all values of $u^+_{\alpha\mathrm{rms}}$ are approximately between 1 and 3, reflecting that the friction velocity u_τ is the suitable scale for the Reynolds tensor. There is a quasi-independence of the Reynolds number using this scale. Secondly, one has $u^+_{1\mathrm{rms}} > u^+_{3\mathrm{rms}} \geq u^+_{2\mathrm{rms}}$ and $u^+_{1\mathrm{rms}}$ reaches its maximum around 2.8 for $x_2^+ \simeq 12$. This anisotropy is expected since only the longitudinal fluctuating velocity is fed by the mean flow, as explained in Chap. 2. For smaller Reynolds numbers such as $3 \times 10^3 \leq \mathrm{Re}_h \leq 4 \times 10^4$, turbulence intensity profiles are independent of Re_h for $x_2^+ \geq 50$. This issue is thoroughly illustrated by the experiments of Wei and Willmarth [687] and of De Graaff and Eaton [605].

Large spatial scales of turbulence have already been mentioned, notably in Sect. 1.4 in order to highlight the efficiency of turbulent transport for momentum, heat or concentration as well as for the definition of a turbulent viscosity in Chap. 2 through a mixing length. A more explicit definition is now introduced and some orders of magnitude are then provided for wall turbulence. A large length scale refers to the notion of spatial coherence of velocity components at two points defined by a correlation coefficient,

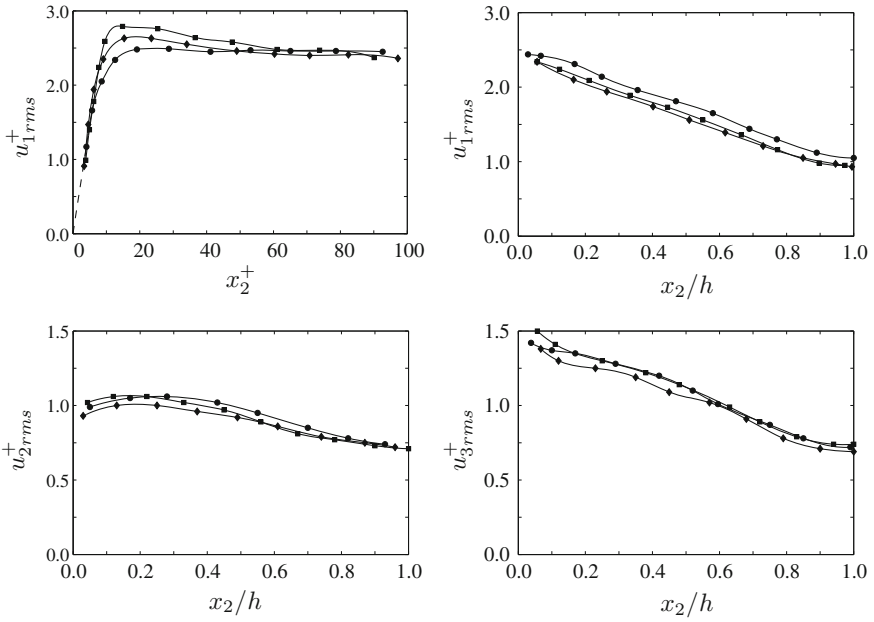

Fig. 3.18 Velocity fluctuation intensity ${u'_\alpha}^+$ in a plane channel of width $2h$ at ■ $\mathrm{Re}_h = 57{,}000$, ♦ $\mathrm{Re}_h = 120{,}000$ and ● $\mathrm{Re}_h = 230{,}000$, measured at $x_1 = 118h$ by Comte-Bellot [604]

$$\mathcal{R}_{\alpha\alpha}^{(k)} = \frac{\overline{u'_\alpha(x_k)u'_\alpha(x'_k)}}{\sqrt{\overline{u'^2_\alpha}(x_k)}\sqrt{\overline{u'^2_\alpha}(x'_k)}} \tag{3.18}$$

where $\alpha = 1, 2$ or 3 indicates the considered velocity component, there is no implicit summation over repeated Greek indices, and $k = 1$, 2 or 3 indicates the selected direction for the separation between the two measurement points $\boldsymbol{x}$ and $\boldsymbol{x}'$. Moreover, the choice of $x'_k \geq x_k$ is most often retained, which for $k = 2$ indicates that the second point is further from the wall than the first one. This information is important, as the turbulent field is non-homogeneous along the normal direction to the wall. For a given point $\boldsymbol{x}$, moving closer or further from the wall through $\boldsymbol{x}'$ is therefore not equivalent. Expression (3.18) leads to the definition of a correlation length relative to the α component and in the direction k, that is

$$L_{\alpha\alpha}^{(k)} = \int_0^\infty \mathcal{R}_{\alpha\alpha}^{(k)}\, d(x'_k - x_k) \tag{3.19}$$

There are 9 possible integral length scales $L_{\alpha\alpha}^{(k)}$ but this complexity has been well explored, both for boundary layers [616, 685], channel [604] and pipe flows [609].

For the plane channel, some results are now summarized below. For the longitudinal components and in the wall zone for $x_2/h \simeq 0.1$, the longitudinal length scale $L_{11}^{(1)} \simeq 0.80h$ is clearly larger than the transverse scales, $L_{11}^{(2)} \simeq 0.15h$ and $L_{11}^{(3)} \simeq 0.05h$, where h is still the half-width of the channel. The longitudinal expansion of the $\mathcal{R}_{11}^{(1)}$ correlation is imposed by the shear induced by the mean velocity gradient $\partial\bar{U}_1/\partial x_2$. An important negative loop induced by the conservation of mass, is necessarily present for $\mathcal{R}_{11}^{(3)}$. As a result, a smaller value of the integral length scale is then found.

Further from the wall, $L_{11}^{(1)}$ increases up to around $x_2/h \simeq 0.3$, and then decreases down to $L_{11}^{(1)} \simeq 0.60h$ on the median plane for $x_2/h \simeq 1$. Therefore, the largest structures are not in the central region of the channel. This can be explained by the interaction of structures issuing from different parts of the wall as described in the previous section.

Finally, regarding components normal to the wall, integral length scales are found to be smaller, with for example $L_{22}^{(1)} \simeq 0.10h$, $L_{22}^{(2)} \simeq 0.12h$, and $L_{22}^{(3)} \simeq 0.03h$ at $x_2/h = 0.1$. An instructive result is, for instance, revealed by comparing the mixing length l_m and $L_{22}^{(2)}$, the most pertinent scale for a transverse transfer ensured by u'_2 fluctuations. With the simplest expression of $l_m = \kappa x_2$, one has $l_m/L_{22}^{(2)} \simeq \kappa/1.2 \simeq 0.33$, at $x_2/h \simeq 0.1$. The mixing length l_m is thus always smaller than the integral length scale $L_{22}^{(2)}$, but of the same order of magnitude, which is expected. The u'_2 velocity component must indeed be conserved over the entire mixing length, corresponding to a near unity correlation coefficient. This is possible only on a length shorter than an integral scale, where the entire correlation curve from 1 down to 0 is taken into account.

Other correlations involving different velocity components and even time delays between the two measurement points $\boldsymbol{x}$ and $\boldsymbol{x}'$ are of interest to better understand wall

turbulence [612, 667]. All these results should also be examined in the simpler case of an homogeneous and isotropic turbulence, without any mean velocity gradient effect, refer to Chap. 6.

3.7 Modeling for a Numerical Simulation

3.7.1 Mixing Length Model

This section is an introduction to turbulence modelling with the aim of numerically calculating the mean velocity profile of a channel flow. Equation (3.4) is used as a starting point in wall variables,

$$\frac{x_2}{h} - 1 - \frac{\overline{u_1' u_2'}}{u_\tau^2} + \frac{d\bar{U}_1^+}{dx_2^+} = 0$$

In order to solve this equation, a closure for the velocity correlation term $-\overline{u_1' u_2'}$ is required, which is usually performed through a turbulent viscosity ν_t, this approach has already been presented in Sect. 2.5. This yields,

$$-\frac{\overline{u_1' u_2'}}{u_\tau^2} = \nu_t^+ \frac{d\bar{U}_1^+}{dx_2^+} \qquad \text{where} \qquad \nu_t^+ = \frac{\nu_t}{\nu}$$

Of course, the expression of ν_t is yet to be determined, and this can be carried out by observing that $\nu_t \sim u' \times l_m$, e.g. the product of a characteristic velocity scale by a mixing or correlation length. Mixing length models are the simplest in this context, since they require no additional equation to solve. They are also known as algebraic or zero equation models, and have been introduced by Prandtl. A first assumption consists of supposing that the mixing length varies linearly with the distance to the wall, that is

$$l_m^+ \simeq \kappa x_2^+$$

where κ is the von Kármán constant, according to expression (3.16) of the mean velocity gradient. For the characteristic velocity scale u', it is assumed that the two time scales l_m/u' and $(d\bar{U}_1/dx_2)^{-1}$ are equals, which yields

$$u' = l_m \frac{d\bar{U}_1}{dx_2} \qquad \text{or} \qquad \frac{u'}{u_\tau} = l_m^+ \frac{d\bar{U}_1^+}{dx_2^+}$$

The turbulent viscosity is thus expressed as,

$$\nu_t^+ = \left(l_m^+\right)^2 \left|\frac{d\bar{U}_1^+}{dx_2^+}\right|$$

and finally, the shear Reynolds stress component is given by

$$-\frac{\overline{u_1' u_2'}}{u_\tau^2} = \left(l_m^+\right)^2 \left|\frac{d\bar{U}_1^+}{dx_2^+}\right| \frac{d\bar{U}_1^+}{dx_2^+}$$

To keep the algebra as simple as possible, only the region over which the total stress τ_t is constant is considered here, that is $x_2/h \ll 1$. The Reynolds number must be however high enough to include the log-law since $x_2^+ = (x_2/h)\,\mathrm{Re}^+ \gg 1$. Hence, the equation governing the mean velocity profile near the wall is

$$\left(\kappa x_2^+\right)^2 \left(\frac{d\bar{U}_1^+}{dx_2^+}\right)^2 + \frac{d\bar{U}_1^+}{dx_2^+} - 1 = 0$$

and the positive root of this quadratic equation is given by

$$\frac{d\bar{U}_1^+}{dx_2^+} = \frac{-1 + \sqrt{1 + 4\,(\kappa x_2^+)^2}}{2\,(\kappa x_2^+)^2} \geq 0 \tag{3.20}$$

In general, this equation is numerically solved by taking $\bar{U}_1^+ = 0$ at $x_2^+ = 0$ as initial condition. However, a tedious calculation can be performed in this simple case to obtain the analytical solution [8, 13],

$$\bar{U}_1^+ = \frac{1}{\kappa} \frac{1 - \sqrt{1 + 4\,(\kappa x_2^+)^2}}{2\,\kappa x_2^+} + \frac{1}{\kappa} \ln\left[2\kappa x_2^+ + \sqrt{1 + 4\,(\kappa x_2^+)^2}\right] \tag{3.21}$$

Expression (3.20) can also be simplified in the two following limit cases $x_2^+ \to 0$ and $x_2^+ \to \infty$. For $x_2^+ \to 0$, a Taylor expansion of the radical in the numerator yields

$$\frac{d\bar{U}_1^+}{dx_2^+} \to 1$$

and therefore, $U_1^+ = x_2^+$ as $x_2^+ \to 0$. This is the velocity law (3.10) found in the viscous sublayer, where molecular viscous effects are preponderant over turbulence. For $x_2^+ \to \infty$, the limit of (3.20) yields

$$\frac{d\bar{U}_1^+}{dx_2^+} \to \frac{1}{\kappa x_2^+}$$

Table 3.2 Behaviour of wall variables in the logarithmic region when using a mixing length model

$U_1^+ = \frac{1}{\kappa}\ln x_2^+ + B$	$\frac{dU_1^+}{dx_2^+} = \frac{1}{\kappa x_2^+}$	$\mathcal{P}^+ \simeq \epsilon^+$
$l_m^+ = \kappa x_2^+$	$\nu_t^+ = \kappa x_2^+$	$\mathcal{P}^+ = \frac{1}{\kappa x_2^+}$

which corresponds to the mean velocity gradient (3.16) found in the log-law. Table 3.2 sums up the behaviour of wall variables in the logarithmic region when using a mixing length model.

3.7.2 The van Driest Model

The model developed in the previous section is not quite satisfactory in practice. Indeed, even though the slope of the log-law is correctly predicted, the additive constant B in (3.13) is underestimated and does not match experimental values. Various modifications have been described in the literature [8]. They aim to reduce the turbulent stresses near the wall, and thus improve the connection with the viscous sublayer. The model proposed by van Driest [442] is one of the most efficient and also holds for compressible wall-bounded flows [441]. The mixing length is modified as follows,

$$l_m^+ = \kappa x_2^+ (1 - e^{-x_2^+/A_0^+}) \qquad \text{with} \qquad A_0^+ \simeq 26 \tag{3.22}$$

The mixing length l_m^+ then decreases as $(\kappa x_2^+)^2$, and therefore faster than κx_2^+ as $x_2^+ \to 0$. The shear Reynolds stress $-\overline{u_1' u_2'}^+$ varies as $(\kappa x_2^+)^4$, indicating its artificial damping near the wall, and the factor $1 - e^{-x_2^+/A_0^+}$ is usually called a damping function. Indeed, the shear Reynolds stress should vary as x_2^{+3} at the wall, as explained in the next section. The log-law is well reproduced with a correct value of the additive constant B, which is not possible by taking $l_m^+ = \kappa x_2^+$. Figure 3.19 illustrates these results. Velocity profiles are obtained by numerically integrating a generalisation of Eq. (3.20) to an arbitrary expression of mixing length l_m^+,

$$\frac{d\bar{U}_1^+}{dx_2^+} = \frac{-1 + \sqrt{1 + 4\,(l_m^+)^2}}{2\,(l_m^+)^2} \geq 0 \tag{3.23}$$

3.7.3 Asymptotic Behaviour Very Near the Wall

The knowledge of the asymptotic behaviour of turbulent statistical quantities near the wall, provides useful information for validating numerical simulations or for assess-

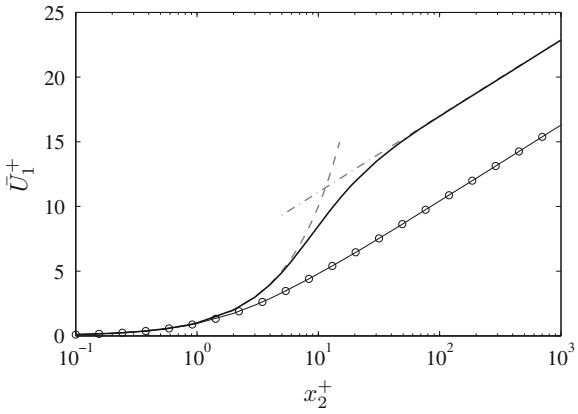

Fig. 3.19 Numerical integration of Eq. (3.23), —o— with the linear mixing length model $l_m^+ = \kappa x_2^+$ and, —— with the van Driest model (3.22). The viscous sublayer law and the log-law are in *dashed* and *mixed lines* respectively. The *open symbols* correspond to the analytical solution (3.21)

ing turbulence models [8, 387]. From a Taylor series of the fluctuating velocity field,

$$u_1' = \sum_n a_n x_2^n \qquad u_2' = \sum_n b_n x_2^n \qquad u_3' = \sum_n c_n x_2^n$$

as x_2 tends to zero, the following expressions can straightforwardly be derived for an incompressible flow near the wall,

$$\begin{cases} u_1' = a_1 x_2 + \cdots \\ u_2' = b_2 x_2^2 + \cdots \\ u_3' = c_1 x_2 + \cdots \end{cases} \qquad \text{with} \qquad b_2 = -\frac{1}{2}\left(\frac{\partial a_1}{\partial x_1} + \frac{\partial c_1}{\partial x_3}\right) \tag{3.24}$$

where all the coefficients are functions of x_1, x_3 and t. As an illustration, this yields for the Reynolds stress components $\overline{u_i' u_j'}$,

$$\overline{u_i' u_j'} \sim \begin{pmatrix} \overline{a_1^2}\, x_2^2 & \overline{a_1 b_2}\, x_2^3 & \overline{a_1 c_1}\, x_2^2 \\ \overline{a_1 b_2}\, x_2^3 & \overline{b_2^2}\, x_2^4 & \overline{b_2 c_1}\, x_2^3 \\ \overline{a_1 c_1}\, x_2^2 & \overline{b_2 c_1}\, x_2^3 & \overline{c_1^2}\, x_2^2 \end{pmatrix} \tag{3.25}$$

For the dissipation, the so-called Hanjalić and Launder [387] equality can be demonstrated,

$$\epsilon = \nu \frac{\partial^2 k_t}{\partial x_2^2} = \nu(\overline{a_1^2} + \overline{c_1^2}) = 2\nu \left(\frac{\partial \sqrt{k_t}}{\partial x_2}\right)^2 \quad \text{at} \quad x_2 = 0 \tag{3.26}$$

as well as that $\epsilon^h = \epsilon - 2\nu(\partial\sqrt{k_t}/\partial x_2)^2 \sim x_2^2$ as $x_2 \to 0$. These results are intensively used in turbulence modelling, see Sect. 9.2.6. They also can be checked

by direct numerical simulation of Navier-Stokes equations, as in the well documented case of the channel flow for instance [621, 622, 640, 642].

3.8 More Complex Boundary Layers

Various complex situations are encountered in practice, as rough walls, asymmetrical geometries, divergent or convergent pipes in the case of confined flows. For boundary layers, wall fluid injection used for the cooling of turbine blades or combustion chambers or wall curvatures effects for wing profiles in aeronautics can be mentioned. Furthermore, the external flow can also be turbulent.

In the following section, the case of a turbulent boundary layer developing on a flate plate in presence of a positive or adverse pressure gradient since a flow detachment can occur, is considered. In contrast with this case, a relaminarisation can occur when the flow is strongly accelerated. The momentum integral equation of von Kármán [22] links the different involved parameters of the boundary layer. It can be derived by integrating (3.5), which leads after some algebra to

$$u_\tau^2 = \frac{d}{dx_1}\left(U_{e1}^2 \delta_\theta\right) - \frac{1}{\rho}\frac{dP_e}{dx_1}\delta_1 \tag{3.27}$$

Thus, a positive pressure gradient induces a decrease of the friction velocity. It is even possible to maintain $u_\tau = 0$ by correctly adjusting the external pressure gradient, as shown by Stratford [679, 680]. Numerical simulations can also complete the picture by providing the instantaneous friction coefficient along the wall [649, 673].

Regarding attached boundary layers, various configurations [602, 670] have been also studied, in particular when an equilibrium is reached not only for the near wall region but also for the external zone [646, 672, 684] when the velocity defect law becomes self-similar. An equilibrium boundary layer requires a pressure gradient such that the so-called Rotta-Clauser [600, 666] parameter β

$$\beta = \frac{\delta_1}{\rho u_\tau^2}\frac{dP_e}{dx_1} = -\frac{\delta_c}{u_\tau}\frac{dU_{e1}}{dx_1} = \text{cst} \qquad \text{with} \qquad \delta_c = \int_0^\infty \frac{U_{e1} - U_1}{u_\tau} dx_2$$

is constant. In its second form, β matches the ratio of two time scales, one specific to the boundary layer δ_c/u_τ, and the other provided by the external flow $(dU_{e1}/dx_1)^{-1}$.

By taking a simplified expression [610, 646, 684] of the freestream velocity $U_{e1} \sim x_1^{-m}$ ensuring an equilibrium boundary layer, the following results can be established. First, the logarithmic law with reference to the wall as well as the standard values of constants are still observed. However, the interval over which this law holds as a function of x_2^+ diminishes as the pressure gradient increases. The wake region is more important and its equilibrium is difficult to reach. Secondly, there is another peak of turbulent kinetic energy production at $x_2/\delta \simeq 0.45$, with energy transfers

towards the wall and the outer region. Thirdly, turbulence intensities normalized by the friction velocity clearly increase compared to the case where there is no pressure gradient. This is expected since according to von Kármán's equation (3.27), the friction velocity u_τ can only decrease when $dP_e/dx_1 > 0$. As an illustration, for $\beta \simeq 20$ or equivalently $m = 0.22$, and near the second peak of kinetic energy production, the following values are observed [672]

$$\overline{u_1'^2}/u_\tau^2 \simeq 55 \quad \overline{u_2'^2}/u_\tau^2 \simeq 24 \quad \overline{u_3'^2}/u_\tau^2 \simeq 36 \quad -\overline{u_1'u_2'}/u_\tau^2 \simeq 16$$

Fourthly, the ratios of turbulence intensity between the various components keep values close to those obtained without any pressure gradient. For $x_2/\delta \simeq 0.45$, one has

$$\overline{u_2'^2}/\overline{u_1'^2} \simeq 0.44 \quad \overline{u_3'^2}/\overline{u_1'^2} \simeq 0.65 \quad -\overline{u_1'u_2'}/\sqrt{\overline{u_1'^2}}\sqrt{\overline{u_2'^2}} \simeq 0.44$$

This result tends to show that the turbulent kinetic energy redistribution mechanism between velocity components caused by the pressure fluctuations is preserved. A similar result is observed for the shear Reynolds stress, which can be useful for turbulence modelling.

3.9 Boundary Layer Equations*

Consider a two-dimensional incompressible mean flow with velocity components $\bar{U}_1(x_1, x_2)$ and $\bar{U}_2(x_1, x_2)$. By assuming that turbulence is homogeneous in the spanwide direction x_3, the Reynolds averaged Navier-Stokes equations are given by

$$\frac{\partial \bar{U}_1}{\partial x_1} + \frac{\partial \bar{U}_2}{\partial x_2} = 0 \tag{3.28}$$

$$\bar{U}_1\frac{\partial \bar{U}_1}{\partial x_1} + \bar{U}_2\frac{\partial \bar{U}_1}{\partial x_2} = -\frac{1}{\rho}\frac{\partial \bar{P}}{\partial x_1} - \frac{\partial \overline{u_1'^2}}{\partial x_1} - \frac{\partial \overline{u_1'u_2'}}{\partial x_2} + \nu\nabla^2\bar{U}_1 \tag{3.29}$$

$$\bar{U}_1\frac{\partial \bar{U}_2}{\partial x_1} + \bar{U}_2\frac{\partial \bar{U}_2}{\partial x_2} = -\frac{1}{\rho}\frac{\partial \bar{P}}{\partial x_2} - \frac{\partial \overline{u_1'u_2'}}{\partial x_1} - \frac{\partial \overline{u_2'^2}}{\partial x_2} + \nu\nabla^2\bar{U}_2 \tag{3.30}$$

The evolution of the mean flow field is assumed to be slow in the streamwise direction x_1 with respect to its evolution in the transverse direction, in agreement with experimental observations. To obtain the boundary layer approximations, the following scales are then introduced,

Furthermore the boundary layer thickening is small, which means that $\delta/L < 1$. To satisfy the conservation of mass (3.28), it is required that

U mean longitudinal velocity scale,
L longitudinal length scale,
V mean transverse velocity scale,
δ transverse length scale,
u fluctuating velocity scale

$$\frac{V}{\delta} \sim \frac{U}{L} \qquad \text{or equivalently,} \qquad V \sim \frac{\delta}{L} U$$

Governing equations can then be simplified as follows. Regarding Eq. (3.29), the order of magnitude is shown below each corresponding term

$$\begin{cases} \bar{U}_1 \dfrac{\partial \bar{U}_1}{\partial x_1} + \bar{U}_2 \dfrac{\partial \bar{U}_1}{\partial x_2} = -\dfrac{1}{\rho} \dfrac{\partial \bar{P}}{\partial x_1} - \dfrac{\partial \overline{u_1'^2}}{\partial x_1} - \dfrac{\partial \overline{u_1' u_2'}}{\partial x_2} + \nu \left(\dfrac{\partial^2}{\partial x_1^2} + \dfrac{\partial^2}{\partial x_2^2} \right) \bar{U}_1 \\ \qquad \sim \dfrac{U^2}{L} \qquad\qquad\qquad\qquad \sim \dfrac{u^2}{L} \quad \sim \dfrac{u^2}{\delta} \qquad \sim \nu \left(\dfrac{U}{L^2}; \dfrac{U}{\delta^2} \right) \end{cases} \tag{3.31}$$

To actually observe the development of a turbulent boundary layer, and not only a laminar one, the dominant term associated with the Reynolds stress tensor must be of the same order as the convection terms

$$\frac{u^2}{\delta} \sim \frac{U^2}{L} \qquad \text{or} \qquad u \sim \left(\frac{\delta}{L} \right)^{1/2} U$$

By taking into account this result, a similar analysis can be carried out for Eq. (3.30) to yield

$$\begin{cases} \bar{U}_1 \dfrac{\partial \bar{U}_2}{\partial x_1} + \bar{U}_2 \dfrac{\partial \bar{U}_2}{\partial x_2} = -\dfrac{1}{\rho} \dfrac{\partial \bar{P}}{\partial x_2} - \dfrac{\partial \overline{u_1' u_2'}}{\partial x_1} - \dfrac{\partial \overline{u_2'^2}}{\partial x_2} + \nu \left(\dfrac{\partial^2}{\partial x_1^2} + \dfrac{\partial^2}{\partial x_2^2} \right) \bar{U}_2 \\ \qquad \sim \dfrac{\delta}{L} \dfrac{U^2}{L} \qquad\qquad\qquad\qquad \sim \dfrac{\delta}{L} \dfrac{U^2}{L} \sim \dfrac{\delta}{L} \dfrac{U^2}{\delta} \qquad \sim \nu \dfrac{\delta}{L} \left(\dfrac{U}{L^2}; \dfrac{U}{\delta^2} \right) \end{cases}$$

The term $\partial \overline{u_2'^2} / \partial x_2$ overwhelms all others. Therefore, it can only be balanced by the pressure term, and the simplified equation reads

$$\frac{1}{\rho} \frac{\partial \bar{P}}{\partial x_2} + \frac{\partial \overline{u_2'^2}}{\partial x_2} = 0$$

Then, by integrating along x_2 from the wall, where $\bar{P} = \bar{P}_w$ and $u_2' = 0$, up to the outer zone where $\bar{P} = P_e$ and $u_2' = 0$, one gets

$$P_e = \bar{P}_w = \bar{P} + \rho \overline{u_2'^2}$$

By comparison to the free shear flow case in Chap. 4, the pressure P_e imposed by the external flow is not necessarily uniform here. The pressure term in Eq. (3.31) thus needs to be kept. Moreover, the dominant viscous term must also be conserved in Eq. (3.31) to ensure the no-slip condition at the wall. By retaining the dominant terms in $\sim U^2/L$, the boundary layer approximation of Eq. (3.29) is then

$$\bar{U}_1 \frac{\partial \bar{U}_1}{\partial x_1} + \bar{U}_2 \frac{\partial \bar{U}_1}{\partial x_2} = -\frac{1}{\rho} \frac{dP_e}{dx_1} - \frac{\partial \overline{u_1' u_2'}}{\partial x_2} + \nu \frac{\partial^2 \bar{U}_1}{\partial x_2^2}$$

and corresponds to Eq. (3.5).

Chapter 4
Free Turbulent Flows: Jets and Wakes

In this chapter, self-similar solutions of free subsonic jets and wakes are established. These solutions can be used to characterize some properties of the mean turbulent flow itself, to assess turbulence models, and also to provide an analytical solution for the mean flow field under some assumptions. The development of a round jet flow is first described, results for a plane jet are then briefly reported, round and plane wake flows are then examined in the two last sections.

4.1 Natural Development of a Free Turbulent Round Jet

Free jet flows have been the subject of numerous experimental as well as numerical studies, particularly in the fields of aeronautics and aeroacoustics where they are produced by the exhaust flow of an aircraft engine for instance. A sketch of the mean velocity field is shown in Fig. 4.1 for a round jet. Three main regions are usually distinguished in the flow development. The first one is the initial region near the nozzle exit, where an annular turbulent mixing layer encloses the potential core of the jet. Inside this core, the flow is quasi-laminar with a constant velocity equal to the jet exit velocity U_j, and its mean position is shown by dotted lines in Fig. 4.1. Turbulence totally penetrates to the jet axis at a distance z_c between $4D$ and $5D$, where D is the nozzle diameter. The merging of the annular shear layer marks the beginning of the transition region, and far downstream, the jet is finally fully developed, at a distance of approximately $15D$. In this region, a constant turbulent intensity is reached on the jet axis, that is $u'_1/U_m = \text{cst}$, where U_m is the local mean axial velocity, and the mean flow is self-similar.

The two Reynolds numbers $\text{Re}_D = U_j D/\nu$ and $\text{Re}_{\delta_\theta} = U_j \delta_\theta/\nu$, where δ_θ is the momentum thickness of the exit boundary layer, and the peak fluctuation intensity u'_1/U_j at the nozzle exit are among the most important parameters to be considered to characterize the initial development of a subsonic jet [537, 538, 566]. For moderate Reynolds numbers $\text{Re}_D \leq 10^5$, the exit boundary layer is laminar and

C. Bailly and G. Comte-Bellot, *Turbulence*, Experimental Fluid Mechanics,
DOI 10.1007/978-3-319-16160-0_4

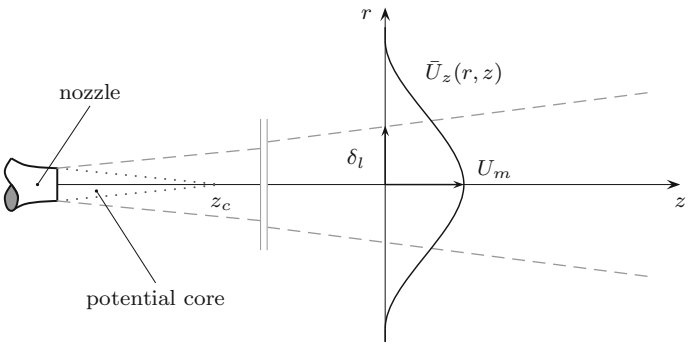

Fig. 4.1 Sketch of the mean velocity field of a round jet in the initial development, and in the region where the flow has reached a self-similar state

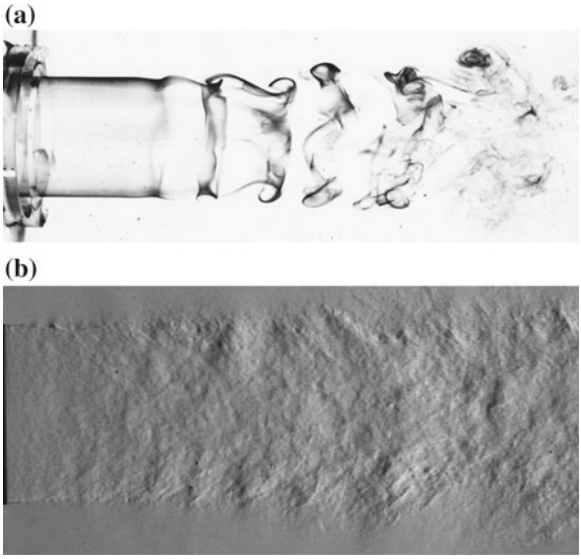

Fig. 4.2 **a** Visualization of a water jet by fluorescent dye injection, $\mathrm{Re}_D = 5570$ with $D = 40$ mm and $U_j \simeq 13\,\mathrm{cm}\cdot\mathrm{s}^{-1}$. Courtesy of Junji Kurima (Kurima, Kasagi and Hirata, Tokyo University, 1983). **b** Schlieren visualization of an air jet at $\mathrm{Re}_D \simeq 8.7\times10^5$ with $D = 38$ mm, $U_j = 293\,\mathrm{m}\cdot\mathrm{s}^{-1}$ and $T_t = T_\infty$, exposure time 3 μs, courtesy of Benoît André and Thomas Castelain (LMFA)

the development of the flow is dominated by vortex pairings occurring in the initial laminar shear layer, as illustrated by Fig. 4.2a. A view of a higher Reynolds number is shown in Fig. 4.2b, for which the incoming boundary layer is turbulent. The overall flow characteristics are then not dependent on the Reynolds number. Between these two asymptotic states, that is for $10^5 \leq \mathrm{Re}_D \leq 2.5 \times 10^5$, the initial shear-layer is transitional. The mean velocity profile is still close to the Blasius laminar solution,

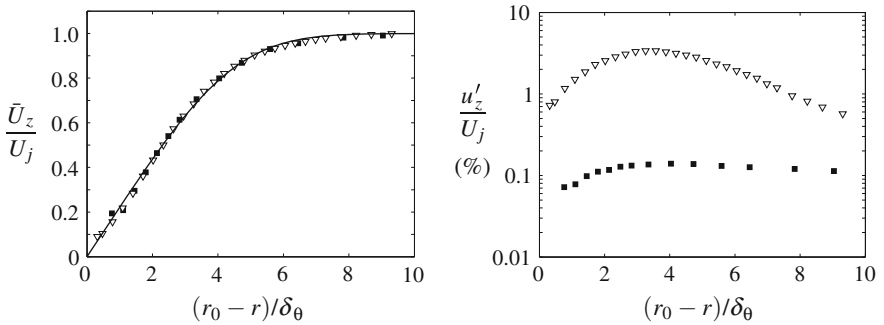

Fig. 4.3 Mean velocity profile $\bar{U}_z$ and fluctuating velocity profile u'_z measured at $z = 0.01D$ for two Reynolds numbers ■ $\mathrm{Re}_D = 6.7 \times 10^4$ and ▽ $\mathrm{Re}_D = 1.3 \times 10^5$ by Fleury [526]. The Blasius profile is also plotted in *solid line* and $r_0 = D/2$ is the nozzle radius

as shown in Fig. 4.3, but streamwise velocity fluctuations grow as Re_D increases. It is not always easy to study the influence of each parameter in experiments, by changing $\mathrm{Re}_{\delta_\theta}$ in keeping the same value for $\mathrm{Re}_D = U_j D/\nu$ for instance, since $\delta_\theta/D \simeq \mathrm{Re}_D^{-1/2}$ at the nozzle exit [526, 537]. More generally, all the parameters are inherently linked and numerical simulations are then an insightful way to prolong experimental studies in carefully controlling the initial conditions [513–515] for instance.

The laminar—turbulent transition in the mixing layer is well described by the linear spatial stability theory introduced in Sect. 1.5. To illustrate this point, the laminar mean velocity profile at the nozzle exit of the jet shown in Fig. 4.2a can be approximated by the following hyperbolic tangent function

$$\bar{U}(z)/U_j = 0.5\,\{1 + \tanh\,[(r_0 - r)/(2\delta_\theta)]\}$$

with $\delta_\theta/r_0 \simeq 0.05$. For an incompressible flow, the most amplified axisymmetric disturbance corresponds to a Strouhal number $\mathrm{St}_{\delta_\theta} = f\delta_\theta/U_j \simeq 0.018$, and is directly associated with the first ring vortex [50]. Viscous effects are found very small for Reynolds numbers $\mathrm{Re}_{\delta_\theta} \leq 300$ according to the work by Morris [53]. Morever, it is essential to include compressible effects for high speed jets by considering the compressible Rayleigh equation (1.19), as shown with the results displayed in Fig. 1.21. The first helicoidal mode $n = 1$ is usually found to be the most amplified disturbance, and amplification rates are reduced. A well-known consequence is the lengthening of the potential core as the Mach number of the jet is increased, thus $z_c/D \simeq 4.2 + 1.1M_j^2$ for isothermal jets [544]. Note that a shock-cell structure is generated inside the supersonic jet core to adapt the pressure at the nozzle exit P_e to the ambient pressure P_∞ for supersonic Mach numbers [550, 558].

4.2 Self-similarity for a Round Jet

A solution for the mean velocity and for the Reynolds shear stress can be determined in the self-similar region, where the jet flow is fully developed. The turbulent flow is assumed incompressible and stationary. As a starting point, the Reynolds averaged Navier-Stokes equations are written for an axisymmetric mean flow, and are simplified through dimensional arguments. A self-similar solution is then sought by introducing a turbulent viscosity to close the governing equations.

4.2.1 Averaged Equations

For a homogeneous and incompressible flow, the mass conservation is simply given by $\nabla \cdot \boldsymbol{u} = 0$, that is in cylindrical coordinates (r, θ, z) where z is aligned along the jet axis

$$\frac{1}{r}\frac{\partial (r u_r)}{\partial r} + \frac{1}{r}\frac{\partial u_\theta}{\partial \theta} + \frac{\partial u_z}{\partial z} = 0$$

The following material derivative operator is introduced to simplify the writing of equations,

$$\frac{Df}{Dt} \equiv \frac{\partial f}{\partial t} + u_r \frac{\partial f}{\partial r} + \frac{u_\theta}{r}\frac{\partial f}{\partial \theta} + u_z \frac{\partial f}{\partial z}$$

and it is recalled below that thanks to the incompressibility condition,

$$\frac{Df}{Dt} = \frac{\partial f}{\partial t} + \frac{1}{r}\frac{\partial (f r u_r)}{\partial r} + \frac{1}{r}\frac{\partial (f u_\theta)}{\partial \theta} + \frac{\partial (f u_z)}{\partial z}$$

Using the D/Dt operator, the Navier-Stokes equations can then be written as follows,

$$\left\{\begin{array}{r} \dfrac{Du_r}{Dt} - \dfrac{u_\theta^2}{r} = -\dfrac{1}{\rho}\dfrac{\partial p}{\partial r} + \nu\left(\nabla^2 u_r - \dfrac{2}{r^2}\dfrac{\partial u_\theta}{\partial \theta} - \dfrac{u_r}{r^2}\right) \\ \dfrac{Du_\theta}{Dt} + \dfrac{u_r u_\theta}{r} = -\dfrac{1}{\rho}\dfrac{1}{r}\dfrac{\partial p}{\partial \theta} + \nu\left(\nabla^2 u_\theta + \dfrac{2}{r^2}\dfrac{\partial u_r}{\partial \theta} - \dfrac{u_\theta}{r^2}\right) \\ \dfrac{Du_z}{Dt} = -\dfrac{1}{\rho}\dfrac{\partial p}{\partial z} + \nu\nabla^2 u_z \end{array}\right.$$

where the Laplacian operator in cylindrical coordinates is given by

$$\nabla^2 f = \frac{1}{r}\frac{\partial}{\partial r}\left(r\frac{\partial f}{\partial r}\right) + \frac{1}{r^2}\frac{\partial^2 f}{\partial \theta^2} + \frac{\partial^2 f}{\partial z^2}$$

The Reynolds decomposition is now introduced into these equations adopting the usual notations for the mean and fluctuating part, that is $u_r = \bar{U}_r + u'_r$, $u_\theta = \bar{U}_\theta + u'_\theta$, $u_z = \bar{U}_z + u'_z$ and $p = \bar{P} + p'$. For a round jet, one has $\bar{U}_\theta = 0$ but $u'_\theta \neq 0$, and furthermore for any mean quantity $\bar{F}$, $\partial \bar{F}/\partial\theta = 0$. Owning to the symmetry of the mean turbulent flow, the turbulence must be homogeneous in the azimuthal direction and thus, $\overline{u'_r u'_\theta} = \overline{u'_z u'_\theta} = 0$. With these assumptions, the averaged mass conservation equation is

$$\frac{1}{r}\frac{\partial\left(r\bar{U}_r\right)}{\partial r} + \frac{\partial \bar{U}_z}{\partial z} = 0$$

Following the approach presented in Chap. 2, the averaged Navier-Stokes equations can be written in the form,

$$\frac{\bar{D}\,\bar{U}_r}{Dt} = -\frac{1}{\rho}\frac{\partial \bar{P}}{\partial r} - \frac{1}{r}\frac{\partial(r\overline{u_r'^2})}{\partial r} - \frac{\partial \overline{u'_r u'_z}}{\partial z} + \frac{\overline{u_\theta'^2}}{r} + \nu\left(\nabla^2 \bar{U}_r - \frac{\bar{U}_r}{r^2}\right) \tag{4.1}$$

$$0 = -\frac{1}{\rho}\frac{1}{r}\frac{\partial \bar{P}}{\partial \theta} \tag{4.2}$$

$$\frac{\bar{D}\,\bar{U}_z}{Dt} = -\frac{1}{\rho}\frac{\partial \bar{P}}{\partial z} - \frac{1}{r}\frac{\partial(r\overline{u'_r u'_z})}{\partial r} - \frac{\partial \overline{u_z'^2}}{\partial z} + \nu\nabla^2 \bar{U}_z \tag{4.3}$$

where the operator $\bar{D}/Dt$ is defined as,

$$\frac{\bar{D}\bar{F}}{Dt} = \frac{1}{r}\frac{\partial\left(r\bar{U}_r\bar{F}\right)}{\partial r} + \frac{\partial\left(\bar{U}_z\bar{F}\right)}{\partial z} = \bar{U}_r\frac{\partial \bar{F}}{\partial r} + \bar{U}_z\frac{\partial \bar{F}}{\partial z}$$

It is straightforward to observe from Eq. (4.2) that the mean pressure can only be a function of r and z, that is $\bar{P} = \bar{P}(r, z)$, which is of course expected for symmetry reasons.

4.2.2 Thin Shear Layer Approximation

The divergence of the thin shear flow flow is quite slow, and boundary-layer approximations, see Sect. 3.9, can be applied to simplify the previous equations. Length (L, δ_l) and velocity (U, V) scales in the axial and radial direction respectively, are introduced to examine the relative amplitude of each term. Only one velocity scale u is chosen for the fluctuating velocity vector $\boldsymbol{u}'$. The boundary-layer approximation requires that $\delta_l/L < 1$, which is in agreement with experimental observations. Variations of the mean flow are smaller in the axial direction than in the radial one. The equation of mass conservation implies that

$$\frac{1}{r}\frac{\partial\left(r\bar{U}_r\right)}{\partial r} + \frac{\partial \bar{U}_z}{\partial z} = 0 \quad \Longrightarrow \quad \frac{V}{\delta_l} \sim \frac{U}{L} \quad \text{or} \quad V \sim \frac{\delta_l}{L}U$$

Considering the averaged Navier-Stokes equation in the axial direction, one has

$$\begin{array}{cccccc} \dfrac{\bar{D}\bar{U}_z}{Dt} = -\dfrac{1}{\rho}\dfrac{\partial \bar{P}}{\partial z} - \dfrac{1}{r}\dfrac{\partial(r\overline{u_r' u_z'})}{\partial r} - \dfrac{\partial \overline{u_z'^2}}{\partial z} + \nu\left[\dfrac{1}{r}\dfrac{\partial}{\partial r}\left(r\dfrac{\partial \bar{U}_z}{\partial r}\right) + \dfrac{\partial^2 \bar{U}_z}{\partial z^2}\right] \\ \dfrac{U^2}{L} \qquad\qquad \dfrac{u^2}{\delta_l} \qquad\quad \dfrac{u^2}{L} \qquad\qquad \nu\left(\dfrac{U}{\delta_l^2}; \dfrac{U}{L^2}\right) \\ (1) \qquad\qquad (2) \qquad\quad (3) \qquad\qquad (4) \end{array} \tag{4.4}$$

The term (3) is negligible with respect to the term (2). Similarly, only the first viscous term in (4) could be retained,

$$(4) \quad \sim \quad \nu\frac{U}{\delta_l^2} = \frac{U^2}{\delta_l}\frac{\nu}{U\delta_l} = \frac{U^2}{L}\frac{L}{\delta_l}\frac{1}{\mathrm{Re}}$$

and viscous effects are very small for usual Reynolds numbers. As an illustration and as already mentioned in the first section, viscous effects are identified for $\mathrm{Re}_{\delta_\theta} \leq 300$, which corresponds to a Reynolds number $\mathrm{Re}_D \sim 10$ with $\delta_\theta / r_0 = 0.05$. Viscous terms will be ignored in what follows. This is a reasonable assumption which can be applied to developing free shear flows far from any wall. The averaged Navier-Stokes equation along z is thus simplified as

$$\frac{\bar{D}\bar{U}_z}{Dt} = -\frac{1}{\rho}\frac{\partial \bar{P}}{\partial z} - \frac{1}{r}\frac{\partial(r\overline{u_r' u_z'})}{\partial r}$$

Moreover, to derive a solution corresponding to a turbulent jet, it is necessary that the terms (1) and (2) have the same order of magnitude. If (2) $\ll$ (1), the laminar solution is recovered and the case (2) $\gg$ (1) is not physically acceptable. Therefore,

$$\frac{U^2}{L} \sim \frac{u^2}{\delta_l} \qquad \text{or} \qquad u \sim \left(\frac{\delta_l}{L}\right)^{1/2} U$$

A similar analysis can be conducted for the averaged Navier-Stokes equation in the radial direction. In terms of order of magnitude, one has

$$\begin{array}{cccccc} \dfrac{\bar{D}\,\bar{U}_r}{Dt} = -\dfrac{1}{\rho}\dfrac{\partial \bar{P}}{\partial r} - \dfrac{\partial \overline{u_r'^2}}{\partial r} - \dfrac{\partial \overline{u_r' u_z'}}{\partial z} - \dfrac{\overline{u_r'^2} - \overline{u_\theta'^2}}{r} + \nu\left(\nabla^2 \bar{U}_r - \dfrac{\bar{U}_r}{r^2}\right) \\ \dfrac{\delta_l}{L}\dfrac{U^2}{L} \qquad\qquad \dfrac{U^2}{L} \qquad \dfrac{\delta_l}{L}\dfrac{U^2}{L} \qquad\qquad\qquad \nu\dfrac{\delta_l}{L}\left(\dfrac{U}{\delta_l^2}; \dfrac{U}{L^2}\right) \\ (1) \qquad\qquad\qquad (2) \end{array}$$

Viscous terms are again negligible, and the term (2) is also discarded. The order of magnitude of the term (1) is larger than all of the other terms, and it can be only balanced by the pressure term. Hence,

$$\frac{1}{\rho}\frac{\partial \bar{P}}{\partial r} + \frac{\partial \overline{u_r'^2}}{\partial r} = 0$$

and by integration in the radial direction from the jet axis to the ambient medium, one obtains $\bar{P} + \rho\overline{u_r'^2} = P_\infty$. This relation can then be used to estimate the order of magnitude of the longitudinal pressure gradient in Eq. (4.4),

$$-\frac{1}{\rho}\frac{\partial \bar{P}}{\partial z} = \frac{\partial \overline{u_r'^2}}{\partial z} \quad \sim \quad U^2\frac{\delta_l}{L}\frac{1}{L} = \frac{\delta_l}{L}\frac{U^2}{L}$$

With respect to terms in U^2/L, the pressure term is found to be negligible in Eq. (4.4). Finally, the governing equations for the mean flow of a round jet are given by

$$\frac{1}{r}\frac{\partial (r\bar{U}_r)}{\partial r} + \frac{\partial \bar{U}_z}{\partial z} = 0 \tag{4.5}$$

$$\frac{1}{r}\frac{\partial (r\bar{U}_r\bar{U}_z)}{\partial r} + \frac{\partial (\bar{U}_z\bar{U}_z)}{\partial z} = -\frac{1}{r}\frac{\partial (r\overline{u_r'u_z'})}{\partial r} \tag{4.6}$$

Conservation of the Momentum Flux

A consequence of the simplified Eq. (4.6) is the conservation of the momentum flux I_z in a cross section of the jet, that is

$$I_z = 2\pi\int_0^\infty \rho\bar{U}_z^2 r dr = \text{cst} \tag{4.7}$$

Starting from Eq. (4.6) rewritten as

$$\frac{\partial (\bar{U}_z\bar{U}_z)}{\partial z} = -\frac{1}{r}\frac{\partial}{\partial r}\left(r\bar{U}_r\bar{U}_z + r\overline{u_r'u_z'}\right)$$

one can shown that dI_z/dz is zero. Indeed,

$$\begin{aligned}\frac{dI_z}{dz} = \int_0^\infty \frac{\partial (\rho\bar{U}_z\,\bar{U}_z)}{\partial z} 2\pi r dr &= -2\pi\rho\int_0^\infty \frac{\partial}{\partial r}\left(r\bar{U}_r\,\bar{U}_z + r\overline{u_r'u_z'}\right) dr \\ &= -2\pi\rho\left[r\bar{U}_r\,\bar{U}_z + r\overline{u_r'u_z'}\right]_0^\infty \\ &= 0\end{aligned}$$

4.2.3 Similarity Solution

The self-similar solution is sought by assuming the following expressions for the mean axial velocity and the Reynolds shear stress,

$$\left\{\begin{array}{l} \bar{U}_z = U_m(z)\, f(\eta) \\ -\eta\, \overline{u_r' u_z'} = U_m^2(z)\, h(\eta) \end{array}\right. \qquad \text{with} \qquad \eta = \frac{r}{\delta_l(z)} \tag{4.8}$$

and where U_m is the mean centerline velocity and δ_l the half-width of the jet, defined usually as the radial distance for which the mean axial velocity is equal to half of the velocity on the axis, see also Fig. 4.1. Thus, one has $f(0) = 1$ and $f(1) = 1/2$ by definition.

The Reynolds shear stress $-\overline{u_r' u_z'}$ is first expressed as a function of $\bar{U}_z$ only. By integrating Eq. (4.6) in the radial direction from the jet axis,

$$r\bar{U}_r\bar{U}_z + \int_0^r \frac{\partial \bar{U}_z^2}{\partial z} r'dr' = -r\overline{u_r' u_z'} \tag{4.9}$$

Moreover, an expression of the mean radial velocity $\bar{U}_r$ can be derived from the mass conservation equation (4.5),

$$r\bar{U}_r = -\int_0^r \frac{\partial \bar{U}_z}{\partial z} r'dr'$$

and can be introduced in Eq. (4.9). Hence,

$$-r\overline{u_r' u_z'} = \int_0^r \frac{\partial \bar{U}_z^2}{\partial z} r'dr' - \bar{U}_z \int_0^r \frac{\partial \bar{U}_z}{\partial z} r'dr'$$

To simplify the algebra, it is also convenient to permute the integration over r and the derivative operator along z, that is

$$-r\overline{u_r' u_z'} = \frac{\partial}{\partial z}\int_0^r \bar{U}_z^2 r'dr' - \bar{U}_z \frac{\partial}{\partial z}\int_0^r \bar{U}_z r'dr' \tag{4.10}$$

The right-hand side of this equation can now be developed by introducing the self-similar profiles defined in (4.8). This yields

$$-r\overline{u_r' u_z'} = \frac{\partial}{\partial z}\int_0^r U_m^2 f^2 r'dr' - U_m f \frac{\partial}{\partial z}\int_0^r U_m f r'dr'$$

The similarity variable η is also introduced in the integrals through the change of variable $r' = \delta_l \eta'$,

$$-r\overline{u_r' u_z'} = \frac{\partial}{\partial z}\left(\delta_l^2 U_m^2 \int_0^\eta f^2 \eta' d\eta'\right) - U_m f \frac{\partial}{\partial z}\left(\delta_l^2 U_m \int_0^\eta f \eta' d\eta'\right)$$

Using Leibniz's rule since the upper bound η of the two integrals is a function of z, it follows that

$$\begin{aligned} -r\overline{u_r' u_z'} &= \frac{d}{dz}(\delta_l^2 U_m^2) \int_0^\eta f^2 \eta' d\eta' + \delta_l^2 U_m^2 f^2 \eta \frac{d\eta}{dz} \\ &\quad - \frac{d}{dz}(\delta_l^2 U_m) U_m f \int_0^\eta f \eta' d\eta' - \delta_l^2 U_m^2 f^2 \eta \frac{d\eta}{dz} \\ &= \frac{d}{dz}(\delta_l^2 U_m^2) \int_0^\eta f^2 \eta' d\eta' - \frac{d}{dz}(\delta_l^2 U_m) U_m f \int_0^\eta f \eta' d\eta' \end{aligned}$$

Thanks to the momentum conservation (4.7)

$$I_z = 2\pi \rho U_m^2 \delta_l^2 \int_0^\infty f^2 \eta d\eta = \text{cst}$$

it is required that $U_m \delta_l = \text{cst}$, and the first term is thus zero on the right-hand side of the previous equation. The similarity function $h(\eta)$ for the Reynolds shear stress profile defined by (4.8) is also introduced on the left-hand side,

$$h(\eta) = -\frac{1}{\delta_l U_m} \frac{d}{dz}(\delta_l^2 U_m) f \int_0^\eta f \eta' d\eta' \tag{4.11}$$

A self-similarity solution is only obtained if the following factor in (4.11) is independent of z,

$$\frac{1}{\delta_l U_m} \frac{d}{dz}(\delta_l^2 U_m) = \text{cst}$$

Recalling that $U_m \delta_l = \text{cst}$, the growth of the jet half-width is found to be linear, $\delta_l \sim z$, and $U_m \sim z^{-1}$. The length scale δ_l and the mean axial velocity U_m of a self-similar round jet are thus given in dimensionless forms by

$$\frac{\delta_l(z)}{D} = a \frac{z - z_0}{D} \qquad \frac{U_m(z)}{U_j} = b \frac{D}{z - z_0} \tag{4.12}$$

where a is the spreading rate and b is the decay constant. The third constant z_0 represents the virtual origin of a self-similar jet generated by a point source of momentum I_z. The jet being definitely not self-similar just beyond the nozzle exit, $z_0 \neq 0$. All these constants are to be determined experimentally or numerically.

4.2.4 Expression of the Radial Profile

The calculation of the function f describing the radial profile of the mean axial velocity (4.8), requires to close the averaged Navier-Stokes equations. A turbulent viscosity is introduced to express the Reynolds shear stress as a function of the mean velocity gradient, refer to Chap. 2,

$$-\overline{u_r' u_z'} = \nu_t \frac{\partial \bar{U}_z}{\partial r} = \frac{\nu_t U_m}{\delta_l} \frac{df}{d\eta} \qquad \text{and,} \qquad -\eta \frac{\overline{u_r' u_z'}}{U_m^2} = h(\eta) = \eta \frac{\nu_t}{U_m \delta_l} \frac{df}{d\eta}$$

The preservation of the self-similar profile h requires that the factor $U_m \delta_l / \nu_t$ must be independent of z. As $U_m \sim z^{-1}$ and $\delta_l \sim z$, the turbulent viscosity is found to be constant in the self-similar jet, $\nu_t = \text{cst}$. This means that there is the same balance between turbulent and viscous effects whatever the distance to the nozzle is. This is an important result indicating that one has a complete similarity for the turbulent round jet. The constant $c \equiv U_m \delta_l / \nu_t$ is thus introduced.

The turbulent closure can be introduced in expression (4.11) to provide

$$\frac{\eta}{c} \frac{df}{d\eta} = -\underbrace{\frac{1}{\delta_l U_m} \frac{d}{dz} (\delta_l^2 U_m)}_{=a} f \int_0^\eta f \eta' d\eta'$$

where the underlined factor is equal to the constant a. Therefore, the function f verifies the following integral equation

$$\frac{\eta}{c} f' + a f \int_0^\eta f \eta' d\eta' = 0$$

where $f' \equiv df/d\eta$. To integrate this differential equation, its is convenient to introduce an auxiliary function F given by,

$$F(\eta) = \int_0^\eta f\left(\eta'\right) \eta' d\eta'$$

By definition, one has $F' = \eta f$ and $F'' = f + \eta f'$. The previous differential equation can thus be written as

$$\frac{1}{ac} \frac{\eta F'' - F'}{\eta} + \frac{F F'}{\eta} = 0$$

so that,

$$\frac{1}{ac} \left[(\eta F')' - 2F' \right] + F F' = 0$$

Noting that $F(0) = 0$ and $F'(0) = 0$, a first integration gives

$$\frac{1}{ac}\left[\eta F' - 2F\right] + \frac{1}{2}F^2 = 0 \qquad \text{or} \qquad \frac{2\eta F - \eta^2 F'}{F^2} = \frac{ac}{2}\eta$$

The previous equation can then be integrated a second time, which yields

$$\frac{\eta^2}{F} = \frac{ac}{4}\eta^2 + \text{cst}$$

To determine this integration constant, the values of F and of its derivatives at the origin are used again. One has $F(0) = 0$, $F'(0) = 0$ and $F''(0) = f(0) = 1$. Therefore,

$$\text{cst} = \lim_{\eta\to 0}\frac{\eta^2}{F} = \lim_{\eta\to 0}\frac{2\eta}{F'} = \lim_{\eta\to 0}\frac{2}{F''} = 2 \qquad \text{and} \qquad F(\eta) = \frac{4\eta^2}{ac\eta^2 + 8}$$

Finally, the expression of the f function describing the radial profile of the mean velocity has been explicitly determined, and can be written as

$$f = \frac{F'}{\eta} = \frac{1}{(d\eta^2 + 1)^2} \qquad \text{with} \qquad d \equiv \frac{ac}{8} \tag{4.13}$$

Note that the condition $f(1) = 1/2$ associated with the definition of the jet half-width requires that $d = \sqrt{2} - 1$.

4.2.5 Some Other Quantities

As already mentioned just above, the different constants involved in the self-similar solution are linked through compatibility relations. Thus, the value of the momentum flux I_z can be calculated at the nozzle exit,

$$I_z = \frac{\pi D^2}{4}\rho U_j^2$$

and also in an arbitrary cross section of the jet using the self-similar solution for the mean axial velocity. Hence,

$$I_z = 2\pi\rho U_m^2\delta_l^2\int_0^\infty f^2\eta d\eta = 2\pi\rho U_m^2\delta_l^2\,\frac{4}{3ac}$$

and by using (4.12), $c = (32/3)ab^2$. Combining this result with the requirement on the constant d in expression (4.13), it yields

$$b = \frac{1}{2a}\left[3(\sqrt{2}-1)\right]^{1/2} \qquad c = \frac{8(\sqrt{2}-1)}{a} \tag{4.14}$$

The knowledge of only one constant is finally required to wholly determine the mean axial velocity profile defined by (4.13). The spreading rate a of the jet is generally chosen. The turbulent viscosity can also be explicitly calculated from the value of the Reynolds number,

$$\frac{\nu_t}{\nu} = \frac{ab}{c}\frac{U_j D}{\nu} = \frac{ab}{c}\mathrm{Re}_D = \frac{3}{32b}\mathrm{Re}_D$$

A jet flow is also characterized by its entrainment, and the flow rate $Q(z)$ provided by the self-similar solution can be calculated. This volume flow rate is given by

$$Q = 2\pi\int_0^\infty \bar{U}_z r dr = 2\pi U_m \delta_l^2 \int_0^\infty f\eta d\eta = Q_j \frac{32ab}{c}\frac{z-z_0}{D}$$

where $Q_j = (\pi D^2/4)U_j$ is the nominal flow rate at the nozzle exit. This relation can be recast in the following dimensionless form

$$\frac{Q}{Q_j} = k_e \frac{z-z_0}{D} \qquad \text{with} \qquad k_e = \frac{32ab}{c} \tag{4.15}$$

where the constant k_e is directly proportional to the spreading rate. The entrainment and the spreading rate are directly associated with the evolution of the mean radial velocity $\bar{U}_r$, which is not zero even far outside of the jet. This velocity can also be determined using the mass conservation. It can be shown that

$$\frac{U_r}{U_m} = g(\eta) = \frac{a}{\eta}\left(\eta^2 f - \int_0^\eta f\eta' d\eta'\right) = \frac{a\eta}{2}\frac{1-d\eta^2}{(1+d\eta^2)^2} \qquad d = \frac{ac}{8}$$

This velocity is positive in the jet core, in agreement with the decrease of the mean axial velocity along the jet axis, and is negative for $\eta \geq 1.5$, corresponding to the entrainement of the surrounding ambient fluid. Note that $\bar{U}_r$ tends towards zero as $-1/\eta$ when $\eta \to \infty$.

4.2.6 Experimental and Numerical Results

Mean Velocity and Reynolds Stress Tensor

Table 4.1 provides some self-similar parameters taken from experiments. The scattering of these data can be attributed to the estimate of the virtual origin of the jet z_0, to a possible influence of the Reynolds number or also to the quality of the facility for preserving the entrainment induced by the jet. The measured radial profile of

Table 4.1 Measured self-similar parameters from stationary/flying hot-wire anemometry (s/fHWA) or from laser-Doppler anemometry (LDA)

M	Re_D	a	b	z_0/D	a^2b^2	Reference
0.15	8.6×10^4	0.086	5.4	3	0.22	Wygnanski et al. [565] (sHWA)
0.12	6.7×10^4	0.08	5.9	−0.5	0.22	Hinze [8]
0.08	1.1×10^4	0.096	6.06	−2.5	0.34	Panchapakesan et al. [549] (fHWA)
0.08	4.5×10^4	0.093	6.09	0.67	0.32	Shiri et al. [555] (LDA)
0.16	9.5×10^4	0.094	5.8	4.0	0.30	Hussein et al. [539] (LDA/fHWA)
0.16	9.5×10^4	0.102	5.9	2.7	0.36	Hussein et al. [539] (sHWA)

Additional data can be found in Lipari and Stansby for water jets [547]

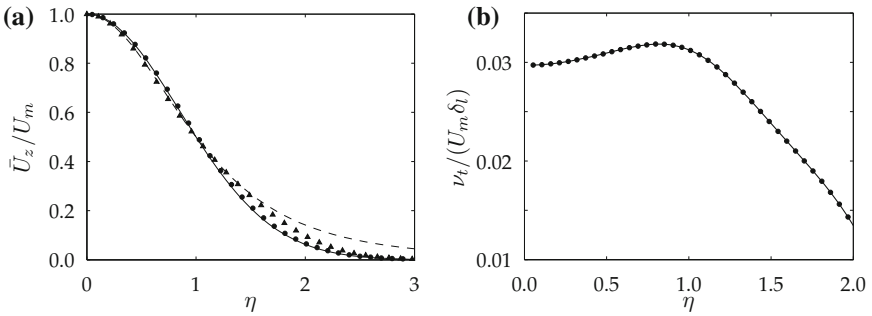

Fig. 4.4 **a** radial profile of the mean longitudinal velocity $\bar{U}_z/U_m = f(\eta)$ measured by Hussein et al. [539] (see also Table 4.1), • laser-Doppler anemometry (LDA) results, ▾ stationary hot-wire anemometry (sHWA) results, – – – self-similar profile $f = 1/(d\eta^2 + 1)^2$, —— Gaussian profile $f = \exp(-\ln 2\,\eta^2)$. **b** normalized turbulent viscosity $\nu_t/(U_m\delta_l)$ computed from LDA results

the mean axial velocity is shown in Fig. 4.4a. The self-similar solution (4.13) is also plotted, as well as the following Gaussian profile,

$$f(\eta) = \exp(-\ln 2\ \eta^2)$$

which is close to observed experimental results. Let us now verify some compatibility relations. From the LDA results of Hussein et al. [539], the normalized turbulent viscosity can be directly computed to provide an estimate of the constant $c = U_m\delta/\nu_t \simeq 32$, by recalling that $c/(ab) = (\nu/\nu_t)\,\mathrm{Re}_D$. The relation involving the constants a and b can also be checked, namely $(ab)^2 = (3/4)(\sqrt{2}-1) \simeq 0.31$, and values are reported in Table 4.1. Note that this value is very close to the last four experiments. Moreover, Ricou and Spalding [552] were able to perform a direct measurement of the jet entrainment. They found a value of $k_e \simeq 0.32$ for the constant

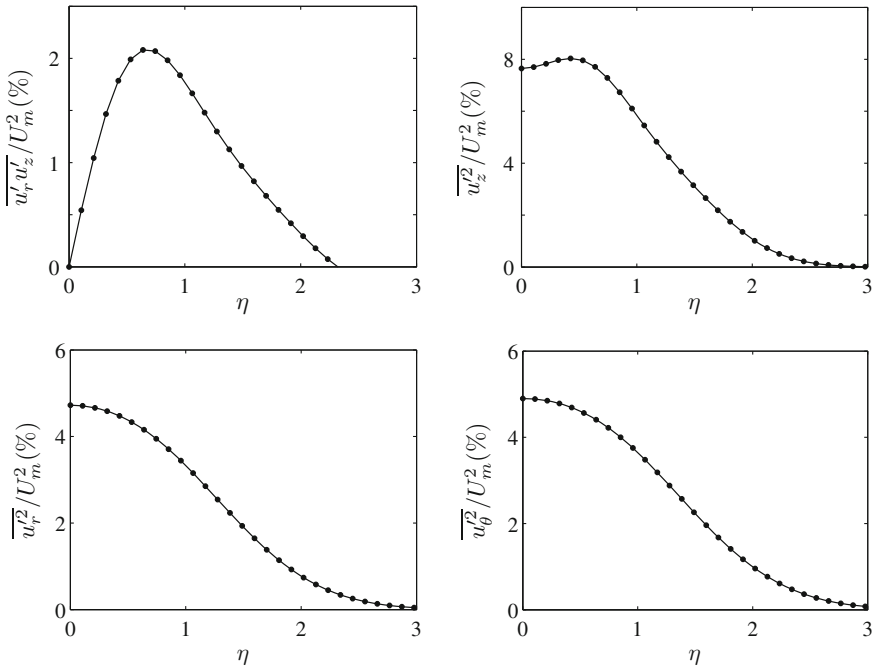

Fig. 4.5 Radial profile of Reynolds stresses measured by Hussein et al. [539] (see also Table 4.1), LDA results

involved in the expression of the volume flow rate (4.15). Note that the predicted self-similar solution does not perfectly match experimental values. Thus, assuming that $a \simeq 0.094$ and according to the compatibility relations (4.14) and (4.15), one should have $b \simeq 5.9$, $c \simeq 35$ and $k_e \simeq 0.51$. The complementarity between experiments and numerical simulations will be discussed in Chap. 8, but an insightfull illustration is given in the next section regarding the turbulent kinetic energy budget.

The normalized radial profiles of the Reynolds stresses are reported in Fig. 4.5 from the data provided by Hussein et al. [539]. Only results obtained by laser-Dopler anemometry have been retained here. They are found in good agreement with flying hot-wire anemometry measurements, but not with stationary HWA data. Indeed, a stationary hot-wire anemometer provide unreliable results far from the jet centerline in reverse flow regions. Turbulense intensities of $u'_z/U_m \simeq 0.28$ and $u'_r/U_m \simeq u'_\theta/U_m \simeq 0.22$ are observed on the jet axis. On the whole, the turbulence of a free jet is far more isotropic than in wall-bounded flows. Moreover, the shear stress profile $\overline{u'_r u'_z}$ is shown in Chap. 2, refer to Fig. 2.3.

Turbulent Kinetic Energy Budget

The turbulent kinetic energy budget has been measured and more recently computed in the self-similar region of a round jet . Using boundary-layer approximations and assuming a high enough Reynolds number to neglect the viscous diffusion, the transport equation for the turbulent kinetic energy k_t can be written as follows,

$$\underbrace{\bar{U}_r\frac{\partial k_t}{\partial r}+\bar{U}_z\frac{\partial k_t}{\partial z}}_{\text{(a)}}=\underbrace{-\overline{u'_r u'_z}\left(\frac{\partial \bar{U}_z}{\partial r}+\frac{\partial \bar{U}_r}{\partial z}\right)-\overline{u'^2_z}\frac{\partial \bar{U}_z}{\partial z}-\overline{u'^2_r}\frac{\partial \bar{U}_r}{\partial r}-\overline{u'^2_\theta}\frac{\bar{U}_r}{r}}_{\text{(b)}}$$
$$\underbrace{-\frac{1}{r}\frac{\partial}{\partial r}\left(\frac{r}{2}\overline{u'^2_i u'_r}\right)-\frac{\partial}{\partial z}\left(\frac{1}{2}\overline{u'^2_i u'_z}\right)}_{\text{(c)}}\underbrace{-\frac{1}{r}\frac{\partial}{\partial r}\left(\frac{r}{\rho}\overline{p'u'_r}\right)-\frac{\partial}{\partial z}\left(\frac{1}{\rho}\overline{p'u'_z}\right)}_{\text{(d)}}\underbrace{\left(-\epsilon^h\right)}_{\text{(e)}} \tag{4.16}$$

where ϵ^h is the homogeneous dissipation, introduced in Sect. 2.6. In this equation, the term (a) represents the convection by the mean flow, the term (b) is the production of k_t, the terms (c) and (d) are the turbulence and pressure transport, and the term (e) is the dissipation. The experimental determination of all these contributions remain difficult, in particular for terms such as the pressure–velocity correlations for instance. As a result, approximations need to be made to estimate the quantities that cannot be measured with accuracy. As an illustration, the results of Panchapakesan and Lumley [549] and of Hussein et al. [539] for a higher Reynolds number, see Table 4.1, are reported in Fig. 4.6. In Panchapakesan and Lumley, the pressure diffusion term (d) is neglected, and the dissipation (e) is obtained as the closing balance of Equation (4.16). In Hussein et al. [539], the energy dissipation is estimated from the assumption of a local axisymmetry of small scales, and the pressure diffusion is then obtained to close the budget. Serious discrepancies are observed between these two approaches. Nowadays, the role of the different terms, in particular the pressure–velocity correlation term, can be clarified using well-resolved numerical simulations. A comparison is shown in Fig. 4.7 between the data of Panchapakesan and Lumley and a large-eddy simulation performed by Bogey and Bailly [512] at the same Reynolds number. The computed pressure diffusion term (d) is found rather small, which finally supports the assumption made by Panchapakesan and Lumley.

The turbulent kinetic energy budget is characterized by an important convection term (a) unlike in wall-bounded flows. This term is indeed equal to zero for a channel or a pipe flow, and remains small for a boundary layer. Moreover, the convection term (a) and the production term (b) have the same order of magnitude. Note also that the term $\overline{u'_r u'^2_\theta}$ involved in the turbulence transport is usually approximated by $\overline{u'^3_r}$, since measurements are made in a plane containing the jet axis. The reader can refer to the review of experimental data by Lipari and Stansby [547] and the simulation results by Bogey and Bailly [512] for budgets of the Reynolds stresses and additional remarks.

Integral Length Scales

The integral length scales $L_{11}^{(1)}$ and $L_{11}^{(2)}$, see the relation (6.4) in Chap. 6, are found to grow linearly with the axial location z. In the first ten diameters along the shear layer at $r = r_0$, one has

$$L_{11}^{(1)} \simeq 2\delta_\theta \qquad L_{11}^{(2)} \simeq \delta_\theta \qquad L_{22}^{(1)} \simeq \delta_\theta$$

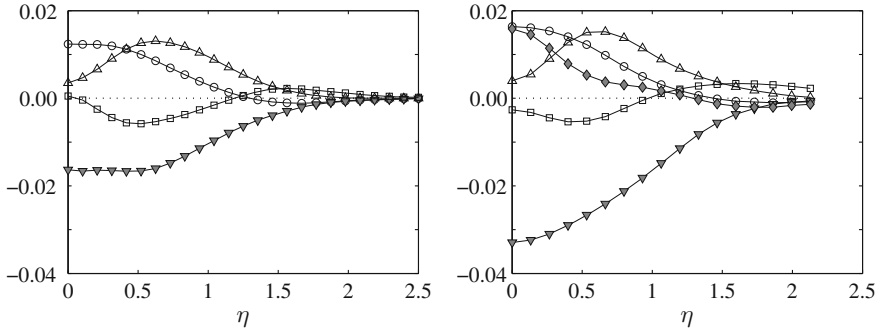

Fig. 4.6 Turbulent kinetic energy budget across the self-similar region of a round jet, experimental data of Panchapakesan and Lumley [549] at *left*, and of Hussein et al. [539] at *right*. ∘ convection (*a*), △ production (*b*), ▼ dissipation (*e*), □ turbulence diffusion (*c*) and ♦ pressure diffusion (*d*). Note that data in solid symbols are not directly measured. All the terms are made dimensionless using U_m and δ_l

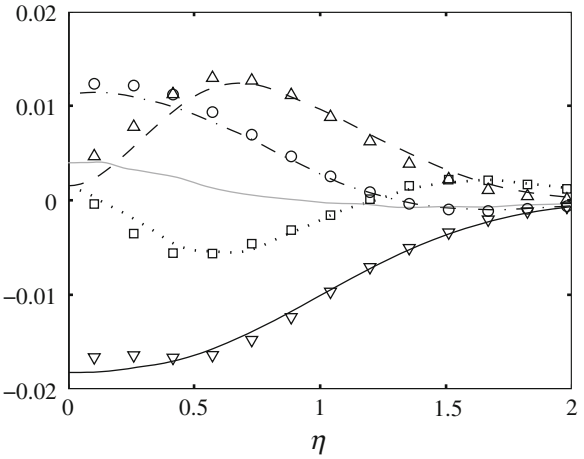

Fig. 4.7 Turbulent kinetic energy budget across the self-similar region of a round jet at $\mathrm{Re}_D = 1.1 \times 10^4$ computed by large-eddy simulation, taken from Bogey and Bailly [512]. Experimental data of Panchapakesan and Lumley [549], ∘ convection (*a*), △ production (*b*), ▽ dissipation (*e*), □ turbulence diffusion (*c*). The computed pressure diffusion (*d*), *in solid gray line*, is neglected in Panchapakesan and Lumley. All the terms are made dimensionless using U_m and δ_l

where compressibility effects are included in the local momentum thickness $\delta_\theta(z)$, as experimentally shown by Fleury et al. [527] for high speed subsonic jets. Thus, no strong deviation is observed from the values expected in isotropic turbulence. The two integral scales $L_{11}^{(1)}$ and $L_{11}^{(2)}$ can indeed be compared to L_f and L_g with $L_f = 2L_g$ in isotropic turbulence, see relation (6.27). The calculation of these scales is usually done in a reference point located at the middle of the separation vector to minimize inhomogeneous effects.

Farther downstream, complete measurements have been performed by Wygnanski and Fiedler [565] in the self-similar region. On the jet axis at $z = 90D$, the axial evolution of the integral length scales is well represented by

$$L_{11}^{(1)} \simeq 0.0385\, z \qquad \text{and} \qquad L_{11}^{(2)} \simeq 0.0157\, z$$

which yields a ratio $L_{11}^{(1)}/L_{11}^{(2)} \simeq 2.4$. Out of the axis, the observed scales are larger, as illustrated by the following values measured at $r/z = 0.1$,

$$L_{11}^{(1)} \simeq 0.062\, z \qquad \text{and} \qquad L_{11}^{(2)} \simeq 0.028\, z$$

The ratio is again very close to the expected value for isotropic turbulence. Note that the largest structures are not observed in the central zone of the jet. The production region of the turbulent kinetic energy is located in an annular region, leading to an intermittency on the jet axis associated with large structures generated in different production regions, as already mentioned for pipe flows in Chap. 3.

4.3 Similarity for a Plane Jet

A plane jet is obtained from a rectangular nozzle with a high aspect ratio, that is the length-to-width ratio, which is assumed to be infinite in the analytical modelling. In practice, the spanwise length must be at least larger than $20l$, where l is the nozzle width as shown in Fig. 4.8. The initial development of the plane jet at the nozzle exit is quite similar to that of a circular jet, again with the particular role played by instability waves in the two mixing layers. The mean flow is found self-similar far downstream, for $x_1/l \geq 25$.

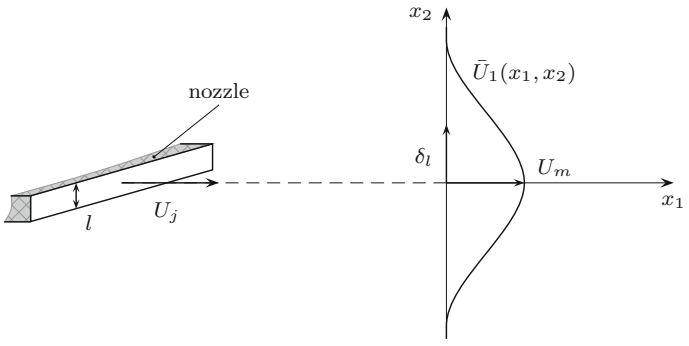

Fig. 4.8 Nozzle exit of a plane jet and self-similar mean velocity profile far downstream. The Reynolds number of the jet is defined as $\mathrm{Re}_l = U_j l/\nu$ where U_j is the exit velocity and l the nozzle width

In the self-similar region, the Reynolds averaged Navier-Stokes equations can be simplified thanks to the boundary layer approximation. For a sufficiently high-Reynolds number flow, one obtains for the longitudinal momentum conservation,

$$\frac{\partial(\bar{U}_1\bar{U}_1)}{\partial x_1} + \frac{\partial(\bar{U}_1\bar{U}_2)}{\partial x_2} = -\frac{\partial\overline{u_1'u_2'}}{\partial x_2} \tag{4.17}$$

whereas the integration of the averaged Navier-Stokes equation in the transverse direction leads to $\bar{P} + \rho\overline{u_2'^2} = P_\infty$. Moreover, the mass conservation is reduced to the incompressibility condition,

$$\frac{\partial\bar{U}_1}{\partial x_1} + \frac{\partial\bar{U}_2}{\partial x_2} = 0$$

The solution is sought in the form of self-affine profiles for $\bar{U}_1$ and $\overline{u_1'u_2'}$

$$\left\{\begin{array}{l} \bar{U}_1 = U_m(x_1)f(\eta) \\ -\overline{u_1'u_2'} = U_m^2(x_1)h(\eta) \end{array}\right. \qquad \text{with} \qquad \eta = \frac{x_2}{\delta_l(x_1)}$$

and where U_m is the maximal velocity on the jet axis and δ_l the local half-width of the jet. The anaytical developments are quite similar to those of the circular jet. The Reynolds shear stress can be calculated by integration of Eq. (4.17) in the transverse direction, which yields

$$-\frac{\overline{u_1'u_2'}}{U_m^2} = h(\eta) = \frac{\left(U_m^2\delta_l\right)'}{U_m^2}\int_0^\eta f^2 d\eta' - \frac{(U_m\delta_l)'}{U_m} f\int_0^\eta f\, d\eta' \tag{4.18}$$

The longitudinal momentum flux I_1 is also conserved for a rectangular jet. Indeed, it is straightforward to show that $dI_1/dx_1 = 0$ by using Eq. (4.17). As a result,

$$I_1 = \int_{-\infty}^{+\infty}\rho\bar{U}_1^2 dx_2 = \rho U_m^2\delta_l\int_{-\infty}^{+\infty} f^2 d\eta = \text{cst}$$

and the first term on the right-hand side in Eq. (4.18) vanishes. Thus, to preserve the self-similarity of the Reynolds shear stress, $U_m^2\delta_l = \text{cst}$ and $(U_m\delta_l)'/U_m = \text{cst}$, which yields the following expressions for the half-width and for the mean longitudinal velocity of a plane jet

$$\frac{\delta_l}{l} = a\,\frac{x_1 - x_0}{l} \qquad \frac{U_m}{U_j} = b\sqrt{\frac{l}{x_1 - x_0}} \tag{4.19}$$

Notations are provided in Fig. 4.8 and a is the spreading rate, b the velocity decay constant and x_0 the virtual origin of the self-similar jet. To determine the velocity

profile f from (4.18), the Reynolds shear stress needs to be modelled, which is usually done through a turbulent viscosity,

$$-\frac{\overline{u_1' u_2'}}{U_m^2} = h(\eta) = \frac{\nu_t}{U_m \delta_l} f'$$

Preservation of the self-similarity requires that $\nu_t/(U_m \delta_l) = \text{cst} \equiv 1/c$ but unlike in the case of the round jet, the turbulent viscosity is no longer constant. It increases with the distance from the nozzle $\nu_t/\nu \sim x_1^{1/2}$, and a complete self-similar solution cannot be obtained. The function f satisfies the following differential equation

$$f' + \frac{ac}{2} f \int_0^\eta f d\eta' = 0$$

and the solution can be written as

$$f(\eta) = \frac{1}{\cosh^2(d\eta)} \tag{4.20}$$

where $d = \sqrt{ac}/2 = 4ab^2/3$. By definition of η and f, there is also a compatibility condition given by $f(1) = 1/2$, or equivalently $d = \cosh^{-1}(\sqrt{2})$.

For completeness, two additional results are mentioned for the self-similar plane jet. The volume rate entrainment per unit length in the spanwise direction is

$$\frac{Q}{Q_j} = \frac{3}{2b}\sqrt{\frac{x_1 - x_0}{l}}$$

where $Q_j = l\, U_j$. The transverse mean velocity can be determined from the mass conservation,

$$\frac{\bar{U}_2}{U_m} = g(\eta) = \frac{a}{2}\left(2\eta f - \int_0^\eta f d\eta'\right) = \frac{a}{2d}\left[\frac{2d\eta}{\cosh^2(d\eta)} - \tanh(d\eta)\right]$$

This velocity is positive near the jet axis, but is negative near the edge of the jet where the ambient fluid is entrained, and takes a significant value $\bar{U}_2 \simeq 0.06 U_m$ as $\eta \to \infty$ featuring a plane flow. Finally, the experimental studies by Heskestad [534], Gutmark and Wygnanski [532] or Everitt and Robins [524] provide the following constant values

$$a \simeq 0.11 \qquad b \simeq 2.5 \qquad c = \frac{U_m \delta_l}{\nu_t} \simeq 30 \tag{4.21}$$

Plane jets can be used for cooling walls in some applications, and the expression of the turbulent viscosity needs to be modified close to the wall, as mentioned in Sect. 2.5.

4.4 Similarity for a Plane Wake

4.4.1 Far Wake Approximation

A self-similar solution can also be derived for wakes, but in a region far enough from the wake-producing body, in a region where the mean flow is nearly parallel, as shown in Fig. 4.9. Governing equations can then be simplified. The flow near the obstacle is generally complex and strongly depends on the shape of the obstacle. For example, the near wake of a circular cylinder is obviously different from that of a square cylinder due to the way the separation of the boundary layers occurs.

To estimate the order of magnitude of the different terms in the averaged Navier-Stokes equations, it must be pointed out that unlike free jets, two velocity scales are required here. The first one, denoted U_{conv}, is used to characterize the convection by the uniform mean flow at $U_{\text{conv}} \sim U_{e1}$, refer to Fig. 4.9 for the notations. Note that there is no external mean pressure gradient here. The second one U_{diff} is used to characterize the diffusion. Hence $U_{\text{diff}} \sim U_m$, where U_m is the axial mean velocity deficit in the wake. Moreover, the transverse mean velocity scale is V, the length scales in the longitudinal and transverse directions are (L, δ_l) and u is the turbulent velocity scale.

The equation for the mass conservation is an obvious example where the diffusion velocity scale appears, which gives for the mean transverse velocity,

$$V \sim \frac{\delta_l}{L} U_m$$

The averaged Navier-Stokes equation in the longitudinal direction is analysed as follows,

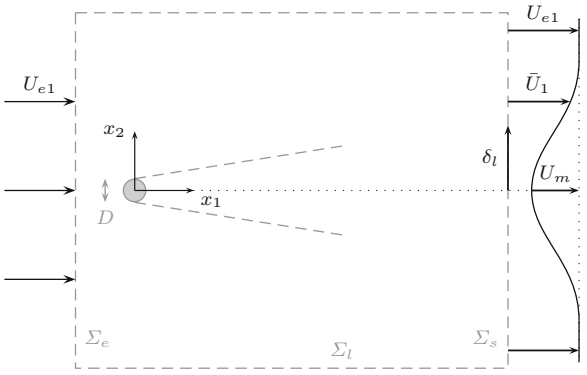

Fig. 4.9 Sketch of a plane far wake. The surface control used to define the drag coefficient (4.27) is shown in *dashed line*. The cross-section Σ_s for which self-similarity is observed, corresponds to $U_m/U_{e1} \leq 0.1$

$$\begin{array}{cccccc} \bar{U}_1\dfrac{\partial \bar{U}_1}{\partial x_1} & +\bar{U}_2\dfrac{\partial \bar{U}_1}{\partial x_2} & = -\dfrac{1}{\rho}\dfrac{\partial \bar{P}}{\partial x_1} & -\dfrac{\partial \overline{u_1'^2}}{\partial x_1} & -\dfrac{\partial \overline{u_1' u_2'}}{\partial x_2} & +\nu\nabla^2\bar{U}_1 \\ U_{e1}\dfrac{U_m}{L} & \dfrac{U_m^2}{L} & & \dfrac{u^2}{L} & \dfrac{u^2}{\delta_l} & \nu\left(\dfrac{U_m}{L^2};\ \dfrac{U_m}{\delta_l^2}\right) \\ (1) & (2) & & (3) & (4) & (5) \end{array} \tag{4.22}$$

The viscous terms are ignored in what follows by considering a sufficiently high Reynolds number wake $\mathrm{Re}_D = U_{e1} D/\nu$, where D is the diameter of the body cross-section. Two additional assumptions are also necessary to continue the study. First, one must postulate that the diffusion velocity scale U_{diff} is smaller than the convection velocity scale U_{conv} by one order of magnitude,

$$U_{\mathrm{diff}} \sim \frac{\delta_l}{L} U_{e1}$$

Secondly, to ensure that a turbulent wake flow is examined, the largest convection term (1) on the left-hand side in (4.22) must be of the same order of magnitude as the dominant turbulent term (4) on the right-hand side,

$$U_{e1}\frac{U_m}{L} \sim \frac{U_m^2}{\delta_l} \sim \frac{u^2}{\delta_l}$$

and thus $u \sim U_m$. It can be shown that the pressure term is negligible by considering the averaged Navier-Stokes in the transverse direction, a similar demonstration has already been developed for jets. The governing equation for the mean flow field is then given by

$$\bar{U}_1\frac{\partial \bar{U}_1}{\partial x_1} = -\frac{\partial \overline{u_1' u_2'}}{\partial x_2}$$

This equation can be further simplified in the far wake region by noting that $\bar{U}_1 \simeq U_{\mathrm{conv}} \simeq U_{e1}$ for the advection operator, and by introducing the deficit velocity $U_{e1} - \bar{U}_1$ in the wake. Hence,

$$U_{e1}\frac{\partial\left(U_{e1} - \bar{U}_1\right)}{\partial x_1} = \frac{\partial \overline{u_1' u_2'}}{\partial x_2} \tag{4.23}$$

The self-similar solution to this equation is sought of the form,

$$\begin{cases} U_{e1} - \bar{U}_1 = U_m\, f(\eta) \\ -\overline{u_1' u_2'} = U_m^2\, h(\eta) \end{cases} \qquad \text{with} \qquad \eta = \frac{x_2}{\delta_l(x_1)}$$

where U_m is the mean longitudinal velocity and δ_l is the half-width of the wake, as illustrated in Fig. 4.9.

4.4.2 Drag Coefficient

To define the drag coefficient C_D, the integral equation for the momentum flux over the control surface $\Sigma = \Sigma_e \cup \Sigma_s \cup \Sigma_l$ shown in Fig. 4.9, is considered. This equation can be written as

$$\int_{\Sigma} \rho \bar{\boldsymbol{U}} \left(\bar{\boldsymbol{U}} \cdot \boldsymbol{n} \right) d\Sigma = -\boldsymbol{F}_{\text{fluid} \to \text{body}}$$

if the pressure is assumed to be constant over Σ, and if the contribution of the Reynolds shear stress can be neglected on the exit surface Σ_s. The drag force is defined as the longitudinal component of $\boldsymbol{F}$,

$$F_1 = \int_{\Sigma_e} \rho U_{e1}^2 d\Sigma - \int_{\Sigma_s} \rho \bar{U}_1^2 d\Sigma - \int_{\Sigma_l} \rho U_{e1} \left(\bar{\boldsymbol{U}} \cdot \boldsymbol{n} \right) d\Sigma \tag{4.24}$$

In this same control volume, the mass conservation is

$$-\int_{\Sigma_e} \rho U_{e1} d\Sigma + \int_{\Sigma_s} \rho \bar{U}_1 d\Sigma + \int_{\Sigma_l} \rho \bar{\boldsymbol{U}} \cdot \boldsymbol{n} \, d\Sigma = 0$$

and illustrates the link between the mass flow deficit in the wake and the mass flux exiting from the lateral surface Σ_l. By multiplying this equation by U_{e1}, it can be combined with (4.24) to introduce the mean deficit velocity in the expression of F_1,

$$F_1 = \int_{\Sigma_s} \rho \bar{U}_1 \left(U_{e1} - \bar{U}_1 \right) d\Sigma = \rho U_{e1}^2 \int_{\Sigma_s} \frac{\bar{U}_1}{U_{e1}} \left(1 - \frac{\bar{U}_1}{U_{e1}} \right) d\Sigma \tag{4.25}$$

In the far wake, one has $F_1 \simeq \rho U_{e1} Q$ where Q is the volumetric flow rate deficit, defined by

$$Q = \int_{\Sigma_s} \left(U_{e1} - \bar{U}_1 \right) d\Sigma \tag{4.26}$$

Note that this flow rate Q is conserved through any cross-section according to (4.23). The drag coefficient C_D of the obstacle is then defined from F_1 by,

$$C_D = \frac{F_1}{\frac{1}{2} \rho U_{e1}^2 S} \tag{4.27}$$

where S is the cross-section area of the body. For two-dimensional plane wakes, the drag per unit length in the spanwise direction is considered. As an illustration, for a cylinder of diameter D, the section area is $S = D \times 1 = D$ and the drag coefficient is written as,

$$C_D = \frac{2\delta_\theta}{D} \simeq \frac{2Q}{U_{e1}D} \quad \text{where} \quad \delta_\theta = \int_{-\infty}^{+\infty} \frac{\bar{U}_1}{U_{e1}}\left(1 - \frac{\bar{U}_1}{U_{e1}}\right) dx_2 \tag{4.28}$$

is the momentum thickness.

4.4.3 Self-similar Solution for a Far Plane Wake

By integrating Eq. (4.23) in the transverse direction,

$$\overline{u_1' u_2'} = U_{e1} \frac{\partial}{\partial x_1} \int_0^{x_2} (U_{e1} - \bar{U}_1) dx_2'$$

the self-similarity for the Reynolds shear stress can then be expressed as

$$-\frac{\overline{u_1' u_2'}}{U_m^2} = h(\eta) = -\frac{U_{e1}}{U_m^2}\frac{d(U_m\delta_l)}{dx_1}\int_0^\eta f d\eta' + \frac{U_{e1}}{U_m}\frac{d\delta_l}{dx_1}\eta f \tag{4.29}$$

Moreover, the conservation of the momentum deficit I_1 for a wake flow provides the additional condition, $\delta_l U_m = \text{cst}$. Indeed,

$$I_1 = \int_{-\infty}^{+\infty} \rho U_{e1}\left(U_{e1} - \bar{U}_1\right) dx_2 = \rho U_{e1} U_m \delta_l \int_{-\infty}^{+\infty} f d\eta = \text{cst}$$

The following laws are thus found for the spreading rate and the velocity deficit of a far plane wake,

$$\frac{\delta_l}{D} = a\sqrt{\frac{x_1 - x_0}{D}} \qquad \frac{U_m}{U_{e1}} = b\sqrt{\frac{D}{x_1 - x_0}} \tag{4.30}$$

where D is the diameter of the cross-section of the body, a and b are the spreading rate and the decay constants of the wake. Equation (4.29) can be recast into a simplified form thanks to the conservation of I_1,

$$-\frac{\overline{u_1' u_2'}}{U_m^2} = \frac{U_{e1}}{U_m}\frac{d\delta_l}{dx_1}\eta f$$

To determine the function f of the transverse mean velocity profile, a turbulent viscosity model is used to express the Reynolds shear stress, $-\overline{u_1' u_2'} = \nu_t \partial\bar{U}_1/\partial x_2$, which yields using self-similar variables,

$$-\frac{\overline{u_1' u_2'}}{U_m^2} = -\frac{\nu_t}{U_m \delta_l}\frac{df}{d\eta}$$

The turbulent viscosity is then found to be a constant. The differential equation which must be satisfied by f is written as,

$$f' = -\frac{U_{e1}\delta_l}{\nu_t}\frac{d\delta_l}{dx_1}\eta f$$

and the solution is given by

$$f(\eta) = \exp\left(-a^2\frac{U_{e1}D}{4\nu_t}\eta^2\right) \tag{4.31}$$

By definition, one obtains $f(1) = 1/2$ which provides a compatibility condition for the constants, and leads to the following simple form for the transverse profile of the mean velocity, $f(\eta) = \exp(-\ln 2\ \eta^2)$. It is not necessary to immediately impose this classical solution of diffusion problems, which here is obtained from self-similarity considerations. As for free jets, various other results can be established. The Reynolds shear stress profile, the flow rate deficit, and the turbulent viscosity are only mentioned below,

$$-\frac{\overline{u_1'u_2'}}{U_m^2} = h(\eta) = \frac{a}{2b}\eta f \qquad \frac{Q}{U_{e1}D} = 2b\sqrt{\frac{\pi\nu_t}{U_{e1}D}} \simeq \frac{C_D}{2} \qquad \frac{\nu_t}{\nu} \simeq \frac{C_D^2}{16\pi b^2}\mathrm{Re}_D$$

and are associated with compatibility relations for the constants,

$$a^2b^2 \simeq \frac{\ln 2}{4\pi}C_D^2 \qquad \frac{\nu_t}{\nu} \simeq \frac{a^2}{4\ln 2}\mathrm{Re}_D \qquad \frac{U_m\delta_l}{\nu_t} = \frac{4b}{a}\ln 2$$

The values of the two constants a and b are not universal. They depend on the type of obstacle, which is well highlighted by the compatibility condition involving the drag coefficient C_D. Furthermore, the b constant cannot be expressed as a function of a only. The ratio ν_t/ν remains constant throughout the whole wake for a given body, and only depends on the Reynolds number Re_D. Thus, ν_t has been introduced in expression (4.31) of the function f. Finally, the calculation of the transverse mean velocity $\bar{U}_2$ turns out to be also interesting. Using the conservation of I_1 in a cross-section, that is $\delta_l U_m = \text{cst}$, the continuity equation provides,

$$\frac{\bar{U}_2}{U_m} = -\frac{d\delta_l}{dx_1}\eta f$$

There is no transverse velocity affinity for $\bar{U}_2/U_m$. Indeed, it remains the term $d\delta_l/dx_1$ which depends on x_1 since the spreading rate is not linear for the plane wake. This is a major difference with respect to free jets, for which $d\delta_l/dx_1 = \text{cst}$. The velocity $\bar{U}_2$ is always negative. Fluid is driven from the external flow to fill the central region of the wake, but $\bar{U}_2$ tends towards zero as $x_2 \to \infty$, in agreement with the conservation of the flow rate deficit Q of the wake.

Experimental studies, particularly the one of Wygnanski et al. [584] , deals with wakes produced by symmetric obstacles, such as cylinders, plates or wing profiles. For the classical case of a cylinder, the drag coefficient is $C_D \simeq 1$, and measurements provide the values

$$a \simeq 0.19 \qquad b \simeq 1.24 \qquad \frac{U_m \delta_l}{\nu_t} \simeq 18$$

Narasimha and Prabhu [576] used two small plates close to each another to obtain a far wake developing faster than with a cylindrical body, and found approximately the same results. These authors introduced another definition of the spreading rate, namely $\delta_l^2 / x_1 \delta_\theta$, using the fact that δ_l^2 is linear in x_1 and that δ_θ is independent of x_1. This speading rate is equal to $2a^2$ in the self-similar region. For more complex configurations, the case of asymmetric wakes for instance, one can refer to the studies by Patel and Scheuerer [414] or Mehta [575]. The case of a wake developing inside an exterior flow with a mean pressure gradient is examined by Narasimha and Prabhu [576].

4.5 Similarity for a Far Axisymmetric Wake

The self-similar solution of an axisymmetric far wake is obtained in the same way. Only the main results are pointed out in the following discussion. Under the same assumptions used for the plane wake, the equation governing the mean axial velocity is given by

$$U_{ez} \frac{\partial \bar{U}_z}{\partial z} = -\frac{1}{r} \frac{\partial}{\partial r} (r \overline{u'_z u'_r})$$

where U_{ez} is the velocity of the external uniform flow. It is convenient to recast this equation by introducing the mean velocity deficit,

$$U_{ez} \frac{\partial (U_{ez} - \bar{U}_z)}{\partial z} = \frac{1}{r} \frac{\partial}{\partial r} (r \overline{u'_z u'_r}) \tag{4.32}$$

For axisymmetric wakes, the momentum thickness δ_θ is also introduced from Eq. (4.25), but it is usually normalized by the perimeter of the body cross-section. For a sphere of diameter D, one has for instance

$$\pi D \times \delta_\theta = 2\pi \int_0^\infty \frac{\bar{U}_z}{U_{ez}} \left(1 - \frac{\bar{U}_z}{U_{ez}}\right) r dr \tag{4.33}$$

and the drag coefficient is

$$C_D = \frac{8\delta_\theta}{D} \simeq \frac{8Q}{\pi D^2 U_{ez}}$$

where Q is the flow rate deficit. The expression of the Reynolds shear stress is obtained by integrating Eq. (4.32) in the radial direction,

$$-\eta\frac{\overline{u_z'u_r'}}{U_m^2} = h(\eta) = -\frac{U_{ez}}{\delta_l U_m^2}\frac{d(U_m\delta_l^2)}{dz}\int_0^\eta f\eta' d\eta' + \frac{U_{ez}}{U_m}\frac{d\delta_l}{dz}f\eta^2$$

and self-similarity is only ensured if the two terms are independent of z on the right-hand side. The first term vanishes by noting that the conservation of the momentum deficit in a cross-section of the wake requires that $U_m\delta_l^2 = \text{cst}$. It is thus straightforward to derive the two following laws for the development of an axisymmetric wake,

$$\frac{\delta_l}{D} = a\left(\frac{z-z_0}{D}\right)^{1/3} \qquad \frac{U_m}{U_{ez}} = b\left(\frac{D}{z-z_0}\right)^{2/3} \tag{4.34}$$

where a and b are two constants linked to the body. The differential equation satisfied by $f(\eta)$ is given by

$$f' = -\frac{U_{ez}\delta_l}{\nu_t}\frac{d\delta_l}{dz}\eta f$$

with $U_m\delta_l/\nu_t = \text{cst} = c$. As a result, the turbulent viscosity varies as $\nu_t/\nu \sim z^{-1/3}$, and only a partial self-similar solution is here obtained. The integration yields,

$$f(\eta) = \exp\left(-\frac{ac}{6b}\eta^2\right) \tag{4.35}$$

A Gaussian profile is again found for the velocity deficit, as for the plane wake, and the condition $f(1) = 1/2$ allows to simplify its expression as follows, namely $f = \exp(-\ln 2\,\eta^2)$. Furthermore, it can be demonstrated that

$$-\frac{\overline{u_r'u_z'}}{U_m^2} = h(\eta) = \frac{a}{3b}\eta f \qquad \frac{\nu_t}{\nu} = \frac{ab}{c}\text{Re}_D\left(\frac{D}{z-z_0}\right)^{1/3}$$

The flow rate deficit normalised with the blocked flow by the obstacle writes

$$\frac{Q}{U_{ez}S} = 24b\frac{\nu_t}{U_{ez}D}\left(\frac{z-z_0}{D}\right)^{1/3} \simeq \frac{C_D}{2}$$

where $S = \pi D^2/4$. Two compatibility conditions link the different constants,

$$a^2 b = \frac{\ln 2}{8}C_D \qquad c = \frac{6b}{a}\ln 2$$

and finally, there is no self-similar profile for the radial mean velocity

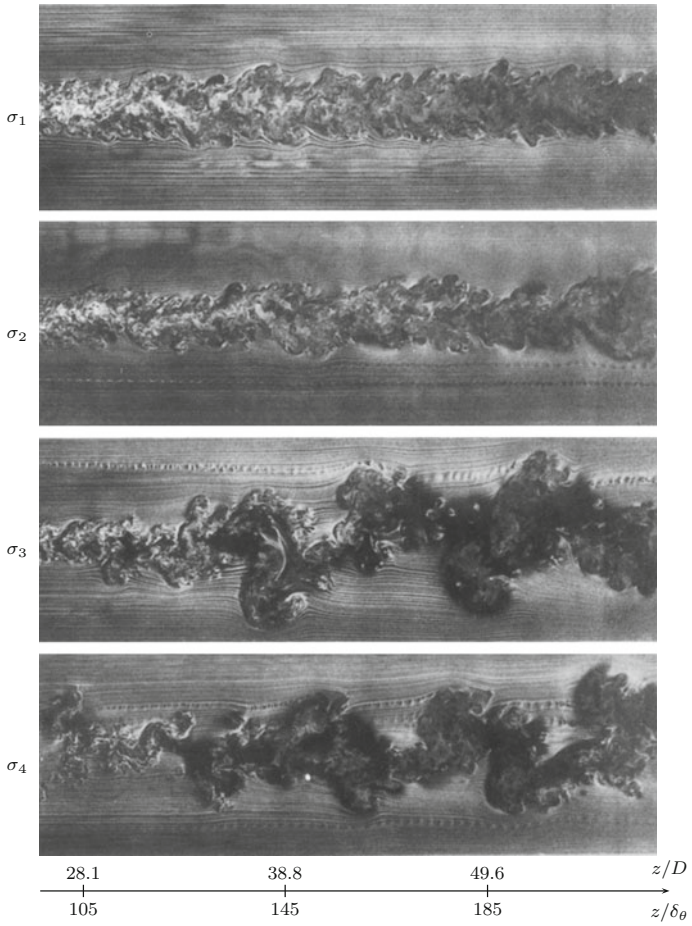

Fig. 4.10 Flow visualization by the smoke wire technique of far wakes generated by axisymmetric screens of solidity $\sigma_1 = 0.49$, $\sigma_2 = 0.62$, $\sigma_3 = 0.84$ and by a solid disk, $\sigma_4 = 1$. All obstacles have the same drag and thus the same momentum thickness, $\delta_\theta = 7.5$ mm at $U_{e1} = 7$ m.s^{-1}, see Sect. 4.5. Hence, the Reynolds number is $\mathrm{Re}_{\delta_\theta} = 3500$. Screen diameters are $D_1 = 37.5$ mm, $D_2 = D_3 = 30.9$ mm and the solid disk diameter is $D = 28$ mm. From Cannon and Glezer [571]

$$\frac{\bar{U}_r}{U_m} = -\frac{d\delta_l}{dz}\eta f$$

The experiments of Chevray [573] for an elongated ellipsoid of 6-to-1 ratio with $C_D \simeq 0.07$, provide an order of magnitude of the spreading rate and decay velocity constants associated with this wake,

$$a \simeq 0.10 \qquad b \simeq 0.60 \qquad c \simeq 25$$

The far wake visualization of a solid disk and three screens of different solidity reported by Cannon and Glezer [571], are shown in Fig. 4.10. The solidity is the ratio of solid to frontal area, which is less than one for a screen. Note the presence of large scale structures for the solid disk and the screens with high solidity.

In practice, the most interesting wakes are those associated with axisymmetric bodies powered by jets or propellers. The persistence of these wakes is often studied in aeronautics or in submarine applications. Of course, the self-similar solution needs to be revisited for wakes produced by self-propelled bodies, refer to Naudascher [577] for instance.

Chapter 5
Vortex Dynamics

A statistical approach to turbulence was adopted in Chap. 2, in which averaged Navier-Stokes equations were considered. Turbulence was found to be maintained through a production term linked to mean velocity gradients. Wall-bounded flows were studied this way in Chap. 3, and free shear flows were similarly examined in Chap. 4. In the present chapter, a more physical point of view is introduced. It is based on the vorticity field which is quite close to the structural eddies that one can observe in a turbulent flow.

5.1 The Biot-Savart Law

Definitions and some classical results regarding vorticity are gathered in this first paragraph. The vorticity field is defined by the relation $\boldsymbol{\omega} = \nabla \times \boldsymbol{u}$, which can be written using suffix notation as $\omega_i = \epsilon_{ijk}\partial u_k/\partial x_j$, where ϵ_{ijk} is the alternating tensor. In what follows, a bounded region of vorticity is considered, also called a vorticity blob. Under this assumption, it can be shown that

$$\int_V \omega_i d\boldsymbol{x} = 0 \tag{5.1}$$

over a sufficiently large volume V, and for $i = 1, \ldots, 3$. One starts by noting the following identity,

$$\frac{\partial}{\partial x_j}\left(\omega_j x_i\right) = \frac{\partial \omega_j}{\partial x_j} x_i + \omega_j \frac{\partial x_i}{\partial x_j} = \omega_j \delta_{ij} = \omega_i$$

where $\partial\omega_j/\partial x_j = 0$ since the vorticity field is solenoidal by definition. Then, use of the divergence theorem gives,

C. Bailly and G. Comte-Bellot, *Turbulence*, Experimental Fluid Mechanics,
DOI 10.1007/978-3-319-16160-0_5

$$\int_V \omega_i d\boldsymbol{x} = \int_V \frac{\partial}{\partial x_j}\left(\omega_j x_i\right) d\boldsymbol{x} = \int_\Sigma \omega_j x_i n_j d\boldsymbol{x} = 0 \tag{5.2}$$

hence the announced result (5.1).

For an incompressible velocity field, $\nabla \cdot \boldsymbol{u} = 0$, and a potential vector such as $\boldsymbol{u} = \nabla \times \boldsymbol{A}$ can be introduced, with the additional condition $\nabla \cdot \boldsymbol{A} = 0$ to ensure uniqueness. This potential vector $\boldsymbol{A}$ verifies a Poisson equation

$$\boldsymbol{\omega} = \nabla \times \boldsymbol{u} = \nabla \times (\nabla \times \boldsymbol{A}) = \nabla (\nabla \cdot \boldsymbol{A}) - \nabla^2 \boldsymbol{A} = -\nabla^2 \boldsymbol{A}.$$

The integral solution to this equation is given by

$$\boldsymbol{A}(\boldsymbol{x}) = \frac{1}{4\pi} \int_V \frac{\boldsymbol{\omega}(\boldsymbol{y})}{|\boldsymbol{x} - \boldsymbol{y}|} d\boldsymbol{y}$$

in free space [21]. The expression of the velocity can then be obtained by taking the curl of $\boldsymbol{A}$,

$$\boldsymbol{u}(\boldsymbol{x}) = \frac{1}{4\pi} \nabla_x \times \int_V \frac{\boldsymbol{\omega}(\boldsymbol{y})}{|\boldsymbol{x} - \boldsymbol{y}|} d\boldsymbol{y} = \frac{1}{4\pi} \int_V \nabla_x \left(\frac{1}{|\boldsymbol{x} - \boldsymbol{y}|} \right) \times \boldsymbol{\omega}(\boldsymbol{y}) d\boldsymbol{y}$$

where the suffix x indicates that the curl or divergence operator is applied at point $\boldsymbol{x}$. By noting that,

$$\frac{\partial}{\partial x_i}\left(\frac{1}{r}\right) = -\frac{1}{r^2}\frac{\partial r}{\partial x_i} = -\frac{1}{r^2}\frac{r_i}{r} \quad \text{with} \quad \boldsymbol{r} = \boldsymbol{x} - \boldsymbol{y}$$

the previous equation can be simplified, yielding the famous Biot-Savart law

$$\boldsymbol{u}(\boldsymbol{x}) = \frac{1}{4\pi} \int_V \frac{\boldsymbol{\omega}(\boldsymbol{y}) \times (\boldsymbol{x} - \boldsymbol{y})}{|\boldsymbol{x} - \boldsymbol{y}|^3} d\boldsymbol{y} \tag{5.3}$$

which provides the velocity field induced by a vorticity distribution. This law was first derived in electromagnetism to calculate the magnetic field induced by an electric current. This connection between velocity and vorticity is non local, which means that every point $\boldsymbol{y}$ in the volume V contributes to the determination of the velocity field at an arbitrary point $\boldsymbol{x}$, not necessarily included in V, as illustrated in Fig. 5.1. Note that a similar result has already been pointed out for the pressure field, refer to expression (1.6).

The velocity field for an observer $\boldsymbol{x}$ in the far field is now examined. By expanding the potential vector $\boldsymbol{A}$ as a Taylor series, one gets

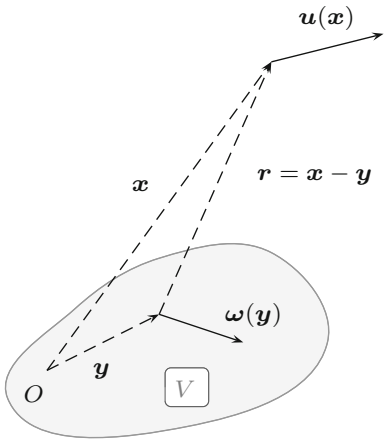

Fig. 5.1 Illustration of Biot-Savart's law. All the points $\boldsymbol{y}$ inside the vorticity blob V contributes to the velocity field at point $\boldsymbol{x}$

$$\boldsymbol{A}(\boldsymbol{x}) = \frac{1}{4\pi}\int_V \frac{\boldsymbol{\omega}(\boldsymbol{y})}{|\boldsymbol{x}-\boldsymbol{y}|}\,d\boldsymbol{y} \simeq \frac{1}{4\pi}\int_V \boldsymbol{\omega}(\boldsymbol{y})\left(\frac{1}{x}+\frac{\boldsymbol{x}\cdot\boldsymbol{y}}{x^3}\right)d\boldsymbol{y}$$
$$\simeq \frac{1}{4\pi x}\left\{\int_V \boldsymbol{\omega}(\boldsymbol{y})\,d\boldsymbol{y} + \int_V \boldsymbol{\omega}(\boldsymbol{y})\,\frac{\boldsymbol{x}\cdot\boldsymbol{y}}{x^2}d\boldsymbol{y}\right\}$$

as $x \to \infty$. The first term is zero according to the relation (5.2). Therefore, one has

$$\boldsymbol{A}(\boldsymbol{x}) \simeq \frac{1}{4\pi}\frac{1}{x^2}\int_V \boldsymbol{\omega}(\boldsymbol{y})\,\frac{\boldsymbol{x}\cdot\boldsymbol{y}}{x}d\boldsymbol{y}$$

and consequently $\boldsymbol{u} = \nabla\times\boldsymbol{A} \sim \mathcal{O}\left(1/x^3\right)$ when $x \to \infty$. This rapid decrease in the hydrodynamic velocity field can be compared to the slow decrease of the acoustic field radiated by the same vorticity blob, which follows a $1/x$ law either for acoustic velocity or pressure in the far field. Obviously, this compressible contribution does not appear here since it has been assumed that $\nabla\cdot\boldsymbol{u} = 0$.

5.2 Vortex Stretching

Kelvin's circulation theorem states that for an inviscid and homentropic flow, submitted to body forces $\boldsymbol{f}$ which can be expressed from a potential $\boldsymbol{f} = \nabla\phi$, the velocity circulation Γ is conserved along a closed material curve $\mathcal{C}$,

$$\frac{d\Gamma}{dt} = \frac{d}{dt}\left(\oint_{\mathcal{C}} \boldsymbol{u}\cdot d\boldsymbol{l}\right) = 0 \tag{5.4}$$

as shown in Fig. 5.2. A brief demonstration is provided below. Starting from the material derivative of the circulation, one has

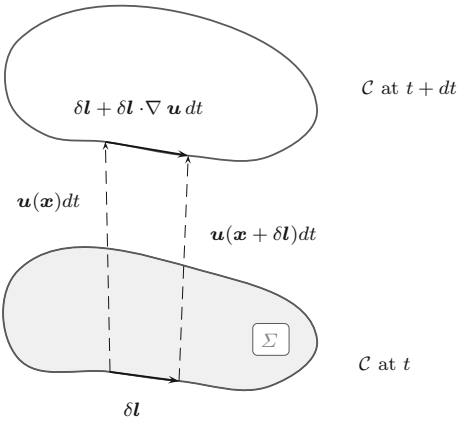

Fig. 5.2 Illustration of Kelvin's circulation theorem, the circulation Γ is conserved along a closed material curve $\mathcal{C}$, or equivalently, the flux of vorticity through the surface Σ closing $\mathcal{C}$. Notice that $d(\delta \boldsymbol{l})/dt = \delta \boldsymbol{l} \cdot \nabla \boldsymbol{u}$, this relation can be straightforwardly derived by considering the velocity difference between the boundaries of $\boldsymbol{\delta}_s$, that is $\boldsymbol{\delta}_s\,(t + dt) = \boldsymbol{\delta}_s\,(t) + \boldsymbol{u}\,(\boldsymbol{x} + \boldsymbol{\delta}_s)\,dt - \boldsymbol{u}\,(\boldsymbol{x})\,dt$

$$\begin{aligned}
\frac{d\Gamma}{dt} &= \oint_{\mathcal{C}} \frac{d\boldsymbol{u}}{dt} \cdot d\boldsymbol{l} + \oint_{\mathcal{C}} \boldsymbol{u} \cdot \frac{d}{dt}(d\boldsymbol{l}) \\
&= \oint_{\mathcal{C}} \left(-\frac{1}{\rho} \nabla p + \nabla \phi \right) \cdot d\boldsymbol{l} + \oint_{\mathcal{C}} \boldsymbol{u} \cdot (d\boldsymbol{l} \cdot \nabla \boldsymbol{u}) \\
&= \oint_{\mathcal{C}} \left(-\frac{1}{\rho} \nabla p + \nabla \phi \right) \cdot d\boldsymbol{l} + \oint_{\mathcal{C}} \nabla \left(\frac{\boldsymbol{u}^2}{2} \right) \cdot d\boldsymbol{l}
\end{aligned}$$

The second and third terms vanish for a closed curve $\mathcal{C}$. Furthermore, if the flow can be considered as homentropic, that is the entropy s is constant, the first term is also zero. Indeed, the density $\rho = \rho(p, s)$ is thus a function only of pressure $\rho = \rho(p)$. By introducing the auxiliary variable

$$\Pi_p = \int \frac{dp}{\rho(p)}$$

the pressure gradient can be written as $\nabla \Pi_p = (1/\rho) \nabla p$. The integration of this term along a closed curve is thus zero and therefore, $d\Gamma/dt = 0$. Moreover, it is straightforward to check that Π_p is the specific enthalpy h for a homentropic perfect gas flow.

Another interesting form of Kelvin's circulation theorem may be written using Stokes' theorem,

$$\frac{d\Gamma}{dt} = \frac{d}{dt} \left(\oint_{\mathcal{C}} \boldsymbol{u} \cdot d\boldsymbol{l} \right) = \frac{d}{dt} \iint_{\Sigma} (\nabla \times \boldsymbol{u}) \cdot d\boldsymbol{x} = \frac{d}{dt} \iint_{\Sigma} \boldsymbol{\omega} \cdot d\boldsymbol{x} = 0$$

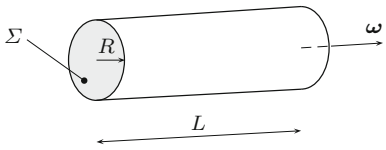

Fig. 5.3 Sketch of an elementary vortex tube

where Σ is the surface closing the curve $\mathcal{C}$. In other words, the flux of vorticity through a material surface is constant. To more concretely illustrate this result, a small elementary vortex tube of length L, radius R with a uniform vorticity ω over its cross-section is considered, see Fig. 5.3. The conservation of the vorticity flux $\pi R^2\omega$ imposes that the product $R^2\omega$ remains constant. Similarly, the conservation of mass yields $R^2 L = \text{cst}$, and finally one gets

$$\omega \sim L \sim \frac{1}{R^2} \tag{5.5}$$

The vortex energy is therefore increased by stretching the vortex tube at the same time as the cross section decreases and the vorticity magnitude ω is amplified. The velocity field induced by the vortex is indeed enhanced, resulting in a larger kinetic energy. The vortex stretching is an essential mechanism for the production of turbulent kinetic energy.

Fluid particles associated with an elementary tube vortex are stretched through velocity gradients of the mean flow. As an illustration, consider the case of a mean shear flow defined by $\bar{U}_1 = \bar{S}x_2$ and $\bar{U}_2 = \bar{U}_3 = 0$. According to relation (2.11), the deviatoric rate-of-strain tensor is

$$\bar{S}_{ij} = \frac{1}{2}\left(\frac{\partial \bar{U}_i}{\partial x_j} + \frac{\partial \bar{U}_j}{\partial x_i}\right) = \frac{\bar{S}}{2}\begin{pmatrix} 0 & 1 \\ 1 & 0 \end{pmatrix}, \quad \text{and} \quad \bar{S}^d_{ij} = \frac{\bar{S}}{2}\begin{pmatrix} 1 & 0 \\ 0 & -1 \end{pmatrix}$$

where $\bar{\boldsymbol{S}}^d$ is the same tensor in a diagonal form obtained by a $\pi/4$ rotation of the frame axes. The principal strain axes are thus also the axes of this rotated coordinate system, as shown in Fig. 5.4. Material lines are stretched in the $\boldsymbol{e}_1 + \boldsymbol{e}_2$ direction, and for a vortex tube, velocity fluctuations are then increased in the perpendicular plane.

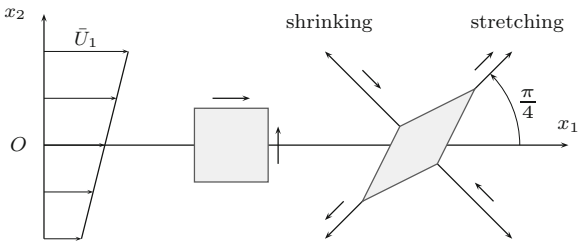

Fig. 5.4 Deformation of a fluid particle by a mean shear flow $\bar{U}_1 = \bar{S}x_2$

5.3 Helmholtz's Equation

The Helmholtz equation is the transport equation for vorticity, which can be established as follows. As a starting point, the curl operator is applied to Navier-Stokes' equation,

$$\nabla \times \left(\frac{\partial \boldsymbol{u}}{\partial t} + \boldsymbol{u} \cdot \nabla \boldsymbol{u} = -\frac{1}{\rho} \nabla p + \nu \nabla^2 \boldsymbol{u} \right)$$

The flow is assumed to be incompressible, that is $\nabla \cdot \boldsymbol{u} = 0$, but with a variable density ρ. A compressible form of the vorticity equation is derived in Sect. 5.8. The convective term can be expressed as $\boldsymbol{u} \cdot \nabla \boldsymbol{u} = \nabla(\boldsymbol{u}^2/2) + \boldsymbol{\omega} \times \boldsymbol{u}$. By using the following vector identity,

$$\nabla \times (\boldsymbol{\omega} \times \boldsymbol{u}) = \boldsymbol{u} \cdot \nabla \boldsymbol{\omega} - \boldsymbol{u} \nabla \cdot \boldsymbol{\omega} - \boldsymbol{\omega} \cdot \nabla \boldsymbol{u} + \boldsymbol{\omega} \nabla \cdot \boldsymbol{u}$$

where $\nabla \cdot \boldsymbol{u} = 0$ and $\nabla \cdot \boldsymbol{\omega} \equiv 0$, the vorticity equation can be rearranged as

$$\frac{\partial \boldsymbol{\omega}}{\partial t} + \boldsymbol{u} \cdot \nabla \boldsymbol{\omega} = \boldsymbol{\omega} \cdot \nabla \boldsymbol{u} - \nabla \times \left(\frac{1}{\rho} \nabla p \right) + \nu \nabla^2 \boldsymbol{\omega}$$

The pressure term can also be simplified, which leads to

$$\nabla \times \left(\frac{1}{\rho} \nabla p \right) = \nabla \left(\frac{1}{\rho} \right) \times \nabla p + \frac{1}{\rho} \nabla \times (\nabla p) = -\frac{1}{\rho^2} \nabla \rho \times \nabla p \tag{5.6}$$

Moreover for a homentropic flow, the pressure is a function only of density, as already mentioned in the previous section. The two vectors $\nabla \rho$ and ∇p are thus aligned and the so-called baroclinic term $-(\nabla \rho \times \nabla p)/\rho^2$ vanishes. The vorticity equation, also known as Helmholtz's equation, is then given by

$$\frac{\partial \boldsymbol{\omega}}{\partial t} + \boldsymbol{u} \cdot \nabla \boldsymbol{\omega} = \boldsymbol{\omega} \cdot \nabla \boldsymbol{u} + \nu \nabla^2 \boldsymbol{\omega} \tag{5.7}$$

Variations of the vorticity $d\boldsymbol{\omega}/dt$ are driven by the source term $\boldsymbol{\omega} \cdot \nabla \boldsymbol{u}$, and by viscous damping. Vortex stretching can thus only be associated with the term $\boldsymbol{\omega} \cdot \nabla \boldsymbol{u}$. To demonstrate that [105], let us consider the evolution of the length of an elementary part $\boldsymbol{\delta_s}$ of a vortex tube. Its material derivative can be written as

$$\frac{d\boldsymbol{\delta_s}}{dt} = \boldsymbol{\delta_s} \cdot \nabla \boldsymbol{u}$$

Consequently for $\delta_s = \boldsymbol{\delta_s} \cdot \boldsymbol{\alpha}$, where $\boldsymbol{\alpha} = \boldsymbol{\omega}/\omega$ is the unit vector aligned with the vorticity vector of the considered element, see the illustration in Fig. 5.5, one has

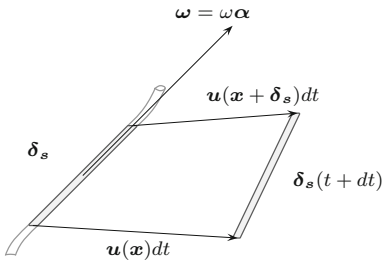

Fig. 5.5 Evolution of an elementary tube vortex $\boldsymbol{\delta_s} = \delta_s\boldsymbol{\alpha}$, where $\boldsymbol{\alpha}$ is the unit vector aligned with the vorticity vector $\boldsymbol{\omega}$

$$\frac{d\delta_s}{dt} = \boldsymbol{\alpha}\cdot(\boldsymbol{\delta_s}\cdot\nabla\boldsymbol{u}) = \frac{\omega_i}{\omega}\left(\delta_s\frac{\omega_j}{\omega}\frac{\partial u_i}{\partial x_j}\right) = \frac{\omega_i\omega_j}{\omega^2}\frac{\partial u_i}{\partial x_j}\delta_s$$

Moreover, according to Helmholtz's equation (5.7) for an inviscid flow, one has

$$\boldsymbol{\omega}\cdot\frac{d\boldsymbol{\omega}}{dt} = \boldsymbol{\omega}\cdot(\boldsymbol{\omega}\cdot\nabla\boldsymbol{u}) \quad \text{which yields,} \quad \frac{d}{dt}\left(\frac{\omega^2}{2}\right) = \omega_i\omega_j\frac{\partial u_i}{\partial x_j}$$

Hence, by comparison of the two previous expressions, it can be inferred that the stretching or shrinking of an elementary vortex tube is gouverned by

$$\frac{1}{\omega^2}\frac{d}{dt}\left(\frac{\omega^2}{2}\right) = \frac{1}{\delta_s}\frac{d\delta_s}{dt}$$

and by integration, this yields $\omega/\delta_s = \text{cst}$. This result is of course in agreement with the expression (5.5). The physical important result is that the elementary length δ_s of a vortex tube is proportional to its vorticity ω. Vortex intensity goes along with stretching of vortex lines and consequently, with an increase in distance between fluid particles. Note that the source term $\boldsymbol{\omega}\cdot\nabla\boldsymbol{u}$ in Helmholtz's equation associated with stretching/shrinking and also tilting, that is the change of orientation of the vorticity vector, is zero for a two-dimensional flow. In other words, a two-dimensional flow is a very particular situation. Vortex stretching, which has been identified as an elementary mechanism for the production of kinetic energy, cannot occur.

Helmholtz's equation (5.7) is in general not the preferred alternative to the Navier-Stokes equation for numerical applications. At least two nonlinear terms must be solved, namely one linked to the material derivative of $\boldsymbol{\omega}$, and the other one to the source term $\boldsymbol{\omega}\cdot\nabla\boldsymbol{u}$. The latter can also be expressed as follows,

$$(\boldsymbol{\omega}\cdot\nabla\boldsymbol{u})_i = \omega_j\frac{\partial u_i}{\partial x_j} = \omega_j\left(e_{ij} + \omega_{ij}\right) = \omega_j e_{ij} = \omega_j s_{ij} \tag{5.8}$$

according to the definition (2.11). Indeed, the antisymmetric part of the rate-of-strain tensor does not contribute to the stretching term. This can be shown by noting that,

$$\omega_j \omega_{ij} = \frac{\omega_j}{2}\left(\frac{\partial u_i}{\partial x_j} - \frac{\partial u_j}{\partial x_i}\right) = -\frac{\omega_j}{2}\epsilon_{ijk}\omega_k = -\frac{\omega_k}{2}\epsilon_{ikj}\omega_j$$

having permuted the two dummy indices j and k. As $\epsilon_{ijk} = -\epsilon_{ikj}$, the half sum of the two previous expressions thus provides $\omega_j \omega_{ij} = 0$. Finally, as with the pressure in Navier-Stokes's equation, vorticity and velocity are connected by the Biot-Savart law (5.3), that is by a non-local relation.

Finally two additional examples are presented to introduce consequences of vortex stretching. The first one is inspired by Tennekes and Lumley [26]. According to expression (5.8), Helmholtz's equation (5.7) can be recast as follows,

$$\frac{\partial \boldsymbol{\omega}}{\partial t} + \boldsymbol{u} \cdot \nabla \boldsymbol{\omega} = \boldsymbol{\omega} \cdot \boldsymbol{s} + \nu \nabla^2 \boldsymbol{\omega} \tag{5.9}$$

This vorticity transport equation can be linearised around a known based flow $\bar{\boldsymbol{U}}$ to study the evolution of a vorticity disturbance $\boldsymbol{\omega}'$ associated with an induced velocity field $\boldsymbol{u}'$. Viscous effects are here neglected to simplify algebra, but could be included [44]. Moreover, the based flow is assumed to be a pure strain flow, which means that the eigenvectors of the strain rate tensor are aligned with the frame axes. A linear based flow is considered for simplicity, $\bar{U}_1 = U_0$, $\bar{U}_2 = \bar{S}x_2$ and $\bar{U}_3 = -\bar{S}x_3$ where U_0 and $\bar{S}$ are two constants. By noting that $\bar{\Omega}_i \equiv 0$, the linearization of Eq. (5.9) gives,

$$\frac{\partial \boldsymbol{\omega}'}{\partial t} + \bar{\boldsymbol{U}} \cdot \nabla \boldsymbol{\omega}' = \boldsymbol{\omega}' \cdot \bar{\boldsymbol{S}}$$

where the strain tensor $\bar{\boldsymbol{S}}$ has only two non-zero terms, $\bar{S}_{22} = \bar{S}$ and $\bar{S}_{33} = -\bar{S}$. A stretching is applied in the x_2 direction, $d\bar{\omega}_2'/d\bar{t} = \bar{S}\omega_2'$, and a compression or shrinking is applied in the x_3 direction, $d\bar{\omega}_3'/d\bar{t} = -\bar{S}\omega_3'$. The linearised vorticity equation can directly be integrated in a Lagrangian frame with the initial conditions $\omega_1' = 0$ and $\omega_2' = \omega_3' = \omega_0$ at $t = 0$. The final result can also be obtained more formally from the following change of variables $(t, \boldsymbol{x}) \rightarrow (\tau, \boldsymbol{\xi})$ with

$$\tau = t \quad \xi_1 = x_1 - U_0 t \quad \xi_2 = x_2 e^{-\bar{S}t} \quad \xi_3 = x_3 e^{\bar{S}t}$$

which provides $\partial\omega_2'/\partial\tau = \bar{S}\omega_2'$ and $\partial\omega_3'/\partial\tau = -\bar{S}\omega_3'$. In both cases, the time evolution of vorticity components is finally given by $\omega_2' = \omega_0 e^{\bar{S}t}$ and $\omega_3' = \omega_0 e^{-\bar{S}t}$ and therefore, vorticity increases since $\omega'^2 = \omega_0^2 \cosh(2\bar{S}t)$. As illustrated in Fig. 5.6,

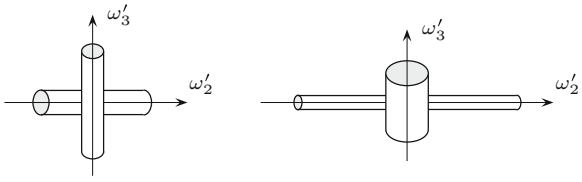

Fig. 5.6 Sketch of vortex tubes submitted to a strain flow in the $x_2 - x_3$ plane, stretching along x_2 and compression along x_3

the velocity field induced by ω_2' is thus reinforced for components u_1' and u_3', and the one induced by ω_3' is reduced for components u_1' and u_2'. As a final result, $u_3'^2$ is increased, $u_2'^2$ is decreased and $u_1'^2$ is expected to fairly increase.

A further view has been given by Bradshaw [3]. Stretching in the x_3 direction for instance, amplifies velocity in the $x_1 - x_2$ plane and also reduces the length scale associated with the flow. As a result, stretching occurs for vorticity components in the $x_1 - x_2$ plane, and velocity is then amplified in the $x_2 - x_3$ and $x_1 - x_3$ planes. The process can be repeated several times as shown by the tree below,

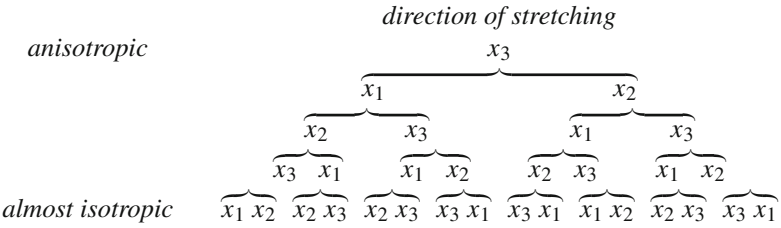

After only a few steps, velocity is equally amplified in all directions and characteristic length scales of the flow become more and more smaller. This so-called energy cascade leading to an isotropic state of turbulence, by which all the directions are equivalent, is of course limited by molecular effects.

These two examples provide a caricatural view of vortex stretching to explain energy transfer between large scales to smaller scales. Isotropic turbulence as well as the cascade energy will be in depth discussed in Chaps. 6 and 7.

5.4 Two Numerical Illustrations

To supplement the previous section, two additional examples are briefly shown so as to underline consequences of developing a turbulent flow in a two dimensional space. In Fig. 5.7, two snapshots of the same flow are displayed, the numerical simulation being performed in three and two dimensions using the same bluff body [574]. The flow goes from the left to the right, and the boundary layer developing around the leading edge is strongly detached. The difference between the two views is striking. In the 2-D simulation, a quasi-periodic vortex shedding of large clockwise vortices is observed from the separation bubble, no mixing occurs with counterclockwise vortical structures and no breakdown of the two-dimensional coherence appears downstream, unlike the 3-D simulation.

In a two-dimensional space, two typical evolutions can be distinguished for a pair of vortices, depending on the sign of their vorticity. The plane mixing layer. is an emblematic example to illustrate the evolution of co-rotative vortices. The mean velocity field is well-described by a hyperbolic tangent profile, which is usually imposed at the entrance of the computational domain,

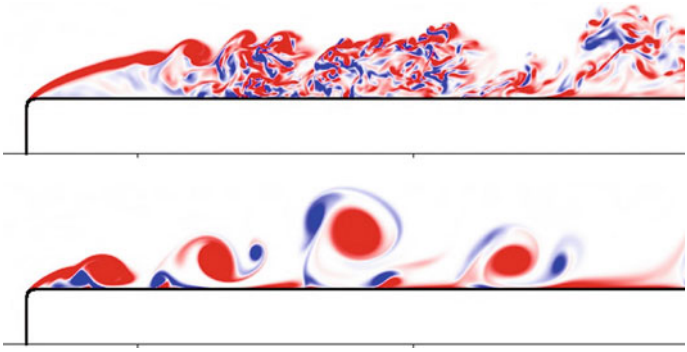

Fig. 5.7 Flow separation behind a rounded leading edge: instantaneous view of the spanwise vorticity ($\omega_z = \pm 5 U_\infty / H$) provided by a 3-D direct numerical simulation in the *top view*, and by a 2-D simulation in the *bottom view*. Case $\eta = 0.125$ where η is the ratio between the curvature radius and the body height H, and with small inflow perturbations $u'/U_\infty = 0.1\,\%$. The Reynolds number is $\mathrm{Re} = U_\infty H/\nu = 2000$. From Lamballais et al. [574]

$$\bar{U}_1(x_2) = \frac{\mathcal{U}_1 + \mathcal{U}_2}{2} + \frac{\mathcal{U}_1 - \mathcal{U}_2}{2} \tanh\left(\frac{2x_2}{\delta_\omega(0)}\right)$$

where $\mathcal{U}_1 \simeq 0.30\, c_0$ and $\mathcal{U}_2 \simeq 0.15\, c_0$ in the present case, and $c_0 \simeq 340\,\mathrm{m \cdot s^{-1}}$ is the speed of sound. The Reynolds number is defined as $\mathrm{Re} = \Delta U \delta_\omega(0)/\nu \simeq 5300$ with $\Delta U = \mathcal{U}_1 - \mathcal{U}_2$, $\delta_\omega(0)$ is the initial vorticity thickness. The reader can also refer to Sect. 1.5.2 for a further description of this flow. The natural development of the mixing layer is numerically obtained by imposing a random excitation. Figure 5.8 displays four snapshots of the vorticity field at four consecutive times [470]. The initial development of the mixing layer is dominated by the development of Kelvin-Helmholtz instability waves, which grow and lead to the first roll-up at about $x_1 \simeq 60\delta_\omega(0)$, and finally to vortices. The mixing layer then contains quasi-isolated co-rotating vortices, but these vortical structures distort and interact with themselves thanks to their induced velocity field. As shown in Fig. 5.8, a merging then occurs between $90\delta_\omega(0) \leq x_1 \leq 150\delta_\omega(0)$, and finally produce a larger vortex as indicated by the intersection between the two solid lines. This coalescence of coherent structures, the so-called vortex pairing, was experimentally revealed by Winant and Browand [497]. An inverse energy cascade occurs since initial vortices of size λ_0 or wavenumber $k_0 = 2\pi/\lambda_0$ generate larger vortices of size $2\lambda_0$, corresponding to the first subharmonic $k_0/2$. This is the only possible evolution in a two-dimensional space, and no breakdown leading to a fully turbulent mixing layer can be observed. As a result, in the present case, the linear expansion of the mean flow [474, 490]

$$\frac{d\delta_\omega}{dx_1} = K_\delta \frac{\mathcal{U}_1 - \mathcal{U}_2}{\mathcal{U}_1 + \mathcal{U}_2} \quad \text{with} \quad 0.170 \leq K_\delta \leq 0.181$$

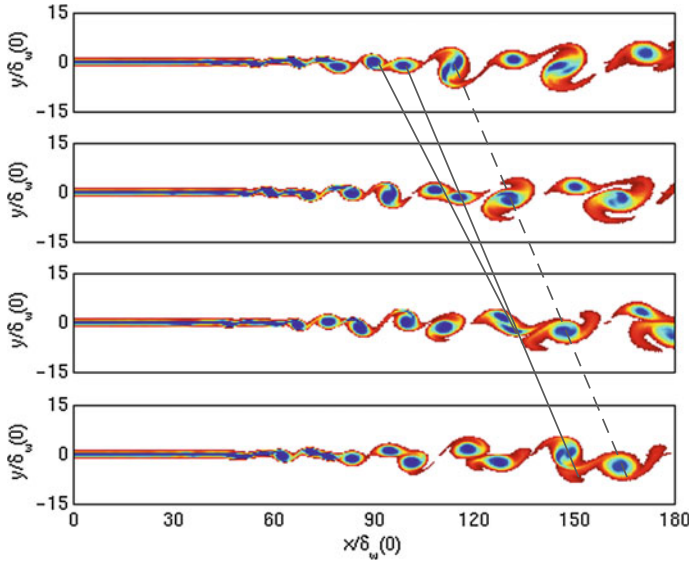

Fig. 5.8 Numerical simulation of a two-dimensional mixing layer. Vorticity snapshots at four consecutive times separated by $17\delta_\omega(0)/U_c$, where U_c is the convection velocity. The velocity of local extrema of vorticity provides an estimation of this convection velocity U_c, as shown with the *dashed line*. The two *solid lines* indicate a vortex pairing. From Bogey et al. [470]

originates from discrete events. Finally, the convection velocity $U_c = (\mathcal{U}_1 + \mathcal{U}_2)/2$ can be estimated by tracking extrema of the vorticity as illustrated by the dashed line.

Moreover, the evolution of a pair of counter-rotating vortices is quite different. They form a dipole of vorticity [1, 159] which moves in an autonomous and chaotic fashion. This situation is rarely found in practice, except for some geophysical flows.

5.5 Transport Equation for the Mean Vorticity

The Reynolds decomposition of the vorticity $\omega_i = \bar{\Omega}_i + \omega_i'$ can be introduced in Helmholtz's equation (5.7) to derive a transport equation on the mean vorticity, as it was done for the Navier-Stokes equations in Chap. 2. By observing that $\partial\omega_j'/\partial x_j = 0$ from the definition of vorticity, and that $\partial u_j'/\partial x_j = 0$ for an incompressible turbulence, it is straightforward to obtain

$$\frac{\partial\bar{\Omega}_i}{\partial t} + \bar{U}_j\frac{\partial\bar{\Omega}_i}{\partial x_j} = \bar{\Omega}_j\frac{\partial\bar{U}_i}{\partial x_j} + \underline{\frac{\partial}{\partial x_j}\left(\overline{\omega_j' u_i'} - \overline{\omega_i' u_j'}\right)} + \nu\frac{\partial^2\bar{\Omega}_i}{\partial x_j\partial x_j} \tag{5.10}$$

The underlined correlation terms are to be modelled in order to close this transport equation. For practical purposes, this equation is seldom solved to obtain a numerical

solution of the mean velocity field. Formulations based on the Reynolds-averaged Navier-Stokes equations are preferred for turbulence modelling.

5.6 Enstrophy

The enstrophy E_ω is defined as the average of one half of the square fluctuating vorticity, namely $E_\omega = \overline{\omega_i'\omega_i'}/2$. A general transport equation can be established for the enstrophy, by susbtracting Eq. (5.10) to Helmholtz's equation (5.7), by multiplying the result by ω_i' and then by applying the average operator. In order to simplify algebra in what follows, it is assumed that the turbulent field is not sustained by a mean flow, that is $\bar{U}_i = 0$ and thus $\bar{\Omega}_i = 0$. Noting $\boldsymbol{\omega}'^2 = \omega_i'\omega_i'$, this leads to

$$\frac{\partial}{\partial t}\left(\frac{\boldsymbol{\omega}'^2}{2}\right) + \boldsymbol{u}' \cdot \nabla\left(\frac{\boldsymbol{\omega}'^2}{2}\right) = \boldsymbol{\omega}' \cdot \left(\boldsymbol{\omega}' \cdot \nabla \boldsymbol{u}'\right) + \boldsymbol{\omega}' \cdot \left(\nu \nabla^2 \boldsymbol{\omega}'\right)$$

The last term associated with molecular viscous effects can be rearranged as,

$$\boldsymbol{\omega}' \cdot \left(\nu \nabla^2 \boldsymbol{\omega}'\right) = \nu \omega_i' \frac{\partial^2 \omega_i'}{\partial x_j \partial x_j} = -\nu \frac{\partial \omega_i'}{\partial x_j}\frac{\partial \omega_i'}{\partial x_j} + \nu \frac{\partial^2}{\partial x_j \partial x_j}\left(\frac{\omega_i'\omega_i'}{2}\right)$$

and consequently, the transport equation for E_ω takes the form,

$$\frac{\partial}{\partial t}\left(\overline{\frac{\boldsymbol{\omega}'^2}{2}}\right) + \nabla\left(\overline{\frac{\boldsymbol{\omega}'^2}{2}\boldsymbol{u}'}\right) = \overline{\boldsymbol{\omega}' \cdot (\boldsymbol{\omega}' \cdot \nabla \boldsymbol{u}')} - \nu \overline{\frac{\partial \omega_i'}{\partial x_j}\frac{\partial \omega_i'}{\partial x_j}} + \nu \frac{\partial^2}{\partial x_j \partial x_j}\left(\overline{\frac{\boldsymbol{\omega}'^2}{2}}\right)$$

for an incompressible turbulence. In order to highlight source terms, diffusion terms are removed by assuming that the turbulence is homogeneous, that is mean quantities are independent of space coordinates. The enstrophy is then governed by,

$$\frac{\partial E_\omega}{\partial t} = \underbrace{\overline{\omega_i'\omega_j'\frac{\partial u_i'}{\partial x_j}}}_{(a)} - \underbrace{\nu \overline{\left(\frac{\partial \omega_i'}{\partial x_j}\right)^2}}_{(b)} \tag{5.11}$$

under the assumptions noted previously. The term (a) is connected to the stretching of vortices as shown in Sect. 5.3, and the term (b) to viscous dissipation. Historically, the term (a) was assumed to be zero by von Kármán [113], but Taylor [152] demonstrated later that this term is not zero and furthermore, must be positive. It expresses that two fluid particles initially close one from the other will be later separated by turbulence in average. For isotropic turbulence, this term takes a very simple form given by expression (6.44), making it experimentally measurable.

The singular behaviour of two-dimensional turbulent flows can be again pointed out, since the transport equation for enstrophy reduces to,

$$\frac{\partial E_\omega}{\partial t} = -\nu \overline{\left(\frac{\partial \omega_i'}{\partial x_j}\right)^2}$$

The enstrophy can thus only decrease, and dynamics of 2-D isotropic turbulence will be discussed in Sect. 7.7. This situation can nevertheless be encountered in geophysical flows. Atmospheric turbulent perturbations are indeed mainly produced by the solar radiation rather than by interactions with the mean flow.

As a final remark, the equation of enstrophy (5.11) can be closed as follows using dimensional arguments,

$$\overline{\omega_i' \omega_j' \frac{\partial u_i'}{\partial x_j}} \simeq A E_\omega^{3/2}$$

where A is a constant. Neglecting viscous effects to simplify calculations, the integration leads to the following time evolution for E_ω,

$$\frac{E_\omega}{E_{\omega 0}} = \frac{1}{\left[1 - A\sqrt{E_{\omega 0}}(t - t_0)/2\right]^2}$$

A singularity is thus obtained for a finite time evolution, and this problem holds by including viscosity. It is still an open question to know if fluid dynamics equations lead to a singularity, or if the singularity is induced by a too simple assumption [489], and will be removed by including compressibility for instance.

5.7 Helicity

The helicity of a flow is usually defined from the following volume integral,

$$\mathcal{H} = \int_V \boldsymbol{u} \cdot \boldsymbol{\omega} \, d\boldsymbol{x} \tag{5.12}$$

and the reader can refer to Moffatt and Tsinober [134] for a review of the properties of this quantity. For instance, it can be shown that $\mathcal{H}$ remains constant from Kelvin's circulation theorem (5.4). Note that $\mathcal{H} \equiv 0$ for a two-dimensional flow.

Helicity is an indicator of the number of linkages of vortex tubes in the volume V. To illustrate this connection between fluid dynamics and topology, the case of two linked vortex tubes T_1 and T_2 is considered, as shown in Fig. 5.9. For this simple flow, $\mathcal{H}$ is the sum of two integrals over each vortex tube,

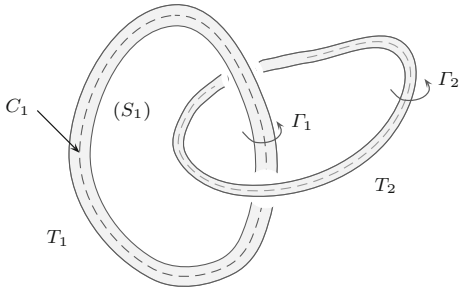

Fig. 5.9 Sketch of two linked vortex tubes T_1 and T_2

$$\mathcal{H} = \int_V \boldsymbol{u} \cdot \boldsymbol{\omega}\, d\boldsymbol{x} = \int_{T_1} \boldsymbol{u} \cdot \boldsymbol{\omega}\, d\boldsymbol{x} + \int_{T_2} \boldsymbol{u} \cdot \boldsymbol{\omega}\, d\boldsymbol{x}$$

The vorticity is assumed to be constant in a section of the two vortices. Therefore, the integration over the tube T_1 results in a line integral over the closed curve C_1

$$\int_{T_1} \boldsymbol{u} \cdot \boldsymbol{\omega}\, d\boldsymbol{x} = \Gamma_1 \oint_{C_1} \boldsymbol{u} \cdot d\boldsymbol{l} \tag{5.13}$$

The circulation along C_1 is equal to the vorticity flux through the surface S_1 closing C_1, associated with the tube T_1. The only possible contribution originates from the second vortex T_2. If this vortex tube crosses S_1, then this vorticity flux is equal to Γ_2, whereas in the opposite case, it is zero. Therefore,

$$\Gamma_1 \oint_{C_1} \boldsymbol{u} \cdot d\boldsymbol{l} = \Gamma_1 \int_{S_1} \boldsymbol{\omega}\, d\boldsymbol{x} = \begin{cases} \Gamma_1 \Gamma_2 \text{ if } C_1 \text{ and } C_2 \text{ are linked,} \\ 0 \text{ else.} \end{cases}$$

The same result is obtained for the integration over the vortex tube T_2 and hence $\mathcal{H} = 2\Gamma_1\Gamma_2$. More generally, the helicity is given by $\mathcal{H} = \pm 2n\Gamma_1\Gamma_2$, where n is the number of linkings, the sign $\pm$ coming from the rotation direction associated with Γ_1 and Γ_2. As mentioned below, $\mathcal{H}$ is preserved under the same assumptions as Kelvin's circulation theorem.

Some statistical properties of helicity in the case of homogeneous and isotropic turbulence are given in Sect. 6.6.

5.8 Equation for the Specific Vorticity*

A more general form of the transport equation of vorticity is shortly derived in what follows. The flow is now assumed to be compressible. By applying the curl operator to Navier-Stokes' equation, it yields

$$\frac{\partial \boldsymbol{\omega}}{\partial t} + \boldsymbol{u} \cdot \nabla \boldsymbol{\omega} = \boldsymbol{\omega} \cdot \nabla \boldsymbol{u} - \boldsymbol{\omega} \nabla \cdot \boldsymbol{u} + \frac{1}{\rho^2} \nabla \rho \times \nabla p + \nu \nabla^2 \boldsymbol{\omega}$$

when the spatial viscosity variations are neglected in the compressible form of the viscous tensor, refer to expression (2.12). From the conservation of mass, the divergence of velocity can be replaced by $(1/\rho) d\rho/dt$, and usually, the transport equation is written for the specific vorticity defined as $\boldsymbol{\omega}/\rho$. Indeed, one has

$$\frac{1}{\rho} \frac{d\boldsymbol{\omega}}{dt} = \frac{\boldsymbol{\omega}}{\rho} \cdot \nabla \boldsymbol{u} - \frac{\boldsymbol{\omega}}{\rho^2} \frac{d\rho}{dt} + \frac{1}{\rho^3} \nabla \rho \times \nabla p + \frac{\nu}{\rho} \nabla^2 \boldsymbol{\omega}$$

and finally, the transport equation for $\boldsymbol{\omega}/\rho$ takes the form,

$$\frac{d}{dt} \left(\frac{\boldsymbol{\omega}}{\rho} \right) = \frac{\boldsymbol{\omega}}{\rho} \cdot \nabla \boldsymbol{u} + \frac{1}{\rho^3} \nabla \rho \times \nabla p + \frac{\nu}{\rho} \nabla^2 \boldsymbol{\omega} \tag{5.14}$$

This equation for compressible flows is similar to Eq. (5.7) for incompressible flows with variable density, if the vorticity is replaced by the specific vorticity $\boldsymbol{\omega}/\rho$.

5.9 Identification of a Vortex*

Identification and localization of vortices are often required for flow visualizations, post-processing or application of a control algorithm for instance. The task occurs both in numerical applications and in experiments, which provide snapshots of the velocity field. The existence of a local maximum of vorticity or a local minimum of pressure appears not to be an adequate condition, and the direct detection of swirling fluid particles from close or spiralling streamlines [475], is also not satisfactory since vortices are usually entangled in a complex way.

For an incompressible flow, the pressure satisfies Poisson's equation (1.5), and the source term of this equation can be recast as follows [471],

$$\frac{1}{\rho} \nabla^2 p = -\frac{\partial u_i}{\partial x_j} \frac{\partial u_j}{\partial x_i} = \omega_{ij} \omega_{ij} - s_{ij} s_{ij}$$

since $e_{ij} = s_{ij}$ for a divergence-free flow. For a region dominated by ω_{ij}, vortices are thus associated with $\nabla^2 p > 0$. This has been formalised later with the so-called Q-criterion [485], where

$$Q = \frac{1}{2} (\omega_{ij} \omega_{ij} - s_{ij} s_{ij}) \tag{5.15}$$

is the second invariant of the velocity gradient tensor $\nabla \boldsymbol{u}$. Indeed, the three invariants usually denoted P, Q and R of a second-order tensor $\boldsymbol{\xi}$ are given by,

$$\begin{cases} P = \mathrm{tr}(\boldsymbol{\xi}) = \xi_{ii} \\ Q = \dfrac{1}{2}\left[\mathrm{tr}^2(\boldsymbol{\xi}) - \mathrm{tr}\left(\boldsymbol{\xi}^2\right)\right] = \dfrac{1}{2}\left[(\xi_{ii})^2 - (\boldsymbol{\xi}^2)_{ii}\right] \\ R = \det(\boldsymbol{\xi}) = \dfrac{1}{6}(\xi_{ii})^2 - \dfrac{1}{2}\xi_{ii}(\boldsymbol{\xi}^2)_{jj} + \dfrac{1}{3}(\boldsymbol{\xi}^3)_{ii} \end{cases}$$

and for the velocity gradient tensor $\xi_{ij} = \partial u_i / \partial x_j$, one gets

$$P = 0 \qquad Q = -\frac{1}{2}\frac{\partial u_i}{\partial x_j}\frac{\partial u_j}{\partial x_i} \qquad R = \det(\nabla \boldsymbol{u})$$

Vorticity regions are thus defined by iso-surfaces of $Q > 0$, as illustrated in Fig. 1.5 for instance. To remove ambiguous results, Jeong and Hussain [487] have proposed a new definition of a vortical motion, the so-called λ_2-criterion, based on the intermediate eigenvalue λ_2 of the symmetric tensor $s_{ik}s_{kj} + \omega_{ik}\omega_{kj}$. A vortex core is identified when $\lambda_2 < 0$. This work has been pursued [482], and at the same time, nonlocal criteria have also been investigated to identify a vortex, see for instance Graftieaux et al. [481] and Berson et al. [469].

Chapter 6
Homogeneous and Isotropic Turbulence

The study of homogeneous and isotropic turbulences is very rewarding for two reasons. On the one hand, it is possible to do an important part of it analytically, and on the other hand, the smallest turbulent structures in most turbulent flows have an almost isotropic behaviour. It is hoped that these small structures, often not represented in numerical simulations, can be modelled correctly.

6.1 Homogeneous Turbulence

A turbulent flow is said to be homogeneous when all its statistical properties are invariant by spatial translation. Thus, the one-point statistical averages such as $\overline{u_1'^2}$ or $\overline{u_1' u_2'}$ do not depend on the observation point $\boldsymbol{x}$. The correlation function at two points of two components of the velocity field only depends on the space vector $\boldsymbol{r}$ separating the points

$$R_{ij}(\boldsymbol{x}, \boldsymbol{r}, t) = \overline{u_i'(\boldsymbol{x}, t)\, u_j'(\boldsymbol{x} + \boldsymbol{r}, t)} = R_{ij}(\boldsymbol{r}, t) \tag{6.1}$$

Figure 6.1 illustrates two widely used correlation functions. The time dependency of the correlation functions are omitted in the following to simplify notations. Moreover, several equations seen in Chap. 2 can be simplified for homogeneous turbulence. For example, the turbulent kinetic energy balance (2.20) becomes

$$\rho \frac{\partial k_t}{\partial t} = -\rho \overline{u_i' u_j'} \frac{\partial \bar{U}_i}{\partial x_j} - \overline{\tau_{ij}' \frac{\partial u_i'}{\partial x_j}} = \mathcal{P} - \rho\epsilon \tag{6.2}$$

The kinetic energy is thus locally supplied by the average flow and dissipated by molecular viscosity, all of the spatial transfers corresponding to the (c), (d) and (e) terms of the Eq. (2.20) being equal to zero. In this situation, the average flow $\bar{U}_i(\boldsymbol{x})$ must be compatible with the existence of homogeneous turbulence. As shown by

C. Bailly and G. Comte-Bellot, *Turbulence*, Experimental Fluid Mechanics,
DOI 10.1007/978-3-319-16160-0_6

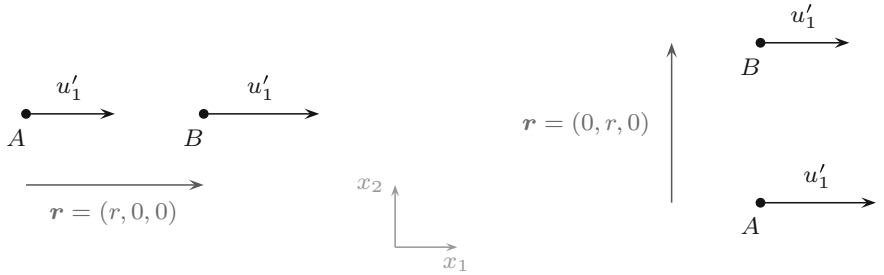

Fig. 6.1 Example of correlation functions at two points A and B separated by vector $\boldsymbol{r}$, at *left* $R_{11}(r, 0, 0)$ and at *right*, $R_{11}(0, r, 0)$

Burgers and Craya [105], a necessary condition is that $\partial \bar{U}_i / \partial x_j = \text{cst}$. Turbulence then stays homogeneous while still being anisotropic. To be more precise, the most general definition of the existence of homogeneous turbulence is $\partial \bar{U}_i / \partial x_j = \Lambda_{ij}(t)$, i.e. the average velocity gradients must be constant, or else only function of time. The description of several cases of anisotropic homogeneous turbulence can be found in the work by Gence [107] and in the experiments of return to isotropy by Le Penven [125].

In homogeneous turbulence, the correlation function R_{ij} at two points and for two components of the velocity field verifies the following properties,

(i) $R_{ij}(\boldsymbol{r}) = R_{ji}(-\boldsymbol{r})$. Indeed,

$$R_{ij}(\boldsymbol{r}) = \overline{u_i'(\boldsymbol{x}) u_j'(\boldsymbol{x} + \boldsymbol{r})} = \overline{u_i'(\boldsymbol{x} - \boldsymbol{r}) u_j'(\boldsymbol{x})} = R_{ji}(-\boldsymbol{r})$$

(ii) $R_{ii}(\boldsymbol{r}) = R_{ii}(-\boldsymbol{r})$, just applying $i = j$ to the previous equation. The correlation function for the same velocity component at two points is then an even function of the $\boldsymbol{r}$ variable between the points. To avoid any ambiguity in the following, Greek characters are used for indexes without summation, noting for the previous function for instance $R_{\alpha\alpha}(\boldsymbol{r})$.

(iii) The Schwarz inequality is obtained for the correlation function by writing

$$\overline{(u_i'(\boldsymbol{x}) + \lambda u_j'(\boldsymbol{x}'))^2} = \overline{u_i'^2(\boldsymbol{x})} + 2\lambda \overline{u_i'(\boldsymbol{x}) u_j'(\boldsymbol{x}')} + \lambda^2 \overline{u_j'^2(\boldsymbol{x}')} \geq 0$$

or else for the reduced discriminant, $\overline{u_i'(\boldsymbol{x}) u_j'(\boldsymbol{x}')}^2 - \overline{u_i'^2(\boldsymbol{x})}\, \overline{u_j'^2(\boldsymbol{x}')} \leq 0$ and finally for the correlation function at two points,

$$\overline{u_i'(\boldsymbol{x}) u_j'(\boldsymbol{x}')} \leq \sqrt{\overline{u_i'^2(\boldsymbol{x})}} \sqrt{\overline{u_j'^2(\boldsymbol{x}')}}$$

This last expression permits us to define the correlation coefficient $\mathcal{R}_{ij}$, which is dimensionless and always between -1 and 1,

$$-1 \leq \mathcal{R}_{ij}(\boldsymbol{x}, \boldsymbol{x}') = \frac{\overline{u_i'(\boldsymbol{x}) u_j'(\boldsymbol{x}')}}{\sqrt{\overline{u_i'^2(\boldsymbol{x})}}\sqrt{\overline{u_j'^2(\boldsymbol{x}')}}} \leq +1 \tag{6.3}$$

6.1.1 Length Scales

To define the size of the largest eddies in the turbulent field, it is useful to have an integral scale L characteristic of the distance on which the correlation function R_{ij} is not equal to zero. More precisely, the $L_{ij}^{(l)}$ scale definition is based on the integration of the correlation coefficient $\mathcal{R}_{ij}$ in the l direction indicated by the unit vector $\boldsymbol{x}_l$

$$L_{ij}^{(l)} = \int_0^\infty \mathcal{R}_{ij}(r\boldsymbol{x}_l) dr \tag{6.4}$$

Among all these scales, two are most useful: the longitudinal integral scale $L_{11}^{(1)}$ which corresponds to $i = j = 1$ and $r\boldsymbol{x}_1 = (r, 0, 0)$, and the transverse integral scale $L_{22}^{(2)}$ for $i = j = 1$ and $r\boldsymbol{x}_2 = (0, r, 0)$. The longitudinal correlation $\mathcal{R}_{11}(r, 0, 0)$ is shown in Fig. 6.2. A micro-scale or Taylor scale is also built using the parabola osculating the correlation function at the origin. To do this, a Taylor polynomial expansion of the component u_α' of velocity at point $\boldsymbol{x}$ in direction β is used,

$$u_\alpha'(\boldsymbol{x} + r\boldsymbol{x}_\beta) = u_\alpha'(\boldsymbol{x}) + r \left.\frac{\partial u_\alpha'}{\partial x_\beta}\right|_{\boldsymbol{x}} + \frac{r^2}{2} \left.\frac{\partial^2 u_\alpha'}{\partial x_\beta^2}\right|_{\boldsymbol{x}} + \cdots$$

Multiplying this expression by u_α' and applying the average operator,

$$R_{\alpha\alpha}(r\boldsymbol{x}_\beta) = \overline{u_\alpha'^2} + r\, \overline{u_\alpha' \frac{\partial u_\alpha'}{\partial x_\beta}} + \frac{r^2}{2} \overline{u_\alpha' \frac{\partial^2 u_\alpha'}{\partial x_\beta^2}} + \cdots$$

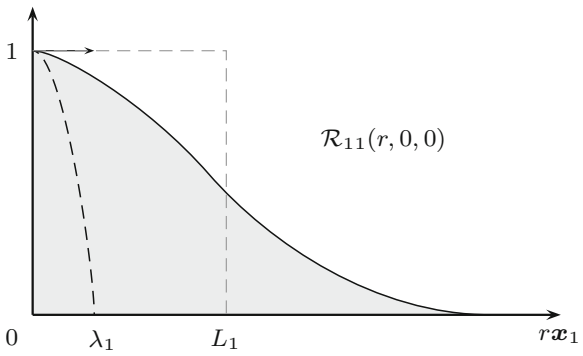

Fig. 6.2 Sketch of the longitudinal correlation function $\mathcal{R}_{11}(r, 0, 0)$ and its associated integral length scale L_1 and Taylor length scale λ_1

where the correlation function is given by $R_{\alpha\alpha}(r\boldsymbol{x}_\beta) = \overline{u'_\alpha(\boldsymbol{x})u'_\alpha(\boldsymbol{x}+r\boldsymbol{x}_\beta)}$. The previous expression can be written as,

$$R_{\alpha\alpha}(r\boldsymbol{x}_\beta) = \overline{u'^2_\alpha} + \frac{r}{2}\frac{\partial \overline{u'^2_\alpha}}{\partial x_\beta} + \frac{r^2}{4}\frac{\partial^2 \overline{u'^2_\alpha}}{\partial x^2_\beta} - \frac{r^2}{2}\overline{\left(\frac{\partial u'_\alpha}{\partial x_\beta}\right)^2} + \cdots$$

and can be simplified for homogeneous turbulence. Indeed, both the second and third terms are equal to zero in this case, which gives the following expression of the correlation coefficient

$$\mathcal{R}_{\alpha\alpha}(r\boldsymbol{x}_\beta) = 1 - \frac{r^2}{2\,\overline{u'^2_\alpha}}\overline{\left(\frac{\partial u'_\alpha}{\partial x_\beta}\right)^2} + \cdots \tag{6.5}$$

Thus, $\mathcal{R}_{\alpha\alpha}$ has a horizontal tangent at the origin. The longitudinal Taylor scale $\lambda_1 = \lambda^{(1)}_{11}$ is then defined using the expression of the correlation coefficient for $\alpha = \beta = 1$

$$\mathcal{R}_{11}(r,0,0) = 1 - \frac{r^2}{\lambda_1^2} + \cdots \quad \text{with} \quad \frac{1}{\lambda_1^2} = -\frac{1}{2}\frac{d^2\mathcal{R}_{11}}{dr_1^2} = \frac{1}{2\overline{u'^2_1}}\overline{\left(\frac{\partial u'_1}{\partial x_1}\right)^2} \tag{6.6}$$

Figure 6.2 illustrates both the osculating parabola and the value of λ_1 obtained at the intersection with the x_1 axis. Of course, there are numerous Taylor scales for α indexes and β directions in a three-dimensional turbulent field. The most used after λ_1 is the transverse Taylor scale $\lambda_2 = \lambda^{(2)}_{11}$, which corresponds to $\alpha = 1$ and $\beta = 2$,

$$\frac{1}{\lambda_2^2} = -\frac{1}{2}\frac{d^2\mathcal{R}_{11}}{dr_2^2} = \frac{1}{2\overline{u'^2_1}}\overline{\left(\frac{\partial u'_1}{\partial x_2}\right)^2} \tag{6.7}$$

Taylor length scales cannot be directly associated with a turbulent structure size playing a particular role. These scales are nonetheless very useful, particularly to give order of magnitudes to terms where products of turbulent quantities derivatives are averaged. Section 6.5 gives a precise example for the average dissipation ϵ of turbulent kinetic energy k_t.

6.1.2 Spectral Tensor of the Velocity Field

Fourier analysis is very convenient for the study of homogeneous turbulence, indeed the turbulence can be described in the spectral space whatever the observation point is. In the case of an inhomogeneous flow, another normal orthogonal mode decomposition must be used [222], also called POD for Proper Orthogonal

Decomposition, see Sect. 6.7. This problem is also present in numerical simulation, where spectral methods can be used only for homogeneous turbulent flows.

A homogeneous turbulent velocity field $\boldsymbol{u}$ without mean velocity is now considered, that is $\bar{U}_i = 0$. Hence $\boldsymbol{u} = \boldsymbol{u}'$ and $\overline{\boldsymbol{u}(\boldsymbol{x}, t)} = 0$. Moreover, in order to shorten the writing, the dependence on t is made implicit, noting for example $\boldsymbol{u}'(\boldsymbol{x}) = \boldsymbol{u}'(\boldsymbol{x}, t)$. The Fourier transform of the velocity field can then be defined by

$$\begin{cases} \hat{\boldsymbol{u}}(\boldsymbol{k}) = \dfrac{1}{(2\pi)^3} \displaystyle\int_{\mathrm{R}^3} \boldsymbol{u}'(\boldsymbol{x})\, e^{-i\boldsymbol{k}\cdot\boldsymbol{x}} d\boldsymbol{x} \\ \boldsymbol{u}'(\boldsymbol{x}) = \displaystyle\int_{\mathrm{R}^3} \hat{\boldsymbol{u}}(\boldsymbol{k}) e^{i\boldsymbol{k}\cdot\boldsymbol{x}} d\boldsymbol{k} \end{cases} \tag{6.8}$$

where $\boldsymbol{k}$ is the wavenumber vector. To simplify, we use improperly the integral sign, reserved to good functions, while we consider distributions. The informed reader can refer to the work of Schwartz [82]. Besides, the basic frame in Fourier space is right-handed and orthonormal, with $\boldsymbol{k}_1$ corresponding to $\boldsymbol{x}_1$. This remark is essential to understand the unidimensional spectra introduced later.

Incompressible Velocity Field

In the case of an incompressible turbulent velocity field, the condition $\nabla \cdot \boldsymbol{u}' = 0$ becomes

$$\nabla \cdot \boldsymbol{u}' = 0 = \int i\boldsymbol{k} \cdot \hat{\boldsymbol{u}}(\boldsymbol{k}) e^{i\boldsymbol{k}\cdot\boldsymbol{x}} d\boldsymbol{k}, \quad \forall \boldsymbol{x}$$

and then,

$$\boldsymbol{k} \cdot \hat{\boldsymbol{u}}(\boldsymbol{k}) \equiv 0, \quad \forall \boldsymbol{k} \tag{6.9}$$

The decomposition of $\boldsymbol{u}'(\boldsymbol{x})$ in Fourier space is actually a sum of transverse waves. This property is very often used to build synthetic turbulent fields to initialize the turbulence in numerical simulation, to study the dispersion of particles or to analyse the propagation of acoustic waves through a turbulent environment. In the local frame of Fourier space represented in Fig. 6.3, the $\hat{\boldsymbol{u}}(\boldsymbol{k})$ vector is then in the plane perpendicular to the wave vector $\boldsymbol{k}$, the rotation angle around $\boldsymbol{k}$ being random because $\hat{\boldsymbol{u}}(\boldsymbol{k})$ is itself random. In this local frame, some calculations become simpler. It was, for example, used by Craya [105] to study sheared homogeneous turbulence.

6.1.3 Spectral Tensor

The spectral tensor ϕ_{ij} is defined as the Fourier transform of the correlation function R_{ij}, i.e.

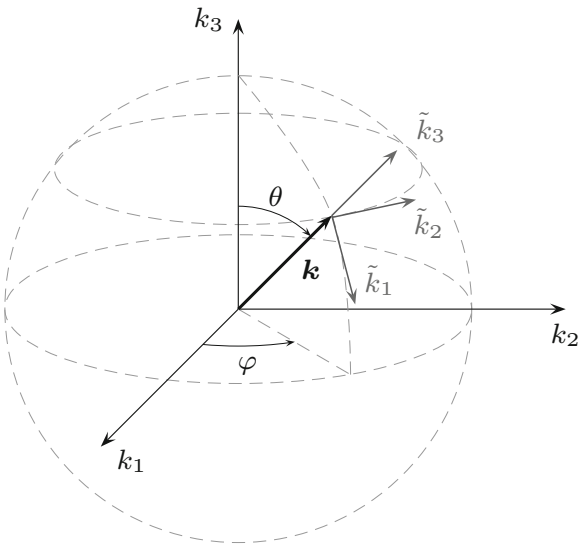

Fig. 6.3 Basic frame (k_1, k_2, k_3) and local frame $(\tilde{k}_1, \tilde{k}_2, \tilde{k}_3)$ in the Fourier space. The Fourier contribution $\hat{\boldsymbol{u}}(\boldsymbol{k})$ is in the plane $(\tilde{k}_1, \tilde{k}_2)$. The orthonormal local frame, also known as the Craya-Herring frame, is defined by analogy with spherical coordinates, $\tilde{k}_3$ is along the wavenumber $\boldsymbol{k}$, $\tilde{k}_1$ is tangent to the meridian circle with increasing θ, $\tilde{k}_2$ is tangent to the parallel circle with increasing φ

$$\begin{cases} \phi_{ij}(\boldsymbol{k}) = \dfrac{1}{(2\pi)^3} \displaystyle\int R_{ij}\,(\boldsymbol{r})\, e^{-i\boldsymbol{k}\cdot\boldsymbol{r}} d\boldsymbol{r} \\ R_{ij}\,(\boldsymbol{r}) = \displaystyle\int \phi_{ij}(\boldsymbol{k}) e^{i\boldsymbol{k}\cdot\boldsymbol{r}} d\boldsymbol{k} \end{cases} \tag{6.10}$$

For instance, when $i = j = 1$ and $\boldsymbol{r} = 0$,

$$\overline{u_1'^2} = \int \phi_{11}\,(\boldsymbol{k})\, d\boldsymbol{k}$$

and $\phi_{11}(\boldsymbol{k})d\boldsymbol{k}$ represents the contribution in $\overline{u_1'^2}$ of the wave vectors between $\boldsymbol{k}$ and $\boldsymbol{k} + d\boldsymbol{k}$. The spectral tensor verifies several properties, including the following

- $\overline{\hat{u}_i^\star(\boldsymbol{k})\hat{u}_j(\boldsymbol{k}')} = \phi_{ij}(\boldsymbol{k}')\delta(\boldsymbol{k} - \boldsymbol{k}')$. Two Fourier components of the velocity field are correlated only if they correspond to the same wavenumber. Indeed

$$\begin{aligned} \overline{\hat{u}_i^\star(\boldsymbol{k})\hat{u}_j(\boldsymbol{k}')} &= \frac{1}{(2\pi)^6} \iint \overline{u_i'(\boldsymbol{x})u_j'(\boldsymbol{x}')}\, e^{i\boldsymbol{k}\cdot\boldsymbol{x}}\, e^{-i\boldsymbol{k}'\cdot\boldsymbol{x}'}\, d\boldsymbol{x}\, d\boldsymbol{x}' \\ &= \frac{1}{(2\pi)^6} \iint R_{ij}(\boldsymbol{r})\, e^{-i\boldsymbol{k}'\cdot\boldsymbol{r}}\, e^{i(\boldsymbol{k}-\boldsymbol{k}')\cdot\boldsymbol{x}}\, d\boldsymbol{x}\, d\boldsymbol{r} \end{aligned}$$

where $\overline{u_i'(\boldsymbol{x})u_j'(\boldsymbol{x}')} = R_{ij}(\boldsymbol{r})$ for homogeneous turbulence, with the notation $\boldsymbol{r} = \boldsymbol{x}' - \boldsymbol{x}$. Besides,

$$\frac{1}{(2\pi)^3} \int e^{i(\boldsymbol{k}-\boldsymbol{k}')\cdot\boldsymbol{x}} d\boldsymbol{x} = \delta(\boldsymbol{k} - \boldsymbol{k}')$$

and then it can be inferred that,

$$\overline{\hat{u}_i^\star(\boldsymbol{k})\hat{u}_j(\boldsymbol{k}')} = \frac{1}{(2\pi)^3}\int R_{ij}(\boldsymbol{r})\, e^{-i\boldsymbol{k}'\cdot\boldsymbol{r}}\, \delta(\boldsymbol{k}-\boldsymbol{k}')d\boldsymbol{r} = \phi_{ij}(\boldsymbol{k})\delta(\boldsymbol{k}-\boldsymbol{k}')$$

- $\phi_{ij}(\boldsymbol{k}) = \phi_{ji}(-\boldsymbol{k}) = \phi_{ji}^\star(\boldsymbol{k})$ provided by $R_{ij}(\boldsymbol{r}) = R_{ji}(-\boldsymbol{r})$. This results shows that ϕ_{ij} is a tensor with Hermitian symmetry.
- $k_i\phi_{ij}(\boldsymbol{k}) = k_j\phi_{ij}(\boldsymbol{k}) = 0$ for an incompressible velocity field. This result comes from (6.9). In physical space, this property corresponds to

$$\frac{\partial R_{ij}(\boldsymbol{r})}{\partial r_i} = \frac{\partial R_{ij}(\boldsymbol{r})}{\partial r_j} = 0$$

Given the previous properties, only four scalar functions are needed to describe completely the spectral tensor ϕ_{ij}. The result is particularly clear in the local frame of Fig. 6.3, where the spectral tensor components are located in the plane perpendicular to $\boldsymbol{k}$, with only two diagnonal real components and two Hermitian symmetry components out of the diagonal. Later in this chapter will be shown the fact that only one function is needed when the turbulence is isotropic.

6.1.4 One-Dimensional Spectra

It is actually difficult to determine the spectral tensor $\phi_{ij}(\boldsymbol{k})$. Indeed, it would be necessary to measure all of the R_{ij} correlations in the three dimensions and then apply a Fourier transform. To have measurable quantities with the experimental techniques as defined in Chap. 10, the longitudinal one-dimensional spectra are introduced,

$$E_{ij}^{(1)}(k_1) = \iint \phi_{ij}(\boldsymbol{k})\, dk_2 dk_3 \tag{6.11}$$

where the upper index (1) indicates the wavenumber component which stays after integration. Some examples are as follows

$$\overline{u_1'^2} = \int_{-\infty}^{+\infty} E_{11}^{(1)}(k_1)\, dk_1 \qquad \overline{u_1'u_2'} = \int_{-\infty}^{+\infty} E_{12}^{(1)}(k_1)\, dk_1$$

More generally, the correlation function R_{ij} can be expressed with the one-dimensional spectrum $E_{ij}^{(1)}$ by:

$$R_{ij}(r_1,0,0) = \int_{\mathrm{R}^3} \phi_{ij}(\boldsymbol{k})\; e^{ik_1r_1}d\boldsymbol{k} = \int_{-\infty}^{+\infty} E_{ij}^{(1)}(k_1)\, e^{ik_1r_1}dk_1$$

and reciprocally by the Fourier transform

$$E_{ij}^{(1)}(k_1) = \frac{1}{2\pi}\int_{-\infty}^{+\infty} R_{ij}\,(r_1, 0, 0)\; e^{-ik_1 r_1} dr_1 \tag{6.12}$$

From these relations can be inferred the longitudinal integral scale L_1 of the turbulence. Indeed, with $k_1 = 0$ and $i = j = 1$ in expression (6.12),

$$E_{11}^{(1)}\,(k_1 = 0) = \frac{1}{2\pi}\int_{-\infty}^{+\infty} R_{11}\,(r_1, 0, 0)\; dr_1 = \frac{1}{2\pi}\,2\,\overline{u_1'^2}\,L_{11}^{(1)}$$

and:

$$L_1 \equiv L_{11}^{(1)} = \pi\frac{E_{11}^{(1)}\,(0)}{\overline{u_1'^2}} \tag{6.13}$$

Similarly, we can also express the Taylor length scale λ_1 with the one-dimensional spectrum,

$$\left(\frac{1}{\lambda_1}\right)^2 \equiv \left(\frac{1}{\lambda_{11}^{(1)}}\right)^2 = \int_0^{\infty} \frac{k_1^2 E_{11}^{(1)}(k_1)}{\overline{u_1'^2}}\, dk_1$$

Transverse one-dimensional spectra can also be defined. For instance $E_{11}^{(2)}(k_2)$ resulting from an integration of $\phi_{11}(\boldsymbol{k})$ on k_1 and k_3 has been used by Kellogg and Corrsin [115] to study the evolution of a special spectral peak generated by a zither in addition to the standard grid producing turbulence.

6.1.5 Turbulent Kinetic Energy

The turbulent kinetic energy k_t can be written, by definition, using the following relations

$$k_t = \frac{1}{2}\overline{\boldsymbol{u}'^2} = \frac{\overline{u_1'^2} + \overline{u_2'^2} + \overline{u_3'^2}}{2} = \frac{1}{2}R_{ii}\,(0) = \frac{1}{2}\int \phi_{ii}(\boldsymbol{k})d\boldsymbol{k}$$

The turbulent kinetic energy spectrum, noted $E\,(k)$, is then introduced

$$E\,(k) = \frac{1}{2}\int_{\Sigma_k} \phi_{ii}(\boldsymbol{k})d\,\Sigma \qquad k_t = \int_0^{\infty} E(k)dk \tag{6.14}$$

As Σ_k is the sphere of radius k in Fourier space, $E(k)dk$ can be interpreted as the contribution to kinetic turbulent energy of wavenumbers of modulus between k and $k + dk$. Of course, the energy distribution over the sphere Σ_k is not necessarily uniform for the turbulence can be anisotropic. In this representation, the tensor $\phi_{ii}(\boldsymbol{k})$ stays function of the direction of vector $\boldsymbol{k}$.

6.1.6 Enstrophy and Dissipation

It is also possible to calculate the spectral tensor Ω_{ij} of the vorticity, which is similar to the tensor ϕ_{ij} for the velocity field. By definition,

$$\overline{\omega_i'(\boldsymbol{x})\omega_j'(\boldsymbol{x}+\boldsymbol{r})} = \int \Omega_{ij}(\boldsymbol{k})\, e^{i\boldsymbol{k}\cdot\boldsymbol{r}} d\boldsymbol{k} \tag{6.15}$$

The calculation of Ω_{ij} is not as easy. It can be demonstrated using the Fourier transform of the vorticity $\hat{\omega}(\boldsymbol{k}) = i\boldsymbol{k} \times \hat{\boldsymbol{u}}(\boldsymbol{k})$, that for an incompressible turbulence [84]

$$\Omega_{ij}(\boldsymbol{k}) = k^2 \left(\delta_{ij} - \frac{k_i k_j}{k^2}\right) \phi_{ll}(\boldsymbol{k}) - k^2 \phi_{ji}(\boldsymbol{k}) \tag{6.16}$$

It is interesting to note that the vorticity spectrum $\Omega_{ij}(\boldsymbol{k})$ is expressed in terms of the spectral tensor $\phi_{ij}(\boldsymbol{k})$. Particularly, for $i = j$ Eq. (6.16) becomes, $\Omega_{ii}(\boldsymbol{k}) = k^2 \phi_{ii}(\boldsymbol{k})$.

The enstrophy spectrum is then given by

$$\frac{\overline{\omega_i'^2}}{2} = \frac{1}{2}\int \Omega_{ii}(\boldsymbol{k}) d\boldsymbol{k} = \frac{1}{2}\int k^2 \phi_{ii}(\boldsymbol{k}) d\boldsymbol{k} = \int_0^\infty k^2 \left(\frac{1}{2}\int_{\Sigma_k} \phi_{ii}(\boldsymbol{k}) d\Sigma\right) dk$$

i.e. introducing the spectrum $E(k)$ of turbulent kinetic energy,

$$\frac{\overline{\omega_i'^2}}{2} = \int_0^\infty k^2 E(k) dk$$

The spectrum of the dissipation ϵ is directly related to the enstrophy spectrum, and then to the turbulent kinetic energy spectrum. Indeed, for homogeneous and incompressible turbulence

$$\rho\epsilon = \frac{1}{2}\mu \overline{\left(\frac{\partial u_i'}{\partial x_j} + \frac{\partial u_j'}{\partial x_i}\right)^2} = \mu \overline{\frac{\partial u_i'}{\partial x_j}\frac{\partial u_i'}{\partial x_j}} = \frac{1}{2}\mu \overline{\left(\frac{\partial u_i'}{\partial x_j} - \frac{\partial u_j'}{\partial x_i}\right)^2} = \mu \overline{\omega_i'^2} \tag{6.17}$$

because,

$$\overline{\frac{\partial u_i'}{\partial x_j}\frac{\partial u_j'}{\partial x_i}} = \frac{\partial^2 \overline{u_i' u_j'}}{\partial x_i \partial x_j} = 0$$

and in the spectral space,

$$\epsilon = \nu \overline{\omega_i'^2} = \nu(\overline{\omega_1'^2} + \overline{\omega_2'^2} + \overline{\omega_3'^2}) = 2\nu \int_0^\infty k^2 E(k)\, dk \tag{6.18}$$

This last expression can also be obtained more directly from the Fourier transform of the velocity field $\boldsymbol{u}'$. According to (6.8), and by taking the conjugate for the second equality

$$\frac{\partial u_i'}{\partial x_j} = i \int k_j \hat{u}_i(\boldsymbol{k}) e^{i\boldsymbol{k}\cdot\boldsymbol{x}} d\boldsymbol{k} = -i \int k_j' \hat{u}_i^\star(\boldsymbol{k}') e^{-i\boldsymbol{k}'\cdot\boldsymbol{x}} d\boldsymbol{k}'$$

and thus,

$$\begin{aligned}
\epsilon &= \nu \overline{\frac{\partial u_i'}{\partial x_j} \frac{\partial u_i'}{\partial x_j}} \\
&= \nu \iint k_j k_j' \, \overline{\hat{u}_i(\boldsymbol{k}) \hat{u}_i^\star(\boldsymbol{k}')} \, e^{i(\boldsymbol{k}-\boldsymbol{k}')\cdot\boldsymbol{x}} \, d\boldsymbol{k} \, d\boldsymbol{k}' \\
&= \nu \iint k_j k_j' \, \phi_{ii}(\boldsymbol{k}) \delta(\boldsymbol{k}-\boldsymbol{k}') \, e^{i(\boldsymbol{k}-\boldsymbol{k}')\cdot\boldsymbol{x}} \, d\boldsymbol{k} \, d\boldsymbol{k}' \\
&= \nu \int k^2 \phi_{ii}(\boldsymbol{k}) d\boldsymbol{k} \\
&= 2\nu \int_0^\infty k^2 E(k) dk
\end{aligned}$$

It must be remembered that for homogeneous turbulence, the energy distribution for a given k is not uniform, but a function of the vector orientation $\boldsymbol{k}$ linked to turbulence anisotropy. Some noteworthy simplifications are made for isotropic turbulence, which is the point of Sect. 6.2.

6.1.7 Rapid Distortion of the Turbulence

Among the numerous problems of homogeneous turbulence, those where the turbulence is suddenly subject to high mean velocity gradients can be distinguished. An approach to study these problems, originally developed by Taylor and then Ribner and Tucker [144] and Batchelor and Proudman [85], is to linearize the equations assuming that there is not enough time for the turbulence to interact with itself. The Rapid Distortion Theory (RDT) is based on the following hypothesis: the characteristic time of the turbulence k_t/ϵ must be larger than the characteristic time of the distortion S^{-1} where S measures the intensity of the mean velocity gradients, i.e.

$$S \frac{k_t}{\epsilon} \gg 1 \qquad S = \sqrt{2\bar{S}_{ij}\bar{S}_{ij}} \tag{6.19}$$

Among the problems usually considered are the turbulence subject to a pure deformation (plane if $\lambda = -1$), to a pure shear or to a pure rotation, then the tensors of the mean velocity gradients are respectively,

$$\frac{\partial \bar{U}_i}{\partial x_j} = \begin{pmatrix} S & 0 & 0 \\ 0 & \lambda S & 0 \\ 0 & 0 & -(\lambda+1)\,S \end{pmatrix}$$

$$\frac{\partial \bar{U}_i}{\partial x_j} = \begin{pmatrix} 0 & S & 0 \\ 0 & 0 & 0 \\ 0 & 0 & 0 \end{pmatrix} \quad \text{and} \quad \frac{\partial \bar{U}_i}{\partial x_j} = \begin{pmatrix} 0 & S & 0 \\ -S & 0 & 0 \\ 0 & 0 & 0 \end{pmatrix}$$

Very often the viscous effects are neglected, though they cause no particular trouble for they are linear, and then the equation governing u_i' can be written

$$\frac{\partial u_i'}{\partial t} + \bar{U}_j \frac{\partial u_i'}{\partial x_j} = -u_j' \frac{\partial \bar{U}_i}{\partial x_j} - \frac{1}{\rho}\frac{\partial p'}{\partial x_i} \tag{6.20}$$

The mean velocity gradients $\partial \bar{U}_i / \partial x_j$ do not depend on $\boldsymbol{x}$ but can be a function of time for homogeneous turbulence. However, it is still possible to return to a Lagrangian description by a variable change, also called Rogallo transformation [465]. An application of this transformation has been seen in Sect. 5.3 to study the pure plane deformation of an eddy using the Helmholtz equation. Another application is presented in Sect. 6.8, with a pure 3-D deformation and a complete turbulence spectrum. The advantage of such an approach is to avoid using a closure for the Reynolds tensor.

Among the essential results provided by RDT is the modelling of the rapid part of the pressure which plays an important role. Indeed, with the Poisson Eq. (1.5) governing the pressure fluctuations for an incompressible flow, one obtains

$$\frac{1}{\rho}\nabla^2 p' = \underbrace{-2\frac{\partial \bar{U}_i}{\partial x_j}\frac{\partial u_j'}{\partial x_i}}_{\text{(a)}} \underbrace{-\frac{\partial u_i'}{\partial x_j}\frac{\partial u_j'}{\partial x_i}}_{\text{(b)}}$$

and two contributions can be distinguished: a rapid part (a) and a slow part (b). In the case of RDT only the rapid contribution is studied and modelled. It is possible to solve the RDT equations numerically and to compare them to direct simulations of the Navier-Stokes equations. To study this topic further, the reader can for instance refer to Cambon and Scott [92], and Sagaut and Cambon [147], for a general overview, and also to the work by Cambon et al. [90, 148, 149].

6.2 Incompressible Isotropic Turbulence

Isotropic turbulence is homogeneous turbulence whose statistical properties are invariant to any axial rotation. Its definition also often includes an invariance to any symmetry. Actually, isotropic turbulence is a turbulent flow where no privileged

observation direction can be found. The first analytical studies on isotropic turbulence were carried out by Taylor [151–153].

To examine the turbulent field, a probing device must be defined. It must be of fixed geometrical configuration, constituted of points if the turbulent quantity is a scalar (temperature, pressure, concentration, …) and of points associated with unit vectors if the measured quantity is a vector (velocity, …). For instance, for pressure-velocity correlation, the pressure variation is considered at point A, and the scalar product $\boldsymbol{u}'_B \cdot \boldsymbol{b}$ is considered at point B where the associated unit vector is $\boldsymbol{b}$. The random variables p'_A and $\boldsymbol{u}'_B \cdot \boldsymbol{b}$ are then obtained. Turbulence is said to be isotropic if the joint probability density of the random variables p'_A and $\boldsymbol{u}'_B \cdot \boldsymbol{b}$ is invariant to any translation or rotation of the probing device, here A, B and $\boldsymbol{b}$, whose geometry is kept the same. The moments of these random variables then also verify these invariance properties. Examples are given in the following.

6.2.1 Double Velocity Correlation at a Point

Let us first consider the particular form of the Reynolds tensor for isotropic turbulence. The probing device is then constituted of only one point A and one associated unit vector $\boldsymbol{a}$, as illustrated in Fig. 6.4. When the probing device is placed such that $\boldsymbol{a}$ is in the x_1 direction, the scalar product $\boldsymbol{u}'_A \cdot \boldsymbol{a}$ gives u'_1. When the deviced is rotated by $\pi/2$, vector $\boldsymbol{a}$ becomes parallel to the x_2 direction and the scalar product $\boldsymbol{u}'_A \cdot \boldsymbol{a}$ gives u'_2. Isotropy implies that it is impossible to statistically distinguish one result from the other, i.e. $\overline{u'^2_1} = \overline{u'^2_2}$. More generally,

$$\overline{u'^2_1} = \overline{u'^2_2} = \overline{u'^2_3} = u'^2 \quad \text{with} \quad u'^2 = \overline{u'^2}$$

Let us now consider the correlation of two velocity components at a same point. The probing device is composed of two unit vectors $\boldsymbol{a}$ and $\boldsymbol{b}$, both associated with point A and the two random variables which are considered are $\boldsymbol{u}'_A \cdot \boldsymbol{a}$ and $\boldsymbol{u}'_A \cdot \boldsymbol{b}$. First the two vectors $\boldsymbol{a}$ and $\boldsymbol{b}$ are chosen respectively parallel to $\boldsymbol{x}_1$ and $\boldsymbol{x}_2$, then the

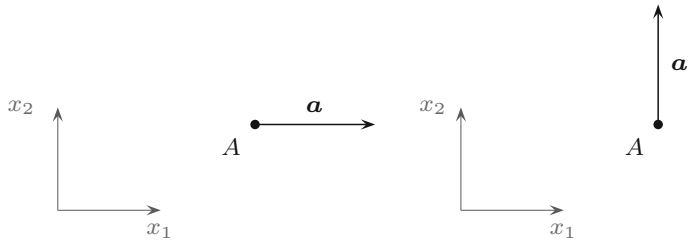

Fig. 6.4 Illustration of the probing device used to measure $\boldsymbol{u}'_A \cdot \boldsymbol{a}$ at point A, which gives u'_1 at left and u'_2 at right when rotating by $\pi/2$

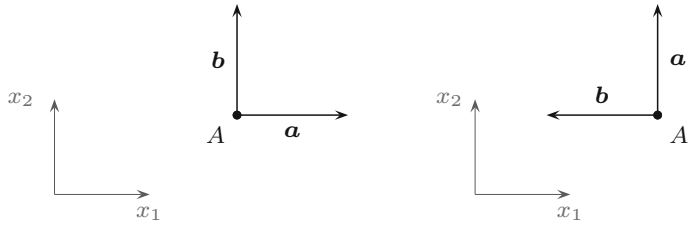

Fig. 6.5 Illustration of the probing device used to measure the double velocity correlation at point A

probing device is rotated by $\pi/2$ in the plane (x_1, x_2), as shows in Fig. 6.5. It can then be inferred that $\overline{u'_1 u'_2} = -\overline{u'_1 u'_2}$ and, consequently, the correlation $\overline{u'_1 u'_2}$ can only be equal to zero. Similarly, it can be demonstrated that $\overline{u'_1 u'_3} = \overline{u'_2 u'_3} = 0$. The Reynolds tensor for isotropic turbulence is thus diagonal and more precisely,

$$\overline{u'_i u'_j} = u'^2 \, \delta_{ij} = \frac{2k_t}{3} \, \delta_{ij} \tag{6.21}$$

It can be shown for similar reasons that triple correlations of the velocity fluctuations at a point are equal to zero, that is $\overline{u'_i u'_j u'_k} = 0$.

6.2.2 Double Velocity Correlation at Two Points

The correlation of the velocity at two points A and B, separated by a vector $\boldsymbol{r}$, is now considered. A unit vector $\boldsymbol{a}$ associated with point A is used, as well as an unit vector $\boldsymbol{b}$ associated with point B. The two vectors $\boldsymbol{a}$ and $\boldsymbol{b}$ are arbitrary. The random variables given by the probing device are $\boldsymbol{u}'_A \cdot \boldsymbol{a}$ and $\boldsymbol{u}'_B \cdot \boldsymbol{b}$, and they lead to the following double correlation function

$$\mathcal{F} = \frac{\overline{(\boldsymbol{u}'_A \cdot \boldsymbol{a})(\boldsymbol{u}'_B \cdot \boldsymbol{b})}}{\sqrt{\overline{\boldsymbol{u}'^2_A}}\sqrt{\overline{\boldsymbol{u}'^2_B}}} = \frac{\overline{u'_{iA} u'_{jB}}(\boldsymbol{r})}{u'^2} a_i b_j = \mathcal{R}_{ij}(\boldsymbol{r}) \, a_i b_j$$

A representation theorem by Robertson [145] indicates that the bilinear form $\mathcal{F}$ must be a function of only the probing device invariants, i.e. of distances and angles, and then of only the following quantities $\boldsymbol{r}^2 = r_i r_i$, $\boldsymbol{a} \cdot \boldsymbol{r} = a_i r_i$, $\boldsymbol{b} \cdot \boldsymbol{r} = b_j r_j$, $\boldsymbol{a} \cdot \boldsymbol{b} = a_i b_i = a_i b_j \delta_{ij}$, and of the volume $(\boldsymbol{a} \times \boldsymbol{b}) \cdot \boldsymbol{r} = \epsilon_{ijk} a_i b_j r_k$. If grouped together correctly, these invariants permit $\mathcal{F}$ to be both linear in a_i and b_j

$$\mathcal{F} = \mathcal{R}_{ij} \, a_i b_j = \alpha(r) r_i r_j a_i b_j + \beta(r) \delta_{ij} a_i b_j + \gamma(r) \epsilon_{ijk} a_i b_j r_k$$

Simplifying by $a_i b_j$, the form of the tensor of the correlation of the velocities at two points can be obtained

$$\mathcal{R}_{ij}(\boldsymbol{r}) = \alpha(r)\, r_i r_j + \beta(r)\, \delta_{ij} + \gamma(r)\, \epsilon_{ijk} r_k \tag{6.22}$$

To the invariance for translation and rotation, is often added for isotropic turbulence the invariance to reflection symmetry condition. For example, a symmetry relative to the first bisector of the coordinate axes leads to $\mathcal{R}_{12}(r_1, r_2, r_3) = \mathcal{R}_{21}(r_2, r_1, r_3)$. But ϵ_{ijk} does not obey the reflection symmetry since $\epsilon_{123} = -\epsilon_{213}$, and then it is necessary that $\gamma = 0$. By the way, this is equivalent to choosing a turbulence without helicity, discussed in Sect. 6.6. Finally, the general form of a second-order isotropic tensor is obtained,

$$\mathcal{R}_{ij}(\boldsymbol{r}) = \alpha(r)\, r_i r_j + \beta(r)\, \delta_{ij} \tag{6.23}$$

Expressed otherwise, the tensor of the double correlation of the velocities at two points can be expressed with only two scalar functions. Instead of keeping $\alpha(r)$ and $\beta(r)$, it is better to choose two other functions whose physical interpretation is known. Thus the longitudinal correlation $\mathcal{R}_{11}(\boldsymbol{r})$ with $\boldsymbol{r} = (r, 0, 0)$ is first chosen and this function is noted $f(r)$. According to (6.23), it can be written

$$f(r) \equiv \mathcal{R}_{11}(r, 0, 0) = \alpha(r)\, r^2 + \beta(r)$$

The second function is the transverse correlation $\mathcal{R}_{11}(\boldsymbol{r})$ with this time $\boldsymbol{r} = (0, r, 0)$. It is usually noted $g(r)$ and, also according to (6.23), it can be written

$$g(r) \equiv \mathcal{R}_{11}(0, r, 0) = \beta(r)$$

Using these new $f(r)$ and $g(r)$ functions to express the tensor of the correlation of the velocities at two points, the following relation established by Kármán and Howarth is obtained [114]

$$\mathcal{R}_{ij}(\boldsymbol{r}) = (f - g)\, \frac{r_i r_j}{r^2} + g \delta_{ij} \tag{6.24}$$

Incompressible Turbulence

The incompressibility of the flow implies an additional condition, and thus $\mathcal{R}_{ij}(\boldsymbol{r})$ can be expressed with only $f(r)$. Indeed, for an incompressible homogeneous turbulence $\nabla \cdot \boldsymbol{u}' = 0$, and

$$\frac{\partial \mathcal{R}_{ij}(\boldsymbol{r})}{\partial r_i} = 0$$

This result can be used on expression (6.24),

$$\frac{\partial \mathcal{R}_{ij}(\boldsymbol{r})}{\partial r_i} = \frac{\partial}{\partial r_i}\left(\frac{f - g}{r^2} r_i r_j + g \delta_{ij}\right) = 0$$

that is

$$\left(\frac{f'-g'}{r^2}-2\frac{f-g}{r^3}\right)\frac{\partial r}{\partial r_i}r_i r_j+\frac{f-g}{r^2}\frac{\partial\left(r_i r_j\right)}{\partial r_i}+g'\delta_{ij}\frac{\partial r}{\partial r_i}=0$$

This expression can be simplified thanks to the two following relations,

$$\frac{\partial r}{\partial r_i}=\frac{r_i}{r}\qquad \delta_{ij}\frac{\partial r}{\partial r_i}=\frac{r_j}{r}$$

Hence,

$$f'\frac{r_j}{r}-2\left(f-g\right)\frac{r_j}{r^2}+\frac{f-g}{r^2}\left(r_j\frac{\partial r_i}{\partial r_i}+r_i\frac{\partial r_j}{\partial r_i}\right)=0$$

$$f'\frac{r_j}{r}+\left(f-g\right)\frac{r_j}{r^2}(-2+N+1)=0$$

$$f'+\frac{f-g}{r}(N-1)=0 \tag{6.25}$$

where $N=2$ in 2-D and $N=3$ in 3-D. In the two cases, the tensor of the correlations $\mathcal{R}_{ij}$ only depends on one scalar function. The 2-D case is developed in Sect. 7.7, and for the 3-D case considered here

$$g=f+\frac{r}{2}f'\quad\text{i.e.}\quad g=\frac{1}{r}\frac{d}{dr}\left(\frac{r^2}{2}f\right) \tag{6.26}$$

This relation, often called the relation of Kármán and Howarth [114], permits us to link the integral scales L_1 and L_2. Assuming that $f(r)$ converges towards zero rapidly enough when $r\to\infty$, one has

$$L_2=\int_0^\infty g dr=\int_0^\infty\left(f+\frac{r}{2}f'\right)dr=L_1+\left[\frac{rf}{2}\right]_0^\infty-\frac{1}{2}\int_0^\infty f dr=\frac{L_1}{2} \tag{6.27}$$

The longitudinal integral scale is thus twice as large as the transverse integral scale for an incompressible isotropic turbulence. According to (6.26),

$$\begin{aligned}\int_0^\infty r g dr&=\int_0^\infty r f dr+\int_0^\infty\frac{r^2}{2}f'dr\\&=\int_0^\infty r f dr+\left[\frac{r^2}{2}f\right]_0^\infty-\int_0^\infty r f dr\\&=0\end{aligned}$$

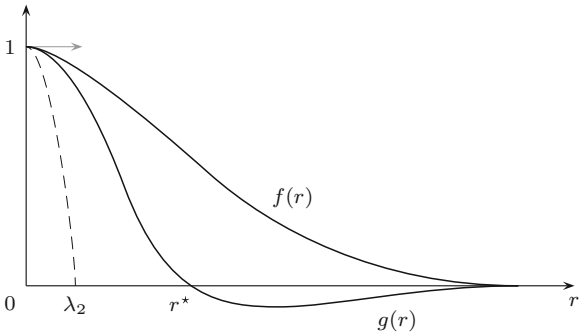

Fig. 6.6 Sketch of the functions $f(r)$ et $g(r)$ for an incompressible and isotropic turbulence in 3-D, and relative position of the Taylor length scale λ_2

The g function curve is expected to cross the abscissa axis. The curves of functions f and g are shown in Fig. 6.6. To take this negative loop into consideration, the following substitute integral scale can be defined

$$\tilde{L}_2 = \int_0^{r^\star} g(r)dr, \quad \text{with} \quad g\left(r^\star\right) = 0, \quad \text{and} \quad g(r) > 0 \quad \text{on} \quad [0, r^\star[.$$

This result can be explained with the incompressibility hypothesis. It is necessary that the correlation

$$g(r) = \overline{u_1'(0,0,0)u_1'(0,r,0)}/u'^2 = \overline{u_2'(0,0,0)u_2'(r,0,0)}/u'^2$$

changes its sign at least once with r for the mass to be conserved.

It is also possible to obtain a relation between the longitudinal Taylor scale λ_1 and the transverse Taylor scale λ_2 deriving relation (6.26) twice

$$g' = f' + \frac{1}{2}f' + \frac{r}{2}f''$$

and

$$g'' = f'' + \frac{1}{2}f'' + \frac{1}{2}f'' + \frac{r}{2}f'''$$

It can be inferred for $r = 0$ that $g''(0) = 2f''(0)$, and considering the definition of Taylor scales (6.6) and (6.7),

$$\frac{1}{\lambda_1^2} = -\frac{f''(0)}{2} \quad \frac{1}{\lambda_2^2} = -\frac{g''(0)}{2} \quad \text{and then,} \quad \lambda_1 = \sqrt{2}\,\lambda_2$$

In the scientific literature, the following notations are often used for an isotropic homogeneous turbulence: $L_f = L_1$, $L_g = L_2$. It is also the case for Taylor scales,

$\lambda_f = \lambda_1$ and $\lambda_g = \lambda_2$. In the following, these notations characteristic of an isotropic homogeneous turbulence will be used.

6.2.3 Double Pressure-Velocity Correlations at Two Points

As for the tensor of the correlations of velocities, the general form of the pressure-velocity correlations at two points for isotropic turbulence can be established. Two points A and B are considered, vector $\boldsymbol{b}$ being associated with the latter. In A is measured the pressure fluctuation p'_A and in B the velocity fluctuation $\boldsymbol{u}'_B$ through the product $\boldsymbol{u}'_B \cdot \boldsymbol{b}$. The following quantity is then considered

$$\mathcal{F} = \frac{\overline{p'_A \left(\boldsymbol{u}'_B \cdot \boldsymbol{b}\right)}}{\sqrt{\overline{p'^2}}\sqrt{\overline{u'^2}}} = \frac{\overline{p'_A u'_{Bi}}}{\sqrt{\overline{p'^2}}\sqrt{\overline{u'^2}}} b_i = \mathcal{P}_i(\boldsymbol{r}) b_i$$

The form $\mathcal{F} = \mathcal{P}_i b_i$ can be function of only the quantities $\boldsymbol{r} \cdot \boldsymbol{b}$ and $\boldsymbol{r}^2$. The linearity in $\boldsymbol{b}$ then provides

$$\mathcal{F} = \mathcal{P}_i b_i = \alpha(r) r_i b_i$$

The $\boldsymbol{b}$ vector being arbitrary, the form of the pressure-velocity correlation can only be $\mathcal{P}_i(\boldsymbol{r}) = \alpha(r)\, r_i$. It can be demonstrated that this correlation is equal to zero for an incompressible turbulence. Indeed, the incompressibility of the velocity field at point B leads to

$$\overline{p'_A \frac{\partial u'_{Bi}}{\partial x_{Bi}}} = \frac{\partial}{\partial x_{Bi}}\left(\overline{p'_A u'_{Bi}}\right) = \frac{\partial}{\partial r_i}\left(\overline{p'_A u'_{Bi}}\right) = 0 \quad \text{or} \quad \frac{\partial \mathcal{P}_i}{\partial r_i} = 0$$

Given the expression of $\mathcal{P}_i$ for isotropic turbulence, one has

$$3\alpha(r) + \alpha'(r)\frac{r_i}{r} r_i = 0$$

which permits to integrate $\alpha(r)$ and express $\mathcal{P}_i(\boldsymbol{r})$ as

$$\mathcal{P}_i(\boldsymbol{r}) = C\,\frac{r_i}{r^3}$$

where C is a constant. Besides, there is a singular point at $r = 0$ because $\mathcal{P}_i$ cannot be infinite, hence C must be zero. Consequently, the pressure-velocity correlation at two points vanishes in isotropic turbulence. This result can be interpreted rather well

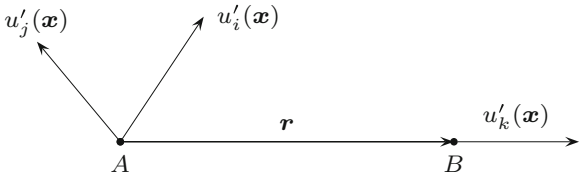

Fig. 6.7 Illustration of the two-point triple velocity correlation

because for isotropic turbulence, $\overline{u_1'^2} = \overline{u_2'^2} = \overline{u_3'^2}$. Thus the pressure does not need to redistribute energy to the different velocity components.

6.2.4 Triple Correlations of the Velocities at Two Points

The tensor of the triple correlations of the velocities at two points also takes a noteworthy form for an incompressible isotropic turbulence. As illustrated in Fig. 6.7, the form considered here is

$$T_{ij,k}(\boldsymbol{r}) = \overline{u'_i(\boldsymbol{x})u'_j(\boldsymbol{x})u'_k(\boldsymbol{x}+\boldsymbol{r})} \quad \text{or else} \quad \mathcal{T}_{ij,k}(\boldsymbol{r}) = \frac{\overline{u'_i(\boldsymbol{x})u'_j(\boldsymbol{x})u'_k(\boldsymbol{x}+\boldsymbol{r})}}{u'^3} \tag{6.28}$$

For similar reasons to those developed in Sect. 6.2.3, it can be demonstrated that for an incompressible isotropic turbulence, this correlation can be expressed with only one scalar function h

$$\mathcal{T}_{ij,k}(\boldsymbol{r}) = (h - rh')\frac{r_i r_j r_k}{2r^3} - \frac{h}{2}\frac{r_k}{r}\delta_{ij} + \frac{1}{4r}\frac{d}{dr}(r^2 h)\left(\delta_{jk}\frac{r_i}{r} + \delta_{ik}\frac{r_j}{r}\right) \tag{6.29}$$

$\mathcal{T}_{ij,k}(\boldsymbol{r})$ is an odd function of $\boldsymbol{r}$, unlike $R_{ij}(\boldsymbol{r})$ which is an even function, and it can also be pointed out that the scalar function $h(r)$ can be interpreted as $h(r) = \mathcal{T}_{11,1}(r, 0, 0)$. The details of the demonstration can be found in Batchelor [84]. Triple correlations between velocity at two points occur when studying the dynamic behaviour of the double correlation because of the nonlinear character of the Navier-Stokes equations.

6.2.5 Spectral Velocity Tensor

As in the case of homogeneous turbulence, the spectral tensor $\phi_{ij}(\boldsymbol{k})$ plays a key role in the description of the isotropic turbulence in Fourier space. Its expression can be directly inferred from the general expression (6.23) of a second-order isotropic tensor by Fourier transform. Then in spectral space,

$$\phi_{ij}(\boldsymbol{k}) = \alpha(k) k_i k_j + \beta(k)\delta_{ij}$$

If the isotropic turbulence is also incompressible, it is necessary that $k_i \phi_{ij} \equiv 0$, i.e. $\alpha(k)\, k^2 + \beta(k) = 0$. The spectral tensor can then be expressed with only one scalar function $\beta(k)$,

$$\phi_{ij}(\boldsymbol{k}) = \beta(k) \left(\delta_{ij} - \frac{k_i k_j}{k^2} \right) \tag{6.30}$$

The $\beta(k)$ function can be expressed as a quantity that can be more easily interpreted. In the 3-D case, the spectrum $E(k)$ of the turbulent kinetic energy defined by (6.14) can be used. According to what was seen above,

$$\phi_{ii} = \phi_{11} + \phi_{22} + \phi_{33} = 2\beta(k)$$

and by definition of $E(k)$,

$$E(k) = \frac{1}{2} \int_{\Sigma_k} \phi_{ii}(\boldsymbol{k}) d\Sigma = 2\pi k^2\, \phi_{ii}(k)$$

And then $\beta(k) = E(k)/4\pi k^2$, because the integration on the sphere of radius k leads only to $4\pi k^2 \phi_{ii}(k)$. The expression of the spectral tensor of an incompressible isotropic turbulence is finally,

$$\phi_{ij}(\boldsymbol{k}) = \frac{E(k)}{4\pi k^2} \left(\delta_{ij} - \frac{k_i k_j}{k^2} \right) \tag{6.31}$$

Usual One-Dimensional Spectra

The knowledge of the spectral tensor given by expression (6.31) permits to express the one-dimensional spectrum $E_{11}^{(1)}$ defined in Sect. 6.1.4, as a function of the spectrum of turbulent kinetic energy $E(k)$. For an incompressible isotropic turbulence,

$$E_{11}^{(1)}(k_1) = \iint \frac{E(k)}{4\pi k^2} \left(1 - \frac{k_1^2}{k^2} \right) dk_2 dk_3$$

To develop this expression, it is convenient to introduce the polar coordinates (σ, φ) in the plane $\mathcal{P}$ perpendicular to the k_1 axis, with $k^2 = k_1^2 + \sigma^2$ as illustrated in Fig. 6.8. Integrating with k_1 fixed,

$$\begin{aligned} E_{11}^{(1)}(k_1) &= \iint \frac{E(\sqrt{k_1^2 + \sigma^2})}{4\pi(k_1^2 + \sigma^2)} \left(1 - \frac{k_1^2}{k_1^2 + \sigma^2} \right) \sigma d\sigma d\varphi \\ &= \frac{1}{2} \int_0^\infty \frac{E(\sqrt{k_1^2 + \sigma^2})}{(k_1^2 + \sigma^2)^2} \sigma^3 d\sigma \end{aligned}$$

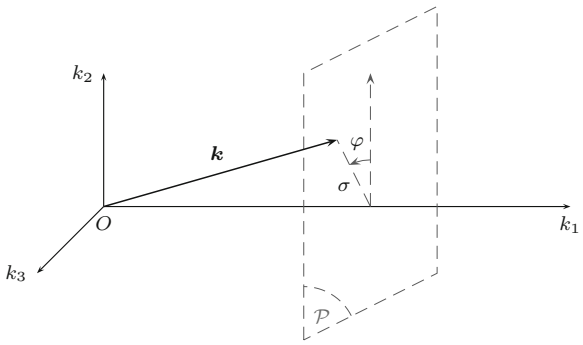

Fig. 6.8 Polar coordinates introduced to obtain expression (6.32)

The variable change $\sigma^2 = k^2 - k_1^2$, $\sigma d\sigma = kdk$ then provides,

$$E_{11}^{(1)}(k_1) = \frac{1}{2}\int_{k_1}^{\infty} \frac{E(k)}{k^4}(k^2 - k_1^2)kdk$$

and finally,

$$E_{11}^{(1)}(k_1) = \frac{1}{2}\int_{k_1}^{\infty} \frac{E(k)}{k}\left(1 - \frac{k_1^2}{k^2}\right)dk \tag{6.32}$$

It is also possible to obtain an expression of the one-dimensional spectra $E_{22}^{(1)}$ and $E_{33}^{(1)}$ in terms of $E(k)$, noting that

$$E_{22}^{(1)}(k_1) = E_{33}^{(1)}(k_1) = \frac{1}{2}\left[E_{22}^{(1)}(k_1) + E_{33}^{(1)}(k_1)\right]$$

Then, using the same variable change as above, one obtains

$$E_{22}^{(1)}(k_1) = E_{33}^{(1)}(k_1) = \frac{1}{4}\int_{k_1}^{\infty} \frac{E(k)}{k}\left(1 + \frac{k_1^2}{k^2}\right)dk \tag{6.33}$$

The two spectra $E_{11}^{(1)}(k_1)$ and $E_{22}^{(1)}(k_1)$ are shown in Fig. 6.9, in the simple case where all the kinetic energy is concentrated on a wavenumber k_0, i.e. $E(k) = \delta(k - k_0)$. The wave vectors which contribute to the energy have their ends on a sphere of radius k_0 and it is the incompressibility condition of the flow which implies different one-dimensional spectra. Particularly, the fact that $E_{11}^{(1)}$ is maximum for $k_1 = 0$ tags all the spectra measured in turbulence.

Let us add that combining the two previous relations, a link between the one-dimensional spectra $E_{11}^{(1)}$ and $E_{22}^{(1)}$ is obtained,

$$E_{22}^{(1)}(k_1) = \frac{1}{2}E_{11}^{(1)}(k_1) - \frac{1}{2}k_1\frac{d}{dk_1}E_{11}^{(1)}(k_1) \tag{6.34}$$

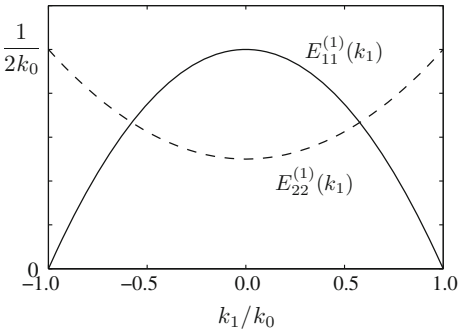

Fig. 6.9 One-dimensional spectra $E_{11}^{(1)}(k_1)$ and $E_{22}^{(1)}(k_1)$ for $E(k) = \delta(k - k_0)$ according to Eqs. (6.32) and (6.33): $E_{11}^{(1)}(k_1) = (1 - k_1^2/k_0^2)/(2k_0)$ and $E_{22}^{(1)}(k_1) = (1 + k_1^2/k_0^2)/(4k_0)$ for $|k_1| \leq k_0$ and $E_{11}^{(1)}(k_1) = E_{22}^{(1)}(k_1) = 0$ for $|k_1| > k_0$. The large difference between the two spectra is due to the incompressibility condition. For example, for $k_1 = k_0$, i.e. a wave vector aligned with the k_1-axis, all the Fourier contributions are in the plane normal to the k_1-axis, so that $\hat{u}_1(k_0) = 0$ and $E_{11}^{(1)}(k_0) = 0$, and $\hat{u}_2(k_0)$ and $E_{22}^{(1)}(k_0)$ are maximum. Similarly, one can consider $k_1 = 0$ and find that $E_{11}^{(1)}(0)$ is maximum and $E_{22}^{(2)}(0)$ is down to zero

This relation in spectral space permits to verify experimentally the isotropy of the turbulence. More precisely, the range of wavenumbers for which the turbulence has an almost isotropic behaviour can be determined. Hence, it bears more meaning than the mere relation between integral scales $L_g = L_f/2$.

Another interesting relation is that expressing the turbulent kinetic energy spectrum $E(k)$ as a function of the one-dimensional spectrum $E_{11}^{(1)}(k_1)$, which can be obtained experimentally. This relation is obtained deriving relation (6.32)

$$\frac{d}{dk_1} E_{11}^{(1)}(k_1) = -\int_{k_1}^{\infty} \frac{E(k)}{k^3} k_1 dk$$

and then deriving a second time with respect to k_1,

$$\frac{d}{dk_1}\left(\frac{1}{k_1}\frac{dE_{11}^{(1)}(k_1)}{dk_1}\right) = \frac{E(k_1)}{k_1^3}$$

and finally,

$$E(k) = k^2 \left.\frac{d^2 E_{11}^{(1)}}{dk_1^2}\right|_{k_1=k} - k \left.\frac{dE_{11}^{(1)}}{dk_1}\right|_{k_1=k} \tag{6.35}$$

6.2.6 Useful Other Results

Numerous other relations can be obtained for an incompressible and three-dimensional isotropic turbulence, see for example Batchelor [84], Hinze [8] or Monin and Yaglom [17]. Let us illustrate a few of them,

- Expression of the integral scale L_f as a function of the spectrum of the turbulent kinetic energy E,

$$L_f = \frac{3\pi}{4} \frac{\displaystyle\int_0^\infty \frac{E(k)}{k} dk}{\displaystyle\int_0^\infty E(k) dk} \tag{6.36}$$

- Relation between the correlation function f and the spectrum of the turbulent kinetic energy E,

$$\begin{cases} f(r) = \dfrac{2}{\overline{u'^2}} \displaystyle\int_0^\infty \left(\frac{\sin(kr)}{k^3 r^3} - \frac{\cos(kr)}{k^2 r^2} \right) E(k) dk \\ E(k) = \dfrac{\overline{u'^2}}{\pi} \displaystyle\int_0^\infty f(r) k^2 r^2 \left(\frac{\sin(kr)}{kr} - \cos(kr) \right) dr \end{cases} \tag{6.37}$$

- Relation between $E(k)$ and the trace $R_{ii}(r)$ of the tensor of the double correlations, without forgetting that $R_{ii} = \overline{u'^2}\, \mathcal{R}_{ii}$,

$$\begin{cases} E(k) = \dfrac{1}{\pi} \displaystyle\int_0^\infty R_{ii}(r) kr \sin(kr) dr \\ R_{ii}(r) = 2 \displaystyle\int_0^\infty E(k) \frac{\sin(kr)}{kr} dk \end{cases} \tag{6.38}$$

- Expression of the dissipation as a function of the velocity field derivatives,

$$\epsilon = \frac{15}{2} \nu \overline{\left(\frac{\partial u_1'}{\partial x_2} \right)^2} = 15 \nu \overline{\left(\frac{\partial u_1'}{\partial x_1} \right)^2} \tag{6.39}$$

- Expression of the dissipation as a function of the Taylor scales,

$$\epsilon = 15 \nu \frac{\overline{u'^2}}{\lambda_g^2} = 30 \nu \frac{\overline{u'^2}}{\lambda_f^2} \tag{6.40}$$

- Expression of the dissipation as a function of the one-dimensional spectrum,

$$\epsilon = 30 \nu \int_0^\infty k_1^2 E_{11}^{(1)}(k_1) dk_1 \tag{6.41}$$

- Average value of the product of two velocity derivatives,

$$Q_{ijlm} = \overline{\frac{\partial u_i'}{\partial x_l}\frac{\partial u_j'}{\partial x_m}} = \overline{\left(\frac{\partial u_1'}{\partial x_2}\right)^2}\left(\delta_{ij}\delta_{lm} - \frac{1}{4}\delta_{il}\delta_{jm} - \frac{1}{4}\delta_{im}\delta_{jl}\right) \tag{6.42}$$

- Expression of the enstrophy spectral tensor [97, 105],

$$\Omega_{ij}(k) = k^2\phi_{ij}(k) = \frac{E(k)}{4\pi}\left(\delta_{ij} - \frac{k_i k_j}{k^2}\right) \tag{6.43}$$

- Expression of the enstrophy production term,

$$\overline{\omega_i'\omega_j'\frac{\partial u_i'}{\partial x_j}} = -\frac{35}{2}\overline{\left(\frac{\partial u_1'}{\partial x_1}\right)^3} = -\frac{35}{2}h'''(0) \tag{6.44}$$

Extending the method to temperature fluctuations in isotropic turbulence, a few pertinent results have been established by Corrsin [103], and Kovasznay et al. [119]

- The correlation between temperature at a point and velocity at another point is equal to zero, similarly to pressure-velocity correlation at two points.
- The correlation between the temperature fluctuations θ_A' and θ_B' at two points A and B take the simple form,

$$\frac{\overline{\theta_A'\theta_B'}}{\overline{\theta'^2}} = m(r)$$

where $r = (r_i r_i)^{1/2}$ is the distance between the two points A and B.
- The three-dimensional power spectrum for the temperature fluctuation field has also a simple form, similar to the trace of $R_{ii}(r)$,

$$\phi_{\theta^2}(\boldsymbol{k}) = \frac{G(k)}{4\pi k^2} \quad \text{with} \quad \overline{\theta'^2} = \int_0^\infty G(k)dk$$

- The one-dimensional spectrum of $\overline{\theta'^2}$ is connected to $G(k)$ by

$$G_{\theta^2}^{(1)}(k_1) = \frac{1}{2}\int_{k_1}^\infty \frac{G(k)}{k}dk \quad \text{and reciprocally,} \quad G(k) = -2k\frac{dG_{\theta^2}^{(1)}(k_1)}{dk_1}\bigg|_{k_1=k}$$

6.3 Experimental Realization of Isotropic Turbulence

The realization of isotropic turbulence in a laboratory is a very useful tool. The experimental study of such a flow permits a better understanding of the nonlinear mechanisms when turbulence is not sustained by mean flow gradients. It also provides quantitative data to refine numerical models.

6.3.1 Experimental Configuration

It is not so easy to achieve isotropic turbulence in a laboratory. The main part of the topic has been described by Comte-Bellot and Corrsin [100, 101]. The basic configuration consists of placing a grid at the beginning of the working section of a wind tunnel where the average velocity is constant. A representation is given in Fig. 6.10. The jets between the bars can be seen, first they stay distinct and then merge and mix, creating homogeneous turbulence downstream in planes parallel to the grid.

The grids used are often composed of two planes of bars perpendicular to each other, as shown in Fig. 6.11. The square section of the bars advantageously implies that the separation of the boundary layers is fixed whatever the Reynolds number is. This ensures stable and repetitive experiments. If the individual jets generated by the grid gradually merge, we can expect that an accurate made grid will produce a reasonably homogeneous field at large enough x_1/M, where M is the mesh spacing

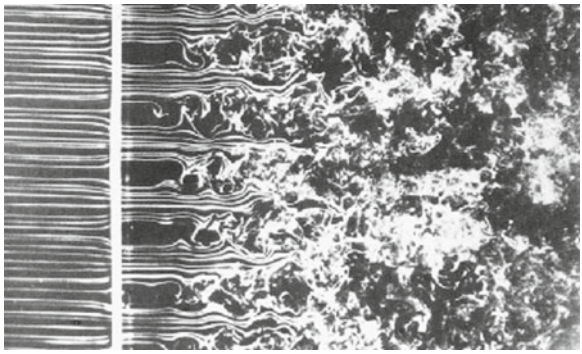

Fig. 6.10 Visualization of turbulence behind a grid using emission lines issued from a wire placed upstream of the grid. The wire is varnished by portions and covered with oil. Applying an electric current, oil burns and generates smoke from the unvarnished parts of the wire. From Corke and Nagib in Van Dyke [28]

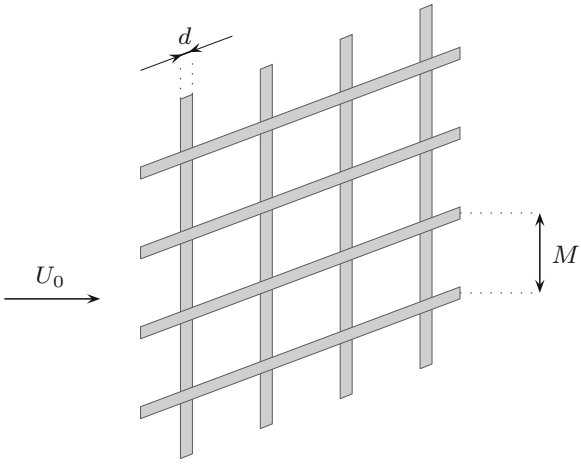

Fig. 6.11 A sketch of a turbulence-generating grid composed of square bars of size d and mesh spacing M. Typically, $d = 1$ cm and $M = 5$ cm

of the grid. Experiments [709] have shown that the solidity of the grid defined by

$$\sigma = \frac{\text{surface obstructed by the grid}}{\text{initial surface}} = \frac{d}{M}\left(2 - \frac{d}{M}\right)$$

should not be too high, usually $\sigma \simeq 0.35$ is a maximum. Otherwise the individual jets coalesce successively into larger and larger jets because of a lack of fluid to drag. The reference Reynolds number is based on M, which can vary from one grid to another, and on the average velocity of the flow U_0 which is adjustable,

$$\mathrm{Re}_M = \frac{U_0 M}{\nu} \simeq 10^4 - 10^5$$

The turbulence level achieved is not very high, $u'/U_0 \simeq 2\,\%$, for a distance of 30 M downstream of the grid. Thus it is important to have a large enough working section, of approximately 20 M, to avoid a contamination by the boundary layers developing along the walls of the wind tunnel. The length of the working section must also be large enough, of approximately 100 to 200 M, to provide significant time for the turbulence to evolve.

There is no reason that a grid perpendicular to the flow creates isotropic turbulence: indeed there are only two symmetry axis. Measures with this configuration provide, $\overline{u_1'^2} = 1.2\,\overline{u_2'^2} = 1.2\,\overline{u_3'^2}$, the component u_1' still being the largest because it is primarily fed by the average flow around the bars. To render the three intensities equal, the solution is to place a flow contraction of ratio $c \simeq 1.27$ at a distance of approximately 18 M of the grid, as indicated in Fig. 6.12. The main effect of the contraction is to stretch the vortices of longitudinal axis, and thus to increase u_2' and u_3'. More precisely, the rapid distortion theory, presented in Sect. 6.1.7, can be used and is developed in Sect. 6.8 to study the case of an axisymmetric contraction.

There are other devices which permit obtention of an almost isotropic turbulence more intense than those created by grids. The innovative idea of Betchov [87] is to use a chamber composed of multiple jets, whose turbulence is extracted by a fan.Grids

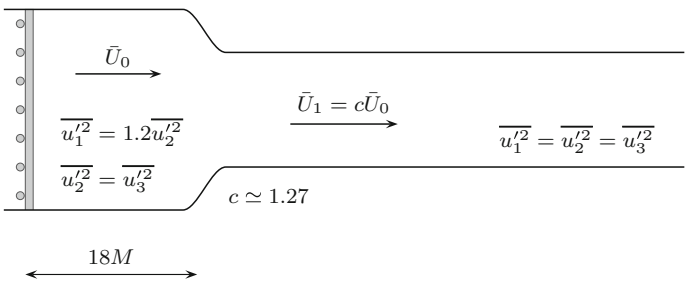

Fig. 6.12 Use of a contraction to generate isotropic turbulence, from Comte-Bellot and Corrsin [100]

with jets have also been suggested, as well as grids associated to small propellers. The most recent and performing device is the one of Mydlarski and Warhaft [137, 138], where the turbulence is created by small flaps of irregular geometry fixed to a grid and driven randomly.

6.3.2 The Turbulence Decay

The observation of the characteristics of turbulence at different distances x_1 downstream of the grid corresponds to the time t which appears in the general equations of turbulence dynamics. Besides, for each distance x_1, the velocity $\bar{U}_1$ allows renewal of the observed phenomenon. This is a simple case where the equivalence between time average and ensemble average can be seen. To know $\overline{u_1'^2}(t)$ for instance, $\overline{u_1'^2}(x_1)$ is measured. As for the partial derivative $\partial/\partial x_1$ of any signal s, which appears for example in the calculation of the dissipation, it can be expressed as a function of the partial derivative with respect to time $\partial/\partial t$ using a frozen turbulence hypothesis on a short period of time, which provides $ds/dt \simeq 0$, i.e.

$$\frac{\partial s}{\partial t} + \bar{U}_1 \frac{\partial s}{\partial x_1} + u_1' \frac{\partial s}{\partial x_1} + u_2' \frac{\partial s}{\partial x_2} + u_3' \frac{\partial s}{\partial x_3} \simeq 0$$

and then

$$\frac{\partial s}{\partial t} \simeq -\bar{U}_1 \frac{\partial s}{\partial x_1} \tag{6.45}$$

keeping the main term where $\bar{U}_1$ is. This approximation is known as the Taylor hypothesis. It is often used in laboratory experiments, even outside the field of homogeneous and isotropic turbulence. For spatial correlations R_{ij}, the separation vector $\boldsymbol{r}$ still corresponds to separations $\Delta x_1 = r_1$, $\Delta x_2 = r_2$ and $\Delta x_3 = r_3$ if two hot-wires are used. However, if only one wire placed in A is used, the frozen turbulence hypothesis associates to a time lag $d\tau$ a space shift $r_1 = -\bar{U}_1 d\tau$, as if the second measured point was upstream of A.

A thorough study of the turbulence decay can be found in Chap. 7, but some simple and essential results can already be mentioned.

Decrease of Turbulence Intensity

The turbulence intensity is found to evolve according to

$$\frac{\overline{u'^2}}{U_0^2} = \frac{1}{A}\left(\frac{tU_0}{M} - \frac{t_0 U_0}{M}\right)^{-n} \quad \text{with} \quad 1.1 \leq n \leq 1.3 \quad \text{and} \quad A \simeq 30 \tag{6.46}$$

The Reynolds number Re_M modifies only slightly n and A [135]. The distance $t_0 U_0$ represents a virtual origin located at a distance of some M downstream of the grid.

Evolution of Spatial Scales

The experiment provides the following laws for the evolution of integral and Taylor scales,

$$\frac{L_g}{M} \simeq 0.06 \left(\frac{tU_0}{M} - \frac{t_0 U_0}{M} \right)^{0.35} \qquad \frac{\lambda_g}{M} \simeq 0.02 \left(\frac{tU_0}{M} - \frac{t_0 U_0}{M} \right)^{0.50} \tag{6.47}$$

It is useful to point out that the exponents of these two relations are not the same. This difference invalidates any simple similarity hypothesis using only one length scale, as is the case for jets and wakes. This attempt, which can be easily developed with the equations of Chap. 7, would imply that both L_g and λ_g scales obey a $t^{0.50}$ evolution. A simple similarity hypothesis would also force any characteristic Reynolds number of the turbulence to stay constant, which can neither be inferred from the experimental data.

Reynolds Number of the Turbulence

From the laws (6.46) and (6.47), Reynolds numbers characteristic of the turbulence, built from L_g, λ_g and u', with the simple notation $u' = \sqrt{\overline{u'^2}}$, change slowly during the turbulence decay,

$$\mathrm{Re}_{L_g} = \frac{u' L_g}{\nu} \simeq (t - t_0)^{-0.30} \quad \text{and} \quad \mathrm{Re}_{\lambda_g} = \frac{u' \lambda_g}{\nu} \simeq (t - t_0)^{-0.15}$$

At large t, when Re_{λ_g} is down to approximately 5 to 10, the nonlinear effects due to both inertia and pressure become negligible. Then viscous effects prevail and lead to a rapid decay of the kinetic energy. This last period is called final period to contrast with the initial period, which was studied above and is of course the most important.

Experimental Value of the Dissipation ϵ

Equation (2.20), to which kinetic energy k_t obeys, becomes for isotropic turbulence

$$\frac{dk_t}{dt} = -\epsilon \quad \text{that is,} \quad \epsilon = -\frac{3}{2} \frac{d\overline{u'^2}}{dt}$$

and various theoretical expressions of ϵ were given in Sect. 6.2.6. The experiment here provides a very interesting independent result, without numerical coefficient the following relation is verified,

$$\epsilon = \frac{u'^3}{L_f} \tag{6.48}$$

Table 6.1 Turbulence data from the experiments reported by Comte-Bellot and Corrsin [101]

tU_0/M		u' cm · s^{-1}	ϵ cm^2 · s^{-3}	L_f cm	$\epsilon L_f/u'^3$
$M = 5.08$ cm	42	22.2	4740	2.40	1.04
	98	12.8	633	3.45	1.04
	171	8.95	174	4.90	1.19
$M = 2.54$ cm	45	20.5	7540	1.20	1.05
	120	10.6	731	1.80	1.10
	240	6.75	145	2.14	1.01
	385	5.03	48.5	2.40	0.91

A comparison with relation (6.48) is shown in the last column. The length L_f is deduced from the measurement of $L_{11}^{(2)}$ for the case $M = 2.54$ cm

Table 6.1 illustrates this result with the data of Comte-Bellot and Corrsin [101], see also Sreenivasan [193]. This expression shows that the dissipation is actually set by the large structures of the turbulence characterized by the two quantities u' and L_f. Small structures must then adapt themselves to the amount of energy to be dissipated. Particularly, small structures are finer for a smaller molecular viscosity.

Characteristic Time of the Turbulence
Relation (6.48) can be written as

$$\epsilon = \frac{u'^2}{L_f/u'}$$

The quantity $\Theta \equiv L_f/u'$ is obviously a time scale, which has a double interest. First, it is built on the characteristics of the energy-containing eddies and second, it rules the turbulence decay in the initial period. Figure 7.8 of Chap. 7 shows that this time also represents an integral scale as a time correlation in the frame moving with velocity $\bar{U}_1$. Thus this characteristic time far exceeds a simple conjuncture using a dimensional analysis.

6.4 Particle Dispersion by Homogeneous Turbulence

As an introduction, in Chap. 1, the role of turbulence as an efficient transport agent was pointed out. Two fundamental dispersion problems are considered here. They were expressed by Taylor [211, 212]. One deals with free-space dispersion by homogeneous and stationary turbulence carried by a constant and uniform velocity while the other deals with dispersion in a very long circular pipe. In both cases, the point is to predict the concentration reduction of a contaminating agent that would of course stay located horizontally to the source point if there was no turbulence.

6.4.1 Free-Space Dispersion

Figure 6.13 illustrates particle dispersion under the effect of a turbulent field, the average size of the cloud created by the arrival points of the particles, some t time after the particles were issued, is searched for. The position $\boldsymbol{X}(\boldsymbol{a}, t)$ reached at time t by the particle which was at A of coordinates $\boldsymbol{a}$ at $t = 0$, is given by

$$\boldsymbol{X}(\boldsymbol{a}, t) = \boldsymbol{a} + \bar{\boldsymbol{U}}t + \int_0^t \boldsymbol{v}(\boldsymbol{a}, t')\, dt' \tag{6.49}$$

where $\boldsymbol{v}(\boldsymbol{a}, t')$ is the velocity encountered by the particle in each point of its trajectory. This velocity is said to be Lagrangian, and is associated with the Euler velocity $\boldsymbol{u}$ by

$$\boldsymbol{v}(\boldsymbol{a}, t') = \boldsymbol{u}\left[\boldsymbol{X}(\boldsymbol{a}, t')\right]$$

To simplify notation, the prime symbol is omitted for velocity variations as well as the initial position $\boldsymbol{a}$. The coordinates of the cloud barycenter are obtained using the statistical average of the different trajectories, $\bar{X}_i(t) = a_i + \bar{U}_i \delta_{i1} t$, and then

$$X_i(t) - \bar{X}_i(t) = \int_0^t v_i(t')dt'$$

It is assumed that the average velocity is constant and has only one non-zero component $\bar{U}_1$. As for the underlying turbulent field, it is assumed to be homogeneous, with the Eulerian meaning of the word, as well as stationary. The random velocity $v_i(t')$ thus becomes stationary for it can be admitted that it corresponds to an Eulerian velocity taken at different times and at different points of the field.

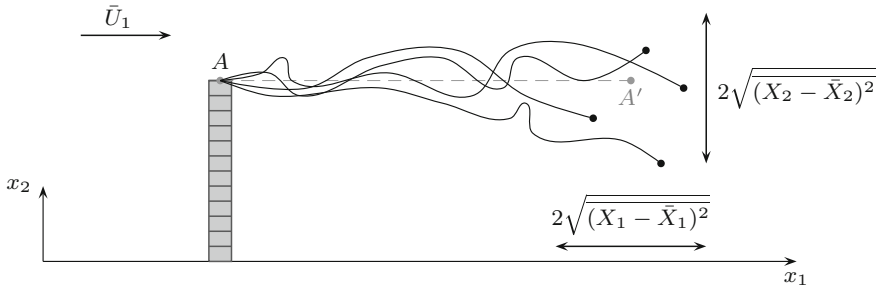

Fig. 6.13 Trajectories of particles released at point A in a turbulent field carried by a constant and uniform mean velocity $\bar{U}_1$. Several realizations are presented showing the positions reached after the same elapsed time t. Without turbulence, all the particles would be at point A' such that $AA' = \bar{U}_1 t$

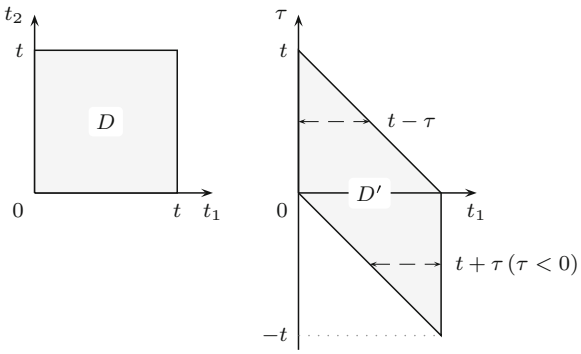

Fig. 6.14 Domains D and D' used to compute the variance of the particle separations

The average quadratic value of a particle distance to the barycenter is,

$$\overline{\left[X_\alpha(t)-\bar{X}_\alpha(t)\right]^2}=\iint_D \overline{v_\alpha(t_1)\,v_\alpha(t_2)}\,dt_1\,dt_2$$

where D is the square area $[0,t]\times[0,t]$ represented in Fig. 6.14. The α index is equal to 1, 2 or 3, without summation, to be able to take into account an anisotropic turbulence. As $v_\alpha(t)$ is stationary, it is interesting to apply the variable change $t_1=t_1$ and $\tau=t_2-t_1$, which leads to the new domain D' where the integration in t_1 is obvious:

$$\begin{aligned}\overline{\left[X_\alpha(t)-\bar{X}_\alpha(t)\right]^2}&=\iint_{D'}\overline{v_\alpha(t_1)v_\alpha(t_1+\tau)}\,dt_1\,d\tau=\overline{v_\alpha^2}\iint_{D'}\mathcal{R}^L_{\alpha\alpha}(\tau)dt_1\,d\tau\\&=\overline{v_\alpha^2}\int_{-t}^{0}(t+\tau)\mathcal{R}^L_{\alpha\alpha}(\tau)\,d\tau+\overline{v_\alpha^2}\int_0^t(t-\tau)\,\mathcal{R}^L_{\alpha\alpha}(\tau)\,d\tau\\&=2\,\overline{v_\alpha^2}\int_0^t(t-\tau)\mathcal{R}^L_{\alpha\alpha}(\tau)\,d\tau \qquad (6.50)\\&=2\,\overline{v_\alpha^2}\,t\int_0^t\left(1-\frac{\tau}{t}\right)\mathcal{R}^L_{\alpha\alpha}(\tau)\,d\tau \qquad (6.51)\end{aligned}$$

The double covariance between the velocity variations of the particle at two times is said to be Lagrangian since the particle is followed in its movement, and $\mathcal{R}^L_{\alpha\alpha}$ is the Lagrangian correlation coefficient. Also $\overline{v_\alpha^2}=\overline{u'^2_\alpha}$ because of the homogeneity and stationarity hypothesis on the turbulent field. For large t, and if $\mathcal{R}^L_{\alpha\alpha}(\tau)$ decreases fast enough with τ, the following approximation value can be made

$$\overline{\left[X_\alpha(t)-\bar{X}_\alpha(t)\right]^2}\simeq 2\,\overline{u'^2_\alpha}\times\Theta^L_{\alpha\alpha}\times t \qquad (6.52)$$

sometimes called Taylor formula, where

$$\Theta_{\alpha\alpha}^{L} = \int_0^{\infty} \mathcal{R}_{\alpha\alpha}^{L}(\tau)\ d\tau$$

The reader can verify that this is correct as soon as $t \gg \Theta_{\alpha\alpha}^{L}$ for a correlation with an exponential form, $\mathcal{R}_{\alpha\alpha}^{L}(\tau) = e^{-\tau/\Theta_{\alpha\alpha}^{L}}$. The most essential result that can be inferred from expression (6.52) is that particle dispersion is governed by $\overline{u_\alpha'^{\,2}} \times \Theta_{\alpha\alpha}^{L}$ which is called turbulent dispersion coefficient, expressed in $\mathrm{m}^2 \cdot \mathrm{s}^{-1}$. It can be pointed out that the $X_i(t)$ values have an almost Gaussian probability density for a sufficiently large t, i.e. for $t \gg \Theta_{\alpha\alpha}^{L}$, by application of the central limit theorem to the sum of the elementary movements which are almost independent of each other.

One of the key points of the problem is the expression of the Lagrangian integral scale $\Theta_{\alpha\alpha}^{L}$ as a function of the fundamental parameters of isotropic turbulence, i.e. L_f and u'. For a grid turbulence, two types of experiment have been conducted,

- A very fine thread is placed in the working section and is slightly heated to tag the passing fluid particles. The transverse profiles of temperature are measured at different distances downstream, and it can be inferred that such a profile is connected to $\overline{(X_2 - \bar{X}_2)^2}$. Far enough downstream, this quantity grows linearly with the distance from the wire, and the slope then provides Θ_{22}^{L}. The experiments of Shlien and Corrsin [208] are conducted in the isotropic turbulence field described in Sect. 6.3, at 42 and 98 M from the grid, where respectively $\mathrm{Re}_{\lambda_g} = 71$ and 65, and they obtain $\Theta_{22}^{L} \simeq 1.25 L_f/u'$.
- Tiny solid particles are individually injected upstream of the grid and their trajectory is monitored. Snyder and Lumley [209] use hollow glass spheres and place approximately ten cameras along the working from section 73 M where $\mathrm{Re}_{\lambda_g} = 51$. They then obtain $\Theta_{22}^{L} \simeq L_f/u'$. Sato and Yamamoto [207] use small polystyrene particles in a water tunnel and follow completely their trajectory with a video camera. They obtain $\Theta_{22}^{L} \simeq 0.6$–$0.3\ L_f/u'$ for $\mathrm{Re}_{\lambda_g} = 20$–$70$ respectively.

A numerical approach is also possible. Yeung and Pope [213] use direct simulations of isotropic turbulence on cubes of sizes 64^3 and 128^3. They find that $\Theta_{22}^{L} \simeq 0.72 L_f/u'$, for a range of Reynolds numbers Re_{λ_g} that can be compared to the one of the experiments.

Thus, for isotropic turbulence, $\Theta_{\alpha\alpha}^{L} \simeq L_f/u'$, and finally the dispersion coefficient has the simple value $\overline{u_\alpha'^{2}} \times \Theta_{\alpha\alpha}^{L} \simeq u' \times L_f$. For instance, with $u' = 0.22\mathrm{m} \cdot \mathrm{s}^{-1}$, $L_f = 0.024$ m and $t = 1$ s, the average size of the cloud as a standard deviation for the half-width is of approximately 2×0.10 m, i.e. more than 8 times the integral scale L_f.

6.4.2 Longitudinal Dispersion in a Circular Pipe

In the case of particles injected into a pipe, the size of the dispersion cloud can also be estimated if the pipe is long enough. Along their random trajectory, the particles necessarily wander across the whole section because of the radial velocity fluctuations and of the walls which confine trajectories, as indicated in Fig. 6.15. Thus the particles see a stationary and homogeneous field, and the result (6.52) can be used again. The cloud moves at the bulk velocity U_d of the flow, and the velocity variations responsible for the longitudinal dispersion are in each point, on the one hand the difference between the local mean velocity and U_d and, on the other hand, the longitudinal velocity fluctuations. Hence,

$$v_1(t') = \bar{U}_1(X_2, t') - U_d + u_1'(\boldsymbol{X}, t')$$

The longitudinal movement of a particle can then be written,

$$X_1(t) = \int_0^t \left[\bar{U}_1(X_2, t') - U_d + u_1'(\boldsymbol{X}, t')\right] dt'$$

which leads for a pipe of section S to

$$\overline{\left[X_1(t) - \bar{X}_1(t)\right]^2} \simeq 2\,\overline{v_1^2} \times \Theta_{11}^L \times t$$

with

$$\overline{v_1^2} \simeq \underbrace{\frac{1}{S}\int_S \overline{(\bar{U}_1 - U_d)^2}\, dS}_{\text{(a)}} + \underbrace{\frac{1}{S}\int_S \overline{u_1'^2}\, dS}_{\text{(b)}}$$

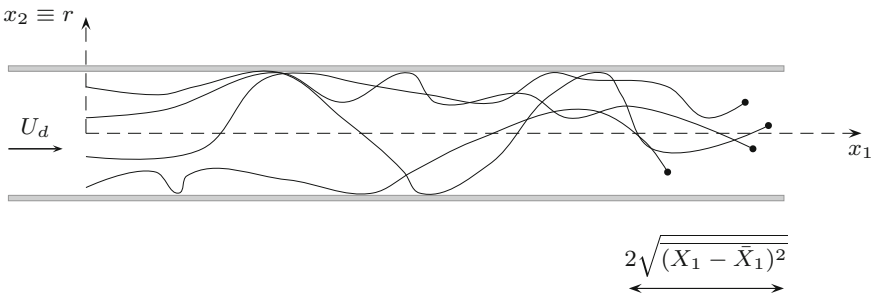

Fig. 6.15 Particle dispersion in a long pipe when the fully developed regime is reached. Trajectories are confined by the walls and at large t, the particles form a cloud homogeneous in the radial direction and centered at $x_1 = U_d t$, where U_d is the bulk velocity

The result must now be expressed as a function of the characteristic scales of the flow, i.e. the radius R of the pipe and the friction velocity u_τ. The term (a) is associated with the mean velocity profile which is convenient to describe using a power law, $\bar{U}_1/\bar{U}_{1\text{axe}} = (1 - r/R)^n$, for describing the whole cross section of the flow. Chosing $n = 6.6$ for a Reynolds Re_D around 2×10^4 close to that used by Taylor in his experiments [212], we obtain

$$(a) = \frac{1}{6.6^2} U_d^2 = \frac{1}{6.6^2} 17.5^2 \times u_\tau^2 \simeq 7.03\, u_\tau^2$$

with $U_d/u_\tau \simeq 17.5$, see Fig. 3.3 in Chap. 3. To assess the (b) term, a linear approximation of the distribution of $\overline{u_1'^2}/u_\tau^2$ is used as a function of the distance to the wall given in Chap. 3, namely $u_1'/u_\tau \simeq 1 + 1.5r/R$, which provides after integration $(b) \simeq 4u_\tau^2$. The main dispersion agent is thus represented by the (a) term. The physics involved is that the transverse velocity fluctuations force the particles not to follow purely longitudinal trajectories.

For the Lagrangian integral scale, the conjecture $\Theta_{11}^L \simeq R/u_\tau$ can be given using the basic scales R and u_τ of a pipe flow, which permits to write

$$\overline{\left[X_1(t) - \bar{X}_1(t)\right]^2} \simeq 2 \times [(a) + (b)] \times \frac{R}{u_\tau} \times t \simeq 2 \times 11.03 \times R \times u_\tau \times t$$

This expression is *a priori* an approximation, but is actually confirmed by Taylor theory [212]. The reader can refer to the complete demonstration, using the frame moving with the bulk velocity, a dispersion coefficient in a section and a mean velocity profile which covers a large range of Reynolds numbers. In the end, the formula demonstrated by Taylor is

$$\overline{\left[X_1(t) - \bar{X}_1(t)\right]^2} = 2 \times 10.1 \times R \times u_\tau \times t \tag{6.53}$$

Figure 6.16 illustrates the passage of a polluting cloud far downstream of the injection point, above an electrical conductibility probe, the pollutant being salt. The time interval between the half-concentration fronts is equal to $\Delta t = 0.316\,\text{s}$. This value is then confirmed by formula (6.53). Using the previous numerical application to assess the friction velocity, it can be written:

$$\overline{\left[X_1(t) - \bar{X}_1(t)\right]^2} = 2 \times 10.1 \times 4.76 \times 10^{-3} \times \frac{2.22}{17.5} \times 7.35 \simeq 8.97 \times 10^{-2}\,\text{m}^2$$

and then for a Gaussian cloud,

$$\Delta t = 2\sqrt{2 \ln 2}\, \frac{\sqrt{8.97} \times 10^{-1}}{2.22} \simeq 0.318\,\text{s}$$

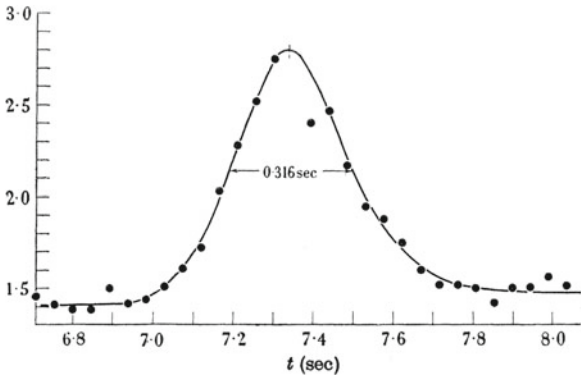

Fig. 6.16 Time trace of a salt cloud in a water pipe recorded at $x_1 = 16.31\,\text{m}$ from the source. $D = 9.525 \times 10^{-3}\,\text{m}$, $U_d = 2.22\,\text{m} \cdot \text{s}^{-1}$ and $\text{Re}_D = 1.9 \times 10^4$. The concentration is maximum at time $t = 7.35\,\text{s}$. From Taylor [212]

where the factor $\sqrt{2\ln 2}$ associates the half-width b to the standard deviation $\sigma = b/\sqrt{2\ln 2}$ for a profile of the form $e^{-x^2/(2\sigma^2)}/(\sigma\sqrt{2\pi})$.

In the radial direction, $i = 2$, the blockage by the walls leads to an uniform distribution of the pollutant. Besides, the variance derivative with respect to t having to be equal to zero, the formula (6.50) shows that the correlation curve $\mathcal{R}^L_{22}(\tau)$ must have a negative loop, which has indeed been observed by Sullivan [210] in a free surface water channel.

To accelerate mixing in industrial pipes, more efficient techniques than natural turbulence have been developed, using chaotic regimes, as described by Ottino [80, 206]. Particularly, there is the Partitioned Pipe Mixer (PPM) technique, where longitudinal plates divide the pipe in two, with a 90° offset between them, forming a shifted lattice.

For dispersion in even more complex situations, as in the atmospheric boundary layer with its different stability conditions, the review of Hunt [202] or the book of Blackadar [201] can be read.

6.5 Approximate Expression of the Dissipation for an Inhomogeneous Turbulence*

The dissipation rate ϵ of the turbulent kinetic energy defined in Sect. 2.4.2 can be written as

$$\rho\epsilon = \overline{\tau'_{ik}\frac{\partial u'_i}{\partial x_k}} = 2\mu\overline{s'^2_{ij}} = 2\mu\,\overline{\frac{1}{4}\left(\frac{\partial u'_i}{\partial x_j} + \frac{\partial u'_j}{\partial x_i}\right)^2} = \mu\underbrace{\overline{\frac{\partial u'_i}{\partial x_j}\frac{\partial u'_i}{\partial x_j}}}_{\text{(a)}} + \mu\underbrace{\overline{\frac{\partial u'_i}{\partial x_j}\frac{\partial u'_j}{\partial x_i}}}_{\text{(b)}}$$

for an incompressible turbulence, and two terms (a) and (b) are in evidence. We will show that term (a) prevails as soon as the Reynolds number is high enough. The orders of magnitude of terms (a) and (b) are,

$$\text{(a)} = \overline{\frac{\partial u_i'}{\partial x_j}\frac{\partial u_i'}{\partial x_j}} \sim \frac{u'^2}{\lambda^2} \qquad \text{(b)} = \overline{\frac{\partial u_i'}{\partial x_j}\frac{\partial u_j'}{\partial x_i}} = \frac{\partial^2(\overline{u_i'u_j'})}{\partial x_i \partial x_j} \sim \frac{u'^2}{L^2}$$

Hence, (a)/(b) $\sim L^2/\lambda^2$. According to relation (6.40), $\epsilon = 15\nu u'^2/\lambda_g^2$ and knowing that $\epsilon = u'^3/L_f$ for isotropic turbulence,

$$\frac{\text{(a)}}{\text{(b)}} \sim \frac{L_f^2}{\lambda_g^2} = \frac{\text{Re}_{L_f}}{15}$$

Therefore, term (a) becomes more and more important compared to term (b) when the Reynolds number increases, and ϵ can then be approximated by

$$\epsilon \simeq \epsilon^h = \nu\overline{\frac{\partial u_i'}{\partial x_j}\frac{\partial u_i'}{\partial x_j}} \tag{6.54}$$

This expression is exact for homogeneous turbulence, and it is thus denoted by ϵ^h. In the literature, this term is sometimes referred as pseudo-dissipation but this denomination is misleading.

6.6 Helicity⋆

During the definition of isotropic turbulence in Sect. 6.2, it was pointed out that statistical properties must be independent of any rotation but also of any reflection symmetry, of the setting of points A and B and of their associated vectors $\boldsymbol{a}$ and $\boldsymbol{b}$. If the reflection symmetry condition is not maintained, then the tensor of the double correlations at two points resumes its complete form (6.22),

$$\mathcal{R}_{ij}(\boldsymbol{r}) = \underbrace{\alpha(r)r_i r_j + \beta(r)\delta_{ij}}_{(1)} + \underbrace{\gamma(r)\epsilon_{ijk}r_k}_{(2)} \tag{6.55}$$

The kinetic energy is still represented by the terms (1) since in the term (2), the application of $i = j$ leads to $\gamma(r)\epsilon_{iik}r_k = 0$. Then the already introduced functions $f(r)$ and $g(r)$ keep their meaning and their role. As for the $\gamma(r)$ function, it can be expressed only with the correlation $h(r) = \mathcal{R}_{23}(r, 0, 0)$ represented in Fig. 6.17 because

$$h(r) = \mathcal{R}_{23}(r, 0, 0) = 0 + 0 + \gamma(r)r$$

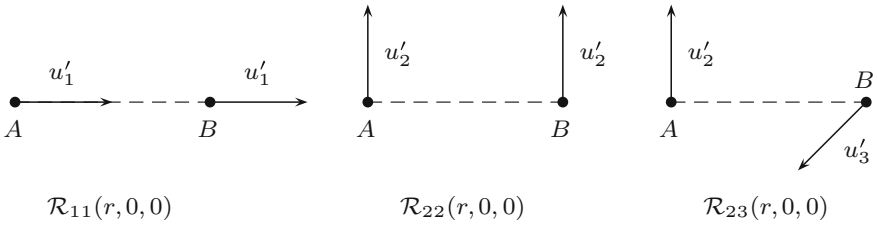

Fig. 6.17 The correlation $h(r) = \mathcal{R}_{23}(r,0,0)$ is specific to helicity. It is shown along the correlations $f(r) = \mathcal{R}_{11}(r,0,0)$ and $g(r) = \mathcal{R}_{22}(r,0,0)$ introduced in Sect. 6.2.2. Note that this $h(r)$ should not be confused with the $h(r)$ involved in expression (6.29)

The $\mathcal{R}_{23}(r,0,0)$ function is of course equal to the other two, $\mathcal{R}_{31}(0,r,0)$ and $\mathcal{R}_{12}(0,0,r)$, which can both be inferred from the first one by circular permutation. Thus, (6.55) can be written as,

$$\mathcal{R}_{ij}(\boldsymbol{r}) = [f(r) - g(r)]\,\frac{r_i r_j}{r^2} + g(r)\delta_{ij} + h(r)\epsilon_{ijk}\frac{r_k}{r} \tag{6.56}$$

The function $h(r)$ is then directly linked to the helicity (5.12) defined in Chap. 5. Indeed, introducing [14] $\bar{h}_e = \overline{u_i'(\boldsymbol{x})\omega_i'(\boldsymbol{x})}$, one has

$$\begin{aligned}
\bar{h}_e &= \lim_{\boldsymbol{x}'\to\boldsymbol{x}} \overline{u_i'(\boldsymbol{x})\omega_i'(\boldsymbol{x}')} \\
&= \lim_{\boldsymbol{x}'\to\boldsymbol{x}} \overline{u_i'(\boldsymbol{x})\,\epsilon_{ijl}\frac{\partial u_l'}{\partial x_j'}(\boldsymbol{x}')} \\
&= \overline{u'^2}\lim_{\boldsymbol{r}\to 0}\epsilon_{ijl}\frac{\partial \mathcal{R}_{il}}{\partial r_j} \\
&= \overline{u'^2}\lim_{\boldsymbol{r}\to 0}\epsilon_{ijl}\frac{\partial}{\partial r_j}\left[(f-g)\frac{r_i r_l}{r^2} + g\delta_{il} + h\,\epsilon_{ilk}\frac{r_k}{r}\right]
\end{aligned}$$

Inside the brackets, the second term leads to $\epsilon_{ijl}\delta_{il}g' r_j/r$. Yet, for any fixed j, $\epsilon_{ijl}\delta_{il} = 0$, because for $i \neq l$, $\delta_{il} = 0$ and for $i = l$, $\epsilon_{ijl} = 0$. Regarding the first term, the derivatives of r_i and r_l with respect to r_j introduce respectively δ_{ij} and δ_{lj}, which leads to contributions equal to zero for the same reasons as above. Also, the derivative of $(f-g)$ with respect to r_j provides $\epsilon_{ijl}(f'-g')r_i r_l r_j/r^3$ and, for each fixed j, there are two equal and opposite terms which neutralize themselves: for example for $j = 2$, $(\epsilon_{123} + \epsilon_{321})\,(f'-g')r_1 r_2 r_3/r^3 = 0$. Finally, taking into account that $\epsilon_{ijl}\epsilon_{ilk} = -\epsilon_{ilj}\epsilon_{ilk} = -2\delta_{jk}$, one obtains

$$\bar{h}_e = -2\overline{u'^2} \lim_{r\to 0} \delta_{jk}\left(h'\frac{r_k}{r}\frac{r_j}{r} + \frac{h}{r}\delta_{kj} - \frac{h}{r^2}r_k\frac{r_j}{r}\right)$$
$$= -2\overline{u'^2} \lim_{r\to 0}\left(h' + 3\frac{h}{r} - \frac{h}{r}\right)$$

The Taylor series of $h(r)$ at $r = 0$ being $h \simeq 0 + h'r + \mathcal{O}(r^2)$, $h' \simeq h/r$, and the outcome is simply,

$$\bar{h}_e = -6\overline{u'^2} \lim_{r\to 0}\left(\frac{h}{r}\right)$$

which provides an explicit relation between the helicity $\bar{h}_e$ and the new double correlation at two points $h(r)$.

The spectral tensor is now considered. The Fourier transform of (6.56) leads to,

$$\phi_{ij}(\mathbf{k}) = \underbrace{\frac{E(k)}{4\pi k^2}\left(\delta_{ij} - \frac{k_i k_j}{k^2}\right)}_{(1)} + \underbrace{i\,\epsilon_{ijk}\gamma_H(k)\frac{k_k}{k}}_{(2)}$$

where (1) is the classic term seen previously, and the (2) term is associated with helicity. The latter is a purely imaginary quantity, which corresponds to the fact that in a Fourier transform, the real part of the spectrum is associated with the even part of the correlation and the imaginary part is associated with the odd part of the correlation.

Just as the spectrum $E(k)$ of kinetic energy was introduced considering the integral of ϕ_{ii} on the $\boldsymbol{k}$ space, the spectrum $H(k)$ of helicity is now defined considering the integral on $\boldsymbol{k}$ of $\phi_{il}\epsilon_{ijl}ik_j$. Indeed this term corresponds to the Fourier transform of $\overline{u'_i\omega'_i} = \overline{u'_i\epsilon_{ijl}\partial u'_l/\partial x_j}$. Then,

$$\bar{h}_e = i^2 \int \epsilon_{ijl}\epsilon_{ilk}\gamma_H(k)\frac{k_k}{k}k_j\, d\boldsymbol{k}$$

Using $i^2 = -1$ and $\epsilon_{ijl}\epsilon_{ilk} = -\epsilon_{ilj}\epsilon_{ilk} = -2\delta_{jk}$, one has

$$\bar{h}_e = 2\delta_{jk}\int \gamma_H(k)\frac{k_k}{k}k_j\, d\boldsymbol{k} = 2\int_0^\infty 4\pi k^2\gamma_H(k)k\, dk$$

The spectrum $H(k)$ of helicity is introduced, it is defined by

$$\bar{h}_e = \int_0^\infty H(k)\, dk \quad \text{and then} \quad \gamma_H(k) = \frac{H(k)}{8\pi k^3}$$

and the spectral tensor form is,

$$\phi_{ij}(\boldsymbol{k}) = \frac{E(k)}{4\pi k^2}\left(\delta_{ij} - \frac{k_i k_j}{k^2}\right) + i\ \epsilon_{ijk}\ \frac{H(k)}{8\pi k^3}\frac{k_k}{k}$$

The realizability condition for $E(k)$ is $E(k) \geq 0$, which is expected when considering the physical meaning of $E(k)$. For $H(k)$, Moffatt [132] shows that it must verify $|H(k)| \leq 2kE(k)$.

The separation, in terms of energy, of $E(k)$ and $H(k)$ must not lead us to think that each quantity changes over time in an independent way. On the contrary, the equations governing $E(k)$ and $H(k)$ are linked, and are complex both to write and solve. For this matter, one can refer to the book of Lesieur [14].

In terms of physics, helicity corresponds to the fact that a vortex is convected by an axial velocity component, this implies a structure developing in an helicoidal way, such as wingtip vortices forming off plane wings. For usual flows, it is generally thought that the large coherent structures of the flows are tridimensional, and have an important helicity as well as a reduced dissipation. The dissipation would more likely appear between these large structures, in thin vorticity layers, as suggested by Tsinober and Levich [155] and Moffatt [488]. Some significative data is obtained by direct numerical simulation, as undertaken by Hussain [486] for a mixing zone. The direct measurement of helicity is very difficult for it requires complex multiple sensors, as the vorticity probes developed by Wallace and Foss [743] or the electromagnetic probes of Kholmyansky et al. [116] tuned upstream of turbulence grids equipped with propellers rotating in a known direction.

6.7 Proper Orthogonal Decomposition*

The Fourier analysis developed above requires infinite turbulent fields. But flows are actually limited to a finite area. The frontier of the turbulent flow can be either a wall, as is the case for pipes and cavities, or a free boundary, as for jets or wakes. Depending on the confinement directions, the Fourier analysis must be replaced by a new decomposition in nonhomogeneous directions. A series of orthogonal functions is chosen to represent well, in terms of average quadratic error minimization, the turbulent kinetic energy integrated on the D domain occupied by the turbulent flow. This technique is named Karhunen-Loève development [223, 224] or more generally POD for Proper Orthogonal Decomposition.

Besides the main objective which is to ensure an analysis of the flow while sticking to physical mechanisms, POD also aims at enabling a prediction of the flow using the notion of dynamical systems. The first theoretical bases have been established by Aubry et al. [215], Berkooz et al. [216], Holmes et al. [222], Lumley [77], Newman [225], or Sirovich [230]. The POD is actually developing rapidly since complete velocity fields are available by numerical simulation of the flow, see Chap. 8, or by particle image velocimetry, see Chap. 10.

Definition and Properties of the Modes

The one-dimensional case is first examined so as to simplify the presentation, by considering a turbulent signal $u_1'(x_1, t)$. This signal is assumed to be centered and stationary, and its decomposition can be expressed as

$$u_1'(x_1, t) = \sum_{n=1}^{\infty} a_n(t)\phi_n(x_1) \tag{6.57}$$

where $\phi_n(x_1)$ is the non-random modal function of rank n, and $a_n(t)$ its random coefficient. The functions $\phi_n(x_1)$ verify an orthogonality condition expressed by a scalar product on a given domain D occupied by the flow

$$\int_D \phi_n(x_1)\phi_m(x_1)dx_1 = \delta_{nm} \tag{6.58}$$

while the functions $a_n(t)$ verify an orthogonality condition on the statistical average, that is

$$\overline{a_n(t)a_m(t)} = \lambda_n \delta_{nm}$$

and thus $\overline{a_n^2} = \lambda_n$. At a point of the field, the average kinetic energy defined by a statistical average, apart from a prefactor 1/2, is given by

$$\begin{aligned}\overline{u_1'^2(x_1, t)} &= \overline{\sum_{n=1}^{\infty} a_n(t)\phi_n(x_1) \sum_{m=1}^{\infty} a_m(t)\phi_m(x_1)} \\ &= \sum_{n=1}^{\infty}\sum_{m=1}^{\infty} \overline{a_n a_m}\ \phi_n(x_1)\phi_m(x_1) \\ &= \sum_{n=1}^{\infty} \lambda_n\ \phi_n(x_1)\phi_n(x_1)\end{aligned}$$

Integrating on the domain D, one gets

$$\int_D \overline{u_1'^2(x_1, t)}dx_1 = \sum_{n=1}^{\infty} \lambda_n$$

The value λ_n thus represents the contribution of the nth mode to the average kinetic energy of the considered turbulent field on the domain D. The decomposition (6.57) is all the more efficient than the number of modes necessary to represent this energy is small. It can be observed that the quadratic average of the projection of the field on a given mode is

$$\overline{\left(\int_D \phi_n(x_1)u_1'(x_1, t)dx_1\right)^2} = \lambda_n$$

and that the reverse formula of (6.57) is given by

$$a_n(t) = \int_D u_1'(x_1, t)\phi_n(x_1)dx_1 \tag{6.59}$$

The spatial covariance $R(x_1, y_1)$ of the velocities at two points x_1 and y_1, still defined by a statistical average, can be transformed in the same way, which provides

$$\begin{aligned} R(x_1, y_1) &= \overline{u_1'(x_1, t)u_1'(y_1, t)} \\ &= \overline{\sum_{n=1}^{\infty} a_n(t)\phi_n(x_1) \sum_{m=1}^{\infty} a_m(t)\phi_m(y_1)} \\ &= \sum_{n=1}^{\infty}\sum_{m=1}^{\infty} \overline{a_n(t)a_m(t)}\ \phi_n(x_1)\phi_m(y_1) \\ &= \sum_{m=1}^{\infty} \lambda_m\ \phi_m(x_1)\phi_m(y_1) \end{aligned}$$

and by taking the scalar product (6.58) with $\phi_n(y_1)$ on the domain D, it yields

$$\int_D R(x_1, y_1)\phi_n(y_1)dy_1 = \lambda_n\phi_n(x_1) \tag{6.60}$$

The two quantities ϕ_n and λ_n are therefore defined by a Fredholm type integral equation. Actually, the minimization of the quadratic error between $u_1'(x_1, t)$ and its approximation by the series (6.57) leads to this equation and to the specified orthogonality conditions. Besides, the kernel $R(x_1, y_1)$ being non-negative and symmetrical, the eigenvalues λ_n are assured to be non-negative, finite and countable. The details of these theoretical developments are explained by Newman [225].

The modes $\phi_n(x_1)$ can be directly obtained by discretizing integral (6.60) on a computational grid. The $\phi_n(x_1)$ are found seeking the eigenvalues of the matrix of spatial correlations $R(x_1, y_1)$. The dimension of this matrix however increases very quickly with the refinement of the mesh.

Turbulent fields provided by numerical simulation of the Navier-Stokes equations can be used to compute the matrix R. Experimentally, hot wire combs or particle image velocimetry (PIV) provide simultaneous measures at several points in space. This last non-intrusive technique has been considerably enhanced since the apparition of CCD cameras, and POD is particularly suitable. The details of the process are considered in the following.

Mode Determination by the Method of Snapshots

The turbulent field $u_1'(x_1, t)$ is observed at n_t different times sufficiently distant from each other for the samples to be independent, and the covariance $R(x_1, y_1)$ at two points to be approximated by an average on the n_t samples. The Fredholm equation

(6.60) can then be written as

$$\int_D \frac{1}{n_t}\left(\sum_{k=1}^{n_t} u_1^{(k)}(x_1)u_1^{(k)}(y_1)\right)\phi_n(y_1)dy_1 = \lambda_n\phi_n(x_1) \tag{6.61}$$

where $u_1^{(k)}(x_1)$ is the kth snapshot of the turbulent field $u_1'(x_1)$. Thus, according to expression (6.59), one has

$$\int_D u_1^{(k)}(y_1)\phi_n(y_1)dy_1 = a_n^{(k)}$$

and (6.61) becomes

$$\frac{1}{n_t}\sum_{k=1}^{n_t} a_n^{(k)}u_1^{(k)}(x_1) = \lambda_n\phi_n(x_1)$$

The modes $\phi_n(x_1)$ are therefore a linear combination of the n_t snapshots, which permits to write

$$\phi_n(x_1) = \sum_{k=1}^{n_t} A_n^{(k)}u_1^{(k)}(x_1) \quad \text{or else} \quad \phi_n(y_1) = \sum_{l=1}^{n_t} A_n^{(l)}u_1^{(l)}(y_1) \tag{6.62}$$

Injection of these two expressions in the initial Eq. (6.61) provides,

$$\int_D \frac{1}{n_t}\left(\sum_{k=1}^{n_t} u_1^{(k)}(x_1)u_1^{(k)}(y_1)\right)\left(\sum_{l=1}^{n_t} A_n^{(l)}u_1^{(l)}(y_1)dy_1\right) = \lambda_n\sum_{k=1}^{n_t} A_n^{(k)}u_1^{(k)}(x_1)$$

Then introducing the correlation matrix $C^{(kl)}$ of size $n_t \times n_t$ between the different snapshots

$$C^{(kl)} = \frac{1}{n_t}\int_D u_1^{(k)}(y_1)\, u_1^{(l)}(y_1)dy_1$$

the previous equation can be recast as follows

$$\sum_{k=1}^{n_t}\sum_{l=1}^{n_t} C^{(kl)}A_n^{(l)}u_1^{(k)}(x_1) = \lambda_n\sum_{k=1}^{n_t} A_n^{(k)}u_1^{(k)}(x_1)$$

or equivalently in matrix form,

$$(\boldsymbol{C}\boldsymbol{A})^T\,\boldsymbol{U} = \lambda\boldsymbol{A}^T\,\boldsymbol{U}$$

with $\boldsymbol{C}$ is the matrix of the $C^{(kl)}$, $\boldsymbol{A}_n$ is the vector of the $A_n^{(l)}$ and $\boldsymbol{U}$ is the vector of the $u_1^{(k)}$. This equation can finally be written as

$$\boldsymbol{C}\boldsymbol{A}_n = \lambda_n \boldsymbol{A}_n \tag{6.63}$$

The eigenvalues of the matrix $C^{(kl)}$ thus provide the n_t first eigenvalues λ_n. This number corresponds to the number of snapshots. The corresponding eigenvectors $A_n^{(k)}$ associated with snapshots $u^{(k)}(x_1)$ by relation (6.62), provide the modes $\phi_n(x_1)$. As the matrix $\boldsymbol{C}$ is of order n_t, with generally $n_t \simeq 100$, the calculations are easy. This method of snapshots has been introduced by Sirovich [230].

Extension to 2 or 3 Dimensions

In the decomposition (6.57), both $\boldsymbol{u}'(\boldsymbol{x}, t)$ and $\boldsymbol{\phi}(\boldsymbol{x})$ are vectors dependent on coordinates x_1, x_2 and x_3, the coefficient $a_n(t)$ remaining a shared coefficient. This decomposition is now explained for the two-dimensional case,

$$u_1'(x_1, x_2, t) = \sum_{n=1}^{\infty} a_n(t)\phi_{n,x_1}(x_1, x_2)$$
$$u_2'(x_1, x_2, t) = \sum_{n=1}^{\infty} a_n(t)\phi_{n,x_2}(x_1, x_2)$$

noting u_1' and u_2' the velocity components and ϕ_{n,x_1} and ϕ_{n,x_2} those of mode $\phi_n(x_1, x_2)$. A scalar product such as (6.58) then becomes,

$$\int_D \left[\phi_{n,x_1}(x_1, x_2)\phi_{m,x_1}(x_1, x_2) + \phi_{n,x_2}(x_1, x_2)\phi_{m,x_2}(x_1, x_2)\right] dx_1 dx_2 = \delta_{nm}$$

which leaves to the λ_n values the meaning of their contribution to kinetic energy $\overline{u_1^2} + \overline{u_2^2}$, still apart from a prefactor 1/2. In the method of snapshots, the matrix $C^{(kl)}$ also involves the kinetic energy of the components, that is in two-dimension

$$C^{(kl)} = \frac{1}{M}\int_D \left[u_1^{(k)}(x_1, x_2)\, u_1^{(l)}(x_1, x_2) + u_2^{(k)}(x_1, x_2)\, u_2^{(l)}(x_1, x_2)\right] dx_1 dx_2$$

and Eq. (6.63) providing eigenvalues of $\boldsymbol{C}$ is preserved. Rowley et al. [226] study the case of a 2-D cavity excited by a grazing flow, for instance. They obtain eigenmodes by the method of snapshots applied to the velocity fields provided by a direct numerical simulation.

Possibility of Complex Modes

Until now only real modes have been considered. However, some authors use complex modes, such as Holmes et al. [222] in a general approach, Aubry et al. [215] for the boundary layer or Citriniti and George [220] for the mixing layer. The integrals on domain D then imply a scalar product of the form $\langle f, g^\star \rangle$ where $\star$ is the conjugate imaginary part. Thus the complex coefficient a_n is given by $\langle u_1', \phi_n^\star \rangle$. It can then be inferred that the real part of a_n is associated with the real part of ϕ_n, and the

imaginary part of a_n to the imaginary part of ϕ_n. Indeed, using $a_n = r_n + ic_n$ and $\phi_n = \Phi_n + i\Psi_n$, it can be written that,

$$r_n(t) + ic_n(t) = \int_D u_1'(x_1, t)\,[\Phi_n(x_1) - i\Psi_n(x_1)]\; dx_1$$

and then,

$$r_n(t) = \int_D u_1'(x_1, t)\Phi_n(x_1)\; dx_1 \qquad c_n(t) = -\int_D u_1'(x_1, t)\Psi_n(x_1)$$

When counting the modes, rank n is sometimes subdivided to consider the Φ_n and Ψ_n that would correspond to $\cos(nx_1)$ and $\sin(nx_1)$ for a homogeneous direction, suggesting an idea of phase shift. All quantities then become real again. This approach is for instance retained by Rowley et al. [226] where two POD modes correspond to only one Rossiter frequency for cavity flow oscillations.

Construction of a Dynamical System

The construction of a dynamical system requires knowledge of the equations of the fluid movement, for example the Navier-Stokes equations. For the modes to appear, the equations need to be multiplied by the mode ϕ_n considered and integrated on the domain D of the flow. This constitutes a projection named the Galerkin projection, which is, for instance, detailed by Holmes et al. [222] The pressure term, the fluid incompressibility, and the limit conditions of domain D require a particular treatment. In the end a system of differential equations governing coefficients $a_n(t)$ is obtained. This system is generally nonlinear, as the Navier-Stokes equations by which it is provided, and its solving is similar to the one of chaotic regimes mentioned in Sect. 1.2 of the introduction chapter. It is hoped that the dynamics of the turbulent field considered can here be followed with only a few modes.

To illustrate the Galerkin projection and the obtention of a dynamical system, the 1-D Burgers equation studied by Chambers [218] and Holmes et al. [222] is considered. The equation and its limit conditions at $x = 0$ and $x = 1$ are,

$$\frac{\partial u}{\partial t} = \nu\frac{\partial^2 u}{\partial x^2} - u\frac{\partial u}{\partial x} \quad \text{with} \quad u(0, t) = u(1, t) = 0$$

The modes of type $\sqrt{2}\sin(n\pi x)$ are known to verify the limit conditions and are used for the decomposition of the velocity field, which can then be written,

$$u(x, t) = \sum_{n=1}^{\infty} a_n(t)\sqrt{2}\sin(n\pi x)$$

The Galerkin projection corresponding to mode p provides for the term $\partial u/\partial t$,

$$\int_0^1 \sum_n \dot{a}_n(t)\sqrt{2}\sin(n\pi x)\sqrt{2}\sin(p\pi x)dx = \dot{a}_p$$

for the viscous term $\nu\partial^2 u/\partial x^2$,

$$-\nu\int_0^1 \sum_n a_n(t)(n\pi)^2\sqrt{2}\sin(n\pi x)\sqrt{2}\sin(p\pi x)dx = -\nu(p\pi)^2 a_p$$

and, for the nonlinear term $u\partial u/\partial x$,

$$\begin{aligned}
&\int_0^1 \left\{ \sum_n a_n\sqrt{2}\sin(n\pi x)\sum_k a_k k\pi\sqrt{2}\cos(k\pi x)\sqrt{2}\sin(p\pi x)\right\}dx \\
&= \sum_n\sum_k 2\sqrt{2}k\pi a_n a_k \int_0^1 \sin(n\pi x)\cos(k\pi x)\sin(p\pi x)dx \\
&= \sum_k \frac{k\pi}{\sqrt{2}} a_k[a_{(p-k)} + a_{(p+k)} - a_{-(p-k)} - a_{-(p+k)}]
\end{aligned}$$

In these calculations, simplifications due to integrals of products of sinus and cosinus on interval [0,1] are taken into account. Finally:

$$\dot{a}_p = -\nu(p\pi)^2 a_p - \frac{\pi}{\sqrt{2}}\sum_k k a_k[a_{(p-k)} + a_{(p+k)} - a_{-(p-k)} - a_{-(p+k)}]$$

Limited to three modes, the system becomes

$$\begin{cases}
\dot{a}_1 = -\pi^2\nu a_1 + \dfrac{\pi}{\sqrt{2}}(a_1 a_2 + a_2 a_3) \\
\dot{a}_2 = -4\pi^2\nu a_2 - \dfrac{\pi}{\sqrt{2}}(a_1^2 - 2a_1 a_3) \\
\dot{a}_3 = -9\pi^2\nu a_3 - \dfrac{\pi}{\sqrt{2}}3a_1 a_2
\end{cases}$$

The nonlinear terms characteristic of dynamical systems appear clearly. A similar example is the one of Kuramoto-Sivashinsky equation which was proposed to modelize interface instabilities and flame fronts,

$$\frac{\partial u}{\partial t} + \frac{\partial^2 u}{\partial x^2} + \frac{\partial^4 u}{\partial x^4} + \frac{1}{2}\left(\frac{\partial u}{\partial x}\right)^2 = 0 \quad 0 \le x \le L$$

with the periodic limit conditions,

$$u(0,t) = u(L,t) \quad \text{and} \quad \frac{\partial u}{\partial x}(0,t) = \frac{\partial u}{\partial x}(L,t)$$

The reader can refer to the work by Holmes et al. [222], with regard to obtaining the dynamical system, with the different possible truncations, and the associated instability study.

6.8 Rapid Distortion: The Case of an Axisymmetric Contraction⋆

The effect of a rapid contraction on an initially isotropic turbulence has been very thoroughly studied by Batchelor [84], who calculated the anisotropy which appears both in the spectral tensor and in the levels of longitudinal and transverse velocity fluctuations. This typical problem also illustrates vorticity dynamics in the case of a Lagrangian approach as well as the interest of Fourier transforms.

To have a Lagrangian approach, the notations $\boldsymbol{u}'(\boldsymbol{a})$ and $\boldsymbol{\omega}'(\boldsymbol{a})$ are used for the velocity and vorticity fluctuations of a fluid particle located at point **a** upstream of the contraction, and the notations $\boldsymbol{u}''(\boldsymbol{x})$ and $\boldsymbol{\omega}''(\boldsymbol{x})$ are used for velocity and vorticity at point $\boldsymbol{x}$ where the same fluid particle is located downstream of the contraction. These fluctuations are measured with respect to axis in uniform translation, with the average upstream velocity for $\boldsymbol{u}'(\boldsymbol{a})$ and with the average downstream velocity for $\boldsymbol{u}''(\boldsymbol{x})$.

During the movement of the particle, its vorticity respects the elongation modifications imposed by the deformation, as seen in Chap. 5 when inertia and viscous forces are neglected, i.e.

$$\frac{\omega''}{\delta s''} = \frac{\omega'}{\delta s'} \quad \text{or} \quad \omega_i''(\boldsymbol{x}) = \frac{\partial x_i}{\partial a_j}\omega_j'(\boldsymbol{a}) \tag{6.64}$$

The strain tensor $\partial x_i/\partial a_j$ expressed for an axisymmetric nozzle of contraction ratio c is,

$$\frac{\partial x_1}{\partial a_1} = c \qquad \frac{\partial x_2}{\partial a_2} = \frac{1}{\sqrt{c}} \qquad \frac{\partial x_3}{\partial a_3} = \frac{1}{\sqrt{c}} \qquad \text{and} \qquad \frac{\partial x_i}{\partial a_j} = 0 \quad \text{for} \quad i \neq j$$

Introducing ϵ_{jpq} symbol to express the components of the vorticity vector, Eq. (6.64) becomes for the i component,

$$\omega_i''(\boldsymbol{x}) = \frac{\partial x_i}{\partial a_j}\epsilon_{jpq}\frac{\partial u_q'(\boldsymbol{a})}{\partial a_p}$$

Using the curl of the two members of the equation with respect to $\boldsymbol{x}$, and considering the r component of the result, with $()_r = \epsilon_{rsi}\partial\omega_i''/\partial x_s$, for an incompressible flow, is obtained

$$-\nabla^2 u_r''(\boldsymbol{x}) = \epsilon_{jpq}\frac{\partial x_i}{\partial a_j}\epsilon_{rsi}\frac{\partial a_l}{\partial x_s}\frac{\partial^2 u_q'(\boldsymbol{a})}{\partial a_p \partial a_l} \tag{6.65}$$

because the strain tensor $\partial x_i/\partial a_j$ is constant. In the left hand-side, the Laplacian directly comes from the classic differential formula,

$$\nabla \times (\nabla \times \boldsymbol{u}) = \nabla(\nabla \cdot \boldsymbol{u}) - \nabla^2 \boldsymbol{u}$$

The right hand-side is more complex. It implies functions at point $\boldsymbol{a}$, thus it is necessary to keep ϵ_{jpq}, ϵ_{rsi} and the strain tensor, expressed in its direct and reciprocal form. Equation (6.65) can be solved by introducing the Fourier transforms of both upstream and downstream fields. These are respectively defined by

$$\boldsymbol{u}'(\boldsymbol{a}) = \int \hat{\boldsymbol{u}}'(\boldsymbol{k})\, e^{i\boldsymbol{k}\cdot\boldsymbol{a}}\, d\boldsymbol{k} \quad \text{and} \quad \boldsymbol{u}''(\boldsymbol{x}) = \int \hat{\boldsymbol{u}}''(\boldsymbol{\xi})\, e^{i\boldsymbol{\xi}\cdot\boldsymbol{x}}\, d\boldsymbol{\xi}$$

and necessarily,

$$\boldsymbol{\xi}\cdot\boldsymbol{x} = \boldsymbol{k}\cdot\boldsymbol{a} \quad \text{that is,} \quad \xi_i = k_j\frac{\partial a_j}{\partial x_i}$$

The reciprocal strain tensor which appears is defined by,

$$\frac{\partial a_1}{\partial x_1} = \frac{1}{c} \qquad \frac{\partial a_2}{\partial x_2} = \sqrt{c} \qquad \frac{\partial a_3}{\partial x_3} = \sqrt{c} \qquad \text{and} \qquad \frac{\partial a_i}{\partial x_j} = 0 \quad \text{for} \quad i \neq j$$

which provides

$$\xi_1 = \frac{k_1}{c}, \quad \xi_2 = k_2\sqrt{c}, \quad \xi_3 = k_3\sqrt{c} \quad \text{and} \quad \xi^2 = k_1^2/c^2 + c(k_2^2 + k_3^2)$$

The Fourier contribution, $\hat{u}_r''(\boldsymbol{\xi})$, to the field downstream of the contraction can then be expressed as

$$\xi^2\hat{u}_r''(\boldsymbol{\xi}) = -\epsilon_{jpq}\epsilon_{rsi}\frac{\partial x_i}{\partial a_j}\frac{\partial a_l}{\partial x_s}k_p k_l \hat{u}_q'(\boldsymbol{k})$$

The multiple indexes do not constitute a great difficulty, for they can actually only take a limited number of values: the usual conditions on ϵ_{rsi} and ϵ_{jpq} apply, and besides only the cases where $i = j$ and $l = s$ must be considered so that the components of the deformation tensor are not equal to zero. For instance, for the axial component $r = 1$, only four combinations are possible,

$$s = l = 2,\ i = j = 3,\ p = 1,\ q = 2 \qquad s = l = 2,\ i = j = 3,\ p = 2,\ q = 1$$
$$s = l = 3,\ i = j = 2,\ p = 3,\ q = 1 \qquad s = l = 3,\ i = j = 2,\ p = 1,\ q = 3$$

which leads to,

$$\hat{u}_1''(\boldsymbol{\xi}) = \frac{k_2^2 + k_3^2}{\xi^2}\hat{u}_1' - \frac{k_1 k_2}{\xi^2}\hat{u}_2' - \frac{k_1 k_3}{\xi^2}\hat{u}_3'$$

The contribution $\hat{u}_r''(\boldsymbol{\xi})$, multiplied by the conjugate quantity corresponding to the l index, provides the components of the spectral tensor $\phi_{lr}''(\boldsymbol{\xi})$ downstream of the contraction. The products $\hat{u}_q'(\boldsymbol{k})\hat{u}_m'^{\star}(\boldsymbol{k})$ which appear correspond to the components of the spectral tensor $\phi_{mq}'(\boldsymbol{k})$ of the upstream turbulent field. In the following, isotropic turbulence is chosen for the upstream side, thus

$$\phi_{ij}'(\boldsymbol{k}) = \frac{E(k)}{4\pi k^2}\left(\delta_{ij} - \frac{k_i k_j}{k^2}\right)$$

which leads to, after the calculations are undertaken, for the downstream spectral tensor

$$\phi_{11}''(\boldsymbol{\xi}) = \frac{E(k)}{4\pi\xi^4}(k_2^2 + k_3^2)$$
$$\phi_{22}''(\boldsymbol{\xi}) + \phi_{33}''(\boldsymbol{\xi}) = \frac{E(k)}{4\pi k^2 \xi^4}\left(c\xi^4 + \frac{k^2 k_1^2}{c^3}\right)$$

The integration with respect to $\boldsymbol{\xi}$ of the first relation provides the energy of the longitudinal fluctuations downstream of the contraction. When compared to the corresponding upstream value,

$$\kappa_1 = \frac{\overline{u_1''^2}}{\overline{u_1'^2}} = \frac{\int \phi_{11}''(\boldsymbol{\xi})\, d\boldsymbol{\xi}}{\int \phi_{11}'(\boldsymbol{k})\, d\boldsymbol{k}} = \frac{\int E(k)(k_2^2 + k_3^2)/\xi^4\, d\boldsymbol{k}}{\int E(k)(k_2^2 + k_3^2)/k^4\, d\boldsymbol{k}}$$

To apply the integrations, the spherical coordinates (k, ϕ, θ), chosen so that $k_1 = k\cos\theta$ and $(k_2^2 + k_3^2)^{1/2} = k\sin\theta$, are introduced. The integrals with respect to k and ϕ appearing in both the numerator and denominator simplify and only the integrals with respect to θ remain. Hence,

$$\begin{aligned}
\kappa_1 &= \left[\int_0^{\pi} \frac{\sin^3\theta}{(c^{-2}\cos^2\theta + c\sin^2\theta)^2}\, d\theta\right] \times \left[\int_0^{\pi} \sin^3\theta\, d\theta\right]^{-1} \\
&= \frac{3}{4c^2}\left[\frac{1+\alpha^2}{2\alpha^3}\ln\left(\frac{1+\alpha}{1-\alpha}\right) - \frac{1}{\alpha^2}\right] \quad \text{where} \quad \alpha^2 = 1 - c^{-3} \\
&\simeq \frac{3}{4c^2}(\ln 4c^3 - 1) \quad \text{for} \quad c \geq 3
\end{aligned}$$

Applying the same for the transverse components, the following can be obtained,

$$\begin{aligned}\kappa_2 &= \frac{\overline{u_2''^2} + \overline{u_3''^2}}{\overline{u_2'^2} + \overline{u_3'^2}} \\ &= c\int_0^\pi \left[1 - c^{-4}\cos^2\theta(c^{-2}\cos^2\theta + c\sin^2\theta)^{-2}\right]\sin\theta d\theta \\ &\quad \times \left[\int_0^\pi (1+\cos^2\theta)\sin\theta d\theta\right]^{-1} \\ &= \frac{3c}{4} + \frac{3}{4c^2}\left[\frac{1}{2\alpha^2} - \frac{1-\alpha^2}{4\alpha^3}\ln\left(\frac{1+\alpha}{1-\alpha}\right)\right] \simeq \frac{3}{4}c \quad \text{for} \quad c \geq 3\end{aligned}$$

The possibility to use the approximated forms of κ_1 and κ_2 for $c \geq 3$ comes from a mere numerical comparison between the exact and approximated formulas. Figure 6.18 represents the values of κ_1 and κ_2 as a function of the contraction ratio c. The increase of the energy of the transverse components and the decrease of the energy of the longitudinal components due to the privileged elongation of vortices with a direction close to the nozzle axis can be observed. As for kinetic energy after contraction, it still increases, the downstream/upstream ratio being $(\kappa_1+2\kappa_2)/3 > 1$ for $c \geq 1$. However, the turbulence intensity $\sqrt{k_t}/\bar{U}_1$ decreases when c increases thanks to the increase of the mean velocity. The downstream/upstream ratio is given by $\sigma_{k_t} = \sqrt{(\kappa_1 + 2\kappa_2)/3}/c$, and is also represented in Fig. 6.18. As a final remark, it must be pointed out that the effect of a convergent nozzle of ratio c is not similar to the effect of a divergent nozzle of ratio $1/c$ since the expressions of κ_1 and κ_2 are not linear in c. Lee [121] has done several numeral predictions on this subject.

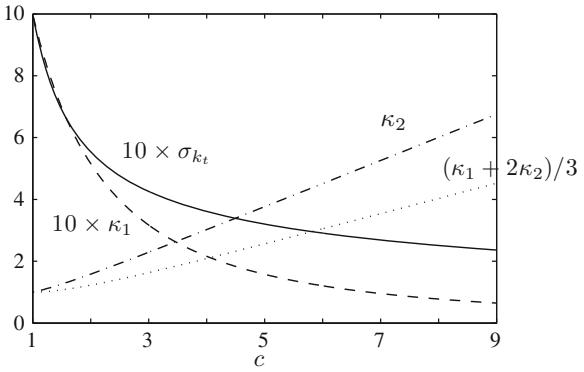

Fig. 6.18 Effect of an axisymmetrical contraction on isotropic turbulence; c is the contraction ratio, κ_1 the downstream/upstream ratio of the turbulent kinetic energy of longitudinal fluctuations, κ_2 a similar ratio for the lateral fluctuations. The turbulence intensity represented by σ_{k_t} is less downstream of the contraction due to the mean velocity increase

Considering again the nozzle of ratio $c \simeq 1.27$ used by Comte-Bellot and Corrsin [100], the previous expressions cannot be applied rigorously because the turbulence upstream of the nozzle is anisotropic, and besides evolves along the nozzle, which is necessarily progressive. The effect of a convergent nozzle of ratio $c = 1.27$ on isotropic turbulence gives $\overline{u_1''^2} = 0.82\overline{u_1'^2}$ and $\overline{u_2''^2} = 1.13\overline{u_2'^2}$, that is an anisotropy ratio of $\overline{u_2''^2}/\overline{u_1''^2} \simeq 1.38$. If this anisotropy is entirely transferred to the upstream turbulence, thus assuming that $\overline{u_1''^2}/\overline{u_2''^2} = 1$, then $\overline{u_1'^2}/\overline{u_2'^2} \simeq 1.38$. Experimentally an upstream anisotropy of approximately 1.20 is observed, as indicated in Sect. 6.3.

Chapter 7
The Dynamics of Isotropic Turbulence

It has been shown in the previous chapter how the description of an isotropic turbulent field can be simplified for an incompressible flow. In physical space, only one scalar function $f(r)$ is necessary to describe the two-point velocity correlations $R_{ij}(\boldsymbol{r})$. In the Fourier space, only the turbulent kinetic energy spectrum $E(k)$ is necessary to describe the corresponding velocity spectral tensor $\phi_{ij}(\boldsymbol{k})$. In this chapter, we consider how these functions $E(k)$ and $f(r)$ evolve with time in a decaying turbulent field.

7.1 Kolmogorov Theory

Kolmogorov had the brilliant idea to draw attention to the small scales of a turbulent field. He then pointed out their universal behaviour. His theory is called the universal equilibrium of small structures and it is certainly the major contribution of the twentieth century to turbulence study.

The Dissipation Scales

In the first chapter were already introduced the length scale l_η and the velocity scale u_η which characterize the dissipative eddies and verify

$$\mathrm{Re} = \frac{l_\eta u_\eta}{\nu} = 1$$

Length l_η can be interpreted as the smallest dimension of the structures or eddies that can be encountered in a turbulent flow. Below this scale, no mechanical energy subsists as it is transformed into thermal energy due to molecular viscosity. The smallest size of dissipative eddies whose length is l_η is uniquely defined by the rate of energy to be dissipated ϵ and by the fluid viscosity ν. Looking for a dimensional description of the form $l_\eta \sim \epsilon^\alpha \nu^\beta$, one necessarily finds $\alpha = 3/4$ and $\beta = -1/4$. Similarly for the velocity, $u_\eta = (\epsilon\nu)^{1/4}$, and as announced above $l_\eta u_\eta/\nu = 1$.

C. Bailly and G. Comte-Bellot, *Turbulence*, Experimental Fluid Mechanics,
DOI 10.1007/978-3-319-16160-0_7

The corresponding Kolmogorov time scale is therefore $\tau_\eta = l_\eta/u_\eta = \nu^{1/2}\epsilon^{-1/2}$. Keeping also in mind the fundamental relation (6.48) obtained experimentally, it appears that two types of scales are available. One characterizes the structures bearing the kinetic energy and the other characterizes the smallest structures of the flow. These two types of scales are gathered below,

$$\text{eddies bearing kinetic energy} \quad \begin{cases} u' & \text{(velocity)} \\ L_f & \text{(length)} \\ L_f/u' & \text{(time)} \end{cases} \qquad \begin{cases} k_t \sim u'^2 \\ \epsilon \sim \dfrac{u'^3}{L_f} \end{cases}$$

$$\text{smallest dissipative scales} \quad \begin{cases} u_\eta = \nu^{1/4}\epsilon^{1/4} & \text{(velocity)} \\ l_\eta = \nu^{3/4}\epsilon^{-1/4} & \text{(length)} \\ \tau_\eta = \nu^{1/2}\epsilon^{-1/2} & \text{(time)} \end{cases} \qquad \mathrm{Re}_\eta = \frac{l_\eta u_\eta}{\nu} = 1$$

Spectrum of Isotropic Turbulence

Let us now consider the spectrum of turbulent kinetic energy for isotropic turbulence, as drawn in Fig. 7.1. The function $E(k)$ reaches its maximum for wavenumbers of approximately $1/L_f$, i.e. for eddies of size L_f, where L_f is the integral length scale. On the same figure also appears the dissipation spectrum $D_\nu(k) = 2\nu k^2 E(k)$. The end of the dissipation spectrum is located at $kl_\eta \sim 1$, whereas its maximum is at $k\lambda_g \sim 1$. In order to characterize the separation between the turbulent kinetic energy spectrum and the dissipation spectrum, the ratio between integral and Kolmogorov scales is considered,

$$\frac{L_f}{l_\eta} = \frac{L_f}{\nu^{3/4}\epsilon^{-1/4}} = \frac{L_f}{\nu^{3/4}(u'^3/L_f)^{-1/4}} = \left(\frac{u' L_f}{\nu}\right)^{3/4}$$

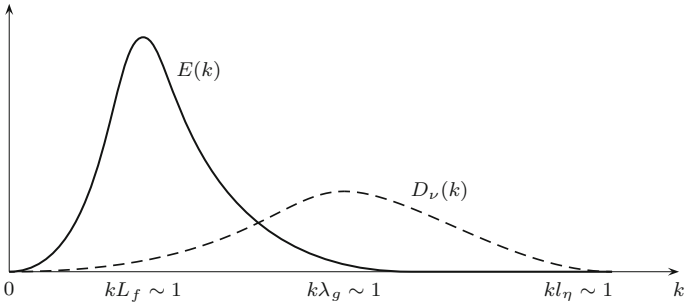

Fig. 7.1 Sketch of the turbulent kinetic energy spectrum $E(k)$ and of the dissipation spectrum $D_\nu(k) = 2\nu k^2 E(k)$

and finally,

$$\frac{L_f}{l_\eta} = \mathrm{Re}_{L_f}^{3/4} \qquad \text{where} \qquad \mathrm{Re}_{L_f} = \frac{u' L_f}{\nu} \tag{7.1}$$

In these expressions, u' represents the root mean square value of the velocity fluctuation. We recall that in isotropic turbulence, $\overline{u_1'^2} = \overline{u_2'^2} = \overline{u_3'^2}$. The Reynolds number Re_{L_f} is built from the scales u' and L_f, and is thus associated with large structures. The Reynolds number based on the transverse Taylor length scale λ_g is also of interest. Using relation (6.40) of Sect. 6.2.6, it can be expressed as

$$\mathrm{Re}_{\lambda_g} = \frac{u'\lambda_g}{\nu} = \frac{\lambda_g^2/\nu}{\lambda_g/u'} = 15\frac{L_f/u'}{\lambda_g/u'} = 15\frac{L_f}{\lambda_g} \sim \frac{\text{time of large eddies}}{\text{time of intermediate eddies}}$$

and,

$$\mathrm{Re}_{\lambda_g}^2 = \frac{u'\lambda_g}{\nu} \times 15\frac{L_f}{\lambda_g} = 15\,\mathrm{Re}_{L_f} \tag{7.2}$$

From these results, it can be noted that the larger the turbulent Reynolds number is, whatever the length scale it is based on is, the more the spectra of turbulent kinetic energy and of dissipation are separate. To illustrate this, the spectra of turbulent kinetic energy and of dissipation obtained for a grid turbulence [101], are shown in Fig. 7.2.

Moreover, an estimate of the Kolmogorov scale l_η is useful to choose the upper frequency to respect when acquiring experimental data, or to set the mesh size for numerical simulations [282]. Let us give as an example a boundary layer whose its Reynolds number is $\mathrm{Re}_\delta = U_{e1}\delta/\nu = 10^5$. Assuming that $u'/U_{e1} \simeq 10\,\%$ and that $L_f \simeq 0.1\delta$, relation (7.1) leads to $l_\eta/\delta \simeq 5.6 \times 10^{-4}$ which shows that the Kolmogorov scale l_η is really small compared to the boundary layer thickness.

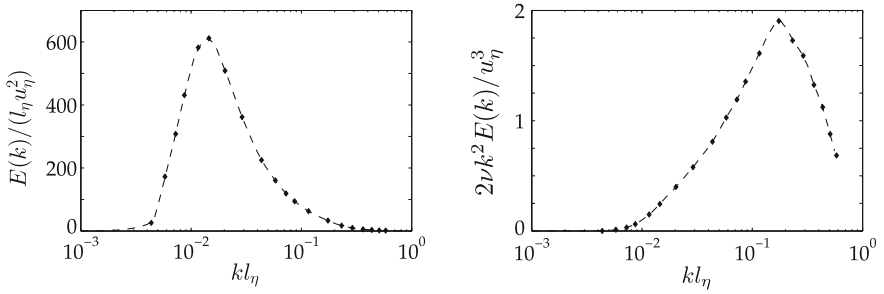

Fig. 7.2 Kinetic energy and dissipation spectra normalized by the Kolmogorov scales for the Comte-Bellot and Corrsin [101] experiments in grid turbulence. Measurements are made at $U_0 t/M = 42$, refer also to Table 6.1, $u' = 22.2\,\mathrm{cm}\cdot\mathrm{s}^{-1}$, $\epsilon = 4740\,\mathrm{cm}^2\cdot\mathrm{s}^{-3}$, $l_\eta = 0.029\,\mathrm{cm}$, $\lambda_g = 0.484\,\mathrm{cm}$, $L_f = 2.40\,\mathrm{cm}$, $\mathrm{Re}_{L_f} = u' L_f/\nu \simeq 355$ and $\mathrm{Re}_{\lambda_g} = u'\lambda_g/\nu \simeq 72$. Note that one decade in wavenumber separates the maxima of the two spectra

Universal Equilibrium Spectra for Small Structures

The turbulence scales adapted to small structures can be used to normalize the spectra. Thus, $E(k)/(l_\eta u_\eta^2)$ is represented as a function of the dimensionless wavenumber kl_η. A single curve limited to $kl_\eta \simeq 1$ is found for the small structures, whatever the type of flow and the Reynolds number is, provided that it is large enough. Figure 7.3 obtained from data by Chapman [173] and Saddoughi and Veeravalli [668, 669] synthesizes

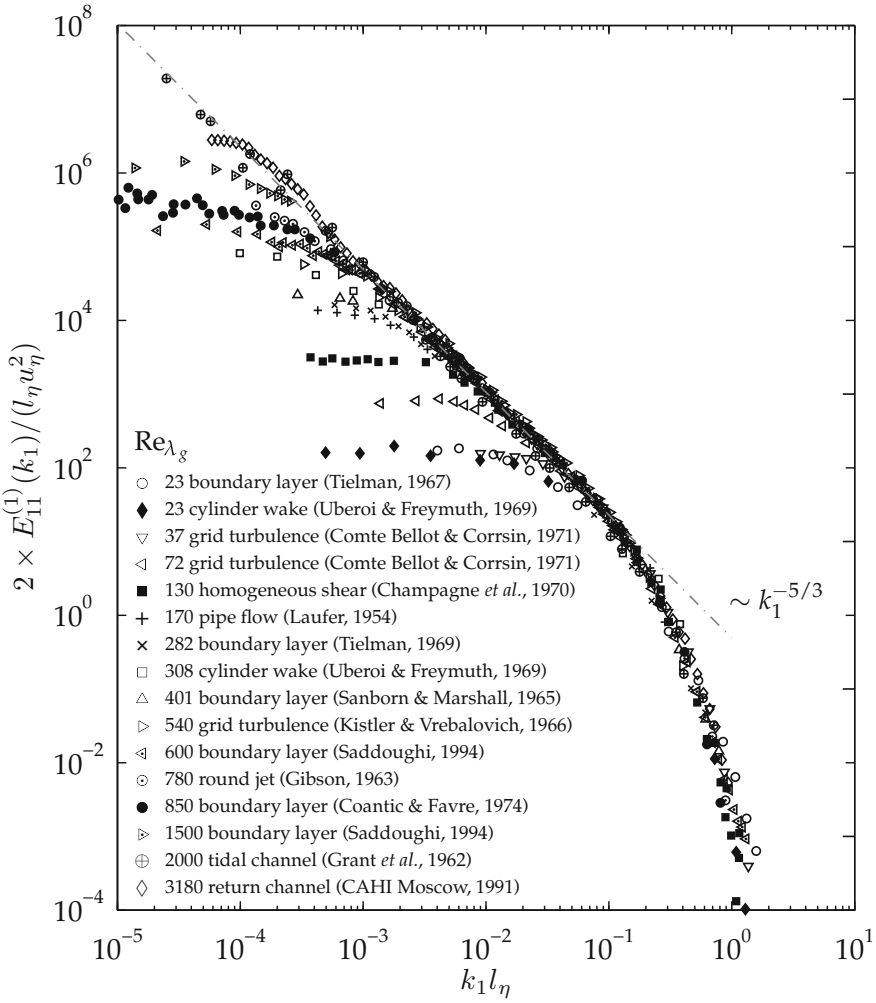

Fig. 7.3 Universal equilibrium of spectra for small structures. The figure deals with the one-dimensional spectrum $E_{11}^{(1)}(k_1)/(l_\eta u_\eta^2)$. Use is made of the data collected by Chapman [173] and Saddoughi and Veeravalli [669]. For all the *curves*, the emergence of an inertial subrange towards smaller k_1 with increasing Reynolds number is observed

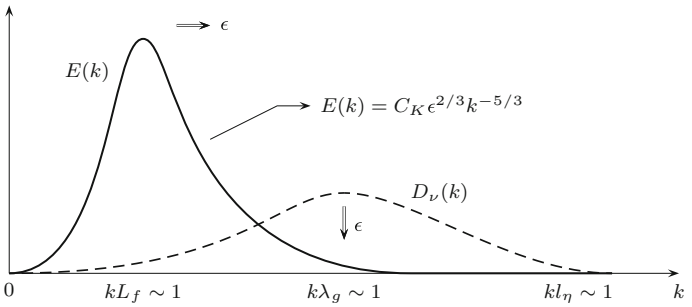

Fig. 7.4 Sketch of the turbulent kinetic energy spectrum $E(k)$ and of the dissipation spectrum $D_\nu(k) = 2\nu k^2 E(k)$ for high Reynolds number isotropic turbulence. The inertial subrange takes place between these two spectra

numerous experiments available in the literature. For large structures, this universal zone extends to values of kl_η increasingly small for a rising Reynolds number.

Inertial Zone of the Spectra

When the turbulent Reynolds number Re_{L_f} or Re_{λ_g} is extremely large, the small wavenumbers associated to eddies containing energy are clearly separated from the large wavenumbers associated with eddies dissipating this energy, as shown in Fig. 7.1. In these conditions, there is a zone, said inertial zone, for which no dissipation appears. The structures of this inertial zone only transfer the kinetic energy to dissipate, set by large structures, to smaller structures that dissipate it. In the general form of the spectrum, where $E(k) = f(k, \nu, \epsilon)$, the molecular viscosity ν no longer appears. Then, apart from a constant prefactor, an expression of the spectrum of the form $E \sim \epsilon^\alpha k^\beta$ can be searched for. The only acceptable combination for the exponents α and β in terms of dimension is then $\alpha = 2/3$ and $\beta = -5/3$, leading to

$$E(k) = C_K \epsilon^{2/3} k^{-5/3} \tag{7.3}$$

This law was established by Kolmogorov [182], formulated from the second-order longitudinal structure function, see Sect. 7.6.2, and $C_K \simeq 1.5$ is known as the Kolmogorov constant [194, 669]. This law is well confirmed experimentally as shown in Fig. 7.3. Particularly, Grant et al. [178] have led a series of measurements in the Discovery Passage, along the Canadian west coast. The Reynolds number based on the depth of the channel and the average velocity was of approximately $\mathrm{Re} \simeq 2.8 \times 10^8$, which must be compared to Reynolds numbers about $\mathrm{Re} \simeq 5 \times 10^5$ obtained in wind tunnels [637]. In Fig. 7.3, the plot deals with the one-dimensional spectra $E_{11}^{(1)}(k_1)$ which are directly measurable. However, it is easily shown that if $E_{11}^{(1)}(k_1) \sim k_1^{-5/3}$, then also $E(k) \sim k^{-5/3}$ by using the relation (6.35).

From a phenomenological point of view, dissipation is conserved through the energy cascade, as illustrated in Fig. 7.4. For eddies of size l and velocity u_l in the inertial zone, one observes a quasi-isotropic behaviour with $u_l^2/(l/u_l) \sim \epsilon$.

The turbulent kinetic energy associated with eddies of size $l \sim 1/k_l$ is then $u_l^2 \sim (\epsilon l)^{2/3} \sim k_l E(k_l)$, and the Kolmogorov law $E(k_l) \sim \epsilon^{2/3} k_l^{-5/3}$ is retrieved. It should be noted here that since E is expected to be a power function of k, it is convenient to introduce the following k-weighted spectrum $kE(k)$

$$\int E(k)dk = \int kE(k)\, d(\ln k) \tag{7.4}$$

The area under the curve $kE(k)$ represents the energy, and integrating with a constant $d(\ln k_l)$, the kinetic energy associated with eddies of size l is $u_l^2 \sim k_l E(k_l)$. This representation often leads to a linear scale for the ordinates, examples are provided later in Figs. 7.6 and 10.13 for instance.

As was stated in the introduction to this section, the inertial zone is present only if the spectra of turbulent kinetic energy and dissipation are separate enough. In the case of free jets for instance, Gibson [531] using work by Corrsin, estimates that in terms of Reynolds number, it is necessary that $\mathrm{Re}_{\lambda_g} = u'\lambda_g/\nu \geq 500$ or $\mathrm{Re}_{L_f} \geq 1.7 \times 10^4$ using relation (7.2), that is $\mathrm{Re}_D = U_j D/\nu \geq 4.2 \times 10^5$ for an inertial zone to appear.

7.2 Equation of Kármán and Howarth

The equation of Kármán and Howarth [114] governs the time evolution of the two-point velocity correlations. The method to find this equation is the following. The velocity and pressure at point A are noted $\boldsymbol{u}'_A$ and p'_A and at point B, $\boldsymbol{u}'_B$ and p'_B. The vector linking points A and B is noted $\boldsymbol{r} = \boldsymbol{x}_B - \boldsymbol{x}_A$. The Navier-Stokes equation is written at point A for component u'_{Ai}, and is then multiplied by the component u'_{Bj} of velocity at point B,

$$u'_{Bj} \times \left(\frac{\partial u'_{Ai}}{\partial t} + \frac{\partial u'_{Ai} u'_{Ak}}{\partial x_{Ak}} = -\frac{1}{\rho}\frac{\partial p'_A}{\partial x_{Ai}} + \nu \frac{\partial^2 u'_{Ai}}{\partial x_{Ak} \partial x_{Ak}} \right)$$

Developing and taking into account that u'_{Bj} is independent from the spatial variable $\boldsymbol{x}_A$, one obtains

$$u'_{Bj}\frac{\partial u'_{Ai}}{\partial t} + \frac{\partial u'_{Ai} u'_{Ak} u'_{Bj}}{\partial x_{Ak}} = -\frac{1}{\rho}\frac{\partial p'_A u'_{Bj}}{\partial x_{Ai}} + \nu \frac{\partial^2 u'_{Ai} u'_{Bj}}{\partial x_{Ak} \partial x_{Ak}}$$

Then the same operation is applied at point B, with the Navier-Stokes equation written in $\boldsymbol{x}_B$ for the component u'_{Bj},

$$u'_{Ai}\frac{\partial u'_{Bj}}{\partial t} + \frac{\partial u'_{Bj} u'_{Bk} u'_{Ai}}{\partial x_{Bk}} = -\frac{1}{\rho}\frac{\partial p'_B u'_{Ai}}{\partial x_{Bj}} + \nu \frac{\partial^2 u'_{Bj} u'_{Ai}}{\partial x_{Bk} \partial x_{Bk}}$$

These two expressions are then added, and the ensemble average is applied to obtain

$$\frac{\partial \overline{u'_{Ai}u'_{Bj}}}{\partial t} + \frac{\partial \overline{u'_{Ai}u'_{Ak}u'_{Bj}}}{\partial x_{Ak}} + \frac{\partial \overline{u'_{Bj}u'_{Bk}u'_{Ai}}}{\partial x_{Bk}} = -\frac{1}{\rho}\left(\frac{\partial \overline{p'_A u'_{Bj}}}{\partial x_{Ai}} + \frac{\partial \overline{p'_B u'_{Ai}}}{\partial x_{Bj}}\right) + \nu\left(\frac{\partial^2 \overline{u'_{Ai}u'_{Bj}}}{\partial x_{Ak}\partial x_{Ak}} + \frac{\partial^2 \overline{u'_{Bj}u'_{Ai}}}{\partial x_{Bk}\partial x_{Bk}}\right)$$

This equation can be simplified noting that for isotropic turbulence, the pressure-velocity correlations at two points are equal to zero and that the following relations are verified

$$\frac{\partial}{\partial x_{Bk}} = \frac{\partial}{\partial r_k} \quad \text{and} \quad \frac{\partial}{\partial x_{Ak}} = -\frac{\partial}{\partial r_k}$$

which leads to

$$\frac{\partial \overline{u'_{Ai}u'_{Bj}}}{\partial t} + \frac{\partial}{\partial r_k}\left(-\overline{u'_{Ai}u'_{Ak}u'_{Bj}} + \overline{u'_{Bj}u'_{Bk}u'_{Ai}}\right) = 2\nu \frac{\partial^2 \overline{u'_{Ai}u'_{Bj}}}{\partial r_k \partial r_k}$$

This relation can be transformed introducing the tensors of double and triple velocity correlations at two points $R_{ij}(\boldsymbol{r}, t)$ and $T_{ij,k}(\boldsymbol{r}, t)$. Particularly, $\overline{u'_{Ai}u'_{Ak}u'_{Bj}} = T_{ik,j}(\boldsymbol{r})$ and $\overline{u'_{Bj}u'_{Bk}u'_{Ai}} = T_{jk,i}(-\boldsymbol{r}) = -T_{jk,i}(\boldsymbol{r})$ since $T_{jk,i}$ is an odd function in $\boldsymbol{r}$ for isotropic turbulence, see Eq. (6.29) and Fig. 7.5. Hence,

$$\underbrace{\frac{\partial R_{ij}}{\partial t}}_{(1)} = \underbrace{\frac{\partial}{\partial r_k}(T_{ik,j} + T_{jk,i})}_{(2)} + \underbrace{2\nu \frac{\partial^2 R_{ij}}{\partial r_k \partial r_k}}_{(3)} \tag{7.5}$$

Equation (7.5) can again be transformed writing R_{ij} as a function of f and $T_{ij,k}$ as a function of h. These two relations are given by (6.24) and (6.29) respectively. Using the spherical coordinates for operators $\partial/\partial r_k$ and $\partial^2/\partial r_k^2$, one finally obtains the equation of Kármán and Howarth [114],

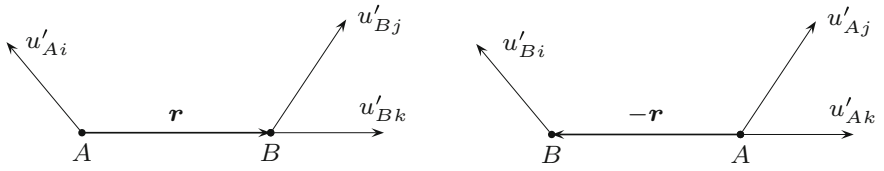

Fig. 7.5 Triple velocity correlations involved in Eq. (7.5)

$$\underbrace{\frac{\partial}{\partial t}(u'^2 f)}_{(1)} = \underbrace{u'^3\left(\frac{4h}{r} + h'\right)}_{(2)} + \underbrace{2\nu u'^2\left(\frac{4f'}{r} + f''\right)}_{(3)} \tag{7.6}$$

where $u'^2 = 2k_t/3$ is a function of time t, and f and h are functions of r and t. In expressions (7.5) and (7.6), the term (1) corresponds to the time variation of the second-order moment of the velocity fluctuations. The term (2) introduces a new unknown, the triple moments of the velocity field associated with the nonlinear interaction of turbulence with itself. Finally, the term (3) represents the dissipation by molecular viscosity.

Hence an assumption is needed for the triple moments so as to resolve the equation governing the second order moment. One can think of writing an equation for the third-order moment, but this will bring fourth-order moments in the equation governing the third-order moment and so on. There is some analytical developments in the literature to close Eq. (7.6). Nonetheless, the closure in spectral space is preferred because the necessary hypotheses can more easily be interpreted.

7.3 Lin Equation

The Lin equation is the equivalent of Eq. (7.5) in spectral space. First it must be remembered that

$$R_{ij}(\boldsymbol{r}, t) = \int \phi_{ij}(\boldsymbol{k}, t)\, e^{i\boldsymbol{k}\cdot\boldsymbol{r}} d\boldsymbol{k}$$

where ϕ_{ij} is the spectral tensor and, similarly, the Fourier transform of the tensor of triple correlations is introduced,

$$T_{ik,j}(\boldsymbol{r}, t) = -i \int \Psi_{ikj}(\boldsymbol{k}, t) e^{i\boldsymbol{k}\cdot\boldsymbol{r}} d\boldsymbol{k}$$

With these definitions, the Fourier transform of Eq. (7.5) is

$$\frac{\partial \phi_{ij}}{\partial t} = k_k(\Psi_{ikj} + \Psi_{jki}) - 2\nu k^2 \phi_{ij}$$

and applying $i = j$, one obtains

$$\frac{\partial \phi_{ii}}{\partial t} = 2k_k \Psi_{iki} - 2\nu k^2 \phi_{ii}$$

Lin's equation is actually the time evolution of the spectrum E of the turbulent kinetic energy. For isotropic turbulence, the spectral tensor ϕ_{ij} can be expressed in terms of E by

$$\phi_{ij}(k) = \frac{E(k)}{4\pi k^2}\left(\delta_{ij} - \frac{k_i k_j}{k^2}\right) \quad \text{and thus,} \quad \phi_{ii}(k) = \frac{E(k)}{2\pi k^2}$$

and the equation established by Lin [127] is beautifully compact,

$$\frac{\partial}{\partial t}E(k,t) = T(k,t) - 2\nu k^2 E(k,t) \tag{7.7}$$

The nonlinear term $T(k,t) = 4\pi k^2 k_k \Psi_{iki}(\boldsymbol{k},t)$ is associated with the triple correlations of velocity variations. The time variation of spectrum E is then due to term T, corresponding to an energy transfer between structures of different sizes, and to the linear viscosity term $2\nu k^2 E(k)$. This equation is not closed since term T is unknown. The expression of spectrum E is determined once the transfer term T is modelled. Lin's equation can really be interpreted after integration on all wavenumbers. Indeed,

$$\underbrace{\frac{\partial}{\partial t}\int_0^\infty E(k,t)dk}_{\partial k_t/\partial t} = \int_0^\infty T\,(k,t)\,dk - \underbrace{2\nu\int_0^\infty k^2 E\,(k,t)\,dk}_{\epsilon}$$

Moreover for isotropic turbulence, the Eq. (2.20) of kinetic energy k_t simplifies in

$$\frac{\partial k_t}{\partial t} = -\epsilon$$

and then, by comparison

$$\int_0^\infty T(k,t)dk = 0$$

The quantity $T(k,t)$ corresponds to the rate of energy transferred to successively smaller and smaller scales of the turbulent field. The function $S(k,t)$ defined by

$$S(k,t) = -\int_0^k T(k',t)dk'$$

represents the energy transferred from all the wavenumbers smaller than k to wavenumbers larger than k, as illustrated in Fig. 7.6 for $\mathrm{Re}_{\lambda_g} = 2078$. This term S thus corresponds to a kinetic energy flux from large structures towards small structures. The transfer term T is always negative for $kl_\eta < 0.02$, and thus corresponds to an energy transfer from large eddies to small ones. In this figure are also represented the spectrum $E(k)$ of the turbulent kinetic energy k_t and the spectrum $D_\nu(k)$ of the dissipation ϵ.

The transfer term $T(k)$ has been measured for instance by Van Atta and Chen [197], and their results are plotted in Fig. 7.7. Transfer terms computed from Comte-Bellot and Corrsin [101] data, have also been reported for the same range of moderate Reynolds numbers.

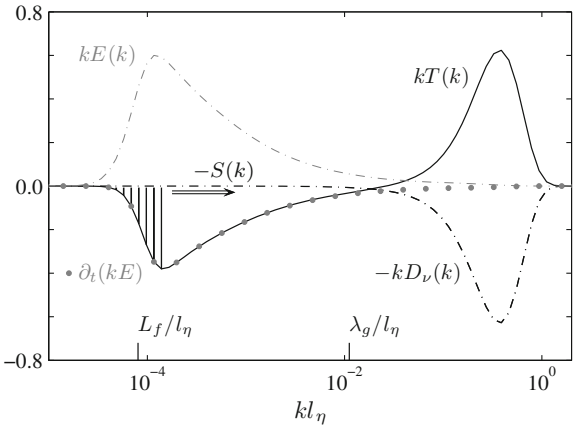

Fig. 7.6 Energy cascade at $\mathrm{Re}_{\lambda_g} \simeq 2078$ according to Lin's equation (7.7) computed by an EDQNM simulation (refer to Fig. 7.17 for details). The energy spectrum $E(k)$ and the flux $S(k)$ are also represented. Note that all terms are multiplied by k according to (7.4). At very high Reynolds number only $T(k) \simeq 0$ in the inertial subrange, and $S(k) \simeq \epsilon$ corresponds to the amount of energy which will be dissipated by the small eddies

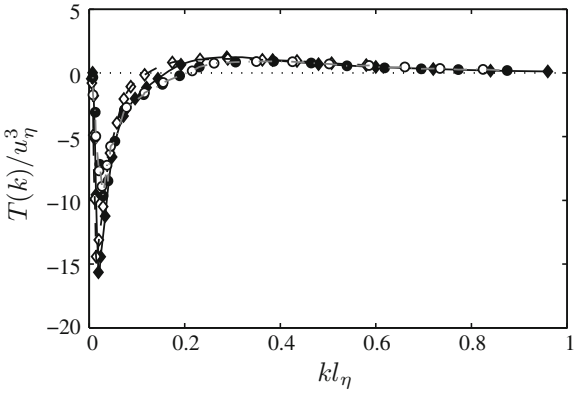

Fig. 7.7 The transfer term $T(k)$ according to Van Atta and Chen [197] measured at $x_1/M = 48$ for two cases of grid turbulence, ($\bullet$ $U_0 = 15.7\,\mathrm{m}\cdot\mathrm{s}^{-1}$, $M = 2.54\,\mathrm{cm}$, $\mathrm{Re}_{\lambda_g} = 49.4$; and $\circ$ $U_0 = 7.7\,\mathrm{m}\cdot\mathrm{s}^{-1}$, $M = 5.08\,\mathrm{cm}$, $\mathrm{Re}_{\lambda_g} = 34.6$), and also calculated from Comte-Bellot and Corrsin [101] data ($\blacklozenge$ at $x_1/M = 42$, $M = 5.08\,\mathrm{cm}$, $\mathrm{Re}_{\lambda_g} = 71.6$; $\lozenge$ at $x_1/M = 98$, $M = 5.08\,\mathrm{cm}$, $\mathrm{Re}_{\lambda_g} = 65.3$). Normalisation is made using Kolmogorov scales

7.4 Lin Equation Closures

Numerous closures have been proposed in the scientific literature for the term $T(k,t)$ of Lin equation (7.7). The simplest hypothesis consists in neglecting the term, $T(k,t) = 0$. Of course, this is not realistic as it assumes that for each class of eddies in the range $[k, k+dk]$, there is a mere viscous dissipation independent from the other classes. In other words, there is no nonlinear interaction. This closure is

valid only for the final period of decay when all small structures have disappeared and only the largest remain. Assuming the spectrum has the form $E(k) \sim k^4$ when $k \to 0$, it can then be shown [84] that the turbulent kinetic energy decreases very rapidly in this final period as

$$k_t(t) \sim (t - t_0)^{-5/2} \qquad t \to \infty$$

Among the different other closures that have been developed and analysed by Hinze [8], some must be mentioned such as those of Obukhov [139], Heisenberg [179], Kovasznay [117] and that of Pao [140, 141], which remains one of the most interesting. Pao's idea was to propose a power law for the energy flux term S, with the constraint that $S(k, t) = \epsilon$ in the inertial zone. Hence,

$$S(k,t) = -\int_0^k T(k',t)dk' = \frac{1}{C_K}\epsilon^{1/3}k^{5/3}E(k,t)$$

where C_K is the Kolmogorov constant. The kinetic energy spectrum obtained after integration of Lin equation then is,

$$E(k) = C_K\epsilon^{2/3}k^{-5/3}\exp\left[-\frac{3C_K}{2}(kl_\eta)^{4/3}\right] \tag{7.8}$$

Some alternative expressions exist to cover also the wavenumbers before the inertial zone. A general form for the turbulent kinetic energy spectrum [20, 102] is

$$E(k) = \alpha_1 C_K(\epsilon L_f)^{2/3}(kL_f)^{-5/3} f_e(kL_f) f_\eta(kl_\eta)L_f$$

where $f_e(kL_f)$ describes the production part, and thus $f_e \to 1$ as $kL_f \to \infty$. Particularly, the von Kármán spectrum [181] is given by

$$f_e(kL_f) = \left[\frac{\alpha_2 kL_f}{\sqrt{1 + (\alpha_2 kL_f)^2}}\right]^{4+5/3} \tag{7.9}$$

with $E(k) \sim k^4$ as $k \to 0$. The values of the two constants α_1 and α_2 are determined by imposing that relations (6.14) and (6.36) must be satisfied by the function $E(k)$,

by using $\epsilon = u'^3/L_f$ and by taking $C_K = 3/2$. It can be shown that

$$\alpha_1 = \frac{110}{27\pi^{1/6}}\left(\frac{\Gamma(5/6)}{\Gamma(1/3)}\right)^{5/3} \simeq 0.80 \qquad \alpha_2 = \frac{1}{\sqrt{\pi}}\frac{\Gamma(1/3)}{\Gamma(5/6)} \simeq 1.34$$

and the spectrum peak is reached for $kL_f = \sqrt{12/5}/\alpha_2 \simeq 1.16$. Though there is now a large number of possibilities offered by numerical simulations, expression (7.9) still remains very useful for modelling purposes. The dissipation part is described by the function $f_\eta(kl_\eta)$, with $f_\eta \to 1$ as $kl_\eta \to 0$. For example, one has $f_\eta(kl_\eta) = \exp[-(3C_K/2)(kl_\eta)^{4/3}]$ for Pao's spectrum (7.8). Other choices [8, 109] and more complete discussions [20, 102, 130] can be found to continue this topic.

7.5 Characteristic Times of Turbulence

7.5.1 The Memory Time of Turbulence

The time scale $\Theta = L_f/u'$ which characterizes the energy containing eddies, has been found experimentally to be important as it fixes the rate of decrease of the kinetic energy (6.48). It is interesting to see that this same time can also be found by integration of the time correlation function

$$R_{11}(\Delta t) = \overline{u_1'(t, \boldsymbol{x})u_1'(t + \Delta t, \boldsymbol{x} + \bar{U}_1 \Delta t)}$$

the turbulence being observed in a frame associated with the average velocity $\bar{U}_1$ in the working section. The wind tunnel experiment for the realization of isotropic turbulence is described in Sect. 6.3. Experimentally, the measurement of space-time correlations requires two probes separated by a distance Δx_1 in the longitudinal direction. The correlation optimum is obtained when the time lag Δt, with which the second signal is observed with respect to the first, verifies $\bar{U}_1 \Delta t = \Delta x_1$ as illustrated in Fig. 7.8. The time provided by the integration of $R_{11}(\Delta t)$ is called an integral time or memory time of turbulence. It closely matches the time provided by $\Theta = L_f/u'$ for isotropic turbulence [101].

7.5.2 The Spectral Times of Turbulence

The memory time notion considered on signal u_i' can be extended to the Fourier components constituting the signal u_i'. A frequency analysis of u_i' and use of the

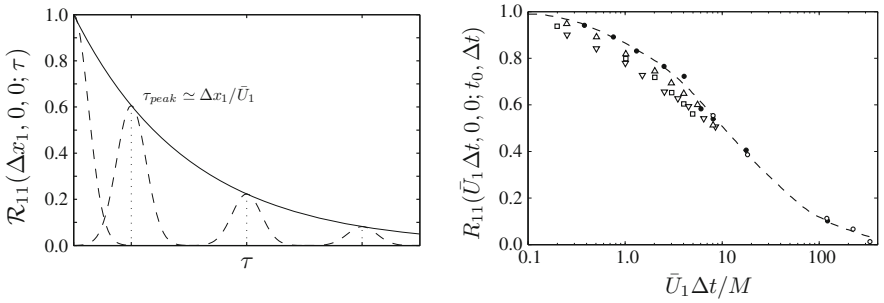

Fig. 7.8 *Left* sketch of the time correlation between two hot-wire probes separated by Δx_1 in *dashed lines*. On each *curve*, the maximum occurs at $\tau_{\text{peak}} = \Delta x_1/\bar{U}_1$. The envelope of these curves in *solid line*, close to the maxima, represents the time correlation in the frame moving at $\bar{U}_1$. The area under the *curve* gives the memory time of turbulence, around L_f/u'. The case $\Delta x_1 = 0$ is the time autocorrelation for which the integral scale is of the order of $L_f/\bar{U}_1$. This time very short compared to the memory time of turbulence, permits to quickly renew the turbulence passing over the probes. *Right* time correlation in a convected frame at the mean velocity $\bar{U}_1$ for fluctuations u_1' in grid turbulence; $\triangle$ $\triangledown$ Favre et al. [612, 613], $\square$ Frenkiel and Klebanoff [106], $\bullet$ $M = 5.08$ and $\circ$ $M = 2.54$ Comte-Bellot and Corrsin [101]

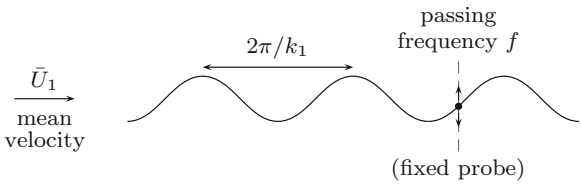

Fig. 7.9 Illustration of Taylor's hypothesis [136, 153] formulated by expression (7.10)

Taylor hypothesis (6.45) permit to link the frequency f to the longitudinal component of the wavenumber

$$k_1 = \frac{2\pi f}{\bar{U}_1} \tag{7.10}$$

where $k_1 \geq 0$ and $f \geq 0$ here, as illustrated in Fig. 7.9. The turbulence being isotropic, these results involving k_1 can be transferred to the wavenumber modulus k, as was already undertaken for spectra in Sect. 6.2.5.

Figure 7.10 illustrates the correlation curves obtained by Comte-Bellot and Corrsin [101]. Here, the notation $R(k, \Delta t)$ without index is similar to $E(k)$. For a given wavenumber modulus k, coherence over time is followed for all the contributions of velocities tangent to the sphere of radius k. Figure 7.10 also represents the integral time existing under each curve corresponding to a given wavenumber modulus. This can be compared to other classic times reported in Fig. 7.10 (right),

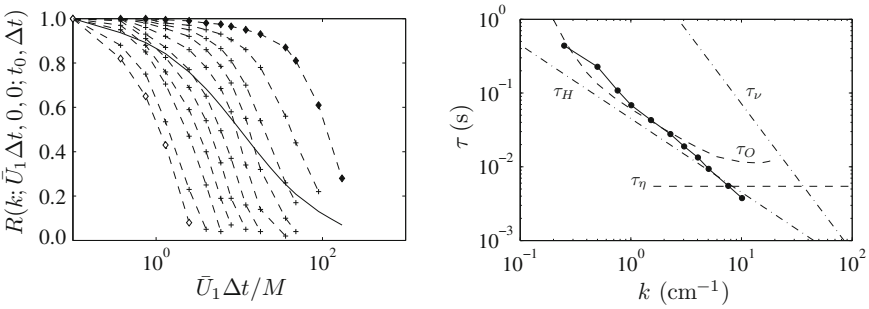

Fig. 7.10 *Left* filtered time-correlation corresponding to Comte-Bellot and Corrsin [101] experiments reported in Fig. 7.8 (right). The wavenumber modulus varies from $k = 0.25\,\mathrm{cm}^{-1}$ (♦) to $k = 10.10\,\mathrm{cm}^{-1}$ (◊). The overall time correlation is plotted in solid line. *Right* comparison with predictions, –·–·– Heisenberg time τ_H, – – – Onsager time τ_O and • Comte-Bellot and Corrsin [101] measurements. Note the rapid decrease of all these *curves* when k increases. The viscous time τ_ν and the Kolmogorov time τ_η are also indicated

$$\begin{aligned}
\tau_O &= \left[k^3 E(k)\right]^{-1/2} && \text{Onsager time}\\
\tau_H &= \left[u' k\right]^{-1} && \text{Heisenberg time}\\
\tau_\nu &= \left[k^2 \nu\right]^{-1} && \text{Viscous time}\\
\tau_\eta &= \nu^{1/2}\epsilon^{-1/2} && \text{Kolmogorov time}
\end{aligned}$$

It can be pointed out that the two first times are built using either data characteristic of the spectrum, for instance Onsager time with k and $E(k)$, or joint data where kinetic energy and wavenumber appear, for instance Heisenberg time with u' and k. The mechanisms responsible for the coherence loss of structures of given wavenumber k are still not completely known. Comte-Bellot and Corrsin have analysed the convection, rotation, and deformation exerted by structures larger than k and the diffusion provided by structures smaller than k.

7.6 Further Details on Kolmogorov Theory⋆

7.6.1 Structure Functions of Velocity⋆

The spectral analysis developed in Sect. 7.1 allowed us to introduce the inertial zone of the universal equilibrium of small structures, and to find the range of wavenumbers to which this balance applies. An expression of this equilibrium in physical space is now searched for. However a simple use of double correlations defined in Chap. 6 is not possible. Indeed these correlations deal with all separations r and not only with the range $L_f \gg r \gg l_\eta$ which corresponds to the inertial subrange of Kolmogorov. Besides, the mere introduction of $E(k) = C_K \epsilon^{2/3} k^{-5/3}$ in relation (6.37) which gives $f(r)$ leads to a divergent integral. Thus the problem has to be considered differently.

Instead of the velocity fluctuation themselves, the difference between velocity fluctuations at two points $\boldsymbol{x}$ and $\boldsymbol{x}+\boldsymbol{r}$ is considered at the same time t, that is $\boldsymbol{u}'(\boldsymbol{x}+\boldsymbol{r},t)-\boldsymbol{u}'(\boldsymbol{x},t)$, as suggested by Kolmogorov [184]. Velocity differences permit to be free from the large scale movements, and are then characteristic of the small and medium structures of turbulence. This approach leads to define structure functions. The second order structure function has the general form

$$F_{ij}(\boldsymbol{r},t)=\overline{[u_i'(\boldsymbol{x}+\boldsymbol{r},t)-u_i'(\boldsymbol{x},t)][u_j'(\boldsymbol{x}+\boldsymbol{r},t)-u_j'(\boldsymbol{x},t)]}$$

The simplifications implied by rotational invariance are easily found, which leads to a local isotropy of the turbulence, as was done for a global isotropy of the field using the tensor R_{ij} of velocity correlations. All details are available in Monin and Yaglom [17]. In the following, time dependency will be omitted to simplify writing.

The form of F_{ij} in the inertial zone is now searched for, and particularly that of the contracted tensor F_{ii},

$$F_{ii}(r)=\overline{\left[u_i'(\boldsymbol{x}+\boldsymbol{r})-u_i'(\boldsymbol{x})\right]^2}$$

Developing this yields

$$F_{ii}(r)=6u'^2-2u'^2\mathcal{R}_{ii}(r)$$

where only the distance r occurs as expected from isotropy. But, according to (6.14) and (6.38) respectively,

$$\frac{3}{2}u'^2=\int_0^\infty E(k)\,dk \qquad \text{and} \qquad u'^2\mathcal{R}_{ii}\,(r)=2\int_0^\infty E(k)\frac{\sin(kr)}{kr}\,dk$$

one obtains

$$F_{ii}(r)=4\int_0^\infty\left[1-\frac{\sin(kr)}{kr}\right]E(k)\,dk$$

The inertial subrange concerns the distances r lying in the range $L_f\gg r\gg l_\eta$, and so as in the integral above, the contribution of small wavenumbers can be neglected due to the term $1-\sin(kr)/(kr)$, and the contribution of large wavenumbers can be neglected since $E(k)$ decreases very rapidly for an increasing k. The part associated with the zone in $k^{-5/3}$ thus provides the main contribution to the integral, which can then be approximated by

$$F_{ii}(r)\simeq 4\int_0^\infty\left[1-\frac{\sin(kr)}{kr}\right]C_K\epsilon^{2/3}k^{-5/3}\,dk$$

To integrate, the variable change $kr=x$ is used

$$F_{ii}(r) \simeq 4C_K(\epsilon r)^{2/3} \int_0^\infty (x - \sin x) x^{-8/3}\, dx$$

and integrating by parts two times,

$$F_{ii}(r) \simeq 4C_K(\epsilon r)^{2/3} \frac{3}{5} \times \frac{3}{2} \int_0^\infty x^{-2/3} \sin x\, dx$$

Finally,

$$F_{ii}(r) \simeq \frac{9}{5} C_K \Gamma\left(\frac{1}{3}\right) (\epsilon r)^{2/3} \simeq 4.82\, C_K\, (\epsilon r)^{2/3}$$

using

$$\int_0^\infty x^{\mu-1} \sin(ax)\, dx = \frac{\Gamma(\mu)}{a^\mu} \sin\left(\frac{\mu\pi}{2}\right) \qquad \text{and} \qquad \Gamma\left(\frac{1}{3}\right) \simeq 2.68$$

In the inertial zone, there is thus a variation in $(\epsilon r)^{2/3}$, which could be predicted by dimensional analysis and besides, the numerical factor is associated with the Kolmogorov constant C_K. In a similar way, though with longer calculations, the second order longitudinal structure function with longitudinal separation can be obtained

$$F_{11}(r, 0, 0) = 2u'^2 [1 - f(r)] = \frac{27}{55} C_K \Gamma\left(\frac{1}{3}\right) (\epsilon r)^{2/3}$$

For the third order structure function, which seems more complex, an exact result is finally obtained because the numerical factor is known but is nontrivial

$$F_{111}(r, 0, 0) = 6u'^3 h(r) = -\frac{4}{5}\epsilon r \qquad L_f \gg r \gg l_\eta \tag{7.11}$$

This result is often called the second Kolmogorov law or law in $-4/5$. To obtain relation (7.11), first the third order structure function $F_{111}(r, 0, 0)$ is expanded taking into account that the triple velocity correlation at two points is an odd function, as indicated in Sect. 6.24, which leads to

$$\begin{aligned} F_{111}(r, 0, 0) &= \overline{\left[u'_1(\boldsymbol{x} + \boldsymbol{r}) - u'_1(\boldsymbol{x})\right]^3} \\ &= -3\overline{u'^2_1(\boldsymbol{x} + \boldsymbol{r}) u'_1(\boldsymbol{x})} + 3\overline{u'_1(\boldsymbol{x} + \boldsymbol{r}) u'^2_1(\boldsymbol{x})} = 6u'^3 h(r) \end{aligned}$$

Then, the Kármán and Howarth equation (7.6) is invoked with $f(r)$ and $h(r)$ expressed in terms of F_{11} and F_{111} using $F_{11} = 2u'^2 [1 - f(r)]$ and $F_{111} = 6u'^3 h(r)$, which gives

$$\frac{\partial}{\partial t}\left(u'^2 - \frac{F_{11}}{2}\right) = \frac{1}{6}\left(F'_{111} + \frac{4}{r}F_{111}\right) - \nu\left(F''_{11} + \frac{4}{r}F'_{11}\right)$$

In the first part of the equation, as time does not appear explicitly in F_{11} but only through ϵ under an almost equilibrium hypothesis, only the derivative of u'^2 remains, that is $\partial u'^2/\partial t = -2\epsilon/3$, yielding

$$-\frac{2\epsilon}{3} \times 6 \simeq \left(F'_{111} + \frac{4}{r}F_{111}\right) - 6\nu\left(F''_{11} + \frac{4}{r}F'_{11}\right)$$

Multiplying by r^4 and integrating give

$$-\frac{4}{5}\epsilon r \simeq F_{111} - 6\nu F'_{11}$$

In the inertial zone, where viscosity ν can be neglected, relation (7.11) is indeed recovered. Maurer et al. [188] brought support to this law. They conducted experiments between two discs rotating in pressurized helium at low temperature, on a large range of Reynolds numbers $20 \leq Re_{\lambda_g} \leq 2100$.

7.6.2 Refinement of Kolmogorov Theory⋆

In experimental investigations with large Reynolds numbers, particularly in the atmosphere, it was observed that some quantities, as the high moments of the velocity derivatives and the structure functions of high order, depend on the Reynolds number, showing that an effect of the integral scale L_f of turbulence is present. The previous classical theory must then be refined to introduce a function of L_f/r, while keeping the already introduced average dissipation rate ϵ. Apart from a numerical constant omitted to simplify the writing, results of the following form are searched for

$$\overline{\left[u'_i(\boldsymbol{x}+\boldsymbol{r},t) - u'_i(\boldsymbol{x},t)\right]^p} \sim (\epsilon r)^{p/3} \times \mathcal{F}(L_f/r) \tag{7.12}$$

where $\mathcal{F}$ depends on the order p. The obtaining of $\mathcal{F}$ is one of the current problems of turbulence. It demands a knowledge of the spatial irregularities of the instantaneous dissipation, or of its intermittency in a time tracking. Several theories describe instantaneous dissipation in terms of probability distributions. They also debate on the geometry of vortex filaments and the reduced space they can occupy. $\mathcal{F}$ contains the randomness of the dissipation and thus becomes function of order p. Three approaches have essentially been suggested and they are compared considering the exponent ζ_p with which r appears in the pth order structure function. The following results are currently available

$$\begin{aligned}
\zeta_p &= \frac{p}{3} && \text{classical theory} \\
\zeta_p &= \frac{p}{3} + \frac{\mu}{18}\left(3p - p^2\right) && \text{log-normal distribution for the dissipation, and } \mu \simeq 0.20 \\
\zeta_p &= \frac{p}{3} + (3 - D)\left(1 - \frac{p}{3}\right) && \text{fractal volumes for the dissipation, and } D \simeq 2.8 \\
\zeta_p &= \frac{p}{9} + 2 - 2\left(\frac{2}{3}\right)^{p/3} && \text{log-Poisson distribution for the dissipation}
\end{aligned} \tag{7.13}$$

Figure 7.11 illustrates the dependency of ζ_p on the order p of the structure function compared to experimental results. This figure leads to several interesting conclusions. First of all, whatever the approach is, the case $p = 3$ provides $\zeta_p = 1$ according to the theory expressed by (7.11). For $p < 3$, the refinement effect is not very marked. Thus the spectra corresponding to a kinetic energy, i.e. to $p = 2$, are only slightly affected. In particular, this confirms the classical law $E(k) \sim k^{-5/3}$ which thus appears to be very solid. This law indeed applies to a large number of different circumstances, from laboratory experiments to tests at sea or in the atmosphere, as shown in Fig. 7.3. For $p > 3$, the internal intermittency effect becomes all the more important as the considered moment is high. This led to numerous studies, by Van Atta and Park [199] up to $p = 9$, by Anselmet et al. [170] up to $p = 18$ and Maurer et al. [188] up to $p = 8$.

The case $p = 2$ and its application to spectrum $E(k)$ is now briefly considered again. As a function of ζ_2, the dependency of $E(k)$ with kL_f can be expressed in the general form

$$E(k) = C_K \epsilon^{2/3} k^{-5/3} (kL_f)^{-(\zeta_2 - 2/3)}$$

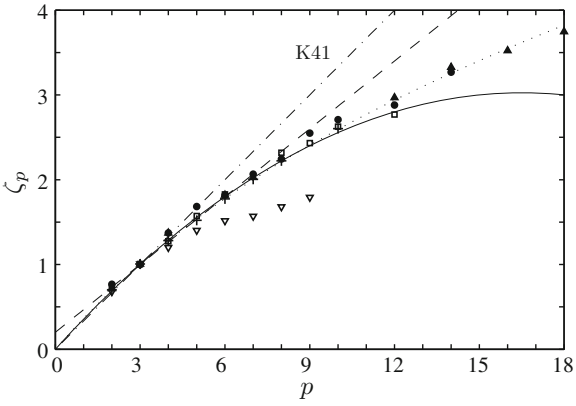

Fig. 7.11 Values of exponent ζ_p according to rank p of the longitudinal structure function: –·–·– classic Kolmogorov theory (K41), —— log-normal law, – – – fractal approach and ····· log-Poisson law, see Eq. (7.13). Symbols corresponds to experimental data collected by Frisch [174], in particular those of Anselmet et al. [170] which are close to the log-Poisson law

The exponent $-(\zeta_2 - 2/3)$ is obtained noting that $p/3$, that is 2/3 here, must be subtracted since it is already taken into account in the passage to spectral space, and that a sign change must be undertaken because the exponent ζ_p corresponds to r, while k implies r^{-1}. This leads to, considering expressions (7.13),

$$\begin{aligned}
E(k) &= C_K \epsilon^{2/3} k^{-5/3} && \text{classical theory} \\
E(k) &= C_K \epsilon^{2/3} k^{-5/3} (kL_f)^{-\frac{\mu}{9}} && \text{log-normal distribution} \\
E(k) &= C_K \epsilon^{2/3} k^{-5/3} (kL_f)^{-\frac{3-D}{3}} && \text{fractal approach} \\
E(k) &= C_K \epsilon^{2/3} k^{-5/3} (kL_f)^{-0.03} && \text{log-Poisson distribution}
\end{aligned}$$

As for the expressions of ζ_p, the log-normal distribution case, which has an historic interest and permits explicit and simple calculations, is developed in the following paragraph. For more recent approaches, one can refer to the work of Frisch [174]. It must be added that for an approach using a fractal volume, as suggested by Frisch [175], the reader must study first non-integer dimension geometry, as for example the famous Menger sponge. In this case a cube is excavated along three directions perpendicular to the center of the faces following an iterative process leading to a reduced volume which becomes fractal. With an excavation section at each iteration of $1/3 \times 1/3$ of edge length, the remaining matter occupies a volume of non-integer dimension $D = \ln 20 / \ln 3 \simeq 2.73$. Finally the approach using a log-Poisson distribution involves a hierarchy of structures associated with the energy cascade and to vorticity filaments. It was suggested by She and Lévêque [190] and She and Waymire [191]. Despite the theoretical complexity, which goes beyond the objectives of this tutorial book, it must be pointed out that the curve obtained for ζ_p is the closest to experiments, without any necessary additional constant.

7.6.3 *Overview of the Log-normal Distribution of the Dissipation⋆*

The basis of a log-normal distribution for the dissipation ϵ_r in a small volume of dimension r relies on a fragmentation process as shown in Fig. 7.12. The idea was suggested by Obukhov [189] and Kolmogorov [184]. For each realization of the turbulent field, the dissipation ϵ_r can be written as

$$\epsilon_r = \alpha_1 \times \alpha_2 \times \cdots \times \alpha_n \times \epsilon_0$$

with $\alpha_1, \alpha_2, \ldots, \alpha_n$ being random. ϵ_0 corresponds to the dissipation in a volume of dimension L_0, which is the initial state of the fragmentation. Numbers $\alpha_1, \alpha_2, \ldots, \alpha_n$ are positive, because a dissipation is always positive and, besides, they are almost independent of each other if the overlap between successive volumes is neglected. Using the logarithm:

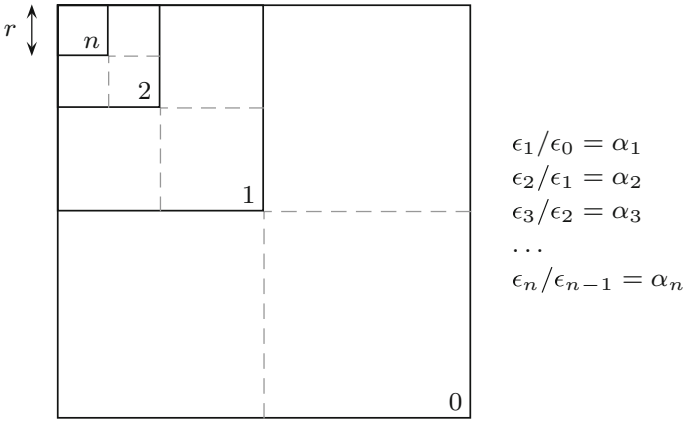

Fig. 7.12 Sketch for one realization illustrating the fragmentation of the volume where energy is dissipated. There is a ratio of 8 at every iteration. The series $\alpha_1, \alpha_2, \ldots, \alpha_n$ represents the ratio between the energy dissipated in two successive volumes. These numbers are random and positive. The last rank n corresponds to the spatial dimension r. This approach is useful to establish the log-normal law

$$\ln \epsilon_r = \ln \epsilon_0 + \underbrace{\ln \alpha_1 + \ln \alpha_2 + \cdots + \ln \alpha_n}_{x}$$

The variable x is then a sum of independent random variables, and according to the central limit theorem x can be assumed to have a normal probability density if n is large enough. Then it can be written that $\ln \epsilon_r = \ln \epsilon_0 + x$ or else $\epsilon_r = \epsilon_0 \exp(x)$ with

$$p(x) = \frac{1}{\sqrt{2\pi\sigma_x^2}} \exp(-x^2/2\sigma_x^2)$$

The variable change from x to ϵ_r is then merely of the form $y = \epsilon_0 \exp(x)$, and this y notation will be kept for a few lines so that the calculation is more understandable. For the same reasons, the notations x and y are improperly used for the non-random values appearing in the probability distributions. The distribution of y can be inferred from the one of x with the classical variable change in a probability distribution, which provides

$$P(y) = \frac{p(x)}{|\partial y/\partial x|} = \frac{1}{\sqrt{2\pi\sigma_x^2}} \frac{\exp[-(\ln y - \ln \epsilon_0)^2/2\sigma_x^2]}{y}$$

The moments of y can now be calculated. For instance, for order q

$$\overline{y^q} = \int_0^\infty y^q P(y)\, dy$$

The variable change $x = \ln y - \ln \epsilon_0$ is quite natural, it is equivalent to $y = \epsilon_0 \exp(x)$. Hence,

$$\overline{y^q} = \epsilon_0^q \frac{1}{\sqrt{2\pi\sigma_x^2}} \int_{-\infty}^{+\infty} \exp(qx - x^2/2\sigma_x^2)\, dx = \epsilon_0^q \exp(q^2\sigma_x^2/2)$$

using

$$\int_{-\infty}^{+\infty} \exp[-(ax^2 + bx + c)]\, dx = \sqrt{\frac{\pi}{a}} \exp[(b^2 - 4ac)/4a]$$

For $q = 1$, $\bar{y}$ becomes the usual dissipation rate ϵ, which appears in all kinetic energy equations. It corresponds to a statistical average on any volume, then particularly on volume r. This permits to link ϵ to ϵ_0, which had no physical meaning by itself

$$\bar{y} = \epsilon_0 \exp(\sigma_x^2/2) = \epsilon \qquad \text{and thus,} \qquad \epsilon_0 = \epsilon \exp(-\sigma_x^2/2)$$

which then provides

$$\overline{y^q} = \epsilon^q \exp\left[q(q-1)\sigma_x^2/2\right] \tag{7.14}$$

For the variance σ_x^2, one uses $\sigma_x^2 = \mu \ln(L_f/r)$ introduced for structure functions and $\sigma_x^2 = \mu \ln(kL_f)$ for spectra, see expression (7.13). This logarithmic form has two advantages. First, it permits a large variation range, with $\sigma_x^2 \simeq 0$ for large separations, $r \sim L_f$, and σ_x^2 large for $r \ll L_f$. Secondly, it allows to continue with simple calculations. The final form of $\overline{y^q}$ is then the following

$$\overline{y^q} = \epsilon^q \left(\frac{L_f}{r}\right)^{\frac{\mu}{2}\, q(q-1)} \tag{7.15}$$

For an energy spectrum, $\overline{\epsilon_r^{2/3}}$ needs to be determined, that is $\overline{y^{2/3}}$, from which the refined Kolmogorov law is easily inferred, the dependency in L_f/r being the same as the one in kL_f

$$E(k) = C_K \epsilon^{2/3} (kL_f)^{\frac{\mu}{2}\times\frac{2}{3}\times(\frac{2}{3}-1)}\, k^{-5/3} = C_K \epsilon^{2/3} k^{-5/3} (kL_f)^{-\mu/9}$$

The structure function of rank p involves $\overline{\epsilon_r^{p/3}}$, that is $q = p/3$, which provides

$$\overline{\left[u_i'(\boldsymbol{x}+\boldsymbol{r},t) - u_i'(\boldsymbol{x},t)\right]^p} \sim (\epsilon r)^{p/3} \times \left(\frac{L_f}{r}\right)^{\frac{\mu}{2}\times\frac{p}{3}\times(\frac{p}{3}-1)}$$

and then,

$$\zeta_p = \frac{p}{3} - \frac{\mu}{2} \times \frac{p}{3} \times \left(\frac{p}{3} - 1\right) = \frac{p}{3} + \frac{\mu}{18}(3p - p^2)$$

This is the formula announced in Sect. 7.6.2. The value of μ is still to be obtained. Van Atta and Chen [198] use the spectrum $\phi_{\epsilon\epsilon}$ of the dissipation which becomes in the inertial zone $\phi_{\epsilon\epsilon}(k) \sim \epsilon^2 k^{-1+\mu}$ in 3-D and similarly, $\phi^{(1)}_{\epsilon\epsilon}(k_1) \sim \epsilon^2 k_1^{-1+\mu}$ for the one-dimensional spectrum in k_1 or in frequency. This provides $\mu \simeq 0.50$. More recent measurements, particularly those of Anselmet et al. [170] provide $\mu \simeq 0.20$. Because of this small value of μ, it can be seen that only the higher moments are to be considered to decide between the different theories. It must be added, so as not to leave the reader with a wrong idea, that the log-normal approach is not the most satisfactory one, and numerous useful comments on this topic can be found in Frisch [174].

7.7 Homogeneous and Isotropic Two-Dimensional Turbulence*

A two-dimensional turbulent field verifies $u_i' \neq 0$ for $i = 1, 2$, the third component u_3' being always equal to zero. For the vorticity vector, only the component ω_3' differs from zero. This case must not be mixed up with that of the average plane turbulent flows, studied in Chaps. 3 and 4, for which the third axis is a principal direction or a homogeneity direction, however with $u_3' \neq 0$.

Whenever an isotropy hypothesis is introduced, the double velocity correlations at two points can be expressed by the relation (6.24). The two basic scalars $f(r)$ and $g(r)$, which notations are kept, have however different properties. Thus the application of the incompressibility condition (6.25) with $N = 2$ provides

$$g = f + rf' \qquad \text{or else} \qquad g = \frac{d}{dr}(rf) \tag{7.16}$$

By integration of $g = f + rf'$, it can be obtained that $L_g = 0$, still assuming a rapid enough decrease of $f(r)$ when $r \to \infty$. The negative loop of the correlation $g(r)$ is more important than that in the 3-D case. This corresponds to the importance of recirculation flows due to the confinement in a plane. Deriving $g = f + rf'$, the new relation between Taylor scales is obtained, i.e. $\lambda_f = \sqrt{3}\,\lambda_g$.

The spectral tensor ϕ_{ij} always has the form (6.30), but indexes i and j only take values 1 or 2, and the wavenumber only has two components k_1 and k_2. The expression of ϕ_{ij} as a function of the spectrum $E(k)$ of kinetic energy is thus modified because: on the one hand kinetic energy is $k_t = (\overline{u_1'^2} + \overline{u_2'^2})/2$, and as a result, $\phi_{ii} = \beta(k)$ and on the other hand the integration surface in the $\boldsymbol{k}$ space is reduced to the circle of radius k, and then $\Sigma_k = 2\pi k$. Finally,

$$\phi_{ij}(\boldsymbol{k}) = \frac{E(k)}{\pi k}\left(\delta_{ij} - \frac{k_i k_j}{k^2}\right) \tag{7.17}$$

The one-dimensional spectra keep their usual definition, but their expressions as a function of $E(k)$ are modified. Particularly those provided by integration of $\phi_{11}(k_1, k_2)$ and of $\phi_{22}(k_1, k_2)$ over k_2, with k_1 fixed, are now

$$\begin{aligned} E_{11}^{(1)}(k_1) &= \frac{2}{\pi}\int_{k_1}^{\infty} \frac{E(k)}{k^2}\sqrt{k^2 - k_1^2}\, dk \\ E_{22}^{(1)}(k_1) &= \frac{2}{\pi}\int_{k_1}^{\infty} \frac{E(k)}{k^2}\frac{k_1^2}{\sqrt{k^2 - k_1^2}}\, dk \end{aligned} \tag{7.18}$$

The relation between these two spectra, which can always serve as a test to characterize the isotropy of the different scales of the field, is

$$E_{22}^{(1)} = -k_1 \frac{dE_{11}^{(1)}}{dk_1} \tag{7.19}$$

Additional relations can also be obtained as in Sect. 6.2.6 for the 3-D case. Several are provided by Sommeria [169]. Here are only mentioned the relations between $f(r)$ and $E(k)$, where Bessel functions appear, which is classical in 2-D,

$$f(r) = 2\left[\int_0^{\infty} E(k)\, dk\right]^{-1} \int_0^{\infty} E(k)\, \frac{\mathrm{J}_1(kr)}{kr}\, dk$$

$$E(k) = \frac{\overline{u'^2}}{2}\, k \int_0^{\infty} \frac{\partial}{\partial r}(r^2 f)\, \mathrm{J}_0(kr)\, dr$$

The only non-zero component Ω_{33} of the spectral tensor of the curl is now calculated. The fluctuating component ω_3' being $\partial u_2'/\partial x_1 - \partial u_1'/\partial x_2$, its Fourier transform is $\hat{\omega}_3 = ik_1\hat{u}_2 - ik_2\hat{u}_1$, which provides,

$$\begin{aligned} \Omega_{33}(\boldsymbol{k}) = \overline{\hat{\omega}_3^{\star}\hat{\omega}_3} &= k_1^2\overline{\hat{u}_2^{\star}\hat{u}_2} + k_2^2\overline{\hat{u}_1^{\star}\hat{u}_1} - k_1k_2\left(\overline{\hat{u}_1^{\star}\hat{u}_2} + \overline{\hat{u}_2^{\star}\hat{u}_1}\right) \\ &= k_1^2\phi_{22} + k_2^2\phi_{11} - k_1k_2\left(\phi_{12} + \phi_{21}\right) \end{aligned}$$

and using (7.17),

$$\Omega_{33}(\boldsymbol{k}) = \frac{E(k)}{\pi k}\left[k_1^2\left(1 - \frac{k_2^2}{k^2}\right) + k_2^2\left(1 - \frac{k_1^2}{k^2}\right) + 2\,\frac{k_1^2k_2^2}{k^2}\right] = \frac{k^2}{\pi k}E(k)$$

To find the spectrum $\Omega(k)$ of the enstrophy, it can be written that

$$\frac{\overline{\omega_3'^2}}{2} = \frac{1}{2}\int_{\mathbf{R}^2} \Omega_{33}(\boldsymbol{k})d\boldsymbol{k} = \frac{1}{2}\int_0^{\infty} \frac{k^2}{\pi k}E(k)\, 2\pi k\, dk = \int_0^{\infty} k^2 E(k)\, dk$$

and then,

$$\Omega(k) = k^2 E(k) \qquad \text{with} \qquad \frac{\overline{\omega_3'^2}}{2} = \int_0^\infty \Omega(k)\, dk$$

As for the dynamics of the two-dimensional turbulence, it is characterized by the absence of elongation of vortex filaments, as was already noted in Chap. 5, which leads to a specific behaviour. To understand this new situation, the approach developed by Batchelor [156] is the most direct one, and is based upon three equations where both the dissipation rate ϵ of turbulent kinetic energy and the dissipation rate ϵ_ω of enstrophy appear. The first equation corresponds to the usual time evolution of turbulent kinetic energy for a homogeneous field without average velocity, i.e. according to (6.17)

$$-\epsilon = \frac{\partial}{\partial t}\left(\frac{\overline{u_i'^2}}{2}\right) = -\nu\overline{\omega_3'^2} \tag{7.20}$$

The second equation deals with the time evolution of enstrophy. It is provided by Eq. (5.11), which now only concerns ω_3' and in which the elongation term (a) is equal to zero,

$$-\epsilon_\omega = \frac{\partial}{\partial t}\left(\frac{\overline{\omega_3'^2}}{2}\right) = 0 - \nu\overline{\left(\frac{\partial \omega_3'}{\partial x_j}\right)^2} \tag{7.21}$$

The absence of elongation of the vortex filaments renders impossible a cascade of kinetic energy towards small structures, but is compatible with a transfer of kinetic energy to large structures. Besides, $\overline{\omega_3'^2}$ decreases faster for a 2-D turbulence than for a 3-D turbulence. For large Reynolds numbers, as $\nu \to 0$, according to the turbulent kinetic energy given by (7.20), $\epsilon \to 0$, and consequently, $\overline{u_i'^2} = \text{cst}$.

In Eq. (7.21), it must also be noted that the role of $\overline{(\partial\omega_3'/\partial x_j)^2}$ is similar to the one of $\overline{\omega_3'^2}$ in Eq. (7.20). It is then useful to remind that for a 3-D turbulence, the dynamics of $\overline{\omega_i'^2}$ was considered to understand the evolution of $\overline{u_i'^2}$. The time evolution of $\overline{(\partial\omega_3'/\partial x_j)^2}$ is now looked for to understand the one of $\overline{\omega_3'^2}$. To do this, the Helmholtz equation (5.7) which governs ω_3' is used,

$$\frac{\partial \omega_3'}{\partial t} + u_j' \frac{\partial \omega_3'}{\partial x_j} = \nu \frac{\partial^2 \omega_3'}{\partial x_j \partial x_j}$$

The derivative $\partial/\partial x_k$ of this equation provides

$$\frac{\partial}{\partial t}\left(\frac{\partial \omega_3'}{\partial x_k}\right) + \frac{\partial u_j'}{\partial x_k}\frac{\partial \omega_3'}{\partial x_j} + u_j' \frac{\partial^2 \omega_3'}{\partial x_j \partial x_k} = \nu \frac{\partial^2}{\partial x_j \partial x_j}\left(\frac{\partial \omega_3'}{\partial x_k}\right)$$

This last relation is then multiplied by $\partial\omega_3'/\partial x_k$, and the statistical average is applied taking into account both incompressibility and homogeneity. The third term in the left hand side simply gives

$$\overline{u_j' \frac{\partial\omega_3'}{\partial x_k} \frac{\partial^2\omega_3'}{\partial x_j \partial x_k}} = \frac{1}{2}\overline{u_j' \frac{\partial}{\partial x_j}\left(\frac{\partial\omega_3'}{\partial x_k}\right)^2} = \frac{1}{2}\frac{\partial}{\partial x_j}\left[\overline{u_j'\left(\frac{\partial\omega_3'}{\partial x_k}\right)^2}\right] = 0$$

Transforming the molecular viscosity term, as in Sect. 5.6, the following equation is finally obtained

$$\frac{1}{2}\frac{\partial}{\partial t}\overline{\left(\frac{\partial\omega_3'}{\partial x_k}\right)^2} = \underbrace{-\overline{\frac{\partial\omega_3'}{\partial x_j}\frac{\partial\omega_3'}{\partial x_k}\frac{\partial u_j'}{\partial x_k}}}_{(a')} \underbrace{-\nu\overline{\left(\frac{\partial^2\omega_3'}{\partial x_j \partial x_k}\right)^2}}_{(b')} \tag{7.22}$$

In Eq. (7.22), the term (a′) is similar to term (a) of Eq. (5.11). The vorticity gradients can then benefit from a production term. One can imagine that the iso-ω_3' contours in the plane containing the velocity variations are distorted, becoming more and more folded and close to one another, enabling an enstrophy transfer to small structures. As a result, for large Reynolds numbers, a direct enstrophy cascade processes can be considered. For the spectrum $\Omega(k)$, the Kolmogorov reasoning can thus be invoked, which leads to search an expression of the form

$$\Omega(k) \sim \epsilon_\omega^\alpha \, k^\beta$$

The dimensional analysis then provides $\alpha = 2/3$ and $\beta = -1$. Remembering relation $\Omega(k) = k^2 E(k)$, one can then obtain the kinetic energy spectrum

$$E(k) \sim \epsilon_\omega^{2/3} \, k^{-3}$$

The direct numerical simulations provide interesting details. Herring et al. [162] have studied the transfer function $T(k)$ of kinetic energy, reproduced in Fig. 7.13. It can clearly be seen that only the large structures are provided with energy. This phenomenon, characteristic of the 2-D case, is called inverse energy cascade.

When turbulence is properly forced around an average wavenumber, as in the analytical approach of Kraichnan [164] or in numerical simulations [157, 160, 161, 168], a double cascade phenomenon is visible: the one of type enstrophy towards small structures and the one of type kinetic energy towards large structures as illustrated in Fig. 7.14. Note that the region in $k^{-5/3}$ corresponds to an inverse energy cascade in 2-D, and not to a direct cascade as in 3-D. Note also the very useful result brought by numerical simulations since dimensional analysis only gives power laws without providing the direction of transfers.

Also, the behaviour of two eddies, whether they are co-rotating or counter-rotating, was already discussed in Sect. 5.4 for the case of the mixing layer. The calculations

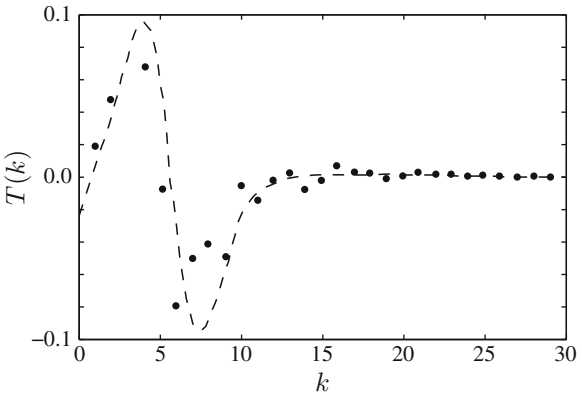

Fig. 7.13 Dimensionless spectral energy transfer rate in 2-D turbulence for $Re_{L_f} = 58.6$ in a periodic square of side 2π (test case I), • numerical simulation, − − − test-field model from Herring et al. [162]. Note the inverse cascade of energy towards large structures, at variance with 3-D turbulence (refer to Fig. 7.7)

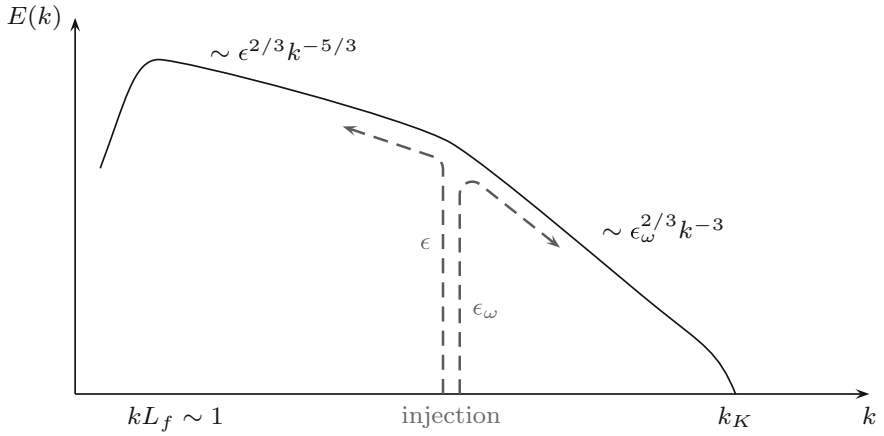

Fig. 7.14 Double energy cascade in forced 2-D turbulence at high Reynolds number, ϵ is the dissipation of kinetic energy and ϵ_ω is the dissipation of enstrophy. According to Kolmogorov similarity, the first inverse cascade obeys a $k^{-5/3}$ law, and the second cascade a k^{-3} law. For the $k^{-5/3}$ law, the Kolmogorov constant is of the order of 10 at variance with 1.5 for 3-D turbulence. The new limit associated with the k^{-3} law is given by $k_K = (\epsilon_\omega/\nu^3)^{1/6}$. From Lesieur [167]

of Couder and Basdevant [159] for a plane wake have also shown the coalescence of two co-rotating whirlwinds and the fact that two counter-rotating vortices form a dipole by mutual inductance, and move away very rapidly along almost straight trajectories. This phenomenon is also observed in Fig. 5.7 for the 2-D simulation of flow separation behind a rounded leading edge. For isotropic turbulence, it is

not impossible that a similar behaviour may appear at certain times, only due to a random arrangement of the vortices which will make them behave one way or the other. This problem, linked to internal intermittence and still pending, is well described in Lesieur [14].

In laboratory experiments, the tests require important confinements, as in the soap film by Couder [158], and Couder and Basdevant [159], the application of an intense magnetic field by Sommeria [169], or the effect of a strong rotation by Hopfinger [163]. The two-dimensional turbulence caught the attention of geo- and astrophysicists as the circumferential extension of the flow is easily 100 times larger than its thickness, permitting the tangential movements to become preponderant.

7.8 Fourier Transform of the Navier-Stokes Equations⋆

To develop more sophisticated closures, the Navier-Stokes equations expressed in wavenumber space are often used. Let us first remember that the Navier-Stokes equations when written in physical space, for an incompressible turbulent field without mean velocity, are

$$\left\{\begin{array}{l} \dfrac{\partial u_i'}{\partial x_i} = 0 \\ \dfrac{\partial u_i'}{\partial t} + \dfrac{\partial u_i' u_j'}{\partial x_j} = -\dfrac{\partial p^\star}{\partial x_i} + \nu \dfrac{\partial^2 u_i'}{\partial x_j \partial x_j} \end{array}\right. \quad \text{where} \quad p^\star = \frac{p'}{\rho}$$

and that the velocity field can be represented by the three-dimensional Fourier integral

$$u_i'(\boldsymbol{x}, t) = \int_{\mathrm{R}^3} \hat{u}_i(\boldsymbol{k}, t) e^{i\boldsymbol{k}\cdot\boldsymbol{x}} d\boldsymbol{k}$$

The Navier-Stokes equations in wavenumber space can therefore be written

$$\left\{\begin{array}{l} i k_i \hat{u}_i = 0 \\ \dfrac{\partial \hat{u}_i}{\partial t} + i k_j \widehat{u_i u_j} = -i k_i \hat{p} - \nu k^2 \hat{u}_i \end{array}\right.$$

The second equation can be simplified. Particularly, the pressure term $\hat{p}$ can be eliminated using Poisson's equation (1.5) seen in Chap. 1, that is

$$\frac{\partial^2 p'}{\partial x_k \partial x_k} = -\frac{\partial^2 u_j' u_l'}{\partial x_j \partial x_l}$$

The Fourier transform gives $k^2\hat{p} = -k_j k_l \widehat{u_j u_l}$. Hence,

$$\left(\frac{\partial}{\partial t} + \nu k^2\right)\hat{u}_i = -ik_j\widehat{u_i u_j} + ik_i\frac{k_j k_l}{k^2}\widehat{u_j u_l}$$
$$= -ik_j\left(\delta_{il} - \frac{k_i k_l}{k^2}\right)\widehat{u_j u_l}$$
$$= -ik_j P_{il}(\boldsymbol{k})\widehat{u_j u_l} \tag{7.23}$$

where the tensor $P_{ij}(\boldsymbol{k}) = \delta_{ij} - k_i k_j/k^2$ is introduced. This operator projects any vector $\boldsymbol{q}$ in a plane perpendicular to $\boldsymbol{k}$, that is $P_{ij}(\boldsymbol{k})q_i\, k_j = 0$. The nonlinear term $\widehat{u_j u_l}$ is still to be evaluated. By definition of the inverse Fourier transform given in expression (6.8)

$$\widehat{u_j u_l}\,(\boldsymbol{k}) = \frac{1}{(2\pi)^3}\int u_j'(\boldsymbol{x})u_l'(\boldsymbol{x})e^{-i\boldsymbol{k}\cdot\boldsymbol{x}}d\boldsymbol{x}$$

and, besides, it is also known that

$$\begin{cases} u_j'(\boldsymbol{x}) = \displaystyle\int \hat{u}_j(\boldsymbol{p})e^{i\boldsymbol{p}\cdot\boldsymbol{x}}d\boldsymbol{p} \\ u_l'(\boldsymbol{x}) = \displaystyle\int \hat{u}_l(\boldsymbol{q})e^{i\boldsymbol{q}\cdot\boldsymbol{x}}d\boldsymbol{q} \end{cases}$$

Hence,

$$\widehat{u_j u_l}\,(\boldsymbol{k}) = \iiint \hat{u}_j(\boldsymbol{p})\hat{u}_l(\boldsymbol{q})\underbrace{\frac{1}{(2\pi)^3}e^{-i(\boldsymbol{k}-\boldsymbol{p}-\boldsymbol{q})\cdot\boldsymbol{x}}d\boldsymbol{x}}_{\delta(\boldsymbol{k}-\boldsymbol{p}-\boldsymbol{q})}\, d\boldsymbol{p}\, d\boldsymbol{q}$$

Finally, the Navier-Stokes equation in the wavenumber space can be written as

$$\left(\frac{\partial}{\partial t} + \nu k^2\right)\hat{u}_i(\boldsymbol{k}) = -ik_j P_{il}\,(\boldsymbol{k})\iint \hat{u}_j(\boldsymbol{p})\hat{u}_l(\boldsymbol{q})\delta(\boldsymbol{k}-\boldsymbol{p}-\boldsymbol{q})\, d\boldsymbol{p}\, d\boldsymbol{q}$$
$$= -\frac{i}{2}P_{ijl}(\boldsymbol{k})\iint \hat{u}_j(\boldsymbol{p})\hat{u}_l(\boldsymbol{q})\delta(\boldsymbol{k}-\boldsymbol{p}-\boldsymbol{q})\, d\boldsymbol{p}\, d\boldsymbol{q} \tag{7.24}$$

where the tensor $P_{ijl}(\boldsymbol{k}) = k_l P_{ij}(\boldsymbol{k}) + k_j P_{il}(\boldsymbol{k})$ is introduced to render the expression symmetrical. The time evolution of the Fourier contribution $\hat{u}_i(\boldsymbol{k}, t)$ is therefore due both to its dissipation and to its nonlinear interaction with two other wavenumbers $\boldsymbol{p}$ and $\boldsymbol{q}$ such that $\boldsymbol{k} = \boldsymbol{p} + \boldsymbol{q}$. Such a group of three is called a triad and can be represented by triangles which can take various shapes as illustrated in Fig. 7.15. Equation (7.24) shows again, under a different form that it is possible, for a fixed $\boldsymbol{k}$, to excite larger wavenumbers, but also smaller ones. Triads have been introduced by Batchelor [84] and Kraichnan [165, 186].

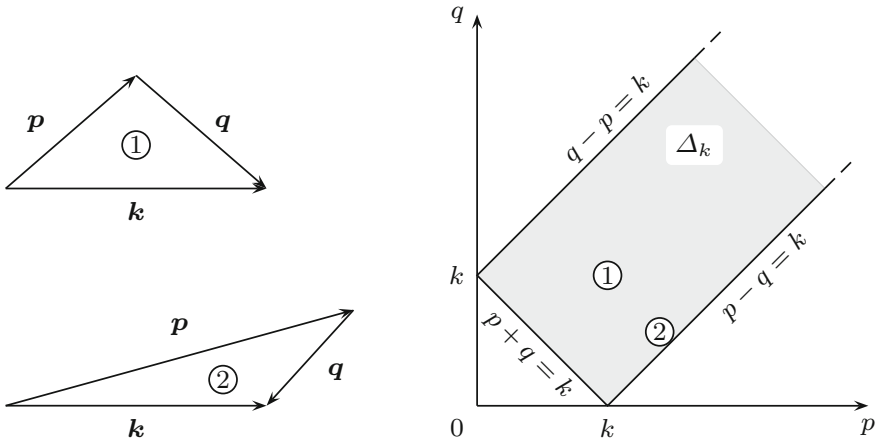

Fig. 7.15 Sketch of triads where $\boldsymbol{k} = \boldsymbol{p}+\boldsymbol{q}$. For a given wavenumber with modulus $\boldsymbol{k}$, the moduli p and q of wavenumbers $\boldsymbol{p}$ and $\boldsymbol{q}$ must lie in the gray domain Δ_k, defined by $|p-q| \leq k \leq p+q$

7.9 Closure with the EDQNM Hypothesis⋆

Equation (7.24) is the starting point of more sophisticated closures than the ones where spectrum $E(k,t)$ is considered. Indeed an expression of the triad interactions directly responsible for the transfer term $T(k,t)$ in Lin equation (7.7) is now searched for. One of the most common hypotheses to close the problem is the EDQNM (Eddy-Damped Quasi-Normal Markovian) hypothesis. In this paragraph, an overview of the emergence of this approach is given.

First of all a description of the time evolution of the correlation $\overline{\hat{u}_i(\boldsymbol{k})\hat{u}_k(\boldsymbol{p})}$ between the spectral contributions of two independent vectors $\boldsymbol{k}$ and $\boldsymbol{p}$ is established. The reason to consider $\overline{\hat{u}_i(\boldsymbol{k})\hat{u}_k(\boldsymbol{p})}$ is that this quantity is linked to the spectral tensor $\phi_{ik}(\boldsymbol{k})$, see Sect. 6.1.3, by the relation

$$\overline{\hat{u}_i(\boldsymbol{k})\hat{u}_k(\boldsymbol{p})} = \phi_{ik}(\boldsymbol{k})\delta(\boldsymbol{k}+\boldsymbol{p}) \tag{7.25}$$

and then linked to the kinetic energy spectrum E using expression (6.31).

As previously stated, omitting the time dependency to simplify notations, it can be inferred from relation (7.24) that

$$\left[\frac{\partial}{\partial t} + \nu(k^2+p^2)\right]\overline{\hat{u}_i(\boldsymbol{k})\hat{u}_k(\boldsymbol{p})} = -\frac{i}{2}P_{ijl}(\boldsymbol{k}) \iint_{\boldsymbol{l}+\boldsymbol{r}=\boldsymbol{k}} \overline{\hat{u}_j(\boldsymbol{l})\hat{u}_l(\boldsymbol{r})\hat{u}_k(\boldsymbol{p})}\, d\boldsymbol{l}\, d\boldsymbol{r} - \frac{i}{2}P_{kjl}(\boldsymbol{p}) \iint_{\boldsymbol{l}+\boldsymbol{r}=\boldsymbol{p}} \overline{\hat{u}_j(\boldsymbol{l})\hat{u}_l(\boldsymbol{r})\hat{u}_i(\boldsymbol{k})}\, d\boldsymbol{l}\, d\boldsymbol{r} \tag{7.26}$$

To determine the time evolution of $\overline{\hat{u}_i(\boldsymbol{k})\hat{u}_k(\boldsymbol{p})}$, the triple velocity correlations appearing in (7.26) must be closed. Millionshchikov [131] and Proudman and Reid [143] have suggested the introduction of a hypothesis of quasi-normality, which

states the following. It is assumed that the four random variables $\hat{u}_i$, $\hat{u}_j$, $\hat{u}_k$ and $\hat{u}_l$ follow a Gaussian distribution for the fourth-order correlation

$$\overline{\hat{u}_i\hat{u}_j\hat{u}_k\hat{u}_l} = \overline{\hat{u}_i\hat{u}_j}\,\overline{\hat{u}_k\hat{u}_l} + \overline{\hat{u}_i\hat{u}_k}\,\overline{\hat{u}_j\hat{u}_l} + \overline{\hat{u}_i\hat{u}_l}\,\overline{\hat{u}_j\hat{u}_k} \tag{7.27}$$

but without implying that the third-order $\overline{\hat{u}_i\hat{u}_j\hat{u}_k}$ be zero, which would normally be the case for Gaussian random variables. This permits the retention of a transfer term not equal to zero in Eq. (7.26). Would it not be the case, turbulence could only decrease over time because of molecular viscosity.

To close the double correlations Eq. (7.26), an additional equation concerning these triple correlations is then written. This equation of course involves fourth-order correlations, but these can be expressed in terms of double correlations using (7.27). The equation of triple correlations is built similarly to (7.26),

$$\begin{aligned}\left[\frac{\partial}{\partial t} + \nu(k^2+p^2+q^2)\right]\overline{\hat{u}_i(\boldsymbol{k})\hat{u}_k(\boldsymbol{p})\hat{u}_m(\boldsymbol{q})} = \\ -\frac{i}{2}P_{ijl}(\boldsymbol{k})\iint_{\boldsymbol{l}+\boldsymbol{r}=\boldsymbol{k}}\overline{\hat{u}_j(\boldsymbol{l})\hat{u}_l(\boldsymbol{r})\hat{u}_k(\boldsymbol{p})\hat{u}_m(\boldsymbol{q})}\,d\boldsymbol{l}\,d\boldsymbol{r} \\ -\frac{i}{2}P_{kjl}(\boldsymbol{p})\iint_{\boldsymbol{l}+\boldsymbol{r}=\boldsymbol{p}}\overline{\hat{u}_j(\boldsymbol{l})\hat{u}_l(\boldsymbol{r})\hat{u}_i(\boldsymbol{k})\hat{u}_m(\boldsymbol{q})}\,d\boldsymbol{l}\,d\boldsymbol{r} \\ -\frac{i}{2}P_{mjl}(\boldsymbol{q})\iint_{\boldsymbol{l}+\boldsymbol{r}=\boldsymbol{q}}\overline{\hat{u}_j(\boldsymbol{l})\hat{u}_l(\boldsymbol{r})\hat{u}_i(\boldsymbol{k})\hat{u}_k(\boldsymbol{p})}\,d\boldsymbol{l}\,d\boldsymbol{r}\end{aligned} \tag{7.28}$$

Expanding the fourth-order correlations with (7.27), the previous equation can be written as

$$\left[\frac{\partial}{\partial t} + \nu(k^2+p^2+q^2)\right]\overline{\hat{u}_i(\boldsymbol{k})\hat{u}_k(\boldsymbol{p})\hat{u}_m(\boldsymbol{q})} = S_{ikm}(\boldsymbol{k},\boldsymbol{p},\boldsymbol{q},t)$$

where S_{ikm} is a function of the double velocity correlations, and where a fully symmetrical relationship $\boldsymbol{k}+\boldsymbol{p}+\boldsymbol{q}=0$ is used for the triad. This equation is then integrated to give

$$\begin{aligned}\overline{\hat{u}_i(\boldsymbol{k})\hat{u}_k(\boldsymbol{p})\hat{u}_m(\boldsymbol{q})} = \left.\overline{\hat{u}_i(\boldsymbol{k})\hat{u}_k(\boldsymbol{p})\hat{u}_m(\boldsymbol{q})}\right|_{t=0} e^{-\nu(k^2+p^2+q^2)t} \\ + \int_0^t S_{ikm}\left(\boldsymbol{k},\boldsymbol{p},\boldsymbol{q},t'\right)e^{-\nu(k^2+p^2+q^2)(t-t')}\,dt'\end{aligned} \tag{7.29}$$

and the factor $\nu(k^2+p^2+q^2)$ which affects S_{ikm} has the simple form of a damping due to viscous molecular dissipation. Now, Eq. (7.29) is injected in (7.26) to obtain an equation involving only $\overline{\hat{u}_i(\boldsymbol{k})\hat{u}_k(\boldsymbol{p})}$ and then the spectrum $E(k,t)$.

For a few years, the Millionshchikov assumption had been thought to be a valuable contribution. However, when computating facilities appeared, Eq. (7.29) would be solved numerically. A major drawback then appears, $E(k,t)$ becomes negative over

time. Even worse is the fact that this energy loss takes place in the region where the spectrum is at its maximum. Orszag [256] thus suggested increasing the damping of S_{ikm}, in other words to force the triple correlations to be less important. Assuming that the turbulence is initially Gaussian, Orszag wrote

$$\overline{\hat{u}_i(\boldsymbol{k})\hat{u}_k(\boldsymbol{p})\hat{u}_m(\boldsymbol{q})} = \int_0^t S_{ikm}(\boldsymbol{k},\boldsymbol{p},\boldsymbol{q},t')e^{-\eta(\boldsymbol{k},\boldsymbol{p},\boldsymbol{q},t')(t-t')}\,dt'$$

where

$$\eta(\boldsymbol{k},\boldsymbol{p},\boldsymbol{q},t) = \nu(k^2+p^2+q^2) + \eta_k(t) + \eta_p(t) + \eta_q(t)$$

The terms in η provide the desired additional damping for triple correlations in the most energetic part region of the spectrum. This new damping is defined by

$$\eta_k(t) = \lambda\sqrt{\int_0^k k'^2 E(k',t)dk'} \quad \text{with} \quad \lambda \simeq 0.218\, C_K^{3/2}$$

The constant λ is determined favoring a connection in the inertial zone. The time $1/\eta_k$ corresponds to the one introduced by Comte-Bellot and Corrsin [101] to characterize the deformation and rotation due to large structures. This new model is called the eddy-damped quasi-normal approximation (EDQN). It must be pointed out that it is still not ensured that $E(k,t)$ be positive.

The EDQN model can be further improved by introducing a memory or relaxing time of the turbulence, dependent on the three wavenumbers of the triad. This modification is based on the work by Leith [124]. The model is then called the Eddy-Damped Quasi-Normal Markovian approximation (EDQNM), and it is written for triple correlations that

$$\begin{aligned}\overline{\hat{u}_i(\boldsymbol{k})\hat{u}_k(\boldsymbol{p})\hat{u}_m(\boldsymbol{q})} &\simeq S_{ikm}(\boldsymbol{k},\boldsymbol{p},\boldsymbol{q},t)\int_0^t e^{-\eta(\boldsymbol{k},\boldsymbol{p},\boldsymbol{q},t')(t-t')}\,dt' \\ &\simeq \underbrace{\frac{1-e^{-\eta(\boldsymbol{k},\boldsymbol{p},\boldsymbol{q},t)}}{\eta(\boldsymbol{k},\boldsymbol{p},\boldsymbol{q},t)}}_{\theta_{kpq}(t)} S_{ikm}(\boldsymbol{k},\boldsymbol{p},\boldsymbol{q},t)\end{aligned}$$

where $\theta_{kpq}(t)$ represents a memory or relaxing time of the turbulence. This model ensures that the spectrum $E(k,t)$ stays positive, whatever the form of the function $\theta_{kpq}(t)$ is.

In the case of isotropic turbulence, using relation (7.25), it can be obtained for the time evolution of the spectrum of turbulent kinetic energy that

$$\frac{\partial E(k)}{\partial t} + 2\nu k^2 E(k) = \int_{\Delta_k} \theta_{kqp} E(q)(xy+z^3)\left[pk^2E(p) - p^3E(k)\right]\frac{dpdq}{pq} \tag{7.30}$$

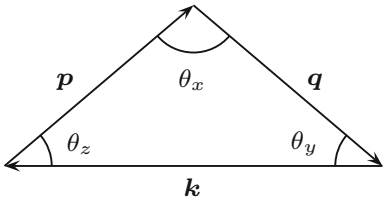

Fig. 7.16 Notations used for the triadic interaction $\boldsymbol{k}+\boldsymbol{p}+\boldsymbol{q}=0$ written in a symmetrical form, θ_x, θ_y and θ_z are the angles opposite to the vectors $\boldsymbol{k}$, $\boldsymbol{p}$ and $\boldsymbol{q}$, $x \equiv \cos\theta_x$, $y \equiv \cos\theta_y$ and $z \equiv \cos\theta_z$. For instance, $x = (p^2+q^2-k^2)/(2pq)$

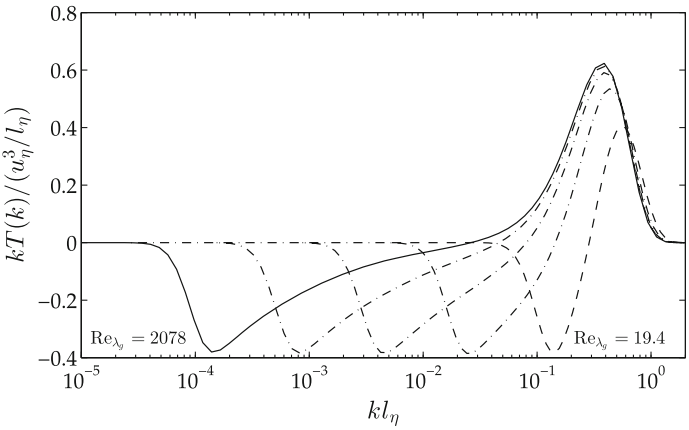

Fig. 7.17 Reynolds number effect on the k-weighted transfer term $T(k)$. Data are normalized by the Kolmogorov scales. Results obtained by EDQNM for $\mathrm{Re}_{\lambda_g} = 19.4$ (*dashed line*), 66.0, 209.1, 659.3 and 2078 (*solid line*). All *curves* merge around $kl_\eta \sim 1$. Also note that $T(k)$ is never zero in the inertial subrange. Courtesy of Touil and Bertoglio

where the integration domain Δ_k is illustrated in Fig. 7.15. The terms x, y and z are the cosinus of the internal angles of the triad, as illustrated in Fig. 7.16.

The closure with an EDQNM model accurately reproduces the decrease of a grid turbulence, as shown by Lesieur [126] and Cambon [94]. This approach is still in progress to take into account the anisotropy of homogeneous turbulence and the rotating effects of the flow [91–93, 96] or compressible effects [367]. The advantage of the EDQNM simulation is also the capacity to study turbulence with large Reynolds numbers [368], which cannot be undertaken easily by direct simulation. As an illustration, the evolution of the transfer term for different Reynolds numbers is shown in Fig. 7.17. The reader can refer to the works of Lesieur [14], and of Cambon and Sagaut [4] on this topic.

Chapter 8
Direct and Large Eddy Simulation of Turbulent Flows

An overview of high-fidelity numerical simulation techniques is presented in this chapter. Advantages and limitations are discussed for research or engineering purposes. These time-dependent approaches are distinguished from mean flow calculations based on the averaged Navier-Stokes equations, which are examined in the next chapter.

8.1 Direct Numerical Simulation

Direct Numerical Simulation (DNS) consists in solving as precisely as possible the complete fluid dynamics equations. The objective is ambitious, as all the scales forming the turbulent kinetic energy spectrum must be computed. The range to be covered can be assessed by taking the integral length scale L_f to estimate the larger ones and the Kolmogorov scale l_η to approximate the smaller ones, and then writing the ratio

$$\frac{L_f}{l_\eta} \sim \frac{L_f}{\nu^{3/4}\epsilon^{-1/4}} \sim \frac{L_f}{\nu^{3/4}(u'^3/L_f)^{-1/4}} \sim \mathrm{Re}_{L_f}^{3/4} \tag{8.1}$$

where $\mathrm{Re}_{L_f} \equiv u' L_f/\nu$. This ratio is proportional to the number of points necessary to build the mesh grid in one direction. The total number of mesh points n_{dof} required to describe all the scales involved in a turbulent spectrum is thus directly linked to the Reynolds number, and more precisely in three dimensions is proportional to

$$n_{\mathrm{dof}} \propto \mathrm{Re}_{L_f}^{9/4} \tag{8.2}$$

Despite the considerable progress in computing resources over the past six decades [234, 239] as illustrated in Fig. 8.1, it is still only possible to reach moderate values of the Reynolds number in direct numerical simulation. Let us consider the example of plane channel flow, a configuration often used for testing numerical simulations and

C. Bailly and G. Comte-Bellot, *Turbulence*, Experimental Fluid Mechanics,
DOI 10.1007/978-3-319-16160-0_8

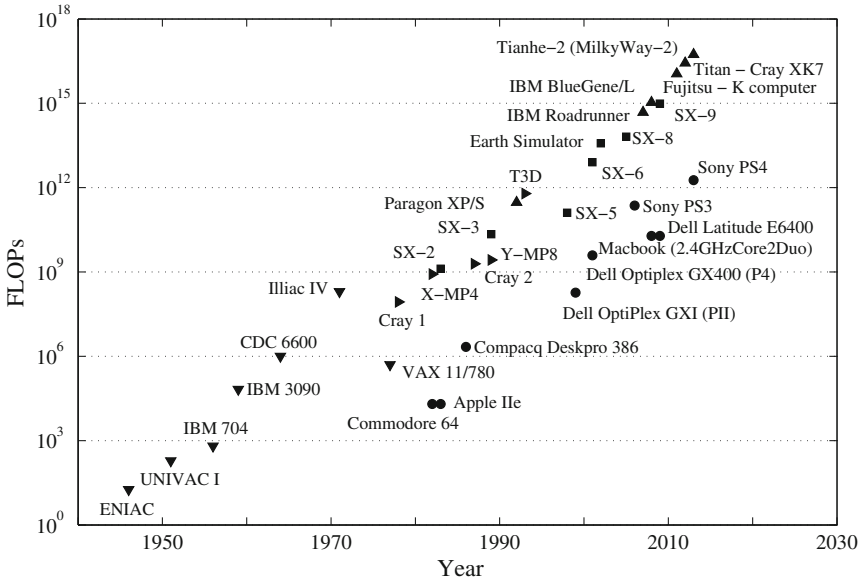

Fig. 8.1 Progress in computing power measured in FLOPs (floating point operations per second). Data from Nordhaus [254], Koomey [247] and the TOP500 project [258]

studying the development of turbulent boundary layers. The grid resolutions of some simulations are collected in Table 8.1. One of the first calculations was performed by Deardorff [286] on a CDC 6600 computer which is listed in Fig. 8.1. He used the largest number of grid points which could be stored in the high-speed memory of the best computer at the time, namely $n_{\mathrm{dof}} = 6720$. This simulation can be compared to the one of Kim et al. [629] using $n_{\mathrm{dof}} = 4 \times 10^6$ grid points and carried out on a Cray XMP. The physical domain is not exactly the same for the different numerical studies, but the width of the channel flow is always $2h$, and the transverse resolution can thus be examined to assess relation (8.1). From the values reported in Table 8.1, one sees that the law $n_2 \sim L_f/l_\eta \sim \mathrm{Re}_{L_f}^{3/4}$ giving the number of points in the wall-normal direction is clearly satisfied by all the different studies.

DNS can provide comprehensive views of turbulence dynamics and enables the assessment of numerous quantities which cannot be found experimentally such as correlations involving pressure. It is also instrumental in validating turbulence models in academic configurations. For industrial flows where Reynolds numbers are too high for a complete DNS, it is sometimes recommended to consider a numerical scale model at a slightly lower Reynolds number to get a reference solution under the assumption that physical mechanisms are preserved.

Table 8.1 Some numerical parameters used for the direct numerical simulation of a plane channel flow of width $2h$, see Fig. 3.1, $n_{\text{dof}} = n_1 \times n_2 \times n_3$, $\text{Re}_h = U_d h/\nu$ where U_d is the bulk velocity, and $\text{Re}^+ = u_\tau h/\nu$

Deardorff [286]	
$n_{\text{dof}} = 24 \times 20 \times 14 = 6720$	
Kim et al. [629]	
$n_{\text{dof}} = 192 \times 129 \times 160 \simeq 4 \times 10^6$	
$\text{Re}_h = 3300$, $\text{Re}^+ = 180$	$(\text{Re}^+)^{3/4}/n_2 \simeq 0.38$
Moser et al. [642]	
$n_{\text{dof}} = 384 \times 257 \times 384 \simeq 38 \times 10^6$	
$\text{Re}_h = 10950$, $\text{Re}^+ = 590$	$(\text{Re}^+)^{3/4}/n_2 \simeq 0.46$
Laadhari [635]	
$n_{\text{dof}} = 512 \times 385 \times 512 \simeq 101 \times 10^6$	
$\text{Re}_h = 20100$, $\text{Re}^+ = 1000$	$(\text{Re}^+)^{3/4}/n_2 \simeq 0.46$
Hoyas and Jiménez [621]	
$n_{\text{dof}} = 6144 \times 633 \times 4608 \simeq 17.9 \times 10^9$	
$\text{Re}_h = 43600$, $\text{Re}^+ = 2003$	$(\text{Re}^+)^{3/4}/n_2 \simeq 0.47$

Note that the longitudinal and spanwise lengths of the computational domain are not the same in the different studies; for instance $4\pi h \times 2h \times 2\pi h$ in Ref. [629] and $8\pi h \times 2h \times 3\pi h$ in Ref. [621]

8.1.1 Numerical Methods

Two main families of numerical methods are used in DNS, namely pseudo-spectral formulations and high-order finite difference schemes. The accuracy of the former to compute spatial derivatives is usually unbeatable since the problem is solved in the spectral space. However, this approach can only be applied simply in periodic flow directions, for example in a decaying turbulence box using Fourier series, or in the transverse direction of a channel flow using orthogonal polynomials. The geometry therefore needs to remain essentially parallelepipedic and be associated with elementary boundary conditions. An alternative is to consider high-order finite difference algorithms, to simulate compressible turbulent flows for instance. A short overview of these two approaches is given in what follows.

8.1.1.1 Pseudo-Spectral Methods

Orszag and Patterson [255, 461, 464] were among the first in the 1970s to make use of the fast Fourier transform for solving fluid dynamics equations. A periodic flow in the three directions is assumed here. The turbulent flow is also homogeneous and incompressible. In the physical space, the Navier-Stokes equation is then written as

$$\frac{\partial \boldsymbol{u}}{\partial t} = \boldsymbol{u} \times \boldsymbol{\omega} - \nabla\left(\frac{p}{\rho} + \frac{1}{2}u^2\right) + \nu \nabla^2 \boldsymbol{u} \tag{8.3}$$

with $\nabla \cdot \boldsymbol{u} = 0$. By taking its Fourier transform and after some rearrangement, one gets

$$\frac{\partial \widehat{\boldsymbol{u}}}{\partial t} = \boldsymbol{P} \cdot \widehat{\boldsymbol{u} \times \boldsymbol{\omega}} - \nu k^2 \widehat{\boldsymbol{u}} \qquad \text{where} \quad P_{ij}(\boldsymbol{k}) = \delta_{ij} - \frac{k_i k_j}{k^2} \tag{8.4}$$

is the projection operator already introduced in Sect. 7.8. It is recalled that $\boldsymbol{P}(\boldsymbol{k})$ projects any vector in a plane perpendicular to $\boldsymbol{k}$ in the solenoidal subspace. Moreover, Eq. (7.23) obtained in that same section is identical to Eq. (8.4) noting that $\boldsymbol{u} \cdot \nabla \boldsymbol{u} = \nabla \left(\boldsymbol{u}^2/2\right) + \boldsymbol{\omega} \times \boldsymbol{u}$. A turbulence box of size L with a regular grid in the three directions is considered, $\boldsymbol{x_l} = (l_1 \Delta x_1, l_2 \Delta x_2, l_3 \Delta x_3)$, where l_i is an integer between 0 and $N_i = L/\Delta x_i$. The periodic boundary conditions are enforced by

$$\boldsymbol{u}\,(\boldsymbol{x} + L\boldsymbol{q}, t) = \boldsymbol{u}\,(\boldsymbol{x}, t)$$

where $\boldsymbol{q}$ is any arbitrary integer vector. To simplify, the mesh is assumed to be identical in the three directions, that is $\Delta x_i = \Delta = L/N$. The smallest wavenumber encountered in the box is $k_L = 2\pi/L$, while the largest resolved wavenumber is π/Δ corresponding to two points per wavelength as illustrated in Fig. 8.2. The velocity vector is then expanded as a series of N^3 Fourier modes

$$\boldsymbol{u}\,(\boldsymbol{x_l}, t) = \sum_{n_1} \sum_{n_2} \sum_{n_3} \hat{\boldsymbol{u}}(\boldsymbol{k_n}, t) e^{i \boldsymbol{k_n} \cdot \boldsymbol{x_l}} \qquad \text{where} \quad -\frac{N}{2} \leq n_i \leq \frac{N}{2} - 1 \tag{8.5}$$

and with $\boldsymbol{k_n} = \boldsymbol{n} k_L = (n_1, n_2, n_3) k_L$. The Fourier coefficients $\hat{\boldsymbol{u}}_{\boldsymbol{n}}$ are given by the following inverse equation, where all the N^3 collocation points $\boldsymbol{x_l}$ are involved

$$\hat{\boldsymbol{u}}(\boldsymbol{k}_n, t) = \frac{1}{N^3} \sum_{l_1} \sum_{l_2} \sum_{l_3} \boldsymbol{u}\,(\boldsymbol{x_l}, t)\, e^{-i \boldsymbol{k_n} \cdot \boldsymbol{x_l}}$$

As noted previously, there is no numerical approximation of the wavenumber when calculating the space derivatives $\boldsymbol{u}$, which explains the great precision of spectral methods. The viscous term is exactly integrated without any associatedstability

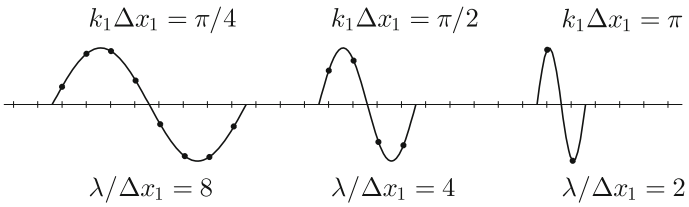

Fig. 8.2 Representation of the number of points per wavelength $\lambda/\Delta x_1$ for a given dimensionless wavenumber $k_1 \Delta x_1$ on a one-dimensional regular grid of spacing Δx_1

condition and in general, a pseudo-spectral method must be implemented to calculate the nonlinear convective term in the physical space. One of the most widely used numerical algorithms is that developed by Rogallo [465], refer also to the reviews by Rogallo and Moin [466] and Hussaini and Zang [460]. The exponential factor in (8.5) is not modified when the index n_i becomes $n_i \pm pN$ where p is any integer, leading to aliasing errors. They can be properly removed [464] by noting, however, that the computational time is significantly increased [467]. Time advancement is usually performed explicitly thanks to a second-order Adams-Bashforth scheme or a self-starting Runge-Kutta scheme, by enforcing the incompressibility condition [466]. Finally, stationary turbulence can be simulated by adding a forcing at each time step [459, 462].

8.1.1.2 Finite Difference Schemes

Let us consider a one-dimensional uniform mesh of spacing Δx_1. An implicit finite-difference approximation f'_i of the first order spatial derivative $\partial f/\partial x_1$ at grid point $x_1 = i\Delta x_1$ can be obtained through the following expression

$$\beta f'_{i-2} + \alpha f'_{i-1} + f'_i + \alpha f'_{i+1} + \beta f'_{i+2} = c\frac{f_{i+3} - f_{i-3}}{6\Delta x_1} + b\frac{f_{i+2} - f_{i-2}}{4\Delta x_1} + a\frac{f_{i+1} - f_{i-1}}{2\Delta x_1} \tag{8.6}$$

based on a Padé-type development, as proposed by Lele [248]. The constants α, β and a, b, c are calculated from a Taylor series of the previous expression to reach the maximum order for a given scheme. An α-family of 6th-order tridiagonal ($\beta = 0$) schemes is obtained with the relations $a = (\alpha + 9)/6$, $b = (32\alpha - 9)/15$ and $c = (-3\alpha+1)/10$ on the coefficients for instance. Two particular values are however of interest, $\alpha = 1/3$ leading to a compact 5-point stencil widely used in computational fluid dynamics, and $\alpha = 3/8$ allowing to reach the 8th order.

Numerical dissipation and dispersion, namely errors in the amplitude and in the propagation speed of the waves, affect the phase velocity for an harmonic plane wave and the group velocity for a wavepacket. To characterize these errors, the exact wavenumber $\boldsymbol{k}$ defined by the Fourier transform of $\partial f/\partial x_j$, that is

$$\widehat{\partial f/\partial x_j} = ik_j\hat{f}$$

can be compared to its approximation $\boldsymbol{k}^s$ provided by the numerical scheme. By taking the Fourier transform of (8.6), the following expression of the effective wavenumber can be derived

$$k_1^s\Delta x_1 = \frac{a\sin(k_1\Delta x_1) + (b/2)\sin(2k_1\Delta x_1) + (c/3)\sin(3k_1\Delta x_1)}{1 + 2\alpha\cos(k_1\Delta x_1) + 2\beta\cos(2k_1\Delta x_1)}$$

Optimized schemes can then be obtained by reducing the formal order of accuracy of the scheme (8.6), and by using the remaining degrees of freedom to minimize the relative error of the modified wavenumber, for instance

$$\int |k_1^s \Delta x_1 - k_1 \Delta x_1| \, d\ln(k_1 \Delta x_1)$$

Explicit schemes are obtained as α goes to zero, the choice $a = 1$, $b = c = 0$ corresponding to the 2nd-order standard scheme and $a = 4/3$, $b = -1/3$, $c = 0$ to the 4th-order scheme. An optimization strategy can be also developed for these schemes, more details can be found in Tam [263] and Bogey and Bailly [236]. Accuracies of the standard and optimized schemes considered above are provided in Table 8.2 with respect to the phase and group velocities. The highest value taken by the modified wavenumber is of importance to determine the stability condition for time advancement, and the last column is an indicator of the scheme's efficiency.

The effective wavenumber is also plotted in Fig. 8.3, as a function of the exact wavenumber in linear scale and as a function of the number of points per wavelength in logarithmic scales. As expected, the error is maximum with $E_{v_\varphi} = 1$ for grid-to-grid oscillations, that is $k_1 \Delta x_1 = \pi$ or $\lambda/\Delta x_1 = 2$, and generally decreases as $\lambda/\Delta x_1$ increases. For the standard finite differences, the decrease is however much more rapid when the order of the scheme becomes higher. For $\lambda/\Delta x_1 = 20$ for example,

Table 8.2 Accuracy limits of some standard central finite-difference schemes (CFD), OFD are the optimized schemes of Bogey and Bailly [236], CoFD is the tridiagonal compact scheme of Lele [248] for $\alpha = 1/3$ (6th-order) and $\alpha = 3/8$ (8th-order), CoFD opt. is the pentadiagonal optimized 4th-order scheme of Lele [248]

Scheme	$E_{v_\varphi} \leq 5 \times 10^{-5}$		$E_{v_g} \leq 5 \times 10^{-4}$			
	$k_1 \Delta x_1\|_{\max}$	$\lambda/\Delta x_1\|_{\min}$	$k_1 \Delta x_1\|_{\max}$	$\lambda/\Delta x_1\|_{\min}$	$k_{\max} \Delta x_1$	$k_{v_\varphi}/k_{\max}$
CFD 2nd-order	0.0986	63.7	0.0323	194.6	1.0000	0.10
CFD 4th-order	0.3439	18.3	0.2348	26.8	1.3722	0.25
CFD 6th-order	0.5857	10.7	0.4687	13.4	1.5860	0.37
CFD 8th-order	0.7882	8.0	0.6704	9.4	1.7306	0.46
CFD 10th-order	0.9550	6.6	0.8380	7.5	1.8374	0.52
CFD 12th-order	1.0929	5.7	0.9768	6.4	1.9208	0.57
OFD 11-pt 4th-order	1.3530	4.6	0.8458	7.4	1.9836	0.68
OFD 13-pt 4th-order	1.3486	4.7	0.7978	7.9	2.1354	0.63
CoFD 6th-order	0.8432	7.5	0.7201	8.7	1.9894	0.42
CoFD 8th-order	1.1077	5.7	0.9855	6.4	2.1334	0.52
CoFD opt. 4th-order	2.4721	7.3	0.7455	8.4	2.6348	0.33

The error criteria on phase and group velocities are defined by $E_{v_\varphi} = |k_1^s \Delta x_1 - k_1 \Delta x_1|/\pi \leq 5 \times 10^{-5}$ and $E_{v_g} = |\partial k_1^s / \partial k_1 - 1| \leq 5 \times 10^{-4}$ respectively. Accuracy limits are equally provided in terms of point-per-wavelength resolution ($\lambda/\Delta x_1$). The highest modified wavenumber $k_{\max} \Delta x_1 = k_1^s \Delta x_1\big|_{\max}$ corresponding to a zero group velocity and the ratio between the highest well-resolved wavenumber k_φ and $k_{\max}$ are also given

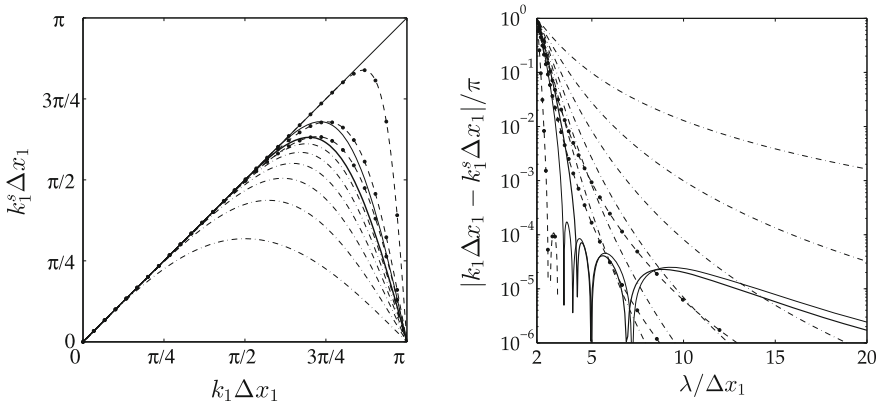

Fig. 8.3 Effective wavenumber $k_1^s \Delta x_1$ as a function of the exact wavenumber $k_1 \Delta x_1$ for spatial differencing methods: *left*, linear representation and *right*, logarithmic scales. –·–·– 2nd, 4th, 6th, 8th, 10th and 12th-order central differences (CFD); –•– tridiagonal 6th-order compact 5-point ($\alpha = 1/3$) and 8th-order ($\alpha = 3/8$) CoFD schemes, pentadiagonal optimized 4th-order scheme (CoFD opt.) of Lele [248]; optimized —— 11-point and —— 13-point schemes (OFD) of Bogey and Bailly [236]

the phase-velocity error E_{v_φ} is around 2×10^{-3} for 2nd order, and 4×10^{-5} for 4th order, but below 10^{-6} for 6th order. With respect to the corresponding standard schemes, the use of optimized schemes allows the reduction in phase errors for short waves, typically with $4 \leq \lambda/\Delta x_1 \leq 10$. As an illustration, the standard 11-point 10th order scheme can be compared to the optimized 11-point 4th-order scheme of Bogey and Bailly [236]. For an explicit $(2n + 1)$-point centered explicit stencil, the maximum order for the truncation error is $2n$.

Finally, it is important to emphasize that accurate numerical schemes, with low dispersive and dissipative errors, are required both in space and time. For time advancement, Runge-Kutta algorithms can also be optimized in Fourier space, as proposed by Berland et al. [233] For frequencies up to four points per wavelength, that is $\omega \Delta t \leq \pi/2$, there are more than three orders of magnitude between the dissipation of the classical Runge-Kutta scheme and the optimized low-storage scheme of Berland et al., both providing a formal 4th-order integration. The time-step range of stability is also increased. The reader can refer to the reviews by Ekaterinaris [243] and Pirozzoli [257], and also refer to associated topics such as boundary conditions [242].

8.1.2 Some Applications of DNS

Several examples of DNS results have already been introduced throughout the text. The case of channel flows for instance is illustrated by Fig. 1.5, is discussed in Sect. 2.6 and recent DNS are quoted in Table 8.1. Topics of interest often stem

from the connection between turbulence and another field of physics. Turbulent combustion, turbulent two-phase flows, acoustic radiation of turbulent flows, magnetohydrodynamics or the use of active control in fluid mechanics can be mentioned. Moin and Mahesh [252] can be referred to for a fairly large overview of the use of DNS in research.

Various studies have been performed for homogeneous and isotropic turbulence in a periodic box, and a review of recent results obtained by DNS can be found in Ishihara, Gotoh and Kaneda [111]. Another model flow to study transition to turbulence through the generation of small turbulent structures by vortex stretching was introduced by Taylor and Green [89, 154]. The generalized Taylor-Green vortex flow is defined as the periodic flow which develops from the following initial solenoidal field

$$\begin{cases} u_1(\boldsymbol{x},0) = (2/\sqrt{3})\sin(\gamma + 2\pi/3)\sin(x_1)\cos(x_2)\cos(x_3) \\ u_2(\boldsymbol{x},0) = (2/\sqrt{3})\sin(\gamma - 2\pi/3)\cos(x_1)\sin(x_2)\cos(x_3) \\ u_3(\boldsymbol{x},0) = (2/\sqrt{3})\sin(\gamma)\cos(x_1)\cos(x_2)\sin(x_3) \end{cases} \tag{8.7}$$

written in non-dimensional form, where the shape factor γ determines the orientation of the initial anisotropic vortex structure. The pressure field can be analytically calculated by solving the Poisson equation (1.5). Two snapshots of the flow computed by DNS are shown in Fig. 8.4. A pseudo-spectral algorithm is used, and more numerical details can be found in Fauconnier et al. [293] The Taylor-Green flow satisfies numerous symmetries, in particular any cross-section plane defined by $x_i = n\pi$ with n integer is never crossed by the flow at any time. This property can be qualitatively distinguished in the reported DNS results. The turbulent flow reaches an isotropic state for $t \simeq 7$ with no memory of the initial conditions for a sufficiently high Reynolds number, namely $\mathrm{Re} \simeq 1 \times 1/\nu \geq 1000$, and the dissipation peak occurs

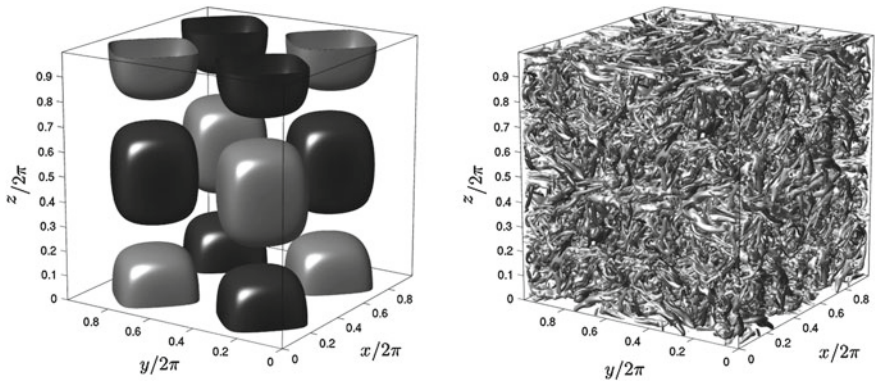

Fig. 8.4 Taylor-Green vortex flow at Re = 3000 on a 384^3 grid at time $t = 0$, see expression (8.7), and DNS at $t = 18$. Turbulent vortex structures are identified with the λ_2 criterion of Jeong and Hussain [487] and are colored by z-vorticity with $(x, y, z) = (x_1, x_2, x_3)$. From Fauconnier et al. [293]

around $t \simeq 9$. Since there is no forcing, the turbulence eventually decays when t goes to infinity. This well-defined configuration can be used to evaluate turbulence models used in large-eddy simulation for instance [293].

8.2 Large Eddy Simulation

In Large Eddy Simulation (LES), the governing equations are obtained by applying a spatial filter to the mass, momentum and energy equations. Only the large scales of the turbulent flow are calculated, and effects of the smallest ones must be taken into account through the addition of a subgrid scale model. The constraint imposed by the Reynolds number on the number of grid points (8.2) can thus be partly relaxed with respect to DNS. The filtering operation is first defined, and the filtered Navier-Stokes equations are then derived. Numerous subgrid scale models have been developed over the last decades. By following Sagaut [339], they can be classified into functional or structural models. Models based on a turbulent eddy viscosity and on an explicit relaxation filtering are here presented. Hybrid approaches such as Detached Eddy Simulation (DES) are finally briefly introduced. The filtered Navier-Stokes equations for a compressible turbulent flow are provided in Sect. 8.4.

8.2.1 Spatial Filtering

In LES, the first element to be introduced is the filtering procedure, which separates the scales to be solved explicitly from those to be modelled, the so-called subgrid scales. The filtered field is mathematically defined by a convolution product in the physical space [312]

$$\bar{u}_i(\boldsymbol{x}, t) = \int G(\boldsymbol{x}, \boldsymbol{y})\, u_i(\boldsymbol{x} - \boldsymbol{y}, t)\, d\boldsymbol{y} = G \star u_i \tag{8.8}$$

where $\bar{u}_i$ is the filtered velocity field, and where the low-pass filter G must satisfy the following normalisation constraint

$$\int G(\boldsymbol{x}, \boldsymbol{y})\, d\boldsymbol{y} = 1 \tag{8.9}$$

This filtering operation is *a priori* not idempotent, that is $\overline{\bar{u}_i} \neq \bar{u}_i$. In other words, the filter G is in general not a projector. Moreover, the derivative operation does not commute with the filtering operation except for a constant filter width in the whole computational domain, that is for a homogeneous filter [302, 303]. For instance, the box or top-hat filter consists in averaging on the mesh size $\Delta = (\Delta x_1 \Delta x_2 \Delta x_3)^{1/3}$, and is defined by

$$G(\boldsymbol{x}-\boldsymbol{y}) = \begin{cases} 1/\Delta^3 & \text{if} \quad |x_i - y_i| \leq \Delta/2 \\ 0 & \text{otherwise.} \end{cases} \tag{8.10}$$

This filter is uniform only on a regular grid. Two other classical filters can be mentioned. The first is the Gaussian filter given by

$$G(\boldsymbol{x}-\boldsymbol{y}) = \left(\frac{6}{\pi}\right)^{3/2} \frac{1}{\Delta^3} \exp\left(-6\frac{(\boldsymbol{x}-\boldsymbol{y})^2}{\Delta^2}\right)$$

The second is a sharp filter defined in the Fourier space. According to the convention for the Fourier transform (6.8), the Fourier transform of the filtered velocity field can be written as $\hat{\bar{\boldsymbol{u}}} = (2\pi)^3 \hat{G} \times \hat{\boldsymbol{u}}$. Consequently, the transfer function is here defined as $G_k \equiv (2\pi)^3 \hat{G}$. The sharp filter in spectral space is then defined by

$$G_k(\boldsymbol{k}) = \begin{cases} 1 & \text{if } |\boldsymbol{k}| \leq k_c = \pi/\Delta \\ 0 & \text{otherwise,} \end{cases} \tag{8.11}$$

and satisfies the normalization condition (8.9), namely $G_k(0) = 1$. In practice, high-order discrete filters are also commonly used in LES algorithms [295, 512]. Using notations already introduced for finite difference schemes, the filtered quantity $\bar{f}$ in the x_1 direction and at point $x_1 = l x_1$ is calculated as

$$\bar{f_l} = f_l - \sigma_f \sum_{j=-n_f}^{n_f} d_j f_{l+j}$$

where σ_f is the filtering strength between 0 and 1. The filter coefficients d_j can be determined by imposing $G_k(\pi) = 0$ to remove shortest waves, and by choosing symmetric coefficients $d_j = d_{-j}$ to ensure no phase-shift and a realizability condition $G_k \geq 0$. The filter order, and consequently the commutation error between the filtering operation and spatial derivatives, can be controlled by cancelling the first moments of G_k [326, 352]. An illustration for a one-dimensional filtering operation is shown in Fig. 8.5. The signal f, the signal $\bar{f}$ filtered by a 4th-order filter, and the small scale part f' are plotted as well as their spectra. The filter cutoff wavenumber is defined as $G_k(k_{c1}\Delta x_1) = 1/2$, corresponding to $k_{c1}\Delta x_1 \simeq 2$ for this filter.

8.2.2 Filtered Navier-Stokes Equations

Before starting, it is important to observe that the decomposition $u_i = \bar{u}_i + u_i'$ associated with the filtered velocity $\bar{u}_i$ for instance, seems similar to the Reynolds decomposition introduced in Chap. 2, but has a completely different meaning here. In large eddy simulation, any variable is decomposed into its filtered part which is calculated, and a small scale part, whose effects must be modelled.

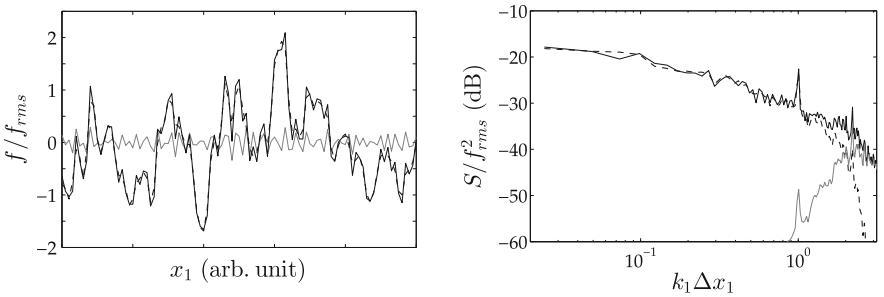

Fig. 8.5 Illustration of the filtering operation on a homogeneous signal $f(x_1)$ (arbitrary units). At *left*, —— signal f, - - - filtered signal $\bar{f}$ by a 4th-order filter G and —— $f' = f - \bar{f}$. All these signals are normalised by the rms value of f. At *right*, power spectral density S as a function of the dimensionless wavenumber $k_1\Delta x_1$, —— for the signal f, - - - for the filtered signal $\bar{f}$ and —— for f'. The relation $S(\bar{f}) = G_k^2 \times S(f)$ is also verified

$$u_i = \bar{u}_i + u_i' \qquad \text{with} \qquad \bar{u}_i = G * u_i \tag{8.12}$$

The time average of a quantity, filtered or not, is denoted by $\langle\cdot\rangle$. For instance, the averaged kinetic energy of the velocity field resolved by LES is $\langle \bar{u}_i^2 \rangle / 2$. The filtered Navier-Stokes equation is obtained by convolution with the filter, and by neglecting commutation errors between differentiation and filtering operations. As mentioned in the previous section, this assumption is reasonable, at least when using high-order filters. Furthermore, the flow is still assumed to be incompressible throughout this chapter, that is $\nabla \cdot \bar{\boldsymbol{u}} = 0$. The compressible case is briefly presented in Sect. 8.5, where the Favre filtering is introduced. The filtered Navier-Stokes equation can be written as follows

$$\frac{\partial(\rho\bar{u}_i)}{\partial t} + \frac{\partial(\rho\bar{u}_i\bar{u}_j)}{\partial x_j} = -\frac{\partial\bar{p}}{\partial x_i} + \frac{\partial\bar{\tau}_{ij}}{\partial x_j} + \frac{\partial t_{ij}}{\partial x_j} \tag{8.13}$$

where $t_{ij} \equiv \rho\bar{u}_i\bar{u}_j - \rho\overline{u_iu_j}$ is the subgrid-scale stress tensor. This tensor is usually split into three contributions as introduced by Leonard [312]

$$\begin{aligned} t_{ij} &= \rho\bar{u}_i\bar{u}_j - \rho\overline{u_iu_j} = \rho\bar{u}_i\bar{u}_j - \rho\overline{(\bar{u}_i + u_i')(\bar{u}_j + u_j')} \\ &= \underbrace{\rho\bar{u}_i\bar{u}_j - \rho\overline{\bar{u}_i\bar{u}_j}}_{(1)} \underbrace{-\rho\overline{u_i'\bar{u}_j} - \rho\overline{\bar{u}_iu_j'}}_{(2)} \underbrace{-\rho\overline{u_i'u_j'}}_{(3)} \end{aligned} \tag{8.14}$$

The term (1) is the Leonard tensor involving only filtered quantities, the cross term (2) involves interactions between resolved and subgrid scales and the term (3) has a form close to that of a Reynolds stress tensor based on subgrid scales. One must pay attention to the sign convention used for the stress tensor t_{ij}, which is sometimes defined with the opposite sign in the literature. The terms (1) and(2)

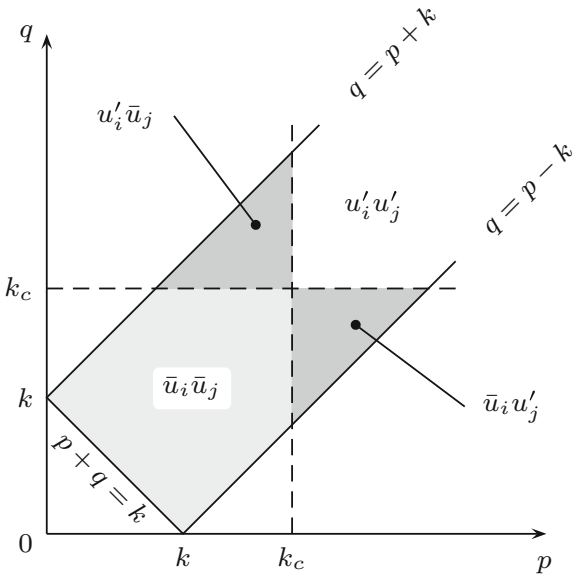

Fig. 8.6 Sketch of triads where $\boldsymbol{k} = \boldsymbol{p} + \boldsymbol{q}$ associated with the Leonard decomposition (8.14), adapted from Sagaut [339]. For a given wavenumber with modulus $\boldsymbol{k}$, the moduli p and q of wavenumbers $\boldsymbol{p}$ and $\boldsymbol{q}$ must lie in the domain defined by $|p - q| \leq k \leq p + q$, refer also to Fig. 7.15. The wavenumber cutoff frequency of the filtering is denoted k_c

should be zero within the framework of the Reynolds decomposition presented in Chap. 2. Moreover, only the terms (2) and (3) are unknown in (8.14) if an explicit filtering is used in the LES algorithm. It must be also mentioned here that this triple decomposition is not Galilean invariant term by term [345]. Germano [296] redefined the triple decomposition (8.14) as

$$t_{ij} = \underbrace{\rho\overline{\overline{u}_i}\,\overline{\overline{u}_j} - \rho\overline{\overline{u}_i u_j}}_{(1)} \underbrace{+\rho(\overline{\overline{u}_i}\,\overline{u'_j} + \overline{u'_i}\,\overline{\overline{u}_j} - \overline{\bar{u}_i u'_j + u_i \bar{u}_j})}_{(2)} \underbrace{-\rho\overline{u'_i u'_j} + \rho\overline{u'_i}\,\overline{u'_j}}_{(3)} \tag{8.15}$$

to meet this requirement. Finally, the Leonard decomposition (8.14) can be visualized in the wavenumber space [339] as shown in Fig. 8.6, following the illustration of triadic interactions presented in Fig. 7.15.

8.2.3 Modelling of Subgrid Scales in LES

Three fundamental sources of error can be identified. The first is associated with the projection leading to the filtered Navier-Stokes equations. The second is linked to the discretization of these equations and has already been illustrated in Sect. 8.1.1.2 for finite difference schemes. Finally, the subgrid-scale modelling represents the third contribution. A complete discussion of the subject, as well as a review of subgrid-scale models, can be found in Sagaut [339].

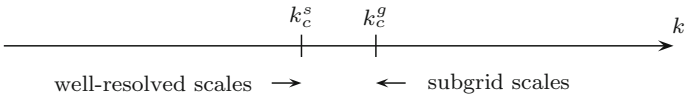

Fig. 8.7 Sketch of scales involved in LES. The cutoff wavenumber of the grid is given by $k_c^g \Delta = \pi$, and the accuracy limit of the spatial numerical differentiation is k_c^s. The transfer function G_k of the low pass filter is chosen to preserve the largest part of the well-resolved scales

In what follows, it is assumed that a filtering operation is applied during the time integration of Eq. (8.13) to control the spectral content of the numerical solution [318], and to ensure a separation between the cutoff wavenumber of the filter k_c, and that of the spatial scheme k_c^g. The error induced by the discretization is thus expected to remain small for the well-resolved scales, as sketched in Fig. 8.7. In practice, the so-called primary filter G introduced in expression (8.8) is often not explicitly defined. It is the transfer function of the differentiation scheme which acts as a low-pass filter, as shown in Fig. 8.3 with some classical finite-difference schemes, and it is merely denoted by $\bar{u}_i$. In other words, the filtering is implicitly obtained through the projection of variables on the mesh. The transfer function is however not known when using unstructured grids for instance.

Finally, subgrid scale models can often be categorized into functional or structural modelling approaches [339]. In the first group, the goal of the subgrid scale model is mainly to preserve the turbulent kinetic energy balance. The model is thus calibrated to recover the dissipation imposed by the energy cascade. Most of these formulations are based on a turbulent viscosity. In the second group, an effort is made to preserve the spectrum of the resolved scales up to the cutoff wavenumber. The transfer function of the filter must be known in this case, which motivates the introduction of an explicit filtering operation in the LES algorithm. These two approaches are briefly presented in the two following sections.

8.2.4 Closure with a Turbulent Viscosity Model

In most of the functional models, the subgrid scale tensor t_{ij} is expressed by introducing a turbulent viscosity written as $\nu_t \sim l \times u$. The models differ in their expression of the velocity scale u, whereas the length scale l is always linked to the width Δ of the filter. Similarly to what has been done in Chap. 2, t_{ij} is expressed from the gradients of the filtered velocity, that is from the components of the resolved velocity. The subgrid scale tensor is written as the sum of its deviator and of its spherical or isotropic parts

$$t_{ij} = t_{ij}^{\mathcal{D}} + t_{ij}^{\mathcal{I}} \qquad \text{with} \qquad \begin{cases} t_{ij}^{\mathcal{D}} = -\rho\overline{u_i' u_j'} + \dfrac{1}{3}\rho\overline{u_k' u_k'}\delta_{ij} \\ t_{ij}^{\mathcal{I}} = -\dfrac{1}{3}\rho\overline{u_k' u_k'}\delta_{ij} = -\dfrac{2}{3}\rho k_{sgs}\delta_{ij} \end{cases} \tag{8.16}$$

and where $t_{ij}^{\mathcal{D}}$ is expressed as

$$t_{ij}^{\mathcal{D}} = 2\mu_t \bar{s}_{ij} \qquad \text{with} \qquad \bar{s}_{ij} = \frac{1}{2}\left(\frac{\partial \bar{u}_i}{\partial x_j} + \frac{\partial \bar{u}_j}{\partial x_i}\right) \tag{8.17}$$

by remembering that the flow is assumed to be incompressible here. The compressible case is introduced in Sect. 8.4. Apart from its sign, the term $t_{ij}^{\mathcal{I}}$ represents the residual energy or the subgrid scale energy k_{sgs}, that is the turbulent kinetic energy part not resolved by the grid. Its average value is given by

$$\langle k_{sgs} \rangle = \int_{\pi/\Delta}^{\infty} E(k)\, dk$$

for a top-hat filter. The filtered Navier-Stokes equation (8.13) can then be written as

$$\frac{\partial(\rho \bar{u}_i)}{\partial t} + \frac{\partial}{\partial x_j}\left(\rho \bar{u}_i \bar{u}_j\right) = -\frac{\partial \bar{p}^{\star}}{\partial x_i} + \frac{\partial}{\partial x_j}\left[(\mu + \mu_t)\frac{\partial \bar{u}_i}{\partial x_j}\right] \tag{8.18}$$

where the isotropic part $t_{ij}^{\mathcal{I}}$ of the subgrid stress tensor t_{ij} is included in the pressure term according to (8.16),

$$\bar{p}^{\star} = \bar{p} - \frac{1}{3} t_{kk} = \bar{p} + \frac{2}{3}\rho k_{sgs}$$

8.2.4.1 Smagorinsky Subgrid Model

Only the expression of the turbulent viscosity is unknown in Eq. (8.18), and the first closure was proposed by Smagorinsky [344]. This turbulent subgrid viscosity ν_t is built by choosing $l = C_s \Delta$ as a length scale and $\bar{s} = \sqrt{2\bar{s}_{ij}\bar{s}_{ij}}$ as a velocity gradient scale. This leads to

$$\nu_t = (C_s \Delta)^2 \sqrt{2\bar{s}_{ij}\bar{s}_{ij}} \qquad \text{where} \qquad \bar{s}_{ij} = \frac{1}{2}\left(\frac{\partial \bar{u}_i}{\partial x_j} + \frac{\partial \bar{u}_j}{\partial x_i}\right) \tag{8.19}$$

where C_s is the so-called Smagorinsky constant. This constant can be estimated assuming that the cutoff wavenumber of the filter $k_c = \pi/\Delta$ is located in the inertial part of the turbulent kinetic energy spectrum, that is when $E(k) \simeq C_K \epsilon^{2/3} k^{-5/3}$. As discussed in the previous chapter, the Reynolds number is implicitly assumed to be large enough to observe an inertial region and an energy cascade. The rate of energy to be dissipated is imposed by the large structures, which are resolved by LES, but the finest scales responsible for dissipation are missing. They are part of the subgrid scales. The value of the turbulent viscosity is then determined in order to realize this dissipation by the resolved scales.

The dissipation corresponds to the energy transferred from the resolved field to the subgrid field, that is

$$\rho\epsilon = \left\langle t_{ij}\frac{\partial \bar{u}_i}{\partial x_j}\right\rangle = 2\langle \mu_t \bar{s}_{ij}^2\rangle = \rho\,(C_s\Delta)^2\,\langle \bar{s}^3\rangle \tag{8.20}$$

The shear magnitude $\bar{s}$ of the filtered field is calculated as follows

$$\langle 2\bar{s}_{ij}\bar{s}_{ij}\rangle = \langle \bar{s}^2\rangle = \int_0^{k_c} 2k^2 E\,(k)\,dk$$

and can be analytically estimated for a cutoff wavenumber k_c located in the inertial zone

$$\langle \bar{s}^2\rangle \simeq \int_0^{k_c} 2k^2 C_K \epsilon^{2/3} k^{-5/3} dk \simeq \frac{3C_K}{2}\left(\frac{\pi}{\Delta}\right)^{4/3}\epsilon^{2/3} \tag{8.21}$$

The value of the constant C_s is obtained by eliminating the dissipation between relations (8.20) and (8.21), which provides

$$C_s = \frac{1}{\pi}\left(\frac{2}{3C_K}\right)^{3/4}\left(\frac{\langle \bar{s}^2\rangle^{3/2}}{\langle \bar{s}^3\rangle}\right)^{1/2} \simeq \frac{1}{\pi}\left(\frac{2}{3C_K}\right)^{3/4} \tag{8.22}$$

Numerically, one finds $C_s \simeq 0.18$ by taking the value $C_K \simeq 1.4$ for the Kolmogorov constant. It is now well established [292, 314, 323] that a more suitable value is about $C_s \simeq 0.10$. A more complete analysis of this model can be found in Meyers and Sagaut [322], in particular regarding the value of the Smagorinsky constant.

A damping function must be introduced to decrease the length scale in the expression of C_s near walls. This difficulty has been already discussed in Chap. 3, refer to relation (3.22). A van Driest type damping function [442] is also used to modify the expression of the turbulent viscosity

$$\nu_t = \left[C_s\Delta(1 - e^{-x_2^+/A_0^+})\right]^2\sqrt{2\bar{s}_{ij}\bar{s}_{ij}} \tag{8.23}$$

It is reminded that the wall variable is given by $x_2^+ = x_2 u_\tau/\nu$. The constant A_0^+ must be adjusted to properly recover the logarithmic law, typically $A_0^+ \simeq 25$. A two layer model can also be developed for near-wall flow regions, as proposed by Flohr and Balaras [266, 294]. Moreover, a complete discussion including the presence of a pressure gradient can be found in Duprat et al. [291].

8.2.4.2 Subgrid Residual Energy

The isotropic part $t_{ij}^{\mathcal{I}}$ of the subgrid tensor (8.16), which is included within the pressure term in (8.18), is often discarded with respect to the pressure term in $\bar{p}^{\star}$. Moin et al. [323] have shown that the ratio between this residual energy term and the pressure is less than 3 % in their simulations dealing with low Reynolds number flows. Introducing the subgrid turbulent Mach number defined by $M_{sgs}^2 = 2k_{sgs}/(\gamma \bar{p}/\bar{\rho})$, it can also be observed that

$$\frac{2}{3}\bar{\rho}k_{sgs} = \frac{\gamma}{3}M_{sgs}^2\bar{p}$$

and Erlebacher et al. [292] consider that $t_{ij}^{\mathcal{I}}$ can be neglected by comparison with the pressure term $\bar{p}$ as long as $M_{sgs} \leq 0.4$.

Within the framework of the Smagorinsky approach, the following expression has nevertheless been proposed [292, 323, 360] for the subgrid scale energy

$$k_{sgs} = C_I \Delta^2 2\bar{s}_{ij}\bar{s}_{ij} = C_I \Delta^2 \bar{s}^2 \tag{8.24}$$

where C_I is a constant. To determine its value, the cutoff wavenumber of the filter is again assumed to be located in the inertial zone of the turbulent kinetic energy spectrum. It can then be written that

$$\langle k_{sgs} \rangle = \int_{\pi/\Delta}^{\infty} E(k)\, dk = C_K \epsilon^{2/3} \int_{\pi/\Delta}^{\infty} k^{-5/3} dk = \frac{3C_K}{2}\epsilon^{2/3}\left(\frac{\pi}{\Delta}\right)^{-2/3}$$

and introducing the expression (8.21) of $\bar{s}^2$ in $k_{sgs} = C_I \Delta^2 \bar{s}^2$, one gets

$$C_I = \frac{1}{\pi^2} \simeq 0.10 \tag{8.25}$$

Finally, a transport equation [309] for the subgrid energy k_{sgs} can also be derived. This approach is used for simulating atmospheric flows for instance.

8.2.4.3 Germano and Lilly Dynamic Models

The classical Smagorinsky model is often found to be too dissipative [279, 310], in particular for transitional flows. This drawback can be partly overcome by a dynamic estimation of the model constant. Germano et al. [298, 300], Lilly [316] and Moin et al. [323] for compressible flows, have developed dynamic formulations of the Smagorinsky model. The constants C_s and C_I are evaluated to adjust locally in space and time to the turbulent flow. The algorithm is based on the Germano identity [297, 319] which allows any subgrid scale tensor calculated at two different filtering levels to be expressed analytically. The underlying assumption is that the turbulent flow is self-similar [267, 325] in the wavenumber band defined by the two filters. The

primary filtering operation of width Δ is still denoted by $\bar{u}_i = G_\Delta * u_i$. An additional test filter $\tilde{u}_i = G_{\tilde{\Delta}} * u_i$ defined on a coarser grid of width $\tilde{\Delta} > \Delta$ is also introduced, and according to the convolution product properties, one has $\tilde{\bar{u}}_i = G_{\tilde{\Delta}} * (G_\Delta * u_i) = G_\Delta * (G_{\tilde{\Delta}} * u_i)$. Thus, by applying the new test filter to the filtered Navier-Stokes equation (8.13), one obtains

$$\frac{\partial(\rho\tilde{\bar{u}}_i)}{\partial t} + \frac{\partial}{\partial x_j}\left(\rho\tilde{\bar{u}}_i\tilde{\bar{u}}_j\right) = -\frac{\partial\tilde{\bar{p}}}{\partial x_i} + \frac{\partial\widetilde{\bar{\tau}_{ij}}}{\partial x_j} + \frac{\partial\mathcal{T}_{ij}}{\partial x_j}$$

where $\mathcal{T}_{ij} \equiv \rho\widetilde{\bar{u}_i\bar{u}_j} - \rho\widetilde{\bar{u}_i}\widetilde{\bar{u}_j}$. This tensor $\mathcal{T}_{ij}$ can be related to the subgrid tensor t_{ij}, see expression (8.14), through the following Germano identity

$$\widetilde{\bar{u}_i}\widetilde{\bar{u}_j} - \widetilde{\bar{u}_i\bar{u}_j} = \bar{u}_i\widetilde{\bar{u}_j} - \widetilde{\bar{u}_i\bar{u}_j} + \widetilde{\bar{u}_i}\widetilde{\bar{u}_j} - \widetilde{\bar{u}_i}\widetilde{\bar{u}_j}$$

which provides in the present case

$$\mathcal{L}_{ij} = \mathcal{T}_{ij} - \tilde{t}_{ij} \qquad \text{with} \qquad \mathcal{L}_{ij} \equiv \rho\widetilde{\bar{u}_i\bar{u}_j} - \rho\widetilde{\bar{u}_i}\widetilde{\bar{u}_j} \tag{8.26}$$

In this relation, the tensor $\mathcal{L}_{ij}$ can be calculated explicitly for the resolved velocity field $\bar{u}_i$. The two subgrid tensors t_{ij} and $\mathcal{T}_{ij}$ are expressed according to the Smagorinsky model using relations (8.17) and (8.19). Hence,

$$\begin{cases} t_{ij}^{\mathcal{D}} = t_{ij} - \dfrac{1}{3}t_{kk}\delta_{ij} = 2C_d\Delta^2\rho\,\bar{s}\,\bar{s}_{ij} \\ \mathcal{T}_{ij}^{\mathcal{D}} = \mathcal{T}_{ij} - \dfrac{1}{3}\mathcal{T}_{kk}\delta_{ij} = 2C_d\tilde{\Delta}^2\rho\,\tilde{\bar{s}}\,\tilde{\bar{s}}_{ij} \qquad \tilde{\bar{s}} \equiv \sqrt{2\tilde{\bar{s}}_{ij}\tilde{\bar{s}}_{ij}} \end{cases}$$

where the dynamic Smagorinsky constant is usually denoted by C_d, and is formally linked to the Smagorinsky constant by $C_d = C_s^2$. This dynamic constant C_d is determined by imposing that the subgrid tensors must satisfy the Germano identity (8.26). Therefore,

$$\begin{aligned} \mathcal{L}_{ij}^{\mathcal{D}} = \mathcal{L}_{ij} - \frac{1}{3}\mathcal{L}_{kk}\delta_{ij} &= \mathcal{T}_{ij}^{\mathcal{D}} - \tilde{t}_{ij}^{\mathcal{D}} \\ &= 2C_d(\tilde{\Delta}^2\rho\,\tilde{\bar{s}}\,\tilde{\bar{s}}_{ij} - \Delta^2\rho\,\widetilde{\bar{s}\,\bar{s}_{ij}}) \\ &\equiv 2C_d\mathcal{M}_{ij} \end{aligned} \tag{8.27}$$

Expression (8.27) can then be used to determine the value of C_d. Contracting this relation using $\bar{s}_{ij}$, one obtains

$$C_d = \frac{1}{2}\frac{\mathcal{L}_{ij}^{\mathcal{D}}\bar{s}_{ij}}{\mathcal{M}_{ij}\bar{s}_{ij}}$$

as derived by Germano et al. [300] However, an ill-posed problem appears in practice, and the final expression to estimate C_d was reformulated by Lilly [316]. The value

of the constant is calculated from (8.27) by minimizing the quantity $\mathcal{L}_{ij}^{\mathcal{D}} - \mathcal{T}_{ij}^{\mathcal{D}} + \tilde{t}_{ij}^{\mathcal{D}}$ using a least-squares method

$$\frac{\partial}{\partial C_d}\left(\mathcal{L}_{ij}^{\mathcal{D}} - 2C_d\mathcal{M}_{ij}\right)^2 = 0$$

which leads to the following expression of C_d

$$C_d = \frac{1}{2}\frac{\mathcal{M}_{ij}\mathcal{L}_{ij}^{\mathcal{D}}}{\mathcal{M}_{kl}\mathcal{M}_{kl}} \tag{8.28}$$

Equation (8.28) provides a dynamic procedure to estimate the Smagorinsky constant $C_d = C_d(\boldsymbol{x}, t)$ and thus to compute the subgrid tensor in (8.13) through the use of an additional test filter. In practice, to avoid negative values or overly large variations of the turbulent viscosity $\nu_t(\boldsymbol{x}, t)$ leading to numerical instability, the numerator and the denominator in (8.28) or more directly ν_t are often averaged in homogeneous directions. Another way to prevent numerical instability is to impose that [339] $\nu + \nu_t \geq 0$. Excessive values of the dynamic constant are also removed by checking that $C_d \leq C_s^2$. Finally, the value $\tilde{\Delta} = 2\Delta$ appears to be a good compromise for the test filter width.

A similar approach can be developed to dynamically determine the constant C_I introduced in expression (8.25) to calculate the subgrid energy [323]. Taking the trace of $\mathcal{L}_{ij}$ and substituting into the subgrid model (8.24) leads to the following relation

$$C_I = \frac{1}{2}\frac{\mathcal{L}_{kk}}{\Delta^2\rho\,\widetilde{\tilde{s}^2} - \tilde{\Delta}^2\rho\,\tilde{\tilde{s}}^2} \tag{8.29}$$

Numerous simulations have been carried out using these dynamical models, and the present discussion can be continued by reading Meneveau and Katz [320], or Jiménez and Moser [306].

To illustrate the behaviour of an LES modelling based on a turbulent viscosity, numerical results obtained from an explicit relaxation filtering are compared to those obtained using the Smagorinsky dynamic model. Reynolds number effects are well reproduced by the first approach, which is presented in the next section. The mean axial velocity and the centerline rms fluctuating velocity of a subsonic round jet are displayed in Fig. 8.8. As the Reynolds number decreases, the generation of vortical structures in the shear layer occurs farther downstream [279], which can be attributed to the decrease of the growth rates of instabilities, due to viscosity effects at low Reynolds numbers. Consequently, the potential core length increases and accordingly, mean axial velocity profiles are shifted in the axial direction to specifically compare the velocity decay rates after the potential core. After the potential core, velocity decays occur faster as the Reynolds number decreases, in accordance with the available experimental data. The effective Reynolds number of the jet at Reynolds $\mathrm{Re}_D = 4.0 \times 10^5$ calculated with the dynamic Smagorinsky

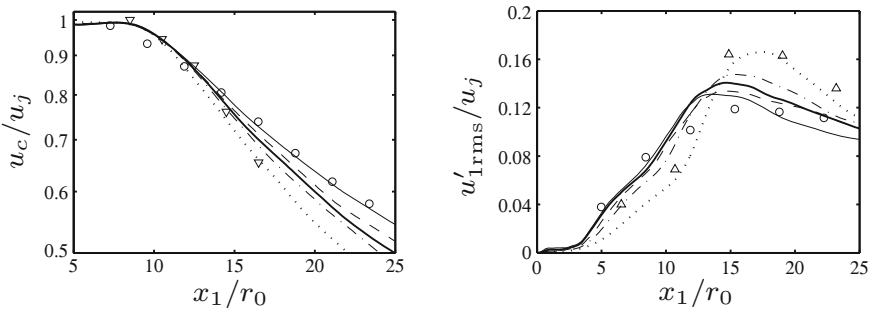

Fig. 8.8 Subsonic round jet at $M = 0.9$. On the *left*, centerline mean axial velocity profile and on the *right*, centerline profile of the rms fluctuating axial velocity, both quantities are normalized by the exit jet velocity u_j. LES results based on an explicit relaxation filtering for different Reynolds numbers, ····· $\mathrm{Re}_D = 2.5 \times 10^3$, –·–·– $\mathrm{Re}_D = 5 \times 10^3$, – – – $\mathrm{Re}_D = 10^4$, —— $\mathrm{Re}_D = 4.0 \times 10^5$, where $D = 2r_0$ is the nozzle diameter. Experimental data of ▽ Stromberg et al. [556] ($\mathrm{Re}_D = 3.6 \times 10^3$), ○ Arakeri et al. [506] ($\mathrm{Re}_D = 5 \times 10^5$) and △ DNS of Freund [528] ($\mathrm{Re}_D = 3.6 \times 10^3$). LES results using the dynamic Smagorinsky model are also reported for —— $\mathrm{Re}_D = 4.0 \times 10^5$. From Bogey and Bailly [279]

model is however artificially decreased by the turbulent viscosity, and reduced down to $\mathrm{Re}_D \simeq u_j D/\nu_t \simeq 8 \times 10^3$ in this example. A similar behaviour is observed for the amplitude of the peak of the axial fluctuating velocity, by noting that this peak increases as the Reynolds number decreases.

8.2.4.4 Velocity Scale Based on a Structure Function

Métais and Lesieur [313, 314, 321] introduced the structure-function model in the physical space as a generalisation of their spectral turbulent viscosity model. The local second-order velocity structure function is defined as

$$F_2(\boldsymbol{x}, \boldsymbol{r}) = \overline{\| \bar{\boldsymbol{u}}(\boldsymbol{x} + \boldsymbol{r}) - \bar{\boldsymbol{u}}(\boldsymbol{x}) \|^2} \tag{8.30}$$

For isotropic turbulence, this function $F_2 = F_2(r)$ can be expressed directly from the spectrum $E(k)$ of the turbulent kinetic energy, as already mentioned in Sect. 7.6.2. The structure function associated with the resolved scales is given by

$$\bar{F}_2(r) = \bar{F}_{ii}(r) = 4 \int_0^{k_c} E(k) \left(1 - \frac{\sin(kr)}{kr}\right) dk$$

and in physical space, the turbulent viscosity is determined as follows

$$\nu_t = C_{FS}\, \Delta \sqrt{\bar{F}_2(\boldsymbol{x}, \Delta)} \qquad \text{with} \qquad C_{FS} \simeq 0.105\, C_K^{-3/2}$$

The structure function is calculated by taking the average of the square of velocity differences between $\boldsymbol{x}$ and the six closest points surrounding $\boldsymbol{x}$ for a three-dimensional Cartesian grid. The structure-function model is expected to be less dissipative in the regions where the flow is almost laminar and more dissipative where the velocity gradients close to the cut-off wavenumber π/Δ are important. This approach nevertheless remains similar to the Smagorinsky model. Indeed, it can be shown [284] that

$$\lim_{\Delta \to 0} \nu_t(\boldsymbol{x}, t) \simeq \sqrt{\frac{2}{3}} (C_s \Delta)^2 \sqrt{2\bar{s}_{ij}\bar{s}_{ij} + \bar{\omega}_{ij}\bar{\omega}_{ij}}$$

To overcome this difficulty and get a less dissipative model for the simulation of the transition of a spatially evolving boundary layer for instance, Ducros et al. [290] introduced a filtered structure function.

8.2.4.5 Spectral Turbulent Viscosity

The concept of a turbulent viscosity can also be introduced in spectral space, at least for homogeneous turbulence. As a starting point, the transport equation of the turbulent kinetic energy spectrum (7.7) or Lin's equation derived in the previous chapter, is considered

$$\left(\frac{\partial}{\partial t} + 2\nu k^2\right) E(k, t) = T(k, t)$$

where the term T can be interpreted in terms of Batchelor-Kraichnan triads from the Fourier transform of the Navier-Stokes equation established in Sect. 7.8. This term is then split into two contributions associated with resolved ($k < k_c$) and unresolved ($k > k_c$) scales, where k_c is the cutoff wavenumber frequency of the top-hat filter (8.11),

$$\left(\frac{\partial}{\partial t} + 2\nu k^2\right) E(k, t) = T_{k<k_c}(k, t) + T_{k>k_c}(k, t)$$

Following Kraichnan [165], a spectral turbulent viscosity denoted $\hat{\nu}_t$ is then introduced to model the unresolved scales,

$$\hat{\nu}_t(k, k_c, t) = -\frac{T_{k>k_c}(k, t)}{2k^2 E(k, t)} \tag{8.31}$$

and the transport equation for E takes the following form

$$\left\{\frac{\partial}{\partial t} + 2\left[\nu + \hat{\nu}_t(k, k_c, t)\right]k^2\right\} E(k, t) = T_{k<k_c}(k, t) \tag{8.32}$$

The term on the right-hand side corresponds to explicit transfers, associated with resolved scales in a large eddy simulation. A model for the spectral viscosity $\hat{\nu}_t$ is however required, and it is of interest to derive an expression of $\hat{\nu}_t$ which is not a function of k. The turbulent kinetic energy at the cutoff wavenumber k_c is $k_c E(k_c)$, which provides $\sqrt{k_c E(k_c)}$ as velocity scale. The spectral turbulent viscosity is then built as

$$\hat{\nu}_t = C\sqrt{\frac{E(k_c)}{k_c}} \tag{8.33}$$

where C is a constant of the model. Its value is determined by following what was done for the Smagorinsky model in physical space. Assuming that k_c lies in the inertial zone of $E(k)$, the dissipation is

$$\epsilon \simeq \int_0^{k_c} 2\hat{\nu}_t k^2 E(k) dk = \hat{\nu}_t \frac{3C_K}{2} \epsilon^{2/3} k_c^{4/3}$$

By identification with expression (8.33), $C = (2/3)C_K^{-3/2} \simeq 0.402$ with $C_K \simeq 1.4$, and the spectral turbulent viscosity takes the form

$$\hat{\nu}_t = \frac{2}{3} C_K^{-3/2} \sqrt{\frac{E(k_c)}{k_c}}$$

A more complete presentation of spectral models for LES can be found in Chollet and Lesieur [283], and Métais and Lesieur [321]. Approaches based on EDQNM models have also been proposed to take into account the energy flux from small to large scales, the subgrid-scale backscatter, in turbulent compressible or rotating flows, see for instance the pioneering studies of Cambon et al. [91, 94], of Bertoglio [86, 272] and also the book of Sagaut and Cambon [147].

8.2.5 LES Based on an Explicit Relaxation Filtering

In the previous section, the subgrid scale tensor t_{ij} in expression (8.17) is computed through the introduction of a turbulent viscosity ν_t. LES models differ from each other mainly by the way in which this viscosity is determined, with the aim of reducing artificial dissipation effects. These efforts will never be fully successful since the functional form for the dissipation remains a Laplacian filter, namely $\sim \nu_t \nabla^2 \bar{u}_i$ in the filtered Navier-Stokes equation (8.13) [289, 332]. As a result, a significant part of the resolved scales is involved and affected by the turbulent viscosity, except for the formulation (8.33) in the spectral space. In this section, LES models are still derived to reproduce the energy transfer to the smallest scales, but by preserving the well-resolved scales of the turbulent flow.

The key role played by the filtering is first highlighted. As for Domaradzki and Adams [288], the spectral truncation induced by the computational grid is denoted by $u_i = u_i^{\mathcal{L}} + u_i^{\mathcal{S}}$ where $u_i^{\mathcal{L}}$ is thus associated with wavenumbers $k < k_c^g$ and $u_i^{\mathcal{S}}$ with wavenumbers $k > k_c^g$ where k_c^g is the Nyquist or smallest wavenumber represented on the grid, by referring to Fig. 8.7. In other words, information regarding $u_i^{\mathcal{S}}$ is definitively lost owing to the grid projection. In connection with the first part of this chapter, one has to satisfy $u_i^{\mathcal{S}} = 0$ in a DNS. Assuming that the spectral truncation commutes with the filtering, the decomposition (8.12) can be recast as follows

$$u_i = \bar{u}_i^{\mathcal{L}} + \underbrace{(u_i^{\mathcal{L}} - \bar{u}_i^{\mathcal{L}}) + u_i^{\mathcal{S}}}_{u_i'}$$

and the filtered Navier-Stokes equation can be rearranged as

$$\frac{\partial(\rho\bar{u}_i^{\mathcal{L}})}{\partial t} + \frac{\partial(\rho\bar{u}_i^{\mathcal{L}}\bar{u}_j^{\mathcal{L}})}{\partial x_j} + \frac{\partial\bar{p}^{\mathcal{L}}}{\partial x_i} - \frac{\partial\bar{\tau}_{ij}^{\mathcal{L}}}{\partial x_j} = \frac{\partial t_{ij}^{\mathcal{L}}}{\partial x_j} + \frac{\partial t_{ij}^{\mathcal{S}}}{\partial x_j} \tag{8.34}$$

where

$$t_{ij}^{\mathcal{L}} \equiv \rho\bar{u}_i^{\mathcal{L}}\bar{u}_j^{\mathcal{L}} - \overline{\rho u_i^{\mathcal{L}} u_j^{\mathcal{L}}}^{\mathcal{L}} \qquad t_{ij}^{\mathcal{S}} \equiv \overline{-\rho\bar{u}_i^{\mathcal{L}}\bar{u}_j^{\mathcal{S}} - \rho\bar{u}_i^{\mathcal{S}}\bar{u}_j^{\mathcal{L}} - \rho\bar{u}_i^{\mathcal{S}}\bar{u}_j^{\mathcal{S}}}^{\mathcal{L}}$$

The left-hand side of Eq. (8.34) is the filtered Navier-Stokes equation written for $u_i^{\mathcal{L}}$. Before discussing the modelling of the two subgrid scale tensors $t_{ij}^{\mathcal{L}}$ and $t_{ij}^{\mathcal{S}}$ on the right-hand side, the possible scale separation between $u_i^{\mathcal{L}}$ and $\bar{u}_i^{\mathcal{L}}$ is briefly illustrated.

A 3-D snapshot of a mixing layer, obtained by large eddy simulation, is displayed in Fig. 8.9. A sketch of the mean velocity profile including usual notations can be found in Sect. 1.5.2. In the laminar flow region $x_1/\delta_{\omega_0} < 5$, instabilities are growing, leading to the roll-up of the mixing interface responsible for the emergence of large-scale organized structures, whose size is comparable with the transverse length scale of the flow. Such vortices are for instance clearly visible around $x_1/\delta_{\omega_0} = 50$. Farther downstream, for about $x_1/\delta_{\omega_0} > 100$, the flow reaches a fully turbulent state with a large range of motion scales typical of high-Reynolds number flows. The spatial derivatives are calculated by using a low-dispersion optimized 11-point finite difference scheme introduced in Sect. 8.1.1.2, associated with the spatial truncation denoted $u_i^{\mathcal{L}}$ of the complete velocity field. A 10th-order standard discrete filter is explicitly applied to obtain the filtered velocity $\bar{u}_i$. Keeping the same accurate spatial scheme, the order of the filter can be changed, allowing the filter cutoff wavenumber k_c to be adjusted. The LES model used in these simulations is discussed later in this section. Numerical results are shown in Fig. 8.10 for the spatially developing mixing layer presented in Fig. 8.9. The order of the filter is increased from top to bottom, and a broadening of the resolved scale bandwidth is clearly visible. It is worth noting that the four snapshots of the flow field show strong similarities. In all cases, coherent

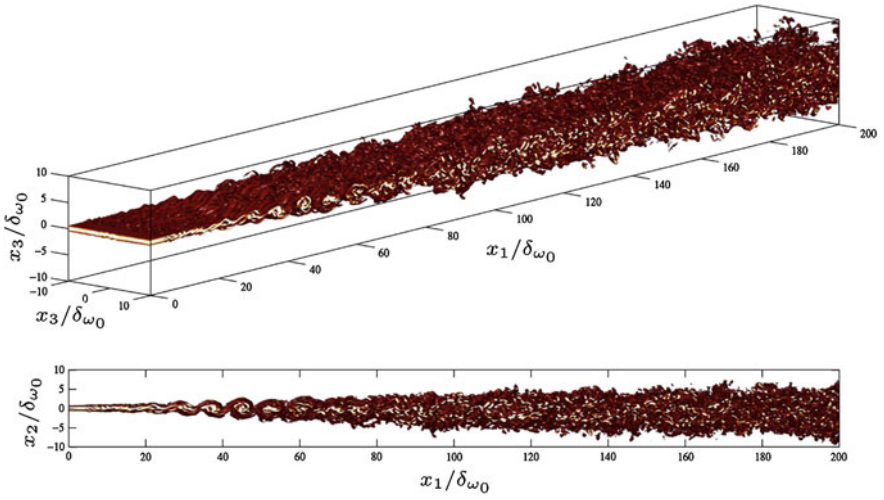

Fig. 8.9 Large eddy simulation based on relaxation filtering (LES-RF) of a mixing layer of convection Mach number $M_c = 0.22$ and of Reynolds number $\mathrm{Re}_{\delta_{\omega 0}} = \delta_{\omega 0} U_c/\nu = 5 \times 10^4$ where $\delta_{\omega 0}$ is the initial vorticity thickness. Snapshot of the modulus of the spanwise vorticity component $|\omega_z|\delta_{\omega_0}/U_c$, from *top* to *bottom*: isometric view and side view. Color scale from -0.5 (*dark*) to 0.2 (*white*). From Berland et al. [271]

vortical structures are generated around $x_1/\delta_{\omega_0} = 25$, vortex breakdown and flow three-dimensionalization is observed in the neighborhood of $x_1/\delta_{\omega_0} = 80$, and a fully turbulent state is eventually reached for $x_1/\delta_{\omega_0} > 150$. This suggests that even though the solutions are different, the key elements of the flow physics are reproduced [271].

The two subgrid scale tensors $t_{ij}^{\mathcal{L}}$ and $t_{ij}^{\mathcal{S}}$ on the right-hand side in Eq. (8.34) are now examined. The first term involves the unknown quantity $u_i^{\mathcal{L}}$, which can be formally recovered by a deconvolution or defiltering procedure,

$$u_i^{\mathcal{L}\star} = Q * \bar{u}_i^{\mathcal{L}}$$

where $Q \simeq G^{-1}$ and thus, $u_i^{\mathcal{L}\star} \simeq u_i^{\mathcal{L}}$. This approach has been retained by Stolz and Adams [349] in their approximate deconvolution model, where the inverse filter Q is estimated by the van Cittert deconvolution

$$Q = \sum_{n=0}^{N} (1 - G)^n$$

with a fixed $N \simeq 5$. Indeed, the series does not converge in general as $N \to \infty$ and must be truncated. Such a procedure allows an explicit calculation of the first subgrid scale term,

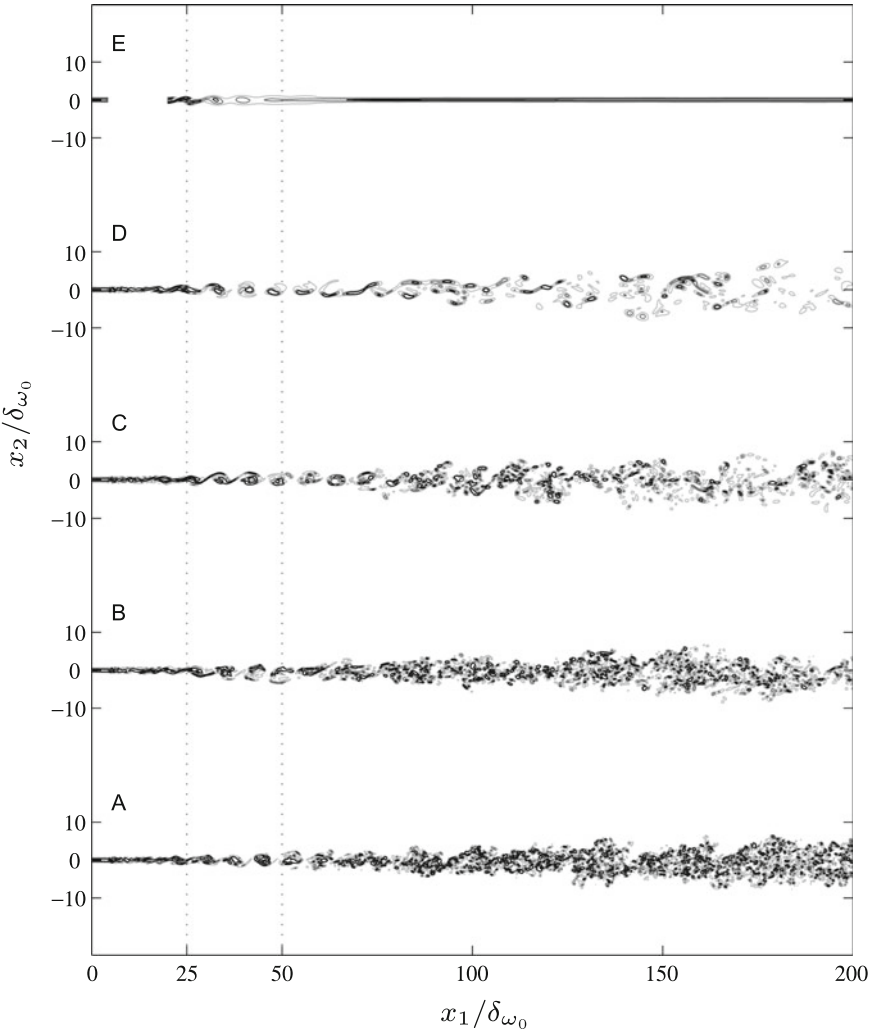

Fig. 8.10 Large eddy simulation of a mixing layer, see Fig. 8.9 for details. Modulus of the spanwise vorticity component in the central plane of the computational domain obtained for various discrete filters used downstream, for $x \geq 50\delta_{\omega_0}$. From *top* to *bottom*, 2nd-order, 4th-order, 6th-order, 8th-order and 10th-order filter. The *vertical dotted lines* indicate the transition region between the upstream and downstream filterings. From Berland et al. [271]

$$t_{ij}^{\mathcal{L}} \simeq \rho \bar{u}_i^{\mathcal{L}} \bar{u}_j^{\mathcal{L}} - \overline{\rho u_i^{\mathcal{L}^\star} u_j^{\mathcal{L}^\star}}^{\mathcal{L}} \tag{8.35}$$

The second subgrid scale tensor $t_{ij}^{\mathcal{S}}$ involves scales beyond the wavenumber cutoff of the grid, which cannot be recovered by deconvolution. It represents the true subgrid scale model mainly associated with the energy cascade. Neglecting this subgrid

scale would lead to a build-up of energy at the cutoff wavenumber. A clever closure was proposed by Stolz et al. [350] to mimic the energy transfer towards scales not represented by the grid

$$\frac{\partial t_{ij}^{\mathcal{S}}}{\partial x_j} = -\chi(1-H) * \rho\bar{u}_i^{\mathcal{L}} \tag{8.36}$$

In this relaxation term, $\chi > 0$ is the inverse of a time scale with which energy is drained at the cutoff wavenumber of a secondary sharp filter H. Using an explicit time integration, $\chi = \sigma_d/\Delta t$ where $0 \leq \sigma_d \leq 1$ is a constant. The choice $H = GQ$ was made in the original model. The one-dimensional transfer functions of both filters G and H are shown in Fig. 8.11 as a function of the dimensionless wavenumber $k_1\Delta x_1$ in grey lines.

The two subgrid scale terms (8.35) and (8.36) do not have the same features. The first term $t_{ij}^{\mathcal{L}}$ does not contain any physical dissipation mechanism. A small numerical dissipation is however produced by the inexact deconvolution procedure. It turns out that its contribution is negligeable, especially using a sharp filter [341, 342] in the wavenumber space, compared to the solution obtained with Eq. (8.34) where only the subgrid term (8.36) is considered. The subgrid scale dissipation is provided entirely by the filtering operation involved in the second term $t_{ij}^{\mathcal{S}}$.

The use of a high-order or selective filtering has also been developed by Visbal and Gaitonde [353], Rizzetta et al. [337] and Bogey and Bailly [275, 509, 512] among others. Following the terminology introduced by the latter authors, an LES based on relaxation filtering (LES-RF) consists in solving the filtered Navier-Stokes equation (8.34) with the relaxation term as the only subgrid scale model

$$\frac{\partial(\rho\bar{u}_i^{\mathcal{L}})}{\partial t} + \frac{\partial(\rho\bar{u}_i^{\mathcal{L}}\bar{u}_j^{\mathcal{L}})}{\partial x_j} + \frac{\partial\bar{p}^{\mathcal{L}}}{\partial x_i} - \frac{\partial\bar{\tau}_{ij}^{\mathcal{L}}}{\partial x_j} = -\chi(1-H) * \rho\bar{u}_i^{\mathcal{L}} \tag{8.37}$$

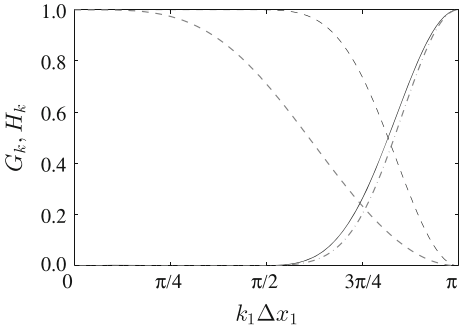

Fig. 8.11 Primary filter – – – G_k and secondary filter –·–·– H_k of the Approximate deconvolution model [350] as a function of the normalized wavenumber $k_1\Delta x_1$. Optimized discrete filter – – – G_k used as relaxation term —— $H_k = 1 - G_k$ in LES based on relaxation filtering [509]

A low-dissipation and low-dispersion discretization scheme, such that the scales discretized at least by four points are neither significantly distorted nor dissipated by the numerical algorithm, is combined with a selective filter. As an illustration, the transfer functions of this filter H and $G = 1-H$ are shown in Fig. 8.11. The accuracy limit for G is around $k_1 \Delta x_1 = \pi/2$ corresponding to 4 points per wavelength, and the formal cutoff wavenumber is around $k_1 \Delta x_1 = 0.82$ corresponding to 2.4 points per wavelength. A theoretical analysis of the numerical algorithm based on the eddy-damped quasi-normal Markovian (EDQNM) modelling [269] can be developed to quantify numerical errors.

In practice [279, 350], numerical results are rather insensitive to the value of the parameter χ in the relaxation term (8.36). The value of the constant can nevertheless be determined by a dynamic procedure [351]. To examine the way in which the energy transfer occurs, a turbulent kinetic energy budget can be numerically calculated, and the contribution of each term can be examined in the wavenumber space including the subgrid dissipation. The energy budget of a subsonic jet [278, 512] has been presented in Sect. 4.2.6, and the channel flow has been studied by Schlatter et al. [342]

As a more simple illustration of the behaviour of the relaxation filtering as subgrid-scale modelling (8.36), isotropic turbulence is considered here. The turbulent kinetic energy spectrum is assumed to be described by a von Kármán spectrum, refer to Sect. 7.4, and is displayed in solid lines for two values of the Reynolds number $\mathrm{Re}_L = u' L/\nu$ in Fig. 8.12, where L represents an integral length scale. In what follows, all spectra are normalized using u' and L. Furthermore, it is assumed that the mesh grid is such that $L/\Delta = \mathcal{O}(10)$, and scales are numerically well resolved with at least 5 points per wavelength, that is $k_c^s = 2\pi/(5\Delta)$. The dimensionless viscous dissipation spectrum $\bar{D}_\nu(k) = 2\nu k^2 \bar{E}(k)$ where $\bar{E}$ is the resolved spectra $\bar{E}(k) = G_k^2(k) E(k)$, is represented by a dashed line. Similarly, the relaxation filtering $\bar{D}_f(k) = 2\chi\,[1 - G_k(k)]\,\bar{E}(k)$ is given by the mixed line. Note that the time evolution of $\bar{E}(k)$ is provided by a Lin equation [269]. For a low arbitrary wavenumber k

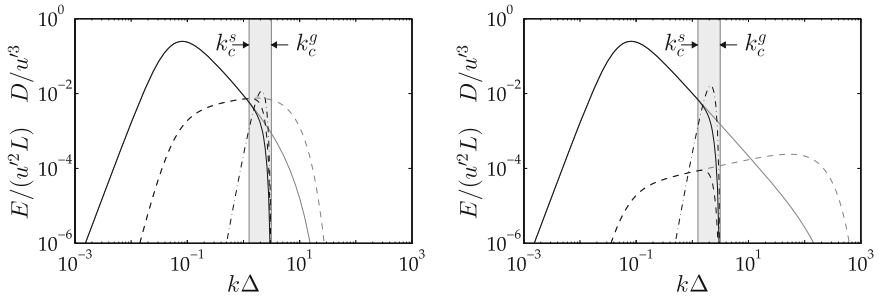

Fig. 8.12 LES based on filtering relaxation, representation of the turbulent kinetic energy spectrum $\bar{E}(k)$ ——, the molecular dissipation $D_\nu(k)$ – – – and the dissipation induced by the explicit filtering $D_f(k)$ –·–·– as a function of the normalized wavenumber $k\Delta$. On the *left*, for a moderate Reynolds number $\mathrm{Re}_L = u' L/\nu = 10^3$ and on the *right*, for a high Reynolds number $\mathrm{Re}_L = 10^5$

and by assuming that $u' = \text{cst}$, it can be shown that

$$\frac{\bar{D}_f(k)}{u'^3} \simeq \text{cst} \qquad \text{and} \qquad \frac{\bar{D}_\nu(k)}{u'^3} \sim \text{Re}_L^{-1}$$

The increase of $\bar{D}_\nu(k)$ as a function of the Reynolds number can be observed in Fig. 8.12. In the well-resolved wavenumber range $0 \leq k \leq k_c^s$, one must have $\bar{D}_f(k) \leq \bar{D}_\nu(k)$ to preserve the physical solution from numerical dissipation. This condition is not fully satisfied for the higher value of the Reynolds number, which highlights the constraint on the mesh imposed by the Reynolds number in large-eddy simulation.

Finally, there are some connections between these approaches and methods involving higher order viscosities, such as hyperviscosity [285] or spectral vanishing viscosity [330]. The reader can refer to the reviews by Domaradzki and Adams [288] and Domaradzki [287] to continue with this topic.

8.3 Classification of Partial Differential Equations*

Second order partial differential equations can be classified as elliptic, parabolic or hyperbolic. The general form of these equations is

$$\sum_{i,j=0}^{n} a_{ij}(\boldsymbol{x}) \frac{\partial^2 f}{\partial x_i \partial x_j} + \sum_{j=0}^{n} b_j(\boldsymbol{x}) \frac{\partial f}{\partial x_j} + c(\boldsymbol{x}) f + d(\boldsymbol{x}) = 0 \qquad \boldsymbol{x} \in \mathbb{R}^{n+1} \quad (8.38)$$

with $a_{ij} = a_{ji}$, and where all the coefficients a_{ij} and b_j are real. Most of the time, $\boldsymbol{x} \in \mathbb{R}^4$ with $x_0 \equiv t$ for the time variable and $(x_i)_{i=1,3}$ for the space variables. The quadratic form Q and the canonical form $\tilde{Q}$ associated with (8.38) are respectively given by

$$Q(\boldsymbol{\xi}) = \sum_{i,j=0}^{n} a_{ij} \xi_i \xi_j \qquad \tilde{Q}(\boldsymbol{\xi}) = \sum_{i=0}^{n} \lambda_i \xi_i^2 \qquad \boldsymbol{\xi} \in \mathbb{R}^{n+1}$$

where the λ_i are the $n+1$ eigenvalues of the symmetric matrix (a_{ij}) with $0 \leq i, j \leq n$.

Equation (8.38) is called elliptic at point $\boldsymbol{x}$ if all the eigenvalues of the canonical form have the same sign, the quadratic form thus being either negative-definite or positive-definite. Elliptic equations are often encountered when solving stationary problems in fluid mechanics. A classical example is the Laplace equation $\nabla^2 T = 0$, with $\lambda_1 = \lambda_2 = \lambda_3 = 1$, $\boldsymbol{\xi} \in \mathbb{R}^3$ for the associated quadratic form and with appropriate boundary conditions. It must be noted that an unsteady problem, of the form $\partial/\partial t$ on the left-hand side and involving spatial derivatives on the right-hand side, with thus $\boldsymbol{\xi} \in \mathbb{R}^4$, is never elliptic.

Equation (8.38) is said to be parabolic at point $\boldsymbol{x}$ if one of the eigenvalues is equal to zero, and the n others have the same sign. Diffusion problems are often modelled by a parabolic equation. An example is the heat equation in a medium at rest

$$\frac{\partial T}{\partial t} = a\nabla^2 T$$

with thus $\lambda_0 = 0$, $\lambda_1 = \lambda_2 = \lambda_3 = 1$ and $\boldsymbol{\xi} \in \mathbb{R}^4$. To solve this equation, it is necessary to provide an initial condition, with a temperature profile $T_0(\boldsymbol{x})$ at $t = 0$ for instance. The boundary layer approximation (3.5) is another example of the parabolization of the steady Navier-Stokes equations,

$$\bar{U}_1 \frac{\partial \bar{U}_1}{\partial x_1} + \bar{U}_2 \frac{\partial \bar{U}_1}{\partial x_2} = -\frac{1}{\rho}\frac{dP_e}{dx_1} - \frac{\partial \overline{u_1' u_2'}}{\partial x_2} + \nu \frac{\partial^2 \bar{U}_1}{\partial x_2^2}$$

with $\lambda_1 = \lambda_3 = 0$, $\lambda_2 = \nu$ and $\boldsymbol{\xi} \in \mathbb{R}^3$, although the external pressure P_e in this type of problem is often provided by an elliptic potential flow outside of the boundary layer.

Finally, Eq. (8.38) is called hyperbolic at point $\boldsymbol{x}$ if and only if n of the $n+1$ eigenvalues have the same sign. A classical example is the wave equation for an acoustic perturbation in a medium at rest of celerity c_∞

$$\frac{\partial^2 p'}{\partial t^2} - c_\infty^2 \nabla^2 p' = 0$$

where the eigenvalues associated with the quadratic form are $\lambda_0 = 1$ and $\lambda_1 = \lambda_2 = \lambda_3 = -c_0^2$. The resolution requires initial conditions for p' and its derivative $\partial p'/\partial t$ at $t = 0$. The Euler equations are also hyperbolic. Equations governing compressible and supersonic flows have a hyperbolic aspect. To solve this type of equation, the associated hypersurface $Q(\boldsymbol{\xi}) = 0$ is often used, permitting to define characteristic curves. The reader can refer to the book of Ockendon and Ockendon [18] for a comprehensive introduction to this topic.

The Navier-Stokes equation

$$\rho\left(\frac{\partial u_i}{\partial t} + u_j \frac{\partial u_i}{\partial x_j}\right) = -\frac{\partial p}{\partial x_i} + \frac{\partial}{\partial x_j}\left[\mu\left(\frac{\partial u_i}{\partial x_j} + \frac{\partial u_j}{\partial x_i}\right) - \frac{2}{3}\mu \frac{\partial u_k}{\partial x_k}\delta_{ij}\right]$$

requires specific comments. Formally this nonlinear equation is parabolic, and its steady formulation is elliptic. Due to the presence of the convection term $u_j \partial u_i/\partial x_j$, the Navier-Stokes equation does not fit into the previously described classification. However, this nonlinear term plays an essential role in fluid dynamics and turbulence, and must be carefully taken into account in numerical algorithms.

A general introduction to computational methods can be found in Ferziger and Perić [244], and a more complete view in the two books by Hirsch [245, 246]. The reader can also refer to the reviews by Colonius [242], Ekaterinaris [243] and more recently Pirozzoli [257] for boundary conditions and high-order numerical algorithms.

8.4 Favre Filtering⋆

A first idea to extend the filtered Navier-Stokes equation (8.13) to compressible flows is to generalize the decomposition (8.12) to the density variable, namely $\rho = \bar{\rho} + \rho'$ with $\bar{\rho} = G * \rho$. In this way, the filtered equations for the mass, momentum and internal total energy ρe_t conservation equations are

$$\frac{\partial \bar{\rho}}{\partial t} + \frac{\partial (\bar{\rho}\bar{u}_i)}{\partial x_i} = \frac{\partial}{\partial x_i}\left(-\overline{\rho u_i} + \bar{\rho}\bar{u}_i\right) \tag{8.39}$$

$$\begin{aligned}\frac{\partial(\bar{\rho}\bar{u}_i)}{\partial t} + \frac{\partial(\bar{\rho}\bar{u}_i\bar{u}_j)}{\partial x_j} &= -\frac{\partial \bar{p}}{\partial x_i} + \frac{\partial \bar{\tau}_{ij}}{\partial x_j} \\ &+ \frac{\partial}{\partial x_j}\left(-\overline{\rho u_i u_j} + \bar{\rho}\bar{u}_i\bar{u}_j\right) + \frac{\partial}{\partial t}\left(-\overline{\rho u_i} + \bar{\rho}\bar{u}_i\right)\end{aligned} \tag{8.40}$$

$$\begin{aligned}\frac{\partial(\bar{\rho}\bar{e}_t)}{\partial t} + \frac{\partial(\bar{\rho}\bar{e}_t\bar{u}_j)}{\partial x_j} &= \frac{\partial}{\partial x_j}\left(-\bar{q}_j + \bar{u}_i\bar{\tau}_{ij} - \bar{u}_j\bar{p}\right) \\ &+ \frac{\partial}{\partial x_j}\left(-\overline{\rho e_t u_j} + \bar{\rho}\bar{e}_t\bar{u}_j + \overline{u_i\tau_{ij}} - \bar{u}_i\bar{\tau}_{ij} - \overline{u_j p} + \bar{u}_j\bar{p}\right) \\ &+ \frac{\partial}{\partial t}\left(-\overline{\rho e_t} + \bar{\rho}\bar{e}_t\right)\end{aligned} \tag{8.41}$$

For the mass conservation equation (8.39), the new term to consider when comparing to the incompressible flow formulation is

$$-\overline{\rho u_i} + \bar{\rho}\bar{u}_i \simeq -\overline{\rho' u_i'} = C_m \Delta^2 \bar{s}\,\frac{\partial \bar{\rho}}{\partial x_i} \qquad \text{where} \qquad \bar{s} = \sqrt{2\bar{s}_{ij}\bar{s}_{ij}}$$

is the shear magnitude of the filtered velocity field. The constant C_m can be determined by a dynamic procedure [273], in the same way as explained in Sect. 8.2.4.3.

An alternative to the formal decomposition of the density consists in introducing density weighted variables for compressible flows. This approach was introduced by Favre [382]. For the reader not familiar with this procedure, it may be useful to first read Sect. 9.3.3 of the Chap. 9 dealing with the Favre-averaged Navier-Stokes equations. In the context of large-eddy simulation, the velocity component u_i, for instance, is decomposed as $u_i = \tilde{u}_i + u_i''$ where the so-called Favre-filtered velocity $\tilde{u}_i$ is defined by $\bar{\rho}\tilde{u}_i = G_\Delta * (\rho u_i)$. This notation should not be confused with that

of the secondary filter introduced in Sect. 8.2.4. As a result, one has

$$u_i = \tilde{u}_i + u_i'' \qquad \text{with} \quad \tilde{u}_i = \frac{\overline{\rho u_i}}{\bar{\rho}} \quad \text{and} \quad \overline{\rho u_i''} = 0$$

The Favre-filtered equations are then given by

$$\frac{\partial \bar{\rho}}{\partial t} + \frac{\partial (\bar{\rho}\tilde{u}_i)}{\partial x_i} = 0 \tag{8.42}$$

$$\frac{\partial}{\partial t}(\bar{\rho}\tilde{u}_i) + \frac{\partial}{\partial x_j}\left(\bar{\rho}\tilde{u}_i\tilde{u}_j\right) = -\frac{\partial \bar{p}}{\partial x_i} + \frac{\partial \bar{\tau}_{ij}}{\partial x_j} + \frac{\partial}{\partial x_j}\left(\bar{\rho}\tilde{u}_i\tilde{u}_j - \widetilde{\rho u_i u_j}\right) \tag{8.43}$$

$$\begin{aligned}\frac{\partial(\bar{\rho}\tilde{e}_t)}{\partial t} + \frac{\partial(\bar{\rho}\tilde{e}_t\tilde{u}_j)}{\partial x_j} &= \frac{\partial}{\partial x_j}\left(-\bar{q}_j + \tilde{u}_i\bar{\tau}_{ij} - \tilde{u}_j\bar{p}\right) \\ &+ \frac{\partial}{\partial x_j}\left(-\widetilde{\rho e_t u_j} + \bar{\rho}\tilde{e}_t\tilde{u}_j + \overline{u_i\tau_{ij}} - \tilde{u}_i\bar{\tau}_{ij} - \overline{u_j p} + \tilde{u}_j\bar{p}\right)\end{aligned} \tag{8.44}$$

The advantage of such a formulation clearly appears when comparing Eqs. (8.42) and (8.39) for instance. However, new unknown terms still need to be modelled for this formulation. The expression of the filtered viscous stress tensor contains an additional term, which is often neglected

$$\bar{\tau}_{ij} = 2\mu\widetilde{s_{ij}} + 2\mu\overline{s_{ij}''} \simeq 2\mu\widetilde{s_{ij}} = \mu\left(\frac{\partial\tilde{u}_i}{\partial x_j} + \frac{\partial\tilde{u}_j}{\partial x_i}\right) - \frac{2}{3}\mu\frac{\partial\tilde{u}_k}{\partial x_k}\delta_{ij}$$

In a similar way, the filtered heat flux is commonly approximated by the following expression

$$\bar{q}_j \simeq \tilde{q}_j = -\lambda\frac{\partial\tilde{T}}{\partial x_j} \qquad \text{with} \quad \lambda = \frac{\mu c_p}{\sigma} \quad \text{and} \quad \bar{p} = \bar{\rho} r\tilde{T}$$

Formulations based on Favre-filtered equations are most often used for compressible flows, but certain authors [273, 324] have nevertheless preferred to solve the system (8.39)–(8.41).

8.5 Compressible Large Eddy Simulation*

*8.5.1 Filtered Navier-Stokes Equations**

Using density weighted variables, the filtered Navier-Stokes equations are given by relations (8.42)–(8.44). The mass conservation equation does not need any modelling, as pointed out above. The filtered equation for momentum conservation can be recast

in the following form

$$\frac{\partial}{\partial t}(\bar{\rho}\tilde{u}_i) + \frac{\partial}{\partial x_j}(\bar{\rho}\tilde{u}_i\tilde{u}_j) = -\frac{\partial \bar{p}}{\partial x_i} + \frac{\partial \bar{\tau}_{ij}}{\partial x_j} + \frac{\partial t_{ij}}{\partial x_j} \tag{8.45}$$

where the subgrid tensor t_{ij} is now defined by $t_{ij} = \bar{\rho}\tilde{u}_i\tilde{u}_j - \widetilde{\bar{\rho}u_iu_j} \simeq -\widetilde{\bar{\rho}u_i''u_j''}$, using notations already introduced in Sect. 8.2.4. When a turbulent viscosity model is chosen to model this tensor, t_{ij} is written as $t_{ij} = t_{ij}^{\mathcal{D}} + t_{ij}^{\mathcal{I}}$ with

$$\begin{cases} t_{ij}^{\mathcal{D}} = -\widetilde{\bar{\rho}u_i''u_j''} + \dfrac{1}{3}\widetilde{\bar{\rho}u_k''u_k''}\delta_{ij} \\ t_{ij}^{\mathcal{I}} = -\dfrac{1}{3}\widetilde{\bar{\rho}u_k''u_k''}\delta_{ij} = -\dfrac{2}{3}\bar{\rho}k_{sgs}\delta_{ij} \end{cases}$$

and the deviator and isotropic parts of t_{ij} are determined as follows

$$\begin{cases} t_{ij}^{\mathcal{D}} = 2\mu_t\tilde{s}_{ij} \qquad \text{with} \qquad \mu_t = \bar{\rho}C_s^2\Delta^2\sqrt{2\tilde{s}_{kl}\tilde{s}_{kl}} \\ t_{ij}^{\mathcal{I}} = -\dfrac{2}{3}\bar{\rho}C_I\Delta^2 2\tilde{s}_{kl}\tilde{s}_{kl}\delta_{ij} \end{cases}$$

where the Favre-filtered tensor $\tilde{s}_{ij}$ is defined by

$$\tilde{s}_{ij} = \frac{1}{2}\left(\frac{\partial \tilde{u}_i}{\partial x_j} + \frac{\partial \tilde{u}_j}{\partial x_i}\right) - \frac{1}{3}\frac{\partial \tilde{u}_k}{\partial x_k}\delta_{ij}$$

The isotropic part $t_{ij}^{\mathcal{I}}$ of the subgrid tensor is directly linked to the residual subgrid energy k_{sgs}. For an ideal gas, one has

$$\frac{2}{3}\bar{\rho}k_{sgs} = \frac{\gamma}{3}M_{sgs}^2\bar{p} \quad \text{where} \quad M_{sgs}^2 = 2k_{sgs}/\left(\gamma\bar{p}/\bar{\rho}\right)$$

and grouping this term with the pressure term in filtered Navier-Stokes equation (8.45), it yields

$$-\frac{\partial}{\partial x_i}\left(\bar{p} + \frac{\gamma}{3}M_{sgs}^2\bar{p}\right) \simeq -\frac{\partial \bar{p}}{\partial x_i} \quad \text{if} \quad M_{sgs} \ll 1$$

Finally, using a turbulent viscosity model, Eq. (8.45) takes the following form

$$\frac{\partial}{\partial t}(\bar{\rho}\tilde{u}_i) + \frac{\partial}{\partial x_j}(\bar{\rho}\tilde{u}_i\tilde{u}_j) = -\frac{\partial \bar{p}}{\partial x_i} + \frac{\partial}{\partial x_j}\left[2(\mu + \mu_t)\tilde{s}_{ij}\right] \tag{8.46}$$

8.5.2 Total Internal Energy Conservation⋆

The conservation of energy is written for the total internal energy ρe_t, defined as the sum of the internal and kinetic energies. The filtered transport equation for $\bar{\rho}\tilde{e}_t$ is

$$\frac{\partial}{\partial t}\left(\bar{\rho}\tilde{e}_t\right)+\frac{\partial}{\partial x_j}\left(\bar{\rho}\tilde{e}_t\tilde{u}_j\right)=\frac{\partial}{\partial x_j}\left(\lambda\frac{\partial\tilde{T}}{\partial x_j}+\tilde{u}_i\bar{\tau}_{ij}-\tilde{u}_j\bar{p}\right)$$
$$+\frac{\partial}{\partial x_j}\underbrace{\left[-\widetilde{\rho e_t u_j}+\bar{\rho}\tilde{e}_t\tilde{u}_j\right]}_{r_j^A}\underbrace{-\widetilde{u_j p}+\tilde{u}_j\bar{p}}_{r_j^B}+\frac{\partial}{\partial x_j}\left[\widetilde{u_i\tau_{ij}}-\tilde{u}_i\bar{\tau}_{ij}\right] \quad (8.47)$$

where the resolved total internal energy is given by

$$\bar{\rho}\tilde{e}_t=\bar{\rho}\tilde{e}+\frac{1}{2}\bar{\rho}\tilde{u}_k\tilde{u}_k+\frac{1}{2}\bar{\rho}\widetilde{u_k''u_k''}$$
$$=\bar{\rho}c_v\tilde{T}+\frac{1}{2}\bar{\rho}\tilde{u}_k\tilde{u}_k+\bar{\rho}k_{sgs}=\frac{\bar{p}}{\gamma-1}+\frac{1}{2}\bar{\rho}\tilde{u}_k\tilde{u}_k+\bar{\rho}k_{sgs} \quad (8.48)$$

with $\bar{p}=\bar{\rho}r\tilde{T}$ for an ideal gas. Following Lesieur and Comte [231], a macro-pressure $p^\star$ and a macro-temperature $T^\star$ defined by

$$p^\star=\bar{p}+\frac{2}{3}\bar{\rho}k_{sgs}\qquad\text{and}\qquad T^\star=\tilde{T}+\frac{1}{c_v}k_{sgs}$$

are introduced, and the residual subgrid energy can then be substituted into (8.46) and (8.47). However new closure problems remain to be solved [292]. One of the most important terms of this equation is the vector r_j^A. It can be written as follows

$$r_j^A=-\widetilde{\rho e_t u_j}+\bar{\rho}\tilde{e}_t\tilde{u}_j$$
$$=\underbrace{-\bar{\rho}\widetilde{\tilde{e}_t\tilde{u}_j}+\bar{\rho}\tilde{e}_t\tilde{u}_j}_{(a)}\underbrace{-\bar{\rho}\widetilde{\tilde{e}_t u_j''}-\bar{\rho}\widetilde{e_t''\tilde{u}_j}}_{(b)}-\bar{\rho}\widetilde{e_t''u_j''}$$

Assuming that the Leonard (a) and cross terms (b) can be neglected, the closure of the term r_j^A is then reduced to the modelling of

$$r_j^A\simeq-\bar{\rho}\widetilde{e_t''u_j''}$$

From Eq. (8.48), one has $e_t''=e_t-\tilde{e}_t=e''+u_k''\tilde{u}_k+u_k''u_k''/2-\widetilde{u_k''u_k''}/2$ which gives after multiplying by $\rho u_j''$ and applying Favre average

$$r_j^A\simeq-\bar{\rho}\widetilde{e''u_j''}-\bar{\rho}\widetilde{u_k''u_j''}\tilde{u}_k-\frac{1}{2}\bar{\rho}\widetilde{u_k''u_k''u_j''}$$

The triple correlation term $\bar{\rho}\widetilde{u_k'' u_k'' u_j''}/2$ is often neglected. Moreover, it is assumed that

$$\widetilde{u_k'' u_j'' \tilde{u}_k} \simeq \widetilde{u_k'' u_j''}\ \tilde{u}_k$$

and the vector r_j^A is approximated by the following expression

$$r_j^A \simeq -\bar{\rho}\widetilde{e_t'' u_j''} \simeq -\bar{\rho} c_v \widetilde{T'' u_j''} - \bar{\rho}\widetilde{u_k'' u_j''}\tilde{u}_k$$

The second term can be directly expressed from the subgrid model, $-\bar{\rho}\widetilde{u_k'' u_j''} = 2\mu_t \tilde{s}_{kj}$. As for the first term, it can be grouped with the vector r_j^B

$$r_j^B = -\overline{u_j p} + \tilde{u}_j \bar{p} = -\overline{u_j'' p} \simeq -r\bar{\rho}\,\widetilde{u_j'' T''}$$

and therefore,

$$-\bar{\rho} c_v \widetilde{T'' u_j''} - r\bar{\rho}\,\widetilde{u_j'' T''} = -\bar{\rho} c_p \widetilde{T'' u_j''}$$

A gradient closure is classically used as in turbulence models, refer to the compressible k_t–ϵ model developed in Sect. 9.3.3 for instance. Hence,

$$-\bar{\rho} c_p \widetilde{T'' u_j''} = \bar{\rho} c_p a_t \frac{\partial \tilde{T}}{\partial x_j}$$

where $\mathrm{Pr}_t = \nu_t / a_t = \mu_t c_p / \lambda_t$ is the turbulent Prandtl number, a_t is the turbulent thermal diffusivity and λ_t is the turbulent thermal conductivity. The terms involving temperature are then recast as follows

$$-\bar{\rho} c_p \widetilde{T'' u_j''} + \lambda \frac{\partial \tilde{T}}{\partial x_j} = \left(\bar{\rho} c_p a_t + \lambda\right) \frac{\partial \tilde{T}}{\partial x_j} = \left(\lambda_t + \lambda\right) \frac{\partial \tilde{T}}{\partial x_j}$$

The last term in brackets in (8.47) is neglected. Finally, the Favre-filtered energy conservation equation takes the form

$$\frac{\partial}{\partial t}(\bar{\rho}\tilde{e}_t) + \frac{\partial}{\partial x_j}(\bar{\rho}\tilde{e}_t \tilde{u}_j) = \frac{\partial}{\partial x_j}\left[(\lambda + \lambda_t)\frac{\partial \tilde{T}}{\partial x_j} + 2\left(\mu + \mu_t\right)\tilde{s}_{ij}\tilde{u}_i - \tilde{u}_j \bar{p}\right] \quad (8.49)$$

The constants of the model C_d and C_I can be numerically determined by a dynamic procedure, using a generalization of expressions (8.28) and (8.29). This is also the case for the turbulent Prandtl number [292, 323].

8.5.3 Variant of the Energy Equation*

Among the numerous other possible formulations for expressing energy conservation, the one proposed by Vreman et al. [356, 357] can be pointed out. These authors attempted to write an exact equation on the total energy part given by (8.48), where only resolved variables appear

$$\bar{\rho}\breve{e} = \bar{\rho}\tilde{e} + \frac{1}{2}\tilde{u}_i\tilde{u}_i \neq \bar{\rho}\tilde{e}_t$$

To achieve this, the kinetic energy transport equation can be subtracted from the total internal energy equation to obtain

$$\frac{\partial}{\partial t}\left(\frac{p}{\gamma-1}\right) + \frac{\partial}{\partial x_j}\left(\frac{\gamma\, p u_j}{\gamma-1}\right) = -\frac{\partial q_j}{\partial x_j} + u_j\frac{\partial p}{\partial x_j} + \tau_{ij}\frac{\partial u_i}{\partial x_j}$$

Applying Favre filtering to this equation

$$\frac{\partial}{\partial t}\left(\frac{\bar{p}}{\gamma-1}\right) + \frac{\partial}{\partial x_j}\left(\frac{\gamma\, \bar{p}\tilde{u}_j}{\gamma-1}\right) = -\frac{\partial \bar{q}_j}{\partial x_j} + \overline{u_j\frac{\partial p}{\partial x_j}} + \overline{\tau_{ij}\frac{\partial u_i}{\partial x_j}} + \frac{\gamma}{\gamma-1}\frac{\partial}{\partial x_j}\left(\bar{p}\tilde{u}_j - \overline{pu_j}\right)$$

So as to form the variable $\bar{\rho}\breve{e}$, the resolved field kinetic energy transport equation obtained from (8.45), is then added

$$\frac{\partial}{\partial t}\left(\frac{\bar{\rho}\tilde{u}_i^2}{2}\right) + \frac{\partial}{\partial x_j}\left(\frac{\bar{\rho}\tilde{u}_i^2}{2}\tilde{u}_j\right) = -\tilde{u}_i\frac{\partial \bar{p}}{\partial x_i} + \tilde{u}_i\frac{\partial \bar{\tau}_{ij}}{\partial x_j} + \tilde{u}_i\frac{\partial t_{ij}}{\partial x_j}$$

to finally obtain

$$\frac{\partial}{\partial t}\left(\bar{\rho}\breve{e}\right) + \frac{\partial}{\partial x_j}\left[\left(\bar{\rho}\breve{e}_t + \bar{p}\right)\tilde{u}_j\right] = -\frac{\partial \bar{q}_j}{\partial x_j} + \tilde{u}_i\frac{\partial t_{ij}}{\partial x_j} + \frac{\partial}{\partial x_j}\left(\tilde{u}_i\bar{\tau}_{ij}\right) + \frac{1}{\gamma-1}\frac{\partial}{\partial x_j}\left(\bar{p}\tilde{u}_j - \overline{pu_j}\right) + \underbrace{\bar{p}\frac{\partial \tilde{u}_j}{\partial x_j} - \overline{p\frac{\partial u_j}{\partial x_j}}} + \underbrace{\overline{\tau_{ij}\frac{\partial u_i}{\partial x_j}} - \bar{\tau}_{ij}\frac{\partial \tilde{u}_i}{\partial x_j}}$$

This is the exact transport equation for the energy variable $\rho\breve{e}$, without any assumption regarding residual subgrid energy or velocity triple correlations. The two last terms represent pressure-dilatation correlations and the turbulent dissipation respectively.

Chapter 9
Turbulence Models

This chapter focuses on turbulent models, which are widely used in a large variety of engineering studies, including atmospheric dynamics and weather forecasting. The objective is to determine the turbulent mean flow from the averaged equations (2.14) and (2.15) established in Chap. 2. A turbulence model is however required to express the unknown Reynolds stress tensor. The most popular approaches are based on Boussinesq's hypothesis (2.24) with the introduction of a turbulent viscosity. A survey of these so-called eddy-viscosity models is presented in this chapter.

For clarity, the Reynolds averaged Navier-Stokes equation is first recalled,

$$\frac{\partial(\rho\bar{U}_i)}{\partial t} + \frac{\partial\left(\rho\bar{U}_i\,\bar{U}_j\right)}{\partial x_j} = -\frac{\partial\bar{P}}{\partial x_i} + \frac{\partial}{\partial x_j}(\bar{\tau}_{ij} - \rho\overline{u_i' u_j'}) \tag{9.1}$$

where $\bar{U}_i$ is the mean velocity, $\bar{\tau}_{ij} = 2\mu\bar{S}_{ij}$ the viscous stress and $-\rho\overline{u_i' u_j'}$ the Reynolds stress. The mean flow is assumed to be incompressible. Section 9.3 is devoted to the specific treatment of the compressible case. Following Boussinesq's hypothesis, see Sect. 2.5, the unknown Reynolds stress tensor is expressed as,

$$-\rho\overline{u_i' u_j'} = 2\mu_t\bar{S}_{ij} - \frac{2}{3}\rho k_t\delta_{ij} \tag{9.2}$$

where $\mu_t = \rho\nu_t$ is the dynamic turbulent viscosity and k_t the turbulent kinetic energy. By noting that μ and μ_t are both in front of the same term $\bar{S}_{ij}$, Eq. (9.1) can be rearranged as follows,

$$\frac{\partial(\rho\bar{U}_i)}{\partial t} + \frac{\partial\left(\rho\bar{U}_i\,\bar{U}_j\right)}{\partial x_j} = -\frac{\partial}{\partial x_i}\left(\bar{P} + \frac{2}{3}\rho k_t\right) + \frac{\partial}{\partial x_j}\left[2(\mu+\mu_t)\bar{S}_{ij}\right] \tag{9.3}$$

The only remaining unknown is now the turbulent viscosity. Turbulence models differ in the way they determine its expression. A classical way consists in writing the turbulent viscosity as the product of a velocity scale by a length scale, and to

C. Bailly and G. Comte-Bellot, *Turbulence*, Experimental Fluid Mechanics,
DOI 10.1007/978-3-319-16160-0_9

solve two additional transport equations to determine these scales. The standard k_t–ϵ model or k_t–ω_t models fall into this family for instance. An alternative approach is to directly write a transport equation for the turbulent viscosity, as in Spalart-Allmaras' model. These models and some extensions are introduced in the following sections.

9.1 Mixing Length Models

In the mixing length models, first introduced by Prandtl, the turbulent viscosity is written as the product of a velocity scale u by a length scale l_m by analogy with the molecular viscosity. It is also assumed that the time scale associated with the mean shear flow $\left|\partial \bar{U}_1/\partial x_2\right|^{-1}$ is proportional to the time scale built from u and l_m, namely

$$\frac{u}{l_m} \sim \left|\frac{\partial \bar{U}_1}{\partial x_2}\right|$$

From the relation $\nu_t \sim u \times l_m$, the expression of the turbulent viscosity can thus be rearranged as follows,

$$\nu_t = l_m^2 \left|\frac{\partial \bar{U}_1}{\partial x_2}\right| \tag{9.4}$$

where the absolute value of the mean flow gradient is taken to ensure a positive value of ν_t. The Reynolds shear stress $-\rho\overline{u_1' u_2'}$ is then determined from Boussinesq's hypothesis (9.2),

$$-\overline{u_1' u_2'} = l_m^2 \left|\frac{\partial \bar{U}_1}{\partial x_2}\right| \frac{\partial \bar{U}_1}{\partial x_2} \tag{9.5}$$

This model has already been applied in Sect. 3.7 to calculate the mean velocity profile of a turbulent boundary layer. It has been shown that the mixing length must be equal to $l_m = \kappa x_2$ in the logarithmic region, and that it must be reduced close to the wall by using a damping function as proposed by Van Driest [442], see expression (3.22).

In a plane mixing layer, the mixing length is $l_m \simeq 0.07\,\delta(x_1)$ where δ is the local thickness of the layer. For other free shear flows, as in jets or wakes, the length scale l_m is also linked to the shear layer thickness. For instance, one obtains approximately $l_m \simeq 0.09\,\delta(z)$ in a round jet, where δ is the width of the annular mixing layer. Further examples can be found in the book by Wilcox [449].

Expression (9.4) can be generalized to an arbitrary mean shear flow by writing $\nu_t = l_m^2 \bar{S}$, where $\bar{S}$ is defined by

$$\bar{S} \equiv \sqrt{2\bar{S}_{ij}\bar{S}_{ij}}$$

The magnitude of the mean vorticity $\bar{\Omega}$ can also be used to define the turbulent viscosity, that is $\nu_t = l_m^2 \bar{\Omega}$ with $\bar{\Omega}^2 \equiv 2\bar{\Omega}_{ij}\bar{\Omega}_{ij}$, as in the Baldwin-Lomax model [364] used in aerodynamics [394, 445].

Mixing length models are easy to implement since the turbulent viscosity is simply determined by an algebraic relation. They are however incomplete since the user must prescribe the suitable evolution of $l_m(\boldsymbol{x}, t)$. This drawback can be removed by solving additional transport equations in order to predict the two scales u and l_m for all points of the computational domain.

9.2 The k_t–ϵ Turbulence Model

One of the most popular two-equation models is undoubtedly the k_t–ϵ turbulence model, introduced by Jones and Launder [392] and formulated by Launder and Spalding [401] in its standard form. In this model, the expression of the turbulent viscosity is built by taking, for the velocity scale, the square root of the turbulent kinetic energy, $u \sim \sqrt{k_t}$, while the length scale is calculated from the dissipation rate of the turbulent kinetic energy. By noting that for homogeneous turbulence, $\epsilon^h \simeq u'^3/L_f$ where $u'^2 = (2/3)k_t$, an expression of the turbulent viscosity can then be derived by choosing l_m proportional to the integral length scale L_f. It yields

$$\nu_t \sim u \times l_m \sim k_t^{1/2} \times k_t^{3/2}/\epsilon^h \qquad \text{and hence,} \qquad \nu_t \equiv C_\mu \frac{k_t^2}{\epsilon^h} \tag{9.6}$$

where C_μ is a constant of the model, which needs to be determined. The estimation of ν_t also requires the knowledge of k_t and ϵ^h. The following sections are devoted to deriving transport equations for these two quantities.

9.2.1 Transport Equation of Turbulent Kinetic Energy

The budget of the turbulent kinetic energy k_t has already been established in Chap. 2, see Eq. (2.20). For the sake of clarity, this equation is rewritten as below

$$\frac{\bar{d}(\rho k_t)}{\bar{d}t} = -\rho\overline{u_i' u_k'}\,\frac{\partial \bar{U}_i}{\partial x_k} - \underbrace{\overline{\tau_{ik}' \frac{\partial u_i'}{\partial x_k}}}_{\text{(a)}} - \frac{1}{2}\frac{\partial}{\partial x_k}\overline{\rho u_i' u_i' u_k'} - \frac{\partial}{\partial x_i}\overline{u_i' p'} + \underbrace{\frac{\partial}{\partial x_k}\overline{u_i' \tau_{ik}'}}_{\text{(b)}} \tag{9.7}$$

The dissipation term (a) and the diffusive transport term (b) can be rearranged as follows

$$\frac{\partial}{\partial x_k}\overline{u_i'\tau_{ik}'} - \overline{\tau_{ik}'\frac{\partial u_i'}{\partial x_k}} = \frac{\partial}{\partial x_k}\left(\mu\frac{\partial k_t}{\partial x_k}\right) + \mu\overline{\frac{\partial u_i'}{\partial x_k}\frac{\partial u_i'}{\partial x_k}}$$
$$= \frac{\partial}{\partial x_k}\left(\mu\frac{\partial k_t}{\partial x_k}\right) - \rho\epsilon^h \tag{9.8}$$

since $\tau_{ik}' = 2\mu s_{ik}'$, and also by using the incompressibility condition $\partial u_k'/\partial x_k = 0$. The homogeneous part of the dissipation ϵ^h has already been introduced when studying the turbulent channel flow, see expression (2.26) and associated comments. It represents a good approximation of the total dissipation rate ϵ for an inhomogeneous turbulent flow at high Reynolds number [429], refer to Sect. 6.5. The transport equation for the turbulent kinetic energy (9.7) thus becomes

$$\frac{\bar{d}(\rho k_t)}{\bar{d}t} = -\rho\overline{u_i'u_k'}\frac{\partial \bar{U}_i}{\partial x_k} - \rho\epsilon^h + \frac{\partial}{\partial x_k}\left(\mu\frac{\partial k_t}{\partial x_k}\right) - \frac{1}{2}\frac{\partial}{\partial x_k}\rho\overline{u_i'u_i'u_k'} - \frac{\partial}{\partial x_i}\overline{u_i'p'} \tag{9.9}$$

Only the two last terms need to be modelled in this expression. Turbulent transport terms such as the triple-correlation term in Eq. (9.9) are usually closed by a gradient-diffusion model. For an arbitrary quantity φ, it is assumed that

$$-\overline{\varphi u_k'} = a_t\frac{\partial \bar{\varphi}}{\partial x_k}$$

where a_t is a diffusion coefficient associated with φ. With $\varphi = u_i'u_i'/2$ in the present case, and by simply including the pressure–velocity correlation in this gradient model, it yields

$$-\frac{\rho}{2}\overline{u_i'u_i'u_k'} - \overline{p'u_k'} = \frac{\mu_t}{\sigma_{k_t}}\frac{\partial k_t}{\partial x_k}$$

where σ_{k_t} is a turbulent Prandtl number, by analogy with the molecular transport, and ν_t/σ_{k_t} is a turbulent diffusivity. The pressure–velocity correlation cannot be directly measured but can be computed by numerical simulations. Its contribution is found to be small in channel flows and in jet flows, see illustrations in Sects. 2.6 and 4.16 respectively, which can justify this approximation. Finally the following transport equation is retained for the turbulent kinetic energy k_t

$$\frac{\bar{d}(\rho k_t)}{\bar{d}t} = \frac{\partial}{\partial x_k}\left[\left(\mu + \frac{\mu_t}{\sigma_{k_t}}\right)\frac{\partial k_t}{\partial x_k}\right] + \mathcal{P} - \rho\epsilon^h \tag{9.10}$$

where $\mathcal{P} = -\rho\overline{u_i'u_k'}\,\partial\bar{U}_i/\partial x_k$ is the production term.

9.2.2 Transport Equation for Dissipation

Derivation of the transport equation for the dissipation ϵ^h for an incompressible homogeneous flow requires much more effort than for the turbulent kinetic energy. Starting from the Navier-Stokes equation on the fluctuating velocity established in Chap. 2 (see Sect. 2.4.1),

$$\frac{\partial\left(\rho u_i'\right)}{\partial t}+\frac{\partial}{\partial x_k}\left[\rho\left(u_i'\bar{U}_k+\bar{U}_i u_k'+u_i'u_k'\right)\right]=-\frac{\partial p'}{\partial x_i}+\frac{\partial}{\partial x_k}\left(\rho\overline{u_i'u_k'}+\tau_{ik}'\right) \quad (9.11)$$

the following equation is then constructed

$$\nu\frac{\partial u_i'}{\partial x_j}\frac{\partial}{\partial x_j}(9.11)$$

and averaged to form an equation on $\rho\epsilon^h=\mu\overline{\partial_{x_j}u_i'\partial_{x_j}u_i'}$, see Eq. (9.8). Details are reported in Sect. 9.7. It is shown that the transport equation can be written as

$$\begin{aligned}\frac{\bar{d}(\rho\epsilon^h)}{\bar{d}t}=&\underbrace{-2\mu\frac{\partial\bar{U}_k}{\partial x_j}\left(\overline{\frac{\partial u_i'}{\partial x_k}\frac{\partial u_i'}{\partial x_j}}+\overline{\frac{\partial u_k'}{\partial x_i}\frac{\partial u_j'}{\partial x_i}}\right)}_{\text{(i)}}\underbrace{-2\mu\overline{u_k'\frac{\partial u_i'}{\partial x_j}}\frac{\partial^2\bar{U}_i}{\partial x_j\partial x_k}}_{\text{(ii)}}\\&\underbrace{-2\mu\overline{\frac{\partial u_i'}{\partial x_j}\frac{\partial u_k'}{\partial x_j}\frac{\partial u_i'}{\partial x_k}}}_{\text{(iii)}}\underbrace{-\mu\frac{\partial}{\partial x_k}\overline{u_k'\frac{\partial u_i'}{\partial x_j}\frac{\partial u_i'}{\partial x_j}}}_{\text{(iv)}}\underbrace{-2\nu\frac{\partial}{\partial x_i}\overline{\frac{\partial u_i'}{\partial x_j}\frac{\partial p'}{\partial x_j}}}_{\text{(v)}}\\&\underbrace{+\mu\frac{\partial^2\epsilon^h}{\partial x_k\partial x_k}}_{\text{(vi)}}\underbrace{-2\rho\nu^2\overline{\frac{\partial^2u_i'}{\partial x_k\partial x_j}\frac{\partial^2u_i'}{\partial x_k\partial x_j}}}_{\text{(vii)}}\end{aligned} \quad (9.12)$$

It is not easy to interpret the different terms and therefore, to propose a rational modelling of this equation. Moreover, numerical simulations often do not provide dissipation-rate budgets [640]. Only a subtle dimensional analysis can be performed to model the dissipation transport equation (9.12), which would be too onerous to reproduce in what follows. An argumentation can be found in Hanjalić and Launder [386, 387] and in Launder [402]. Finally, the modelled transport equation for the dissipation is taken as follows

$$\frac{\bar{d}(\rho\epsilon^h)}{\bar{d}t}=\underbrace{\frac{\partial}{\partial x_k}\left[\left(\mu+\frac{\mu_t}{\sigma_\epsilon}\right)\frac{\partial\epsilon^h}{\partial x_k}\right]}_{\text{(a)}}+\underbrace{\frac{\epsilon^h}{k_t}\left(C_{\epsilon1}\mathcal{P}-C_{\epsilon2}\rho\epsilon^h\right)}_{\text{(b)}\quad\text{(c)}} \quad (9.13)$$

in the k_t–ϵ model, where σ_ϵ, $C_{\epsilon 1}$ and $C_{\epsilon 2}$ are three constants of the model. This semi-empirical equation has the same structure as that of Eq. (9.10) for the turbulent kinetic energy k_t. Transport of the dissipation rate along the mean flow is balanced by three terms. The turbulent diffusion term (a) represents terms (iv), (v) and (vi) in Eq. (9.12), where the viscous diffusion term (vi) can be neglected at high Reynolds numbers. The production term (b) is associated with term (iii), one can indeed refer to Sect. 5.2 where it is shown that this term is associated with vortex stretching. The destruction term (c) is associated with term (vii). These two terms (b) and (c) dominate all the other terms in the transport equation but, in view of their apparent difference, they should be both kept. Finally, it can be shown [387, 402] that the terms (i) and (ii) vary as $\mathrm{Re}_t^{-1/2}$ and as Re_t^{-1} respectively, and may thus be neglected relative to other terms. The turbulent Reynolds number is defined by $\mathrm{Re}_t = k_t^2/(\nu\epsilon^h)$.

9.2.3 Transport Equation of Energy

Several forms of the energy equation have been introduced in Chap. 2. The enthalpy equation (2.4) is first considered,

$$\frac{\partial(\rho h)}{\partial t} + u_j \frac{\partial(\rho h)}{\partial x_j} = \frac{\partial}{\partial x_j}\left(\frac{\lambda}{c_p}\frac{\partial h}{\partial x_j}\right) + \frac{\partial p}{\partial t} + u_j \frac{\partial p}{\partial x_j} + \tau_{ij}\frac{\partial u_i}{\partial x_j} \tag{9.14}$$

written for an ideal gas law, that is $dh = c_p dT$. As usual, the Reynolds decomposition for the enthalpy is introduced $h = \bar{H} + h'$ and the averaging operator is applied to derive a transport equation of the mean enthalpy,

$$\frac{\bar{d}(\rho\bar{H})}{\bar{d}t} = \frac{\partial}{\partial x_j}\left(\frac{\lambda}{c_p}\frac{\partial \bar{H}}{\partial x_j} - \overline{\rho u_j' h'}\right) + \frac{\partial \bar{P}}{\partial t} + \frac{\partial(\bar{U}_j\bar{P})}{\partial x_j} + \frac{\partial \overline{u_j' p'}}{\partial x_j} + \bar{\tau}_{ij}\frac{\partial \bar{U}_i}{\partial x_j} + \rho\epsilon \tag{9.15}$$

In numerical simulations, the turbulent diffusion term through fluctuating pressure is often neglected in the energy equation. Moreover, the dissipation is approximated by $\epsilon \simeq \epsilon^h$ according to Eq. (9.13). The velocity-enthalpy correlation term is expressed from a gradient model,

$$-\overline{\rho u_j' h'} \simeq \frac{\mu_t}{\mathrm{Pr}_t}\frac{\partial \bar{h}}{\partial x_j}$$

where Pr_t is a turbulent Prandtl number defined by $\mathrm{Pr}_t \equiv \nu_t/a_t$, and a_t is a turbulent thermal diffusivity. This number can be estimated experimentally in sheared mean flows for instance [8]. From the following relation,

$$\mathrm{Pr}_t = \frac{\nu_t}{a_t} = \frac{-\overline{u_1' u_2'}}{\partial\bar{U}_1/\partial x_2} \times \left(\frac{-\overline{h' u_2'}}{\partial\bar{h}/\partial x_2}\right)^{-1} \tag{9.16}$$

values of the turbulent Prandtl number are found between $0.6 \leq \mathrm{Pr}_t \leq 1$, and the recommended value [449, 451] in the k_t–ϵ model is $\mathrm{Pr}_t \simeq 0.85$ for boundary layer flows, and $\mathrm{Pr}_t \simeq 0.5$ for free shear flows. It is also convenient to introduce a turbulent thermal conductivity λ_t, with $a_t = \lambda_t/(\rho c_p)$, to model the correlation between fluctuating velocity and temperature. From the Reynolds decomposition of the temperature $T = \bar{T} + \theta'$, it is assumed that

$$-\overline{u_i'\theta'} = a_t \frac{\partial \bar{T}}{\partial x_i}$$

The particular case $\mathrm{Pr}_t = 1$ corresponds to the Reynolds analogy [370], for which turbulent momentum and thermal transfers lead to similar turbulent boundary layer profiles for the mean velocity and temperature. Finally, the ideal gas law provides a relation between the mean temperature and pressure, that is $\bar{P} = \rho r \bar{T}$.

As a further illustration, the transport equation for the specific internal energy e is also briefly examined for an ideal gas, that is, with $p = (\gamma - 1)\rho e$. This equation can be written as

$$\frac{\partial}{\partial t}\left(\rho e + \rho\frac{u_i^2}{2}\right) + \frac{\partial}{\partial x_j}\left[\left(\rho e + \rho\frac{u_i^2}{2} + p\right)u_j\right] = \frac{\partial}{\partial x_j}\left(\lambda\frac{\partial T}{\partial x_j} + u_i\tau_{ij}\right)$$

The Reynolds decomposition is then introduced, with $e = \bar{E} + e'$, and the total mean energy is defined by $\bar{E}_t \equiv \bar{E} + \bar{U}_i\bar{U}_i/2 + k_t$. A mean equation is obtained by applying the averaging operator. More details can be found in reviews by Vandromme [443] or by Knight [394]. Only the simplified usual form of this equation is given below,

$$\frac{\partial(\rho\bar{E}_t)}{\partial t} + \frac{\partial}{\partial x_j}\left[\left(\rho\bar{E}_t + \bar{P} + \frac{2}{3}\rho k_t\right)\bar{U}_j\right] = \frac{\partial}{\partial x_j}\left[(\lambda + \lambda_t)\frac{\partial \bar{T}}{\partial x_j} + 2(\mu + \mu_t)\bar{U}_i\bar{S}_{ij}\right]$$

where the gradient-diffusion assumption has again been used for second-order correlation terms.

As mentioned in the introduction, when the density is assumed constant, the mean temperature is a passive scalar. The mean velocity field is consequently not coupled to the transport equation for energy. This is no longer the case for an incompressible flow with variable density, that is $\bar{\rho} = \bar{\rho}(\bar{T})$, and when buoyancy effects are taken into account. The gravity force $-\rho g\delta_{3i}$ is then included in the Navier-Stokes equation, and the Boussinesq approximation [14, 405] is usually applied to derived averaged equations. Density variations are thus neglected in the fluid dynamics equations, except for terms involving buoyant effects. For instance, this leads to an additional term in the turbulent kinetic energy equation (9.7). Usually denoted $\mathcal{G}$, this term is expressed as $\mathcal{G} = \bar{\rho}g\beta\overline{\theta' u_3'}$, where the coefficient of thermal expansion is $\beta = 1/\bar{T}$

for an ideal gas. A transport equation for the temperature variance $\overline{\theta'^2}$ can also be established and modelled, a review is provided by Hanjalić [385].

9.2.4 High-Reynolds-Number Form of the Model

Equations of the k_t–ϵ turbulence model for an incompressible flow at high-Reynolds number are summarized in what follows. The mean flow field is governed by

$$\begin{aligned}
\frac{\partial \bar{U}_i}{\partial x_i} &= 0 \\
\frac{\bar{d}(\rho \bar{U}_i)}{\bar{d}t} &= -\frac{\partial}{\partial x_i}\left(\bar{P} + \frac{2}{3}\rho k_t\right) + \frac{\partial}{\partial x_j}\left[(\mu + \mu_t)\,\bar{S}_{ij}\right] \\
\frac{\bar{d}(\rho \bar{H})}{\bar{d}t} &= \frac{\partial}{\partial x_j}\left[\left(\frac{\mu}{\mathrm{Pr}} + \frac{\mu_t}{\mathrm{Pr}_t}\right)\frac{\partial \bar{H}}{\partial x_j}\right] + \frac{\partial \bar{P}}{\partial t} + \frac{\partial(\bar{U}_j \bar{P})}{\partial x_j} + \bar{\tau}_{ij}\frac{\partial \bar{U}_i}{\partial x_j} + \rho\epsilon^h
\end{aligned}$$

where the turbulent viscosity is expressed from the turbulent kinetic energy k_t and the dissipation for a homogeneous flow ϵ^h, as $\mu_t = C_\mu \rho k_t^2/\epsilon^h$. The heart of the model consists of the two transport equations for k_t and ϵ^h, which take the following form,

$$\left\{\begin{aligned}
\frac{\bar{d}(\rho k_t)}{\bar{d}t} &= \frac{\partial}{\partial x_k}\left[\left(\mu + \frac{\mu_t}{\sigma_{k_t}}\right)\frac{\partial k_t}{\partial x_k}\right] + \mathcal{P} - \rho\epsilon^h \\
\frac{\bar{d}(\rho \epsilon^h)}{\bar{d}t} &= \frac{\partial}{\partial x_k}\left[\left(\mu + \frac{\mu_t}{\sigma_\epsilon}\right)\frac{\partial \epsilon^h}{\partial x_k}\right] + \frac{\epsilon^h}{k_t}\left(C_{\epsilon 1}\mathcal{P} - C_{\epsilon 2}\rho\epsilon^h\right)
\end{aligned}\right. \tag{9.17}$$

where the production term is given by $\mathcal{P} = 2\mu_t \bar{S}_{ij}^2$. The model contains five constants which have been determined by comparison with experimental data for simple flows [401]. As an illustration, the case of the constant $C_{\epsilon 2}$ is examined in the next section. Finally, the following values are retained in the standard form of the model,

$$C_\mu = 0.09 \quad C_{\epsilon 1} = 1.44 \quad C_{\epsilon 2} = 1.92 \quad \sigma_{k_t} = 1.0 \quad \sigma_\epsilon = 1.3 \tag{9.18}$$

Knowledge of k_t and ϵ^h provides an estimation of the turbulent velocity scale $u' = \sqrt{2k_t/3}$ and of an integral length scale from $L_f \simeq u'^3/\epsilon^h$. Moreover, from the expression of the turbulent viscosity $\nu_t = u' \times l_m = C_\mu k_t^2/\epsilon^h$, the mixing length is given by $l_m \simeq \sqrt{3/2} C_\mu k_t^{3/2}/\epsilon^h$.

The k_t–ϵ turbulence model has been successfully used in various configurations. The mean flow field computed behind a ducted diaphragm is shown in Fig. 9.1 for instance. More precisely, streamlines are plotted in different vertical planes to take into account the three-dimensional nature of the mean velocity field. The jet-like flow coming from the diaphragm aperture is attached to the top wall due to the Coanda

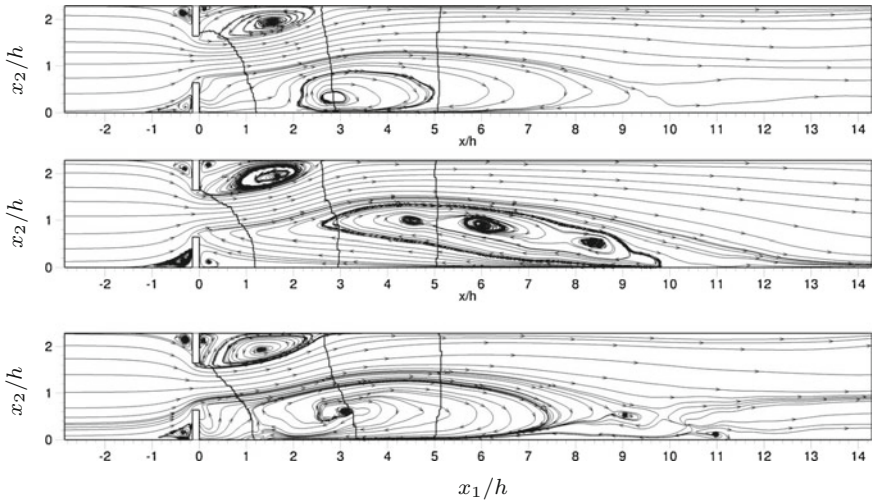

Fig. 9.1 Computed mean flow field behind a diaphragm [416] by using the standard k_t–ϵ model. The duct height is $2.29h$ and the duct span is $w = 2.86h$ where $h = 35\,\text{mm}$ is the aperture size. The Reynolds number based on h and on the maximum mean velocity $\bar{U}_m = 20\,\text{m} \cdot \text{s}^{-1}$ is $\text{Re}_h = 4.8 \times 10^4$. Streamlines in x_1x_2-planes computed with the $\bar{U}_1$ and $\bar{U}_2$ components of the 3-D mean velocity field at three spanwise locations $x_3/w = 0.1$, 0.5 and 0.9

effect, and there is a reattachment to the bottom wall in the second part of the outlet duct.

Unfortunately, as for most of the turbulence models, adaptations are required for specific flows such as for axisymmetric jets [418, 438, 439] or for radial jets [406, 420] to name a few. Boundary layer flows are discussed in Sect. 9.2.6.

9.2.5 Determination of the Constant $C_{\epsilon 2}$

The k_t–ϵ model can be written for specific flows in order to determine the empirical constants. Consider, for instance, the case of decaying turbulence behind a grid, for which experimental results have been presented in Sect. 6.3. The two transport equations (9.17) take the simplified form,

$$\begin{cases} U_0 \dfrac{\partial k_t}{\partial x_1} \simeq -\epsilon^h \\ U_0 \dfrac{\partial \epsilon^h}{\partial x_1} \simeq -C_{\epsilon 2} \dfrac{(\epsilon^h)^2}{k_t} \end{cases}$$

where U_0 is the uniform mean flow velocity. These two equations can then be combined as follows,

$$\frac{1}{\epsilon^h} U_0 \frac{\partial \epsilon^h}{\partial x_1} = -C_{\epsilon 2} \frac{\epsilon^h}{k_t} = C_{\epsilon 2} \frac{1}{k_t} U_0 \frac{\partial k_t}{\partial x_1}$$

and solved to obtain

$$\frac{\epsilon^h}{\epsilon_{h0}} = \left(\frac{k_t}{k_{t0}} \right)^{C_{\epsilon 2}}$$

where k_{t0} and ϵ_{h0} are two constants. Therefore, the solutions for the turbulent kinetic energy and the dissipation rate are

$$\frac{k_t}{k_{t0}} = \left[1 + (C_{\epsilon 2} - 1) \frac{\epsilon_0}{k_{t0}} \frac{x_1}{U_0} \right]^{-\frac{1}{C_{\epsilon 2} - 1}} = \left(1 + \frac{x_1}{\Theta_{c0} U_0} \right)^{-n}$$

and

$$\frac{\epsilon^h}{\epsilon_{h0}} = \left(1 + \frac{x_1}{\Theta_{c0} U_0} \right)^{-(n+1)}$$

where the two constants are given by

$$C_{\epsilon 2} = \frac{n+1}{n} \qquad \Theta_{c0} = \frac{1}{C_{\epsilon 2} - 1} \frac{k_{t0}}{\epsilon_{h0}} = n \frac{k_{t0}}{\epsilon_{h0}}$$

The constants k_{t0} and ϵ^h_{h0} correspond to the initial values at time $t = x_1/U_0 = 0$, and an integral time scale of turbulence is defined by $\Theta_c = k_t/\epsilon^h$. The measured value [100, 135] of n is $n \simeq 1.3$, which yields $C_{\epsilon 2} \simeq 1.77$. This is not exactly the recommended standard value in (9.18), which results from other additional factors. Finally, the evolution of the turbulent viscosity $\nu_t = C_\mu k_t^2/\epsilon^h$ is given by

$$\frac{\nu_t}{\nu_{t0}} = \left(1 + \frac{x_1}{\Theta_{c0} U_0} \right)^{1-n}$$

which indicates that decaying turbulence is not a self-similar flow since $n \neq 1$, as already noted in Sect. 6.3.

9.2.6 Low-Reynolds-Number Form of the k_t–ϵ Model

Treatment of wall-bounded flows requires modifications of the k_t–ϵ turbulence model in its standard form (9.17). The first low-Reynolds versions of the model were introduced by Jones and Launder [392] and by Launder and Sharma [400]. The model of Chien [374] is one of the several significant developments, and reviews can be found in Patel et al. [415] in Celić and Hirschel [372] and in Wilcox's book [449]. Two main

changes are introduced in these models. First, the constants are now functions of a turbulent Reynolds number defined as $\mathrm{Re}_t = k_t^2/(\nu\epsilon)$, which tends to zero as $x_2 \to 0$, and also of the wall distance x_2^+. For instance, C_μ becomes $C_\mu \times f_\mu(\mathrm{Re}_t, x_2^+)$. The Van Driest model (3.22) introduced in Chap. 3 is an example of such semi-empirical damping functions. Secondly, an additional term is included in the dissipation equation. From the equation for k_t, the value of the dissipation at the wall verifies [387]

$$\epsilon^h(x_2 = 0) = \nu \frac{\partial^2 k_t}{\partial x_2^2}\bigg|_{x_2=0} = 2\nu \left(\frac{\partial \sqrt{k_t}}{\partial x_2}\right)^2\bigg|_{x_2=0}$$

and moreover, it can be shown that $\epsilon = \epsilon^h$ at $x_2 = 0$. The dissipation equation is then often written for an auxiliary variable $\epsilon^h - \epsilon^h|_{x_2=0}$ for numerical purposes, in order to apply a Dirichlet boundary condition and to ensure a bounded value of the Reynolds number at the wall.

An alternative to low-Reynolds-number forms of turbulence models, which requires a relatively fine mesh near the wall with $\Delta x_2^+ \simeq 1$, is to use wall functions. This alternative is simple to implement but is based on a strong hypothesis. The first point of the mesh in the normal direction to the wall is indeed assumed to be in the logarithmic region of a boundary layer. Values of ν_t and k_t can thus be imposed at this point, as well as the value of ϵ^h or $\partial\epsilon^h/\partial x_2$.

9.2.7 Realisability and Unsteady Simulations

Turbulence models should satisfy additional constraints, imposed by fundamental physics principles such as the invariance of the formulation by a Galilean transformation [434], or by realisability conditions for the Reynolds stress tensor for instance. An introduction to this topic can be found in Schumann [427], and it follows that

$$\overline{u'_\alpha u'_\alpha} \geq 0 \qquad \overline{u'_\alpha u'_\beta}^2 \leq \overline{u'_\alpha u'_\alpha}\ \overline{u'_\beta u'_\beta} \qquad \det(\overline{u'_\alpha u'_\beta}) \geq 0$$

where the second relation is the Schwarz inequality. Recall that there is no summation on Greek indices.

The renormalisation group (RNG) approach provides a more general framework, and was applied by Yakhot et al. [452] to the k_t–ϵ turbulence model. In the resulting RNG k_t–ϵ model, a new set of constants, see (9.18), is obtained in the high-Reynolds number approximation,

$$C_\mu = 0.085 \quad C_{\epsilon 1} = 1.42 \quad C_{\epsilon 2} = 1.68 \quad \sigma_{k_t} = \sigma_\epsilon = 0.7194$$

Moreover, an additional term must be considered in the dissipation equation, and can be included by replacing the constant $C_{\epsilon 2}$ by the function $C^{\star}_{\epsilon 2} = C_{\epsilon 2} + C_{\mu}\eta^3(1 - \eta/\eta_0)/(1 + \beta\eta^3)$ where $\eta = \bar{S}k_t/\epsilon$, $\eta_0 = 4.38$ and $\beta \simeq 0.012$. In practice, this smart approach has a rather weak influence on turbulence model closures and results.

This is a good opportunity to make a digression about unsteady simulations of Reynolds-averaged Navier-Stokes equations. Unsteady RANS (URANS) simulations can be obtained through the use of a time-marching algorithm. The value of the constant C_{μ}, and as a result ν_t, is also often decreased [366]. Consider a mean shear flow $\bar{U}_1 = \bar{U}_1(x_2)$ with $\bar{U}_2 = \bar{U}_3 = 0$. Schwarz's inequality for $\alpha = 1$ and $\beta = 2$ gives

$$\begin{aligned}
\left(2\nu_t \bar{S}_{12}\right)^2 &\leq \left(\frac{2}{3}k_t - 2\nu_t \bar{S}_{11}\right)\left(\frac{2}{3}k_t - 2\nu_t \bar{S}_{22}\right) \\
\left(2\nu_t \bar{S}_{12}\right)^2 &\leq (2k_t/3)^2 \\
9C_{\mu}^2 \bar{S}_{12}^2 &\leq (\epsilon^h/k_t)^2
\end{aligned}$$

by noting that $\bar{S}_{12} \neq 0$ and $\bar{S}_{11} = \bar{S}_{22} = 0$. There is thus an implicit low-pass filter imposed by the mean shear and controlled by the value of C_{μ}. As a result, no development of the energy cascade can occur with grid refinement in numerical simulations. Examples and discussions can be found in Spalart [430] and Iaccarino et al. [389]

9.3 The k_t–ϵ Model for Compressible Flows

9.3.1 Favre-Averaged Navier-Stokes Equation

The opportunity is taken in this chapter to introduce the Favre average in order to extend the k_t–ϵ turbulence model to compressible flows or to variable density flows. A natural first idea to generalize Reynolds-averaged Navier-Stokes equations for compressible flows consists in applying the Reynolds decomposition to the density, by writing $\rho = \bar{\rho} + \rho'$. Consider for instance the conservation of mass. One obtains

$$\frac{\partial \bar{\rho}}{\partial t} + \frac{\partial}{\partial x_i}\left(\bar{\rho}\bar{U}_i + \overline{\rho' u_i'}\right) = 0$$

A new unknown appears with the correlation $\overline{\rho' u_i'}$ and needs to be modelled. It is relatively easy to guess consequences for other governing equations when the density decomposition is introduced. To overcome, at least in part, this difficulty, Favre [382] proposed to define a new averaging operator defined by

$$\widetilde{F} \equiv \frac{\overline{\rho f}}{\bar{\rho}} \tag{9.19}$$

corresponding to a density-weighted average, and Favre's average is indicating by an over-tilde sign. This means that for any variable f, one has the following Favre decomposition

$$f = \widetilde{F} + f'' \quad \text{with} \quad \overline{\rho f''} = 0 \quad \text{but with} \quad \overline{f''} = -\frac{\overline{\rho' f'}}{\bar{\rho}} \neq 0$$

Note that the fluctuation f'' is non-centered. Returning to the mass conservation equation, the Favre decomposition is then introduced for the velocity, that is $u_i = \widetilde{U}_i + u_i''$, which yields

$$\frac{\partial(\bar{\rho} + \rho')}{\partial t} + \frac{\partial}{\partial x_i}\left(\rho \widetilde{U}_i + \rho u_i''\right) = 0$$

By taking the statistical average of this equation, one obtains

$$\frac{\partial \bar{\rho}}{\partial t} + \frac{\partial}{\partial x_j}(\bar{\rho}\widetilde{U}_j) = 0$$

This compressible form of the mass conservation has the same structure as the incompressible form obtained by using the Reynolds variable decomposition, which clearly illustrates the interest of the Favre averaging. The Reynolds and Favre averaging are equivalent for incompressible flows, and only differ when significant density fluctuations occur.

The Favre decomposition is now considered for all variables, except for density and pressure. Moreover, the property (2.1) regarding the product of two variables f and g, takes the form

$$\overline{\rho f g} = \bar{\rho}\widetilde{F}\widetilde{G} + \overline{\rho f'' g''} \tag{9.20}$$

From these rules, the Favre-averaged Navier-Stokes equation are straightforward to derive

$$\frac{\partial(\bar{\rho}\widetilde{U}_i)}{\partial t} + \frac{\partial(\bar{\rho}\widetilde{U}_i\widetilde{U}_j)}{\partial x_j} = -\frac{\partial \bar{P}}{\partial x_j} + \frac{\partial}{\partial x_j}\left(\bar{\tau}_{ij} - \overline{\rho u_i'' u_j''}\right)$$

and again, the structure of the averaged Navier-Stokes equation is preserved for compressible flows. The Boussinesq assumption for the closure of the Reynolds tensor $-\overline{\rho u_i'' u_j''}$ is generalized as follows,

$$-\overline{\rho u_i'' u_j''} = 2\mu_t \widetilde{S}_{ij} - \frac{2}{3}\bar{\rho} k_t \delta_{ij} \quad \text{where} \quad \widetilde{S}_{ij} = 2\left(\frac{\partial \widetilde{U}_i}{\partial x_j} + \frac{\partial \widetilde{U}_j}{\partial x_i}\right) - \frac{1}{3}\frac{\partial \widetilde{U}_k}{\partial x_k}\delta_{ij}$$

according to relation (2.11) for the deviatoric part of the mean velocity gradient tensor. The turbulent kinetic energy is now defined by

$$k_t = \frac{1}{2}\widetilde{u_i'' u_i''} = \frac{1}{2}\frac{\overline{\rho u_i'' u_i''}}{\bar{\rho}}$$

To keep notations as simple as possible, we will still continue to denote k_t as the turbulent kinetic energy when Favre averaging is used. There is generally no ambiguity in interpretation. The transport equation for the conservation of enthalpy (9.14) is established in the same way. This yields, for an ideal gas,

$$\begin{aligned}\frac{\partial(\bar{\rho}\widetilde{H})}{\partial t} + \frac{\partial(\bar{\rho}\widetilde{H}\widetilde{U}_j)}{\partial x_j} = \frac{\partial}{\partial x_j}\left(\frac{\lambda}{c_p}\frac{\partial \widetilde{H}}{\partial x_j} - \overline{\rho u_j'' h''}\right) + \frac{\partial \bar{P}}{\partial t} + \widetilde{U}_j \frac{\partial \bar{P}}{\partial x_j} \\ + \overline{u_j''}\frac{\partial \bar{P}}{\partial x_j} + \overline{u_j''\frac{\partial p'}{\partial x_j}} + \widetilde{\tau}_{ij}\frac{\partial \widetilde{U}_i}{\partial x_j} + \bar{\rho}\epsilon \end{aligned} \tag{9.21}$$

The Reynolds decomposition is applied to the heat flux $q_j = -(\lambda/c_p)\partial h/\partial x_j$, but the mean component is approximated by $\bar{Q}_j \simeq -(\lambda/c_p)\partial \widetilde{H}/\partial x_j$. This is a quite reasonable approximation for mean molecular transport terms. Similarly, the dissipation term is approximated by $\bar{\tau}_{ij} \simeq \widetilde{\tau}_{ij} = 2\mu \widetilde{S}_{ij}$. Finally, the ideal gas law is directly given by $\bar{P} = r\overline{\rho T} = \bar{\rho} r \widetilde{T}$.

Using the density-weighted averaging clearly simplifies the derivation of the mean flow equations with respect to the usual Reynolds decomposition for the density. Some difficulties nevertheless appear, in the new term $\overline{u_j''}\partial \bar{P}/\partial x_j$ since fluctuations are non-centered, or in the correlation term between the pressure gradient and the fluctuating velocity, $\overline{u_j''\partial p'/\partial x_j}$. By observing that $u_i' = u_i'' - \overline{u_i''}$, the latter can be rearranged as follows,

$$\overline{u_j''\frac{\partial p'}{\partial x_j}} = \overline{u_j'\frac{\partial p'}{\partial x_j}} = \underbrace{\frac{\partial \overline{u_j' p'}}{\partial x_j}}_{\text{(a)}} - \underbrace{\overline{p'\frac{\partial u_j'}{\partial x_j}}}_{\text{(b)}}$$

The first term (a) is a turbulent transport term while the second term (b) is the so-called pressure-dilatation correlation, where the dilatation is the divergence of the fluctuating velocity field, denoted $d' \equiv \nabla \cdot \boldsymbol{u}'$.

The transport equation for the turbulent kinetic energy is more tedious to establish, and details are provided in Sect. 9.8. This equation can take the following form,

$$\frac{\partial(\bar{\rho}k_t)}{\partial t}+\frac{\partial(\bar{\rho}k_t\widetilde{U}_j)}{\partial x_j}=-\overline{\rho u_i'' u_j''}\frac{\partial\widetilde{U}_i}{\partial x_j}-\overline{\tau_{ij}\frac{\partial u_i''}{\partial x_j}}$$
$$-\frac{1}{2}\frac{\partial}{\partial x_j}\overline{\rho u_i'' u_i'' u_j''}-\frac{\partial}{\partial x_i}\overline{p' u_i'}+\frac{\partial}{\partial x_j}\overline{u_i''\tau_{ij}}$$
$$-\overline{u_i''}\frac{\partial\bar{P}}{\partial x_i}-\overline{p'\frac{\partial u_i'}{\partial x_i}} \tag{9.22}$$

and can be compared to its incompressible form (9.9). The convection of k_t by the mean flow is now balanced by a production term related to the mean shear, a destruction term related to viscous effects, three diffusion transport terms, and two new contributions arising from the non-centered fluctuation of the velocity, that is $\overline{u_j''}\neq 0$, and from the compressible feature of the fluctuating velocity, that is $d'\neq 0$.

The term $\overline{u_j''}\partial\bar{P}/\partial x_j$ in Eqs. (9.21) and (9.22), which is related to the turbulent mass flux, can be modelled through a diffusion-gradient assumption,

$$\mathcal{G}_f\equiv-\overline{u_i''}\frac{\partial\bar{P}}{\partial x_i}=\frac{\overline{\rho' u_i'}}{\bar{\rho}}\frac{\partial\bar{P}}{\partial x_i}=-\frac{1}{\bar{\rho}}\frac{\mu_t}{\mathrm{Pr}_t}\frac{\partial\bar{\rho}}{\partial x_i}\frac{\partial\bar{P}}{\partial x_i} \tag{9.23}$$

as proposed by Jones [391] or by Sarkar and Balakrishnan [423] for instance, where Pr_t is the turbulent Prandtl number previously introduced, see expression (9.16). Other strategies are possible, and the reader may refer to Krishnamurty and Shyy [397] or to the book by Wilcox [449]. Modelling of the pressure-dilatation correlation $\overline{p'd'}$ in Eq. (9.22), is discussed in the next section since a similar dilatational term also appears in the equation for the dissipation rate.

9.3.2 Compressible Form of the Dissipation Rate

The transport equation for the dissipation rate in the incompressible form of the k_t–ϵ model is semi-empirical, as discussed previously in this chapter. It is therefore illusive to derive an exact equation in the compressible case, and to model this equation in a second step. The approximation of the exact dissipation rate ϵ by its expression for a homogeneous flow ϵ^h is still retained, but must be now reformulated for compressible turbulence. As a starting point, one has

$$\bar{\rho}\epsilon=\overline{\tau_{ij}\frac{\partial u_i''}{\partial x_j}}=2\overline{\mu s_{ij}e_{ij}''}=2\overline{\mu e_{ij}e_{ij}''}-\frac{2}{3}\overline{\mu d d''}\simeq 2\nu\overline{\rho e_{ij}''e_{ij}''}-\frac{2}{3}\nu\overline{\rho d''^2}$$

by assuming a constant molecular viscosity ν, and where $d''=\nabla\cdot\boldsymbol{u}''$. The dissipation rate is then split into two contributions associated with the incompressible part of the velocity in the first term, and with dilatation in the second one. The following relationship can be obtained using the Favre average defined by (9.19),

$$\bar{\rho}\epsilon = 2\mu\widetilde{e''_{ij}e''_{ij}} - \frac{2}{3}\mu\widetilde{\rho d''^2}$$
$$= \mu\widetilde{\omega''_i\omega''_i} + \frac{4}{3}\mu\widetilde{d''^2} + \underline{2\mu\frac{\partial^2\widetilde{u''_iu''_j}}{\partial x_i\partial x_j} - 4\mu\frac{\partial}{\partial x_j}\widetilde{u''_jd''}}$$

where the underlined term is usually neglected. This assumption holds for high-Reynolds number flows or for homogeneous turbulence. The dissipation rate is then given by

$$\epsilon^h = \epsilon^h_s + \epsilon^h_d \quad \text{with} \quad \bar{\rho}\epsilon^h_s \equiv \mu\widetilde{\omega''_i\omega''_i} \quad \text{and} \quad \bar{\rho}\epsilon^h_d \equiv \frac{4}{3}\mu\widetilde{d''^2} \tag{9.24}$$

The dissipation rate related to the incompressible part of the velocity, also called the solenoidal dissipation rate ϵ^h_s, is computed from a transport equation similar to the one of the k_t–ϵ model in its incompressible form. Therefore, only the dilatational dissipation ϵ^h_d including compressibility effects, needs to be modelled. Various modellings have been proposed in the literature for ϵ^h_d, as well as for the pressure-dilatation correlation $\overline{p'd'}$. Many of them are built as follows, $\epsilon^h_d = f(M_t) \times \epsilon^h_s$ where f is a function of the turbulent Mach number M_t defined by

$$M_t = \frac{\sqrt{2k_t}}{\bar{c}}$$

The reader may refer to the pioneering studies by Zeman [454–456] and by Sarkar et al. [422–424] Variants and applications to shear flows can be found in Lakshmanan and Abdol-Hamidn [398] in Dash et al. [377] or in Krishnamurty and Shyy [397] among others. A more general overview can be found in Chassaing et al. [373] or in Gatski and Bonnet [384] for turbulence modelling aspects.

9.3.3 Compressible Form of the k_t–ϵ Model

The full equations of the k_t–ϵ turbulence model in its compressible form are presented below. Equations for the mean flow are similar to the incompressible case provided that the Favre averaging (9.19) is used, and that the complete expression of the deviatoric part of the mean velocity gradient tensor (2.11) is considered. Thus, the conservation of mass and of momentum can be written as follows,

$$\frac{\partial\bar{\rho}}{\partial t} + \frac{\partial(\bar{\rho}\widetilde{U}_j)}{\partial x_j} = 0$$
$$\frac{\partial(\bar{\rho}\widetilde{U}_i)}{\partial t} + \frac{\partial(\bar{\rho}\widetilde{U}_i\widetilde{U}_j)}{\partial x_j} = -\frac{\partial}{\partial x_i}\left(\bar{P} + \frac{2}{3}\rho k_t\right) + \frac{\partial}{\partial x_j}\left[(\mu + \mu_t)\,\widetilde{S}_{ij}\right]$$

These equations must be associated with a conservation equation for energy, such as Eq. (9.21) for the mean enthalpy. The turbulent viscosity μ_t is now defined from the turbulent kinetic energy and from the total dissipation $\epsilon^h = \epsilon_s^h + \epsilon_d^h$,

$$\mu_t = C_\mu \bar{\rho} \frac{k_t^2}{\epsilon^h}$$

as explained in the previous paragraph. The two transport equations for k_t and the incompressible part of the dissipation rate ϵ_s^h take the following form,

$$\left\{ \begin{array}{l} \dfrac{\partial(\bar{\rho}k_t)}{\partial t} + \dfrac{\partial(\bar{\rho}k_t\widetilde{U}_j)}{\partial x_j} = \dfrac{\partial}{\partial x_j}\left[\left(\mu + \dfrac{\mu_t}{\sigma_{k_t}}\right)\dfrac{\partial k_t}{\partial x_j}\right] + \mathcal{P} + \mathcal{G}_f - \bar{\rho}\epsilon^h \\ \dfrac{\partial(\bar{\rho}\epsilon_s^h)}{\partial t} + \dfrac{\partial(\bar{\rho}\epsilon_s^h\widetilde{U}_j)}{\partial x_j} = \dfrac{\partial}{\partial x_j}\left[\left(\mu + \dfrac{\mu_t}{\sigma_\epsilon}\right)\dfrac{\partial \epsilon_s^h}{\partial x_j}\right] + \dfrac{\epsilon_s^h}{k_t}\left[C_{\epsilon 1}(\mathcal{P} + \mathcal{G}_f) - C_{\epsilon 2}\bar{\rho}\epsilon_s^h\right] \end{array} \right.$$

The compressible part of the dissipation rate is computed from a specific model, which usually takes the following general form $\epsilon_d^h = f(M_t) \times \epsilon_s^h$. The production term $\mathcal{P}$ is given by

$$\mathcal{P} = -\overline{\rho u_i'' u_j''}\frac{\partial \widetilde{U}_i}{\partial x_j} = 2\mu_t(\widetilde{S}_{ij})^2 - \frac{2}{3}(\mu_t \nabla\cdot\widetilde{\mathbf{U}} + \bar{\rho}k_t)(\nabla\cdot\widetilde{\mathbf{U}})$$

by generalising Boussinesq's assumption. Finally, the values (9.18) of the constants established for the incompressible form of the model are still used.

Applications to free shear flows of these compressible and high-Reynolds-number forms of the k_t–ϵ model can be found in Dash et al. [375, 376] or in Thies and Tam [439]. Regarding perfectly expanded supersonic jets, numerical predictions obtained by different approaches are discussed in Barber and Chiappetta [365]. A conservative form of the model has been derived by Sinha and Balasridhar [428]. As an illustration, the case of a supersonic round jet at Mach number $M_j = 2$ is considered in Fig. 9.2. The turbulent mean flow is calculated from a compressible form of the $k_t - \epsilon$ model including the model of Zaman [454] for the compressible part of the dissipation and the term (9.23). The turbulent kinetic energy field is represented through the quantity $k_t^{1/2}/U_j$, which indicates a normalised level of velocity fluctuations. In the present case for the hot jet at $T_j/T_\infty \simeq 2.8$, $k_t^{1/2}/U_j$ reaches around 15 % in the annular shear-layer. The jet exit temperature and the ambient temperature are respectively denoted T_j and T_∞, U_j is the jet exit velocity. The faster decrease of the velocity with increasing jet temperature is reasonably well retrieved by the model. Note that the small wiggles for the hot-jet mean velocity profile are caused by a slight mismatch between the jet exit pressure and the ambient pressure in the calculation.

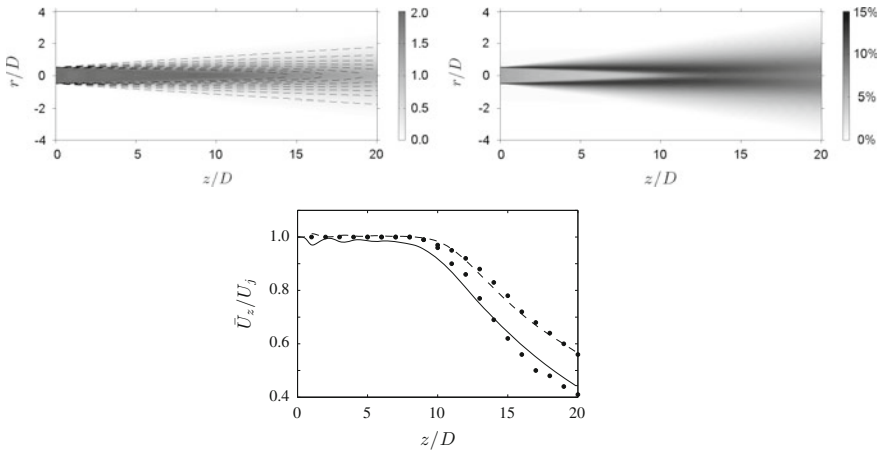

Fig. 9.2 Turbulent mean flow of a round supersonic jet at $M_j = 2$ computed from a compressible form of the k_t–ϵ model [507]. At the *top*, maps of the Mach number and of $\sqrt{k_t}/U_j$ for a hot jet, $T_j/T_\infty \simeq 2.8$. At the *bottom*, computed mean axial velocity profiles for a cold jet $T_j/T_\infty \simeq 1$ – – – and a hot jet $T_j/T_\infty \simeq 2.8$ ——— , and measurements of Seiner et al. [554] •. All axis are normalised by the nozzle diameter D, and the Reynolds number of the cold jet is $\mathrm{Re}_D \simeq 4.3 \times 10^6$

9.4 The k_t–ω_t Turbulence Model

Turbulence models based on k_t and ω_t are currently widely used. The turbulent viscosity is still built with the knowledge of two turbulent scales, namely the turbulent kinetic energy k_t and the specific dissipation rate $\omega_t \sim \epsilon^h/k_t$. This variable ω_t has the dimension of a frequency, and can be linked to the square of enstrophy, where enstrophy is the root mean square fluctuating vorticity. This quantity was introduced in Chap. 5. The first two-equation turbulence model was historically proposed by Kolmogorov [396, 433], and it is precisely based on k_t and ω_t.

Various formulations have been developed and improved in the literature, but the transport equation for the turbulent kinetic energy often retains the following usual form,

$$\frac{\bar{d}(\rho k_t)}{\bar{d}t} = \frac{\partial}{\partial x_j}\left[\left(\mu + \frac{\mu_t}{\sigma_{k_t}}\right)\frac{\partial k_t}{\partial x_j}\right] + \mathcal{P} - \beta^\star \rho \omega_t k_t \tag{9.25}$$

where $\beta^\star$ is a constant of the model. Its structure is quite similar to Eq. (9.10), and there is even a direct link between these two equations by the change of variable $\epsilon^h = \beta^\star \omega_t k_t$ with $\beta^\star = C_\mu$. The general form of the transport equation for the specific dissipation rate ω_t is given by

$$\frac{\bar{d}(\rho\omega_t)}{\bar{d}t} = \underbrace{\frac{\partial}{\partial x_j}\left[\left(\mu + \frac{\mu_t}{\sigma_\omega}\right)\frac{\partial \omega_t}{\partial x_j}\right] + \frac{\alpha}{\nu_t}\mathcal{P} - \beta\rho\omega_t^2}_{\text{(a)}}$$
$$+ \underbrace{2(1-F_1)\frac{\rho\sigma_{\omega 2}}{\omega_t}\frac{\partial k_t}{\partial x_j}\frac{\partial \omega_t}{\partial x_j}}_{\text{(b)}} \tag{9.26}$$

The three terms collected in (a) are respectively a diffusion term, a production term and a destruction term. This transport equation, by including only (a) on the right-hand side, has the same structure as Eq. (9.13). Combined with Eq. (9.25), they provide the baseline k_t–ω_t model derived by Wilcox [446]. Standard values of the constants are $\sigma_{k_t} = 0.5$, $\sigma_\omega = 0.5$, $\beta = 3/40$ and $\alpha = \beta/\beta^\star - \sigma_\omega\kappa^2\sqrt{\beta^\star}$. In this model, the turbulent viscosity is expressed as

$$\mu_t = \rho\frac{k_t}{\omega_t} \tag{9.27}$$

The additional cross-diffusion term (b) has been introduced by Menter [410], and comes from the transformation of Eq. (9.13). This change of variable mentioned above from ϵ^h to ω_t, also provides values for the constants $\beta = C_\mu(C_{\epsilon 2} - 1)$ and $\sigma_\omega = \sigma_\epsilon$. In the shear stress model of Menter, known as the $k_t - \omega_t -$ SST model and combining Eqs. (9.25) and (9.26), each constant is calculated as the sum of the value provided by the model of Wilcox and weighted by F_1, and of the value provided by the transformation of the k_t–ϵ model and weighted by $1 - F_1$, where F_1 is a blending function [410]. Furthermore, the turbulent viscosity is now a more complex function, written symbolically as $\mu_t = \mu_t(k_t/\omega_t, k_t/\omega)$. Through another blending function, the turbulent viscosity becomes proportional to k_t/ω in boundary layer flows, where ω is the norm of the vorticity, and μ_t is given by expression (9.27) elsewhere. As pointed out by Menter [410], the production term $\mathcal{P}$ in (9.25) must therefore be computed according to the two definitions of the turbulent viscosity in the SST model.

Successive variants and numerical applications can be found in Wilcox [449, 450]. The k_t–ω_t turbulence model proves to be numerically robust, especially for the prediction of wall boundary flows, and does not require damping functions. A weak point of this model is its sensitivity to freestream values in external aerodynamics and improvements have been proposed to correctly represent free stream turbulence [395, 408, 432]. Extensions to compressible flows [421, 448] have also been considered.

9.5 The Spalart and Allmaras Turbulence Model

An alternative to the determination of the turbulent viscosity for evaluating the unknown Reynolds stress tensor in (9.1) is to solve a transport equation for ν_t. In this way, a complete turbulence model is also obtained. A possible starting point

is to consider the expression of the turbulent viscosity, e.g. relation (9.27) for the k_t–ω_t model. It is then straightforward to derive the following transport equation,

$$\frac{\bar{d}\nu_t}{\bar{d}t} = \frac{1}{\omega_t}\frac{\bar{d}k_t}{\bar{d}t} - \frac{k_t}{\omega_t^2}\frac{\bar{d}\omega_t}{\bar{d}t}$$

in which the formulation of each term must then be revisited to remove the dependence with respect to k_t and ω_t. Independently, Menter [411] has developed a turbulent viscosity equation derived from the k_t–ϵ model.

One of the most popular turbulence models for aeronautical applications in this framework, is the Spalart and Allmaras model [431]. A semi-empirical transport equation is assembled term by term to match selected requirements, which yields

$$\frac{\bar{d}\breve{\nu}_t}{\bar{d}t} = c_{b_1}\breve{\Omega}\breve{\nu}_t + \frac{1}{\mathrm{Pr}_t}\left\{\nabla\cdot\left[(\nu+\breve{\nu}_t)\nabla\breve{\nu}_t\right] + c_{b_2}(\nabla\breve{\nu}_t)^2\right\} - c_{w_1}f_w\left(\frac{\breve{\nu}_t}{d_w}\right)^2 \quad (9.28)$$

for the auxiliary variable $\widetilde{\nu}_t$ related to the turbulent viscosity by $\nu_t = \breve{\nu}_t f_{\nu_1}$, and where c_{b_1}, c_{b_2} and c_{w_1} are three constants. The function f_{ν_1} allows the viscosity to be equal to $\nu_t = \kappa u_\tau d_w$ in all regions of a boundary layer, where d_w is the transverse distance to the wall. The first term $c_{b_1}\breve{\Omega}\breve{\nu}_t$ is a production term, where $\breve{\Omega}$ is a vorticity magnitude sensor equal to $u_\tau/(\kappa x_2)$ in the logarithmic region of a boundary layer and equal to the mean vorticity magnitude $\bar{\Omega}$ elsewhere. The second term in brackets describes diffusion in a non conservative form for $\breve{\nu}_t$. The third term is a destruction term and f_w is a damping function associated with near-wall corrections [431].

9.6 Concluding Remarks

Numerical results obtained from different turbulent-viscosity models have been compared in the literature, for instance in Menter [409], in Singer [232], in Wilcox [449] or in Celić and Hirschel [372]. A first view of these models can also be obtained by writing simplified equations in the case of usual flows, in order to well understand their behaviour. The compressible form of the k_t–ϵ has been introduced in Sect. 9.3, but similar corrections can be made for other models, as formalized in Catris and Aupoix [369]. Realisability conditions can also be enforced in the different models. More specific topics including rough walls, rotating flows, adverse pressure gradient flows or shock wave boundary layer interaction are deliberately not addressed here.

The k_t–ϵ turbulence model is not as commonly used for predicting aerodynamic flows [372] with respect to the $k_t-\omega_t-$SST model or the Spalart-Allmaras model for example. Alternative approaches have also been developed [425, 426] for turbulent-viscosity turbulence models. To relax the constitutive relation based on Boussinesq's hypothesis (9.2), a transport equation must be solved for each of the six Reynolds stresses $-\overline{\rho u_i' u_j'}$. One of the first Reynolds stress models (RSM) was developed by

Hanjalić and Launder [386] to compute the anisotropy in a channel flow, induced by a smooth wall on one side and a rough wall on the other. Full second-moment Reynolds stress models have been deeply investigated by Lumley [250], Launder [399], Gatski and Speziale [383, 436] and Speziale et al. [437]. Transport equations for Reynolds stresses were initially combined with a transport equation for the dissipation, see for instance Eq. (9.13), in order to have access to a turbulence length scale. A transport equation for the specific dissipation rate ω_t can also be used [371, 449].

9.7 Equation for the Dissipation in Incompressible Homogeneous Turbulence*

Starting from the Navier-Stokes equation for the fluctuating velocity (9.11) developed below for an incompressible flow, and by assuming a constant molecular viscosity μ,

$$\frac{\partial\left(\rho u_i'\right)}{\partial t}+\frac{\partial}{\partial x_k}\left[\rho\left(u_i'\bar{U}_k+\bar{U}_i u_k'+u_i'u_k'\right)\right]= -\frac{\partial p'}{\partial x_i}+\frac{\partial}{\partial x_k}\left(\overline{\rho u_i'u_k'}+\mu\frac{\partial u_i'}{\partial x_k}\right) \tag{9.29}$$

the following equation is then built

$$\nu\frac{\partial u_i'}{\partial x_j}\frac{\partial}{\partial x_j}\left[\text{Eq. (9.29)}\right]$$

Using the incompressibility condition for the mean and for the fluctuating velocity fields, each term can be recast as follows,

$$(1)\quad \nu\overline{\frac{\partial u_i'}{\partial x_j}\frac{\partial}{\partial x_j}\frac{\partial(\rho u_i')}{\partial t}}=\frac{1}{2}\frac{\partial(\rho\epsilon^h)}{\partial t}$$

$$(2)\quad \nu\overline{\frac{\partial u_i'}{\partial x_j}\frac{\partial}{\partial x_j}\frac{\partial}{\partial x_k}(\rho u_i'\bar{U}_k)}=\frac{1}{2}\bar{U}_k\frac{\partial(\rho\epsilon^h)}{\partial x_k}+\mu\frac{\partial\bar{U}_k}{\partial x_j}\overline{\frac{\partial u_i'}{\partial x_k}\frac{\partial u_i'}{\partial x_j}}$$

$$(3)\quad \nu\overline{\frac{\partial u_i'}{\partial x_j}\frac{\partial}{\partial x_j}\frac{\partial}{\partial x_k}(\rho\bar{U}_i u_k')}=\mu\frac{\partial\bar{U}_i}{\partial x_k}\overline{\frac{\partial u_i'}{\partial x_j}\frac{\partial u_k'}{\partial x_j}}+\mu\overline{u_k'\frac{\partial u_i'}{\partial x_j}\frac{\partial^2\bar{U}_i}{\partial x_j\partial x_k}}$$

$$(4)\quad \nu\overline{\frac{\partial u_i'}{\partial x_j}\frac{\partial}{\partial x_j}\frac{\partial}{\partial x_k}(\rho u_i'u_k')}=\mu\overline{\frac{\partial u_i'}{\partial x_j}\frac{\partial u_k'}{\partial x_j}\frac{\partial u_i'}{\partial x_k}}+\frac{\mu}{2}\frac{\partial}{\partial x_k}\overline{u_k'\frac{\partial u_i'}{\partial x_j}\frac{\partial u_i'}{\partial x_j}}$$

$$(5)\quad \nu\overline{\frac{\partial u_i'}{\partial x_j}\frac{\partial}{\partial x_j}\frac{\partial p'}{\partial x_i}}=\nu\frac{\partial}{\partial x_i}\overline{\frac{\partial u_i'}{\partial x_j}\frac{\partial p'}{\partial x_j}}$$

$$(6)\quad \nu\frac{\partial u_i'}{\partial x_j}\frac{\partial}{\partial x_j}\frac{\partial}{\partial x_k}(\overline{\rho u_i'u_k'})=0$$

$$(7)\quad \rho\nu^2\overline{\frac{\partial u_i'}{\partial x_j}\frac{\partial}{\partial x_j}\frac{\partial^2 u_i'}{\partial x_k\partial x_k}} = \frac{\mu}{2}\frac{\partial^2\epsilon^h}{\partial x_k\partial x_k} - \rho\nu^2\overline{\frac{\partial^2 u_i'}{\partial x_k\partial x_j}\frac{\partial^2 u_i'}{\partial x_k\partial x_j}}$$

The transport equation for the dissipation in an incompressible homogeneous flow is thus obtained by grouping all the previous terms, and by multiplying them all by a factor of 2 to obtain Eq. (9.12). It yields,

$$\begin{aligned}\frac{\partial(\rho\epsilon^h)}{\partial t} + \frac{\partial(\rho\epsilon^h\bar{U}_k)}{\partial x_k} &= -2\mu\frac{\partial\bar{U}_k}{\partial x_j}\left(\overline{\frac{\partial u_i'}{\partial x_k}\frac{\partial u_i'}{\partial x_j}} + \overline{\frac{\partial u_k'}{\partial x_i}\frac{\partial u_j'}{\partial x_i}}\right) - 2\mu\overline{u_k'\frac{\partial u_i'}{\partial x_j}}\frac{\partial^2\bar{U}_i}{\partial x_j\partial x_k}\\ &\quad - 2\mu\overline{\frac{\partial u_i'}{\partial x_j}\frac{\partial u_k'}{\partial x_j}\frac{\partial u_i'}{\partial x_k}} - \mu\frac{\partial}{\partial x_k}\overline{u_k'\frac{\partial u_i'}{\partial x_j}\frac{\partial u_i'}{\partial x_j}} - 2\nu\frac{\partial}{\partial x_i}\overline{\frac{\partial u_i'}{\partial x_j}\frac{\partial p'}{\partial x_j}}\\ &\quad + \mu\frac{\partial^2\epsilon^h}{\partial x_k\partial x_k} - 2\rho\nu^2\overline{\frac{\partial^2 u_i'}{\partial x_k\partial x_j}\frac{\partial^2 u_i'}{\partial x_k\partial x_j}}\end{aligned}$$

9.8 Favre-Averaged Turbulent Kinetic Energy Equation*

Starting from the Navier-Stokes equation, written in its non-conservative form, it is possible to establish an equation for the turbulent kinetic energy $\bar{\rho}k_t = \overline{\rho u_i'' u_i''}/2$. The exact Navier-Stokes equation is multiplied by u_i'', that is

$$u_i''\left\{\rho\frac{\partial u_i}{\partial t} + \rho u_j\frac{\partial u_i}{\partial x_j} = -\frac{\partial p}{\partial x_i} + \frac{\partial\tau_{ij}}{\partial x_j}\right\}$$

Let us examine each term of this equation. The term which involves a time derivative can be written as

$$\begin{aligned}u_i''\rho\frac{\partial u_i}{\partial t} &= \rho u_i''\frac{\partial\widetilde{U}_i}{\partial t} + \rho u_i''\frac{\partial u_i''}{\partial t}\\ &= \rho u_i''\frac{\partial\widetilde{U}_i}{\partial t} + \rho\frac{\partial}{\partial t}\left(\frac{u_i''^2}{2}\right)\\ &= \rho u_i''\frac{\partial\widetilde{U}_i}{\partial t} + \frac{\partial}{\partial t}\left(\rho\frac{u_i''^2}{2}\right) - \frac{u_i''^2}{2}\frac{\partial\rho}{\partial t}\end{aligned}$$

Taking the statistical average of this last relation, it yields

$$\overline{u_i''\rho\frac{\partial u_i}{\partial t}} = \underbrace{\overline{\rho u_i''}}_{=0}\frac{\partial \widetilde{U}_i}{\partial t} + \frac{\partial}{\partial t}\underbrace{\overline{\rho\frac{u_i''^2}{2}}}_{\equiv \bar{\rho}k_t} - \overline{\frac{u_i''^2}{2}\frac{\partial \rho}{\partial t}} \tag{9.30}$$

A similar development for the convection term leads to

$$u_i''\rho u_j\frac{\partial u_i}{\partial x_j} = \rho u_i''\widetilde{U}_j\frac{\partial \widetilde{U}_i}{\partial x_j} + \rho u_i''u_j''\frac{\partial \widetilde{U}_i}{\partial x_j} + \rho u_i''u_j\frac{\partial u_i''}{\partial x_j} \tag{9.31}$$

The last term of (9.31) which still involves u_j, can be recast as follows,

$$\begin{aligned}\rho u_i''u_j\frac{\partial u_i''}{\partial x_j} &= \rho u_j\frac{\partial}{\partial x_j}\left(\frac{u_i''^2}{2}\right)\\ &= \frac{\partial}{\partial x_j}\left(\rho u_j\frac{u_i''^2}{2}\right) - \frac{u_i''^2}{2}\frac{\partial(\rho u_j)}{\partial x_j}\\ &= \frac{\partial}{\partial x_j}\left(\widetilde{U}_j\,\rho\frac{u_i''^2}{2} + \rho\frac{u_j''u_i''u_i''}{2}\right) - \frac{u_i''^2}{2}\frac{\partial(\rho u_j)}{\partial x_j}\end{aligned} \tag{9.32}$$

Thus, by grouping expressions (9.31) and (9.32), and by applying the statistical averaging, one obtains

$$\begin{aligned}\overline{u_i''\rho u_j\frac{\partial u_i}{\partial x_j}} = &\underbrace{\overline{\rho u_i''}}_{=0}\widetilde{U}_j\frac{\partial \widetilde{U}_i}{\partial x_j} + \overline{\rho u_i''u_j''}\frac{\partial \widetilde{U}_i}{\partial x_j}\\ &+ \frac{\partial}{\partial x_j}\underbrace{\left(\widetilde{U}_j\rho\overline{\frac{u_i''^2}{2}}\right)}_{=\widetilde{U}_j\bar{\rho}k_t} + \frac{1}{2}\frac{\partial}{\partial x_j}\overline{\rho u_j''u_i''u_i''} - \overline{\frac{u_i''^2}{2}\frac{\partial(\rho u_j)}{\partial x_j}}\end{aligned} \tag{9.33}$$

For the pressure term, one obtains

$$\begin{aligned}-\overline{u_i''\frac{\partial p}{\partial x_i}} &= -\overline{u_i''\frac{\partial \bar{P}}{\partial x_i}} - \overline{u_i''\frac{\partial p'}{\partial x_i}}\\ &= \underbrace{-\overline{u_i''}\frac{\partial \bar{P}}{\partial x_i}}_{\text{(a)}} - \frac{\partial}{\partial x_i}\overline{p'u_i''} + \underbrace{\overline{p'\frac{\partial u_i''}{\partial x_i}}}_{\text{(b)}}\end{aligned} \tag{9.34}$$

The two terms (a) and (b) are specific to compressible flows. The term (a) is usually denoted G_f and the term (b) is called the pressure-dilatation correlation. Finally, the viscous term is rearranged as

$$\overline{u_i'' \frac{\partial \tau_{ij}}{\partial x_j}} = \frac{\partial}{\partial x_j} \overline{u_i'' \tau_{ij}} - \underbrace{\overline{\tau_{ij} \frac{\partial u_i''}{\partial x_j}}}_{\equiv \bar{\rho}\epsilon} \tag{9.35}$$

The transport equation (9.22) for the turbulent kinetic energy k_t is finally obtained by summing the different contributions, namely expressions (9.30), (9.33)–(9.35), which leads to [449]

$$\begin{aligned} \frac{\partial(\bar{\rho} k_t)}{\partial t} + \frac{\partial(\bar{\rho} k_t \widetilde{U}_j)}{\partial x_j} = & -\overline{\rho u_i'' u_j''} \frac{\partial \widetilde{U}_i}{\partial x_j} - \overline{\tau_{ij} \frac{\partial u_i''}{\partial x_j}} \\ & - \frac{1}{2} \frac{\partial}{\partial x_j} \overline{\rho u_i'' u_i'' u_j''} - \frac{\partial}{\partial x_i} \overline{p' u_i''} + \frac{\partial}{\partial x_j} \overline{u_i'' \tau_{ij}} \\ & - \overline{u_i''} \frac{\partial \bar{P}}{\partial x_i} - \overline{p' \frac{\partial u_i''}{\partial x_i}} \end{aligned}$$

Note that by adding the two terms (9.30) and (9.33), the conservation of mass has been used

$$\overline{\frac{u_i''^2}{2} \underbrace{\left[\frac{\partial \rho}{\partial t} + \frac{\partial(\rho u_j)}{\partial x_j} \right]}_{=0}} = 0$$

Chapter 10
Experimental Methods

Three methods are frequently used to measure turbulent flows: thermal anemometry, laser Doppler anemometry and particle image velocimetry. Thermal anemometry delivers continuous signals for velocity and fluid temperature at one or several points. It makes use of tiny sensors introduced in the flow. Wall shear stress measurements are also possible with sensors integrated in the wall. Laser Doppler anemometry, based on the frequency shift of illuminated particles carried by the flow, provides velocity at one or several points in the flow at a large series of discrete times. Particle image velocimetry, where cameras observe the displacement of small particles by the flow, provides instantaneous velocity maps at a moderate frequency rate. These methods are successively presented in this chapter.

10.1 Thermal Anemometry

10.1.1 Main Lines of Operation

Thermal anemometry relies on the use of a fine metallic wire, usually made of platinum or tungsten, which is heated electrically and exposed to a flowing fluid. Its temperature, which is a function of the fluid temperature, fluid velocity, and the rate of heating, may be determined by measuring its electrical resistance. For a metallic wire, a quasi-linear relation links the electrical resistance of the wire R_w to its temperature T_w

$$R_w = R_0[1 + \chi(T_w - T_0)] \tag{10.1}$$

where R_0 is the wire resistance at a reference temperature T_0, and χ the first order temperature coefficient of resistivity of the wire material, provided by the manufacturer, also measurable using a thermostat or an heated jet. The wire, if it were an ideal sensor, i.e. without any mass, heat capacity, and boundary layer on its surface,

C. Bailly and G. Comte-Bellot, *Turbulence*, Experimental Fluid Mechanics,
DOI 10.1007/978-3-319-16160-0_10

would respond instantaneously to any velocity or temperature change occurring in the flow. Its heat balance would then be simply written

$$0 = R_w^\star I_w^{\star 2} - (T_w^\star - T)F(u_n) \tag{10.2}$$

where $R_w^\star$ is the resistance of the ideal wire, $I_w^\star$ the current intensity through it, $T_w^\star - T$ the temperature difference between the wire temperature $T_w^\star(t)$ and the incoming flow temperature $T(t)$, and $F(u_n)$ a function of the velocity component u_n normal to the wire. The first term is the Joule energy brought to the wire, and the second the heat loss by forced convection, the wire being comparable with a two-dimensional body, as explained by Knudsen and Katz [10] or Corrsin [709]. The difference $T_w^\star - T$ is a driving factor for the cooling rate of the wire, and in hot-wire anemometry it leads to the overheat ratio of the wire defined by

$$a_w^\star = \frac{T_w^\star - T}{T} \simeq \frac{R_w^\star - R}{R} \tag{10.3}$$

where R is the resistance of the unheated wire placed in the flow, given by Eq. (10.1) for the temperature T. A real wire, although very fine, is not devoid of mass and heat capacity. The heat balance of a real wire has now a more complicated form

$$m_w c_w \frac{dT_w}{dt} = R_w I_w^2 - (T_w - T)F(u_n) \tag{10.4}$$

The left-hand side of (10.4) expresses the rate of change of heat kept by the real wire, where m_w is the mass of the wire and c_w the specific heat of the wire material. The wire resistance is now denoted by R_w, the wire temperature by T_w, and the electrical current by I_w, all without the star index, as the variables of a real wire differ from those of an ideal wire.

An anemometer is the association of a hot-wire sensor and an electronic circuit. By itself or combined with a special data processing technique, any anemometer has to properly correct the thermal inertia of the real wire so that Eq. (10.2) is recovered and permits proper values to be obtained for the instantaneous velocity $u_n(t)$. Over the years [701], different types of anemometers have been developed according to the way the wire is operated: at constant current, which leads to the Constant Current Anemometer—in brief CCA, at constant resistance or temperature, which leads to the Constant Temperature Anemometer—in brief CTA, at constant voltage across the wire, which leads to the Constant Voltage Anemometer—in brief CVA.

Hot-wire anemometry is usually reserved for low turbulence levels. All governing equations can thus be linearized around a mean operating point, leading to two very useful results: expression of the time constant of the wire, and definition of the wire sensitivity coefficients to velocity and temperature fluctuations. However, an exception exists for CVAs where a recent approach permits to cope with large velocity fluctuations [695].

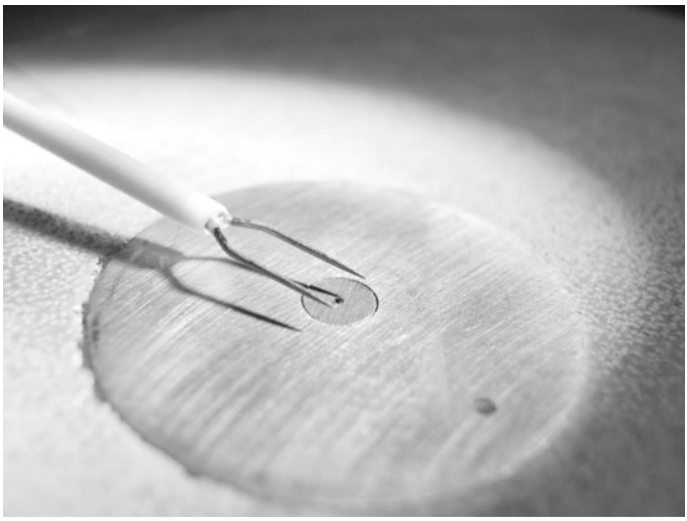

Fig. 10.1 Hot-wire sensor and wall pressure pinhole microphone to investigate a turbulent boundary layer. Courtesy of Edouard Salze (LMFA)

10.1.2 The Wires and Their Positions in a Turbulent Flow

Typical wires have a diameter d_w in the range 1–5 μm and a length l_w in the range 1–3 mm, see Fig. 10.1. Choosing a wire is always a compromise. On one hand, the aspect ratio, l_w/d_w, has to be large to offer a correct directional response [709]. On the other hand, the length l_w has to be small to provide local measurements [750]. The whole probe which consists of a stem, two broaches also called prongs, and the sensing wire has also to be built to reduce aerodynamic perturbations [692, 702, 703].

The two usual configurations for hot wires are illustrated in Fig. 10.2. For a single wire placed normal to the mean flow $\bar{U}_1$, the instantaneous velocity $u_n(t)$ cooling the wire is given by Pythagoras' theorem as

$$u_n(t) = \left[(\bar{U}_1 + u_1'(t))^2 + u_3'(t)^2\right]^{1/2}$$

which simplifies for small fluctuations into

$$u_n(t) \simeq \bar{U}_1 + u_1'(t) + \frac{1}{2}\frac{u_1'^2(t) + u_3'^2(t)}{\bar{U}_1} \simeq \bar{U}_1 + u_1'(t)$$

Fluctuations $u_2'(t)$ are not included, being of no cooling effect since they are parallel to the wire. When the second order terms are not small, it becomes interesting to move the wire longitudinally at a constant speed to create an artificial higher mean

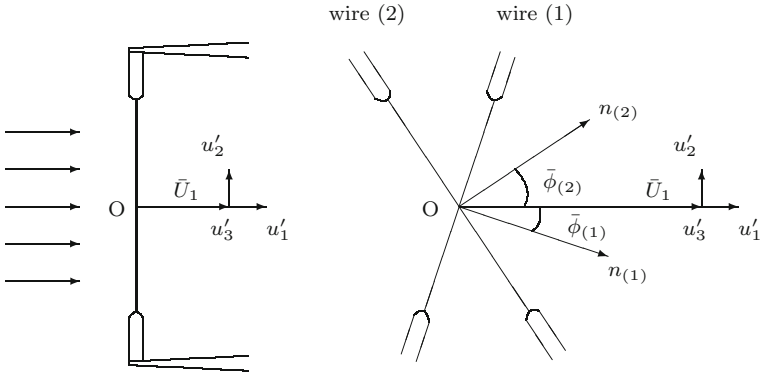

Fig. 10.2 Two classic positions for hot wires. On the *left*, a single wire is set normal to the mean velocity and responds to $u_n \simeq \bar{U}_1 + u_1'$. On the *right*, two wires are inclined to the mean flow, and respond to $u_{n(1)} \simeq \left(\bar{U}_1 + u_1'\right)\cos\bar{\phi}_{(1)} - u_2'\sin\bar{\phi}_{(1)}$ for wire (1) with normal $n_{(1)}$, and to $u_{n(2)} \simeq \left(\bar{U}_1 + u_1'\right)\cos\bar{\phi}_{(2)} + u_2'\sin\bar{\phi}_{(2)}$ for wire (2) with normal $n_{(2)}$

velocity $\bar{U}_1$. This technique is called *the flying hot-wire* as the wire acts as an airplane through the flow. It was initiated by Panchapakesan and Lumley [549] for jets and quickly adopted by Hussein et al. [539] who clearly showed the difference between a stationary probe and a moving one. Complex flows around airfoils can also be captured using flying hot wires as explained by Bruun [699].

Probes more robust than wires consist of a thin metallic material deposited on a small quartz cylinder, and overcoated by a thin layer of quartz. They respond in a similar way to wires and permit measurements in water, liquid metals, and gases in industrial conditions.

The right-hand side of Fig. 10.2 illustrates an X-probe which consists of two wires closely spaced and inclined with respect with the mean flow. This set-up permits to measure $u_1'(t)$ and $u_2'(t)$ and to deduce the Reynolds stress $-\rho\overline{u_1'u_2'}$ which is a fundamental quantity in all turbulent flows. Figure 10.2 is sketched for a known mean velocity direction $\bar{U}_1$. Nevertheless, an X-probe may be used, even if the mean velocity direction is not known, but one has to check that the velocity lies in the plane (1)–(2) to ensure $u_3'(t) \simeq 0$. In that case an exact 90° angle between the two wires simplifies the approach [699]. Other configurations of interest are:

- three hot-wire probes give access to the three velocity components in a 3-D flow. Commercial probes are provided with mutually orthogonal wires to ease calibration and data processing since the probe frame has to be connected to the flow frame [699, 704],
- arrays of single or X wires are used to investigate mixing layers and orthogonal modes decomposition [220],
- arrays of 4–12 wires distributed on tetrahedrons permit to obtain the vorticity components [743],

Table 10.1 Physical properties of hot-wire and hot-film materials († annealed) at $T_0 = 293\,\mathrm{K}$: ρ_e electrical resistivity, χ temperature coefficient of resistivity, ρ density, c specific heat and λ thermal conductivity

Material	$\rho_e\ \Omega\cdot\mathrm{m}$	$\chi\ \mathrm{K}^{-1}$	$\rho\ \mathrm{kg}\cdot\mathrm{m}^{-3}$	$c\ \mathrm{J}\cdot\mathrm{kg}^{-1}\cdot\mathrm{K}^{-1}$	$\lambda\ \mathrm{W}\cdot\mathrm{m}^{-1}\cdot\mathrm{K}^{-1}$
Copper	$1.6\ 10^{-8}$	$+4.0\ 10^{-3}$	8 900	385	400
Nickel	$7.0\ 10^{-8}$	$+6.0\ 10^{-3}$	8 900	438	90
Platinum	$1.1\ 10^{-7}$	$+3.9\ 10^{-3}$	21 500	130	70
Pt-10 %Rh	$1.9\ 10^{-7}$	$+1.7\ 10^{-3}$	19 900	150	40
Silver	$1.6\ 10^{-8}$	$+3.8\ 10^{-3}$	10 500	235	428
Tungsten	$6.0\ 10^{-8}$	$+3.7\ 10^{-3}$	19 300	140	170
Tungsten†	$6.0\ 10^{-8}$	$+4.1\ 10^{-3}$	19 300	140	170

- for temperature measurements, an additional cold wire is placed close to a single wire or an X-wire. It behaves as a resistance thermometer [708],
- finally, thin films can be glued onto walls to obtain wall-shear stresses.

Electrical and thermal properties of materials used for most hot wires are reported in Table 10.1. Some basic values can therefore be estimated, such as the reference resistance R_0 given by the classical expression $R_0 = 4\rho_e l_w/\pi d_w^2$ where ρ_e is the electrical resistivity of the wire material. For example, $R_0 \simeq 3.3\,\Omega$ for a $5\,\mu\mathrm{m}$ tungsten wire, 2 mm long, and $R_0 \simeq 28\,\Omega$ for a $2.5\,\mu\mathrm{m}$ tungsten wire, 3 mm long. For $a_w^\star = 0.80$, the resistances become 6 and $50\,\Omega$ for these two wires respectively and the wire temperatures are then around 500 K, a limit which should be respected to avoid wire deformations.

10.1.3 Heat Transfer Relationship for Ideal Wires

Cooling laws associated with heat transfer by forced convection around long cylinders, a geometry well suited to describing hot wires, are available in many books or reviews, by Knudsen and Katz [10] or Comte-Bellot [704] among others. These laws are expressed in terms of dimensionless groups which make them general. For forced convection and subsonic flows, the relationship is

$$\mathrm{Nu}^\star = \mathcal{A}\,\mathrm{Pr}^{0.20} + \mathcal{B}\,\mathrm{Pr}^{0.33}\,\mathrm{Re}^n \tag{10.5}$$

with $\mathcal{A} \simeq 0.20$–0.30, $\mathcal{B} \simeq 0.60$–0.65, $n \simeq 0.45$–0.50, and the following notations

$$\mathrm{Re} = \frac{\rho u_n d_w}{\mu} \qquad \mathrm{Nu}^\star = \frac{R_w^\star I_w^{\star 2}}{\pi l_w \lambda (T_w^\star - T)} \qquad \mathrm{Pr} = \frac{\mu}{\lambda}$$

Table 10.2 Physical properties of usual fluids and substrates for hot films at $T_0 = 293\,\mathrm{K}$

Fluid/wall	Pr	γ	$\rho\,\mathrm{kg\cdot m^{-3}}$	$c_p\,\mathrm{J\cdot kg^{-1}\cdot K^{-1}}$	$\lambda\,\mathrm{W\cdot m^{-1}\cdot K^{-1}}$	$\mu\,\mathrm{kg\cdot m^{-1}\cdot s^{-1}}$
Air	0.71	1.40	1.2	1 005	0.0257	$1.82\ 10^{-5}$
Helium	0.70	1.66	0.17	5 180	0.157	$1.86\ 10^{-5}$
Water	7.0		1 000	4 180	0.60	$1.00\ 10^{-3}$
Mercury	0.022		13 600	140	9.3	$1.55\ 10^{-3}$
Quartz			2 650	710	6–11	
Kapton			1 420	1 090	0.10–0.35	
Plexiglas			1 190	1 470	0.21	
Tufnol			1 320	1 500	0.29	
Wood			580	2 500	0.13	

for the Reynolds and Nusselt numbers of the wire and for the Prandtl number of the fluid. Variables without subscript denote the value at the fluid temperature T in subsonic flows. In supersonic flows, the stagnation temperature T_t seen by the wire when not heated replaces the static temperature T [3, 723]. Table 10.2 indicates values of the physical parameters at the reference temperature of $T_0 = 293\,\mathrm{K}$. Some laws available in the literature [704] slightly differ from (10.5) mainly by the correcting factor $0.5(T_w^\star + T)^{0.18}$. This introduces complexity and is left outside the scope of this presentation. For experiments in air, Eq. (10.5) takes the simple form

$$\mathrm{Nu}^\star \simeq 0.24 + 0.56\,\mathrm{Re}^{0.50} \tag{10.6}$$

Returning to the physical parameters themselves, i.e. to u_n, R, $R_w^\star$, $I_w^\star$, and using the general heat balance Eq. (10.2), (10.6) then becomes

$$\frac{R_w^\star I_w^{\star 2}}{R_w^\star - R} = A + B\sqrt{u_n} \tag{10.7}$$

where

$$A \simeq 0.24\frac{\pi l_w \lambda}{R_0 \chi} \quad \text{and} \quad B \simeq 0.56\frac{\pi l_w \lambda}{R_0 \chi}\sqrt{\rho d_w/\mu}$$

The relation (10.7) is known as King's law [722]. Although audaciously established assuming a potential flow around the wire, it highlights two main properties: the nonlinearity of the heat exchange law of the wire, as illustrated in Fig. 10.3, and the robustness of the law regarding supersonic flows, as illustrated in Fig. 10.4. The first property reveals a problem one has to cope with when doing turbulence measurements, the second property shows the usefulness of hot-wire anemometry for high speed flows.

The fluid characteristics ρ, μ and λ which enter into A and B depend on the temperature T. One can estimate this effect by assuming power laws of the form [30] $\rho \sim T^{-1}$, $\mu \sim T^{0.80}$, $\lambda \sim T^{0.80}$, which gives $A \sim T^{0.80}$ and $B \sim T^{0.80-0.50-0.40} \sim T^{-0.10}$. Hence B is almost independent of T. Moreover, $B\sqrt{u_n}$ becomes more and more important compared to A when u_n increases, so that one can admit that the fluid temperature appears only through R in Eq. (10.7).

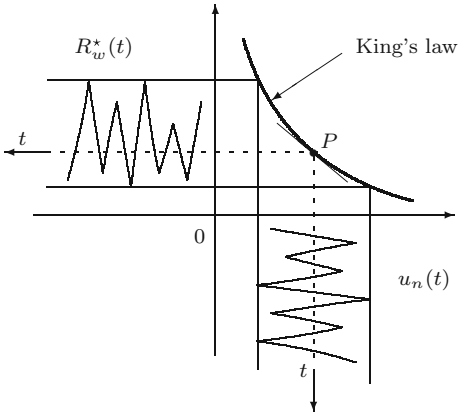

Fig. 10.3 Time variation of the wire resistance $R_w^\star(t)$ with the velocity $u_n(t)$ when the wire is fed by a constant current, according to King's law (10.7). Note the curve nonlinearity. For small amplitudes, the curve may be approximated by its tangent at the mean operating point P

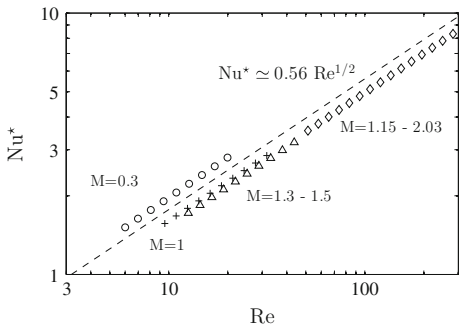

Fig. 10.4 King's law for different Mach numbers M, in continuous regime, Knudsen number Kn < 0.01. Note that $\mathrm{Nu}^\star$ becomes independent of M as soon as M ≥ 1.3. Data from Barre et al. [693] for $0.3 \leq \mathrm{M} \leq 1.5$, and Kovszanay [723] for $1.15 \leq \mathrm{M} \leq 2.03$

10.1.4 Constant Current Anemometer

A diagram of a Constant Current Anemometer (CCA) is shown in Fig. 10.5. For preliminary tests, the wire is incorporated in a Wheatstone bridge to measure R and adjust I_w for a chosen $a_w^\star$. Afterwards, only the left part of the bridge is kept. The DC part is recorded per se and the AC part is the input to a high gain amplifier which includes a resistance-capacity (R-C) network to compensate the wire thermal lag, an approach valid for low turbulence levels. CCAs were developed around 1930 by Dryden and Kuethe [710] and were used for many years, for example, by Klebanoff and Diehl [632] for boundary layers, by Corrsin and Uberoi [521] for heated jets, by Comte-Bellot and Corrsin [100, 101] for grid turbulence, by Kovasznay [723, 724], Morkovin [732] or Barre et al. [693] for supersonic flows.

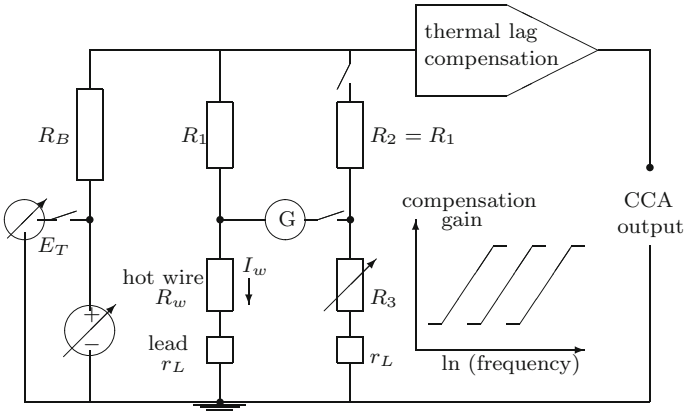

Fig. 10.5 Block diagram of a Constant Current Anemometer (CCA). The large resistance R_B imposes a constant current in the wire. A gain increase with frequency, shown in the insert, and a phase lead are applied to the AC part of the wire signal to compensate the thermal lag. The compensation circuit is correctly adjusted when a square-wave input signal gives a square-wave output signal

The equations governing the resistance $R_w(t)$ of a real wire and the resistance $R_w^\star(t)$ of the corresponding ideal wire, are obtained from (10.1), (10.2) and (10.4)

$$\frac{m_w c_w}{R_0 \chi}\frac{dR_w}{dt} = R_w I_w^2 - (R_w - R) f[u_n(t)] \tag{10.8}$$

$$0 = R_w^\star I_w^2 - (R_w^\star - R) f[u_n(t)] \tag{10.9}$$

where $f(u_n) = F(u_n)/(R_0\chi)$. Of course, all variables should mention that the wire is operated by a CCA, but for simplification R_w stands for $R_w|_{\mathrm{CCA}}$, $R_w^\star$ for $R_w^\star|_{\mathrm{CCA}}$ and I_w for $I_w|_{\mathrm{CCA}}$ or $I_w^\star|_{\mathrm{CCA}}$. The elimination of $f[u_n(t)]$ between Eqs. (10.8) and (10.9) gives

$$\frac{m_w c_w}{R_0 \chi}\frac{1}{RI_w^2}\frac{dR_w}{dt} = \frac{R_w^\star - R_w}{R_w^\star - R}$$

and provides also the compact equation

$$\frac{m_w c_w}{R_0 \chi}\frac{1}{RI_w^2}\frac{dR_w}{dt} + \frac{R_w - R}{R_w^\star - R} = 1 \tag{10.10}$$

first established by Corrsin [709]. Thus $R_w(t)$ is governed by a first-order differential equation which is nonlinear because $R_w^\star$ is time dependent. Before considering that general case, let us examine the widely used simplifications for low turbulence levels.

At low turbulence levels, that is for small fluctuations, the above equations can be linearized and two notable results emerge, the concept of the time constant and the concept of sensitivity coefficients. Linearization implies splitting of all variables into

their mean and fluctuating parts assumed of small amplitude. Thus $R_w^\star = \bar{R}_w^\star + r_w'^\star$ with $r_w'^\star \ll \bar{R}_w^\star$, $R_w = \bar{R}_w + r_w'$ with $r_w' \ll \bar{R}_w$, and $R = \bar{R} + r'$ with $r' \ll \bar{R}$. Substitution in Eq. (10.10) gives, after some algebra, $\bar{R}_w = \bar{R}_w^\star$ and

$$\frac{m_w c_w}{R_0 \chi} \frac{\bar{R}_w - \bar{R}}{\bar{R} I_w^2} \frac{dr_w'}{dt} + r_w' = r_w'^\star \tag{10.11}$$

The differential equation governing $r_w'(t)$ now has constant coefficients, and the factor in front of dr_w'/dt has the dimension of a time. This factor is called the *time constant* of the wire when operated in a constant-current mode. For clarity, we note it $\bar{M}_w^{\mathrm{CCA}}$, so that

$$\bar{M}_w^{\mathrm{CCA}} \frac{dr_w'}{dt} + r_w' = r_w'^\star \quad \text{with} \quad \bar{M}_w^{\mathrm{CCA}} = \frac{m_w c_w}{R_0 \chi} \frac{1}{I_w^2} \frac{\bar{R}_w - \bar{R}}{\bar{R}} \tag{10.12}$$

whatever the nature of the fluctuation, velocity or temperature. Two other forms can also be written using Eq. (10.6) or (10.7)

$$\bar{M}_w^{\mathrm{CCA}} = (1 + \bar{a}_w) \frac{d_w^2}{4} \frac{\rho_w c_w}{\lambda \bar{\mathrm{Nu}}} \quad \text{or} \quad \bar{M}_w^{\mathrm{CCA}} = \frac{m_w c_w}{\chi R_0} \frac{1}{f(\bar{U}_n)} (1 + \bar{a}_w) \tag{10.13}$$

As orders of magnitude, for a tungsten wire with $d_w = 5\,\mu\mathrm{m}$, $\bar{M}_w^{\mathrm{CCA}} = 420\,\mu\mathrm{s}$, $\bar{U}_n = 50\,\mathrm{m.s}^{-1}$ and $\bar{a}_w = 0.80$. For $\bar{U}_n = 100\,\mathrm{m.s}^{-1}$, $\bar{M}_w^{\mathrm{CCA}}$ is reduced to $305\,\mu\mathrm{s}$. The fact that $\bar{M}_w^{\mathrm{CCA}}$ decreases when $\bar{U}_n$ increases, allows the investigation of high speed flows. The solution of Eq. (10.12) has the classic exponential form

$$r_w' = r_w'^\star \exp(-t/\bar{M}_w^{\mathrm{CCA}}) \qquad \text{and} \qquad \bar{M}_w^{\mathrm{CCA}} j\omega \, \hat{r_w'} + \hat{r_w'} = \hat{r_w'^\star}$$

in the time space, see Fig. 10.6, and in the frequency space respectively. The amplitude loss $a/a^\star$ and the phase lag ψ of a real wire compared to the ideal wire are thus

$$a/a^\star = \left[1 + (\bar{M}_w^{\mathrm{CCA}} \omega)^2\right]^{-1/2} \qquad \text{with} \qquad \tan\psi = \bar{M}_w^{\mathrm{CCA}} \omega$$

The purpose of the compensation amplifier is to correct the amplitude loss and the phase lag, and thereby recover the ideal signal $r_w'^\star$. In practice, the output voltage $e'^\star = r_w'^\star I_w$ is acquired during the experiment.

Also for small fluctuations, sensitivity coefficients can be defined. Taking the log derivative of King's law (10.7), when I_w is a constant, and recalling that $R = R_0[1 + \chi(T - T_0)]$, one obtains for the fluctuations

$$\frac{r_w'^\star}{\bar{R}_w^\star} = -\frac{\bar{a}_w^\star}{2} \frac{B\sqrt{\bar{U}_n}}{A + B\sqrt{\bar{U}_n}} \frac{u_n'}{\bar{U}_n} + \frac{\chi \bar{T}}{1 + \chi(\bar{T} - T_0)} \frac{\theta'}{\bar{T}}$$

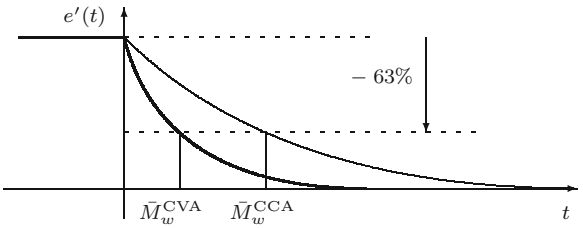

Fig. 10.6 Response of a constant current anemometer to a square-wave signal added to the current heating the wire and comparison with the similar curve corresponding to a constant voltage anemometer. Each curve obeys an exponential decay and the time constant is the time at which the drop is $1 - e^{-1} \simeq 63\,\%$. Note that $\bar{M}_w^{\mathrm{CVA}} < \bar{M}_w^{\mathrm{CCA}}$, refer to Eqs. (10.13) and (10.28)

At sufficiently large velocities, $B\sqrt{\bar{U}_n} \gg A$, and from Table 10.1, $\chi\bar{T} \simeq 1$ and $\chi(\bar{T} - T_0) \ll 1$ if T stays close to T_0. The previous equation can thus be written in a simple form,

$$\frac{r'^{\star}_w}{\bar{R}^{\star}_w} = -\frac{\bar{a}^{\star}_w}{2}\frac{u'_n}{\bar{U}_n} + \frac{\theta'}{\bar{T}}$$

which gives at the CCA output,

$$\frac{e'^{\star}_{\mathrm{CCA}}}{\bar{E}^{\star}_{CCA}} = S^{\mathrm{CCA}}_{u'_n}\frac{u'_n}{\bar{U}_n} + S^{\mathrm{CCA}}_{\theta'}\frac{\theta'}{\bar{T}} \tag{10.14}$$

where

$$S^{\mathrm{CCA}}_{u'_n} = -\frac{\bar{a}^{\star}_w}{2} \times C_C \qquad S^{\mathrm{CCA}}_{\theta'} = 1 \times C_C \qquad C_C = \frac{\bar{R}^{\star}_w}{\bar{R}^{\star}_w + R_1 + r_L}$$

The factors $S^{\mathrm{CCA}}_{u'_n}$ and $S^{\mathrm{CCA}}_{\theta'}$ are the CCA sensitivity coefficients to velocity and temperature fluctuations respectively. Comparison with other anemometers is reported in Table 10.3.

For large fluctuations, the time dependence which appears through the coefficients of Eq. (10.10) introduces higher harmonics in the solution due to parametric

Table 10.3 Sensitivity coefficient of anemometers according to King's law, when $B\sqrt{\bar{U}_n} \gg A$, $\chi T \simeq 1$ and $\chi(T - T_0) \ll 1$

	CCA	CTA	CVA
$S_{u'_n}$	$-\frac{1}{2}\,\bar{a}^{\star}_w \times C_C$	$\frac{1}{4}$	$\frac{\bar{a}^{\star}_w}{2(1+2\bar{a}^{\star}_w)} \times L_S$
$S_{\theta'}$	$1 \times C_C$	$-\frac{1}{2\bar{a}^{\star}_w}$	$\frac{1}{1+2\bar{a}^{\star}_w} \times L_S$

See expressions (10.14) and (10.31) for the factors C_C and L_S respectively

excitation. This problem was pointed out by Corrsin [709] using Fourier series, then studied by Comte-Bellot and Schon [707] using an analog computer. Numerical results are reported by Comte-Bellot [704]. These harmonics generated at the wire level are not at all suppressed by the compensating circuit. Even worse, they are amplified as if they were true turbulence. Large errors appear on odd moments, such as the skewness factors, due to cross moments between harmonics, but fortunately mean quadratic values and power spectral densities (PSD) are only slightly affected.

10.1.5 Constant Temperature Anemometer

A diagram of a Constant Temperature Anemometer (CTA) is given in Fig. 10.7. The idea is to use an electronic feedback amplifier to maintain the wire at a nearly constant resistance. Thus $dR_w/dt \simeq 0$ gives $dT_w/dt \simeq 0$ thanks to Eq. (10.1), and in Eq. (10.4), any thermal lag effect due to the wire is suppressed. The wire overheat is chosen once and for all by adjusting the resistance R_3 in the adjacent lower arm of the bridge. The factor m which appears in the right arm of the bridge is called the *bridge ratio*. Often $m = 20$ so that most of the supply current goes through the active left arm of the bridge which includes the wire rather than through the passive right arm. Also, the top resistance R_1 is chosen to be large compared to R_w, usually 20 or 50 Ω to increase the CTA output voltage and ease its acquisition. In Fig. 10.7 all resistances are expressed in terms of the resistance $R_w^\star$ that the equivalent ideal wire would have. Thus, if $R_w^\star = 5\,\Omega$ and $R_1 = 20\,\Omega$, $n = 4$.

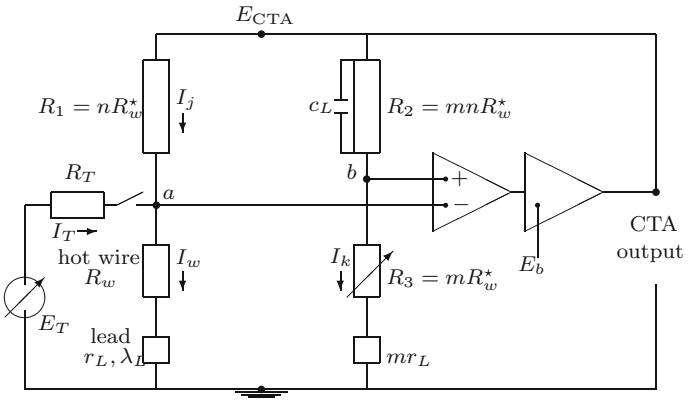

Fig. 10.7 Block diagram of a constant temperature anemometer (CTA). The Wheatstone bridge is kept balanced at all times by a feedback amplifier, so that the wire resistance R_w is maintained constant. The current intensity I_w sent back to the wire is the leading indicator, it increases when the incident flow velocity increases, it decreases when the incident flow temperature increases. The CTA ouput E_{CTA} mimics the I_w change

The CTA was pioneered by several independent workers around 1950, e.g. by Weske [745], Ossofsky [734], and Ling and Hubbard [721, 728] making use of the newly existing operational amplifiers. Many studies were later conducted to improve the circuitry, its comprehension and stability, for example by Perry [735], Fingerson [711], Watmuff [744], Weiss et al. [749] and most importantly by Freymuth [713, 714, 716–718].

For an ideal CTA where the bridge is kept perfectly balanced at all times, the current intensity $I^\star_w(t)$ obeys King's law (10.7) where $R^\star_w = \text{cst}$. The top bridge voltage $E^\star_{CTA}(t)$ is thus

$$E^\star_{CTA}(t) = (R_1 + R^\star_w + r_L)\left[\frac{R^\star_w - R}{R^\star_w}\left(A + B\sqrt{u_n(t)}\right)\right]^{1/2} \tag{10.15}$$

where $R^\star_w$ denotes $R^\star_w|_{CTA}$. Of course, that value differs from that associated with a CCA. The curve relating $E^\star_{CTA}$ to u_n at a given flow temperature is the CTA calibration. It is then common practice to admit that any measured $E_{CTA}(t)$ value is the ideal $E^\star_{CTA}(t)$ quantity, and to invert the curve to deduce $u_n(t)$ from an acquired signal. Several procedure are described for single or X-wires, using polyfit polynomials [698] or look-up tables [729].

Sensitivity coefficients can also be defined for small fluctuations in that ideal situation. The log derivative of (10.15) yields for the incident velocity fluctuations

$$\frac{e'^\star_{CTA}}{\bar{E}^\star_{CTA}} = S^{CTA}_{u'_n}\frac{u'_n}{\bar{U}_n} \qquad \text{with} \qquad S^{CTA}_{u'_n} = \frac{1}{4}\frac{B\sqrt{\bar{U}_n}}{A + B\sqrt{\bar{U}_n}} \simeq \frac{1}{4}$$

and for the incident temperature fluctuations

$$\frac{e'^\star_{CTA}}{\bar{E}^\star_{CTA}} = S^{CTA}_{\theta'}\frac{\theta'}{\bar{T}} \quad \text{with} \quad S^{CTA}_{\theta'} = -\frac{1}{2\bar{a}^\star_w}\frac{\chi\bar{T}}{1 + \chi(\bar{T} - T_0)} \simeq -\frac{1}{2\bar{a}^\star_w}$$

the approximate values being based on the conditions $B\sqrt{\bar{U}_n} \gg A, \chi \simeq 1/\bar{T}$, $\bar{T} \simeq T_0$.

For a real CTA, the electronic circuit implies more parameters than in the ideal CTA that was considered above. According to the well accepted analysis of Freymuth [713, 716], three equations are needed to model a CTA. The first deals with the bridge, the second with the feedback amplifier and the third with the hot wire.

For the bridge, the voltage difference $\delta = V_b - V_a$ constitutes the input signal to the feedback amplifier. As there are many reactances in the circuit, the cable inductance λ_L, the capacitance C_L, see Fig. 10.7, and often additional ones in the lower right arm of the bridge, lumping all these into a single term M_B is convenient as suggested by Freymuth [713] and used by Weiss et al. [749]. Ohm and Kirchhoff laws for the circuit then give

$$\delta = \frac{nR_w^\star(R_w^\star - R_w)}{(nR_w^\star + R_w^\star + r_L)(nR_w^\star + R_w + r_L)} E + M_B \frac{dE}{dt} - \frac{nR_w^\star}{R_T} \frac{R_w + r_L}{nR_w^\star + R_w + r_L} E_T \tag{10.16}$$

where E stands for E_{CTA}, R_w for $R_w|_{CTA}$, $R_w^\star$ for $R_w^\star|_{CTA}$. The voltage for an electronic test is E_T.

The feedback amplifier usually has two stages [718], each one characterized by a first-order frequency response. The gain-bandwidth products of these stages are GBP_1 and GBP_2. Those are inalterable and characterize their dynamics. Hence, $GBP_1 = G_1/2\pi M_1$, and $GBP_2 = G_2/2\pi M_2$ where the gains of the stages are denoted by G_1 and G_2 and their first-order time constants by M_1 and M_2. Furthermore, it is assumed that the second stage generates a constant but adjustable offset voltage E_b. Combining the dynamic responses of the two amplifier stages leads to

$$M'' \frac{d^2E}{dt^2} + M' \frac{dE}{dt} + E = E_b + G\delta \tag{10.17}$$

where $G = G_1G_2$, $M' = M_1 + M_2$ and $M'' = M_1M_2$.

For the hot wire, the energy balance is directly deduced from Eqs. (10.1) and (10.4)

$$\frac{m_w c_w}{\chi R_0} \frac{dR_w}{dt} = \frac{R_w}{(nR_w^\star + R_w + r_L)^2} E^2 - (R_w - R) f(U_n) \tag{10.18}$$

There are three unknowns, δ, R_w and E, and to solve Eq. (10.16)–(10.18) one has to find a way of estimating G, M', M'', E_b, and M_B. This requires the linearization of the equations and the use of the electronic test signal e'_T.

To linearize CTA equations, small perturbations are defined as follows, δ', r' and e' around the mean (or static) values $\bar{\delta} = 0$, $\bar{R}_w = R_w^\star$ and $\bar{E} = E_b$. Substitution in Eqs. (10.16)–(10.18) gives

$$\delta' = -\bar{E} \frac{nR_w^\star}{(nR_w^\star + R_w^\star + r_L)^2} r' + M_B \frac{de'}{dt} - \frac{nR_w^\star}{R_T} \frac{R_w^\star + r_L}{(nR_w^\star + R_w^\star + r_L)} e'_T \tag{10.19}$$

$$M'' \frac{d^2e'}{dt^2} + M' \frac{de'}{dt} + e' = G\delta' \tag{10.20}$$

$$\frac{m_w c_w}{\chi R_0} \frac{1}{f(\bar{U}_n)} \frac{dr'}{dt} + \left[1 - \frac{(nR_w^\star - R_w^\star + r_L)}{nR_w^\star + R_w^\star + r_L} \frac{(R_w^\star - R)}{R_w^\star}\right] r' = 2\frac{(R_w^\star - R)}{\bar{E}} e' - (R_w^\star - R) \frac{1}{f(\bar{U}_n)} \frac{df}{d\bar{U}_n} u'_n \tag{10.21}$$

The elimination of δ' is achieved by combining (10.19) and (10.20). The resulting equation between e' and r' is then derived with respect to time so that dr'/dt can be eliminated using (10.21). The important result is that a third-order linear differential equation with constant coefficients now governs e', its form is

$$C_3\frac{d^3e'}{dt^3}+C_2\frac{d^2e'}{dt^2}+C_1\frac{de'}{dt}+e'=C_u u'_n+C_t e'_T+C_{tt}\frac{de'_T}{dt} \tag{10.22}$$

and the most important factor is C_3

$$C_3=M''\frac{1}{G}\frac{m_w c_w}{\chi R_0}\frac{1}{f(\bar{U}_n)}\frac{(nR^\star_w+R^\star_w+r_L)^2}{2(R^\star_w-R)nR^\star}$$

which gives the cut-off frequency of a CTA, $f_c=2\pi(C_3)^{-1/3}$. Figure 10.8 illustrates the pulse response specific to a 3rd-order system submitted to an electronic square wave input. Using that signature, Freymuth [713] gave a practical rule, $f_c=1/(1.3\tau_0)$, where τ_0 is the time at which the pulse crosses the time axis for the first time. Figure 10.9 displays an experimental result and a numerical simulation. The transfer function output/input, as considered by Weiss et al. [749] see Fig. 10.10, is a useful addition. Adjustment of a CTA has to be conducted at every mean operating point as $f(\bar{U}_n)$ appears in C_3. At least, an adjustement at the highest flow velocity, rather than at the lowest one, is advised to obtain stability. At high velocity the feedback effect is minimal, since the wire thermal lag is small, insuring oscillation-free behaviour at lower velocities.

The effect of wire overheat is illustrated in Fig. 10.11. For a good feedback efficiency, the wire overheat has to be high. Hence, it is often advised to set $\bar{a}_w=0.80$, but values of $\bar{a}_w$ down to 0.20 may still work for RMS and PSD measurements if the frequency correction suggested by Weiss et al. [746] is included. However, the cold wire technique that one would like to use to obtain instantaneous temperature fluctuations is ruled out.

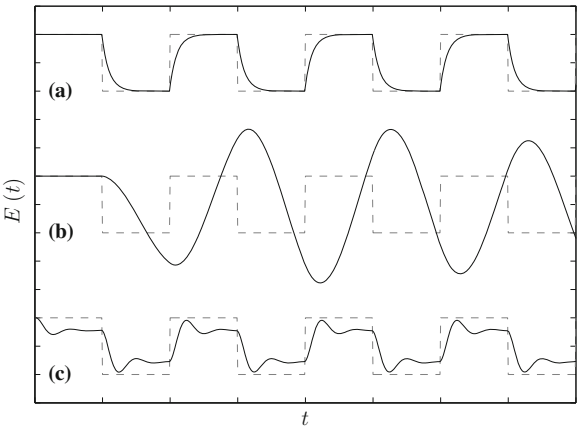

Fig. 10.8 Square-wave responses (arbitrary units): **a** exponential decay for a 1st order system, the case of a CCA or a CVA, see also Fig. 10.6; **b** oscillations for a 2nd order system; **c** a large initial pulse followed by small decaying oscillations for a 3rd order system

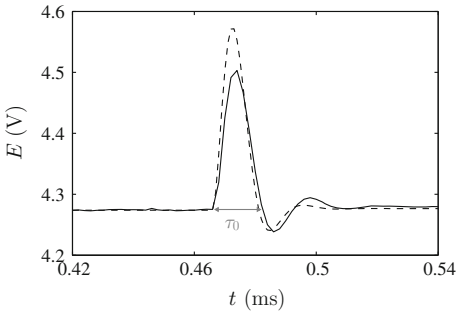

Fig. 10.9 Pulse for a 5 µm tungsten wire, − experimental curve, −− numerical simulation using (10.16)–(10.18). The CTA is a DISA 55M10, $n = 3.47$. $\bar{U}_n = 10\,\mathrm{m\cdot s^{-1}}$, $a_w = 0.80$, $f_T = 100\,\mathrm{kHz}$, $e'_T = 100\,\mathrm{mV}$ peak to peak, $R_4 = 1000\,\Omega$, $G = 1000$, $M' = 2.22 \times 10^{-5}\,\mathrm{s}$, $M'' = 1.23 \times 10^{-10}\,\mathrm{s^2}$, $E_b = 1.99\,\mathrm{V}$, $M_B = -8.55 \times 10^{-9}\,\mathrm{s}$, $r_L = 1\,\Omega$. Courtesy of Julien Weiss (ÉTS Montréal)

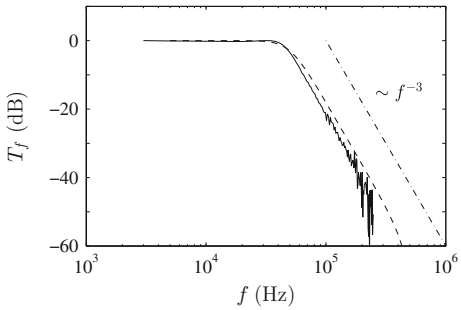

Fig. 10.10 Transfer function for the same conditions as in Fig. 10.9. The curve presents a plateau up to $f_c \simeq 40\,\mathrm{kHz}$ and afterwards a −60 dB/decade slope characteristic of a 3rd order system. Courtesy of Julien Weiss (ÉTS Montréal)

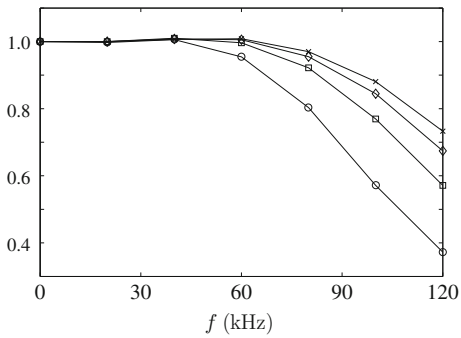

Fig. 10.11 Improvement of a CTA frequency response with wire overheat $a_w = 0.20$ ∘, 0.40 □, 0.60 ⋄, 0.80 ×. Same conditions as in Fig. 10.9, except for E_b which are 0.8, 1.6, 2.4 and 3.4 V for the four a_w values respectively. Courtesy of Julien Weiss (ÉTS Montréal)

Input signals with large amplitudes induce nonlinearity because of a joint effect between the electronic circuit and the thermal inertia of the wire. Freymuth [714] pointed out that a second harmonic is generated, of the order of 20 % of the fundamental signal, around half the cut-off frequency $f_c/2$. Confirmation of this result is brought by Weiss et al. [749] with experimental tests and numerical simulations.

10.1.6 Constant Voltage Anemometer

Figure 10.12 illustrates the Constant Voltage Anemometer (CVA) principle. There are two independent circuits to operate the hot wire, one to fix the wire voltage V_w and the other to modify the wire current I_w according to the incident flow. In the voltage output $E_{T_c}^{\mathrm{CVA}}$, the lower index T_c recalls that the instantaneous output voltage depends on the capacity C. The CVA concept was elaborated by Mangalam et al. [730] and Sarma [736] in the 1990s. Prototypes and commercial units were then widely used, in high-speed boundary layers by Sarma et al. [739], Comte-Bellot and Sarma [706] and Weiss et al. [748], in shock tubes by Norris and Chokani [733], in pulsed synthetic jets by Truzzi et al. [741].

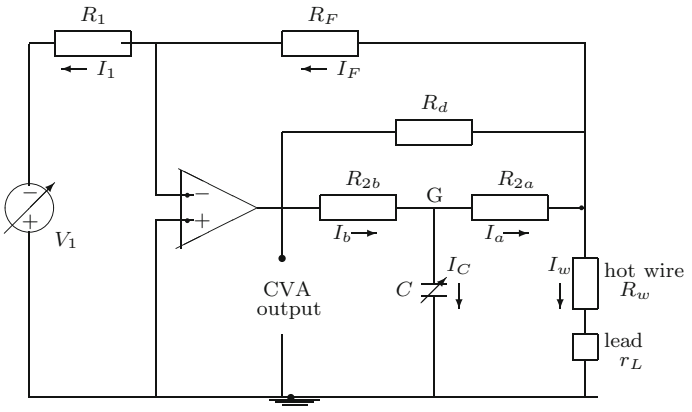

Fig. 10.12 Block diagram of a Constant Voltage Anemometer (CVA). The wire voltage $V_w = (R_w + r_L)I_w$ is fixed by the DC supply V_1 and resistances R_1 and R_F. The current through the wire whose intensity I_w changes with turbulence is supplied by a feedback amplifier, the only path is through resistance $R_{2a} + R_{2b}$, chosen large so as to yield a large voltage output $E_{T_c}^{\mathrm{CVA}}$

The Ohm–Kirchhoff laws applied to the network of Fig. 10.12 give

$$\begin{aligned} -R_1 I_1 + V_1 &= 0 \\ V_w - R_F I_F &= 0 \\ V_w &= (R_w + r_L) I_w \\ E_{Tc}^{\mathrm{CVA}} - R_{2b} I_b &= V_G \\ V_G - R_{2a} I_a &= V_w \\ I_c &= C dV_G/dt \\ I_b &= I_a + I_c \\ I_a &= I_w + I_F \end{aligned} \tag{10.23}$$

where R_w stands for $R_w|_{\mathrm{CVA}}$ and I_w for $I_w|_{\mathrm{CVA}}$. Resistor R_d, which is large compared to $R_{2a} + R_{2b}$, is neglected in the above equations. If needed the complete equations are available in Sarma [736]. From (10.23) one can easily deduce $V_w = V_1 R_F / R_1$, which shows that the wire voltage V_w is indeed constant, as V_1 is a stable DC source. The setting of V_w is made by adjusting V_1 manually or by a PC. After some algebra, one deduces from (10.23) the CVA instantaneous output voltage

$$E_{Tc}^{\mathrm{CVA}} = V_w \left[1 + R_2 \left(\frac{1}{R_F} + \frac{1}{R_w + r_L} \right) + T_c R_2 \frac{d}{dt} \left(\frac{1}{R_w + r_L} \right) \right] \tag{10.24}$$

where $R_2 = R_{2a} + R_{2b}$. Note that $T_c = R_{2a} R_{2b} C / R_2$ is a time constant whose interest is presented further below.

The equations governing the resistance R_w of the real wire and the resistance $R_w^\star$ of the corresponding ideal wire, are issued from (10.1), (10.2) and (10.4)

$$\frac{m_w c_w}{R_0 \chi} \frac{dR_w}{dt} = R_w \frac{V_w^2}{(R_w + r_L)^2} - (R_w - R) f(u_n) \tag{10.25}$$

$$0 = R_w^\star \frac{V_w^2}{(R_w^\star + r_L)^2} - (R_w^\star - R) f(u_n) \tag{10.26}$$

The basic equation which links R_w to $R_w^\star$ is then obtained by eliminating $f(u_n)$

$$\frac{1}{V_w^2} \frac{m_w c_w}{R_0 \chi} \frac{dR_w}{dt} = \frac{R_w}{(R_w + r_L)^2} - \frac{R_w^\star}{(R_w^\star + r_L)^2} \frac{R_w - R}{R_w^\star - R} \tag{10.27}$$

This is the equivalent of Eq. (10.10) for a CVA. The linearization of Eq. (10.27) leads after some algebra to

$$\bar{M}_w^{\mathrm{CVA}} \frac{dr'_w}{dt} + r'_w = r'^\star_w$$

with

$$\bar{M}_w^{\mathrm{CVA}} = \frac{m_w c_w}{R_0 \chi} \frac{1}{f(\bar{U}_n)} \frac{1 + \bar{a}_w^\star}{(1 + 2\bar{a}_w^\star)} \times L_M \tag{10.28}$$

where $\bar{M}_w^{\mathrm{CVA}}$ is the time constant of the wire when operated in a constant voltage mode. The factor $L_M = (1 + r_L/\bar{R}_w^\star)/\left[1 + r_L/\bar{R}_w^\star(1 + 2\bar{a}_w^\star)\right]$ is due [705] to the cable resistance r_L: it reaches 10 % when $\bar{R}_w^\star \simeq 5\ \Omega$, $\bar{a}_w^\star \simeq 0.80$ and $r_L \simeq 1\Omega$. Thanks to the dividing factor $(1 + 2\bar{a}_w^\star)$ which appears explicitly in (10.28), M_w^{CVA} is smaller than M_w^{CCA}, see also Fig. 10.6. The measurement of $\bar{M}_w^{\mathrm{CVA}}$ makes use of an additional CVA board [739] which includes a square wave generator.

The correction of the thermal lag of the real wire is based on the linearized form [696] of Eq. (10.24)

$$e'_{Tc} = -\frac{R_2}{(\bar{R}_w^\star + r_L)^2} V_w \left(r'_w + T_c \frac{dr'_w}{dt} \right) \tag{10.29}$$

which shows that T_c already brings a partial correction, as the fully corrected signal which is desired is

$$e'^\star = -\frac{R_2}{(\bar{R}_w^\star + r_L)^2} V_w \left(r'_w + \bar{M}_w^{\mathrm{CVA}} \frac{dr'_w}{dt} \right) \tag{10.30}$$

Obtention of a software procedure to connect the raw signal acquired at the CVA output e'_{Tc} to the fully corrected signal $e'^\star$ can be established as follows. The difference between (10.29) and (10.30) gives

$$e'^\star - e'_{Tc} = -\frac{R_2}{(\bar{R}_w^\star + r_L)^2} V_w (\bar{M}_w^{\mathrm{CVA}} - T_c) \frac{dr'_w}{dt}$$

and furthermore, the difference between (10.30) derived with respect to t and multiplied by T_c, and (10.29) derived with respect to t and multiplied by $\bar{M}_w^{\mathrm{CVA}}$, gives

$$T_c \frac{de'^\star}{dt} - \bar{M}_w^{\mathrm{CVA}} \frac{de'_{Tc}}{dt} = -\frac{R_2}{(\bar{R}_w^\star + r_L)^2} V_w (T_c - \bar{M}_w^{\mathrm{CVA}}) \frac{dr'_w}{dt} = e'_{Tc} - e'^\star$$

and finally,

$$e'^\star(t) = e'_{Tc}(t) + \bar{M}_w^{\mathrm{CVA}} \frac{de'_{Tc}(t)}{dt} - T_c \frac{de'^\star(t)}{dt}$$

In terms of the ith and $(i-1)$th samples acquired at a sampling frequency f_s this gives

$$e'^\star(i) = \frac{e'_{Tc}(i) + \bar{M}_w^{\mathrm{CVA}} f_s \left[e'_{Tc}(i) - e'_{Tc}(i-1) \right] + T_c f_s\, e'^\star(i-1)}{1 + T_c f_s}$$

This two-step procedure has two advantages, it ensures a constant frequency bandwidth whatever the flow conditions or wire overheat [739], and it increases the efficiency of data acquisition.

To express the CVA sensitivity coefficients, Eq. (10.24) where T_c is set to zero is now linearized and differentiated. After some developments [705], one obtains

$$\frac{e'^{\star}}{\bar{E}^{\star}_{\mathrm{CVA}}} = S^{\mathrm{CVA}}_{u'_n}\frac{u'_n}{\bar{U}_n} + S^{\mathrm{CVA}}_{\theta'_a}\frac{\theta'}{\bar{T}}$$

where

$$S^{\mathrm{CVA}}_{u'_n} = \frac{1}{2}\frac{\bar{a}^{\star}_{w}}{(1+2\bar{a}^{\star}_{w})}L_S \quad \text{and} \quad S^{\mathrm{CVA}}_{\theta'} = \frac{1}{(1+2\bar{a}^{\star}_{w})}L_S \tag{10.31}$$

The factor $L_S = \left[1+(\bar{R}^{\star}_{w}+r_L)\,(1/R_2+1/R_F)\right]^{-1}\left[1+r_L/\bar{R}^{\star}_{w}(1+2\bar{a}^{\star}_{w})\right]^{-1}$ involves the CVA circuit and the wire cable resistance r_L. It is around 8 % when $\bar{R}^{\star}_{w} \simeq 5\,\Omega$, $a^{\star}_{w} \simeq 0.80$, $r_L \simeq 1\,\Omega$, $R_2 = 100\,\Omega$ and $R_F = 400\,\Omega$.

When large fluctuations are present, all equations are nonlinear, especially Eq. (10.27) where the time-dependent coefficients are clearly visible, resulting in the generation of higher harmonics in the CVA response due to parametric excitation. A procedure to eliminate all nonlinearities is proposed by Berson et al. [695, 696]. It can be entirely conducted during data processing, and has three steps. First, Eq. (10.24) is solved to deduce $R_w(t)$ from E^{CVA}_{Tc}. Secondly, Eq. (10.27) is solved to deduce $R^{\star}_{w}(t)$ from $R_w(t)$, and third, $f(u_n(t))$ is obtained from $R^{\star}_{w}(t)$ and the calibration data set. At this point, note the clear advantage of CVAs over CCAs or CTAs.

10.1.7 Some Additional Remarks

The calibration of a probe is a prerequisite for any turbulent investigation. Indeed, one has to know how to connect the anemometer output to the incident velocity, yaw angle and possibly pitch angle of the wire. For calibration the probe is placed in a smooth flow, such as the potential core of a jet or the free stream over a boundary layer, to quickly collect accurate data. The incident velocity must cover the range of interest. It is usually measured with a Pitot tube, except at low velocities where rotating arms or linearly moving carriages are needed [699]. For X-wires, a rotating ring is added to change the yaw angle of the probe, usually in the range between 45 and +45°. Enough data must be acquired so that the calibration tables or curves can be inverted to obtain instantaneous velocity components when subsequently conducting experiments in a turbulent flow. Details regarding this important topic are available in Lueptow et al. [729], Browne et al. [698] or van Dijk and Nieuwstadt [742]. At this point, note that all calibration data are obtained in a smooth flow where no time dependence occurs. They therefore deal with ideal wires without thermal lag, and are associated with quantities denoted by a star superscript in the preceding sections.

When performing turbulence measurements, the flow temperature might differ from the reference temperature at which the calibration was recorded. If the difference is only of a few degrees, one can shift the calibration curve using the sensitivity coefficients listed in Table 10.3. For larger differences, calibration curves at different temperatures are needed, as reported by Brunn [699]. With a CVA, a cold/hot sequence for the wire, just adjusting V_w as shown by Sarma and Comte-Bellot [737], avoids the use of an extra thermocouple to get the flow temperature.

The two ends of a wire which are soldered to metallic broaches are necessarily at ambient temperature or close to it. Very demonstrative temperature distributions along hot wires were obtained by Champagne et al. [700] using an infrared detector. There are at least two consequences. The wire has a sensitivity greater in its central part than near its ends, and a fraction of the Joule heating goes towards the broaches instead of being convected away by the flow. Many papers are devoted to this subject, by Corrsin for CCAs [709] or by Li for CTAs [726]. For a 5 µm tungsten wire, 2 mm long and overheated at $a_w = 0.80$, the thermal loss to the broaches is 20, 11 and 9 % at $\bar{U}_1 = 10, 30, 60\,\mathrm{m.s}^{-1}$ respectively [704].

The velocity value indicated by a wire cannot be a perfectly local one, because the wire can only provide an average value over its length. The small scales of turbulence are obviouly the most affected and an early example is provided by Wyngaard [750] who studied turbulence in the atmosphere. Analytical expressions and numerical simulations, as well as a lot of work on the subject, are given in the review by Comte-Bellot [704].

When placed close to a wall, for $x_2 u_\tau/\nu \leq 5$, a wire is submitted to an extra heat exchange with the wall, and an ordinary calibration curve is obviously no longer valid. The only way to cope with this problem has been suggested by Khoo et al. [627] who calibrates the wire in a Poiseuille flow between two disks, the bottom one is at rest and the top one is rotating at a constant speed. The velocity profile is thus known analytically over the gap where the wire is placed for calibration.

The background noise of an anemometer is usually white noise that is amplified by the electronic circuit and hence results in a f^2 spectrum at the anemometer output. It is an important quantity to know as it limits the highest part of the spectra where turbulence contributions are small. Noise measurements are easy with CCAs or CVAs, just using a resistance in place of the wire [747]. For CTAs, one has to keep the wire connected to maintain the CTA stability and to place the wire in an enclosure which insures $u_i(t) = 0$. Numerical estimates have been developed by Freymuth [712] or Weiss and Comte-Bellot [747].

The wire support, i.e. broaches and stem, creates aerodynamic perturbations which have to be minimized. Ligrani and Willmarth [727] even manufactured a subminiature probe to approach a wall. Nowadays, with commercial probes, the only possibility is to estimate the importance of the pertubation and its consequence on the angular sensitivity as suggested by Adrian et al. [692] for X-wires and 3-D probes. For supersonic flows, stubs are advised to be kept near the broaches so that the shocks attached to the broaches do not perturb the active part of the wire [723].

10.1.8 Illustrative Examples

10.1.8.1 Measurement of $u_1'(t)$, $\overline{u_1'^2}$, $E_{11}^{(1)}$ and $L_{11}^{(1)}$

All these quantities concern the longitudinal velocity fluctuation $u_1'(t)$ and a single hot wire oriented normal to the mean velocity $\bar{U}_1$ suffices, see Fig. 10.2. The anemometer output must be acquired versus time at a high enough sampling frequency f_s and over a sufficient observation time Δt to cover the whole expected turbulence spectrum. For CCAs within the assumption of small fluctuations presented in Sect. 10.1.4, use of the sensitivity coefficient indicated in Table 10.3 suffices to obtain $u_1'(t)$. For CTAs, after having checked that all turbulence frequencies are well below the cut-off frequency of the feedback circuit, the perfect response presented in Sect. 10.1.5 may be used for small and large fluctuations. Thus, $u_1(t)$ is first obtained by inverting the calibration curve, then $\bar{U}_1$ is computed and finally $u_1'(t)$ is obtained by the difference $u_1(t) - \bar{U}_1$. For CVAs and small fluctuations the software correction described in Sect. 10.1.6 and use of the sensitivity coefficient indicated in Table 10.3 are sufficient. For CVAs and large fluctuations, the Berson et al. routine [695] presented in Sect. 10.1.6 is easy to program.

The power spectrum $\psi(f)$ of $u_1'(t)$ in the frequency domain f is easily obtained by a signal processing routine. This spectrum $\psi(f)$ and the one-dimensional spectrum $E_{11}^{(1)}(k_1)$ defined in Chap. 6 are such that

$$\overline{u_1'^2} = \int_0^\infty \psi(f)\, df = \int_{-\infty}^{+\infty} E_{11}^{(1)}(k_1)\, dk_1 = 2\int_0^\infty E_{11}^{(1)}(k_1)\, dk_1$$

The link between the two spectra is provided by the Taylor hypothesis which connects f and k_1 by stating that over a short time a turbulent structure is convected over the wire by the mean velocity $\bar{U}_1$, see Sect. 7.5.2. Hence, it can be written

$$k_1 = \frac{2\pi}{\bar{U}_1} f \qquad dk_1 = \frac{2\pi}{\bar{U}_1}\, df \qquad \text{and} \qquad E_{11}^{(1)}(k_1) = \frac{\bar{U}_1}{4\pi}\, \psi\left(f = \frac{\bar{U}_1}{2\pi}\, k_1\right)$$

Spectra are plotted on log-log scales when power laws are of interest and on lin-lin scales when a direct estimate of the energy is desired. This is illustrated by Fig. 10.13. One has just to write

$$\overline{u_1'^2} = \int_0^\infty E_{11}^{(1)}(k_1)\, dk_1 = \int_0^\infty k_1\, E_{11}^{(1)}(k_1)\, d\ln k_1$$

and to plot $k_1 E_{11}$ versus $\ln(k_1)$. For the correlation length $L_{11}^{(1)}$, one has to remember, see Sect. 6.1.4, that

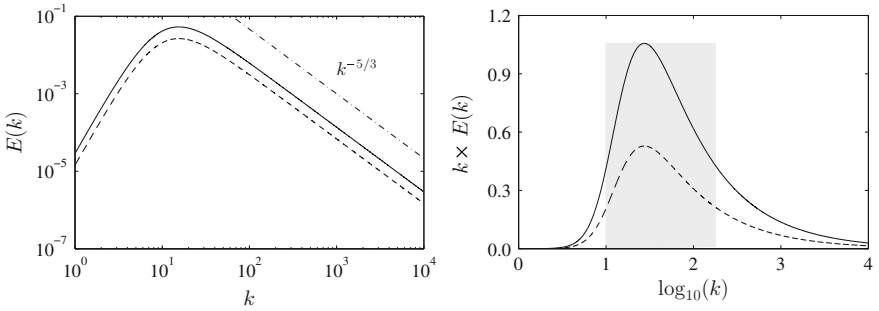

Fig. 10.13 Plots of two von Kármán $E(k)$ spectra, in *solid line* for $k_t = 3$ and in *dashed line* for $k_t = 1.5$ (arbitrary units here). On the *left*, k and $E(k)$ on log-log scales to observe the $-5/3$ law. On the *right*, $\ln(k)/\ln(10)$ and $k \times E(k)$ on linear scales. This latter plot clearly shows the factor 2 between the two energy spectra. Moreover, the first mean rule of an integrale allows the turbulent kinetic energy k_t to be estimated *by eye*. Indeed, for the largest spectrum, use of the equivalent area of the *grey rectangle* gives $1.25 \times \ln(10) \times 1.05 \simeq 3$

$$E_{11}^{(1)}(0) = \frac{1}{2\pi} \int_{-\infty}^{+\infty} R_{11}(r_1, 0, 0)\, dr_1 = 2\, \frac{\overline{u_1'^2}}{2\pi}\, L_{11}^{(1)}$$

which gives

$$L_{11}^{(1)} = \frac{\pi}{\overline{u_1'^2}}\, E_{11}^{(1)}(0) = \frac{1}{4} \bar{U}_1\, \frac{\psi(0)}{\overline{u_1'^2}}$$

10.1.8.2 Measurement of $u_1'(t)$, $u_2'(t)$ and $-\rho\overline{u_1' u_2'}$

As soon as component u_2' is considered, an X wire is needed and two anemometer channels are required. For small fluctuations, Fig. 10.2 illustrates the connection of u_2' with variations in the flow direction relative to the wire, i.e. $d\phi_{(1)} = +u_2'/\bar{U}_1$ and $d\phi_{(2)} = -u_2'/\bar{U}_1$. Commercial probes are often available with orthogonal wires, so that the half sum of the two anemometer outputs is directly related to u_1' and the half difference to u_2'. Sensitivity coefficients indicated in Table 10.3 are then used around a mean velocity given by $\bar{U}_1 \cos(\pi/4)$. The full reconstruction of the $u_1(t) - u_2(t)$ velocity field requires bilinear interpolation schemes which insure that a unique velocity vector is obtained and followed in time. The procedure using calibration curves is well described for CTAs by Browne et al. [698]. Additional references are available in reviews [699, 704].

10.1.8.3 Measurement of $\theta'(t)$, $\overline{\theta'^2}$ and $\overline{u_1'\theta'}$

If only variances and correlations are required, a single hot wire, placed normal to the mean velocity and operated at different overheat ratios can be used. The responses lead to a system of algebraic equations where the unknowns are $\overline{u_1'^2}$, $\overline{\theta'^2}$ and $\overline{u_1'\theta'}$. Alternatively, if one desires to know the instantaneous fluctuation $\theta'(t)$, an almost unheated wire acting as a resistance thermometer is needed, this approach is called the *cold wire* technique.

For the multiple overheat ratio method, a wire oriented normal to $\bar{U}_1$ responds to both u_1' and θ', as mentioned by Corrsin [708]. For small fluctuations, the anemometer response can be expressed using the sensitivity coefficients given in Table 10.3

$$\frac{e'^{\star}}{\bar{E}} = S_{u_1'} \frac{u_1'}{\bar{U}_1} + S_{\theta'} \frac{\theta'}{\bar{T}} \tag{10.32}$$

Squaring and averaging this response yields

$$\frac{\overline{e'^{\star 2}}}{\bar{E}^2} = S_{u_1'}^2 \frac{\overline{u_1'^2}}{\bar{U}_1^2} + S_{\theta'}^2 \frac{\overline{\theta'^2}}{\bar{T}^2} + S_{u_1'} S_{\theta'} \overline{u_1'\theta'} \tag{10.33}$$

Coefficients $S_{u_1'}$ and $S_{\theta'}$ are independent functions of $\bar{a}_w^{\star}$, thus choosing different $\bar{a}_w^{\star}$ values leads to a system of algebraic linear equations which is easily solved for the three unknowns $\overline{u_1'^2}$, $\overline{\theta'^2}$ and $\overline{u_1'\theta'}$. At least three values of $\bar{a}_w^{\star}$ are needed, but a larger number improves the accuracy. CVAs are best suitable for this method, as $\bar{a}_w^{\star}$ is easily adjusted using the external command of V_w without modifying the frequency response of the anemometer.

For the cold wire method, a hot wire is operated at an extremely low overheat ratio. It works as a resistance thermometer and responds to θ' only. Indeed one can observe in Table 10.3 that $S_{\theta'} \gg S_{u_1'}$ when $\bar{a}_w^{\star}$ tends towards zero. The wire can be operated by a CCA or a CVA. A CTA is not appropriate as the feedback loop looses efficiency as seen in Sect. 10.1.5. Even if it is fine, the wire has thermal inertia. From relations (10.13) and (10.28), one obtains

$$\bar{M}_w^{\mathrm{CCA}} = \bar{M}_w^{\mathrm{CVA}} = \frac{m_w c_w}{\chi R_0} \frac{1}{f(\bar{U}_1)} \qquad \text{when} \qquad \bar{a}_w^{\star} \to 0 \tag{10.34}$$

Two substantial extensions can be brought to (10.34). The acceptance of large velocity amplitudes and the possibility to introduce instantaneous velocity values in the function f. Indeed, the general heat balance of the wire, given by (10.8) for a CCA and by (10.25) for a CVA, can be explicited in both types of system as

$$\frac{1}{f\left[u_1(t)\right] - I_w^2} \frac{m_w c_w}{\chi R_0} \frac{dR_w(t)}{dt} + R_w(t) = R_w^{\star}(t)$$

For a cold wire $I_w \simeq 0.3\,\mathrm{mA}$, a constant value for a CCA and a nearly constant value for a CVA, so that $I_w^2 \simeq 1.10^{-7}\,\mathrm{A}^2$. Regarding $f(u_1) = A + B\sqrt{u_1}$, an estimate is possible for the chosen wire and the flow under consideration, using expressions of A and B indicated after Eq. (10.7), for example $f(u_1) \simeq 1 \times 10^{-4}\,\mathrm{A}^2$, so that $f[u_1(t)] \gg I_w^2$. The above differential equation thus simplifies to

$$\mathcal{M}_w(t)\frac{dR_w(t)}{dt} + R_w(t) = R_w^\star(t) \qquad \mathcal{M}_w(t) = \frac{m_w c_w}{\chi R_0}\frac{1}{f[u_1(t)]} \tag{10.35}$$

for either a CCA or a CVA. Formulation (10.34) was used by Lemay et al. [725] on the axis of a hot jet. Formulation (10.35) with the *in situ* measurement of $1/f[u_1(t)]$ was pioneered by Berson et al. [696] in an acoustic resonant tube. Once (10.34) or (10.35) is resolved for $R_w^\star$, the flow temperature T is obtained by using the relationship $T(t) = T_0 + (R_w^\star(t) - R_0)/(R_0\chi)$.

10.1.8.4 Measurement of $\overline{\theta_t'^2}$ and $\overline{(\rho u_1)'\theta_t'}$ in Supersonic Flows

In a supersonic flow, there are three inherent variables, ρ, u_1 and T, leaving aside the velocity components u_2, u_3 and the pressure p connected to T by the state law of the gas. Upstream of the wire, there is a detached bow shock whose thickness and distance to the wire depends on the flow [723, 740]. In all cases, the wire is subjected to a subsonic flow and the heat-transfer law mentioned in Sect. 10.1.3 still holds, as illustrated in Fig. 10.4. However, one has to note that the wire now responds to the mass flow rate ρu_1 and to the total temperature $T_t = T[1 + (\gamma - 1)/2\,M^2]$. Two assumptions are then usually introduced to proceed further. First, all fluctuations are assumed of small amplitude permitting the use of the sensitivity coefficients given in Table 10.3. Indeed complete calibration data would require complex wind tunnels. Secondly, a *strong* Reynolds analogy is introduced which states that the correlation coefficient between θ' and u_1' is around -1, i.e.

$$\frac{\overline{u_1'\theta'}}{\sqrt{\overline{u_1'^2}}\sqrt{\overline{\theta'^2}}} = -1$$

Gaviglio [719] reports several examples for boundary layers over adiabatic or heated walls. The underlying mechanism is that the warm low speed fluid heading away from the wall creates $u_1' < 0$ and $\theta' > 0$. It can be compared to the momentum transfer across an ordinary isothermal boundary layer, as seen in Sect. 2.4.2, where the low speed flow heading away from the wall creates $u_1' < 0$ and $u_2' > 0$, with a correlation coefficient of the order or -0.40. Gaviglio [719] also reports that in a subsonic boundary layer over a heated wall, the correlation between θ' and u_1' is of the order of -0.60. In a supersonic flow one therefore refers to a strong Reynolds analogy as the correlation between θ' and u_1' is much higher. Other experimental results are

reported by Barre et al. [693], Comte-Bellot and Sarma [706] and Weiss et al. [748] for boundary layers.

Another approach to analyse the results is suggested by Kovasznay [724] and Morkovin [732] who introduce three distinct modes of disturbance for the field: the vorticity mode, the entropy mode and the sound-wave mode. This allows one mode to be completely neglected, for example the acoustic mode is usually neglected inside boundary layers or jets.

10.1.8.5 Measurement of the Wall Shear Stress τ_w

The measurement of the wall shear stress τ_w gives access to the friction velocity $u_\tau = (\tau_w/\rho)^{1/2}$ whose importance has been seen in Chap. 3. A hot film is flush-mounted on a wall, as sketched in Fig. 10.14. The thermal law for its cooling was studied by Lévêque as reported by Knudsen and Katz [10] and by Haritonidis [720]. The main assumptions are as follows: steady laminar flow along x_1, constant film temperature T_w and constant outside temperature T_∞. The general equation governing the temperature T in the thermal boundary layer is

$$u_1 \frac{\partial T}{\partial x_1} + u_2 \frac{\partial T}{\partial x_2} + u_3 \frac{\partial T}{\partial x_3} = \alpha \frac{\partial^2 T}{\partial x_2^2}$$

and as $u_2 = u_3 = 0$, it can be simplified as

$$Cx_2 \frac{\partial T}{\partial x_1} = \alpha \frac{\partial^2 T}{\partial x_2^2}$$

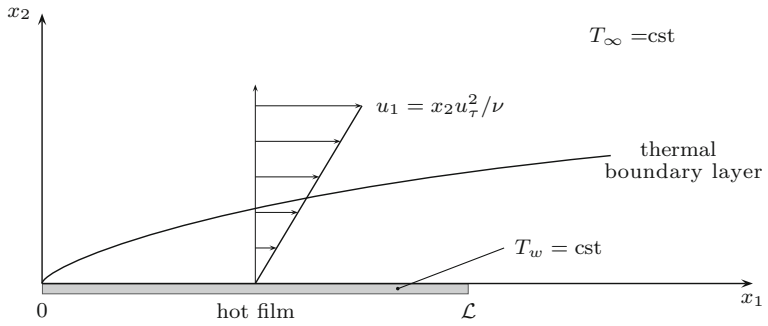

Fig. 10.14 Shear stress τ_w. Approximate dimensions are: width $\mathcal{L} \simeq 0.1$ mm along the flow direction x_1, thickness about 2000 Å along x_2, spanwise extent $l \simeq 1$ mm along x_3. The material is usually platinum or nickel. The thermal boundary along the film is supposed to be fully included in the viscous sublayer of the flow

where $\alpha = \lambda/\rho c_p$ is the thermal diffusivity of the fluid and $C = u_\tau^2/\nu$ the slope of the velocity profile in the viscous sublayer according to $u_1^+ = x_2^+$. This equation can be recast into an ordinary differential equation

$$\frac{d^2T}{d\eta^2} + 3\eta^2 \frac{dT}{d\eta} = 0$$

using the new variable $\eta = x_2(C/9\alpha x_1)^{1/3}$. The solution is written as

$$\frac{T_w - T}{T_w - T_\infty} = \frac{1}{0.893} \int_0^\eta \exp(-\eta'^3)\, d\eta' \quad \text{where} \quad \int_0^\infty \exp(-\eta'^3)\, d\eta' \simeq 0.893$$

The heat flux to the wall dq_{x_1} at location x_1 is therefore

$$\begin{aligned} dq_{x_1} &= -\lambda \left.\frac{\partial T}{\partial x_2}\right|_{x_2=0} = -\lambda \left(\frac{C}{9\alpha x_1}\right)^{1/3} \left.\frac{\partial T}{\partial \eta}\right|_{\eta=0} \\ &= \frac{\lambda}{0.893} \left(\frac{C}{9\alpha x_1}\right)^{1/3} (T_w - T_\infty) \end{aligned}$$

and the amount of heat taken away by the flow is

$$dq_{\mathcal{L}} = l \int_0^{\mathcal{L}} dq_{x_1} dx_1 = \frac{l\lambda}{0.893} \frac{3}{2} \left(\frac{C\mathcal{L}^2}{9\alpha}\right)^{1/3} (T_w - T_\infty)$$

This amount of heat is also the Joule energy provided to the film, so that

$$\frac{R_w I_w^2}{R_w - R} = b' \tau_w^{1/3} \qquad \text{with} \qquad b' = \frac{1}{0.893} \frac{3}{2} \frac{l\lambda}{R_0 \chi} \left(\frac{\mathcal{L}^2 \rho c_p}{9\mu\lambda}\right)^{1/3} \tag{10.36}$$

An additive constant a' is usually introduced in this law because of the heat loss to the substrate as pointed out by Bellhouse and Schultz [694]. Thermal insulation beneath the hot film is therefore advisable and Table 10.2 indicates some useful materials. Being non intrusive, arrays of wall hot films can be incorporated on airfoils to locate transition or track shock waves. Experiments in flight are reported by Moes, Sarma and Mangalam [731] or on high speed ground vehicles by Sarma and Moes [738]. Calibration of a film and the corresponding anemometer is usually conducted in the fully developed region of a channel or pipe flow, as the wall shear stress is connected to the easily measured longitudinal pressure gradient $\tau_w = -hd\bar{P}_w/dx_1$ for a plane channel and $\bar{\tau}_w = -(D/4)d\bar{P}_w/dx_1$ for a circular pipe. For a boundary layer, one can use the classic relations between the friction coefficient c_f and the Reynolds number, as documented by Schlichting [22].

10.2 Laser Doppler Anemometry

10.2.1 Principle

In this optical measurement technique, the velocity at a point of the turbulent field is inferred from the frequency variation appearing in the light scattered by very small particles which are illuminated by a laser and convected by the flow. Figure 10.15 represents one of these particles of velocity $\boldsymbol{u}$.

The light scattered by the particles has been subjected to two consecutive Doppler effects. The first occurs when the incident laser beam hits the particle. This is a fixed source—mobile observer scenario. The frequency perceived by the moving observer differs from the at-rest frequency, by the number of peaks per second encountered due to the observer's movement. This number is positive if the observer is approaching the source, and negative if the observer is moving away from it. The Doppler shift is thus

$$\Delta f = -\frac{\boldsymbol{u}\cdot\boldsymbol{e}_i}{\lambda} \qquad \text{that is,} \qquad \frac{\Delta f}{f} = -\frac{\boldsymbol{u}\cdot\boldsymbol{e}_i}{c}$$

where f is the laser frequency, $\boldsymbol{e}_i$ the unit vector for the incident beam, λ the laser's wavelength and c the speed of light, both in the medium of interest. So as to simplify the time interval considered in the previous illustration was of 1 second, but a shorter one Δt can be considered to enable velocity $\boldsymbol{u}$ to be constant on that time interval.

The second Doppler effect arises when the particle reflects the incident light. This is now a mobile source—fixed observer scenario. The modified wavelength λ' separating two successive peaks emitted by the source is

$$\lambda' = \lambda - \boldsymbol{u}\cdot\boldsymbol{e}_s T$$

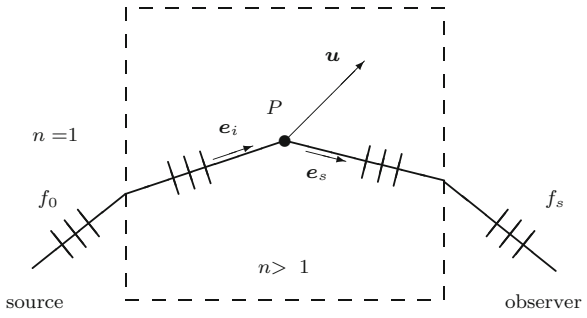

Fig. 10.15 Doppler effect for a particle P moving at velocity $\boldsymbol{u}$ in a non-dispersive medium. The light received by the particle is along direction $\boldsymbol{e}_i$ and the light scattered by the particle is along direction $\boldsymbol{e}_s$. The Doppler frequency shift arises twice, when the mobile particle is illuminated by the laser and when the mobile particle emits scattered light

where T is the source period and $\boldsymbol{e}_s$ the unit vector for the scattered beam direction. Accordingly,

$$\Delta\lambda = -\boldsymbol{u}\cdot\boldsymbol{e}_s T \qquad \text{and} \qquad \frac{\Delta f}{f} = -\frac{\Delta\lambda}{\lambda} = \frac{\boldsymbol{u}\cdot\boldsymbol{e}_s}{c}$$

To the first order, the two Doppler effects add, which gives

$$\frac{\Delta f}{f} = -\frac{\boldsymbol{u}\cdot\boldsymbol{e}_i}{c} + \frac{\boldsymbol{u}\cdot\boldsymbol{e}_s}{c}$$

In laser Doppler anemometry, this relation is usually written as

$$\Delta f = f_s - f_0 = \frac{1}{\lambda}\boldsymbol{u}\cdot(\boldsymbol{e}_s - \boldsymbol{e}_i) \tag{10.37}$$

to highlight the shift $f_s - f_0$ which can be measured, with f_0 the laser frequency and f_s the frequency of the scattered beam, these two frequencies remaining unchanged when crossing interfaces between two media. The wavelength λ in the considered medium is linked to the wavelength in air λ_0 through refractive index n, by $\lambda = \lambda_0/n$. It is important to observe that velocity $\boldsymbol{u}$ appears linearly in expression (10.37).

The direct measurement of shift $f_s - f_0$ according to expression (10.37) requires the collection of the scattered signal in a certain direction $\boldsymbol{e}_s$, which is possible only with small aperture optical sytems. The signal-to-noise ratio is thus small, even if several particles are present at the measured point. This method was used in the past but is now being abandoned in favor of a new method which will be presented in the following section. However it has still a historical interest. With such a device called *reference beam*, Yeh and Cummins [771] showed that the Doppler effect could be used to measure flow velocities.

10.2.2 The Dual-Beam LDA

In this device, the particle is illuminated by two beams from the same laser and forming a small angle 2θ between them, as represented in Fig. 10.16. The technique was proposed around 1970 by Lehmann [760] and by vom Stein and Pfeifer [770]. A historic presentation can be found in Buchhave, George and Lumley [755]. The direction of the incoming beam is $\boldsymbol{e}_{i1}$ for the first and $\boldsymbol{e}_{i2}$ for the second. Doppler shifts appearing for the light scattered by the particle due to each incoming beam are

$$f_{s1} - f_0 = \frac{1}{\lambda}\boldsymbol{u}\cdot(\boldsymbol{e}_s - \boldsymbol{e}_{i1}) \qquad \text{and} \qquad f_{s2} - f_0 = \frac{1}{\lambda}\boldsymbol{u}\cdot(\boldsymbol{e}_s - \boldsymbol{e}_{i2})$$

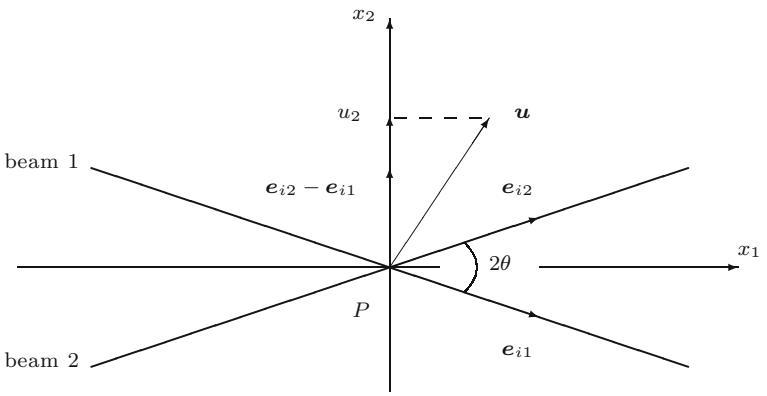

Fig. 10.16 Velocity component u_2 measured by a dual-beam laser Doppler anemometer, this component is along the external bisector of the two incident beams $\boldsymbol{e}_{i1}$ and $\boldsymbol{e}_{i2}$

Combining these two expressions, it can be written

$$\Delta f = f_{s1} - f_{s2} = \frac{1}{\lambda}\boldsymbol{u} \cdot (\boldsymbol{e}_{i2} - \boldsymbol{e}_{i1})$$

It is seen that Δf is independent of the observation direction $\boldsymbol{e}_s$ of scattered light.

This dual-beam device thus has several advantages. Scattered light can be collected by a large aperture optical system, the provided signal is thus strong. The relationship between Δf and the velocity $\boldsymbol{u}$ is always linear. The measured velocity component, given by the scalar product $\boldsymbol{u} \cdot (\boldsymbol{e}_{i2} - \boldsymbol{e}_{i1})$, is along the external bisector of directions $\boldsymbol{e}_{i1}$ and $\boldsymbol{e}_{i2}$. If the internal bisector of the two beams is chosen as the x_1 axis, then it is the velocity component along x_2 which is measured, i.e. u_2. As the angle 2θ is small, a simple calculation based on the parallelogram built from vectors $\boldsymbol{e}_{i2}$ and $-\boldsymbol{e}_{i1}$ gives

$$\Delta f = 2\frac{1}{\lambda}u_2 \sin\theta \qquad \text{and} \qquad u_2 = \frac{\lambda}{2\sin\theta}\Delta f \tag{10.38}$$

Interference fringes appear in the overlapping volume of the two beams, as represented on Fig. 10.17. They are perpendicular to direction x_2, thus crossed normally by the velocity component u_2. This observation helps the user remember the measured velocity component. The fringe spacing d_f, calculated from the optical path difference of the beams represented in Fig. 10.17, is

$$d_f = \frac{1}{2}\frac{\lambda}{\sin\theta}$$

Indeed, beam 1 propagates according to $\exp[i(\omega t - kx_1 \cos\theta + kx_2 \sin\theta)]$ and beam 2 according to $\exp[i(\omega t - kx_1 \cos\theta - kx_2 \sin\theta)]$ where $k = 2\pi/\lambda$. Their superposition

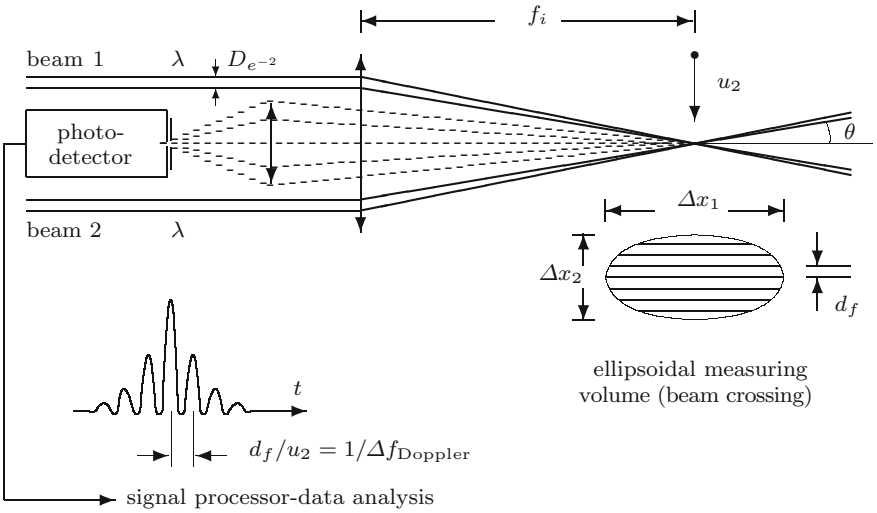

Fig. 10.17 Schematic of a dual-beam arrangement. The backscattered light represented by a *dashed line* is collected by a lens of aperture D_r and focal length f_r, which ensures the convergence towards the diaphragm of the photodetector. The measured velocity component is u_2 which is normal to the fringes

during interference leads to the appearance of the modulation factor $\cos^2(kx_2 \sin\theta)$ for the light intensity distribution. The bright fringes occur whenever $\cos(kx_2 \sin\theta)$ is a multiple of π. The fringe spacing d_f is such that $kd_f \sin\theta = 2\pi d_f \sin\theta/\lambda = \pi$ which gives $d_f = \lambda/2\sin\theta$.

The fringe spacing d_f is the same whatever the medium where the measurement is carried out. This medium can for instance be water ($n \simeq 1.33$) and the laser located in air ($n_0 \simeq 1$). Indeed, Snell's law gives $\lambda_0 = n\lambda$ and $\sin\theta_0 = n\sin\theta$. Therefore,

$$d_f = \frac{1}{2}\frac{\lambda}{\sin\theta} = \frac{1}{2}\frac{\lambda_0}{n\sin\theta} = \frac{1}{2}\frac{\lambda_0}{\sin\theta_0} \tag{10.39}$$

Finally, no calibration on the considered velocities is required. However, the direction of the device must be adjusted to reach a given component of the turbulent field. Angle $2\theta_0$ in air is obtained by measuring the distance d_0 separating the impacts of the two laser beams on a screen located at a great distance D_0 of the probe volume, then $2\theta_0 \simeq d_0/D_0$.

10.2.3 Implementation of a Dual-Beam LDA

Figure 10.17 provides the experimental set-up of a dual-beam LDA with scattered light collected in the backward direction. The optical system on the incident side

should be noted. The initially parallel beams from the same laser equipped with a beam splitter converge towards the measurement point due to the lens of focal length f_i. In its plane section, the laser beam presents a Gaussian light intensity distribution and its lateral dimension is defined as the distance to the axis at which intensity is reduced by a prefactor $1/e^2$, hence the notation $D_{e^{-2}}$. Near the focus point, the width of the beam becomes $d_{e^{-2}}$

$$d_{e^{-2}} = \frac{4 f_i \lambda}{\pi D_{e^{-2}}}$$

For this calculation which requires the transformation of a Gaussian beam after passing through a focus point, Drain [757] or Trolinger [765] can be read. The quantity $d_{e^{-2}}$ is important, for it appears in the dimension of the probe volume.

The probe volume is an ellipsoid of revolution about its major axis x_1, and its section by plane x_1, x_2 is represented in Fig. 10.17. Its dimensions, inferred from simple geometric considerations, are the following, where f_i is the incident side focal length,

$$\begin{aligned}
&\text{Length:} && \Delta x_1 = \frac{d_{e^{-2}}}{\sin\theta} = \frac{4 f_i \lambda}{\pi D_{e^{-2}}} \frac{1}{\sin\theta} \\
&\text{Diameter:} && \Delta x_2 = \frac{d_{e^{-2}}}{\cos\theta} = \frac{4 f_i \lambda}{\pi D_{e^{-2}}} \frac{1}{\cos\theta} \\
&\text{Fringe spacing:} && d_f = \frac{1}{2} \frac{\lambda}{\sin\theta} \\
&\text{Number of fringes:} && N = \frac{\Delta x_2}{d_f} = \frac{8 f_i}{\pi D_{e^{-2}}} \frac{\sin\theta}{\cos\theta}
\end{aligned}$$

For example, let us consider $\lambda_0 = 514.5\,\text{nm}$, the green spectral line of an ionized Argon laser, $f_0 \simeq 6 \times 10^{14} \pm 3 \times 10^9\,\text{Hz}$, coherence length $3 \times 10^8/(2 \times 3 \times 10^9) \simeq 5\,\text{cm}$, $D_{e^{-2}} = 1.1\,\text{mm}$, $f_i = 250\,\text{mm}$, $2\theta = 8°$, which leads to $\Delta x_1 = 2.13\,\text{mm}$, $\Delta x_2 = 150\,\mu\text{m}$, $d_f = 3.68\,\mu\text{m}$ and $N = 40$. If the velocity of the flow is $u_2 = 10\,\text{m.s}^{-1}$, the Doppler shift is $\Delta f = 2.725\,\text{MHz}$ and the transit time through the volume is at most of $15\,\mu\text{s}$.

The short coherence length of a laser, approximately of 5 cm as indicated above, requires that the optical paths of the two beams be very close to one another, thus explaining the symmetric devices often built. When the laser system is located far away, a large focal length f_i is required, and a suitable number of fringes in the probe volume can be conserved increasing $D_{e^{-2}}$ with a beam expander. A fiber optical system can also be used to reach the measurement point, and then conserve the use of small focal lengths.

The Doppler shift Δf is not dependent on the sign of velocity u_2. Fortunately, this can be corrected by introducing a Bragg cell on one of the laser beams, which allows its frequency to be increased, and whose principle is reminded in Fig. 10.18. With the Bragg cell, there is a constant frequency shift between the two incident beams. The probe volume fringes, instead of being fixed, are now moving with a

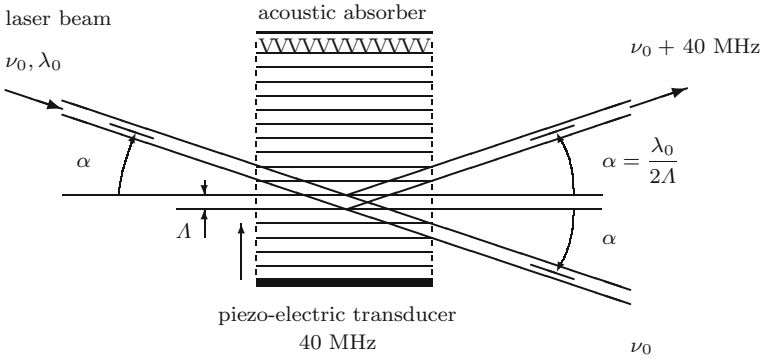

Fig. 10.18 Sketch of an acousto-optical modulator, also called a Bragg cell. The acoustic wave creates a moving diffraction grating. Intensity is maximal along a direction α such that the travel path difference created by two acoustic planes is a multiple of the laser wave length, i.e. $2\Lambda \sin\alpha = n\lambda_0$, and $\alpha = \lambda_0/2\Lambda$ for $n = 1$ and α small

constant velocity. Zones where flow recirculations exist can thus be studied. Bragg cells providing 40 and 80 MHz shifts can be bought. Experimentally, the smallest possible shift must be used due to the signal-to-noise ratio, as is seen later on.

The particles used to tag the flow have diameter of approximately 1 μm. They have to be small enough to follow the flow, but large enough to maintain sufficient scattered signal intensity [757, 759, 766]. In air the particles used include incense smoke, polystyrene latex, di-ethyl-hexyl-sebacate (DEHS), paraffin or olive oil sprays in trichlorethylene, and silicon dioxide or titanium oxide. In water, particles naturally present are often sufficient. If not, polystyrene or titanium oxide can be used. In all cases, the concentration has to be adjusted so that there is at most a single particle in the probe volume.

The tagging is often done upstream of the studied zone. In the case of free boundary turbulent flows, such as jets for example, it is preferable to inject particles both in the flow itself and the surrounding ambient air, so as to have measurements in both the turbulent and external zones. Hussein, Capp and George [539] thus fill a large volume surrounding the jet before beginning the experiments, and then turn the wind tunnel on. Besides, measurements close to the walls are always difficult. Few particles are present due to the small velocities, and they tend to get stuck on the portholes.

The response time of the particles must also be estimated and controlled by experiments. Tests are done in oscillating acoustic flows up to 100 kHz or in a normal shock wave [752, 759, 761, 762]. For the particle motion, among the forces applying to the particle, only Stokes viscous drag is retained in most papers, e.g. by Mazumder and Kirsch [762] or Boutier [753]. Equation governing the particle velocity $\boldsymbol{u}_P$ is thus given by

$$\rho_P \frac{\pi d_P^3}{6} \frac{d\boldsymbol{u}_P}{dt} = 3\pi\mu_f d_P(\boldsymbol{u} - \boldsymbol{u}_P)$$

where $\boldsymbol{u}$ denotes the fluid velocity. The time constant of the particle is then simply

$$\tau_P = \rho_P \frac{d_P^2}{18\mu} = \frac{\rho_P}{\rho} \frac{d_P^2}{18\nu}$$

where μ is the dynamical viscosity of the fluid and ν its kinematic viscosity. Thus, in the case of air, $\tau_P \simeq 4\,\mu$s for $d_P = 1\,\mu$m, $\rho_P/\rho \simeq 10^3$ and $\nu = 1.5 \times 10^{-5}\,\mathrm{m}^2.\mathrm{s}^{-1}$.

The scatterring pattern of the particle must also be estimated, according to Mie theory. This will help selecting an LDV operating in near-forward or near-backward scattering mode, most of the time the decision being imposed by the physical accessibility of the flow. An example of a Mie diagram is given in Fig. 10.21.

The signal provided by the photodetector is constituted of short pulses as represented in Fig. 10.17. These pulses appear randomly and are often noisy due to parasitic reflections. They also contain a low frequency associated with the Gaussian distribution of light intensity in the beams, and can have only a few cycles of the useful Doppler frequency. However, recent progress in very fast digital techniques permits, for a pulse, to know the transit time and to calculate the FFT with several sampling frequencies: this is necessary because the frequency to be treated is not yet known. The best fit is then kept to provide the most exact possible velocity value. In addition, a validation process can be applied to keep the values provided by particles that have gone through the central part of the probe volume. The value of the average velocity is then obtained by weighting each measured velocity value by its transit time, which leads to

$$\bar{U} = \frac{\Sigma u^{(j)} \tau_t^{(j)}}{\Sigma \tau_t^{(j)}}$$

where $u^{(j)}$ is the j particle velocity, and $\tau_t^{(j)}$ the transit time of this particle j. This perfectly corresponds to the definition of time average in Chap. 2. The same process is followed for the average quadratic value of velocity variations.

The obtention of a quasi continuous velocity signal from the randomly occurring burst data requires an interpolation. The Sample and Hold technique (SNH) illustrated in Fig. 10.19 is simple and efficient. The reconstructed velocity signal is formed by sampling at the arrivals of valid signal bursts and holding these values until another valid burst arrives. The reconstructed signal can then be read at equidistant times and classic FFT used to compute spectra. The steps in the sampled and hold signals lead to a white noise spectrum which vanishes in the limit of high data density, i.e. of high flow seeding. Adrian and Yao [751] analysed and illustrated that process by using wide band white noise signals. They show that PSD estimates are valid only up to a frequency of $f = \dot{n}/(2\pi)$ where $\dot{n}$ is the mean particle rate, which is a rather stringent condition. Improvements are suggested by Nobach et al. [763] and by Simon and Fitzpatrick [764], and comparisons with hot wire anemometry data are conducted by Velte et al. [769] for axial jets and 2-D cylindrical wakes.

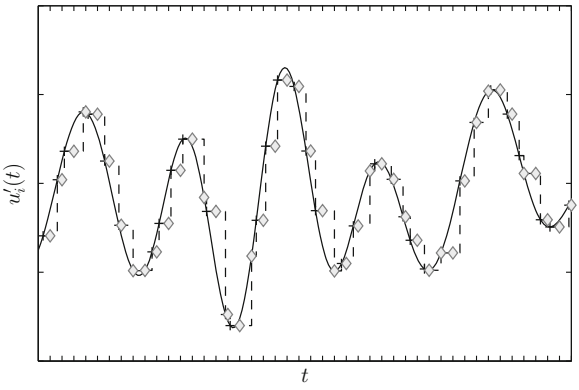

Fig. 10.19 Illustration of the sample and hold technique (SNH): —— assumed velocity $u_i(t)$ to be measured, + measured velocity by particles, – – – zeroth-order reconstructed velocity trace by the SNH technique and ◊ regular resampled signal to run classic FFT programs

The intensity of the signal provided by the photodetector is a function of numerous parameters: the laser power, the characteristics of the optical system during both emission and detection, the particles themselves through their diffusing properties, their elasticity, their index compared to that of the medium considered. These last points affect in particular the angle chosen to collect scattered light.

The quantification of all these effects is difficult, but the essential elements are included in the synthesis by Fingerson and Menon [758]. The Signal-to-Noise Ratio (SNR) can be written as

$$\mathrm{SNR} \simeq \eta_{\mathrm{PM}} P_0 \frac{1}{\Delta f} \left[\frac{D_{e-2}}{f_i} \frac{D_r}{f_r} \right]^2 d_P^2 \, \overline{GV}^2$$

where η_{PM} is the quantum efficiency of the photodetector, P_0 the laser power and $\overline{GV}$ a factor taking into account the visibility of the particle. The other quantities have already been introduced, see Fig. 10.17.

Two aspects must be commented on. First, the factor $\overline{GV}$ corresponds to the properties of the scattered light, according to Mie theory. Of note is a large level difference between forward scattering and backward scattering. The backward scattering device is often preferred, although it suffers from a 20 dB handicap, for the optical system is more compact and easier to handle. Secondly, the Doppler factor Δf increases linearly with velocity. Thus, if $\Delta f \simeq 3$ MHz for 10 m.s^{-1}, then $\Delta f \simeq 150$ MHz for 500 m.s^{-1}, only corresponding to Mach 1.5. The larger the velocity is, the more difficult it is to measure. Moreover, if a Bragg cell is used, an additional 40 or 80 MHz appears, again diminishing the SNR. In that case, the particle has such a short transit time inside the probe volume that it does not have the time to emit a high intensity signal.

Fingerson and Menon [758] report for instance in air, with polystyrene particles and a Doppler shift of $\Delta f = 10$ MHz the following values of SNR

34 dB for 0.5 μm particles and forward scattering,
18 dB for 0.5 μm particles and backward scattering,
50 dB for 2 μm particles and forward scattering,
37 dB for 2 μm particles and backward scattering.

Two perpendicular velocity components can be obtained rather easily, for example u_1 and u_2, by setting two laser Doppler anemometers so that the probe volumes overlap normally. When a single particle goes through both volumes, a simultaneaous measurement of the two components u_1 and u_2 is possible, which then permits to obtain the Reynolds tension $-\overline{\rho u_1' u_2'}$ associated with velocity variations. Such a measurement can be performed with only one Argon laser. Apart from the green spectrum line $\lambda_0 = 514.5\,\text{nm}$, this laser provides a blue spectrum line, $\lambda_0' = 488\,\text{nm}$ of same power, i.e. 0.5 W on each line for a 1 W laser.

The extension to the measurement of three components is more difficult, for the adjustments are more complex. In theory, a third laser spectrum line can be used, but its power is much smaller than those of the main lines. Another solution consists in using a single powerful line and placing three Bragg cells with different frequencies on each of the beams.

The use of optical fibers leads to compact devices, where the probe is located near to the flow, while heavy parts such as the laser and the photodetector can be kept at a large distance, with distances greater than 10 m being easily achieved. Focal lengths used thus stay small and ensure a good precision. However the laser/fiber junctions have to be made very carefully, through fiber holes of very small diameter, approximately of 5 μm, to conserve the power of the laser.

Other devices allow even greater miniaturization so as to obtain measurements in different points. Both the velocity and diameter of the particles can be determined at the same time for instance. For all these developments, the reader can refer to the review by Boutier [754].

Recent work aims at using single-mode laser diodes with a fluted substrate. The coherence length, around 50 m, is two orders of magnitude greater than that of a gas laser. The wavelength is of approximately 800 nm. Also the PN junctions of the semiconductors being very sensitive to temperature, a temperature stabilization is necessary. When detecting, the classical photodetector can be replaced with avalanche photodiodes (APDs) which ensure a very fair signal-to-noise ratio. The main advantage is to have a very compact device, and extensible to the three velocity components. Various articles by Dopeide et al. [756] can be very useful here.

10.2.4 Additional Comments

Due to the linearity of its response, laser Doppler anemometry is well adapted to high turbulence levels, up to 100 % for the boundaries of a jet and the backward flows encountered in detachment zones or in recirculation zones such as near wakes and

backward facing steps. As no probe is placed in the flow, hostile environments can be studied, such as reactive flows or flames.

Of course some limitations exist. The considered medium must be transparent. The probe volume is not as small as that of a hot-wire anemometer. Signals provided are not continuous, which limits the determination of turbulence spectra to a few decades. The fact that seeding particle velocity rather than fluid velocity is measured can be of importance, particularly in very high velocity flows. The adjustement of some elements, such as filters or sampling frequency, requires a sound knowledge of optical techniques.

10.3 Particle Image Velocimetry

Particle Image Velocimetry (PIV) is based on the displacement of small tracers introduced into the flow, and followed by a rapid digital camera. It classically allows to determine a velocity field over a plane. When only two velocity components included in a plane are considered, PIV is noted 2D-2C PIV. When the velocity component perpendicular to the observation plane is also needed, it is noted 2D-3C PIV, also called Stereoscopic PIV. Volumetric measurement techniques are being developed and this recent technique is noted 3D-3C PIV.

10.3.1 Principle of 2D-2C PIV

Figure 10.20 provides the sep-up of a 2D-2C PIV device. Particles introduced in the field are illuminated in the zone of interest by a thin luminous plane sheet. The thickness of the sheet is of approximately 1 mm and it is obtained from a laser beam and a cylindrical lens. If an average flow velocity prevails, it is better to place the luminous sheet parallel to this velocity. Typically, dual cavity pulsed lasers are used. The first light pulse, from the first cavity, is emitted at time t and the second, from the second cavity, at time $t' = t + \Delta t$. An optical system with an axis perpendicular to the laser sheet forms the images of the particles on a plane, and the two successive images are recorded by a double exposure camera, the first image in the first frame, and the second image in the second frame of the camera. From the movement of the images between the two snapshots, the velocity components u_1 and u_2 in the observation plane are obtained, according to the following expressions

$$u_1 = \frac{\Delta x_1}{\Delta t} = -\frac{\Delta X_1}{M_0 \Delta t} \quad \text{and} \quad u_2 = \frac{\Delta x_2}{\Delta t} = -\frac{\Delta X_2}{M_0 \Delta t} \tag{10.40}$$

X_1 and X_2 are the axes of the image plane, parallel to axes x_1 and x_2 of the object plane, ΔX_1, ΔX_2 and Δx_1, Δx_2 the components of the respective movements of images and particles during time interval Δt, and M_0 the transverse magnification

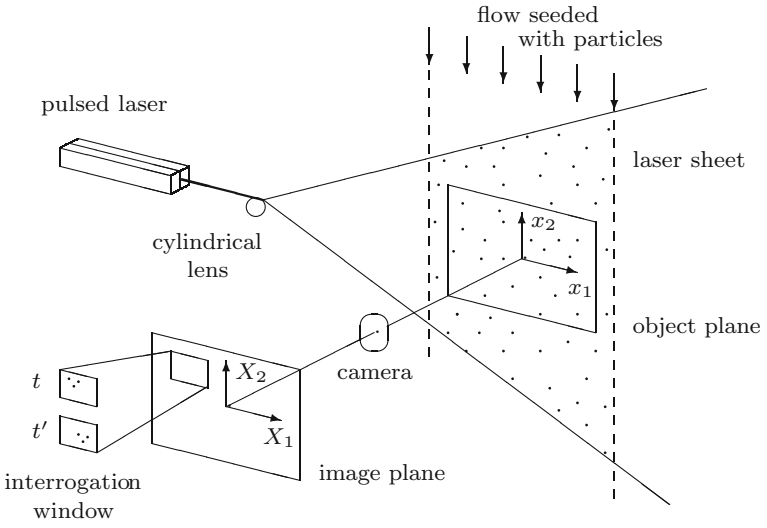

Fig. 10.20 Typical layout and main elements in a 2D-2C PIV system, measurement of two velocity components in a plane, by particle image velocimetry

of the optical system, i.e. the image/object ratio. M_0 is in fact negative, because the image is reversed. Time t is chosen to enable conditional averages, the laser being triggered conditionally to the studied phenomena. Time t' must be adapted to encountered velocities so that particles remain in the view field during the time interval $\Delta t = t' - t$. Generally, Δt is of a few μs, but can range from less than 1 μs to a number of ms.

The movement of particle pairs is obtained by cross-correlation between the two images I and I' corresponding to times t and t'. This correlation is realized by Fast Fourier Transform (FFT). The treatment is not applied to the entire image, it only concerns a fraction of it, termed an interrogation window. Indeed, the essential hypothesis of PIV is that the velocity of the flow is uniform over the interrogation window's small surface. The velocity assigned to the center of the window corresponds to the tallest peak of the cross-correlation function [786] The velocities obtained from each window are then assembled to obtain the total field. A validation step is then necessary to ensure that the obtained velocities are continuous.

The idea to use the images of particles in movement in a flow goes back to some 30 years ago. The studies by Adrian [774] and by Westerweel et al. [794] give, for the first a very interesting historical overview of this technique, and for the second the current state of art.

10.3.2 Implementation of 2D-2C PIV

As in laser Doppler anemometry, the particles used in PIV have to follow properly the flow to be studied. In air, their diameter is often of approximately 1 μm. Melling [783] provides a very useful synthesis on particles that can be used, and the means by which they can be injected into the flow. Optimal concentration is such that between 7 and 10 pairs of images are found in each interrogation window. The reason why these numbers appear is detailed later on. It must also be pointed out that concentration has to be roughly homogeneous over the entire studied field.

In 2D-2C PIV, observations are carried out normal to the luminous plane, i.e. perpendicular to the incoming beam. Thus the intensity of scattered light is small, see Fig. 10.21. Accordingly, when compared to forward and backward scattering used in laser Doppler anemometry, the respective 10^6 and 10^2 factors are lost. The laser to be used for PIV must therefore be powerful, or the camera very sensitive.

A continuous laser is rarely appropriate, however it is usually sufficient for experiences in water or air at small velocities, after having been fitted with an electronic shutter or a rotating mirror. A pulsed laser is always better.

Up to 10 Hz, one can use a Nd:YAG laser. Active ions are Neodym Nd^{+3}, and the host material is a monocrystal of Yttrium-Aluminium-Garnet. The duration of a pulse is of approximately 5–10 ns and emitted energy can reach 400 mJ. The wavelength naturally emitted is 1064 nm, and a frequency doubler leads to $\lambda = 532$ nm, which is well suitable to the sensitivity of cameras. A Nd:YAG laser has two parallel cavities to obtain the time interval Δt adapted to desired measurements, but a single frequency doubler is generally sufficient.

For high time resolution [792], up to 10 kHz, one uses diode-pumped Nd:YLF lasers, constituted of neodym crystals doped with ytrium and lithium fluoride. The emitted energy is around 20 mJ/pulse, with a maximum around 1 kHz. Two independent oscillators allow the pulse separation and the pulse energy to be controlled. The natural wavelength is 1053 nm, transformed into 527 nm by a frequency doubler.

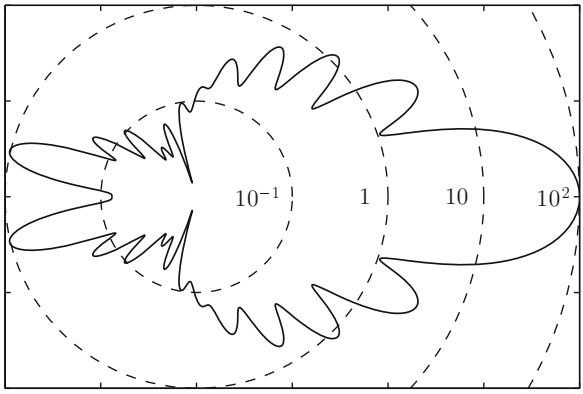

Fig. 10.21 Scattering phase function for a $d_P = 2\,\mu$m oil particle in air with a wavelength of $\lambda = 532$ nm, corresponding to a Mie parameter of $2\pi/(\lambda/n_{\text{air}}) \times (d_P/2) \simeq 11.8$

The dimension d_τ of the image of a particle is an important quantity that must be known both absolutely and relatively to the dimension p_x of a pixel of the recording cameras. This dimension d_τ, of course, depends on diameter d_P of the particle injected in the flow, but also in an essential way on the diffraction of the collecting optical system. The classical result on the Airy disc, the reader can refer to Raffel et al. [786] or Stanislas and Monnier [791] for details, provides

$$d_\tau = \left[(|M_0|d_P)^2 + d_{\text{diff}}^2\right]^{1/2} \quad \text{with} \quad d_{\text{diff}} = 2,44 f_\sharp (|M_0| + 1)\lambda \tag{10.41}$$

where M_0 is the linear nominal magnification of the optical system, $f_\sharp$ the ratio between the focal length f of the objective and its aperture diameter D_a, also called relative aperture, λ the wavelength of the laser. For instance, for $d_P = 1\,\mu\text{m}$, $|M_0| = 1/4$ and $\lambda = 532\,\text{nm}$, one has $d_\tau = 4.7$, 6.6, 9.1, 13.0, 17.8 and 26.0 μm, respectively for $f_\sharp = 2.8$, 4.0, 5.6, 8.0, 11 and 16.

Thus, the dimension of the image of a 1 μm particle is of approximately 15 μm. It must also be noted that for small particles, of some microns, it is always the d_{diff} term which prevails in expression (10.41).

The depth of field δx_3 of the chosen optical system can also be estimated assuming that the motion blur on the image of a particle located slightly out of the targeted plane is approximately equal to the diameter of the image of the particle, see Stanislas and Monnier [791]. This leads to

$$\delta x_3 = 4.8 \left(\frac{1 + |M_0|}{|M_0|}\right)^2 f_\sharp^2 \lambda$$

i.e. $\delta x_3 = 2\,\text{mm}$ for $|M_0| = 1/4$, $\lambda = 532\,\text{nm}$ and $f_\sharp = 5.6$. This δx_3 quantity corresponds to the thickness to assign to the laser sheet so that the images are not blurred.

Charge-Coupled Device (CCD) cameras allow high quality images to be recorded up to around 15 Hz. The basic element is the pixel, an abbreviation of picture element, whose typical size is $10\,\mu\text{m} \times 10\,\mu\text{m}$, or even $7\,\mu\text{m} \times 7\,\mu\text{m}$ in very recent experiments. This sensor can convert photons into electric charges. Arrays with a minimum of 1000×1000 pixels constitute the recording area of the camera.

To ensure that each pixel is saved after the first image, there are temporary storage locations next to each pixel column. These slightly cover the active part of the pixels, so that microlenses are located above of each pixel to better collect incident light. The transfer of an image to storage is done in less than 1 μs. Then, the second image can be taken and stored. When all the columns have been stored, the successive temporal data enters an analog-digital converter (ADC). This element being unique, it imposes the low frequency operation of CCD cameras.

High speed digital imaging, up to around 10,000 frames per second, is possible with cameras using the Complementary Metal Oxide Semiconductor (CMOS) technology. As a MOS is transistor-like, the received photons change the voltage of the grid between the source and the drain. The term complementary concerns an

additional logic circuit which can be incorporated. The pixel dimension is around $20\,\mu\text{m} \times 20\,\mu\text{m}$. The rapidity of the recording comes from the fact that each pixel has its own ADC.

Figure 10.22 illustrates an interrogation window with approximately ten particles, at time t, image I and at time t', image I'. These images are obviously distinct on the camera but their superposition clearly shows movements $1 \rightarrow 1', 2 \rightarrow 2', \ldots$ which must be identical to create a peak in the cross-correlation of images I and I'. The position of this peak provides quantities $\Delta X_1, \Delta X_2$ to be introduced into relations (10.40) to obtain u_1, u_2. Away from the peak, there is noise. It essentially comes from type $1 - 2'$ or $2 - 1'$ separations which are random, type $3 - 3'$ or $4 - 4'$ separations where the particle is not in the interrogation window at one or the other of the two instants t or t', movements, such as $5 - 5'$, which do not obey the hypothesis of a uniform velocity field in the window. These limitations are analysed by numerous authors, particularly Westerweel [793] or Raffel et al. [786], mainly in terms of height of the cross-correlation peak.

The concentration of useful image pairs, entirely contained in the interrogation window, is an essential factor to obtain a proper peak. The right-hand plot in Fig. 10.22 shows that 7–10 pairs must be used to approach a 100 % success rate. Factor $N_e = N_0 \times F_1 \times F_2$ is the actual concentration of the particles, with N_0 the concentration injected, and F_1 and F_2 the percentages of pairs of particles remaining in the window despite lateral entries and exits, and entries and exits perpendicular to the laser sheet. Keane and Adrian [774], and Adrian [774], have analysed different PIV techniques, by numerical simulation, and the average curve is extracted in Fig. 10.22.

At this point, the choice of Δt as a function of flow velocity is essential, a large Δt being suited to small velocities, and inversely a small Δt being suited to large velocities. In the case of an oscillating flow, the adjustment is to be done at each instant, which is the case for acoustic fields. The input necessary for the triggering

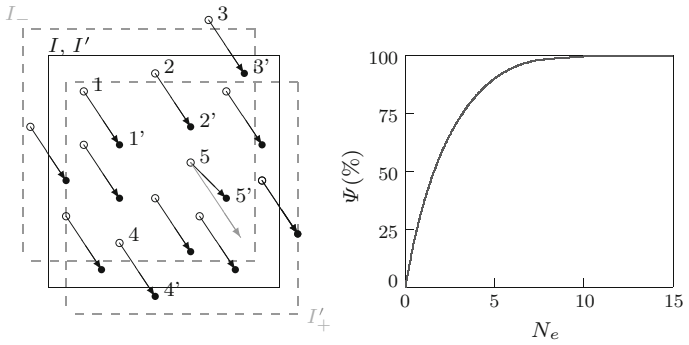

Fig. 10.22 On the *left*, pairs of particle images at time t and t' which lead to a correlation peak, *white circles* at time t, *black circles* at time t'. Each particle is numbered 1, 2, …The shifted windows I_- and I'_+ are in *dashed lines*, they allow more particle pairs to be caught. On the *right*, the probability to detect the correlation peak according to the number of particle pairs, adapted from Adrian [773]

of the images is then directly furnished by the acoustic source or by an auxiliary microphone.

Cross-correlation on images I and I' is obtained using Fourier transforms, which is quicker than using 2-D cross-correlation in the physical space. The Fourier transform of images I and I' is first formed, and then the product of the first transform by the conjugate of the second. An inverse Fourier transform is then applied to this product, which leads to the desired cross-correlation.

Interrogation windows have power-of-two dimensions, i.e. typically 16^2, 32^2, 64^2 or 128^2pixels due to Fourier transforms to be applied. Given the dimension of a pixel, $p_x = 10\,\mu\text{m}$, and magnification M_0, for instance $|M_0| = 1/4$, these dimensions correspond respectively to 0.64, 1.28, 2.56 mm^2 in the observed physical field.

For the FFT, an iterative algorithm is used which includes two essential substeps, the first to enhance displacement estimation, the second to reduce the window dimension. Starting for example from a 64^2 window, the best possible displacement value is determined, i.e. $\Delta \boldsymbol{X}_a^{64}$. Then from this approximated value, the I window is shifted upstream by $-0.5\Delta \boldsymbol{X}_a^{64}$ and the I' window downstream by $+0.5\Delta \boldsymbol{X}_a^{64}$, as represented by a dashed gray line in Fig. 10.22. The cross-correlation between I_- and I'_+ windows is then formed. This method allows more image pairs contributing to cross-correlation to be caught, for instance pair 4–4′. The same calculation can be carried out several times to enhance the final displacement, noted $\Delta \boldsymbol{X}_e^{64}$. This is most important at large flow velocities due to large movements appearing. The second substep consists in dividing the 64^2 pixel window in four 32^2 pixel windows. For each of these windows the approximated movement is assumed to be the one just obtained, thus $\Delta \boldsymbol{X}_a^{32} = \Delta \boldsymbol{X}_e^{64}$, and the cross-correlation peak between windows shifted by $-0.5\Delta \boldsymbol{X}_a^{32}$ and $+0.5\Delta \boldsymbol{X}_a^{32}$ is searched for, as indicated previously. This can be applied again; the method often stops at 16^2 pixel windows.

To enhance the separation power of the measurement, a partial overlap of the interrogation windows is also used. A 50 % overlap leads to decreasing the distance between the centers of the windows by two, and thus to quadruple the number of points finally obtained on the considered field. This overlap is usually applied at the final stage, on the smallest windows.

The previous methods lead to a ± 0.5 pixel precision on the detection of a cross-correlation peak. This precision can be increased by fitting a Gaussian curve to the peaks occurring on adjacent pixels, as described by Westerweel [793]. An illustration is given in Fig. 10.23 showing different particle sizes relative to the pixel dimension. Using the maximum of the Gaussian curve to locate the particle image, the precision can be improved down to around ± 0.05 pixel. Other approaches are proposed, for example by Lynch and Scarano [782] who track the patterned fluid element within a chosen interrogation window, along its individual trajectory throughout an image sequence.

For a simple lens, geometrical optics laws provide the magnification $|M_0| = D_3/d_3$ with D_3 the distance from the image plane to the lens, and d_3 the distance from the object plane to the lens. However, a camera is composed of several lenses and the casing occupies a volume difficult to estimate. The laser sheet is actually

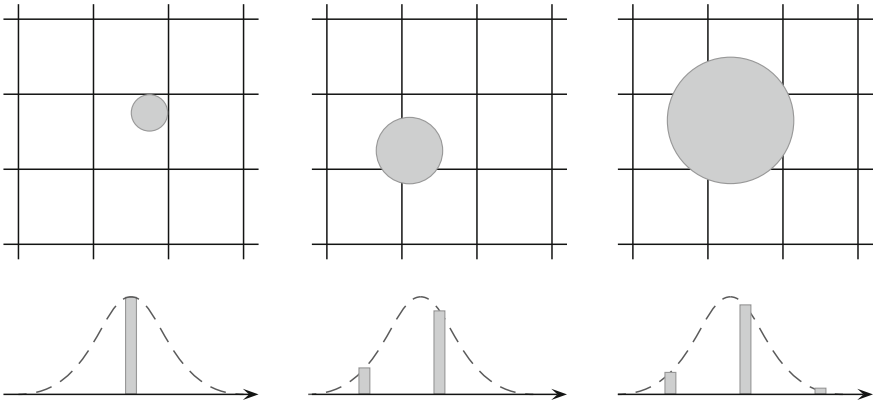

Fig. 10.23 Gaussian curve fitting to pixel data, the exact location for the particle is taken at the curve maximum, hence an accuracy of ± 0.05 px

replaced by a calibration plate which covers the zone to be studied. This device is a thin glass plate on which white dots or crosses are engraved forming a square grid. All the characteristics of the plate image are picked up, which permits to obtain the position of the particles in the object plane and the local value of the magnification to be used in place of M_0.

When all displacements have been calculated on the interrogation windows and the velocities are obtained, the validity of the resulting vectors must be verified. First, all displacements not sufficiently distinguishable from noise are eliminated, as well as too disparate values of velocity. Then, all velocities are compared to their neighbours. A widely used algorithm, described by Raffel et al. [786], is based on the average and standard deviation of velocities on the 8 positions surrounding a given point, i.e.

$$m_u(i,j) = \frac{1}{N}\sum_{n=1}^{N} u(n) \quad \text{and} \quad \sigma_u^2(i,j) = \frac{1}{N}\sum_{n=1}^{N}\left[u(n) - m_u(i,j)\right]^2$$

with $N = 8$. The condition to verify is

$$| u(i,j) - m_u(i,j) | < \epsilon_{\text{threshold}} \qquad \text{with} \qquad \epsilon_{\text{threshold}} = C_2\sigma_u(i,j)$$

where C_2 is an adjustable coefficient, C_2 often between 2 and 3, depending on the type of flow, e.g. laminar or turbulent, and on the turbulence level. At points where the velocity vector is eliminated, it is replaced with an average value of neighbouring points.

10.3.3 Examples of 2D-2C PIV

2D-2C PIV is often used to highlight the movement of large structures or of vortex zones. Adrian et al. [586] have thus studied the development of bursts and hairpins on a flat-plane boundary layer, see Fig. 3.13. Raffel et al. [786] present numerous examples concerning aerodynamics, such as wingtip vortices or the transonic zone above a profile.

In active flow control, PIV allows results to be assessed during an experimental campaign. Figure 10.24 illustrates the re-attachment of a separation zone downstream from a circular cylinder due to a pulsed jet, studied by Béra et al. [569]. Here the average fields are considered, the average is produced from 30 acquisitions at random times. The study of the pulsed jet serving as control is also interesting in itself. It was carried out conditionally at different phases of the pulsation cycle [775]. Figure 10.25 provides two views of the pulsed jet corresponding to blowing and to sucking phases. The most important result is the bifurcation phenomenon of the velocity field slightly above the jet orifice during sucking. The vortex produced during the blowing phase still follows its ascending path even when aspiration has already begun near the orifice.

Spatial velocity fields obtained by PIV can be analysed to obtain important characteristics of the flow, such as the vorticity component perpendicular to the laser sheet or the normal modes in the laser sheet plane. For vorticity, the definition $\omega_3 = \partial u_2/\partial x_1 - \partial u_1/\partial x_2$ can be used, or the angular momentum of the velocities

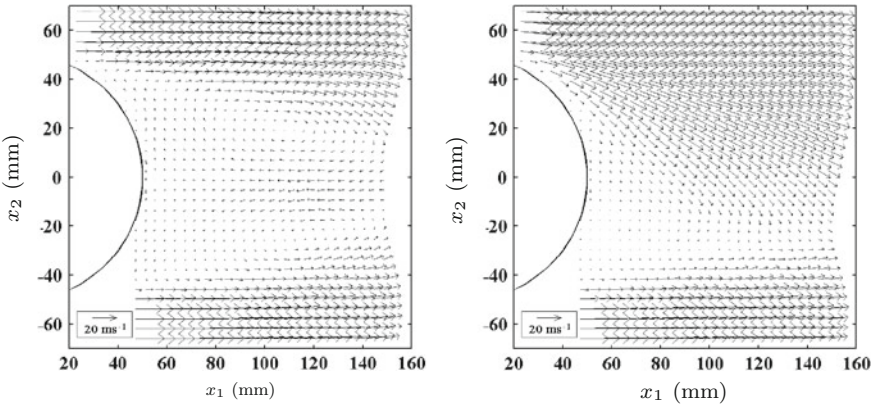

Fig. 10.24 Flow reattachment on the downstream side of a *circular* cylinder by active control. Cylinder diameter 10 cm, incident flow velocity 20 m.s^{-1}. On the *left*, without control, on the *right* control by a 200 Hz pulsed jet issued from a 2-D 1.5 mm slot located at 110° from the stagnation line. Use of 2D-2C PIV system, CCD camera 1008×1018 pixels, $|M_0|$=1/6, $f_\sharp = 2.8$, $\Delta t = 50\,\mu$s, interrogation window 32^2. Courtesy of Jean-Christophe Béra, see also Béra et al. [569]

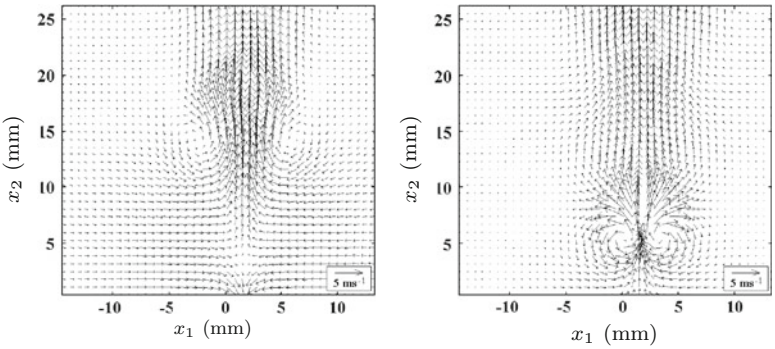

Fig. 10.25 Velocity maps for the 2D pulsed jet used in Fig. 10.24. On the *left*, during the sucking phase and on the *right*, during the blowing phase. Courtesy of Jean-Christophe Béra, see also Béra et al. [775]

around a point P, as proposed by Graftieaux et al. [481]

$$\omega_3(P) = \frac{1}{N^2 - 1} \sum_{i=1}^{N} \frac{\boldsymbol{r}_{PQ_i} \times \boldsymbol{u}(Q_i)}{|\boldsymbol{r}_{PQ_i}| \; |\boldsymbol{u}(Q_i)|} \tag{10.42}$$

where the Q_i are points distributed on a square of side N, centered on P, $\boldsymbol{u}(Q_i)$ the velocity vector at Q_i, $\boldsymbol{r}_{PQ_i}$ the separation vector between P and Q_i, generally $N = 5$.

10.3.4 2D-3C or Stereoscopic PIV

The examples in Figs. 10.24 and 10.25 correspond to bidimensional flows, those to which 2D-2C PIV must be restrained. In the case of a tridimensional flow, 2D-2C PIV leads to favoring times when the velocity component perpendicular to the laser sheet is almost equal to zero, which implicitly leads to conditional averages. Furthermore, the velocity component u_3 leads to a particle movement through the thickness of the laser sheet, as represented in Fig. 10.26. The position of the particle inferred from the image is thus incorrect, and all the more so since observation angle θ is large. Prasad and Jensen [785] estimate that error can reach 10 % when $\Delta x_1 \simeq \Delta x_3$ and $\theta = 5°$.

A PIV technique adapted to the simultaneous determination of three velocity components is thus necessary. This is 2D-3C PIV, also called Stereoscopic PIV, which still retains the principle of a laser sheet to light the zone of interest in the flow. The Stereoscopic PIV is based on the addition of a second optical system to be able to observe the flow from two different angles [785]. In the first set-up developed in the literature, called *shifting device*, two cameras are located on a plane parallel to the laser sheet. This device has a constant magnification, but the optical system uses large angles θ which degrades image sharpness and creates distortions. The

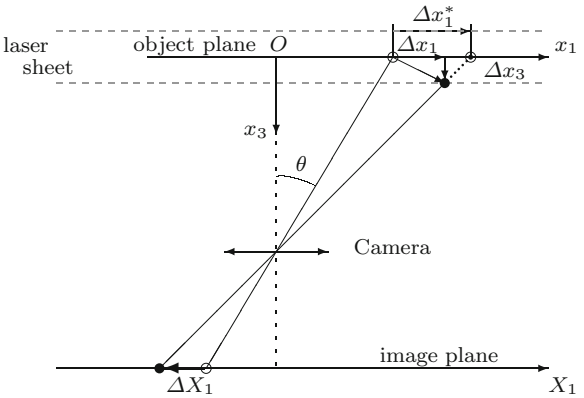

Fig. 10.26 Influence of a velocity component perpendicular to the laser sheet. The ΔX_1 observed in the image plane is erroneously connected to $x_1 + \Delta x_1^*$ instead of $x_1 + \Delta x_1$

rotating device is preferred, see Fig. 10.27, with use of the Scheimpflug rule [778]. For each camera, the object plane, the lens plane and the image plane have a shared intersection line. It must also be pointed out that the optical system now uses very small angles and scattered light is collected from a favorable angle.

Figure 10.28 illustrates the Scheimpflug rule using ray tracing. Images A' and B' of points A and B are obtained aligned on a line passing through I. The alignment of the image points on line IO' can be demonstrated using geometrical optics laws for a thin lens, i.e.

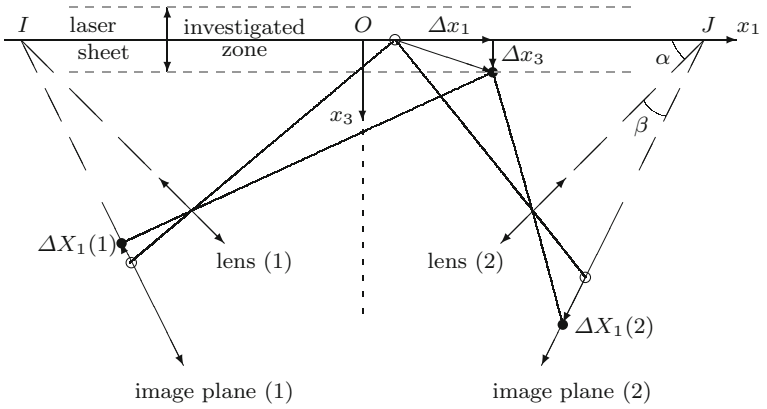

Fig. 10.27 Stereo viewing PIV system to resolve the out of plane velocity component, for two cameras located on the same side of the laser sheet and symmetrically placed with respect to Ox_3. According to Scheimpflug's rule, the object plane, the image plane and the lens plane all intersect at a common line, I or J. $\Delta X_1(1)$ and $\Delta X_1(2)$ are linear functions of the particle displacements Δx_1 and Δx_3, and their combination provides the velocity component u_1 and u_3. Either $\Delta X_2(1)$ or $\Delta X_2(2)$ can be used to obtain the velocity component u_2

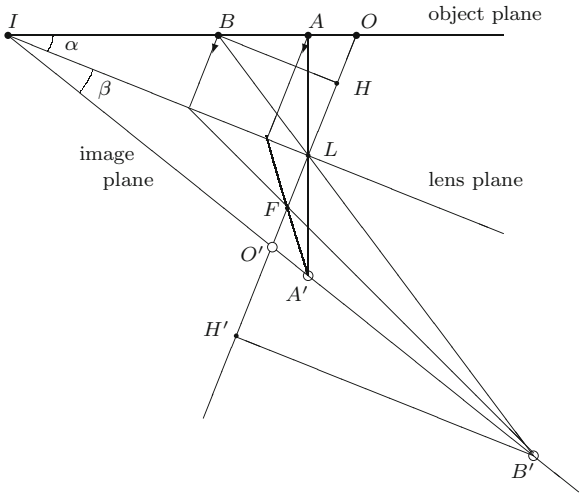

Fig. 10.28 Scheimpflug rule: points A et B of the object plane give images in A' et B' on the line IO'. Geometrical tracing using the rays going straight through the lens center L and the rays parallel to the optic axis OO' going through the lens focus F

$$\frac{1}{LO}+\frac{1}{LO'}=\frac{1}{f}\qquad\frac{1}{LH}+\frac{1}{LH'}=\frac{1}{f}\quad\text{and}\quad\frac{B'H'}{BH}=\frac{LH'}{LH}\tag{10.43}$$

with L the center of the lens, f its focal length, O' the image of O, H and H' the projections on the optical axis of point B and of its image B'. These laws allow the coordinates of points O' and B', and the components of vectors IO' and IB', to be calculated in the framework formed by the lens and its optical axis. Forming the cross product of these two vectors, it is found that it is equal to zero for any B' and thus for any B on the Ox_1 axis.

The first law (10.43) also implies a relation between f, α, β and length $D = IO$ which specifies the position of the hinge

$$f=\frac{D\ \sin\alpha}{1+\tan\alpha/\tan\beta}$$

In a Scheimpflug device, the sharpness of the image is ensured, but magnification $M = \Delta X_1/\Delta x_1$ depends on the position of the object point. This is already visible in Fig. 10.28, observing object points A and B, and their images A' and B'. Relations already used above easily provide the abscissa X of the image of point x

$$X_1(x_1)=-D\,x_1\,\frac{\cos\alpha}{\cos\beta}\,\tan\beta\,\frac{1}{(D-x_1)\tan\alpha-x_1\tan\beta}$$

and local magnification M

$$M(x_1)=\frac{\Delta X_1}{\Delta x_1}=X_1\left[\frac{1}{x_1}-\frac{\tan\alpha+\tan\beta}{D\ \tan\alpha-x_1(\tan\alpha+\tan\beta)}\right]\tag{10.44}$$

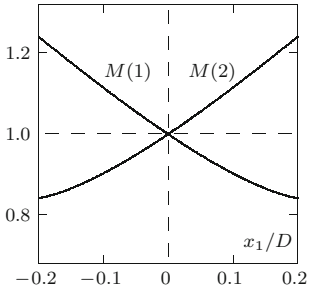

Fig. 10.29 Lateral magnification of cameras (1) and (2), as a function of x_1/D, for the Scheimpflug set-up shown in Fig. 10.28, $\alpha = 45°$, $\beta = 8°$, $OI = D = 50\,\text{cm}$, $M(1)$ et $M(2)$ are made dimensionless by $M_0 \simeq -0.10$

To simplify the expression, x_1 is used instead of $(x_1, 0, 0)$ and X_1 instead of $(X_1(1), 0, 0)$ relative to camera (1). For camera (2) in Fig. 10.28, the position of the image and magnification are given by the same expressions, substituting $-x_1$ by x_1.

Figure 10.29 represents variations of magnification values $M(1)$ and $M(2)$ of cameras (1) and (2) of Fig. 10.28. These magnification values are normalized by the value of magnification $M_0 = -A'O'/AO$, when A tends to O, and A' to O', respectively along x and X axes, i.e.

$$M_0 = -\frac{\cos\alpha}{\cos\beta}\,\frac{\tan\beta}{\tan\alpha}$$

The chosen values, $\alpha = 45°$ and $\beta = 8°$, are the typical values allowed by cameras used in Stereoscopic PIV. The two curves are of course antisymmetric. If the two cameras are located on either side of the laser sheet, as in the device by Willert [796], then $M(1) = M(2)$.

In current experiments, the particle constituting the object point is located in a tridimensional space and Δx_1, Δx_2, Δx_3 must be determined. The expressions serving to reconstruct this 3-D field have been studied by numerous authors, particularly Lawson and Wu [781], Soloff et al. [790], Raffel et al. [786] and Prasad [784]. They are too complex to be given here, but are included in numerous analysis softwares. The main parameters are obtained using a calibration grid with two levels of landmark points, simulating separations along x_1, x_2 and x_3. The calibration grid must be precisely aligned with the laser sheet [777].

Stereoscopic PIV is required to determine lateral velocity components in a flow which has an important longitudinal velocity. Studies by Castelain et al. [776] concern a Mach 0.9 jet subject to the impact of 6–24 micro-jets near the nozzle. The modifications induced by the micro-jets have been followed by the determination of the three velocity components, with their average values, time variations and rms, spatial correlations, and completed by the determination of vorticity. Figure 10.30 represents the field of the longitudinal vorticity component, ω_1, inferred from lateral velocity components u_2 and u_3 by use of criterion (10.42). The alternating vortices created by the micro-jets are very important and affect the jet development both in the mixing zone and the potential cone. The acoustic consequences are beneficial.

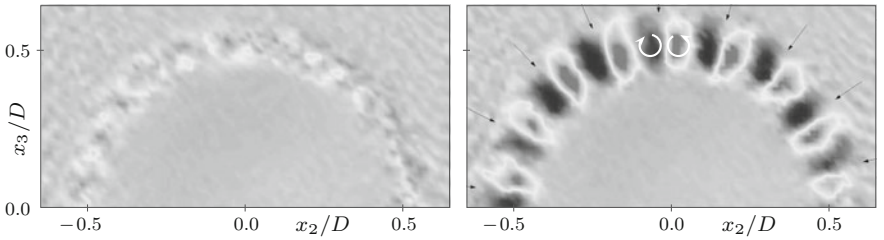

Fig. 10.30 Vorticity field $\omega_1 D/U_j$ in a Mach 0.9 jet. On the *left*, baseline jet, and on the *right*, the same jet impacted by 18 microjets, marked by *arrows*. StereoPIV with $\Delta t = 1.6\,\mu$s, $M \simeq 0.9$, CCD 1280×1024, 16^2 interrogation window, $\alpha = 45°$, $\beta = 8°$ and $OI = 50$ cm. Courtesy of Thomas Castelain (LMFA). See also Castelain et al. [776]

Noise reductions appear in far field, from 1 to 3 dB, depending on the observation direction.

The current major developments in the measurement of three dimensional velocity fields use the tomographic technique where three velocity components are estimated in a volumetric domain. Principles and practice are available in Scarano [787]. A fully described example dealing with Eulerian and Lagragian data in a turbulent boundary layer is provided by Schröder et al. [789].

References

General references are indicated in the first section, and references specific to the chapter topics are then listed in subsequent sections.

General References

1. Batchelor, G.K.: An Introduction to Fluid Dynamics. Cambridge University Press, Cambridge (1967)
2. Bernard, P.S., Wallace, J.M.: Turbulent Flows. Wiley, Hoboken (2002)
3. Bradshaw, P.: An Introduction to Turbulence and its Measurement. Pergamon Press, Oxford (1971)
4. Cambon, C., Sagaut, P.: Homogeneous Turbulence Dynamics. Cambridge University Press, Cambridge (2008)
5. Candel, S.: Mécanique des Fluides, 2nd edn. Dunod Université, Paris (1996)
6. Davidson, P.A., Kaneda, Y., Moffatt, K., Sreenivasan, K.R.: A Voyage Through Turbulence. Cambridge University Press, Cambridge (2011)
7. Guyon, E., Hulin, J.P., Petit, L., Mitescu, C.: Physical Hydrodynamics, 2nd edn. Oxford University Press, Oxford (2014)
8. Hinze, J.O.: Turbulence, 2nd edn. McGraw-Hill International Book Company, New York (1975)
9. Kleine, H., Settles, G.S.: The art of shock waves and their flowfields. Shock Waves **17**, 291–307 (2008)
10. Knudsen, J.G., Katz, D.L.: Fluid Dynamics and Heat Transfer. McGraw-Hill Book Company, New York (1958)
11. Lamb, H.: Hydrodynamics, 2nd edn. Dover Publications, New York (1993)
12. Landau, L.D., Lifchitz, E.M.: Fluid Mechanics, a Course of Theoretical Physics, 2nd edn, vol. 6. Pergamon Press, Oxford (1966)
13. Landahl, M.T., Mollo-Christensen, E.: Turbulence and Random Processes in Fluid Mechanics. Cambridge University Press, Cambridge (1992)
14. Lesieur, M.: Turbulence in Fluids: Stochastic and Numerical Modelling. 4th revised and enlarged edn. Kluwer Academic Publishers, Springer, Berlin (2008)
15. Libby, P.A.: Introduction to Turbulence. Taylor, Francis (1996)
16. Lumley, J.L., Panofsky, H.A.: The Structure of Atmospheric Turbulence. Interscience, New York (1964)

C. Bailly and G. Comte-Bellot, *Turbulence*, Experimental Fluid Mechanics,
DOI 10.1007/978-3-319-16160-0

17. Monin, A.S., Yaglom, A.M.: Statistical fluid mechanics: mechanics of turbulence. In: Lumley, J.L. (ed.) MIT Press, Cambridge (1971)
18. Ockendon, H., Ockendon, J.R.: Waves and Compressible Flow. Springer, New York (2000)
19. Panton, R.L.: Incompressible Flows, 2nd edn. Wiley, New-York (1996)
20. Pope, S.B.: Turbulent Flows. Cambridge University Press, Cambridge (2000)
21. Saffman, P.G.: Vortex Dynamics. Cambridge University Press, Cambrige (1992)
22. Schlichting, H., Gersten, K.: Boundary Layer Theory. Springer, Berlin (2000)
23. Settles, G.S.: Schlieren and Shadowgraph Techniques. Visualizing Phenomena in Transparent Media. Springer, Heidelberg (2001)
24. Smits, A.J., Dussauge, J.-P.: Turbulent Shear Layers in Supersonic Flow, 2nd edn. Springer Sciences+Business Media Inc, New York (2006)
25. Tavoularis, S.: Measurement in Fluid Mechanics. Cambridge University Press, Cambridge (2005)
26. Tennekes, H., Lumley, J.L.: A First Course in Turbulence. MIT Press, Cambridge (1972)
27. Tropea, C., Yarin, A.L., Foss, J.F. (eds.): Handbook of Experimental Fluid Mechanics. Springer, Berlin (2007)
28. Van Dyke, M.: An Album of Fluid Motion. The Parabolic Press, Stanford (1982)
29. Versluis, M.: High-speed imaging in fluids. Exp. Fluids **54**(1458), 1–35 (2013)
30. White, F.: Viscous Flows. McGraw-Hill Inc, New-York (1991)

Stability

31. Arnal, D.: Boundary layer transition: predictions based on linear theory. In: FDP/VKI Special Course on Progress in Transition Modelling. AGARD report 793 (1993)
32. Batchelor, G.K., Gill, A.E.: Analysis of the stability of axisymmetric jets. J. Fluid Mech. **14**, 529–551 (1962)
33. Betchov, R., Criminale, W.O.: Spatial instability of the inviscid jet and wake. Phys. Fluids **9**(2), 359–362 (1966)
34. Betchov, R., Criminale, W.O.: Stability of Parallel Flows. Academic Press, New York (1967)
35. Chomaz, J.M.: Global instabilities in spatially developing flows: non-normality and nonlinearity. Annu. Rev. Fluid Mech. **37**, 357–392 (2005)
36. Criminale, W.O., Jackson, T.L., Joslin, R.D.: Theory and Computation of Hydrodynamic Stability. Cambridge University Press, Cambridge (2003)
37. Drazin, P.G., Reid, W.H.: Hydrodynamic Stability. Cambridge University Press, Cambridge (1981)
38. Gaster, M.: A note on the relation between temporally-increasing and spatially-increasing disturbances in hydrodynamic stability. J. Fluid Mech. **14**, 222–224 (1962)
39. Godrèche, C., Manneville, P. (eds.): Hydrodynamics and Nonlinear Instabilities. Cambridge University Press, Cambridge (1998)
40. Haertig, J.: Étude du couplage entre champs moyen, cohérent et turbulent dans un jet libre rond excité. Thèse d'État, rapport ISL-R115/83 (1983)
41. Ho, C.-M., Huerre, P.: Perturbed free shear layers. Annu. Rev. Fluid Mech. **16**, 365–424 (1984)
42. Huerre, P., Monkewitz, P.A.: Local and global instabilities in spatially developing flows. Annu. Rev. Fluid Mech. **22**, 473–537 (1990)
43. Huerre P., Rossi, M.: Hydrodynamic instabilities in open flows. In: Hydrodynamics and Nonlinear Instabilities. Cambridge University Press, Cambridge (1998)
44. Lagnado, R.R., Phan-Thien, N., Leal, L.G.: The stability of two-dimensional linear flows. Phys. Fluids **27**(5), 1094–1101 (1984)
45. Lin, C.C.: The Theory of Hydrodynamic Stability. Cambridge University Press, Cambridge (1955)

46. Mattingly, G.E., Criminale, W.O.J.: Disturbance characteristics in a plane jet. Phys. Fluids **14**(11), 2258–2264 (1971)
47. Michalke, A.: On the inviscid instability of the hyperbolic-tangent velocity profile. J. Fluid Mech. **19**, 543–556 (1964)
48. Michalke, A.: On spatially growing disturbances in an inviscid shear layer. J. Fluid Mech. **23**(3), 521–544 (1965)
49. Michalke, A.: The instability of free shear layers. Prog. Aerosp. Sci. **12**, 213–239 (1972)
50. Michalke, A.: Survey of jet instability theory. Prog. Aerosp. Sci. **21**, 159–199 (1984)
51. Michalke, A., Hermann, G.: On the inviscid instability of a circular jet with external flows. J. Fluid Mech. **114**, 343–359 (1982)
52. Monkewitz, P.A., Huerre, P.: Influence of the velocity ratio on the spatial instability of mixing layers. Phys. Fluids **25**(7), 1137–1143 (1982)
53. Morris, P.J.: The spatial viscous instability of axisymmetric jets. J. Fluid Mech. **77**(3), 511–529 (1976)
54. Reed, H., Saric, W.S., Arnal, D.: Linear stability theory applied to boundary layers. Annu. Rev. Fluid Mech. **28**, 389–428 (1996)
55. Schmid, P.J., Hennigson, D.S.: Stability and Transition in Shear Flows. Applied Mathematical Sciences, vol. 142. Springer, New York (2001)
56. Squire, H.B.: On the stability of three-dimensional disturbances of viscous flows between parallel walls. Proc. Roy. Soc. Lond. A **142**, 621–628 (1933)
57. Tam, C.K.W.: Excitation of instability waves in a two-dimensional shear by sound. J. Fluid Mech. **89**(2), 357–371 (1978)
58. Tam, C.K.W., Hu, F.Q.: On the three families of instability waves of high-speed jets. J. Fluid Mech. **201**, 447–483 (1989)
59. Tam, C.K.W., Burton, D.E., Sound generated by instability waves of supersonic flows. Part 1: two-dimensional mixing layers. J. Fluid Mech. **138**, 249–271 (1984)
60. Tam, C.K.W., Burton, D.E.: Sound generated by instability waves of supersonic flows. Part 2: Axisymmetric jets. J. Fluid Mech. **138**, 273–295 (1984)
61. Tatsumi, T., Gotoh, K.: The stability of free boundary layers between two uniform streams. J. Fluid Mech. **7**, 433–441 (1960)
62. Wazzan, A.R.: Spatial stability of Tollmien-Schlichting waves. Prog. Aerosp. Sci. **16**(2), 99–127 (1975)
63. Wazzan, A.R., Gazley Jr, C., Smith, A.M.O.: Tollmien-Schlichting waves and transition. Prog. Aerosp. Sci. **18**, 351–392 (1979)

Additional References Mentioned in Introduction

64. Aref, H.: Stirring by chaotic advection. J. Fluid Mech. **143**, 1–21 (1984)
65. Aref, H.: Something old, something new. Phil. Trans. R. Soc. Lond. A **366**, 2649–2670 (2008)
66. Aris, R.: Vectors, Tensors and the Basic Equations of Fluid Mechanics. Dover Publications Inc, New York (1962)
67. Bergé, P., Pomeau, Y., Vidal, C.: Order Within Chaos: Towards a Deterministic Approach to Turbulence. Wiley-Interscience, Hermann (1987)
68. Corrsin, S.: Interpretation of viscous terms in the turbulent energy equation. J. Aeronaut. Sci. **20**, 853–854 (1953)
69. Deissler, R.G.: On the Nature of Navier-Stokes Turbulence. NASA, TM 101983 (1989)
70. Dimotakis, P.E.: The mixing transition in turbulent flows. J. Fluid Mech. **409**, 69–98 (2000)
71. Greenspan, M.: Propagation of sound in five monoatomic gases. J. Acoust. Soc. Am. **28**(4), 644–648 (1956)
72. Greenspan, M.: Rotational relaxation in nitrogen, oxygen and air. J. Acoust. Soc. Am. **31**(2), 155–160 (1959)

73. Heisenberg, W.: Nonlinear problems in physics. Phys. Today **20**(5), 27–33 (1967)
74. Karim, S.M., Rosenhead, L.: The second coefficient of viscosity in liquids and gases. Rev. Mod. Phys. **24**(2), 108–116 (1952)
75. Lorenz, E.N.: Deterministic nonperiodic flow. J. Atmos. Sci. **20**, 130–141 (1963)
76. Lighthill, M.J.: Viscosity effects in sound waves of finite amplitude. In: Batchelor, G.K., Davies, R.M. (eds.) Surveys in Mechanics. Cambridge University Press, Cambridge (1956)
77. Lumley, J.L.: Stochastic Tools in Turbulence. Academic Press, New York (1970)
78. Manneville, P.: Instabilities, Chaos and Turbulence. Imperial College Press, London (2010)
79. Ott, E.: Chaos in Dynamical Systems. Cambridge University Press, Cambridge (1993)
80. Ottino, J.M.: The Kinematics of Mixing: Stretching, Chaos and Transport. Cambridge University Press, Cambridge (1989)
81. Ruelle, D., Takens, F.: On the nature of turbulence. Commun. Math. Phys. **20**, 167–192 (1971)
82. Schwartz, L.: Méthodes mathématiques pour les sciences physiques. Hermann, Paris (1997)

Homogeneous Turbulence, Isotropy, Anisotropy

83. Batchelor, G.K.: The theory of axisymmetric turbulence. Proc. Roy. Soc. Lond. A **186**, 480–502 (1946)
84. Batchelor, G.K.: The Theory of Homogeneous Turbulence. Cambridge University Press, Cambridge (1953)
85. Batchelor, G.K., Proudman, I.: The effect of rapid distortion of a fluid in turbulent motion. Q. J. Mech. Appl. Math. **7**(1), 121–152 (1954)
86. Bertoglio, J.P.: Homogeneous turbulent field within a rotating field. AIAA J. **20**, 1175–1181 (1982)
87. Betchov, R.: An inequality concerning the production of vorticity in isotropic turbulence. J. Fluid Mech. **1**, 497–504 (1956)
88. Betchov, R.: On the fine structure of turbulence flows. J. Fluid Mech. **3**, 205–216 (1957)
89. Brachet, M.E., Meiron, D.I., Orszag, S.A., Nickel, B.G., Morf, R.H., Frish, U.: Small-scale structure of the Taylor-Green vortex. J. Fluid Mech. **130**, 411–452 (1983)
90. Brachet, M.E., Meiron, D.I., Orszag, S.A., Nickel, B.G., Morf, R.H., Frish, U.: Étude spectrale d'un champ turbulent incompressible soumis à des effets couplés de déformation et de rotation, imposés extérieurement. thèse d'Etat, Université Claude Bernard, Lyon I, 1982–25 (1982)
91. Brachet, M.E., Meiron, D.I., Orszag, S.A., Nickel, B.G., Morf, R.H., Frish, U.: Turbulence and vortex structures in rotating and stratified flows. Eur. J. Mech. B/Fluids **20**, 489–510 (2001)
92. Cambon, C., Scott, J.: Linear and nonlinear models of anisotropic turbulence. Annu. Rev. Fluid Mech. **31**, 1–53 (1999)
93. Cambon, C., Jacquin, L.: Spectral approach to non-isotropic turbulence subjected to rotation. J. Fluid Mech. **202**, 295–317 (1989)
94. Cambon, C., Jeandel, D., Mathieu, J.: Spectral modelling of homogeneous non-isotropic turbulence. J. Fluid Mech. **104**, 247–262 (1981)
95. Cambon, C., Mansour, N.N., Godeferd, F.S.: Energy transfer in rotating turbulence. J. Fluid Mech. **337**, 303–332 (1997)
96. Cambon, C., Rubinstein, R., Godeferd, F.S.: Advances in wave turbulence: rapidly rotating flows. New J. Phys. **6**, 1–28 (2004)
97. Champagne, F.H.: The fine-scale structure of the turbulent velocity field. J. Fluid Mech. **86**(1), 67–108 (1978)
98. Chandrasekhar, S.: The theory of axisymmetric turbulence. Phil. Trans. Roy. Soc. Lond. A **242**, 557–577 (1950)
99. Eyink, G.L., Sreenivasan, K.R.: Onsager and the theory of hydrodynamic turbulence. Rev. Mod. Phys. **78**, 87–135 (2006)

100. Comte-Bellot, G., Corrsin, S.: The use of a contraction to improve the isotropy of grid-generated turbulence. J. Fluid Mech. **25**(4), 657–682 (1966)
101. Comte-Bellot, G., Corrsin, S.: Simple Eulerian time correlation of full- and narrow-band velocity signals in grid-generated, isotropic turbulence. J. Fluid Mech. **48**(2), 273–337 (1971)
102. Coantic, M., Lasserre, J.J.: On pre-dissipative 'bumps' and a Reynolds-number-dependent spectral parameterization of turbulence. Eur. J. Mech. B/Fluids **18**, 1027–1047 (1999)
103. Corrsin, S.: The decay of isotropic temperature fluctuations in an isotropic turbulence. J. Aeronaut. Sci. **18**, 417–423 (1951)
104. Corrsin, S., Karweit, M.: Fluid line growth in grid-generated isotropic turbulence. J. Fluid Mech. **39**(1), 87–96 (1969)
105. Craya, A.: Contribution à l'analyse de la turbulence associée à des vitesses moyennes. Publications scientifiques et techniques du Ministère de l'Air, Paris, PST-345 (1958)
106. Frenkiel, F.N., Klebanoff, P.S.: Space-time correlations in turbulence. In: Pai, S.I. (ed.) Dynamics of Fluids and Plasmas, pp. 257–274. Academic Press, New-York (1966)
107. Gence, J.N.: Homogeneous turbulence. Annu. Rev. Fluid Mech. **15**, 201–222 (1983)
108. Godeferd, F.S., Lollini, L.: Direct numerical simulations of turbulence with confinement and rotation. J. Fluid Mech. **393**, 257–307 (1999)
109. Helland, K.N., Van Atta, C.W., Stegen, G.R.: Spectral energy transfer in high Reynolds number turbulence. J. Fluid Mech. **79**(2), 337–359 (1977)
110. Ishida, T., Davidson, P.A., Kaneda, Y.: On the decay of isotropic turbulence. J. Fluid Mech. **564**, 455–475 (2006)
111. Ishihara, T., Gotoh, T., Kaneda, Y.: Study of high-Reynolds number isotropic turbulence by direct numerical simulation. Annu. Rev. Fluid Mech. **41**, 165–180 (2009)
112. Kaneda, Y., Ishihara, T.: High-resolution direct numerical simulation of turbulence. J. Turbul. **7**(20), 1–17 (2006)
113. von Kármán, T.: The fundamentals of the statistical theory of turbulence. J. Aeronaut. Sci. **4**(4), 131–138 (1937)
114. von Kármán, T., Howarth, L.: On the statistical theory of isotropic turbulence. Proc. Roy. Soc. Lond. A **164**, 192–215 (1938)
115. Kellogg, R.M., Corrsin, S.: Evolution of a spectrally local disturbance in grid-generated, nearly isotropic turbulence. J. Fluid Mech. **96**(4), 641–669 (1980)
116. Kholmyansky, M., Kit, E., Teitel, M., Tsinober, A.: Some experimental results on velocity and vorticity measurements in turbulent grid flows with controlled sign of mean helicity. Fluid Dynamics Research **7**, 65–75 (1991)
117. Kovasznay, L.S.G.: Spectrum of locally isotropic turbulence. J. Aeronaut. Sci. **15**(12), 745–753 (1948)
118. Kovasznay, L.S.G.: The spectrum of locally isotropic turbulence. Phys. Rev. **73**(9), 1115–1116 (1948)
119. Kovasznay, L.S.G., Uberoi, M.S., Corrsin, S.: The transformation between one- and three-dimensional power spectra for an isotropic scalar fluctuation field. Phys. Rev. **76**(8), 1263–1264 (1949)
120. Kuo, A.Y.-S., Corrsin, S.: Experiment on the geometry on the fine-structure regions in fully turbulent fluid. J. Fluid Mech. **56**(3), 447–479 (1972)
121. Lee, M.J.: Distorsion of homogeneous turbulence by axisymmetric strain and dilatation. Phys. Fluids A **1**(9), 1541–1557 (1989)
122. Lee, S., Lele, S.K., Moin, P.: Simulation of spatially evolving turbulence and the applicability of Taylor's hypothesis in compressible flow. Phys. Fluids A **4**(7), 1521–1530 (1992)
123. Leith, C.E.: Diffusion approximation to inertial transfer in isotropic turbulence. Phys. Fluids **10**(7), 1409–1416 (1967)
124. Leith, C.E.: Atmospheric predictability and two-dimensional turbulence. J. Atmos. Sci. **28**(2), 145–161 (1971)
125. Le Penven, L., Gence, J.N., Comte-Bellot, G.: On the approach to isotropy of homogeneous turbulence: effect of the partition of kinetic energy among the velocity components. In: Davies, S.H., Lumley, J.L. (eds.) Frontiers in Fluid Mechanics. Commemoration 65th birthday Corrsin S, pp. 1–21. Springer, Berlin (1985)

126. Lesieur, M., Schertzer, D.: Amortissement auto-similaire d'une turbulence à grand nombre de Reynolds. J. de Mécanique **17**(4), 609–646 (1978)
127. Lin, C.C.: Note of the law of decay of isotropic turbulence. Proc. Natl. Acad. Sci. U.S.A. **34**, 540–543 (1948)
128. Mathieu, J., Scott, J.: An Introduction to Turbulent Flows. Cambridge University Press, Cambridge (2000)
129. McComb, W.D.: The Physics of Fluid Turbulence. Clarendon Press, Oxford (1991)
130. Meyers, Y., Meneveau, C.: A functional form for the energy spectrum parametrizing bottleneck and intermittency effects. Phys. Fluids **20**(065109), 1–7 (2008)
131. Millionshchikov, M.D.: Theory of homogeneous isotropic turbulence. C.R. Acad. Sci. USSR (Dokl. Akad. Nauk SSSR), **22**, 236–240 (1941), and Izv. Akad. Nauk SSSR Ser. Geogr. Geofiz. **5**, 433–446 (1941)
132. Moffatt, H.K.: The degree of knottedness of tangled vortex lines. J. Fluid Mech. **35**, 117–129 (1969)
133. Moffatt, H.K.: Some developments in the theory of turbulence. J. Fluid Mech. **106**, 27–47 (1981)
134. Moffatt, H.K., Tsinober, A.: Helicity in laminar and turbulent flows. Annu. Rev. Fluid Mech. **24**, 281–312 (1992)
135. Mohamed, M.S., Larue, J.C.: The decay power law in grid-generated turbulence. J. Fluid Mech. **219**, 195–214 (1990)
136. Moin, P.: Revisiting Taylor's hypothesis. J. Fluid Mech. **640**, 1–4 (2009)
137. Mydlarski, L., Warhaft, Z.: On the onset of high-Reynolds-number grid-generated wind tunnel turbulence. J. Fluid Mech. **320**, 331–368 (1996)
138. Mydlarski, L., Warhaft, Z.: Passive scalar statistics in high-Péclet-number grid turbulence. J. Fluid Mech. **358**, 135–175 (1998)
139. Obukhov, A.M.: Spectral energy distribution in a turbulent flow. Izv. Akad. Nauk SSSR **5**, 453–566 (1941)
140. Pao, Y.H.: Structure of turbulent velocity and scalar fields at large wavenumbers. Phys. Fluids **8**(6), 1063–1075 (1965)
141. Pao, Y.H.: Transfer of turbulent energy and scalar quantities at large wavenumbers. Phys. Fluids **11**(6), 1371–1372 (1968)
142. Proudman, I.: A comparison of Heisenberg's spectrum of turbulence with experiment. Proc. Camb. Phil. Soc. Math. Phys. Sci. **47**, 158–176 (1951)
143. Proudman, I., Reid, W.H.: On the decay of a normally distributed and homogeneous turbulent velocity field. Phil. Trans. Roy. Soc. Lond. A **247**, 163–189 (1954)
144. Ribner, H.S., Tucker, M.: Structure of Turbulence in a Contracting Stream. NACA Report 1113 (1953)
145. Robertson, H.P.: The invariant theory of isotropic turbulence. Proc. Camb. Phil. Soc. **36**, 209–223 (1940)
146. Saffman, P.G.: On the fine-scale structure of vector fields convected by a turbulent fluid. J. Fluid Mech. **16**, 545–572 (1963)
147. Sagaut, P., Cambon, C.: Homogeneous Turbulence Dynamics. Cambridge University Press, Cambridge (2008)
148. Salhi, A., Cambon, C.: An analysis of rotating shear flow using linear theory and DNS and LES results. J. Fluid Mech. **347**, 171–195 (1997)
149. Simone, A., Coleman, G.N., Cambon, C.: The effect of compressibility on turbulent shear flow: a rapid-distortion-theory and direct-numerical-simulation study. J. Fluid Mech. **330**, 307–338 (1997)
150. Sposito, G.: A note on helicity conservation in steady fluid flows. J. Fluid Mech. **363**, 325–332 (1998)
151. Taylor, G.I.: Statistical theory of turbulence, Part I. Proc. Roy. Soc. Lond. A **151**, 421–444 (1935)
152. Taylor, G.I.: Production and dissipation of vorticity in a turbulent fluid. Proc. Roy. Soc. Lond. A **164**, 15–23 (1938)

153. Taylor, G.I.: The spectrum of turbulence. Proc. Roy. Soc. Lond. A **164**, 476–490 (1938)
154. Taylor, G.I., Green, A.E.: Mechanism of the production of small eddies from large ones. Proc. R. Soc. Lon. A **158**, 499–521 (1937)
155. Tsinober, A., Levitch, E.: On the helical nature of three dimensional coherent structures in turbulent flows. Phys. Lett. A **99**, 321–324 (1983)

Two-Dimensional Turbulence

156. Batchelor, G.K.: Computation of the energy spectrum in homogeneous two-dimensional turbulence. Phys. Fluids **12**(Supplement II), 233–239 (1969)
157. Brachet, M.E., Meneguzzi, M., Politano, H., Sulem, P.L.: The dynamics of freely decaying two-dimensional turbulence. J. Fluid Mech. **194**, 333–349 (1988)
158. Couder, Y.: Two-dimensional grid turbulence in a thin liquid film. J. Phys. Lett. **45**(8), 353–360 (1984)
159. Couder, Y., Basdevant, C.: Experimental and numerical study of vortex couples in two-dimensional flows. J. Fluid Mech. **173**, 225–251 (1986)
160. Frisch, U., Sulem, P.L.: Numerical simulations of the inverse cascade in two-dimensional turbulence. Phys. Fluids **28**, 438 (1984). Erratum Phys. Fluids 27(8), 1921–1923 (1984)
161. Herring, J.R., McWilliams, J.C.: Comparison of direct numerical simulation of two-dimensional turbulence with two-point closure: the effect of intermittency. J. Fluid Mech. **153**, 229–242 (1985)
162. Herring, J.R., Orszag, S.A., Kraichnan, R.H., Fox, D.G.: Decay of two-dimensional homogeneous turbulence. J. Fluid Mech. **66**(3), 417–444 (1974)
163. Hopfinger, E.J., Griffiths, M., Mory, M.: The structure of turbulence in homogeneous and stratified rotating fluids. J. de Mécanique Théorique et Appliquée (Special issue) 21–44 (1983)
164. Kraichnan, R.H.: Inertial ranges in two-dimensional turbulence. Phys. Fluids **10**(7), 1417–1423 (1967)
165. Kraichnan, R.H.: Eddy viscosity in two and three dimensions. J. Atmos. Sci. **33**, 1521–1536 (1976)
166. Kraichnan, R.H., Montgomery, D.: Two-dimensional turbulence. Rep. Prog. Phys. **43**, 549–619 (1980)
167. Lesieur, M.: Introduction à la turbulence bidimensionnelle. J. de Mécanique Théorique et Appliquée (Special issue) 5–20 (1983)
168. Siggia, E.D., Aref, H.: Point-vortex Simulation of the inverse energy cascade in two-dimensional turbulence. Phys. Fluids **24**(1), 171–173 (1981)
169. Sommeria, J.: Experimental study of the two-dimensional inverse energy cascade in a square box. J. Fluid Mech. **170**, 139–168 (1986)

Kolmogorov Theory—Turbulent Kinetic Energy Spectrum

170. Anselmet, F., Gagne, Y., Hopfinger, E.J., Antonia, R.A.: High-order velocity structure functions in turbulent shear flows. J. Fluid Mech. **140**, 63–89 (1984)
171. Antonia, R.A., Ould-Rouis, M., Anselmet, F., Zhu, Y.: Analogy between predictions of Kolmogorov and Yaglom. J. Fluid Mech. **332**, 395–409 (1997)
172. Belin, F., Maurer, J., Tabeling, P., Willaime, H.: Velocity gradient distributions in fully developed turbulence: an experimental study. Phys. Fluids **9**(12), 3843–3850 (1997)
173. Chapman, D.R.: Computational aerodynamics developement and outlook. AIAA J. **17**(12), 1293–1301 (1979)

174. Frisch, U.: Turbulence, the Legacy of A.N. Kolmogorov, 2nd edn. Cambridge University Press, Cambridge (2001)
175. Frisch, U., Sulem, P.L., Nelkin, M.: A simple dynamical model of intermittent fully developed turbulence. J. Fluid Mech. **87**(4), 719–736 (1978)
176. Garg, S., Warhaft, Z.: On the small scale structure of simple shear flow. Phys. Fluids **10**(3), 662–673 (1998)
177. Gibson, C.H., Schwarz, W.H.: The universal equilibrium spectra of turbulent velocity and scalar fields. J. Fluid Mech. **16**, 365–384 (1963)
178. Grant, H.L., Stewart, R.W., Moilliet, A.: Turbulence spectra from a tidal channel. J. Fluid Mech. **12**, 241–268 (1962)
179. Heisenberg, W.: On the theory of statistical and isotropic turbulence. Proc. Roy. Soc. Lond. A **195**, 402–406 (1948)
180. Heisenberg, W.: 1958 On the statistical theory of turbulence. Translation of Zur statistischen theorie der turbulenz. Zeitschrift für Physik **124** (1948) NACA TM 1431
181. von Kármán, T.V.: Progress in the statistical theory of turbulence. J. Mar. Res. **7**, 252–264 (1948)
182. Kolmogorov, A.N., The local structure of turbulence in incompressible viscous fluid for very large Reynolds number. C.R. Acad. Sci. USSR (Dokl. Akad. Nauk SSSR), **30**(4) (1941). English translation in Proc. Roy. Soc. Lond. A **434**, 9–13 (1991)
183. Kolmogorov, A.N., 1941, Dissipation of energy in the locally isotropic turbulence. C. R. Acad. Sci. U.S.S.R. (Dokl. Akad. Nauk. SSSR), 32(1) (1941) English translation in Proc. Roy. Soc. Lond. A 434, 15–17 (1991)
184. Kolmogorov, A.N.: A refinement of previous hypotheses concerning the local structure of turbulence in a viscous incompressible fluid at high Reynolds number. J. Fluid Mech. **13**(1), 82–85 (1962)
185. Kraichnan, R.H.: Pressure field within homogeneous anisotropic turbulence. J. Acoust. Soc. Am. **28**(1), 64–72 (1956)
186. Kraichnan, R.H.: The structure of isotropic turbulence at very high Reynolds numbers. J. Fluid Mech. **5**(4), 497–543 (1959)
187. Kraichnan, R.H.: Eddy viscosity in two and three dimensions. J. Atmos. Sci. **33**, 1521–1536 (1976)
188. Maurer, J., Tabeling, P., Zocchi, G.: Statistics of turbulence between two counterrotating disks in low-temperature Helium gas. Europhys. Lett. **26**(1), 31–36 (1994)
189. Obukhov, A.M.: Some specific features of atmospheric turbulence. J. Fluid Mech. **13**, 77–81 (1962)
190. She, Z.S., Lévêque, E.C.: Universal scaling laws in fully developed turbulence. Phys. Rev. Lett. **72**(3), 336–339 (1994)
191. She, Z.S., Waymire, E.C.: Quantized energy cascade and log-Poisson statistics in fully developed turbulence. Phys. Rev. Lett. **74**(2), 262–265 (1995)
192. Shih, T.H., Reynolds, W.C., Mansour, N.N.: A Spectrum model for weakly anisotropic turbulence. Phys. Fluids A **2**(8), 1500–1502 (1990)
193. Sreenivasan, K.R.: On the scaling of the turbulence energy dissipation rate. Phys. Fluids **27**(5), 1048–1051 (1984)
194. Sreenivasan, K.R.: On the universality of the Kolmogorov constant. Phys. Fluids **7**(11), 2778–2784 (1995)
195. Sreenivasan, K.R., Antonia, R.A.: The phenomenology of small-scale turbulence. Annu. Rev. Fluid Mech. **29**, 435–472 (1997)
196. Uberoi, M.S.: 1963, Energy transfer in isotropic turbulence. Phys. Fluids **6**(8), 1048–1056 (1963)
197. Van Atta, C.W., Chen, W.Y.: Measurements of spectral energy transfer in grid turbulence. J. Fluid Mech. **38**(4), 743–763 (1969)
198. Van Atta, C.W., Chen, W.Y.: Structure functions of turbulence in the atmospheric boundary layer over the ocean. J. Fluid Mech. **44**(1), 145–159 (1970)

199. Van Atta, C.W., Park, J.: Statistical self-similarity and inertial subrange turbulence. In: Rosenblatt, M., Van Atta, C. (eds.) Statistical Models and Turbulence. Lecture Notes in Physics, vol. 12, pp. 402–426. Springer, Berlin (1972)
200. Yaglom, A.M.: A.N. Kolmogorov as a fluid mechanician and founder of a school in turbulence research. Annu. Rev. Fluid Mech. **26**, 1–22 (1994)

Turbulent Dispersion

201. Blackadar, A.K.: Turbulence and Diffusion in the Atmosphere. Lectures in Environmental Sciences. Springer, Berlin (1997)
202. Hunt, J.C.R.: Turbulent diffusion from sources in complex flows. Annu. Rev. Fluid Mech. **17**, 447–485 (1985)
203. Kraichnan, R.H.: Diffusion by a random velocity field. Phys. Fluids **13**(1), 22–31 (1970)
204. Kraichnan, R.H.: Convection of a passive scalar by a quasi-uniform random straining field. J. Fluid Mech. **64**(4), 737–762 (1974)
205. Kraichnan, R.H.: Diffusion of passive-scalar and magnetic fields by helical turbulence. J. Fluid Mech. **77**(4), 753–768 (1976)
206. Ottino, J.M.: Mixing, chaotic advection and turbulence. Annu. Rev. Fluid Mech. **22**, 207–253 (1990)
207. Sato, Y., Yamamoto, K.: Lagrangian measurement of fluid-particle motion in an isotropic turbulent field. J. Fluid Mech. **175**, 183–189 (1987)
208. Shlien, D.J., Corrsin, S.: A measurement of Lagrangian velocity autocorrelation in approximately isotropic turbulence. J. Fluid Mech. **62**, 255–271 (1974)
209. Snyder, W.H., Lumley, J.L.: Some measurements of particle velocity autocorrelation functions in a turbulent flows. J. Fluid Mech. **48**, 41–71 (1971)
210. Sullivan, P.J.: Longitudinal dispersion within a two-dimensional turbulent shear flows. J. Fluid Mech. **49**, 551–576 (1971)
211. Taylor, G.I.: Diffusion by continuous movements. Proc. Lond. Math. Soc. Ser. **2**(20), 196–212 (1921)
212. Taylor, G.I.: The dispersion of matter in turbulent flow through a pipe. Proc. Roy. Soc. Lond. A **223**, 446–468 (1954)
213. Yeung, P.K., Pope, S.B.: Lagrangian statistics from direct numerical Simulations of isotropic turbulence. J. Fluid Mech. **207**, 531–586 (1989)

Mode Decomposition and Spectral Analysis

214. Aubry, N.: Use of experimental data for an efficient description of turbulent flows. Appl. Mech. Rev. **43**, 240–245 (1990)
215. Aubry, N., Holmes, P., Lumley, J.L., Stone, E.: The dynamics of coherent structures in the wall region of a turbulent boundary layer. J. Fluid Mech. **192**, 115–173 (1988)
216. Berkooz, G., Holmes, P., Lumley, J.L.: The proper orthogonal decomposition in the analysis of turbulent flows. Annu. Rev. Fluid Mech. **25**, 539–575 (1993)
217. Bergmann, M., Cordier, L., Brancher, J.-P.: Optimal rotary control of the cylinder wake using proper orthogonal decomposition reduced-order model. Phys. Fluids **17**(097101), 1–21 (2005)
218. Chambers, D.H., Adrian, R.J., Moin, P., Stewart, D.S., Sung, H.J.: Karhunen-Loève expansion of Burgers' model of turbulence. Phys. Fluids **31**(9), 2573–2582 (1988)
219. Chatterjee, A.: An introduction to the proper orthogonal decomposition. Curr. Sci. **78**(7), 808–817 (2000)

220. Citriniti, J.H., George, W.K.: Reconstruction of the global velocity field in the axisymmetric mixing layer utilizing the proper orthogonal decomposition. J. Fluid Mech. **418**, 137–166 (2000)
221. Gloerfelt, X.: Compressible proper orthogonal decomposition/Galerkin reduced-order model of self-sustained oscillations in a cavity. Phys. Fluids **20**(115105), 1–22 (2008)
222. Holmes, P., Lumley, J.L., Berkooz, G.: Turbulence, Coherent Structures, Dynamical Systems and Symmetry. Cambridge University Press, Cambridge (1996)
223. Karhunen, K.: Zur spektral theorie stochastischer prozesse. Annu. Acad. Sci. Fennicae Ser. A (J. Math. Phys.) **34**, (1–7) (1946)
224. Loève, M.: Sur la covariance d'une fonction aléatoire. C. R. Acad. Sci. Paris **220**, 295–296 (1945)
225. Newman, A.J.: Model Reduction via the Karhunen-Loeve Expansion, Part I: An exposition, Part II: Some elementary examples. Technical report, Institute for System Research, University of Maryland, 20742 (1996)
226. Rowley, C.W., Colonius, T., Murray, R.M.: Dynamical Models for Control of Cavity Oscillations. AIAA Paper 2001–2126 (2001)
227. Rowley, C.W., Williams, D.R.: Dynamics and control of high-Reynolds-number flow over open cavities. Annu. Rev. Fluid Mech. **38**, 251–276 (2006)
228. Rowley, C.W., Mezić, I., Bagheri, S., Schlatter, P., Hennigson, D.S.: Spectral analysis of nonlinear flows. J. Fluid Mech. **641**, 115–127 (2009)
229. Schmid, P.J.: Dynamic mode decomposition of numerical and experimental data. J. Fluid Mech. **656**, 5–28 (2010)
230. Sirovich, L.: Turbulence and the dynamics of Coherent structures, Part I: Coherent structures, Part II: Symmetries and transformations. Q. Appl. Math. **XLV**, 561–582 (1987)

Numerical Simulations of Turbulent Flows

General References, Direct Numerical Simulation

231. Agard: Special course on modern theoretical and experimental approaches to turbulent flow structure and its modelling. Report 755 (1987)
232. Agard: Progress in transition modelling. Report 793 (1994)
233. Berland, J., Bogey, C., Bailly, C.: Low-dissipation and low-dispersion fourth-order Runge-Kutta algorithm. Comput. Fluids **35**(10), 1459–1463 (2006)
234. Birnbaum, J., Williams, S.R.: Physics and the information revolution. Phys. Today **53**(1), 38–42 (2000)
235. Bogey, C., Bailly, C.: Three-dimensional non-reflective boundary conditions for acoustic simulations: far field formulation and validation test cases. Acta Acust. **88**(4), 463–471 (2002)
236. Bogey, C., Bailly, C.: A family of low dispersive and low dissipative explicit schemes for noise computation. J. Comput. Phys. **194**(1), 194–214 (2004)
237. Bogey, C., Marsden, O.: Direct numerical simulation of the turbulent development of a round jet at Reynolds number 11 000. In: Parallel computing: from multicores and GPU's to petascale, advances in parallel computing, vol. 19, 513–519, IOS Press, ISBN 978-1-60750-529-7 (2010)
238. Bradshaw, P.: Turbulence, with the contributions of Fernholz H.-H. In: Johnston, J.P., Woods, J.D., Reynolds, W.C., Cebeci, T., Launder, B.E., Lumley J.L. (eds.), 2nd edn. Springer, Berlin (1978)
239. Brenner, A.E.: The computing revolution and the physics community. Phys. Today **49**(10), 24–30 (1996)
240. Colonius, T., Lele, S.: Computational aeroacoustics: progress on nonlinear problems on sound generation. Prog. Aerosp. Sci. **40**, 345–416 (2004)

241. Choi, H., Moin, P.: Effects of the computational time step on numerical solutions of turbulent flows. J. Comput. Phys. **113**, 1–4 (1994)
242. Colonius, T.: Modeling artificial boundary conditions for compressible flows. Annu. Rev. Fluid Mech. **36**, 315–345 (2004)
243. Ekaterinaris, J.A.: High-order accurate, low numerical diffusion methods for aerodynamics. Prog. Aerosp. Sci. **41**, 192–300 (2005)
244. Ferziger, J.H., Perić, M.: Computational Methods for Fluid Dynamics. Springer, Berlin (1996)
245. Hirsch C.: Numerical computation of internal and external flows. Fundamentals of Computational Fluid Dynamics, vol. 1, 2nd edn. Butterworth-Heinemann, Oxford (2007)
246. Hirsch C.: Numerical computation of internal and external flows. Computational Methods for Inviscid and Viscous Flows, vol. 2, 2nd edn. Butterworth-Heinemann, Oxford (2007)
247. Koomey, J.G., Berard, S., Sanchez, M., Wong, H.: Implications of historical trends in the electrical efficiency of computing. IEEE Annu. Hist. Comput. **33**(3), 46–54 (2011)
248. Lele, S.K.: Compact finite difference schemes with spectral-like resolution. J. Comput. Phys. **103**(1), 16–42 (1992)
249. Lele, S.K.: Computational aeroacoustics: a review. AIAA Paper 97 0018 (1997)
250. Lumley, J.L.: Computational modeling of turbulent flows. Adv. Appl. Mech. **18**, 123–176 (1978)
251. Mahesh, K., Lele, S.K., Moin, P.: The influence of entropy fluctuations on the interaction of turbulence with a shock wave. J. Fluid Mech. **334**, 353–379 (1997)
252. Moin, P., Mahesh, K.: Direct numerical simulation: a tool in turbulence research. Annu. Rev. Fluid Mech. **30**, 539–578 (1998)
253. Moore, G.E.: Cramming more components onto integrated circuits. Electronics **38**(8), 114–117 (1965)
254. Nordhaus, W.D.: Two centuries of productivity growth in computing. J. Econ. Hist. **67**(1), 128–159 (2007)
255. Orszag, S.A.: Numerical methods for the simulation of turbulence. Phys. Fluids **12**(Supplement II), 250–257 (1969)
256. Orszag, S.A.: Analytical theories of turbulence. J. Fluid Mech. **41**(2), 363–386 (1970)
257. Pirozzoli, S.: Numerical methods for high-speed flows. Annu. Rev. Fluid Mech. **43**, 163–194 (2011)
258. The top 500 computer sites. http://www.top500.org/
259. Rai, M.M., Moin, P.: Direct simulations of turbulent flow using finite-difference schemes. J. Comput. Phys. **96**, 15–53 (1991)
260. Reynolds, W.C.: The potential and limitations of direct and large eddy simulations. In: Lumley, J.L. (ed.) Whither turbulence ? turbulence at the Crossroads, pp. 313–343. Berlin, Lectures notes in Physics, Springer (1990)
261. Reynolds, W.C.: Computation of turbulent flows. Annu. Rev. Fluid Mech. **8**, 183–208 (1976)
262. Spalart, P.R., Moser, R.D., Rogers, M.M.: Spectral methods for the Navier-Stokes equations with one infinite and two periodic directions. J. Comput. Physics **96**, 297–324 (1991)
263. Tam, C.K.W.: Computational aeroacoustics: an overview of challenges and applications. Int. Journal Comput. Fluid Dyn. **18**, 547–567 (2004)

Large Eddy Simulation

264. Akhavan, R., Kang, S., Mangiavacchi, N.: Subgrid-scale interactions in a numerically simulated planar turbulent jet and implications for modelling. J. Fluid Mech. **408**, 83–120 (2000)
265. Akselvoll, K., Moin, P.: Large-eddy simulation of turbulent confined coannular jets. J. Fluid Mech. **315**, 387–411 (1996)
266. Balaras, E., Benocci, C., Piomelli, U.: Two-layer approximate boundary conditions for large-eddy simulations. AIAA J. **34**(6), 1111–1119 (1996)

267. Bardina, J., Ferziger, J.H., Reynolds, W.C.: Improved subgrid scale models for large eddy simulation. AIAA Paper 80–1357 (1980)
268. Bardina, J., Ferziger, J.H., Rogallo, R.S.: Effect of rotation on isotropic turbulence: computation and modelling. J. Fluid Mech. **154**, 321–336 (1985)
269. Berland, J., Bogey, C., Bailly, C.: A study of differentiation errors in large-eddy simulations based on EDQNM theory. J. Comput. Phys. **227**(18), 8314–8340 (2008)
270. Berland, J., Bogey, C., Bailly, C.: Investigation using statistical closure theory of the influence of the filter shape on scale separation in large-eddy-simulations. J. Turbul. **9**(21), 1–22 (2008)
271. Berland, J., Lafon, P., Daude, F., Crouzet, F., Bogey, C., Bailly, C.: Filter shape dependence and effective scale separation in large-eddy simulations based on relaxation filtering. Comput. Fluids **47**(1), 65–74 (2011)
272. Bertoglio, J.P.: Etude d'une turbulence anisotrope: modélisation de sous-maille et approche statistique. thèse d'État, Université Claude Bernard, Lyon I (1986)
273. Boersma, B.J., Lele, S.K.: Large eddy simulation of a Mach 0.9 turbulent jet, AIAA Paper 99–1874 (1999)
274. Bhat, G.S., Narasimha, R.: A volumetrically heated jet: large-eddy structure and entrainment characteristics. J. Fluid Mech. **325**, 303–330 (1996)
275. Bogey, C., Bailly, C.: LES of a high Reynolds high subsonic jet: effects of the subgrid scale modellings on flow and noise. AIAA Paper 2003–3557 (2003)
276. Bogey, C., Bailly, C.: Effects of inflow conditions and forcing on subsonic jet flows and noise. AIAA J. **43**(5), 1000–1007 (2005)
277. Bogey, C., Bailly, C.: Decrease of the effective Reynolds number with eddy-viscosity subgrid-scale modeling. AIAA J. **43**(2), 437–439 (2005)
278. Bogey, C., Bailly, C.: Large eddy simulations of transitional round jets: Influence of the Reynolds number on flow development and energy dissipation. Phys. Fluids **18**(065101), 1–14 (2006)
279. Bogey, C., Bailly, C.: Large eddy simulations of round free jets using explicit filtering with/without dynamic Smagorinsy model. Int. J. Heat Fluid Flow **27**, 603–610 (2006)
280. Bogey, C., Bailly, C.: Turbulence and energy budget in a self-preserving round jet: direct evaluation using large-eddy simulation. J. Fluid Mech. **627**, 129–160 (2009)
281. Boris, J.P., Grinstein, F.F., Oran, E.S., Kolbe, R.L.: New insights into large eddy simulation. Fluid Dyn. Res. **10**, 199–228 (1992)
282. Choi, H., Moin, P.: Grid-point requirements for large eddy simulation: Chapman's estimates revisited. Phys. Fluids **24**(011702), 1–5 (2012)
283. Chollet, J.P., Lesieur, M.: Parameterization of small scales of three-dimensional isotropic turbulence utilizing spectral closures. J. Atmos. Sci. **38**, 2747–2757 (1981)
284. Comte, P., Ducros, F., Silvestrini, J., David, E., Lamballais, E., Métais, O., Lesieur, M.: Simulation des grandes échelles d'écoulements transitionnels. AGARD conference proceedings 551, application of direct and large simulation to transition and turbulence, 14–1–14–12 (1994)
285. Dantinne, G., Jeanmart, H., Winckelmans, G.S., Legat, V., Carati, D.: Hyperviscosity and vorticity-based models for subgrid scale modeling. Appl. Sci. Res. **59**, 409–420 (1998)
286. Deardorff, J.W.: A numerical study of three-dimensional turbulent channel flow at large Reynolds numbers. J. Fluid Mech. **41**(2), 453–480 (1970)
287. Domaradzki, J.A.: Large eddy simulations without explicit eddy viscosity models. Int. J. Comput. Fluid Dyn. **24**(10), 435–447 (2010)
288. Domaradzki, J.A., Adams, N.A.: Direct modelling of subgrid scales of turbulence in large eddy simulations. J. Turbul. **3**(024), 1–19 (2002)
289. Domaradzki, J.A., Yee, P.P.: The subgrid-scale estimation model for high Reynolds number turbulence. Phys. Fluids **12**(1), 193–196 (2000)
290. Ducros, F., Comte, P., Lesieur, M.: Large-eddy simulation of transition to turbulence in a boundary layer developing spatially over a flat plate. J. Fluid Mech. **326**, 1–36 (1996)
291. Duprat, C., Balarac, G., Métais, O., Congedo, P.M., Brugière, O.: A wall-layer model for large-eddy simulations of turbulent flows with/out pressure gradient. Phys. Fluids **23**(015101), 1–12 (2011)

292. Erlebacher, G., Hussaini, M.Y., Speziale, C.G., Zang, T.A.: Toward the large-eddy simulation of compressible turbulent flows. J. Fluid Mech. **238**, 155–185 (1992)
293. Fauconnier, D., Bogey, C., Dick, E.: On the performance of relaxation filtering for large-eddy simulation. J. Turbul. **14**(1), 22–49 (2013)
294. Flohr, P., Balaras, E.: Large eddy simulation of a turbulent boundary layer. Von Kármán Institute, Rhode Saint Genèse, Technical Note 187 (1995)
295. Gaitonde, D.V., Visbal, M.R.: Padé-type higer-order boundary filters for the Navier-Stokes equations. AIAA J. **38**(11), 2103–2112 (2000)
296. Germano, M.: A proposal for a redefinition of the turbulent stresses in the filtered Navier-Stokes equations. Phys. Fluids **29**(7), 2323–2324 (1986)
297. Germano, M.: Turbulence: the filtering approach. J. Fluid Mech. **238**, 325–336 (1992)
298. Germano, M.: A statistical formulation of the dynamic model. Phys. Fluids **8**(2), 565–570 (1996)
299. Germano, M.: A new deconvolution method for large-eddy simulation. Phys. Fluids **21**(045107), 1–3 (2009)
300. Germano, M., Piomelli, U., Moin, P., Cabot, W.H.: A dynamic subgrid-scale eddy viscosity model. Phys. Fluids A *3*(7), 1760–1765. Erratum in *3*(12), 3128 (1991)
301. Ghosal, S.: An Analysis of numerical errors in large-eddy simulations of turbulence. J. Comput. Phys. **125**, 187–206 (1996)
302. Ghosal, S.: Mathematical and physical constraints on large eddy simulation of turbulence. AIAA J. **37**(4), 425–433 (1999)
303. Ghosal, S., Moin, P.: The basic equations for the large eddy simulation of turbulent flows in complex geometry. J. Comput. Phys. **118**(1), 24–37 (1995)
304. Horiuti, K.: The role of the Bardina model in large eddy simulation of turbulent channel flow. Phys. Fluids A **1**(2), 426–428 (1989)
305. Huai, X., Joslin, R.D., Piomelli, U.: Large eddy simulation of transition to turbulence in boundary layers. Theoret. Comput. Fluid Dyn. **9**, 149–163 (1997)
306. Jiménez, J., Moser, R.D.: Large-eddy simulations: where are we and what can we Expect? AIAA J. **38**(4), 605–612 (2000)
307. Kannepalli, C., Piomelli, U.: 2000, Large-eddy simulation of a three-dimensional shear-driven turbulent boundary layer. J. Fluid Mech. **423**, 175–203 (2000)
308. Kawai, S., Larsson, J.: Wall-modeling in large eddy simulation: length scales, grid resolution and accuracy. Phys. Fluids 24(1), 015105, 1–10 (2012)
309. Kosović, B.: Subgrid-scale modelling for the large-eddy simulation of high-Reynolds-number boundary layers. J. Fluid Mech. **336**, 151–182 (1997)
310. Kuerten, J.G.M., Geurts, B.J., Vreman, A.W., Germano, M.: Dynamic inverse modeling and its testing in large-eddy simulations of the mixing noise. Phys. Fluids **11**(12), 3778–3785 (1999)
311. Lenormand, E., Sagaut, P.: Ta Phuoc, L., Comte, P.: Subgrid-scale models for large-eddy simulations of compressible wall bounded flows. AIAA J. **38**(8), 1340–1350 (2000)
312. Leonard, A.: Energy cascade in large-eddy simulations of turbulent fluid flows. Adv. Geophys. A **18**, 237–248 (1974)
313. Lesieur, M.: Looking for turbulence structures: a numerical exploration. Flow, Turbul. Combust. **66**, 477–494 (2001)
314. Lesieur, M., Métais, O.: New trends in large-eddy simulations of turbulence. Annu. Rev. Fluid Mech. **28**, 45–82 (1996)
315. Lesieur, M., Comte, P., Métais, O.: Numerical simulations of coherent vortices in turbulence. Appl. Mech. Rev. **48**(3), 121–149 (1995)
316. Lilly, D.K.: A proposed modification on the Germano subgrid-scale closure method. Phys. Fluid A **4**(3), 633–635 (1992)
317. Liu, S., Meneveau, C., Katz, J.: On the properties of similarity subgrid-scale models as deduced from measurements in a turbulent jet. J. Fluid Mech. **275**, 83–119 (1994)
318. Lund, T.S.: The use of explicit filters in large eddy simulation. Comput. Math. Appl. **46**, 603–616 (2003)

319. Meneveau, C.: Germano identity-based subgrid-scale modeling: a brief survey of variations on a fertile theme. Phys. Fluids **24**(121301), 1–14 (2012)
320. Meneveau, C., Katz, J.: Scale-Invariance and turbulence models for large-eddy simulation. Annu. Rev. Fluid Mech. **32**, 1–32 (2000)
321. Métais, O., Lesieur, M.: Spectral large-eddy simulation of isotropic and stably stratified turbulence. J. Fluid Mech. **239**, 157–194 (1992)
322. Meyers, J., Sagaut, P.: On the model coefficients for the standard and the variational multi-scale Smagorinsky model. J. Fluid Mech. **569**, 287–319 (2006)
323. Moin, P., Squires, K., Cabot, W., Lee, S.: A dynamic subgrid-scale model for compressible turbulence and scalar transport. Phys. Fluids A **3**(11), 2746–2757 (1991)
324. Morris, P.J., Long, L.N., Scheidegger, T.E., Boluriaan, S.: Simulations of supersonic jet noise. Int. J. Aeroacoustics **1**(1), 17–41 (2002)
325. Muschinski, A.: A Similarity theory of locally homogeneous and isotropic turbulence generated by a Smagorinski-type LES. J. Fluid Mech. **325**, 239–260 (1996)
326. Najjar, F.M., Tafti, D.K.: Study of discrete test filters and finite difference approximations for the dynamic subgrid-scale stress model. Phys. Fluids **8**(4), 1076–1088 (1996)
327. Neto, A.S., Grand, D., Métais, O., Lesieur, M.: A numerical investigation of the coherent vortices in turbulence behind a backward-facing step. J. Fluid Mech. **256**, 1–25 (1993)
328. Olsson, M., Fuchs, L.: Large eddy simulation of the proximal region of a spatially developing circular jet. Phys. Fluids **8**(8), 2125–2137 (1996)
329. O'Neil, J., Meneveau, C.: Subgrid-scale stresses and their modelling in a turbulent plane wake. J. Fluid Mech. **349**, 253–293 (1997)
330. Pasquetti, R.: Spectral vanishing viscosity method for large eddy simulation of turbulent flows. J. Sci. Comput. **27**, 365–375 (2006)
331. Piomelli, U., Ferziger, J., Moin, P.: New approximate boundary conditions for large eddy simulations of wall-bounded flows. Phys. Fluids A **1**(6), 1061–1068 (1989)
332. Porter, D.H., Woodwrad, P.R., Pouquet, A.: Inertial Range structures in decaying compressible turbulent flows. Phys. Fluids **10**(1), 237–245 (1998)
333. Pruett, D.C.: Eulerian time-domain filtering for spatial large-eddy simulation. AIAA J. **38**(9), 1634–1642 (2000)
334. Pruett, D.C.: Toward the de-mystification of LES. Third AFOSR international conference on direct numerical simulation and large eddy simulation (TAICDL), University of Texas, 1–8 (2001)
335. Pruett, C.D., Sochacki, J.S.: On Taylor-series expansions of residual stress. Phys. Fluids **13**(9), 1578–2589 (2001)
336. Pruett, C.D., Thomas, B.C., Grosch, C.E., Gatski, T.B.: A Temporal Approximate Deconvolution model for large-eddy simulation. Phys. Fluids **18**(028104), 1–4 (2006)
337. Rizzetta, D.P., Visbal, M.R., Blaisdell, G.A.: A time-implicit high-order compact differencing and filtering scheme for large-eddy simulation. Int. J. Num. Meth. Fluids **42**, 665–693 (2003)
338. Rodi, W., Ferziger, J.H., Breuer, M., Pourquié, M.: Status of large eddy simulation: results of a workshop. J. Fluids Eng. **119**, 248–262 (1997)
339. Sagaut, P.: Large eddy simulation for imcompressible flows. An introduction, 3rd edn. Springer, Paris (2006)
340. Salvetti, M.V., Banerjee, S.: A priori tests of a new dynamic subgrid-scale model for finite-difference large-eddy simulations. Phys. Fluids **7**(11), 2831–2847 (1995)
341. Schlatter, P., Stoltz, S., Kleiser, L.: LES of transitional flows using the approximate deconvolution model. Int. J. Heat Fluid Flow **25**, 549–558 (2004)
342. Schlatter, P., Stoltz, S., Kleiser, L.: An analysis of the SGS energy budget for deconvolution- and relaxation-based models in channel flow. In: Proceedings of Direct and Large-Eddy Simulation VI, vol. 10, pp. 135–142, Springer, Berlin (2006)
343. Schumann, U.: Subgrid scale model for finite difference simulations of turbulent flows in plane channels and annuli. J. Comput. Phys. **18**, 376–404 (1975)
344. Smagorinsky, J.S.: General circulation experiments with the primitive equations: I. the basic experiment. Mon. Weath. Rev. *91*(3), 99–164 (1963)

345. Speziale, C.G.: Galilean invariance of subgrid-scale stress models in the large-eddy simulation of turbulence. J. Fluid Mech. **156**, 55–62 (1985)
346. Speziale, C.G., Erlebacher, G., Zang, T.A., Hussaini, M.Y.: The subgrid-scale modeling of compressible turbulence. Phys. Fluids **31**(4), 940–942 (1998)
347. Spyropoulos, E.T., Blaisdell, G.A.: Large-eddy simulation of a spatially evolving supersonic turbulent boundary-layer flows. AIAA J. **36**(11), 1983–1990 (1998)
348. Squires, K., Zeman, O.: On the subgrid-scale modeling of compressible turbulence. In: Center for Turbulence Research, Stanford, Proceedings of the Summer Program, pp. 47–59 (1990)
349. Stolz, S., Adams, N.A.: An approximate deconvolution procedure for large-eddy simulation. Phys. Fluids **11**(7), 1699–1701 (1999)
350. Stolz, S., Adams, N.A., Kleiser, L.: An approximate deconvolution procedure for large-eddy simulation with application to incompressible wall-bounded flow. Phys. Fluids **13**(4), 997–1015 (2001)
351. Stolz, S., Adams, N.A., Kleiser, L.: The approximate deconvolution model for large-eddy simulations of compressible flows and its application to shock-turbulent-boundary-layer interaction. Phys. Fluids **13**(10), 2985–3001 (2001)
352. Vasilyev, O.V., Lund, T.S., Moin, P.: A general class of commutative filters for LES in complex geometries. J. Comput. Phys. **146**, 82–104 (1998)
353. Visbal, M.R., Gaitonde, D.V.: High-order-accurate methods for complex unsteady subsonic flows. AIAA J. **37**(10), 1231–1239 (1999)
354. Visbal, M.R., Rizzetta, D.P.: Large-eddy simulation on curvilinear grids using compact differencing and filtering schemes. J. Fluids Eng. **124**, 836–847 (2002)
355. Vreman, B., Geurts, B., Kuerten, H.: Realizability conditions for the turbulent stress Tensor in large-eddy simulation. J. Fluid Mech. **278**, 351–362 (1994)
356. Vreman, B., Geurts, B., Kuerten, H.: Subgrid-modelling in LES of compressible flows. Appl. Sci. Res. **54**, 191–203 (1995)
357. Vreman, B., Geurts, B., Kuerten, H.: Large-eddy simulation of the turbulent mixing layer. J. Fluid Mech. **339**, 357–390 (1997)
358. Woodruff, S.L., Seiner, J.M., Hussaini, M.Y.: Grid-size dependence in the large-eddy simulation of Kolmogorov flows. AIAA J. **38**(4), 600–604 (2000)
359. Yang, K.S., Ferziger, J.H.: Large-eddy simulation of turbulence obstacle flows using a dynamic subgrid-scale model. AIAA J. **31**(8), 1406–1413 (1993)
360. Yoshizawa, A.: Statistical theory for compressible turbulent shear flows, with the application to subgrid modeling. Phys. Fluids **29**(7), 2152–2164 (1986)
361. Yuan, L.L., Street, R.L., Ferziger, J.H.: Large-eddy simulations of a round jet in crossflow. J. Fluid Mech. **379**, 71–104 (1999)
362. Zang, T.A., Dahlburg, R.B., Dahlburg, J.P.: Direct and large-eddy simulations of three-dimensional compressible Navier-Stokes turbulence. Phys. Fluids A **4**(1), 127–140 (1992)
363. Zang, Y., Street, R.L., Koseff, J.R.: A dynamic mixed subgrid-scale model and its application to turbulent recirculating flows. Phys. Fluids **5**, 3186–3196 (1993)

Turbulence Models

364. Baldwin, B.S., Lomax, H.: Thin layer approximation and algebraic model for separated turbulent flows. AIAA Paper 78–257 (1978)
365. Barber, T.J., Chiappetta, L.M., DeBonis, J.R., Georgiadis, N.J., Yoder, D.A.: Assessment of parameters influencing the prediction of shear-layer mixing. J. Propul. Power **15**(1), 45–53 (1999)
366. Bastin, F., Lafon, P., Candel, S.: Computation of jet mixing noise due to coherent structures: the plane jet case. J. Fluid Mech. **335**, 261–304 (1997)

367. Bertoglio, J.-P., Bataille, F., Marion, J.-D.: Two-point closure for weakly compressible turbulence. Phys. Fluids **13**(1), 290–310 (2001)
368. Bos, W.J.T., Chevillard, L., Scott, J., Rubinstein, R.: Reynolds number effect on the velocity increment skewness in isotropic turbulence. Phys. Fluids **24**(015108), 1–21 (2012)
369. Catris, S., Aupoix, B.: Density correlations for turbulence models. Aerosp. Sci. Technol. **4**, 1–11 (2000)
370. Cebeci, T., Smith, A.M.O.: Analysis of turbulent boundary layers. In: Applied Mathematics and Mechanics, vol. 18. Academic Press, New York (1974)
371. Cecora, R.-D., Eisfeld, B., Probst, A., Crippa, S., Radespiel, R.: Differential reynolds stress modeling for aeronautics. AIAA Paper 2012–0465 (2012)
372. Celić, A., Hirschel, E.H.: Comparison of eddy-viscosity turbulence models in flows with adverse pressure gradient. AIAA J. **44**(10), 2156–2169 (2006)
373. Chassaing, P., Anselmet, F., Joly, L., Sarkar, S.: Variable density fluid turbulence. Kluwer Academic Publishers, Dordrecht (2002)
374. Chien, K.Y.: Predictions of channel and boundary-layer flows with a Low-Reynolds turbulence model. AIAA J. **20**(1), 33–38 (1982)
375. Dash, S.M., Sinha, N., Kenzakowski, D.C.: The critical role of turbulence modeling in the predictions of supersonic jet structure for acoustic applications. AIAA Paper 92–02-206 (1992)
376. Dash, S.M., Kenzakowski, D.C., Seiner, J.M., Bhat, T.R.S.: Recent advances in jet flowfield simulation: Part I - Steady flows, AIAA Paper 93–4390, Part II - Unsteady flows, AIAA Paper 93–4391 (1993)
377. Dash, S.M., Kenzakowski, D.C., Sinha, N., Hosangadi, A.: Simulation of high-speed jets: turbulence and two-phase flows modeling. AIAA Paper 92–3440 (1992)
378. Du Vachat, R.: Realizability inequalities in turbulent flows. Phys. Fluids **20**(4), 551–556 (1977)
379. Durbin, P.A.: Near-Wall turbulence closure modeling without damping functions. Theoret. Comput. Fluid Dyn. **3**, 1–13 (1991)
380. Durbin, P.A.: On the $k-\epsilon$ stagnation point anomaly. Int. J. Heat Fluid Flow **17**, 89–90 (1996)
381. Emami, B., Bussmann, M., Tran, H.: Application of realizability and shock unsteadiness to $k-\epsilon$ simulations of under-expanded supersonic free jets. J. Fluids Eng. **132**(041104), 1–7 (2010)
382. Favre, A.: Équations des gaz turbulents compressibles (I) et (II). Journal de Mécanique 4(3), 361–390, 4(4), 391–421 (1965)
383. Gatski, T.B., Speziale, C.G.: On explicit algebraic stress models for complex turbulent flows. J. Fluid Mech. **254**, 59–78 (1993)
384. Gatski, T.B., Bonnet, J.P.: Compressibility, turbulence and high speed flow. Elsevier, Paris (2009)
385. Hanjalić, K.: One-point closure models for buoyancy-driven turbulent flows. Annu. Rev. Fluid Mech. **34**, 321–347 (2002)
386. Hanjalić, K., Launder, B.E.: A Reynolds stress model of turbulence and its application to thin shear flows. J. Fluid Mech. **52**(4), 609–638 (1972)
387. Hanjalić, K., Launder, B.E.: Contribution towards a Reynolds-stress closure for low-Reynolds-number turbulence. J. Fluid Mech. **74**(4), 593–610 (1976)
388. Hussain, A.K.M.F.: Coherent structures—reality and myth. Phys. Fluids **26**(10), 2816–2850 (1983)
389. Iaccarino, G., Ooi, A., Durbin, P.A., Behnia, M.: Reynolds averaged simulation of unsteady separated flow. Int. J. Heat Fluid Flow **24**, 147–156 (2003)
390. Jakirlić, S., Hanjalić, K.: A new approach to modelling near-wall turbulence energy and stress dissipation. J. Fluid Mech. **459**, 139–166 (2002)
391. Jones, W.P.: Models for turbulent flows with variable density and combustion. In: Prediction methods for turbulent flows, Lecture series 1979–2, von Kármán Institute for Fluid Dynamics, Rhode Saint Genèse (1979)
392. Jones, W.P., Launder, B.E.: The prediction of laminarization with a two-equation model of turbulence. Int. J. Heat Mass Transf. **15**, 301–314 (1972)

393. Kourta, A., Ha Minh, H.: Modified turbulence model to predict unsteady separated flows. 7th International Conference on Numerical Methods in Laminar and Turbulent Flows, Stanford (1991)
394. Knight, D.D.: Numerical simulation of compressible turbulent flows using the Reynolds-averaged Navier-Stokes equation. In: Turbulence in compressible flows, AGARD Report 819 (1997)
395. Kok, J.C.: Resolving the dependence on freestream values for the $k-\omega$ turbulence model. AIAA J. **38**(7), 1292–1295 (2000)
396. Kolmogorov, A.N.: Equations of turbulent motion of an incompressible fluid. Izvestia Acad. Sci. USSR Phys. **6**(1–2), 56–58 (1942)
397. Krishnamurty, V.S., Shyy, W.: Study of compressibility modifications to the $k-\epsilon$ model. Phys. Fluids *9*(9), 2769–2788 (1997). See also erratum, *9*(12), 3938
398. Lakshmanan, B., Abdol-Hamid, K.S.: Investigation of supersonic jet plumes using an improved two-equation turbulence model. J. Propul. Power **10**(5), 736–741 (1994)
399. Launder, B.E.: Second-moment closure: present and future? Int. J. Heat Fluid Flow **10**(4), 282–300 (1989)
400. Launder, B.E., Sharma, B.I.: Application of the energy-dissipation model of turbulence to the calculation of flows near a spinning disc. Lett. Heat Mass Transf. **1**, 131–138 (1974)
401. Launder, B.E., Spalding, D.B.: The numerical computation of turbulent flows. Comput. Methods Appl. Mech. Eng. **3**(2), 269–289 (1974)
402. Launder, B.E., Reynolds, W.C., Rodi, W.: Turbulence models and their applications. CEA-EDF-INRIA, vol. 56, Eyrolles, Paris (1984)
403. Lebrère, L., Buffat, M., Le Penven, L., Dillies, B.: Application of Reynolds stress modeling to engine flow calculation. J. Fluids Eng. **118**, 710–721 (1996)
404. Lee, J., Taulbee, D.B., Holden, M.S.: Study of turbulence on supersonic compression surfaces using Reynolds stress model. AIAA J. **30**(7), 1738–1746 (1992)
405. Lilly, D.K.: A comparison of incompressible, anelastic and Boussinesq dynamics. Atmos. Res. **40**, 143–151 (1996)
406. Malin, M.R.: Prediction of radially spreading turbulent jets. AIAA J. **26**(6), 750–752 (1988)
407. Mathieu, J., Jeandel, D.: La simulation des modèles de turbulence et leurs applications. CEA-EDF-INRIA, vol. 55. Eyrolles, Paris (1984)
408. Menter, F.R.: Influence of freestream values on $k-\omega$ turbulence model predictions. AIAA J. **30**(6), 1657–1659 (1992)
409. Menter, F.R.: Performance of popular turbulence models for attached and separated adverse pressure gradient flows. AIAA J. **30**(8), 2066–2072 (1992)
410. Menter, F.R.: Two-equation eddy-viscosity turbulence models for engineering applications. AIAA J. **32**(8), 1598–1605 (1994)
411. Menter, F.R.: Eddy viscosity transport equations and their relation to the $k-\epsilon$ model. J. Fluids Eng. **119**, 876–884 (1997)
412. Menter, F.R., Langtry, R., Völker, S.: Transition modelling for general purpose CFD codes. Flow Turbul. Combust. **77**, 277–303 (2006)
413. Papamoschou, D., Debiasi, M.: Noise measurements in supersonic jets treated with the Mach wave elimination method. AIAA J. **37**(2), 154–160 (1999)
414. Patel, V.C., Scheuerer, G.: Calculation of two-dimensional near and far wakes. AIAA J. **20**(7), 900–907 (1982)
415. Patel, V.C., Rodi, W., Scheuerer, G.: Turbulence models for near-wall and low Reynolds number flows: a review. AIAA J. **23**(9), 1308–1319 (1985)
416. Piellard, M., Bailly, C.: Validation of a hybrid CAA method. Application to the case of a ducted diaphragm at low Mach number. AIAA Paper 2008–2873 (2008)
417. Pollard, A., Martinuzzi, R.: Comparative study of turbulence models in predicting turbulent pipe flow, Part II: Reynolds stress and $k-\epsilon$ models. AIAA J. **27**(12), 1714–1721 (1989)
418. Pope, S.B.: An explanation of the turbulent round-jet/plane-jet anomaly. AIAA J. **16**(3), 279–281 (1978)

419. Rhee, G.H., Sung, H.J.: Generation of inflow conditions in a Reynolds-averaged Navier-Stokes closure. AIAA J. **38**(3), 545–547 (2000)
420. Rubel, A.: On the vortex stretching modification of the $k-\epsilon$ turbulence model: radial jets. AIAA J. **23**(7), 1129–1130 (1995)
421. Rumsey, C.L.: Compressibility considerations for $k-\omega$ turbulence models in hypersonic boundary-layer applications. J. Spacecraft Rockets **47**(1), 11–20 (2010)
422. Sarkar, S., Erlebacher, G., Hussaini, M.Y., Kreiss, H.O.: The analysis and modelling of dilatational terms in compressible turbulence. J. Fluid Mech. **227**, 473–493 (1991)
423. Sarkar, S., Balakrishnan, L.: Application of a Reynolds stress turbulence model to the compressible shear layer. AIAA J. **29**(5), 743–749 (1991)
424. Sarkar, S.: The pressure-dilatation correlation in compressible flows. Phys. Fluids A **4**(12), 2674–2682 (1992)
425. Schiestel, R.: Multiple-time-scale modeling of turbulent flows in one point closures. Phys. Fluids **30**(3), 722–731 (1987)
426. Schiestel, R.: Modeling and simulation of turbulent flows. Wiley-ISTE, London (2008)
427. Schumann, U.: Realizability of Reynolds-stress turbulence models. Phys. Fluids **20**(5), 721–725 (1977)
428. Sinha, K., Balasridhar, S.J.: Conservative formulation of the $k-\epsilon$ turbulence model for shock - turbulence interaction. AIAA J. **51**(8), 1872–1882 (2013)
429. Sinha, K., Candler, G.V.: Turbulent dissipation-rate equation for compressible flows. AIAA J. **41**(6), 1017–1021 (2003)
430. Spalart, P.R.: Strategies for turbulence modelling and simulations. Int. J. Heat and Fluid Flow **21**, 252–263 (2000)
431. Spalart, P.R., Allmaras, S.R.: A One-Equation turbulence model for Aerodynamic flows. AIAA Paper 92–0439 (1992)
432. Spalart, P.R., Rumsey, C.L.: Effective inflow conditions for turbulence models in aerodynamic calculations. AIAA J. **45**(10), 2544–2553 (2007)
433. Spalding, D.B.: Kolmogorov's two-equation model of turbulence. Proc. Roy. Soc. Lond. A **434**, 211–216 (1991)
434. Speziale, C.G.: Invariance of turbulence closure models. Phys. Fluids **22**(6), 1033–1037 (1979)
435. Speziale, C.G.: Turbulence modeling for time-dependent RANS and VLES: a review. AIAA Journal **36**(2), 173–184 (1998)
436. Speziale, C.G., Gatski, T.B.: Analysis and modelling of anisotropies in the dissipation rate of turbulence. J. Fluid Mech. **344**, 155–180 (1997)
437. Speziale, C.G., Sarkar, S., Gatski, T.B.: Modeling the pressure-strain correlation of turbulence: an invariant dynamical systems approach. J. Fluid Mech. **227**, 245–272 (1991)
438. Tam, C.K.W., Ganesan, A.: Modified $k-\epsilon$ turbulence model for calculating hot jet mean flows and noise. AIAA J. **42**(1), 26–34 (2004)
439. Thies, A.T., Tam, C.K.W.: Computation of turbulent axisymmetric and nonaxisymmetric jet flows using the $k-\epsilon$ model. AIAA J. **34**(2), 309–316 (1996)
440. Turpin, G., Troyes, J.: Validation of a two-equation turbulence model for axisymmetric reacting and non-reacting flows. AIAA Paper 2000–3463 (2000)
441. Van Driest, E.R.: Turbulent boundary layer in compressible fluids. J. Aero. Sci. **18**(3), 145–160, 216 (1951)
442. Van Driest, E.R.: On turbulent flows near a wall. J. Aero. Sci. **23**, 1007–1011 (1956)
443. Vandromme, D.: Turbulence modeling for compressible flows and implementation in Navier-Stokes solvers. In: Introduction to the modeling of turbulence, Lecture Series 1993–02, Feb. 08–11, von Kármán Institute for Fluid Dynamics, Rhode Saint Genèse (1993)
444. Vandromme, D., Zeman, O.: Response of a supersonic boundary layer to a compression Corner, pp. 247–258. Proccedings of Center for Turbulence Research, Stanford (1992)
445. Visbal, M., Knight, D.: The Baldwin-Lomax turbulence model for two-dimensional shock-wave/boundary-layer interactions. AIAA J. **22**(7), 921–928 (1984)

446. Wilcox, D.C.: Reassessment of the scale-determining equation for advanced turbulence models. AIAA J. **26**(11), 1299–1310 (1988)
447. Wilcox, D.C.: Multiscale model for turbulent flows. AIAA J. **26**(11), 1311–1320 (1988)
448. Wilcox, D.C.: Dilatation-dissipation corrections for advanced turbulence models. AIAA J. **30**(11), 2639–2646 (1992)
449. Wilcox, D.C.: Turbulence modeling for CFD. DCW Industries, California, USA (2006)
450. Wilcox, D.C.: Formulation of the $k - \omega$ turbulence model revisited. AIAA J. **46**(11), 2823–2838 (2008)
451. Yakhot, V., Orszag, S.A., Yakhot, A.: Heat transfer in turbulent fluids-I. pipe flow. Int. J. Heat Mass Transf. **30**(1), 15–22 (1987)
452. Yakhot, V., Orszag, S.A., Thangam, S., Gatski, T.B., Speziale, C.G.: Development of turbulence for shear flows by a double expansion technique. Phys. Fluids A **4**(7), 1510–1520 (1992)
453. Yang, Z., Shih, T.H.: New time scale Based $k - \epsilon$ model for near-wall turbulence. AIAA Journal **31**(7), 1191–1198 (1993)
454. Zeman, O.: Dilatation-dissipation: the concept and application in modeling compressible mixing layers. Phys. Fluids A **2**(2), 178–188 (1990)
455. Zeman, O.: On the decay of compressible isotropic turbulence. Phys. Fluids A **3**(5), 951–955 (1991)
456. Zeman, O.: A new model for Super/Hypersonic turbulent boundary layers. AIAA Paper 93–0897 (1993)
457. Zeman, O., Blaisdell, G.A.: New Physics and models for compressible turbulent flows. In: Johansson, A.V., Alfredsson, P.H. (eds.) Advances in turbulence, vol. 3, pp. 445–454. Springer, Berlin (1991)

Usual Turbulent Flows

Turbulence Box

458. Chen, S., Shan, X.: High-resolution turbulence simulations using the connection machine-2. Comput. Phys. **6**(6), 643–646 (1992)
459. Eswaran, V., Pope, S.B.: An examination of forcing in direct numerical simulations of turbulence. Comput. Fluids **16**(3), 257–278 (1988)
460. Hussaini, M.Y., Zang, T.A.: Spectral methods in fluid mechanics. Annu. Rev. Fluid Mech. **19**, 339–367 (1987)
461. Orszag, S.A., Patterson, G.S.: Numerical simulation of three-dimensional homogeneous isotropic turbulence. Phys. Rev. Lett. **28**(2), 76–79 (1972)
462. Overholt, M.R., Pope, S.B.: A deterministic forcing scheme for direct numerical simulations of turbulence. Comput. Fluids **27**(1), 11–28 (1998)
463. Passot, T., Politano, H., Sulem, P.L., Angilella, J.R., Meneguzzi, M.: Instability of strained vortex layers and vortex tube formation in homogeneous turbulence. J. Fluid Mech. **282**, 313–338 (1995)
464. Patterson, G.S., Orszag, S.A.: Spectral calculations of isotropic turbulence: efficient removal of aliasing interactions. Phys. Fluids **14**, 2538–2541 (1971)
465. Rogallo, R.S.: Numerical experiments in homogeneous turbulence. NASA TM 81315 (1981)
466. Rogallo, R.S., Moin, P.: Numerical simulation of turbulent flows. Annu. Rev. Fluid Mech. **16**, 99–137 (1984)
467. Vincent, A., Meneguzzi, M.: The spatial structure and statistical properties of homogeneous turbulence. J. Fluid Mech. **225**, 1–20 (1991)
468. Vincent, A., Meneguzzi, M.: The dynamics of vorticity tubes in homogeneous turbulence. J. Fluid Mech. **258**, 245–254 (1994)

Mixing Layers and Vortices

469. Berson, A., Michard, M., Blanc-Benon, P.: Vortex identification and tracking in unsteady flows. C. R. Mécanique, Acad. Sci. Paris, **337**, 61–67 (2009)
470. Bogey, C., Bailly, C., Juvé, D.: Numerical simulation of the sound generated by vortex pairing in a mixing layer. AIAA J. **38**(12), 2210–2218 (2000)
471. Bradshaw, P., Koh, Y.M.: A note on Poisson's equation for pressure in a turbulent flow. Phys. Fluids **24**(4), 777 (1981)
472. Browand, F.K., Ho, C.-M.: The mixing-layer: an example of quasi two-dimensional turbulence, pp. 99–120. Journal de Mécanique Théorique et Appliquée, Special issue (1983)
473. Brown, G.L., Rosko, A.: The effect of density difference on the turbulent mixing layer. In: Turbulent shear flows, AGARD-CP-93, 23–1 23–12 (1971)
474. Brown, G.L., Rosko, A.: On density effects and large structure in turbulent mixing layers. J. Fluid Mech. **64**(4), 775–816 (1974)
475. Chong, M.S., Perry, A.E., Cantwell, B.J.: A general classification of three-dimensional flow fields. Phys. Fluids A **2**(5), 765–777 (1990)
476. Cohen, J., Marasli, B., Levinski, V.: The interaction between the mean flow and coherent structures in turbulent mixing layers. J. Fluid Mech. **260**, 81–94 (1994)
477. Corcos, G.M., Lin, S.J.: The mixing layer: deterministic models of a turbulent flow. Part 2. The origin of the three-dimensional motion. J. Fluid Mech. **139**, 67–95 (1984)
478. Corcos, G.M., Sherman, F.S.: The mixing layer: deterministic models of a turbulent flow. Part 1. Introduction and the two-dimensional flow. J. Fluid Mech. **139**, 29–65 (1984)
479. Dimotakis, P.E., Brown, G.L.: The mixing layer at high Reynolds number: large-structure dynamics and entrainment. J. Fluid Mech. **78**(3), 535–560 (1976)
480. Foss, J.K., Zaman, K.B.M.Q.: Large and small scale vortical motions in a shear layer perturbed by tabs. J. Fluid Mech. **382**, 207–329 (1999)
481. Graftieaux, L., Michard, M., Grosjean, N.: Combining PIV, POD and vortex identification algorithms for the study of unsteady turbulent swirling flows. Meas. Sci. Technol. **12**, 1422–1429 (2001)
482. Haller, G.: An objective definition of a vortex. J. Fluid Mech. **525**, 1–26 (2005)
483. Ho, C.M., Huang, L.S.: Subharmonics and vortex merging in mixing layers. J. Fluid Mech. **119**, 443–473 (1982)
484. Huang, L.S., Ho, C.M.: Small-scale transition in a plane mixing layer. J. Fluid Mech. **210**, 475–500 (1990)
485. Hunt, J.C.R., Wray, A.A., Moin, P.: Eddies, streams, and convergence zones in turbulent flows, pp. 193–208. Center for turbulence Research, Proceedings of the Summer Program (1988)
486. Hussain, A.K.M.F.: Coherent structures and turbulence. J. Fluid Mech. **173**, 303–356 (1986)
487. Jeong, J., Hussain, F.: On the identification of a vortex. J. Fluid Mech. **285**, 69–94 (1995)
488. Moffatt, K.H.: Magnetostatic equilibria and analogous Euler flows of arbitrary complex topology. Part 1. Fundamentals. J. Fluid Mech. **159**, 359–378 (1985)
489. Moffatt, K.H.: The interaction of skewed vortex pairs: a model for blow-up of the Navier-Stokes equations. J. Fluid Mech. **409**, 51–68 (2000)
490. Papamoschou, D., Roshko, A.: The compressible turbulent shear layer: an experimental study. J. Fluid Mech. **197**, 453–477 (1988)
491. Roshko, A.: Structure of turbulent shear flows: a new look. AIAA J. **14**(10), 1349–1357 (1976)
492. Samimy, M., Elliott, G.S.: Effects of compressibility on the characteristics of free shear layers. AIAA J. **28**(3), 439–445 (1990)
493. Slessor, M.D., Bond, C.L., Dimotakis, P.E.: Turbulent shear-layer mixing at high Reynolds numbers: effects of inflow conditions. J. Fluid Mech. **376**, 115–138 (1998)
494. Stanley, S., Sarkar, S.: Simulations of spatially developing two-dimensional shear layers and jets. Theoret. Comput. Fluid Dyn. **9**, 121–147 (1997)
495. Sunyach, M.: Contribution à l'étude des frontières d'écoulements turbulents libres. thèse d'État, Université de Lyon, No. 1971–37 (1971)

496. Wills, J.A.B.: On convection velocities in turbulent shear flows. J. Fluid Mech. **20**(3), 417–432 (1964)
497. Winant, C.D., Browand, F.K.: Vortex pairing: the mechanism of turbulent mixing-layer growth at moderate Reynolds number. J. Fluid Mech. **63**(2), 237–255 (1974)
498. Vreman, A.W., Sandham, N.D., Luo, K.H.: Compressible mixing layer growth rate and turbulence characteristics. J. Fluid Mech. **320**, 235–258 (1996)
499. Wygnanski, I., Oster, D., Fiedler, H., Dziomba, B.: On the perseverance of a quasi-two-dimensional eddy-structure in a turbulent mixing layer. J. Fluid Mech. **93**(2), 325–335 (1979)
500. Zaman, K.B.M.Q., Hussain, A.K.M.F.: Natural large-scale structures in the axisymmetric mixing layer. J. Fluid Mech. **138**, 325–351 (1984)
501. Zeman, O.: Similarity in Supersonic mixing layers. AIAA J. **30**(5), 1277–1283 (1992)

Jets

502. Antonia, R.A., Browne, L.W.B.: The destruction of temperature fluctuations in a turbulent plane jet. J. Fluid Mech. **134**, 67–83 (1983)
503. Antonia, R.A., Mi, J.: Temperature dissipation in a turbulent round jet. J. Fluid Mech. **250**, 531–551 (1993)
504. Antonia, R.A., Van Atta, C.W.: On the correlation between temperature and velocity dissipation fields in a heated turbulent jet. J. Fluid Mech. **67**(2), 273–288 (1975)
505. Antonia, R.A., Browne, L.W.B., Rajagopalan, S., Chambers, A.J.: On the organized motion of a turbulent plane jet. J. Fluid Mech. **134**, 49–66 (1983)
506. Arakeri, V.H., Krothapalli, A., Siddavaram, V., Alkistar, M.B.: Lourenco, L: On the use of microjets to suppress turbulence in a M=0.9 axisymmetric jet. J. Fluid Mech. **490**, 75–98 (2003)
507. Bailly, C., Lafon, P., Candel, S.: Subsonic and supersonic jet noise predictions from statistical source models. AIAA J. **35**(11), 1688–1696 (1997)
508. Bickley, W.G.: The plane jet. Philos. Mag. **7**(23), 727–731 (1937)
509. Bogey, C., Bailly, C.: Large eddy simulations of transitional round jets: influence of the Reynolds number on flow development and energy dissipation. Phys. Fluids **18**(065101), 1–14 (2006)
510. Bogey, C., Bailly, C.: Computation of a High-Reynolds number jet and its radiated noise using large eddy simulation based on explicit filtering. Comput. Fluids **35**, 1344–1358 (2006)
511. Bogey, C., Bailly, C.: An analysis of the correlations between the turbulent flow and the sound pressure field of turbulent jets. J. Fluid Mech. **583**, 71–97 (2007)
512. Bogey, C., Bailly, C.: Turbulence and energy budget in a self-preserving round jet: direct evaluation using large-eddy simulation. J. Fluid Mech. **627**, 129–160 (2009)
513. Bogey, C., Bailly, C.: Influence of nozzle-exit boundary-layer conditions on the flow and acoustic fields of initially laminar jets. J. Fluid Mech. **663**, 507–538 (2010)
514. Bogey, C., Marsden, O., Bailly, C.: Influence of initial turbulence level on the flow and sound fields of a subsonic jet at a diameter-based Reynolds number of 10^5. J. Fluid Mech. **701**, 352–385 (2012)
515. Bogey, C., Marsden, O.: Identification of the effects of the nozzle-exit boundary-layer thickness and its corresponding Reynolds number in initially highly disturbed subsonic jets. Phys. Fluids **25**(055106), 1–27 (2013)
516. Boersma, B.J., Brethouwer, G., Nieuwstadt, F.T.M.: A numerical investigation on the effect of the inflow conditions on the self-similar region of a round jet. Phys. Fluids **10**(4), 899–909 (1998)
517. Bradbury, L.J.L.S.: The structure of a self-preserving turbulent plane jet. J. Fluid Mech. **23**(1), 31–64 (1965)

518. Bradshaw, P., Ferriss, D.H., Johnson, R.F.: Turbulence in the noise-producing region of a circular jet. J. Fluid Mech. **19**(4), 591–624 (1964)
519. Catrakis, H.J., Dimotakis, P.E.: Mixing in turbulent jets: scalar measures and isosurface geometry. J. Fluid Mech. **317**, 369–406 (1996)
520. Chevray, R., Tutu, N.K.: Intermittency and preferential transport of heat in a round jet. J. Fluid Mech. **88**(1), 133–160 (1978)
521. Corrsin, S., Uberoi, M.S.: Spectra and diffusion in a round turbulent jet. NACA Report 1040 (1951)
522. Crow, S.C., Champagne, F.H.: Orderly structure in jet turbulence. J. Fluid Mech. **48**(3), 547–591 (1971)
523. Darisse, A., Lemay, J., Benzaïssa, A.: LDV measurements of well converged third order moments in the far field of a free turbulent round jet. Exp. Therm. Fluid Sci. **44**, 825–833 (2013)
524. Everitt, K.W., Robins, A.G.: The development and structure of turbulent plane jets. J. Fluid Mech. **88**(3), 563–583 (1978)
525. Fisher, M.J., Davies, P.O.A.L.: Correlation measurements in a non-frozen pattern of turbulence. J. Fluid Mech. **18**(1), 97–116 (1964)
526. Fleury, V.: Superdirectivité, bruit d'appariement et autres contributions au bruit de jet subsonique. Ph.D. Thesis ECL - No. 2006–18 (2006)
527. Fleury, V., Bailly, C., Jondeau, E., Michard, M., Juvé, D.: Space-time correlations in two subsonic jets using dual particle image velocimetry measurements. AIAA J. **46**(10), 2498–2509 (2008)
528. Freund, J.B.: Noise sources in a low-Reynolds-number turbulent jet at Mach 0.9. J. Fluid Mech. **438**, 277–305 (2001)
529. Freymuth, P.: On transition in a separated laminar boundary layer. J. Fluid Mech. **25**(4), 683–704 (1966)
530. George, W.K., Abrahamsson, H., Eriksson, J., Karlsson, R.I., Löfdahl, L., Wosnik, M.: A similarity theory for the turbulent plane wall jet without external stream. J. Fluid Mech. **425**, 367–411 (2000)
531. Gibson, M.M.: Spectra of turbulence in a round jet. J. Fluid Mech. **15**(2), 161–173 (1963)
532. Gutmark, E., Wygnanski, I.: The planar turbulent jet. J. Fluid Mech. **73**(3), 465–495 (1976)
533. Gutmark, E., Parr, T.P., Hanson, D.M., Schadow, K.C.: Coherent and random structure in reacting jets. Exp. Fluids **10**, 147–156 (1990)
534. Heskestad, G.: Hot-wire measurements in a plane turbulent jet. J. Appl. Mech. **32**, 721–734 (1965)
535. Heskestad, G.: Hot-wire measurements in a radial turbulent jet. J. Appl. Mech. **33**, 417–424 (1966)
536. Hill Jr, W.G., Jenkins, R.C., Gilbert, B.L.: Effects on the initial boundary-layer state on turbulent jet mixing. AIAA J. **14**(11), 1513–1514 (1976)
537. Hussain, A.K.M.F., Zedan, M.F.: Effects of the inital condition on the axisymmetric free shear layer: effects of the initial momentum thickness. Phys. Fluids **21**(7), 1100–1112 (1978)
538. Hussain, A.K.M.F., Zedan, M.F.: Effects of the initial condition on the axisymmetric free shear layer: effect of the initial fluctuation level. Phys. Fluids **21**(9), 1475–1481 (1978)
539. Hussein, H.J., Capp, S.P., George, W.K.: Velocity measurements in a high-Reynolds-number, momentum-conserving, axisymmetric, turbulent jet. J. Fluid Mech. **258**, 31–75 (1994)
540. Islam, M.T., Ali, M.A.T.: Mean velocity and static pressure distributions of a circular jet. AIAA J. **35**(1), 196–197 (1997)
541. Keiderling, F., Kleiser, L., Bogey, C.: Numerical study of eigenmode forcing effects on jet flow development and noise generation mechanisms. Phys. Fluids **21**(045106), 1–22 (2009)
542. Lau, J.C.: Effects of exit Mach number and temperature on mean-flow and turbulence characteristics in round jets. J. Fluid Mech. **105**, 193–218 (1981)
543. Lau, J.C., Fisher, M.J., Fuchs, H.V.: The intrinsic structure of turbulent jets. J. Sound Vib. **22**(4), 379–406 (1972)

544. Lau, J.C., Morris, P.J., Fisher, M.J.: Measurements in subsonic and supersonic free jets using a laser velocimeter. J. Fluid Mech. **93**(1), 1–27 (1979). See also Lau et al. J. Fluid Mech. **102**, 353–366 (1979)
545. Laufer, J.: New trends in experimental turbulence research. Annu. Rev. Fluid Mech. **7**, 307–326 (1975)
546. Lighthill, M.J.: On sound generated aerodynamically - I. General theory. Proc. Roy. Soc. Lond. A **211**(1107), 564–587 (1952)
547. Lipari, G., Stansby, P.K.: Review of experimental data on incompressible turbulent round jets. Flow Turbul. Combust. **87**, 79–114 (2011)
548. Malmström, T.G., Kirkpatrick, A.T., Christensen, B., Knappmiller, K.D.: Centerline velocity decay measurements in low-velocity axisymmetric jets. J. Fluid Mech. **346**, 363–377 (1997)
549. Panchapakesan, N.R., Lumley, J.L.: Turbulence measurements in axisymmetric jets of air and helium. Part 1. Air jet. J. Fluid Mech. **246**, 197–223 (1993)
550. Powell, A.: On Prandtl's formulas for supersonic jet cell length. Int. J. Aeroacoustics **9**(1, 2), 207–236 (2010)
551. Ramaprian, B.R., Chandrasekhara, M.S.: LDA measurements in plane turbulent jets. J. Fluids Eng. **107**, 264–271 (1985)
552. Ricou, F.P., Spalding, D.B.: Measurements of entrainment by axisymmetrical turbulent jets. J. Fluid Mech. **11**, 21–32 (1961)
553. Sami, S.: Balance of turbulence energy in the region of jet-flow establishment. J. Fluid Mech. **29**(1), 81–92 (1967)
554. Seiner, J.M., Ponton, M.K., Jansen, B.J., Lagen, N.T.: The effects of temperature on supersonic jet noise emission. AIAA Paper 92–06-048 (1992)
555. Shiri, A., George, W.K., Naughton, J.W.: Experimental study of the far field of incompressible swirling jets. AIAA J. **46**(8), 2002–2009 (2008)
556. Stromberg, J.L., McLaughlin, D.K., Troutt, T.R.: Flow field and acoustic properties of a Mach number 0.9 jet at low Reynolds number. J. Sound Vib. **72**(2), 159–176 (1980)
557. Tailland, A., Mathieu, J.: Jet pariétal. Journal de Mécanique **6**(1), 103–131 (1967)
558. Tam, C.K.W.: Supersonic jet noise. Annu. Rev. Fluid Mech. **27**, 17–43 (1995)
559. Tam, C.K.W., Jackson, J.A., Seiner, J.M.: A multiple-scales model of the shock-cell structure of imperfectly expanded supersonic jets. J. Fluid Mech. **153**, 123–149 (1985)
560. Thomas, F.O., Goldschmidt, V.W.: Structural characteristics of a developing turbulent planar jet. J. Fluid Mech. **163**, 227–256 (1986)
561. Villermaux, E., Innocenti, C.: On the geometry of turbulent mixing. J. Fluid Mech. **393**, 123–147 (1999)
562. Villermaux, E., Rehab, H.: Mixing in coaxial jets. J. Fluid Mech. **425**, 161–185 (2000)
563. Witze, P.O.: Centerline velocity decay of compressible free jets. AIAA J. **12**(4), 417–418 (1974)
564. Witze, P.O., Dwyer, H.A.: The turbulent radial jet. J. Fluid Mech. **75**(3), 401–417 (1976)
565. Wygnanski, I., Fiedler, H.: Some measurements in the self-preserving jet. J. Fluid Mech. **38**(3), 577–612 (1969)
566. Zaman, K.B.M.Q.: Effect of initial condition on subsonic jet noise. AIAA J. **23**(9), 1370–1373 (1985)

Wakes and Detached Flows

567. Achenbach, E.: Distribution of local pressure and skin friction around a circular cylinder in cross-flow up to Re$= 5 \times 10^6$. J. Fluid Mech. **34**(4), 625–639 (1968)
568. Batham, J.P.: Pressure Distributions on circular cylinders at critical Reynolds numbers. J. Fluid Mech. **57**(2), 209–228 (1973)

569. Béra, J.C., Michard, M., Sunyach, M., Comte-Bellot, G.: Changing lift and drag by jet oscillation: experiments on a circular cylinder with turbulent separation. Eur. J. Mech. B - Fluids **19**, 575–595 (2000)
570. Blackburn, H.M., Henderson, R.D.: A study of two-dimensional flows Past an oscillating cylinder. J. Fluid Mech. **385**, 255–286 (1999)
571. Cannon, S.C.E., Glezer, A.: Observations of large-scale structures in wakes behind axisymmetric bodies. Exp. Fluids **14**, 447–450 (1993)
572. Carmody, T.: Establishment of the wake behind a disk. J. Basic Eng. **86**(4), ser. D, 869–882 (1964)
573. Chevray, R.: The turbulent wake of a body of revolution. J. Basic Eng. **90**(2), ser. D, 275–284 (1968)
574. Lamballais, E., Silvestrini, J., Laizet, S.: Direct numerical simulation of flow separation behind a rounded leading edge: study of curvature effects. Int. J. Heat Fluid Flow **31**, 295–306 (2010)
575. Mehta, J.M.: Self-preservation of turbulent wakes. AIAA J. **26**(1), 93–96 (1989)
576. Narasimha, R., Prabhu, A.: Equilibrium and relaxation in turbulent wakes. J. Fluid Mech. **54**, 1–17 (1972)
577. Naudascher, E.: Flow in the wake of self-propelled bodies and related sources of turbulence. J. Fluid Mech. **22**, 625–656 (1965)
578. Roshko, A.: Experiments on the flow past a cylinder at very high Reynolds number. J. Fluid Mech. **10**, 345–356 (1960)
579. Seifert, A., Bachart, T., Koss, G., Shepshelovitch, M., Wygnanski, I.: Oscillatory blowing: a tool to delay the boundary-layer separation. AIAA J. **31**(11), 2052–2060 (1993)
580. Sunyach, M., Ffowcs Williams, J.E.: Contrôle actif des oscillations dans les cavités excitées par des écoulements. C. R. Acad. Sci. Paris **303**(12), IIb, 1085–1088 (1986)
581. Tsinober, A.B., Shtern, A.G., Shcherbinin, E.V.: The influence of Re number on the position of the separation point of a boundary layer. J. Eng. Phys. Thermophys. **8**(1), 87–88 (1965)
582. Uberoi, M.S., Freymuth, P.: Turbulent energy balance and spectra of the axisymmetric wake. Phys. Fluids **13**(9), 2205–2210 (1970)
583. Williamson, C.H.K.: Vortex dynamics in the cylinder wake. Annu. Rev. Fluid Mech. **28**, 477–539 (1996)
584. Wygnanski, I., Champagne, F., Marasli, B.: On the large-scale structures in two-dimensional, small deficit, turbulent wakes. J. Fluid Mech. **168**, 31–71 (1986)

Wall-Bounded Flows

585. Adrian, R.J.: Hairpin vortex organization in wall turbulence. Phys. Fluids **19**(041301), 1–16 (2007)
586. Adrian, R.J., Meinhart, C.D., Tomkins, C.D.: Vortex organization in the outer region of the turbulent boundary layer. J. Fluid Mech. **422**, 1–54 (2000)
587. Andreopoulos, J., Durst, F., Zaric, Z., Jovanovic, J.: Influence of Reynolds number on characteristics of turbulent wall boundary layers. Exp. Fluids **2**, 7–16 (1984)
588. Antonia, R.A., Kim, J.: Low-Reynolds-number effects on near wall turbulence. J. Fluid Mech. **276**, 61–80 (1994)
589. Antonia, R.A., Teitel, M., Kim, J., Browne, L.W.B.: Low Reynolds number effects in a fully developed turbulent channel flows. J. Fluid Mech. **236**, 579–605 (1992)
590. Bandyopadhyay, P.: Large structure with a characteristic upstream interface in turbulent boundary layer. Phys. Fluids **23**, 2326–2327 (1980)
591. Barenblatt, G.I.: Scaling Laws for fully developed turbulent shear flows. Part 1. Basic hypotheses and analysis, Part 2. Processing of experimental data. J. Fluid Mech. **248**, 513–529 (1993)

592. Boussinesq, J.: Essai sur la théorie des eaux courantes. In: Mémoires présentés par divers savants, Acad. Sci. Paris **23**, 1–680 (1877)
593. Bradshaw, P., Perot, J.B.: A note on turbulent energy dissipation in the viscous wall region. Phys. Fluids A **5**(12), 3305–3306 (1993)
594. Buschmann, M.H., Gad-el-Hak, M.: Debate concerning the mean-velocity profile of a turbulent boundary layer. AIAA J. **41**(4), 565–572 (2003)
595. Cantwell, B., Coles, D., Dimotakis, P.: Structure and entrainment in the plane of symmetry of a turbulent spot. J. Fluid Mech. **87**(4), 641–672 (1978)
596. Chauhan, K.A., Monkewitz, P.A., Nagib, H.M.: Criteria for assessing experiments in zero pressure gradient boundary layers. Fluid Dyn. Res. **41**, 1–23 (2009)
597. Chen, C.-H.P., Blackwelder, R.F.: Large-scale motion in a turbulent boundary layer: a study using temperature contamination. J. Fluid Mech. **89**(1), 1–31 (1978)
598. Choi, H., Moin, P.: On the space-time characteristics of wall-pressure fluctuations. Phys. Fluids A **2**(8), 1450–1460 (1990)
599. Christensen, K.T., Adrian, R.J.: Statistical evidence of hairpin vortex packets in wall turbulence. J. Fluid Mech. **431**, 433–443 (2001)
600. Clauser, F.H.: Turbulent boundary layers in adverse pressure gradients. J. Aero. Sci. **21**, 91–108 (1954)
601. Coles, D.: Measusrements in the boundary layer of a smooth flat plate in a supersonic flow. Ph.D. Thesis, California Institute of Technology (1953)
602. Coles, D.: The law of the wake in the turbulent boundary layer. J. Fluid Mech. **1**(2), 191–226 (1956)
603. Comte-Bellot, G.: Coefficients de dissymétrie et d'aplatissement, spectres et corrélations en turbulence de conduite. J. de Mécanique **2**(2), 105–128 (1963)
604. Comte-Bellot, G.: Écoulement turbulent entre deux plaques planes parallèles. Publications scientifiques et techniques du ministère de l'Air, Paris, PST-419 (1965). See also: Bradshaw, P., (ed.): Turbulent flow between two parallel walls. Aeronautical Research Council 31609, FM 4102 (1969)
605. De Graaff, D.B., Eaton, J.K.: Reynolds-number scaling of the flat-plate turbulent boundary layer. J. Fluid Mech. **422**, 319–346 (2000)
606. Dixit, S.A., Ramesh, O.N.: Pressure-gradient-dependent logarithmic laws in sink flow turbulent boundary layers. J. Fluid Mech. **615**, 445–475 (2008)
607. Dol, H.S., Hanjalic, K., Versteegh, T.A.M.: A DNS-based thermal second-moment closure for buoyant convection at vertical walls. J. Fluid Mech. **391**, 211–247 (1999)
608. Dussauge, J.P., Smith, R.W., Smits, A.J., Fernholz, H., Finley, P.J., Spina, E.F: Turbulent boundary layers in subsonic and supersonic flows. Saric, W.S., (ed.): AGARDograph, AG-335 (1996)
609. Eggels, J.G.M., Unger, F., Weiss, M.H., Westerweel, J., Adrian, R.J., Friedrich, R., Nieuwstadt, F.T.M.: Fully developed turbulent pipe flow: a comparison between direct numerical simulation and experiment. J. Fluid Mech. **268**, 175–209 (1994)
610. Falkner, V.M., Skan, W.: Some approximate solutions of the boundary layer equations. Phil. Mag. **12**(7), 865–896 (1931)
611. Farabee, T.M., Casarella, M.J.: Spectral features of wall pressure fluctuations beneath turbulent boundary layers. Phys. Fluids A **3**(10), 2410–2420 (1991)
612. Favre, A.J.: Review of space-time correlations in turbulent fluids. J. Appl. Mech. **32**, 241–257 (1965)
613. Favre, A.J., Gaviglio, J.J., Dumas, R.J.: Further space-time correlations of velocity in a turbulent boundary layer. J. Fluid Mech. **3**(4), 344–356 (1958)
614. Gad-el-Hak, M., Bandyopadhyay, P.R.: Reynolds number effects in wall-bounded flows. Appl. Mech. Rev. **47**(8), 307–365 (1994)
615. George, W.K.: Recent advancements toward the understanding of turbulent boundary layers. AIAA J. **44**(11), 2435–2449 (2006)
616. Grant, H.L.: The large eddies of turbulent motion. J. Fluid Mech. **4**(2), 149–190 (1958)

617. Grek, G.R., Kozlov, V.V., Titarenko, S.V.: An experimental study of the influence of riblets on transition. J. Fluid Mech. **315**, 31–49 (1996)
618. Hanjalić, K., Launder, B.E.: Fully developed asymmetric flow in a channel. J. Fluid Mech. **51**(2), 301–335 (1972)
619. Head, M.R., Bandyopadhyay, P.: New aspects of turbulent boundary-layer structure. J. Fluid Mech. **107**, 297–338 (1981)
620. Hof, B., Juel, A., Mullin, T.: Scaling of the turbulence transition threshold in a pipe. Phys. Rev. Lett. **91**(24), 244502, 1–4 (2003)
621. Hoyas, S., Jiménez, J.: Scaling of the velocity fluctuations in turbulent channels up to $\mathrm{Re}_\tau = 2003$. Phys. Fluids **18**(011702), 1–4 (2006)
622. Hoyas, S., Jiménez, J.: Reynolds number effects on the Reynolds-stress budgets in turbulent channels. Phys. Fluids **20**(101511), 1–8 (2008)
623. Huang, P.G., Coleman, G.N., Bradshaw, P.: Compressible turbulent channel flows: DNS results and modelling. J. Fluid Mech. **305**, 185–218 (1995)
624. Jiménez, J., Pinelli, A.: The autonomous cycle of near-wall turbulence. J. Fluid Mech. **389**, 335–359 (1999)
625. Johansson, A.V., Alfredsson, P.H.: On the structure of turbulent channel flows. J. Fluid Mech. **122**, 295–314 (1982)
626. Josserand, M.A., Lauchle, G.C.: Modeling the wavevector-frequency spectrum of boundary-layer wall pressure during transition on a flat plate. J. Vib. Acoust. **112**, 523–534 (1990)
627. Khoo, B.C., Chew, Y.T., Teo, C.J.: On near-wall hot-wire measurements. Exp. Fluids **29**, 448–460 (2000)
628. Kim, J., Moin, P.: Application of a fractional-step method to incompressible Navier-Stokes equations. J. Comput. Phys. **59**, 308–323 (1985)
629. Kim, J., Moin, P., Moser, R.: Turbulence Statistics in fully developed channel flow at low Reynolds number. J. Fluid Mech. **177**, 133–166 (1987)
630. Kim, H.T., Kline, S.J., Reynolds, W.C.: The production of turbulence near a smooth wall in a turbulent boundary layer. J. Fluid Mech. **50**(1), 133–160 (1971)
631. Klebanoff, P.S.: Characteristics of turbulence in a boundary-layer with zero pressure gradient. NACA Report 1247 (1955). Formerly NACA TN 3178 (1954)
632. Klebanoff, P.S., Diehl, F.W.: Some features of artificially thickened fully developed turbulent boundary layers with zero pressure gradient. NACA TR 1110 (1952)
633. Kline, S.J., Reynolds, W.C., Schraub, F.A., Runstadler, P.W.: The structure of turbulent boundary layers. J. Fluid Mech. **30**(4), 741–773 (1967)
634. Kovasznay, L.S.G., Kibens, V., Blackwelder, R.F.: Large-scale motion in the intermittent region of a turbulent boundary layer. J. Fluid Mech. **41**, 283–325 (1970)
635. Laadhari, F.: Reynolds number effect in the dissipation function in wall-bounded flows. Phys. Fluids **19**(038101), 1–4 (2007)
636. Laufer, J.: Investigation of turbulent flow in a two-dimensional channel. NACA TR 1053 (1951)
637. Laufer, J.: The structure of turbulence in fully developed pipe flow. NACA T.R. 1174 (1954)
638. Le, H., Moin, P., Kim, J.: Direct numerical simulation of turbulent flow over a backward-facing step. J. Fluid Mech. **330**, 349–374 (1997)
639. Lin, J., Laval, J.P., Foucaut, J.M., Stanislas, M.: Quantitative characterization of coherent structures in the buffer layer of near-wall turbulence. Part 1: streaks. Exp. Fluids **45**, 999–1013 (2008)
640. Mansour, N.N., Kim, J., Moin, P.: Reynolds-stress and dissipation-rate budgets in a turbulent channel flow. J. Fluid Mech. **194**, 15–44 (1988)
641. Moin, P., Kim, J.: The structure of the vorticity field in turbulent channel flow. Part 1. Analysis of instantaneous fields and statistical correlations. J. Fluid Mech. **155**, 441–464 (1985)
642. Moser, R.D., Kim, J., Mansour, N.N.: Direct numerical simulation of turbulent channel flow up to $\mathrm{Re}_\tau = 590$. Phys. Fluids **11**(4), 943–945 (1999)
643. Marquillie, M., Ehrenstein, U., Laval, J.-P.: Instability of streaks in wall turbulence with adverse pressure gradient. J. Fluid Mech. **681**, 205–240 (2011)

644. Marusic, I., McKeon, B.J., Monkewitz, P.A., Nagib, H.M., Smits, A.J., Sreenivasan, K.R.: Wall-bounded turbulent flows at high Reynolds numbers: recent advances and key issues. Phys. Fluids **22**(065103), 1–24 (2010)
645. McKeon, B.J., Swanson, C.J., Zagarola, M.V., Donnelly, R.J., Smits, A.J.: Friction factors for smooth pipe flow. J. Fluid Mech. **511**, 41–44 (2004)
646. Mellor, G.L., Gibson, D.M.: Equilibrium turbulent boundary layers. J. Fluid Mech. **24**, 225–253 (1966)
647. Mullin, T.: Experimental studies of transition to turbulence in a pipe. Annu. Rev. Fluid Mech. **43**, 1–24 (2011)
648. Na, Y., Moin, P.: The structure of wall-pressure fluctuations in turbulent boundary layers with adverse pressure gradient and separation. J. Fluid Mech. **377**, 347–373 (1998)
649. Na, Y., Moin, P.: Direct numerical simulation of a separated turbulent boundary layer. J. Fluid Mech. **374**, 379–405 (1998)
650. Nagib, H.M., Chauhan, K.A., Monkewitz, P.E.: Approach to an asymptotic state for zero pressure gradient turbulent boundary layers. Phil. Trans. R. Soc. A. **365**, 755–770 (2007)
651. Nagib, H.M., Chauhan, K.A.: Variations of von Kármán coefficient in canonical flows. Phys. Fluids **20**(101518), 1–10 (2008)
652. Örlü, R., Schlatter, P.: On the fluctuating wall-shear stress in zero pressure-gradient turbulent boundary layer flows. Phys. Fluids **23**(021704), 1–4 (2011)
653. Örlü, R., Schlatter, P.: Comparison of experiments and simulations for zero pressure gradient turbulent boundary layers at moderate Reynolds numbers. Exp. Fluids **54**(1547), 1–21 (2013)
654. Österlund, J.M.: Experimental studies of zero-pressure-gradient turbulent boundary-layer flow. Ph.D. Thesis, Department of Mechanics, Royal Institute of Technology, Stockholm (1999)
655. Österlund, J.M., Johansson, A.V., Nagib, H.M., Hites, M.H.: A note on the overlap region in turbulent boundary layers. Phys. Fluids **12**(1), 1–4 (2000)
656. Panton, R.L.: Scaling turbulent wall layers. J. Fluids Eng. **112**, 425–432 (1990)
657. Panton, R.L.: A Reynolds stress function for wall layers. J. Fluids Eng. **119**, 325–330 (1997)
658. Panton, R.L.: Overview of the self-sustaining mechanisms of wall turbulence. Prog. Aerosp. Sci. **37**, 341–383 (2001)
659. Prandtl, L.: Recent results of turbulence research. NACA Technical Memorendum 720 (1933)
660. Procaccia, I., Sreenivasan, K.R.: The state of art in hydrodynamics turbulence: past successes and future challenges. Physica D. **237**, 2167–2183 (2008)
661. Rai, M.M., Moin, P.: Direct numerical simulation of transition and turbulence in a spatially evolving boundary layer. J. Comput. Phys. **109**, 169–192 (1993)
662. Reynolds, O.: An experimental investigation of the circumstances which determine whether the motion of water shall be direct or sinuous, and of the law of resistance in parallel channels. Phil. Trans. Roy. Soc. Lond. **174**, 935–982 (1883)
663. Reynolds, O.: On the dynamical theory of incompressible viscous fluid and the determination of the criterion. Phil. Trans. Roy. Soc. Lond. **186**, 123–164 (1885)
664. Robinson, S.K.: Coherent motions in the turbulent boundary layer. Annu. Rev. Fluid Mech. **23**, 601–639 (1991)
665. Rott, N.: Note on the history of the Reynolds number. Annu. Rev. Fluid Mech. **22**, 1–11 (1990)
666. Rotta, J.: On the theory of turbulent boundary layer. NACA TM 1344 (1953)
667. Sabot, J., Comte-Bellot, G.: Intermittency of coherent structures in the core region of fully developed turbulent pipe flow. J. Fluid Mech. **74**, 767–796 (1976)
668. Saddoughi, S.G.: Local isotropy in complex turbulent boundary layers at high Reynolds number. J. Fluid Mech. **348**, 201–245 (1997)
669. Saddoughi, S.G., Veeravalli, S.V.: Local isotropy in turbulent boundary layers at high Reynolds number. J. Fluid Mech. **268**, 333–372 (1994)
670. Schloemer, H.H.: Effects of pressure gradient on turbulent-boundary-layer wall-pressure fluctuations. J. Acoust. Soc. Am. **42**(1), 93–113 (1967)
671. Shaikh, F.N.: Investigation of transition to turbulence using white-noise excitation and local analysis techniques. J. Fluid Mech. **348**, 29–83 (1997)

672. Skåre, P.E., Krogstad, P.-A.: A turbulent equilibrium boundary layer near separation. J. Fluid Mech. **272**, 319–348 (1994)
673. Skote, M., Hennigson, D.S., Henkes, R.A.W.M.: Direct numerical simulation of self-similar turbulent boundary layers in adverse pressure gradients. Flow Turbul. Combust. **60**, 47–85 (1998)
674. Smith, C.R., Metzier, S.P.: The characteristics of low-speed streaks in the near-wall region of a turbulent boundary layer. J. Fluid Mech. **129**, 27–54 (1983)
675. Smits, A.J., McKeon, B.J., Marusic, I.: High-Reynolds number wall turbulence. Annu. Rev. Fluid Mech. **43**, 353–375 (2011)
676. Spalart, P.R.: Direct simulation of a turbulent boundary layer up to $R_\theta = 1410$. J. Fluid Mech. **187**, 61–98 (1988)
677. Spalart, P.R.: Theoretical and numerical study of a three-dimensional turbulent boundary layer. J. Fluid Mech. **205**, 319–340 (1989)
678. Spalart, P.R., Watmuff, J.H.: Experimental and numerical study of a turbulent boundary layer with pressure. J. Fluid Mech. **249**, 337–371 (1993)
679. Stratford, B.S.: The prediction of separation of the turbulent boundary layer. J. Fluid Mech. **5**, 1–16 (1959)
680. Stratford, B.S.: An experimental flow with zero skin friction throughout its region of pressure rise. J. Fluid Mech. **5**, 17–35 (1959)
681. Tardu, S.F.: Characteristics of single and multiple bursting events in the inner layer. Part 1: vita events. Exp. Fluids **20**, 112–124 (1995)
682. Tardu, S.F.: Characteristics of single and multiple bursting events in the inner layer. Part 2: level-crossing events. Exp. Fluids **33**, 640–652 (1995)
683. Tardu, S.F.: Stochastic synchronization of the near wall turbulence. Phys. Fluids **20**(045105), 1–8 (2008)
684. Townsend, A.A.: The structure of turbulent shear flows. Cambridge University Press, Cambridge (1980)
685. Tritton, D.J.: Some new correlation measurements in a turbulent boundary layer. J. Fluid Mech. **28**(3), 439–462 (1967)
686. Wallace, J.M., Eckelmann, H., Brodkey, R.S.: The wall region in turbulent shear flow. J. Fluid Mech. **54**(1), 39–48 (1972)
687. Wei, T., Willmarth, W.W.: Reynolds-number effects on the structure of a turbulent channel flows. J. Fluid Mech. **204**, 57–95 (1989)
688. Wosnik, M., Castillo, L., George, W.K.: A theory for turbulent pipe and channel flows. J. Fluid Mech. **421**, 115–145 (2000)
689. Zagarola, M.V., Smits, A.J.: Mean-flow scaling of turbulent pipe flow. J. Fluid Mech. **373**, 33–79 (1998)
690. Zhang, Y.-S., Bi, W.-T., Hussain, F., She, Z.-S.: A generalized Reynolds analogy for compressible wall-bounded turbulent flows. J. Fluid Mech. **739**, 392–420 (2014)
691. Zhou, J., Adrian, R.J., Balachandar, S., Kendall, T.M.: Mechanisms for generating coherent packets of hairpin vortices in channel flows. J. Fluid Mech. **387**, 353–396 (1999)

Experimental Methods

Hot-Wire Anenometry

692. Adrian, R.J., Johnson, R.E., Jones, B.G., Merati, P., Tung, A.T.C.: Aerodynamic disturbances of hot wire probes and directional sensitivity. J. Phys. E: Sci. Instrum. **17**, 62–71 (1984)
693. Barre, S., Dupont, P., Dussauge, J.P.: Hot-wire measurements in turbulent Transonic flows. Eur. J. Mech. B/ Fluids **11**, 439–454 (1992)

694. Bellhouse, B.J., Schultz, D.L.: The measurement of fluctuating skin friction in air with heated thin-film gauges. J. Fluid Mech. **32**, 675–680 (1968)
695. Berson, A., Blanc-Benon, P.h., Comte-Bellot, G.: A strategy to eliminate all nonlinear effects in constant-voltage hot-wire anemometry. Rev. Sci. Instrum. **80**(045102), 1–7 (2009)
696. Berson, A., Poignand, G., Blanc-Benon, P.H., Comte-Bellot, G.: Capture of instantaneous temperature in oscillating flows: use of constant-voltage anemometry to correct the thermal lag of cold wires operated by constant-current anemometry. Rev. Sci. Instrum. **81**(015102), 1–8 (2010)
697. Berson, A., Blanc-Benon, P.H., Comte-Bellot, G.: On the use of hot-wire anemometry in pulsating flows. A comment on "A critical review on advanced velocity measurement techniques in pulsating flows". Meas. Sci. Technol. **21**(128001), 1–5 (2010)
698. Browne, L.W.B., Antonia, R.A., Chua, L.P.: Calibration of X-probes for turbulent flow measurements. Exp. Fluids **7**, 201–208 (1989)
699. Bruun, H.H.: Hot-wire anemometry, principles and signal analysis. Oxford University Press, Oxford (1995)
700. Champagne, F.H., Sleicher, C.A., Wehrmann, O.H.: Turbulence measurements with inclined hot-wires Part 1. Heat transfer experiments with inclined hot-wire. J. Fluid Mech. **28**(1), 153–175 (1967)
701. Comte-Bellot, G.: Hot-wire anemometry. Annu. Rev. Fluid Mech. **8**, 209–231 (1976)
702. Comte-Bellot, G.: Hot-wire and hot-film anemometers. In: Richards, B.E. (ed.) Measurement of Unsteady Fluid dynamic Phenomena, pp. 123–162. Hemisphere Publ. Corp., Washington DC, (1977)
703. Comte-Bellot, G.: Hot-wire anemometry. In: Johnson, R.W. (ed.) Handbook of Fluid Dynamics, pp. 1–29. CRC Press, Boca Raton, Florida, chap. 34, (1998)
704. Comte-Bellot, G.: Thermal anemometry. In: reference, [27] section 5.2.1, 229–283 and section 5.2.7, 446–456 (2007)
705. Comte-Bellot, G., Weiss, J., Béra, J.C.: Lead-resistance effects in a constant voltage anemometer. Rev. Sci. Instrum. **75**(6), 2075–2081 (2004)
706. Comte-Bellot, G., Sarma, G.R.: Constant voltage anemometer: practice in supersonic flows. AIAA J. **39**(2), 261–270 (2001)
707. Comte-Bellot, G., Schon, J.P.: Harmoniques créés par excitation paramétrique dans les anémomètres à fil chaud à intensité constante. Int. J. Heat Mass Transf. **12**, 1661–1677 (1969)
708. Corrsin, S.: Extended application of the hot wire anemometer. Rev. Sci. Instrum. **18**, 469–471 (1947)
709. Corrsin, S.: Turbulence: Experimental methods. In: Flugge, S. (ed.) Handbuch der Physik/Encyclopedia of Physics, 8(2), pp. 524–590. Springer-Verlag, Berlin (1963)
710. Dryden, H.L., Kuethe, A.M.: The measurement of fluctuations of air speed by the hot-wire anemometer, NACA TR 320 (1929)
711. Fingerson, L.M.: Thermal anemometry, current state, and future directions. Rev. Sci. Instrum. **65**, 285–300 (1994)
712. Freymuth, P.: Noise in hot-wire anemometers. Rev. Sci. Instrum. **39**, 550–557 (1968)
713. Freymuth, P.: Frequency response and electronic testing for constant-temperature hot-wire anemommeters. J. Phys. E: Sci. Instrum. **10**, 705–710 (1977)
714. Freymuth, P.: Further investigation of the nonlinear theory for constant-temperature anemometers. J. Phys. E: Sci. Instrum. **10**, 710–713 (1977)
715. Freymuth, P.: Hot-wire anemometry at very high frequencies: effect of electronic noise. Meas. Sci. Technol. **8**, 115–116 (1997)
716. Freymuth, P.: Interpretations in the control theory of thermal anemometers. Meas. Sci. Technol. **8**, 174–177 (1997)
717. Freymuth, P.: On higher order dynamics of constant-temperature hot-wire anemometers. Meas. Sci. Technol. **9**, 534–535 (1998)
718. Freymuth, P., Fingerson, L.M.: Second or third order control theory for constant-temperature hot-wire anemometers? Exp. Fluids **23**, 175–176 (1997)

719. Gaviglio, J.: Reynolds analogies and experimental study of heat transfer in the supersonic boundary layer. Int. J. Heat Mass Transf. **30**(5), 911–926 (1987)
720. Haritonidis, J.H.: The measurement of wall shear stress. Adv. Fluid Mech. Measur. **45**, 229–261 (1989)
721. Hubbard, P.G.: Operating manual for the Iowa Institute of Hydraulics Research hot-wire and hot-film anemometers. Stud. Eng. Bull. **37** (1957)
722. King, L.V.: On the convection of heat from small cylinders in a stream of fluid. Phil. Trans. Roy. Soc. Lon. A **214**, 373–432 (1914)
723. Kovasznay, L.S.G.: The hot-wire anemometer in supersonic flows, J. Aero. Sci. **17**, 565–572, cont'd 584 (1950)
724. Kovasznay, L.S.G.: Turbulence in supersonic flows. J. Aero. Sci. **20**, 657–675 (1953)
725. Lemay, J., Benaissa, A., Antonia, R.A.: Correction of cold-wire response for mean temperature dissipation rate measurements. Exp. Thermal Fluid Sci. **27**, 133–143 (2003)
726. Li, J.D.: Dynamic response of constant-temperature hot-wire systems in turbulence velocity measurements. Meas. Sci. Technol. **15**, 1835–1847 (2004)
727. Ligrani, P.M., Bradshaw, P.: Spatial resolution and measurement of turbulence in the viscous sublayer using miniature hot-wire probes. Exp. Fluids **5**, 407–417 (1987)
728. Ling, S.C., Hubbard, P.G.: The hot-films anemometers. A new device for fluid mechanics research. J. Aero. Sci. **23**, 890–891 (1956)
729. Lueptow, R.M., Breuer, K.S., Haritonidis, J.H.: Computer-aided calibration of X-probes using a look-up table. Exp. Fluids **6**, 115–118 (1988)
730. Mangalam, S.M., Sarma, G.R., Kuppa, S., Kubendran, L.R.: A new approach to high-speed flows measurements using constant voltage hot film anemometry. AIAA Paper 92–3957 (1992)
731. Moes, T.R., Sarma, G.R., Mangalam, S.M.: Flight demonstration of a shock location sensor using constant voltage anemometry. NASA TM-4806 (1997)
732. Morkovin, M.V.: Fluctuations and hot-wire anemometry in compressible flows. AGARDograph **24** (1956)
733. Norris, J.D., Chokani, N.: Rapid scanning of overheat ratios using a constant voltage anemometer. AIAA J. **41**(8), 1619–1621 (2003)
734. Ossofsky, E.: Constant temperature Operation of the hot-wire anemometer at high frequency. Rev. Sci. Instrum. **19**(12), 881–889 (1948)
735. Perry, A.E.: Hot-wire anemometry. Clarendon Press, Oxford (1982)
736. Sarma, G.R.: Transfer function analysis of the constant voltage anemometer. Rev. Sci. Instrum. **69**, 2385–2391 (1998)
737. Sarma, G.R., Comte-Bellot, G.: Automated constant voltage anemometer for measurements with fluid temperature drifts. Rev. Sci. Instrum. **73**(3), 1313–1317 (2002)
738. Sarma, G.R., Moes, J.R.: Demonstration of skin friction measurements featuring in situ estimation of conduction loss using constant voltage anemometers and surface hot-films. Rev. Sci. Instrum. **76**(5), 55102, 1–6 (2005)
739. Sarma, G.R., Comte-Bellot, G., Faure, T.: Software corrected hot wire thermal lag for the constant voltage anemometer featuring a constant bandwith at the selected compensation setting. Rev. Sci. Instrum. **69**, 3223–3231 (1998)
740. Spina, E.F., McGinley, C.B.: Constant-temperature anemometry in critical issues and sample results. Exp. Fluids **17**, 365–374 (1994)
741. Truzzi, G.E., Sarma, G.R., Chokani, N.: Constant voltage anemometer operated hot wire at subsonic speeds over wide overheats in unsteady flows. Rev. Sci. Instrum. **73**(12), 4363–4368 (2002)
742. van Dijk, A., Nieuwstadt, F.T.M.: The calibration of (multi-) hot-wire probes. 2. Velocity-calibration. Exp. Fluids **36**, 550–564 (2004)
743. Wallace, J.M., Foss, J.F.: The measurement of vorticity in turbulent flows. Annu. Rev. Fluid Mech. **27**, 469–514 (1995)
744. Watmuff, J.H.: An investigation of the constant-temperature hot-wire anemometer. Exp. Therm. Fluid Sci. **11**, 117–134 (1995)

745. Weske, J.R.: A hot-wire circuit with very small thermal lag, NACA TN 881 (1943)
746. Weiss, J., Knauss, H., Wagner, S.: Method for the determonation of frequency response and signal to noise ratio for constant-temperature hot-wire anemometers. Rev. Sci. Instrum. **72**(3), 1904–1909 (2001)
747. Weiss, J., Comte-Bellot, G.: Electronic noise in a constant voltage anemometer. Rev. Sci. Instrum. **75**(5), 1290–1296 (2004)
748. Weiss, J., Chokani, N., Comte-Bellot, G.: Constant-temperature and constant-voltage anemometer use in a Mach 2.5 flow. AIAA J. **43**(5), 1140–1143 (2005)
749. Weiss, J., Berson, A., Comte-Bellot, G.: Investigation of nonlinear effects in constant-temperature anemometers. Meas. Sci. Technol. **24**(085302), 1–8 (2013)
750. Wyngaard, J.C: Measurement of small-scale turbulence structure with hot-wires. J. Sci. Instrum, J. Phys. E, series 2, 1, 1105–1108 (1968)

Laser Doppler Anemometry

751. Adrian, R.J., Yao, C.S.: Power spectra of fluid velocities measured by laser Doppler velocimetry. Exp. Fluids **5**, 17–28 (1987)
752. André, B., Castelain, T., Bailly, C.: Experimental exploration of underexpanded supersonic jets. Shock Waves **24**, 21–32 (2014)
753. Boutier, A.: Introduction to laser velocimetry techniques, basic LDV—one component system, advanced systems—multicomponent systems, advanced and non-conventional systems, accuracy of laser Doppler velocimetry. von Kármán Institute, Rhode Saint Genèse, Lecture Series - Laser velocimetry (1991)
754. Boutier, A.: Métrologie optique en mécanique des fluides: un état de l'art en 1996. In: Trinité M. (ed.) 5ème congrès francophone de vélocimétrie laser, Rouen, 24–27 septembre, 1–11 (1996)
755. Buchhave, P., George Jr, W.K., Lumley, J.L.: The measurement of turbulence with the laser-Doppler anemometer. Annu. Rev. Fluid Mech. **11**, 443–504 (1979)
756. Dopheide, D., Strunck, V., Pfeifer, H.J.: Miniaturized multicomponent laser Doppler anemometers using high-frequency pulsed diodes lasers and new electronic signal acquisition systems. Exp. Fluids **9**, 309–316 (1990)
757. Drain, L.E.: The Laser Doppler Technique. Wiley (1980)
758. Fingerson, L.M., Menon, R.K.: Laser Doppler velocimetry. In: Johnson, R.W. (ed.) Handbook of Fluid Dynamics, CRC Press, Boca Raton, Florida, chap. 35, 1–18 (1998)
759. Hunter, W.W., Nichols, C.E.: Wind tunnel seeding systems for laser velocimeters, proceedings of workshop NASA Langley, March 19–20, NASA CP-2393 (1985)
760. Lehmann, B.: Geschwindigkeitsmessung mit laser-Doppler-anemometer verfahren. Wissenschaftliche Berichte AEG-Telefunken **41**, 141–145 (1968)
761. Maxwell, B.R., Seasholtz, R.G.: Velocity lag of solid particles in oscillating gases and in gases passing through normal shock waves, NASA Report TN D-7490 (1974)
762. Mazumder, M.K., Kirsch, K.J.: Flow tracing fidelity of scattering aerosol in laser Doppler velocimetry. Appl. Opt. **14**, 894–901 (1975)
763. Nobach, H., Müller, E., Tropea, C.: Efficient estimation of power spectral density from laser Doppler anemometer data. Exp. Fluids **14**, 499–509 (1998)
764. Simon, L., Fitzpatrick, J.: An improved sample-and-hold reconstruction procedure for estimation of power spectra from LDA data. Exp. Fluids **37**, 272–280 (2004)
765. Trolinger, J.D.: Laser applications in flow diagnostics. In: Ginoux, J.J. (ed.), AGARDograph No. 296 (1988)
766. Tropea, C.: Tracer particles. In: reference, [27] section 5.3.2, 287–296 (2007)
767. Tropea, C.: Laser Doppler anemometry: recent developments and future challenges. Meas. Sci. Technol. **6**, 605–619 (1995)

768. Tropea, C., Scarano, F., Westerweel, J.: Laser Doppler techniques. In: reference, [27] section 5.3.1, 296–309 (2007)
769. Velte, C.M., George, W.K., Buchhave, P.: Estimation of burst-mode LDA power spectra. Exp. Fluids **55**, 1674–1693 (2014)
770. vom Stein, H.D., Pfeifer, H.J.: A Doppler difference method for velocity measurements. Metrologia **5**, 59–61 (1969)
771. Yeh, Y., Cummins, H.Z.: Localized fluid flow measurements with an He-Ne laser spectrometer. Appl. Phys. Lett. **4**, 176–178 (1964)

Particle Image Velocimetry

772. Adrian, R.J.: Particule-Image techniques for experimental fluid mechanics. Annu. Rev. Fluid Mech. **23**, 261–304 (1991)
773. Adrian, R.J.: Dynamic ranges of velocity and spatial resolution of particle image velocimetry. Meas. Sci. Technol. **8**, 1393–1398 (1997)
774. Adrian, R.J.: Twenty years of particle image velocimetry. Exp. Fluids **39**, 159–169 (2005)
775. Béra, J.C., Michard, M., Grosjean, N., Comte-Bellot, G.: Flow analysis of two-dimensional pulsed jets by particle image velocimetry. Exp. Fluids **31**, 519–532 (2001)
776. Castelain, T., Sunyach, M., Juvé, D., Béra, J.-C.: Jet-noise reduction by impinging microjets: an acoustic investigation testing microjet parameters. AIAA J. **46**(5), 1081–1087 (2008)
777. Coudert, S.J.M., Schon, J.P.: Back-projection algorithm with misalignment corrections for 2D3C stereoscopic PIV. Meas. Sci. Technol. **12**, 1371–1381 (2001)
778. Hinsch, K.D.: Three-dimensional particle velocimetry. Meas. Sci. Technol. **6**, 742–753 (1995)
779. Host-Madsen, A., McCluskey, D.R.: On the accuracy and reliability of PIV measurements. 7th International Symposium Application of Laser Techniques to Fluid Mechanics, 11–14 July, Lisbon, Portugal (1994)
780. Keane, R.D., Adrian, R.J.: Optimisation of particle image velocimeters. Part II: multiple-pulsed system. Meas. Sci. Technol. **2**, 963–974 (1991)
781. Lawson, N.J., Wu, J.: Three-dimensional particle image velocimetry: experimental error analysis of a digital angular stereoscopic system. Meas. Sci. Technol. **8**, 1455 (1997)
782. Lynch, K., Scarano, F.: A high-order time-accurate interrogation method for time-resolved PIV. Meas. Sci. Technol. **24**(035305), 1–16 (2013)
783. Melling, A.: Tracer particles and seeding for particle image velocimetry. Meas. Sci. Technol. **8**, 1406–1416 (1997)
784. Prasad, A.K.: Stereoscopic particle image velocimetry. Exp. Fluids **29**, 103–116 (2000)
785. Prasad, A.K., Jensen, K.: Scheimpflug stereocamera for particle image velocimetry in liquid flows. Appl. Opt. **34**(30), 7092–7099 (1995)
786. Raffel, M., Willert, C.E., Kompenhans, J.: Particule Image Velocimetry—A Practical Guide. Springer, Berlin (1998)
787. Scarano, F.: Tomographic PIV: principles and practice. Meas. Sci. Technol. **24**(012001), 1–28 (2013)
788. Scarano, F., Westerweel, J.: Particle image velocimetry. In reference, [27] section 5.3.3, 309–362 (2007)
789. Schröder, A., Geisler, R., Staack, K., Elsinga, G.E., Scarano, F., Wieneke, B., Henning, A., Poelma, A., Westerweel, J.: Eulerian and Lagrangian views of a turbulent boundary layer flow using time-resolved tomographic PIV. Exp. Fluids **50**, 1071–1091 (2011)
790. Soloff, S.M., Adrian, R.J.: Liu Z-C: Distortion compensation for generalized stereoscopic particle image velocimetry. Meas. Sci. Technol. **8**, 1441–1454 (1997)
791. Stanislas, M., Monnier, J.C.: Practical aspects of image recording in particle image velocimetry. Meas. Sci. Technol. **8**, 1417–1426 (1997)

792. Wernet, M.P.: Temporally resolved PIV for space-time correlations in both cold and hot jet flows. Meas. Sci. Technol. **18**, 1387–1403 (2007)
793. Westerweel, J.: Fundamentals of digital particle image velocimetry. Meas. Sci. Technol. **8**, 1379–1392 (1997)
794. Westerweel, J., Elsinga, G.E., Adrian, R.J.: Particle image velocimetry for complex and turbulent flows. Annu. Rev. Fluid Mech. **45**, 409–436 (2013)
795. Westerweel, J., Draad, A.A., van der Hoeven, J.G.: Th, van Oord, J.: Measurements of fully-developed turbulent pipe flow with digital particle image velocimetry. Exp. Fluids **20**, 165–177 (1996)
796. Willert, C.: Stereoscopic digital particle image velocimetry for application in wind tunnel flows. Meas. Sci. Technol. **8**, 1465–1479 (1997)

Author Index

C. Bailly and G. Comte-Bellot, *Turbulence*, Experimental Fluid Mechanics,
DOI 10.1007/978-3-319-16160-0

Subject Index

C. Bailly and G. Comte-Bellot, *Turbulence*, Experimental Fluid Mechanics,
DOI 10.1007/978-3-319-16160-0